

**ANNALS OF THE UNIVERSITY OF CRAIOVA  
ANNALES DE L'UNIVERSITÉ DE CRAIOVA**

---

---

**ANALELE  
UNIVERSITĂȚII  
DIN CRAIOVA**

**SERIA: INGINERIE ELECTRICĂ  
SERIE: ELECTRICAL ENGINEERING  
SÉRIE: INGÉNIERIE ÉLECTRIQUE**

**Anul/Year/Année 40  
No. 40, Vol. 40, Issue 1, 2016**

**December 2016**

---

---

**ISSN 1842 - 4805**

**EDITURA UNIVERSITARIA**

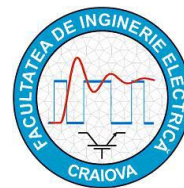
---

---

## ANNALS OF THE UNIVERSITY OF CRAIOVA



13, A.I. Cuza Str., CRAIOVA 200585  
ROMANIA



---

We exchange publications with similar  
institutions of country and from abroad

## ANNALES DE L'UNIVERSITÉ DE CRAIOVA

Rue A.I. Cuza, No. 13, CRAIOVA 200585  
ROUMANIE

---

On fait des échanges des publications avec les  
institutions similaires du pays et de l'étranger

---

---

This journal is published by the Faculty of Electrical Engineering from the University of Craiova.  
The authors are fully responsible for the originality of their papers and for accuracy of their notes.

*This volume has benefited by the financial support of the Association for Support of Engineering Education.*

### Editorial board

Prof.dr.ing. Ioan POPA editor in chief, Universitatea din Craiova, Romania  
Conf.dr.ing. Mircea DRIGHICIU - editor in chief, Universitatea din Craiova, Romania  
Prof.dr.ing. Dan MIHAI, Universitatea din Craiova, Romania  
Prof.dr.ing. Marian CIONTU, Universitatea din Craiova, Romania  
Prof.dr.ing. Sergiu IVANOV, Universitatea din Craiova, Romania  
Prof.dr.ing. Lucian MANDACHE, Universitatea din Craiova, Romania  
Prof.dr.sc. Ivan YACHEV, Universitatea tehnica din Sofia, Bulgaria  
Prof.dr.ing. Leszek CZARNECKI-Life Fellow IEEE, Louisiana State University, USA  
Prof.dr.ing. Slavoljub ALEKSIC, Universitatea din Nic, Serbia  
Prof.dr.ing. Sergey RYVKIN, Institutul Stintelor de control, V.I.Trapeznikov, Russia  
Prof.dr.ing. Mihai IORDACHE, Universitatea Politehnica Bucuresti, Romania  
Prof.dr.ing. Victor SONTEA, Universitatea Tehnica a Moldovei, Moldova  
Prof.dr.ing. Iuliu DELESEGA, Universitatea Politehnica din Timisoara, Romania  
Prof.dr.ing. Dumitru-Marcel ISTRATE, Universitatea Tehnica "Gh. Asachi", Iasi, Romania  
Prof.dr.ing. Miroslav PRSA, Universitatea din Novisad, Serbia  
Prof.dr.ing. Maria BROJBOIU, Universitatea din Craiova, Romania  
Prof.dr.ing. Mihai GAVRILAȘ, Universitatea Tehnica Gh.Asachi, Iasi, Romania  
Conf.dr.ing. Daniela DANCIU, Universitatea din Craiova, Romania  
Prof.dr.ing. Nicolae MUNTEAN, Universitatea Politehnica Timisoara, Romania  
Prof.dr.ing. Calin MUNTEANU, Universitatea Tehnica Cluj-Napoca, Romania  
Prof.dr.ing. Leonardo-Geo MĂNESCU, Universitatea din Craiova, Romania  
S.I.dr.ing. Ioana Gabriela SIRBU, Universitatea din Craiova, Romania

## REVIEWERS COMMITTEE

Lia-Elena ACIU - *Transilvania University of Brasov, Romania*  
Maricel ADAM – *"Gh. Asachi" Technical University of Iasi, Romania*  
Mihaela ALBU – *University "Politehnica" of Bucharest, Romania*  
Slavoljub ALEKSIC – *University of Nis, Serbia*  
Horia BALAN – *Technical University of Cluj-Napoca, Romania*  
Gheorghe BALUTA – *"Gh. Asachi" Technical University of Iasi, Romania*  
Alexandru BITOLEANU – *University of Craiova, Romania*  
Maria BROJBOIU – *University of Craiova, Romania*  
Aurel CAMPEANU – *University of Craiova, Romania*  
Emil CAZACU – *University "Politehnica" of Bucharest, Romania*  
Mihai CERNAT – *Transilvania University of Brasov, Romania*  
Marian CIONTU – *University of Craiova, Romania*  
Daniel Cristian CISMARU – *University of Craiova, Romania*  
Grigore CIVIDJIAN – *University of Craiova, Romania*  
Zlata CVETCOVIC – *University of Nis, Serbia*  
Leszek CZARNECKI - *Louisiana State University, USA*  
Daniela DANCIU – *University of Craiova, Romania*  
Sonia DEGERATU – *University of Craiova, Romania*  
Iuliu DELESEGA – *University "Politehnica" of Timisoara, Romania*  
Silvia-Maria DIGA – *University of Craiova, Romania*  
Peter DINEFF – *Technical University of Sofia, Bulgaria*  
Radu DOBRESCU – *University "Politehnica" of Bucharest, Romania*  
Mircea-Adrian DRIGHICIU – *University of Craiova, Romania*  
Laurentiu Marius DUMITRAN – *University "Politehnica" of Bucharest, Romania*  
Sorin ENACHE – *University of Craiova, Romania*  
Virgiliu FIRETEANU – *University "Politehnica" of Bucharest, Romania*  
Dan FLORICAU – *University "Politehnica" of Bucharest, Romania*  
Cristian FOSALAU – *"Gh. Asachi" Technical University of Iasi, Romania*  
Teodor Lucian GRIGORIE – *University of Craiova, Romania*  
Micea-Dan GUSA – *"Gh. Asachi" Technical University of Iasi, Romania*  
Stefan HARAGUS – *University "Politehnica" of Timisoara, Romania*  
Elena HELEREA – *Transilvania University of Brasov, Romania*  
Eugen HNATIUC – *"Gh. Asachi" Technical University of Iasi, Romania*  
Kemal HOT – *Polytechnic of Zagreb, Croatia*  
Eugen IANCU – *University of Craiova, Romania*  
Nathan IDA – *University of Akron, USA*  
Maria IOANNIDES – *National Technical University of Athens, Greece*  
Valentin IONITA – *University "Politehnica" of Bucharest, Romania*  
Mihai IORDACHE – *University "Politehnica" of Bucharest, Romania*  
Marcel ISTRATE – *"Gh. Asachi" Technical University of Iasi, Romania*  
Sergiu IVANOV – *University of Craiova, Romania*  
Virginia IVANOV – *University of Craiova, Romania*  
Wilhelm KAPPEL – *National Research and Development Institute for Electrical Engineering (ICPE – CA) Bucharest, Romania*  
Liviu KREINDLER – *University "Politehnica" of Bucharest, Romania*  
Gheorghe LIVINT – *"Gh. Asachi" Technical University of Iasi, Romania*  
Dumitru Dorin LUCHACHE – *"Gh. Asachi" Technical University of Iasi, Romania*

Lucian MANDACHE – *University of Craiova*, Romania  
Leonardo-Geo MANESCU – *University of Craiova*, Romania  
Gheorghe MANOLEA – *University of Craiova*, Romania  
Andrei MARINESCU – *Research, Development and Testing National Institute for Electrical Engineering Craiova (ICMET)*, Romania  
Iliana MARINOVA – *Technical University of Sofia*, Bulgaria  
Claudia MARTIS – *Technical University of Cluj-Napoca*, Romania  
Ernest MATAGNE – *Université Catholique de Louvain*, Belgium  
Dan MIHAI – *University of Craiova*, Romania  
Alexandru MOREGA – *University “Politehnica” of Bucharest*, Romania  
Mihaela MOREGA – *University “Politehnica” of Bucharest*, Romania  
Nazih MOUBAYED – *Lebanese University*, Lebanon  
Calin MUNTEANU – *Technical University of Cluj-Napoca*, Romania  
Florin MUNTEANU – *“Gh. Asachi” Technical University of Iasi*, Romania  
Valentin NAVRAPESCU – *University “Politehnica” of Bucharest*, Romania  
Mitica Iustinian NEACĂ – *University of Craiova*, Romania  
Ciprian NEMES – *“Gh. Asachi” Technical University of Iasi*, Romania  
Petre-Marian NICOLAE – *University of Craiova*, Romania  
Dragoș NICULAE - *University “Politehnica” of Bucharest*, Romania  
Petru NOTINGHER – *University “Politehnica” of Bucharest*, Romania  
Teodor PANA – *Technical University of Cluj-Napoca*, Romania  
Ioan POPA – *University of Craiova*, Romania  
Dan POPESCU – *University of Craiova*, Romania  
Daniela POPESCU – *University of Craiova*, Romania  
Mihaela POPESCU – *University of Craiova*, Romania  
Miroslav PRSA – *University of Novi-Sad*, Serbia  
Mircea M. RADULESCU – *Technical University of Cluj Napoca*, Romania  
Benoit ROBYNS – *Ecole des Hautes Etude d’Ingénieur de Lille*, France  
Constantin ROTARU – *Military Technical Academy*, Romania  
Alex RUDERMAN – *Elmo Motion Control Ltd*, USA  
Sergey RYVKIN – *Trapeznikov Institute of Control Sciences*, Russia  
Alexandru SALCEANU – *“Gh. Asachi” Technical University of Iasi*, Romania  
Cristina Gabriela SARACIN – *University “Politehnica” of Bucharest*, Romania  
Constantin SARMASANU – *“Gh. Asachi” Technical University of Iasi*, Romania  
Dan SELISTEANU – *University of Craiova*, Romania  
Victor SONTEA – *Technical University of Moldova*, Moldova  
Alexandru STANCU – *“A.I. Cuza” University of Iasi*, Romania  
Florian STEFANESCU – *University of Craiova*, Romania  
Viorel STOIAN – *University of Craiova*, Romania  
Ryszard STRZELECKI – *University of Technology Gdansk*, Poland  
Flavius-Dan SURIANU – *University “Politehnica” of Timisoara*, Romania  
Lorand SZABO – *Technical University of Cluj-Napoca*, Romania  
Radu-Adrian TIRNOVAN – *Technical University of Cluj-Napoca*, Romania  
Raina TZENEVA – *Technical University of Sofia*, Bulgaria  
Ioan VADAN – *Technical University of Cluj-Napoca*, Romania  
Viorel VARVARA – *“Gh. Asachi” Technical University of Iasi*, Romania  
Ion VLAD – *University of Craiova*, Romania  
Ivan YATCHEV – *Technical University of Sofia*, Bulgaria

This issue is dedicated to the 65<sup>th</sup> anniversary of  
Higher education in electrical engineering at Craiova  
and to the 40<sup>th</sup> year of uninterrupted apparition of the  
journal Annals of the University of Craova, Electrical  
Engineering series



## CONTENTS

Professor Aurel CAMPEANU at his 80 <sup>th</sup> anniversary .....	IX
Professor Grigore CIVIDJIAN at his 80 <sup>th</sup> anniversary .....	XI
<i>Comparison of the Conservative Power Theory (CPT) with Budeanu's Power Theory</i> – Leszek S. Czarnecki	1
<i>Modeling and Torque Ripple Control in Faulty SPMSM</i> – Elmehdi Bahri, Remus Pusca, Raphael Romary, Driss Belkhaty .....	9
<i>Digital Control for the Air Pressure with Multi-Characteristics Selection</i> – Dan Mihai .....	17
<i>Study of the Reactive Power Side Effects for Tariff and Compensation Purpose at the Transmission Networks'Users</i> – Leonardo Geo Mănescu, Denisa Ruşinaru, Marian Ciontu, Cosmin Buzatu, Eugen Butoarcă, Miron Alba .....	25
<i>Evaluating RMS of Linearly Variable Magnitude Waveforms by Using FFT and WPT. Theory and Practice</i> – Ileana-Diana Nicolae, Petre-Marian Nicolae, Diana Cristina Maria, Scărlătescu Lucian .....	33
<i>On the Implementation of FBD-Theory Concepts in the Control of Active DC-Traction Substations</i> – Mihaela Popescu, Alexandru Bitoleanu, Mircea Dobriceanu .....	39
<i>New Aspects on the Frequency Splitting and Bifurcation Phenomena in Wireless Power Transfer Systems</i> – Mihai Iordache, Andrei Marinescu, Ioana-Gabriela Sîrbu, Lucian Mandache, Dragoş Niculae, Lavinia Iordache.....	46
<i>Power Control and Energetic Performances of an Induction Heating System Destined for Drying of Current Transformers</i> – Alexandru Bitoleanu, Mihaela Popescu, Dinu Roxan Doboşeriu .....	54
<i>Some Considerations Concerning Radiated Emissions Produced by a Board Display</i> – Petre-Marian Nicolae, Ileana-Diana Nicolae, Relu-Adrian Aipu .....	60
<i>Development of a Barrier Structure Actuated by Three Shape Memory Alloy Springs</i> – Sonia Degeratu, Costel Cărămidă, Laurenţiu Alboteanu, Irina Boncea, Daniela Coman, Monica S. Stăicuş, Gabriela Tont ....	66
<i>Energetic Analysis of the Drying Process of Current Transformers from 110 kV Ciungetu Power Station</i> – Dinu Roxan Doboşeriu, Alexandru Bitoleanu, Mihaela Popescu .....	74
<i>Improving the Power Quality and Controllability of PV Power Plants for Microgrids Integration</i> – Luminiţa Barote, Corneliu Marinescu, Ioan Şerban, Daniel Munteanu .....	80
<i>Simulation and Implementation of Sensorless Control Using Estimators in Electric Drives with High Dynamic</i> – Marcel Nicola, Dumitru Sacerdoţianu, Adrian Hurezeanu .....	86
<i>Monitoring and Analysis of the Electrical Parameters for an Industrial Consumer using LabVIEW Environment</i> – Claudiu-Ionel Nicola, Viorica Voicu, Sebastian Popescu, Maria Cristina Niţu, Daniela Iovan, Marian Duţă, Alin Benea, Silviu Andreescu .....	94
<i>Modeling and Simulation of the Coal Flow Control System for the Longwall Scraper Conveyor</i> – Olimpiu Stoicuţă, Teodor Pană.....	101
<i>Design and Simulation of Wireless Power Transfer Systems</i> – Mihai Iordache, George Andronescu, Victor Bucată, Maria-Lavinia Iordache (Bobaru), Marilena Stăculescu, Dragoş Niculae .....	109

<i>Small Scale Model of Automatic Barrier Powered by Photovoltaic Panel</i> – Laurențiu Alboteanu, Gheorghe Manolea, Alexandru Novac .....	115
<i>Dynamic Regime Electromagnetic Torque in Brushless Direct Current Motors</i> – Ion Vlad, Sorin Enache, Monica Adela Enache .....	123
<i>Enhancing the dynamic frequency of microgrids by means of PV power plants with integrated energy storage</i> – Daniel Munteanu, Ioan Șerban, Corneliu Marinescu, Luminița Barote .....	129
<i>The Analysis of Magnetic Field Measurements in a Public Access Area</i> – Georgiana Roșu, Octavian Baltag .....	135
<i>Comparisons Among p - Channel, n-Channel and Mixed n/p Channel OTFTs</i> – Cristian Ravari, Georgeta Alecu .....	141
<i>On the Immunity of Data Acquisition Systems Used in Power Systems</i> – Livia-Andreea Dina, Ileana-Diana Nicolae, Petre-Marian Nicolae, Dorina-Mioara Purcaru .....	147
<i>Aspects of Behavior Regarding Certain Electronic Equipment Subject to Electrostatic Discharge</i> – Mircea-Emilian Ardeleanu, Paul Nicolescu .....	153
<i>Load Flow Analysis of Unbalanced Distribution Networks using Symmetrical Components Based Software</i> – Denisa Rușinaru, Leonardo Geo Mănescu, Marian Ciontu, Miron Alba .....	159
<i>Technical Aspects Regarding Electromagnetic Compatibility Compliance of the Electric and Electronic Integrated Systems</i> – Stoica Dan, Cosereanu Liviu, Enache Mihai, Ploșniță Albert, Mazăre Petru .....	168
<i>Electromagnetic Shielding System for Information and Communication Equipments</i> – Stoica Dan, Cosereanu Liviu, Enache Mihai, Boteanu Adina, Ploșniță Albert .....	173

## Professor Aurel CAMPEANU at his 80<sup>th</sup> anniversary

Professor Aurel Câmpeanu was born on the 6-th of August 1935, in Calafat town, Dolj County. He followed secondary-school classes at «Nicolae Bălcescu» Popular College in Craiova, which graduated with praiseworthy diploma in 1953. In 1953 he was admitted without exam at the Faculty of Electrotechnics of the Institute of Electrical Machines and Apparatus in Craiova. In 1958 he graduated the Faculty of Electrotechnics in Craiova as part of the Polytechnic Institute from Bucharest, obtaining engineer diploma.



He started his professional activity as an electrotechnical engineer in the Central Laboratory of Electroputere Factory in Craiova (1958 – 1963). In 1963 he occupied the position of university assistant and then lecturer at the Department of Electrical Machines in the framework of the Faculty of Electrotechnics of the Polytechnical Institute of Timișoara where he collaborated with Academician Professor Toma DORDEA. In 1969 he presented his thesis for a doctor's degree entitled «*Study of two mechanically coupled synchronous machines, connected to a common network*», under the guidance of Academician Toma DORDEA, obtaining PhD title.

Since 1970 he has been going on his higher education and research activity in the framework of the University of Craiova, Faculty of Electrotechnics, where he occupied successively positions from lecturer to full professor. Since 2005 he is honorary professor in the framework of the Faculty of Electrical Engineering.

Testing engineer in Electroputere Factories – Central Laboratory.

In this quality he had the following contributions:

- he carried out *Testing Method in heating for transformers with three windings of high power and unequal*, which made dispatch possible, with important economic consequences, towards beneficiaries of transformers rated at 5/3/2 MVA (for India) and 40/30/30 MVA (for Poland); that method was acknowledged as an invention;

- he established a *method of recoverable test for synchronous machines rated at powers which sensitively exceed the power of the testing stands*. That made possible the industrial test, including in heating and avoiding, on this basis, the operation problems. That method was acknowledged as an invention and included in the IEC-60034-2 Standard elaborated by the International Electrotechnical Commission, regarding tests of electrical machines;

- he directly participated in homologating all the machines and transformers which were to be manufactured, including the motors and generators of the first generation of electrical diesel railway engines.

Teacher at the Polytechnic Institute in Timișoara.

This period is fundamentally marked by the presence of Academician Toma Dordea. The first meeting had taken place, without professor's knowledge, in the third year of studies, when Academician Toma Dordea came to Craiova as a President of the State Exam. He frequently expressed his gratitude to Professor's essential contribution in his professional formation as well as in a larger context.

Beside the current academic activity as an assistant and lecturer and the participation in research projects with Electromotor Factory Timișoara:

- he worked for elaborating, under Professor's coordination, the doctorate thesis "*Study of two mechanically coupled synchronous machines, connected to a common network*", original research, which carried out theoretical bases of a particular operation regime of synchronous machine and which had as a final purpose the method acknowledged as an invention and tested in Electroputere Factory;

- the publication activity and participating at conferences became a major preoccupation.

Teacher at the University of Craiova

He followed all the university stages of lecturer and professor, the disciplines taught being those afferent to electrical machines; he was head of department, pro-rector and dean. Professor Campeanu considers student as a close partner, that any failure must be equally assumed by teacher, too, which cannot be a simple provider of professional information, however high.

Concomitantly, he persevered in the activity of scientific research, constantly appreciated as being compulsory for a professor. His research activity has materialized in:

- over 200 scientific papers published in the most prestigious Romanian reviews ("Revue roumaine des sciences techniques – Série Electrotechnique et Energétique") and international reviews ("Electrical

Engineering-AfE”) or in outstanding international conferences ICEM (Vilamoura, Marseille, Rome, Helsinki), ELECTROMOTION (Patras, Bologna, Bodrum, Marrakesh, Lausanne, Lille) PEMC (Warsaw, Budapest), SPEEDAM (Capri, Ischia), EUROCON (Warsaw) IPEMC (Shanghai), IEMDC (Antalya) OPTIM (Braşov), AECE (Bucharest), ICED (Rome, Helsinki) PCIM (Nuremberg) EDPE (Dubrovnic) ACEMP (Kusadasi) etc.

- 13 books; among them, “Electrical machines. Basic problems, special and of optimal operation” was awarded the “Traian Vuia Prize” of the Romanian Academy; two books which approach present problems regarding modelling and simulation of alternating current machines published in the Academy Publishing House are appreciated by Academician Toma Dordea as publications elaborated at a high scientific level which surely satisfy the necessity of perfecting specialists which work in the area of electrical machines design and performant electrical drives, university teaching staff, master students and trainers for a doctor’s degree;

- research contracts, being Director of Grant with World Bank and Director of Tempus I, II Programs; these referred to perfecting and modernizing through advanced studies and doctorate at the Faculty of Electromechanics of the University of Craiova; all the teaching staff got mobilities in university centres in France, Belgium, Spain, Italy and all the laboratories of the faculty were modernized etc.

The favourite research area of Professor Aurel Câmpeanu has been connected with dynamic regimes of electrical machines, with an original approach, activity materialized in papers and books acknowledged in our country and abroad. Among the original contributions of Professor Profesorului Aurel Câmpeanu we can mention:

1. Elaborating the theory of a general method of testing in heating for transformers with three windings of high power and unequal;
2. Elaborating the generalized unitary theory of dynamic mathematical models of induction machine using representative vectors;
3. Elaborating the unitary theory of dynamic mathematical models of synchronous machine considering saturation and magnetic asymmetry;

Acknowledgements of scientific activity in our country and abroad.

Here are a few reference points of professional and scientific acknowledgement of Professor Aurel Câmpeanu:

- Permanent expert from Romania at International Electrotechnical Comitee IEC-WG 28 (present at meetings in Madrid, Toronto, Paris, Montréal, Zurich, Berlin, St. Petersburg, Helsinki, Heidelberg, Brno, Milano, London etc.);

- “Traian Vuia Prize” of the Romanian Academy (1991);

- Titular member of the Academy of Technical Sciences of Romania. Vice-president of the section Electrotechnics - Energetics, President of ASTR – territorial branch of Craiova;

- Doctor-Honoris Causa of the Technical University of Moldova- Chişinău, North University of Baia Mare, “Gh. Asachi” Technical University - Iaşi, “Stefan cel Mare” University - Suceava, “Eftimie Murgu” University - Reşiţa;

- Invited Professor with papers to universities from abroad (France, Belgium, Spain, Switzerland, Canada);

- Invited Professor to the International Conference of European Universities, CESAER, (Belgium) with the theme “Transfer of technology from universities towards industry”;

- Honour Distinction of the Senate of the Technical University of Cluj - Napoca;

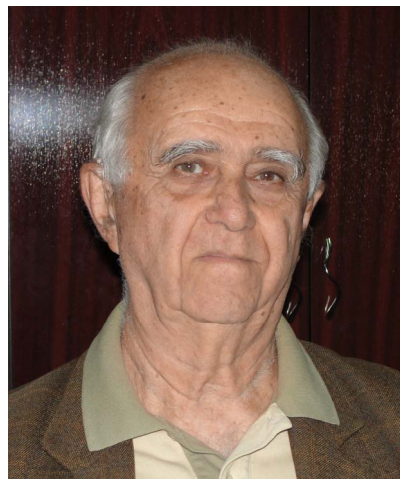
- Diploma of Honoured Emeritus Professor of the University of Craiova;

This is the survey of an activity devoted to professional and responsible formation of over 50 generations of engineers, from among over 45 in the framework of the University of Craiova, in general to scientific knowledge.

Prof.dr.ing. Ioan C. POPA

## Professor Grigore CIVIDJIAN at his 80<sup>th</sup> anniversary

Professor Grigore A. Cividjian was born in Chişinău (Republic of Moldova) on 12 January 1936. He followed the National College Carol I in Craiova between the years 1946 and 1953, when the name of this famous school was Popular College « Nicolae Bălcescu ». He graduated from the Craiova Institute of Electrical Machines and Apparatus in 1958 and sustained his graduated work in Polytechnic Institute of Bucharest in the summer of



1963, obtaining the engineer diploma in electrical machines and apparatus. In 1966 he began the doctoral study in theoretical electricity at Gh. Asachi Polytechnic Institute of Iassy with Professor dr. doc. ing. Gheorghe VASILIU, considered worthy successor of illustrious Dragomir Hurmuzescu and Ştefan Procopiu and also the mathematical study at University of Craiova. He sustained the thesis entitled “Contributions to the optimization of the parameters of shading coils from the electromagnets of control apparatus” and obtained his doctor (PhD) diploma in theoretical electricity in Polytechnic Institute of Iassy in 1970. In the next year he graduated from the University of Craiova with license in mathematics.

He began his activity as worker in local industry enterprise ILMET Craiova in 1958 in the metrological verification of high pressure mechanical installations, measuring instruments and electrical elevators and from May 1960 he is electrical installations designer in project institute DSAPC Craiova.

In September 1967 he was transferred as assistant in the new opened University of Craiova, in 1969 is promoted as lecturer and from 1977 he won a contest for associated professor of Electrical Apparatus.

In 1972 he made a 1 month formation stage in Bucharest Polytechnic Institute in *modeling the electric and magnetic fields* and in 1973 a 3 month formation stage in *switching arc phenomena* in the Sankt Petersburg Polytechnic institute.

In 1990 as result of contest he become university professor and PhD supervisor. In 1997 he is awarded with the title of professor emeritus of the Craiova University.

From 2006 he is consulting professor, associated to the Electrical Engineering faculty and director of the IEETE research center.

Prof. G. A. Cividjian was head of the department of Electrical Apparatus between 1990 and 2004 and along the years gave the following courses: Electrical apparatus (equipment), Statistical models and reliability (both in Romanian and French), Computer aided design of electrical apparatus, Special problems of electrical apparatus-switching in vacuum and SF<sub>6</sub>, Electro-physical devices (in Romanian and French). However his courses were at a high scientific level, sometimes difficult to understand, he was very appreciated by the students, being very close to them.

As invited professor he gave some lectures in the University of Perugia (Italy, 1999) and in Technical University of Sofia (Bulgaria, 2001). He participated with contributions at international doctoral schools as Budva (Serbia and Montenegro, 2004), Ohrid (Macedonia, 2005), Nis, CEMBEF (Serbia, 2009).

He made short documentation visits in several universities as Lancashire from Preston (GB), TEI Patras (GR), Bochum (D), University of Toulouse (F) by program Tempus, INSA Lyon (F) by program Erasmus, University of Sherbrooke, Ecole Polytechnique de Montréal, Ecole de Technologie Supérieure (Canada), University of Nis (YU), Technical University of Brno (CZ), University of Delft (NL).

The research was and is his permanent activity, materialized in large part with solutions for practical problems occurring in industry or research institutions. From 2001 prof. G. A. Cividjian is the director of the Research Center for Electrical Energy Engineering and Ecological Technology (IEETE) of University of Craiova. His research activity can be summarized as follows:

146 published research papers in national and international revues as “Rev. Roum. Sci. Tech. Electrotechnique et Energetique », « Electrotehnica, » « Studii si cercetari ale Academiei – Fizica si Stiinte Tehnice, » and « Archiv für elektrotechnik », « Elektrotehnika », « Izv. VUZ - Elektromehanika », « Elektrichestvo », “IEEE Transactions on Magnetics”, “Compel”, “Serbian Journal of Electrical Engineering”, “Electrical Engineering (PI)”, or in proceedings of international conferences as “Modelling, Simulation & Control, A, AMSE Press”, “Accelerators'92, Seventh Conference on Applied Accelerators, St. Petersburg, 16-18 June, 1992, “Seventh Int. Conf. on Switching Arc Phenomena, SAP' 93”, “The 5-th International Conference on Electrical Fuses and their Applications, ICEFA'95, 25th - 27th Sept., 1995, VDE Verlag, Technical University Ilmenau, Germany”, “7-th

International IGTE Symposium on Numerical Field Calculation in Electrical Engineering, Proceedings, p. 1, Graz, Austria, Sept. 23-25, 1996”, “Numelec' 97, Seconde Conférence Européenne sur les Méthodes Numériques en Electromagnétisme, 19-21 mars, 1997, Ecole Centrale de Lyon, France”, “International Symposium on Short-circuit currents in Power systems, Brussels (Belgium), 8-10 October, 1998”, *Symposium on Physics of Switching Arc*, TU Brno (Czech Rep.), 1994 – 2005.  
Researcherid h-index = 4.

Prof. G. A. Cividjian is the author of the textbooks “Aparate electrice, Reprografia Universitatii din Craiova, 1970, 1972”, «Aparate electrice – Izolatie si arc, 1996” and the first author of the textbook , “Modèles statistiques et fiabilité, Université de Craiova, 2003”. He contributed as coauthor at two monographs on electrical technologies (coordinated by F. T. Tanasescu e. a.) published in Romanian Editura Academiei (2002) si Editura AGIR (2011) with the chapters on Magnetic separation (I. Bahrin, G. Cividjian), pp. 346-392 and respectively Acoustic emission (N. Cividjian, G. Cividjian) pp. 549-598 and also at the proceeding of selected papers edited by S. Wiak and E. Napieralska-Juszak: Computer field models of electromagnetic devices, IOS press, Amsterdam, Berlin, Oxford, Tokyo, Washington DC, 2010, 935 p.:with Exact expression of corner reluctances in a magnetic circuit of rectangular section, (E. Matagne, G. A. Cividjian and Virginie Kluyskens), pp.134-142;

- He coordinated also 37 scientific research projects and is co-author of 3 invention brevets.

The main research directions of his activity are the modeling of electric and physical phenomena and processes, the optimization of electrical equipment and statistical models in engineering. Between his original contributions can be cited:

1. Optimization of the parameters of electromagnet shading coils with and without consideration of leakage flux;
2. Internal and external inductance of the coils with rectangular cross-section and application to the electromagnet design.
3. Contribution to the theory development of fragmented core transformers and of high voltage direct current cascade generators for industrial and medical accelerators.
4. Modeling the potential 2D strong no uniform fields: formulas for “corner permeance (capacitance)”, ‘corner force”, “constriction permeance”, “distorted constriction resistance” etc.
5. Modeling the physical processes in electrical apparatus and equipment; black-box arc model, lightning surges in transformers, thermal field diffusion in cylindrical items.

The research activity of prof. Cividjian is largely recognized in the world. He is member of several professional and scientific organizations as Romanian Electrical Committee CER (CT8), ASER (electrostatics), ACER (electrical compatibility), Fuse Club, member of IBC Advisory Council. He is also member of several scientific committees of international conferences as ICATE, SIELA, PES, SAP and member of editorial board of revues as Serbian Journal of Electrical Engineering and Annals of the University of Craiova – Electrical engineering. He was or is expert evaluator for INTAS, GACR (Czech Scientific Foundation), GNSF (Georgian National Science Foundation), FP-7 and voluntary reviewer for prestigious revues as IEEE Transaction on Magnetics (SUA) and COMPEL - The international journal for computation and mathematics in electrical and electronic engineering.

This is a short review of an activity dedicated to the professional formation of 49 generations of engineers and of an distinguished scientific research activity of the professor Grigore A. Cividjian.

Prof. dr. ing. Ioan C. POPA

# Comparison of the Conservative Power Theory (CPT) with Budeanu's Power Theory

Leszek S. Czarnecki, *IEEE Life Fellow*

Louisiana State University / School of Electrical Engineering and Computer Science, Baton Rouge, USA  
lczar1@lsu.edu

**Abstract** - It is shown in this paper that the Conservative Power Theory (CPT) describes power properties of electrical circuits in a way which has a strong analogy to this description in terms of Budeanu's power theory which misinterprets the power phenomena in such circuits. Also, similarly as Budeanu's power theory, the CPT does not create right fundamentals for the power factor improvement by reactive compensation. Moreover, Budeanu's power theory is no less "conservative" than the Conservative Power Theory, thus both theories can be referred to as conservative ones.

**Keywords:** power definitions, reactive current, reactive power, distortion power, Currents' Physical Components, CPC.

## I. INTRODUCTION

The first power theory of electrical systems with nonsinusoidal voltages and currents was suggested [3] by Budeanu in 1927. It was a response to Steinmetz experiment performed in 1892, which challenged the concept of the reactive power [1]. The Conservative Power Theory (CPT), presented in [15] by Tenit and his co-workers in 2003, seems to be the latest attempt aimed at developing such a theory. Comparison of these two power theories is just the subject of this paper.

The power theory of electrical systems is focused on two questions that are fundamental for the electrical engineering: **(i) why can the apparent power  $S$  be higher than the active power  $P$**  and **(ii) how can this difference be reduced?** The first question is cognitive in its nature, the second question is practical.

The period of 76 years which separates these two concepts of the power theory was filled with numerous attempts, com-piled in [22], aimed at providing answers to these two questions. In effect of these attempts the difference between the apparent and the active powers,  $S$  and  $P$ , can be now explained in terms of power related phenomena in electrical loads. Fundamentals of compensation, i.e., reduction of the difference between these two powers, in the presence of distortion and asymmetry were developed as well. Development of the Currents' Physical Components (CPC) – based power theory [9, 16] was crucial for the present state of the knowledge on the power properties of systems with nonsinusoidal and asymmetrical voltages and currents and on compensation in such systems.

The CPC – based power theory was developed in the frequency-domain, i.e., using the concept of harmonics. In this respect the development of the CPC-based theory has followed Budeanu's frequency-domain approach.

The Conservative Power Theory (CPT) has occurred after the development of the CPC – based power theory was almost completed. It seems that development of the CPT was motivated by an old postulate formulated by Fryze [4] in 1931, that the power theory should be formulated in the time-domain, i.e., without any use of the concept of harmonics and such a theory should be based on the load current decomposition into orthogonal components.

The CPT satisfies Fryze's postulates, nonetheless, it describes the power properties of electrical loads in a way, which has a strong analogy to description of these properties in terms of Budeanu's power theory. Unfortunately, as it was demonstrated in papers [11, 12], Budeanu's power theory misinterprets power phenomena in electrical circuits and it does not provide any fundamentals for their compensation. As it will be shown in this paper the same applies to the CPT.

Development of the CPT started in 2003 in paper [15], where mathematical fundamentals of the CPT for single-phase systems were presented with an extension to poly-phase networks. Later the CPT was focused mainly on three-phase systems [17, 19, 20]. It disseminates in electrical engineering and provides CPT – based interpretations of the power related phenomena in electrical systems and fundamentals for their compensation. Unfortunately, as it will be shown in this paper, the power quantities and the load current components introduced by the CPT are not associated with physical phenomena in the load. It applies first of all to the quantity called in the CPT the "reactive energy"  $W$ . The same applies to the reactive and void currents as well to the unbalanced current. These new quantities defined in the CPT can contribute to major misinterpretations of power phenomena and to erroneous conclusions as to methods of reactive compensators design.

The power theory of single-phase systems with nonsinusoidal voltages and currents developed by Budeanu, introduced a new definition of the reactive power  $Q$ , denoted in this paper as  $Q_B$ , and introduced a concept of the distortion power  $D_B$  to the power theory. This theory has gained almost common acceptance [10] in the electrical engineering community and was supported by some standards, such as [8], [13] or [14]. In 1987 it was challenged in [11], where it was demonstrated that the reactive power  $Q_B$  as defined by Budeanu is not associated with the energy oscillation between the load and the supply source. Moreover, it was demonstrated that the distortion power  $D_B$  is not associated with the mutual distortion of the load voltage and current. It was also demonstrated that there is no relation between the power factor improvement and reduction of the reactive power

$Q_B$ . Consequently, Budeanu's power theory had to be abandoned for other concepts. It also disappeared from the IEEE 1459 Standard [18].

The CPT, although formulated mathematically in a substantially different way than Budeanu's power theory, shares with that theory the same incapability for explanation of the power related phenomena in electrical systems and the same incapability for providing right fundamentals for compensation. In fact, some conclusions of the CPT, formulated in the time-domain, are identical to those of Budeanu's theory, formulated in the frequency-domain. Moreover, the adjective "conservative", which is pivotal for the CPT to such a degree, that it is used in its name, can be applied in the same sense to Budeanu's reactive power  $Q_B$ , which does not have any physical interpretation and any practical application. In both cases *conservativeness* has nothing in common [20] with the Law of Conservation of Energy (LCE). The conservation property of the "reactive energy"  $W$  in the CPT and the reactive power  $Q_B$  in Budeanu's power theory has only mathematical, but not physical fundamentals.

Conclusions on interpretations of very confusing power properties, drawn from studies of real and complex systems, where various phenomena are superimposed, might not be credible. These studies should be done on systems, where the number of different power related phenomena is reduced as much as possible. It means that to be valid and credible in poly-phase systems with a full complexity, these interpretations, definitions and conclusions have to be credible when applied to single-phase and even to purely reactive systems. A statement to be valid in the whole set of power systems has to be valid in every sub-set of such systems. Single-phase and purely reactive loads are just sub-sets of the set of three-phase loads. Therefore, to obtain credible conclusions, this paper investigates how the CPT interprets the power related phenomena in such, strongly simplified systems.

## II. "REACTIVE ENERGY" $W$

The reactive current in the CPT is defined as

$$i_{rT}(t) \stackrel{\text{df}}{=} \frac{W}{\|\hat{u}\|^2} \hat{u}(t) \quad (1)$$

where

$$W \stackrel{\text{df}}{=} (\hat{u}, i) \stackrel{\text{df}}{=} \frac{1}{T} \int_0^T \hat{u}(t) i(t) dt \quad (2)$$

denotes "a reactive energy" as defined in the CPT. Symbol  $(x, y)$  denotes the scalar product of periodic quantities  $x(t)$  and  $y(t)$ ; symbol  $\|x\|$  denotes the rms value of  $x(t)$ , while symbol  $\hat{u}$  denotes the unbiased voltage integral:

$$\hat{u}(t) = \int_0^t u(\tau) d\tau - \frac{1}{T} \int_0^T \left[ \int_0^t u(\tau) d\tau \right] dt. \quad (3)$$

The name of quantity  $W$  "a reactive energy" is written in quotation marks because the quantity  $W$  for a capacitor is negative, while energy cannot be negative. Any quantity, even with the energy dimension, that can be negative cannot be regarded as "energy". Index "T" in the

definition (1) was used in this paper to differentiate the reactive current as defined in the CPT from the reactive currents defined in other power theories.

A new concept of the reactive current  $i_{rT}(t)$ , introduced by the CPT as defined by (1), has the physical interpretation entirely founded on the physical interpretation of the "reactive energy"  $W$ . Thus, what the "reactive energy" is?

This term does not exist in the first papers on the CPT, meaning in [15] and [17]. Its mathematical definition was provided without any physical interpretation. Its interpretation can be found in [20], namely

"...the reactive energy accounts for inductive and capacitive energy stored in the load circuit."

To verify this interpretation of the "reactive energy", let us calculate the energy  $E$  stored in an ideal LC load, shown in Fig. 1, supplied with a sinusoidal voltage

$$u(t) = \sqrt{2}U \cos \omega_1 t.$$

The energy stored in such a reactive load is

$$E = \frac{1}{2} Li_L^2(t) + \frac{1}{2} Cu^2(t) = \frac{U^2}{\omega^2 L} \sin^2 \omega t + CU^2 \cos^2 \omega t. \quad (4)$$

Now, let us calculate the "reactive energy"  $W$  of the same reactive load. The unbiased voltage integral is equal to

$$\hat{u}(t) = \sqrt{2} \frac{U}{\omega} \sin \omega t \quad (5)$$

thus the "reactive energy"  $W$  of such a reactive load is

$$W = (\hat{u}, i) = \frac{1}{T} \int_0^T \hat{u}(t) [i_L(t) + i_C(t)] dt = \left( \frac{1}{\omega^2 L} - C \right) U^2 \quad (6)$$

This is not the energy  $E$  stored, as specified by (4), in the LC load, shown in Fig. 1. Thus the interpretation of the "reactive energy"  $W$ , as presented in [20], is not right. It is even more visible at a resonance in that load, when  $1/\omega L = \omega C$ . At such a condition, the "reactive energy"  $W$  is zero, while the energy stored in the load is

$$E = \frac{U^2}{\omega} \left( \frac{1}{\omega L} \sin^2 \omega t + \omega C \cos^2 \omega t \right) = \frac{1}{\omega^2 L} U^2. \quad (7)$$

Doubts about whether the opinion expressed in [20] is right can be strengthened by results of analysis of a purely resistive circuit with a TRIAC, shown in Fig. 2.

At sinusoidal supply voltage

$$u(t) = \sqrt{2}U \sin \omega_1 t$$

the load current at the TRIAC firing angle  $\alpha$  has the waveform as shown in Fig. 3.

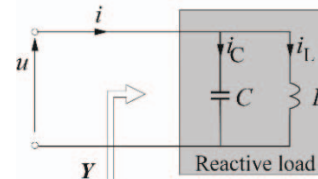


Fig. 1. Ideal reactive load.

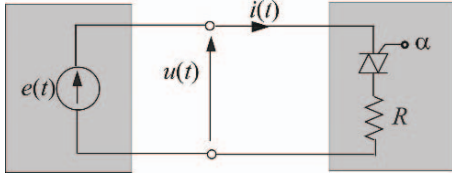
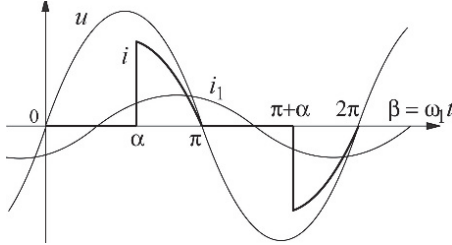


Fig. 2. Resistive load with periodic switch.


 Fig. 3. Voltage, current and the current fundamental harmonic  $i_1$  waveforms in resistive circuit with TRIAC.

The load current in such a circuit can be decomposed into harmonics

$$i(t) = \sum_{k=1}^{\infty} i_k(t) = i_1(t) + \sum_{k=2}^{\infty} i_k(t) \quad (8)$$

with the current fundamental harmonic

$$i_1(t) = \sqrt{2} I_1 \sin(\omega_1 t - \varphi_1) \quad (9)$$

i.e., shifted with respect to the voltage as shown in Fig. 3. The unbiased integral of the supply voltage is

$$\hat{u}(t) = -\sqrt{2} \frac{U}{\omega} \cos \omega_1 t \quad (10)$$

and consequently, the “reactive energy”  $W$  is equal to

$$\begin{aligned} W = (\hat{u}, i) &= \sum_{n=1}^{\infty} (\hat{u}_n, i_n) = (\hat{u}, i_1) = \\ &= \frac{1}{T} \int_0^T \hat{u}(t) i_1(t) dt = \frac{U I_1}{\omega_1} \sin \varphi_1. \end{aligned} \quad (11)$$

Thus, loads without any capability of energy storage could have a “reactive energy”  $W$ . This confirms the previous conclusion that the “reactive energy”  $W$  is not associated with the phenomenon of energy storage.

The “reactive energy”  $W$  was defined originally by (2) in the time-domain. In such a way the CPT follows Fryze’s concept [4] of defining power quantities without any use of harmonics. This confines insight into the meaning of this quantity, however.

Thus, let us express the “reactive energy”  $W$  of a purely reactive load in the frequency-domain, assuming that the supply voltage is nonsinusoidal and composed of harmonics of the order  $n$  from a set  $N$ , namely, that it is equal to

$$u(t) = \sum_{n \in N} u_n(t) = \sqrt{2} \sum_{n \in N} U_n \cos n \omega_1 t. \quad (12)$$

The unbiased integral of such a voltage is

$$\hat{u}(t) = \sum_{n \in N} \hat{u}_n(t) = \sqrt{2} \sum_{n \in N} \frac{U_n}{n \omega_1} \sin n \omega_1 t. \quad (13)$$

A purely reactive load has the admittance for harmonic frequency of the  $n^{\text{th}}$  order harmonic equal to

$$Y_n = G_n + jB_n = jB_n$$

i.e., with  $G_n = 0$ . If for the  $n^{\text{th}}$  order harmonic the load is inductive, then  $B_n < 0$  and

$$i_n(t) = \sqrt{2} |B_n| U_n \sin n \omega_1 t.$$

If for such a harmonic the load is capacitive, i.e.,  $B_n > 0$ , then

$$i_n(t) = -\sqrt{2} |B_n| U_n \sin n \omega_1 t.$$

Therefore, the current of a purely reactive load can be expressed in the form

$$i(t) = \sum_{n \in N} i_n(t) = -\sqrt{2} \sum_{n \in N} \text{sgn}\{B_n\} |B_n| U_n \sin n \omega_1 t. \quad (14)$$

The “reactive energy”  $W$  of such a reactive LC load is

$$W = (\hat{u}, i) = \sum_{n \in N} (\hat{u}_n, i_n) = \sum_{n \in N} W_n = -\sum_{n \in N} \text{sgn}\{B_n\} |B_n| \frac{U_n^2}{n \omega_1} \quad (15)$$

Individual terms  $W_n$  of this sum can be, depending on the sign of the load susceptance  $B_n$ , positive or negative, thus they can cancel mutually. This mutual cancellation of the harmonic “reactive energies”  $W_n$  resembles mutual cancellation of harmonic reactive powers  $Q_n$  in Budeanu’s definition [3] of the reactive power  $Q_B$ .

$$Q_B = \sum_{n \in N} U_n I_n \sin \varphi_n = \sum_{n \in N} Q_n. \quad (16)$$

This mutual cancellation was of one of the major deficiencies of Budeanu’s reactive power [11, 12] definition, for which it was eventually abandoned in the power theory.

Formula (15) for the “reactive energy”  $W$  has a strong analogy with definition of the reactive power  $Q_B$ . This is particularly visible if (16) is rearranged for reactive loads to the form.

$$Q_B = \sum_{n \in N} U_n I_n \sin \varphi_n = -\sum_{n \in N} \text{sgn}\{B_n\} |B_n| U_n^2 \quad (17)$$

Individual terms in Budeanu’s definition of the reactive power  $Q_B$  stand for the amplitude of the energy oscillation at the frequency of individual harmonics, since the bidirectional component of the instantaneous power  $p(t)$  of the  $n^{\text{th}}$  order harmonic is equal to

$$\tilde{p}_n = U_n I_n \sin \varphi_n \sin 2n \omega_1 t = Q_n \sin 2n \omega_1 t. \quad (18)$$

The sum (16) of these amplitudes  $Q_n$ , i.e., Budeanu’s reactive power  $Q_B$ , does not specify, as shown in [11], any physical phenomenon in the circuit, however.

Thus the “reactive energy”  $W$ , when expressed in the frequency-domain, look a lot like the reactive power suggested at the beginning of the power theory

development. In particular, it occurs to be almost identical with the reactive power  $Q_1$  defined in 1925 [2] by Illović.

Namely, according to Illović, the reactive power should be defined as the quantity measured by a wattmeter with the resistor in the voltage branch replaced by an inductor  $L$ .

Such a device, assuming that it is ideal and lossless, measures the quantity

$$Q_1 = \sum_{n \in N} \frac{1}{n} U_n I_n \sin \varphi_n \quad (19)$$

According to Illović, just this is one of the quantities that should be regarded as the reactive power at nonsinusoidal supply voltage.

Assuming that the voltage branch is lossless, then at terminals of a purely reactive LC load such an instrument measures the quantity

$$Q_1 = \sum_{n \in N} \frac{1}{n} U_n I_n \sin \varphi_n = - \sum_{n \in N} \operatorname{sgn}\{B_n\} |B_n| \frac{U_n^2}{n} = \omega_1 W \quad (20)$$

Thus, Illović's reactive power  $Q_1$  and the "reactive energy"  $W$  differ mutually only by the dimensional coefficient  $\omega_1$ . Consequently, there is no physical phenomenon in the load that could be characterized by the quantity  $W$ , called in the CPT "a reactive energy".

### III. CONSERVABILITY OF "REACTIVE ENERGY" $W$

The "reactive energy"  $W$  satisfies the Conservative Property. It means that in any circuit confined by a sphere with zero energy transfer and composed of  $K$  branches, as shown in Fig. 4,

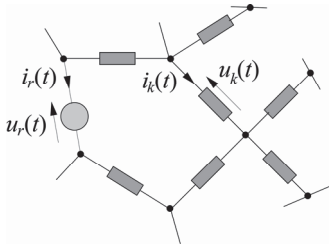


Fig. 4. Circuit with  $K$  branches.

the sum of "reactive energies" of individual branches  $W_k$  is equal to zero, i.e.,

$$\frac{1}{T} \int_0^T \sum_{k=1}^K \hat{u}_k(t) i_k(t) dt = \sum_{k=1}^K W_k = 0 \quad (21)$$

This is a very important property. It enables balancing the "reactive energies" and verification of its calculation. Also, if a quantity satisfies the conservative property, this might indicate that this quantity has a physical nature. Such argument was sometimes used in discussions on the physical nature of Budeanu's reactive power. It also satisfies the conservative property, i.e.,

$$\sum_{k=1}^K \sum_{n \in N} U_{kn} I_{kn} \sin \varphi_{kn} dt = \sum_{k=1}^K Q_{Bk} = 0 \quad (22)$$

The conservative property can be an outcome of one of two more fundamental principles. One of them is the Law

of Conservation of Energy (LCE). The second principle is the Tellegen Theorem [5]. According to the LCE, if in any circuit confined by a sphere with zero energy transfer and composed of  $K$  branches, and if energy  $E_k$  is transferred to the  $k$ -branch, then

$$\sum_{k=1}^K E_k = \text{Const.} \quad (23)$$

Since the instantaneous power of the  $k$ -branch is

$$\frac{dE_k}{dt} = p_k(t) \quad (24)$$

thus the conservative property of the instantaneous power

$$\sum_{k=1}^K \frac{dE_k}{dt} = \sum_{k=1}^K p_k(t) = 0 \quad (25)$$

is a direct conclusion from the Law of Conservation of Energy.

As emphasized in [15], the conservative property of the "reactive energy"  $W$ , with the importance of this property reflected in the name of the Conservative Power Theory, is a conclusion from the Tellegen Theorem.

This Theorem, concluded by Tellegen from Kirchoff Laws in [5], seems to be not commonly known because it was developed not long ago. Since it is crucial for this discussion on the conservative property of the "reactive energy"  $W$ , its meaning is explained below.

According to this Theorem, if we have two circuits of the identical topologies, as shown in Fig. 5,

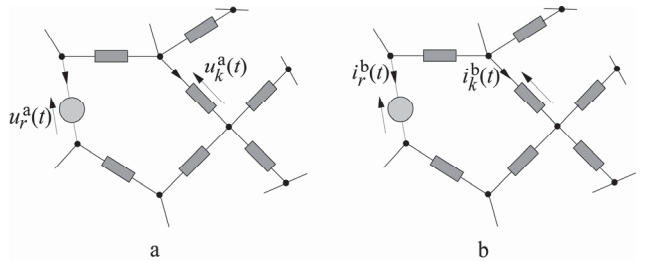


Fig. 5. Two circuits with identical topology.

then the sum of voltage-currents products over all  $K$  branches with voltages taken from the circuit in Fig. 5(a) and the currents taken from the circuit in Fig. 5(b) is equal to zero, i.e.,

$$\sum_{k=1}^K u_k^a(t) i_k^b(t) \equiv 0 \quad (26)$$

The voltage-current products in (26) do not stand for any physical quantity, however, because voltages are taken from one circuit while the currents are taken from the other one. Nonetheless, such non-physical products have the conservative property. This property is also valid for any integral operations performed on voltages and currents in these two circuits. Therefore, assuming that

$$u_k^a(t) \equiv \hat{u}_k(t), \quad i_k^b(t) \equiv i_k(t) \quad (27)$$

from the Tellegen Theorem (26) we obtain

$$\sum_{k=1}^K u_k^a(t) i_k^b(t) = \sum_{k=1}^K \hat{u}_k(t) i_k(t) \equiv 0, \quad (28)$$

and hence

$$\frac{1}{T} \int_0^T \sum_{k=1}^K \hat{u}_k(t) i_k(t) dt = \sum_{k=1}^K \langle \hat{u}_k, i_k \rangle = \sum_{k=1}^K W_k \equiv 0. \quad (29)$$

It means that the conservative property of the reactive energy  $W$  does not strengthen arguments for its physical nature. This has a strong analogy with the conservative property of the reactive power as defined by Budeanu.

Budeanu's reactive power  $Q_B$  can be expressed as demonstrated in [7]

$$Q_B = \sum_{n \in N} U_n I_n \sin \varphi_n = \frac{1}{T} \int_0^T u(t) H\{i(t)\} dt \quad (30)$$

where

$$H\{i(t)\} = PV \frac{1}{\pi} \int_{-\infty}^{\infty} \frac{i(\tau)}{\tau - t} dt \quad (31)$$

is the Hilbert Transform of the load current  $i(t)$ . Symbol PV denotes the principal value of the integral.

Assuming that in circuits in Fig. 5(a) and (b)

$$u_k^a(t) \equiv u_k(t), \quad i_k^b(t) \equiv H\{i_k(t)\} \quad (32)$$

then from Tellegen Theorem

$$\sum_{k=1}^K u_k^a(t) i_k^b(t) = \sum_{k=1}^K u_k(t) H\{i_k(t)\} \equiv 0. \quad (33)$$

Hence

$$\begin{aligned} \frac{1}{T} \int_0^T \sum_{k=1}^K u_k(t) H\{i_k(t)\} dt &= \sum_{k=1}^K \frac{1}{T} \int_0^T u_k(t) H\{i_k(t)\} dt = \\ &= \sum_{k=1}^K Q_{Bk} = 0. \end{aligned} \quad (34)$$

The conservative property of Budeanu's reactive power  $Q_B$  is not a consequence of the LCE, i.e., a physical principle, but only the Tellegen Theorem, which is a sort of mathematical, but not a physical property of electrical systems. Consequently, the CPT is no more conservative than Budeanu's power theory. From the fact, that the "reactive energy"  $W$  has a conservative property, we should not draw the conclusion that it is a physical quantity. The same was with Budeanu's reactive power  $Q_B$ .

#### IV. THE REACTIVE CURRENT $i_{rT}(t)$

The previous section has demonstrated that the physical interpretation of reactive current  $i_{rT}(t)$  in the CPT cannot be founded on the "reactive energy", since it does not have such interpretation. Thus, what the reactive current  $i_{rT}(t)$  is?

Definition (1) of this current shows that it can be regarded as a current of an ideal inductor, since

$$i_{rT}(t) = \frac{W}{\|\hat{u}\|^2} \hat{u}(t) = \frac{1}{L_e} \hat{u}(t) \quad (35)$$

where

$$L_e = \frac{\|\hat{u}\|^2}{W}. \quad (36)$$

It means that with respect to the "reactive energy"  $W$  at the supply voltage  $u(t)$ , the purely reactive load is equivalent to an inductor of inductance  $L_e$ . Such an inductor draws the current  $i_{rT}(t)$  from the supply source.

Since the physical meaning of the "reactive energy"  $W$  in the CPT is not clear, not clear is also the physical meaning of the reactive current  $i_{rT}(t)$ . Its meaning can be clarified using the Currents' Physical Components (CPC) power theory [16]. Namely, at the supply voltage

$$u(t) = \sqrt{2} \operatorname{Re} \sum_{n \in N} U_n e^{jn\omega_1 t} \quad (37)$$

the reactive current defined in the CPT is

$$i_{rT}(t) = \sqrt{2} \operatorname{Re} \sum_{n \in N} \frac{1}{jn\omega_1 L_e} U_n e^{jn\omega_1 t}. \quad (38)$$

This is not the reactive current as defined by Shepherd and Zakikhani [6], namely the current

$$i_r(t) = \sqrt{2} \operatorname{Re} \sum_{n \in N} jB_n U_n e^{jn\omega_1 t} \quad (39)$$

meaning, the current which occurs in the supply lines due to a phase-shift between the voltage and current harmonics. The current  $i_{rT}(t)$  is only a part of that reactive current  $i_r(t)$ .

According to the CPT the reactive current  $i_{rT}(t)$  can be compensated entirely by a capacitor connected as shown in Fig. 6.

The "reactive energy" of the capacitor is

$$W_C = (\hat{u}, i_C) = - \sum_{n \in N} \frac{n\omega_1 C}{n\omega_1} U_n^2 = -C \sum_{n \in N} U_n^2 = -C \|\hat{u}\|^2. \quad (40)$$

Thus a shunt capacitor of capacitance

$$C = \frac{W}{\|\hat{u}\|^2} \quad (41)$$

compensates the "reactive energy"  $W$  entirely. It changes the CPT reactive current  $i_{rT}(t)$  to

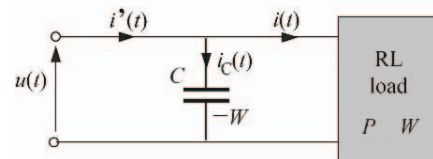


Fig. 6. RL load with a capacitor which compensates the "reactive energy"  $W$ .

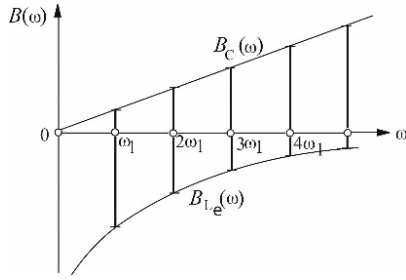


Fig. 7. Change of inductor and capacitor susceptance with harmonic order.

$$i_{rT}(t) = \sqrt{2} \operatorname{Re} \sum_{n \in N} j(n\omega_1 C - \frac{1}{n\omega_1 L_e}) U_n e^{jn\omega_1 t}. \quad (42)$$

The susceptance of the capacitor  $C$  changes with the harmonic order in a different way than the susceptance of the equivalent inductance  $L_e$ , as shown in Fig. 7, however.

Thus, reduction of the reactive current  $i_{rT}(t)$  does not result from (42), but from reduction of the “reactive energy”  $W$  to zero and an increase of the equivalent inductance  $L_e$  to infinity. The true reactive current  $i_r(t)$ , as defined by (39), is not compensated, however. The CPT ignores the fact that the compensating capacitor can affect also the void current.

#### V. THE VOID CURRENT $i_v(t)$

The load current according to the CPT is composed of the active, reactive and the void currents

$$i(t) = i_a(t) + i_{rT}(t) + i_v(t) \quad (43)$$

where the void current is defined as

$$i_v(t) = i(t) - [i_a(t) + i_{rT}(t)]. \quad (44)$$

The void current  $i_v(t)$ , as defined by (29), is not expressed in terms of voltage and the load parameters, which are specified in the frequency-domain, however, but in the time-domain. The physical meaning of this current is not clear. This meaning can be clarified in the frequency-domain, with the CPC-based power theory.

Since the active current  $i_a(t)$  is equal to

$$i_a(t) \stackrel{\text{df}}{=} G_e u(t) = \sqrt{2} \operatorname{Re} \sum_{n \in N} G_e U_n e^{jn\omega_1 t}, \quad G_e = \frac{P}{\|u\|^2} \quad (45)$$

while the reactive current  $i_{rT}(t)$  is given by (38), thus the void current can be expressed as

$$\begin{aligned} i_v &= i - i_a - i_{rT} = \\ &= \sqrt{2} \operatorname{Re} \sum_{n \in N} [(G_n + jB_n) - G_e - \frac{1}{jn\omega_1 L_e}] U_n e^{jn\omega_1 t}. \end{aligned} \quad (46)$$

This formula shows that the void current is in fact a compound quantity. It contains in-phase component

$$i_s(t) = \sqrt{2} \operatorname{Re} \sum_{n \in N} (G_n - G_e) U_n e^{jn\omega_1 t} \quad (47)$$

revealed [9] in CPC and called *scattered current*. It contains also a quadrature component, i.e., composed of current harmonics shifted by  $\pi/2$  with respect to the voltage harmonics

$$i_{vr}(t) = \sqrt{2} \operatorname{Re} \sum_{n \in N} j(B_n + \frac{1}{n\omega_1 L_e}) U_n e^{jn\omega_1 t} \quad (48)$$

Thus,

$$i_v(t) = i_s(t) + i_{vr}(t). \quad (49)$$

The quadrature component of the void current has the rms value

$$\|i_{vr}\| = \sqrt{\sum_{n \in N} (B_n + \frac{1}{n\omega_1 L_e})^2 U_n^2}. \quad (50)$$

When a capacitor is connected as shown in Fig. 6 to compensate the “reactive energy”  $W$ , then the supply current does not contain the reactive current  $i_{rT}(t)$ . The quadrature component of the void current changes to

$$i_{vr}(t) = \sqrt{2} \operatorname{Re} \sum_{n \in N} j(B_n + n\omega_1 C) U_n e^{jn\omega_1 t}. \quad (51)$$

Its rms value changes to

$$\|i_{vr}\| = \sqrt{\sum_{n \in N} (B_n + n\omega_1 C)^2 U_n^2} \quad (52)$$

Thus capacitive compensation of the reactive current  $i_{rT}(t)$  changes the void current rms value. Moreover, this change increases with the harmonic order  $n$ . Thus, compensation of the reactive current  $i_{rT}(t)$  cannot be separated from its effect on the void current  $i_{vr}(t)$  rms value increase. This is illustrated numerically on an example of effects of compensation of the “reactive energy”  $W$  of RL load shown in Fig. 8. To have these effects clearly visible, it was assumed that the fifth order harmonic of the supply voltage has the rms value  $U_5$  equal to the fundamental harmonic rms value  $U_1$ . It is, of course, unrealistically strong distortion, but we could expect that conclusions of the CPT are valid irrespective of the level of the supply voltage distortion.

At the supply voltage harmonics complex rms (crms) values

$$U_1 = U_5 = 100e^{j0^\circ} \text{ V}, \quad \|u\| = 100\sqrt{2} \text{ V}$$

the crms values of the load current harmonics are

$$I_1 = 70.7e^{-j45^\circ} \text{ A}, \quad I_5 = 19.9e^{-j79^\circ} \text{ A}, \quad \|i\| = 73.4 \text{ A}$$

so that, assuming that the supply voltage frequency is normalized to  $\omega_1 = 1$  rad/s, the “reactive energy”, is

$$W = \operatorname{Re} \sum_{n=1,5} \frac{U_n}{jn\omega_1} (Y_n U_n)^* = 0.538 \times 10^4 \text{ J.}$$

Capacitance of a shunt capacitor for the “reactive energy”  $W$  of the load compensation is equal to

$$C = \frac{W}{\|u\|^2} = 0.269 \text{ F.}$$

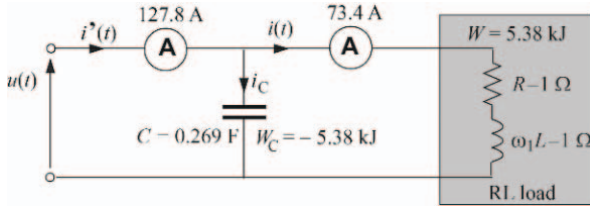


Fig. 8. Results of compensation of the “reactive energy”  $W$  of RL load.

The capacitor compensates the “reactive energy”  $W$  of the load, but it changes the crms values of the supply current harmonics to

$$I'_1 = 55.1e^{-j24.8^\circ} \text{ A}, I'_3 = 115.3e^{j88.0^\circ} \text{ A}, \|i\| = 127.8 \text{ A}$$

The results of compensation of this “energy” are shown in Fig. 8.

The “reactive energy”  $W$  of the compensated load is zero, but the compensator increases the void current rms value. Consequently, instead of improving the power factor, it was worsened.

## VI. DISTORTION POWER

According to the CPT, the load current of a purely reactive single-phase LC load is composed only of the reactive  $i_{rT}(t)$  current and the void  $i_v(t)$  current.

$$i(t) = i_{rT}(t) + i_v(t) \quad (53)$$

The supply current of a purely reactive load contains neither the active current, as defined in Fryze’s power theory [4], nor the scattered current, as defined in the CPC-based power theory [9, 16].

The reactive and void currents are mutually orthogonal, so that their rms values satisfy the relationship

$$\|i\|^2 = \|i_{rT}\|^2 + \|i_v\|^2. \quad (54)$$

Multiplying this formula by the square of the supply voltage rms value  $\|u\|$ , the power equation of reactive loads is obtained. It has the form

$$S^2 = Q_T^2 + D_T^2. \quad (55)$$

According to [20], the quantity

$$D_T = \|i_v\| \times \|u\| \quad (56)$$

is a distortion power of the load. In some papers on the CPT, such as [17], this quantity is called a void power.

The concept of a distortion power occurred for the first time in Budeanu’s power theory. It was defined as

$$D_B \stackrel{\text{df}}{=} \sqrt{S^2 - P^2 - Q_B^2}. \quad (57)$$

Indices T and B were used in (55 – 57) to distinguish distortion powers in Budeanu’s and in the CPT power theories. Despite having the same name, these are two different quantities.

Distortion power  $D_B$  is interpreted as a measure of the effect of the voltage and current mutual distortion on the apparent power  $S$  of the load. This interpretation was challenged in [11, 12], where it was demonstrated that

such interpretation was not right. There is no relation between distortion power  $D_B$  and the voltage and current mutual distortion.

Let us check whether distortion power  $D_T$  defined in the CPT is related to the load voltage and current mutual distortion. This is done below with a numerical analysis of a purely reactive load shown in Fig. 9

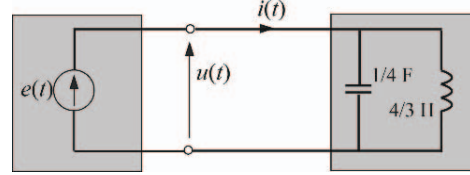


Fig. 9. Circuit with reactive load.

supplied with the voltage:

$$u(t) = \sqrt{2}(100 \sin \omega_1 t + 30 \sin 3\omega_1 t) \text{ V}, \omega_1 = 1 \text{ rad/s.}$$

The admittances of such a load for the voltage harmonics are  $Y_1 = -j1/2 \text{ S}$  and  $Y_3 = j1/2 \text{ S}$ . The “reactive energy”  $W$  of such load is equal to

$$W = - \sum_{n \in \{1, 3\}} \text{sgn}\{B_n\} |B_n| \frac{U_n^2}{n\omega_1} = 4.85 \text{ kJ.}$$

Since

$$\|\hat{u}\| = \sqrt{\sum_{n \in \{1, 3\}} \left(\frac{U_n}{n\omega_1}\right)^2} = \sqrt{\left(\frac{U_1}{\omega_1}\right)^2 + \left(\frac{U_3}{3\omega_1}\right)^2} = 100.50 \text{ V s}$$

the rms value of the reactive current  $i_{rT}(t)$  is

$$\|i_{rT}\| = \left\| \frac{W}{\|\hat{u}\|^2} \hat{u}(t) \right\| = \frac{|W|}{\|\hat{u}\|} = 48.26 \text{ A.}$$

The load current rms value is

$$\|i\| = \sqrt{\sum_{n \in \{1, 3\}} (Y_n U_n)^2} = \sqrt{(0.5 \times 100)^2 + (0.5 \times 30)^2} = 52.20 \text{ A.}$$

Since the active current does not exist in this circuit, the rms value of the void current is equal to

$$\|i_v\| = \sqrt{\|i\|^2 - \|i_{rT}\|^2} = \sqrt{52.2^2 - 48.26^2} = 19.90 \text{ A}$$

so that the distortion power

$$D_T = \|i_v\| \|u\| = 19.90 \times 104.40 = 2.08 \text{ kVA.}$$

The load current is equal to

$$\begin{aligned} i(t) &= \sqrt{2} \left[ 50 \sin \left( \omega_1 t - \frac{\pi}{2} \right) + 15 \sin \left( 3\omega_1 t + \frac{\pi}{2} \right) \right] = \\ &= \sqrt{2} \left[ 50 \sin \omega_1 \left( t - \frac{T}{4} \right) + 15 \sin 3\omega_1 \left( t - \frac{T}{4} \right) \right] \text{ A} = \\ &= \frac{1}{2} u \left( t - \frac{T}{4} \right). \end{aligned}$$

The load current is only shifted versus the voltage by  $T/4$ , as shown in Fig. 10. In spite of non-zero distortion power  $D_T$ , the voltage and current are not mutually distorted.

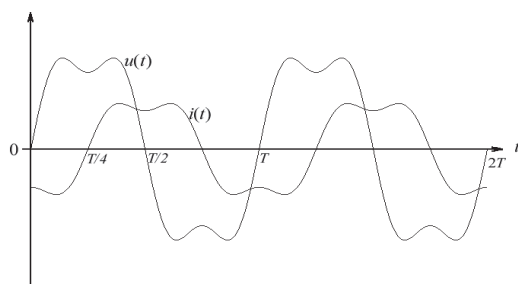


Fig. 10. Waveforms of the voltage and current.

It demonstrates that there is no relation between distortion power  $D_T$  and distortion of the load current with respect to the supply voltage.

This conclusion has a strong analogy to the conclusion on the distortion power  $D_B$  in Budeanu's power theory. Both in the CPT and in Budeanu's power theory, the name "distortion power" of  $D_B$  and  $D_T$  quantities suggests a relationship between these powers and the voltage and current mutual distortion. There is not such a relationship between these powers and the voltage and current distortion, however. The concept of these powers in both cases contributes to misinterpretation of power related phenomena in systems with nonsinusoidal voltage.

## VII. CONCLUSIONS

It was demonstrated in this paper that the Conservative Power Theory occurs to be a sort of return to its initial phase, to Budeanu concept. Although, unlike Budeanu's power theory, it is formulated in the time-domain and generalized to unbalanced three-phase loads, it has all deficiencies of Budeanu's power theory. The CPT follows Fryze's approach to power theory, meaning it is based on the current orthogonal decomposition, but repeats some of its deficiencies. Namely, just as Fryze's concept did not explain the physical meaning of the reactive current,  $i_{rF}(t)$ , the CPT also does not provide physical interpretation of the reactive current  $i_{rT}(t)$ , because the "reactive energy"  $W$  is not a physical quantity. Consequently, the void current  $i_v(t)$  also does not have any physical meaning. It is associated in the CPT with distortion power  $D_T$ , but similarly as it was with Budeanu's distortion power  $D_B$ , there is no relationship between distortion power  $D_T$  and the voltage and current mutual distortion. It means that the Conservative Power Theory misinterprets power related phenomena in electrical circuits. Moreover, the Conservative Power Theory is no more "conservative" than Budeanu's power theory.

Like Budeanu's power theory the CPT does not provide right fundamentals for reactive compensation, because compensation of the reactive current  $i_{rT}(t)$  as defined in the CPT can change the rms value of the void current and consequently, its compensation, as shown in this paper, can increase the supply current rms value, thus degrade the power factor.

Received on July 1, 2016

Editorial Approval on November 15, 2016

## REFERENCES

- [1] Ch.P. Steinmetz, "Is a phase-shift in the current of an electric arc?" (in German), *Elektrotechnische Zeitschrift*, Heft 42, pp. 567-568, 1892.
- [2] M.A. Illović, "Definition et mesure de la puissance et de l'énergie réactives," *Bull. Soc. Franc. Electriciens*, 1925.
- [3] C.I. Budeanu, "Puissances réactives et fictives," *Institut Romain de l'Énergie*, Bucharest, 1927.
- [4] S. Fryze, "Active, reactive and apparent power in circuits with nonsinusoidal voltages and currents," (in Polish), *Przegląd Elektrotechniczny*, z.7, z.8, (1931), z.22, (1932).
- [5] B.D.H. Tellegen, "A general network theorem with applications," *Philips Research Reports*, (Philips Research Lab.) No. 7, 1952.
- [6] Shepherd, P. Zakikhani, "Suggested definition of reactive power for nonsinusoidal systems," *Proc. IEE*, 119, No. 9, pp. 1361-1362, 1972.
- [7] Z.J. Nowomiejski, "Analysis of electrical circuits with periodic, non-sinusoidal quantities," (in German), *Akademische Verlagsgesellschaft*, Leipzig, 1967.
- [8] German Standard, DIN, "Wechselstromgrossen", pp. 303-310, 1972.
- [9] L.S. Czarnecki, "Considerations on the reactive power in nonsinusoidal situations," *IEEE Trans. Instr. Meas.*, Vol. 34, No. 3, 1984.
- [10] M. Hasler, J. Neirynek, *Circuits nonlinéaires*, Press Polytechniques Romandes, Lausanne, 1985.
- [11] L.S. Czarnecki, "What is wrong with the Budeanu concept of reactive and distortion powers and why it should be abandoned," *IEEE Trans. Instr. Meas.*, Vol., 1987, IM-36, No. 3, pp. 834-837, Sept. 1987.
- [12] L.S. Czarnecki, "Budeanu and Fryze: Two frameworks for interpreting power properties of circuits with nonsinusoidal voltages and currents," *Archiv fur Elektrotechnik*, (81), N. 2, pp. 5-15, 1997.
- [13] The New IEEE Standard Dictionary of Electrical and Electronics Terms, *IEEE Inc.*, New York, 1997.
- [14] IEEE Trial Use Standard for the Measurement of Electric Power Quantities Under Sinusoidal, Nonsinusoidal, Balanced and Unbalanced Conditions. IEEE 1459-2000.
- [15] P. Tenti, P. Mattavelli, "A time-domain approach to power terms definitions under non-sinusoidal conditions", *Proc. of the Sixth Int. Workshop on Power Definitions and Measurements under Nonsinusoidal Conditions*, 2003.
- [16] L.S. Czarnecki, "Currents' Physical Components (CPC) concept: a fundamental for power theory," *Przegląd Elektrotechniczny*, R84, No. 6/2008, pp. 28-37, 2008.
- [17] F.P. Marafao, A. Costabeber, P. Tenti, "Application of Conservative Power Theory to cooperative control of distributed compensators in smart grids," *International School on Nonsinusoidal Currents and Compensation, ISNCC 2010*, Łagów, Poland, 2010.
- [18] IEEE Trial Use Standard for the Measurement of Electric Power Quantities Under Sinusoidal, Nonsinusoidal, Balanced and Unbalanced Conditions. IEEE 1459-2010.
- [19] P. Tenti, H.K.M. Parades, P. Mattavelli, "Conservative Power Theory, a framework to approach control and accountability issues in smart grids," *IEEE Trans. on Pow. Elect.*, Vol. 26, No. 3, pp. 664-673, 2011.
- [20] H.K.M. Parades, F.P. Marafao, P. Mattavelli, P. Tenti, "Application of Conservative Power Theory to load and line characterization and revenue metering", *2012 Int. Workshop on Applied Measurements for Power Systems*, DOI: 10.1109/AMPS.2012.6343993, pp. 1-6, 2012.
- [21] L.S. Czarnecki, "Critical comments on the Conservative Power Theory (CPT)", *Proc. of International School on Nonsinusoidal Currents and Compensation, ISNCC 2015*, Łagów, Poland.
- [22] L.S. Czarnecki, "From Steinmetz to Currents' Physical Components (CPC): History of the power theory development", *13th Int. Conf. on Applied and Theoretical Electricity (ICATE 2016)*, 2016, Craiova, Romania.

# Modeling and Torque Ripple Control in Faulty SPMSM

Elmehdi Bahri<sup>\*†</sup>, Remus Pusca<sup>†</sup>, Raphael Romary<sup>†</sup> and Driss Belkhat<sup>\*</sup>

<sup>\*</sup>LSET, Cadi Ayyad University, BP. 549, Marrakech, Morocco, dbelkhat@gmail.com

<sup>†</sup>Univ. Artois, EA. 4025 LSEE, F-62400, Bethune, France, remus.pusca@univ-artois.fr

**Abstract** - This paper presents a model of a Surface Permanent Magnet Synchronous Motor which can be used in a faulty case and a torque ripple control approach developed to be applied if the faulty case is detected. Two faulty cases are considered for study, the first consider an asymmetry between the stator phases of the motor created by unbalanced number of turns and the second a short circuit between the stator windings of the motor. Proposed torque ripple control use a phasor approach to provides the current reference for stator asymmetry and an injection of an inverse current for stator short circuit fault in order to decrease the motor torque ripple. The torque control has been implemented using a model of surface permanent magnet synchronous motor based on the dynamic equations. Simulation and experimental results highlight the link between the faulty and the torque ripple and show the possibility to decrease in this case the torque ripples by changing a balanced sinusoidal current reference by unbalanced one. In practical tests the impact of the unbalanced system of currents in the torque variation is studied using an analysis of vibratory harmonic measured at twice of the supply frequency.

**Keywords:** SPMSM, stator fault modeling, torque ripple control.

## I. INTRODUCTION

Surface Permanent Magnet Synchronous Motors (SPMSM) are widely used in various applications such as airplanes, industry, electric vehicles, etc ... These machines have multiple advantages like high performance, high torque density, robust construction and no use of brushes [1,2]. However, torque ripples generated by SPMSM and iron losses in the rotor are factors that hinder their use and reduce SPMSM efficiency [3-5].

The unbalanced of magnetic field in an electric motor, the demagnetization of the rotor, a short circuit between turns or rotor eccentricity, leads to increase the torque ripple and also the losses [6-8]. In these cases the global system reliability can decrease if the control of the currents is not adjusted for taking into account the motor fault [9, 10]. This is true for some specific applications such as those related to electric vehicles or aircraft systems.

Reducing torque ripple in a healthy synchronous motor has been the subject of several researches and different strategies have been proposed. The best known method is to control the stator currents to compensate the torque ripple. These currents are calculated by several methods, some of them uses the decomposition of the electromo-

tive force in Fourier series to determine a limited number of current harmonics while others use the finite element method to estimate their parameters (amplitude, frequency) [11-13] or methods developed for determination of harmonic currents through an analytical modeling approach and an optimization criterion [14].

In the case of a faulty synchronous motor the torque ripple increases. As solution, some works develop methods based on dynamic modeling of the faulty machine that use mathematical development with voltages, flux and currents, separated in direct and inverse components [15].

Another method developed for multiphase motors use a phasor approach and the electromotive force to compute the optimal current references in order to maintain a smooth torque and minimal joule losses [16].

The aim of presented work is to compensate the torque ripple in a faulty case. The proposed method is based on control strategy of the stator currents obtained by a product of two phasors, the stator flux space phasor and current space phasor. A simplified analytical model of a SPMSM is used to elaborate the control strategy developed to decrease the effect of the fault. The considered fault is a stator's winding asymmetry and the proposed strategy control allows one to decrease the torque ripple and to maintain motor performance near the healthy case one. In this paper, the stator's winding asymmetry is generated by about 5.5 % lack of turns of the phase "A" of the motor.

This paper is organized as follows: in section II the model developed of the surface permanent magnet synchronous motors is presented. In section III the approach used to calculate the reference currents in order to reduce the torque ripple is given. Simulation results are presented in the last section of the paper to validate the proposed approach.

## II. SPMSM ANALITICAL MODEL

The developed model to simulate the SPMSM operating is a three-phase dynamic model based on the equivalent electrical circuit. This model enables to consider the stator winding asymmetry fault easily. However it does not take into account the iron losses and saturation [10].

The electrical model considered is shown in Fig.1. With this model, it is possible to introduce the fault (unbalance number of turns between the three phases of the motor stator windings) by adapting the different machine parameters for each phase.

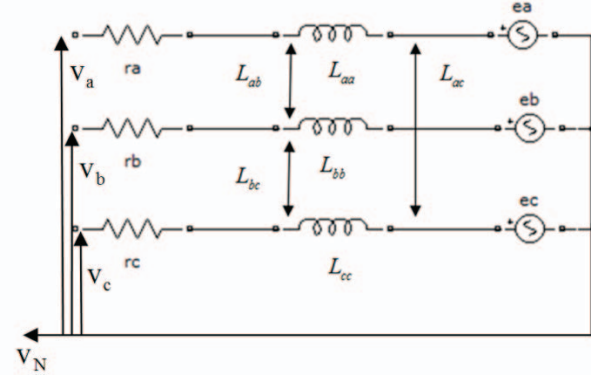


Fig. 1. Electrical model of the SPMSM used for simulation of the winding asymmetry fault.

In this model  $r_a, r_b, r_c, L_{aa}, L_{bb}, L_{cc}$  are the resistances and the main cyclic self inductances of each stator phase,  $e_a, e_b, e_c$  are the electromotive forces and  $L_{ab}, L_{bc}, L_{ac}$  are the mutual inductances of stator windings.

#### A. Electrical Equations

In the proposed model the following electrical equations are considered:

$$V_{abc} = r_{abc} i_{abc} + \frac{d\psi_{abc}}{dt} \quad (1)$$

$$\psi_{abc} = L_{abc} i_{abc} + \psi_{rabc} \quad (2)$$

where  $i_{abc}$  are the stator currents,  $\psi_{abc}$  the stator flux and  $V_{abc}$  the phase-to-neutral voltage. These parameters can be expressed as:

$$V_{abc} = \begin{bmatrix} V_a \\ V_b \\ V_c \end{bmatrix} \quad e_{abc} = \begin{bmatrix} e_a \\ e_b \\ e_c \end{bmatrix} \quad i_{abc} = \begin{bmatrix} i_a \\ i_b \\ i_c \end{bmatrix} \quad \psi_{abc} = \begin{bmatrix} \psi_a \\ \psi_b \\ \psi_c \end{bmatrix}$$

$$r_{abc} = \begin{bmatrix} r_a & 0 & 0 \\ 0 & r_b & 0 \\ 0 & 0 & r_c \end{bmatrix} \quad L_{abc} = \begin{bmatrix} L_{aa} & L_{ab} & L_{ac} \\ L_{ba} & L_{bb} & L_{bc} \\ L_{ca} & L_{cb} & L_{cc} \end{bmatrix} \quad \psi_{rabc} = \begin{bmatrix} \psi_{ra} \\ \psi_{rb} \\ \psi_{rc} \end{bmatrix}$$

where  $L_{abc}$  is the inductance matrix,  $\psi_{rabc}$  the phasor of rotor flux and  $e_{abc}$  the electromotive force vector. In this model it is considered that the neutral point is not connected, therefore the sum of the stator currents is equal to zero:

$$i_a + i_b + i_c = 0 \quad (3)$$

the stator fluxes are defined as:

$$\begin{aligned} \psi_a &= L_{aa} i_a + L_{ab} i_b + L_{ac} i_c + \psi_{ra} \\ \psi_b &= L_{ba} i_a + L_{bb} i_b + L_{bc} i_c + \psi_{rb} \\ \psi_c &= L_{ca} i_a + L_{cb} i_b + L_{cc} i_c + \psi_{rc} \end{aligned} \quad (4)$$

Considering the flux in each coil expressed with only  $i_a$

and  $i_b$  currents (4) can be expressed as:

$$\begin{aligned} \psi_a &= (L_{aa} - L_{ac}) i_a + (L_{ab} - L_{ac}) i_b + \psi_{ra} \\ \psi_b &= (L_{ba} - L_{bc}) i_a + (L_{bb} - L_{bc}) i_b + \psi_{rb} \\ \psi_c &= (L_{ca} - L_{cc}) i_a + (L_{cb} - L_{cc}) i_b + \psi_{rc} \end{aligned} \quad (5)$$

In the developed SPMSM model for healthy and faulty case, (1-5) are used to determine the expression of flux and currents. In presence of the fault, the potential of the neutral point can vary. For modeling, equations independent of neutral point can be used:

$$\frac{d\psi_a}{dt} - \frac{d\psi_b}{dt} = V_a - V_b - r_a i_a + r_b i_b \quad (6)$$

$$\frac{d\psi_a}{dt} - \frac{d\psi_c}{dt} = V_a - V_c - (r_a + r_c) i_a - r_c i_b$$

The current expressions are obtained from (5) and (3):

$$\begin{aligned} i_a &= \frac{B(\psi_a - \psi_c) - D(\psi_a - \psi_b - \psi_{ra} + \psi_{rb})}{BC - AD} \\ i_b &= \frac{C(\psi_a - \psi_b - \psi_{ra} + \psi_{rb}) - A(\psi_a - \psi_c)}{BC - AD} \\ i_c &= -i_a - i_b \end{aligned} \quad (7)$$

where  $A = L_{aa} - L_{ac} - L_{ba} + L_{bc}$ ;  $B = L_{ab} - L_{ac} - L_{bb} + L_{bc}$ ;  $C = L_{aa} - L_{ac} - L_{ca} + L_{cc}$  and  $D = L_{ab} - L_{ac} - L_{cb} + L_{cc}$

#### B. Electromagnetic Torque

In the considered model, the electromagnetic torque is obtained from vector product between the flux and the current space phasors. It can be expressed:

$$T_e = \frac{3p}{2} [\Psi_s \wedge i_s] \quad (8)$$

where  $p$  is the pole pair number.  $\Psi_s$  and  $i_s$  are the space vector of the flux and the stator current defined as:

$$\Psi_s = \frac{2}{3} [\psi_a + a\psi_b + a^2\psi_c] \quad (9)$$

$$i_s = \frac{2}{3} [i_a + ai_b + a^2i_c] \quad (10)$$

with  $a = \exp(i2\pi/3)$ .

#### C. Mechanical Equation

The SPMSM rotor angular speed  $\Omega$  is obtained from classical mechanical equation:

$$J \frac{d\Omega}{dt} = T_e - f_f \Omega - T_r \quad (11)$$

where  $J$  is the moment of inertia,  $T_e$  the electromagnetic torque,  $T_r$  the load torque and  $f_f$  the friction parameter. The rotor angular speed is used to calculate the angular position:

$$\theta = \int \Omega dt \quad (12)$$

#### D. SPMSM Simulation Model

##### 1) Principle for healthy case and faulty case

The bloc diagram presented in Fig 2 shows the principle of the simulation used in the considered model. The rotor flux values are stored in recording tables. Then they are read as a function of the angle  $\theta$  of the rotor position. In this model a sine signal is considered for simulation but in real case this parameter can be obtained from integration of electromotive forces which are previously identified using the SPMSM in alternator mode:

$$\psi_{rabc} = \int e_{abc} dt \quad (13)$$

The rotor position angle is obtained from electromagnetic and load torque using (11) and (12). For torque calculation the phasor approach given by (8),(9) and (10) is used. At the end of the bloc diagram, the currents  $i_a, i_b, i_c$  supplying the SPMSM are obtained from electrical equations where the stator flux given by (4) at  $t=t-\Delta t$  ( $\Delta t$  simulation step) is also used as input value.

##### 2) SPMSM parameters

To simulate the faulty case, 1/18 lack of turns of the phase "A" winding is considered. Each phase is composed of 6 elementary coils with distribution presented in Fig. 3.

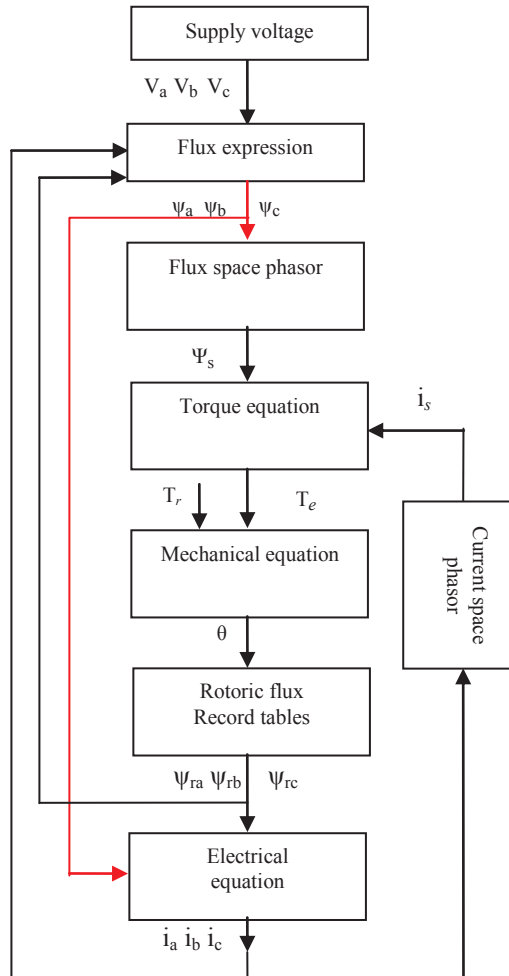


Fig. 2. Bloc diagram of the SPMSM model used in simulation for healthy and faulty case.

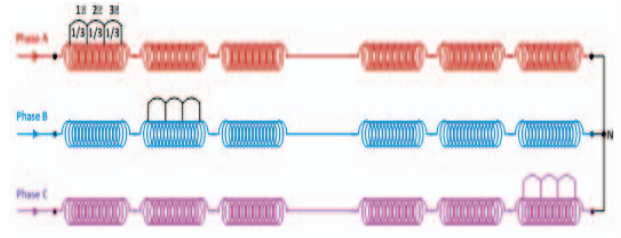


Fig.3. Turns distribution of the SPMSM used for simulation of the winding asymmetry fault. The first 1/3 turns of the first elementary coil of the phase "A" are not supplied by  $V_a$  voltage in the faulty case.

The fault corresponds to 1/3 of the first elementary coil of the phase "A". This lack of turns introduces a change for each corresponding parameters taken in consideration by a step changing at  $t=30s$  from healthy to faulty parameters value during simulation.

The parameter values used in simulation for healthy and faulty case are presented in Table I where the subscript "f" means that the resistances and the inductances are related to the faulty case.

In practical case the determination of the SPMSM parameters in the healthy and faulty case is based on the method presented in [17] which use the magnetomotive force (mmf) generated by the stator winding in healthy and faulty case to calculate the inductance. The following relationship is used:

$$L_{xy} = \mu_0 RL \int_0^{2\pi} N_x(\alpha_s) N_y(\alpha_s) e^{-j(\alpha_s)} d\alpha_s \quad (14)$$

where:  $L_{xy}$  is the self inductance ( $x=y$ ), mutual inductance ( $x \neq y$ ) between windings  $x$  and  $y$ ;  $\mu_0$  permeability of vacuum;  $R$  the radius of the stator;  $L$  the length of the slots;  $N_x(\alpha_s), N_y(\alpha_s)$  are magnetomotive force the of the windings 'x' respectively 'y' crossed by a unit current;  $e$  thickness of the air gap;  $\alpha_s$  the angular abscissa of a point in the air gap in a stator reference. The numerical values applied in simulation are:  $V_A, V_B, V_C = 200$  V,  $J=0.002$  Nm<sup>2</sup>,  $F_f=0.0075$ .

#### III. PHASOR APPROACH FOR ESTIMATE THE REFERENCE CURRENTS IN ASYMMERTY FAULT

The objective of the presented application is the reduction of torque ripple which increases in faulty case. According to the study of the torque equation, this one is derived from a vector product between the flux space vector and current space vector.

TABLE I.  
PARAMETERS USED FOR SPMSM MODELISATION IN HEALTHY AND FAULTY CASE

$r_a$ ( $\Omega$ )	$r_b$ ( $\Omega$ )	$r_c$ ( $\Omega$ )	$L_{aa}$ (mH)	$L_{bb}$ (mH)	$L_{cc}$ (mH)	$L_{ab}$ (mH)	$L_{ac}$ (mH)	$L_{ba}$ (mH)
3.56	3.56	3.56	74.3	74.3	74.3	-37.2	-37.2	-37.2
$L_{bc}$ (mH)	$L_{ca}$ (H)	$L_{cb}$ (H)	$L_{aaf}$ (H)	$L_{abf}$ (H)	$L_{acf}$ (H)	$L_{baf}$ (H)	$L_{caf}$ (H)	$r_{af}$ ( $\Omega$ )
-37.2	-37.2	-37.2	70.2	-35.1	-35.1	-35.1	-35.1	3.362

Therefore, to produce a maximum torque, it is necessary that the current and the flux are in quadrature. In the basic control of the synchronous machine, the current is forced to move following the q axis ( $i_d=0$ ). This procedure will not be verified in the case of a faulty machine where the rotor flux is no longer along the “d” axis [18]. So the control must respect following proprieties:

1) following a constant torque

$$T_e = \frac{3p}{2} (\psi_d i_q - \psi_q i_d) = cst \quad (15)$$

2) having a maximum torque (the flux is in quadrature whit the current

$$\psi_d i_d = -\psi_q i_q \quad (16)$$

where  $i_d$  and  $i_q$  are direct and quadrature components of the space phasor of the stator reference current. From (15) it can be written:

$$\begin{cases} i_d = -\frac{\psi_q i_q}{\psi_d} \\ i_q = -\frac{\psi_d i_d}{\psi_q} \end{cases} \quad (17)$$

Replacing (17) in the torque equation, the current reference giving constant torque without variations is obtained:

$$\begin{cases} i_d = -\frac{2T_e}{3p} \frac{\psi_q}{\psi_q^2 + \psi_d^2} \\ i_q = \frac{2T_e}{3p} \frac{\psi_d}{\psi_q^2 + \psi_d^2} \end{cases} \quad (18)$$

The direct and quadrature components of the flux space phasor  $\psi_d$  and  $\psi_q$  used in (18) are obtained from (9) and (5) considering the real and imaginary components of the space phasor flux:

$$\begin{cases} \psi_d = \text{Re}(\psi_s) \\ \psi_q = \text{Im}(\psi_s) \end{cases} \quad (19)$$

The global scheme of the phasor approach used to determine the current references for each phase of the motor is presented in Fig. 4a and a detailed implementation in matlab simulink of the phasor approach in Fig. 4b.

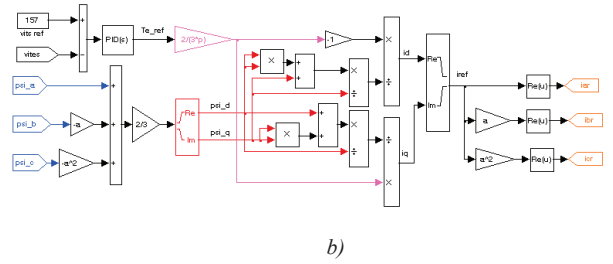
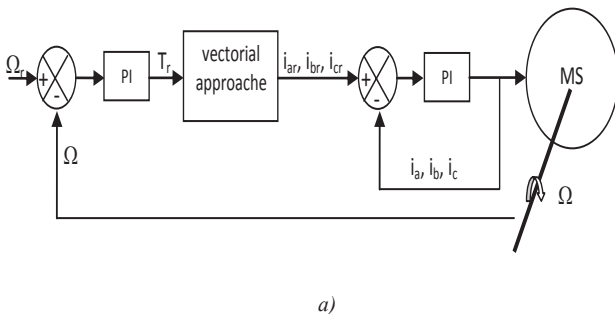


Fig.4. Control loop applied to SPMSM a) scheme of global phasor control loop b) matlab implementation of phasor approach.

In matlab implementation the proportional integral constant values of the PI blocs used in the control loop for torque reference  $T_r$  are  $K_{t_p}=2$ ,  $K_{t_i}=1$  and for current references are  $K_{c_p}=1000$ ,  $K_{c_i}=500$ .

#### IV. APPROACH FOR ESTIMATE THE REFERENCE CURRENTS IN INTER-TURNS SHORT CIRCUIT FAULT

If a stator inter-turns short circuit appear it induces torque ripple at twice of supply frequency and reduces the average torque [19, 20]. The torque harmonic component at twice of supply frequency mainly provides from the stator inverse sequence space harmonics of magnetomotive force (mmf) at  $h = -2$  and by the fundamental rotor space harmonics flux density. In order to reduce this torque harmonic it is necessary to cancel the mmf at  $h=-2$ , for the considered machine with 2 pole pairs [21].

The SPMSM is assumed to be supplied with sine currents. The strategy for calculation of stator currents to decrease the space harmonic stator mmf at  $h = -2$  in the case of a stator inter-turn short circuit in one phase winding is performed using the complex notation of the mmf components. So in order to decrease the negative sequence mmf of faulty SPMSM, an analytical method is developed which allow to determine the rms value  $I_i$  which must be injected in the global current references [21].

For study it is considered a stator elementary coil composed of two beams, one of them has a side inserted into the slot 3 and the other side inserted into the slot 10. In the case when the short-circuit fault occurs in this coil the relationship used between the direct current and the inverse current [22] used to compensate the harmonic of rank  $h=-2$  is given by:

$$\underline{I}_i = \frac{I_d \sum_{j=3,10} e^{j(-2\beta_j^s + \varphi_{dj})} - I_{cc} \sum_{j=3,10} e^{j(-2\beta_j^s + \varphi_{ccj})}}{\sum_{j=1}^{N_t} e^{j(-2\beta_j^s + \varphi_{ij})}} \quad (20)$$

where  $I_{cc}$  is the rms value of the current in the coil where occurs the inter-turn short circuit and  $I_d$  the rms value of direct balanced currents system. The other parameters presented in (20) are:

$\beta_j^s$  : angular position of the stator slot  $j$ .

$\varphi_{dj}$  : phase angle of  $I_d$  current in the slot  $j$ .

$\varphi_{ccj}$  : phase angle of  $I_{cc}$  in the slot  $j$ .

$\varphi_{ij}$  : phase angle of inverse current  $I_i$  in the slot  $j$ .

$N_t^s$  : total stator slot number.

Equation (20) leads to decrease the mmf space harmonic of rank  $h=-2$ , and then to reduce the torque ripple at twice the supply frequency. To simplify this equation, it is put in following form:

$$\bar{I}_i = \frac{I_d B - I_{cc} A}{C} \quad (21)$$

with A, B and C

$$A = \sum_{j=3,10} e^{j(-2\beta_j^s + \varphi_{csj})}, B = \sum_{j=3,10} e^{j(-2\beta_j^s + \varphi_{dj})},$$

$$C = \sum_{j=1}^{N_t^s} e^{j(-2\beta_j^s + \varphi_{sj})}$$

In Fig.5 it is presented the diagram computation method of the temporal corrected current reference able to decrease the torque ripple. To validate this control strategy, first a direct balanced currents system of  $I_d$  rms value and  $f$  frequency is considered. The inverse current  $\bar{I}_i$  is given by (20), and the reference current  $\bar{I}_{ar}$ ,  $\bar{I}_{br}$ ,  $\bar{I}_{cr}$  to cancel torque ripple at  $2f$  is calculated. Finally the time current references  $\dot{i}_{ar}$ ,  $\dot{i}_{br}$ ,  $\dot{i}_{cr}$  are reconstructed. In following expressions “ $a$ ” is a complex number:  $a = e^{j2\pi/3}$ .

## V. SIMULATION RESULTS

The simulation model of the SPMSM has been realized using MATLAB / Simulink. In order to test the torque regulation, a fault is simulated at  $t=30s$ .

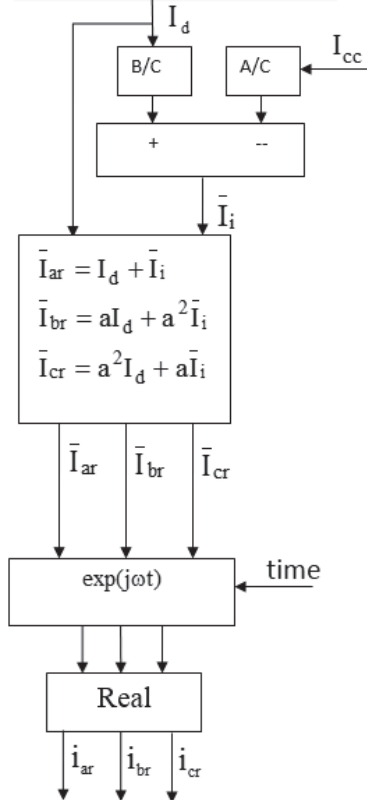


Fig. 5. Diagram computation of the temporal corrected currents reference

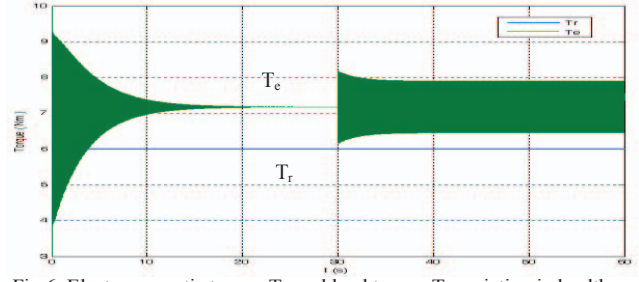


Fig.6. Electromagnetic torque  $T_e$  and load torque  $T_r$  variation in healthy and faulty case for SPMSM supplied by balanced system of currents. Fault simulated at  $t=30s$ .

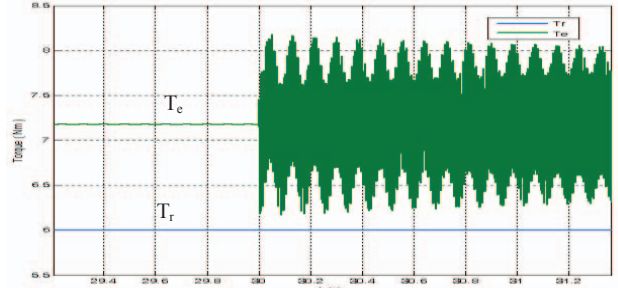


Fig.7. Zoom of electromagnetic and load torque ( $T_e$  and  $T_r$ ) around to faulty case for motor supplied by balanced system of currents.

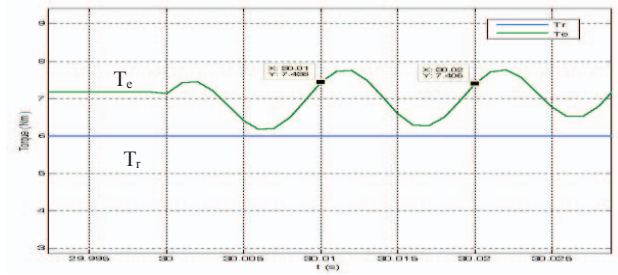


Fig.8. Zoom of electromagnetic and load torque ( $T_e$  and  $T_r$ ) at  $t=30s$  to faulty case for motor supplied by balanced system of currents. Torque undulation at 100 Hz.

The fault is located in the first elementary section of the phase “A” by reducing its number of turns of two thirds of one elementary section. To analyze the impact of the current on the torque and speed variation, two cases are studied: the first one considers the motor supplied by a balanced system of currents, the second one considers the motor supplied by currents obtained with phasor approach presented in (18).

In this case the motor is integrated in a control loop in order to maintain the control law during the healthy and faulty cases.

The variation of electromagnetic and load torques ( $T_e$ ,  $T_r$ ) for SPMSM supplied by balanced system of currents is shown in Fig. 6. In this case, the load torque remains constant at 6 Nm until the fault appear at  $t=30s$ .

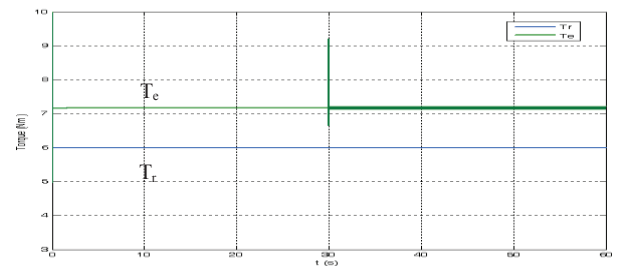


Fig.9. Electromagnetic  $T_e$  and load torque  $T_r$  variation in healthy and faulty case for SPMSM supplied by unbalanced system of currents during the fault. Fault simulated at  $t=30s$ .

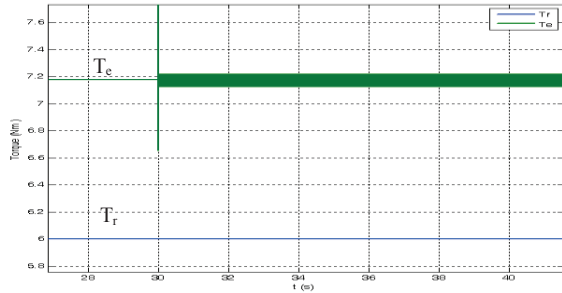


Fig. 10. Zoom of electromagnetic and load torque ( $T_e$  and  $T_r$ ) around to faulty case for SPMSM supplied by unbalanced system of currents during the fault.

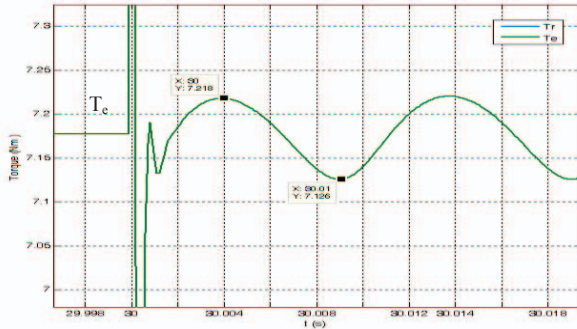
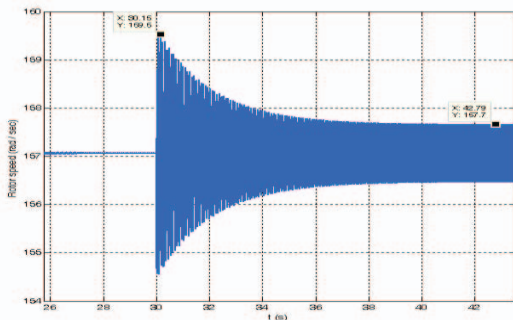


Fig. 11. Zoom of electromagnetic torque ( $T_e$ ) at  $t=30s$  to faulty case for SPMSM supplied by unbalanced system of currents. Torque undulation at 100 Hz.

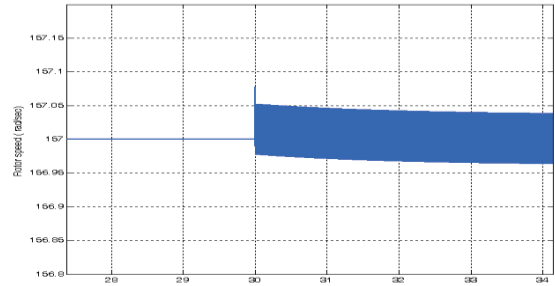
The Fig. 7 shows a zoom around the time when the fault occurs. It can be remarked the torque variation between  $T_{min}= 6.2Nm$  and  $T_{max}= 8.2Nm$ . In Fig. 8 it is shown a zoom of the torque variation for the first two periods after the fault appearance. It can be noticed the electromagnetic torque variation at 100Hz frequency which corresponds to the double frequency of the supply currents (50Hz).

The torque variation can be demonstrated in practical tests by analyzing the spectrums of an accelerometer. The amplitude of vibration harmonic at 100Hz given by the accelerometer increases in faulty case.

The next simulation presented in Fig. 9 shows the variations of electromagnetic and load torques for SPMSM integrated in a control loop using a flux space vector control. Here the reference currents are calculated for each phase in order to decrease the torque variation so, during the faulty case the motor is supplied by unbalanced system of currents. Figure 10 shows a zoom of the Fig.9 around the time when the fault occurs and Fig. 11 a zoom of the torque variation for the first two periods after the fault appearance. It can be noticed that in presence of a flux control, one can obtain an important decrease of the torque variation ( $T_{min}= 7.12 Nm$  and  $T_{max}= 7.22 Nm$ ) compared to the case without phasor flux control.



a)

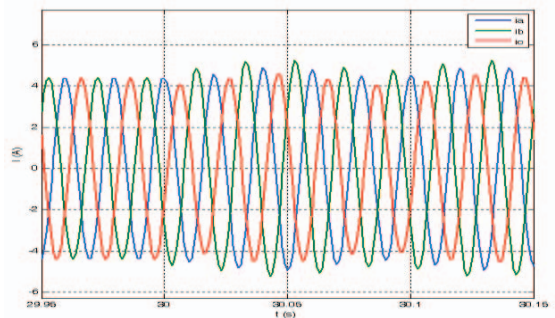


b)

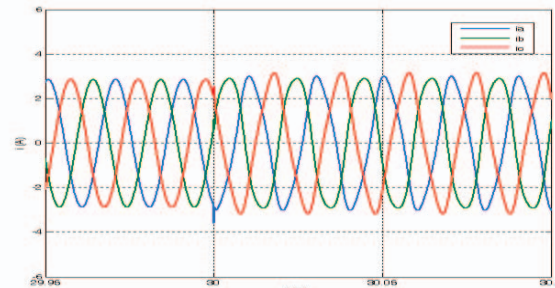
Fig. 12. Speed variation during the faulty case for SPMSM supplied by: a) balanced system of currents, b) unbalanced system of currents.

The variation of the rotor speed around of  $t=30s$  is presented in Fig. 12. In the case of a faulty SPMSM supplied by balanced system of currents (Fig.12.a) the speed variation takes values between  $\Omega_{min}= 156.5 rad/sec$  and  $\Omega_{max}= 157.7 rad/sec$ . For a faulty SPMSM supplied by unbalanced system of currents (Fig. 12.b) like in the case of the torque, the speed variation is much decrease (between  $\Omega_{min}= 156.98 rad/sec$  and  $\Omega_{max}= 157.5 rad/sec$ ) and the time of transient state is reduced.

Figure 13.a shows the currents variation for a motor supplied by balanced system of currents during the faulty case (starting at  $t=30s$ ) and Fig. 13.b shows the currents waveform for SPMSM integrated in a control loop with unbalanced currents during faulty operation. In this case a control in quadrature between the stator flux and the currents is considered. It can be remarked a higher amplitude of the currents in Fig. 13.a and more variation during the faulty state in correlation with more important torque ripple as shown in Fig. 6, Fig. 7 and Fig.8. The decrease of the current amplitude in Fig.13.b for the same load and electromagnetic torque can be explained by the optimization of the quadrature control.



a)



b)

Fig. 13. Current variation during the faulty case for SPMSM supplied by: a) system without currents control b) unbalanced system of currents.

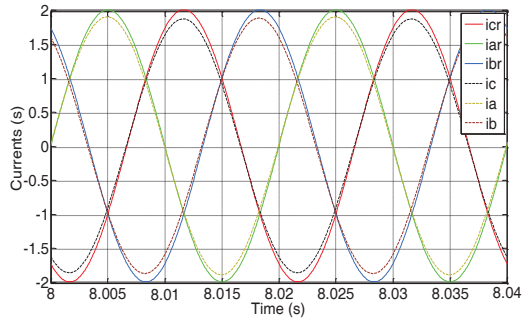


Fig. 14. Balanced stator currents supplying the faulty SPMSM: the reference and supply current.

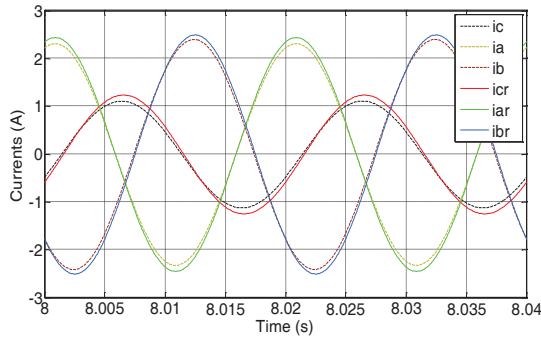


Fig. 15. Corrected stator currents for the faulty SPMSM: the reference and supply current.

The simulation case for a short-turn introduced into the first elementary section located in the winding phase A (Fig.3) is presented in the next simulations.

In Fig. 14 is simulated the currents variation for faulty SPMSM supplied by balanced currents and in Fig. 15 the currents variation faulty SPMSM supplied by corrected currents. In considered faulty case the short-turns current has a peak value of 14A with the same frequency as the supply currents and the inverse current is  $I_i = 0.53A$  rms value. It can be remarked that the currents are still regulated and the references make an unbalanced system.

### VI. EXPERIMENTAL RESULTS

Simulations presented in paragraph V shows that it is possible to reduce the torque variation for asymmetry or short circuit in the stator windings of SPMSM by using adapted unbalanced current references. In experimental tests the influence of unbalanced currents in the decrease of torque variation if a faulty appears is bring to the fore by using an accelerometer sensor as shown in Fig. 16.



Fig. 16. Measurement of SPMSM vibrations in faulty case.

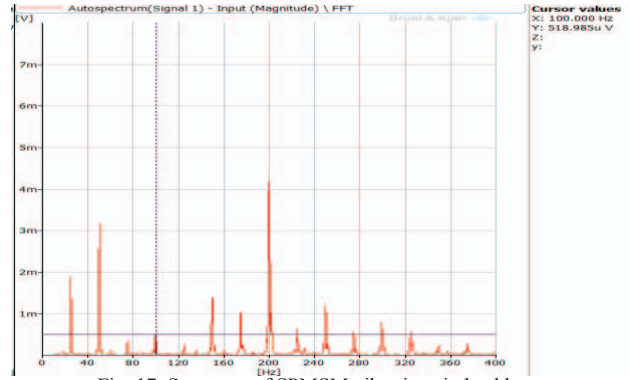


Fig. 17. Spectrum of SPMSM vibrations in healthy case.

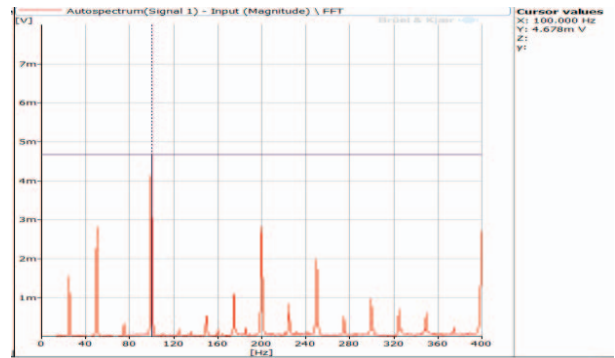


Fig. 18. Spectrum of SPMSM vibrations in faulty case.

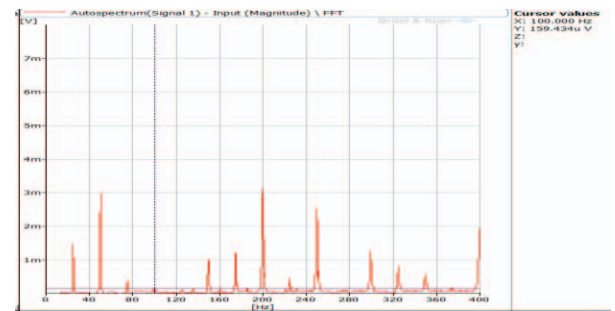


Fig. 19. Spectrum of SPMSM vibrations in faulty case after injection of inverse current.

The accelerometer sensor is connected to a frequency analyzer Brüel&Kjær 3560 which give the FFT spectrum of measured signal.

The spectrums for healthy machine, machine with short-turn faulty in the windings of the phase A and machine with correction by injection of an inverse current  $I_i$  are presented in Fig. 17, Fig. 18 and Fig. 19. Analyzing the accelerometer spectrum we can remarked in Fig. 17 the vibration harmonic measured at frequency 100Hz (rank  $h=2$ ) have  $519\mu V$  amplitude; in Fig. 18 the same harmonic increase at  $4670\mu V$  and in Fig. 19 after correction with imbalanced currents the amplitude of harmonic at frequency 100Hz decrease at  $159.43\mu V$ . This experimental test confirms the possibility to decrease the torque ripple by using specific non-balanced supply currents.

### VII. CONCLUSION

This paper proposes a model for a Surface Permanent Magnets Synchronous Motor (SPMSM) which allows to study the motor torque ripple and an adapted current con-

trol in healthy and faulty case. The simulation result has shown the link between the presence of the fault in the motor and the increase of the torque ripple. As solution to reduce the torque ripples it is proposed, an adequate control of the currents using a phasor approach for asymmetry fault or injection of an inverse current for short-circuit fault. This approach is based on the use of unbalanced currents.

The simulation has been tested considering an asymmetry created by unbalanced number of turns in the motor stator windings and a short circuit in the stator windings of the SPMSM phase A. This solution does not affect the motor operation but we must mention here that the variation of absorbed power from supply has an important increase and this solution must be correlated in practical applications with the performances of the available supply used for the global system

Received on October 1, 2016

Editorial Approval on November 11, 2016

#### REFERENCES

- [1] S.Li, C.Xia, X.Zhou, "Disturbance rejection control method for permanent magnet synchronous motor speed-regulation system", *Mechatronics*, vol. 22, pp. 706–714, 2012.
- [2] C.A. Borghi, D. Casadei, M. Fabbri, and G.Serra "Reduction of the Torque Ripple in Permanent Magnet Actuators by a Multi-Objective Minimization Technique", *IEEE Trans. Magn.* vol. 34, pp. 2869-2872, 1998.
- [3] Y. M. Abdel-Rady, "A newly designed instantaneous-torque control of direct-drive PMSM servo actuator with improved torque estimation and control characteristics", *IEEE Trans. Ind. Electron.*, vol. 54, pp. 2864 – 2873, 2007.
- [4] G. Pellegrino, P. Guglielmi, A. Vagati, F. Villata, "Core losses and torque ripple in IPM machines: dedicated modeling and design tradeoff", *IEEE Trans. Ind. Appl.* vol. 46, pp. 2381-2391, 2010.
- [5] C. Mademlis, N. Margaris, "Loss minimization in vector-controlled interior permanent-magnet synchronous motor drives", *IEEE Trans. Ind. Electron.* vol. 49, pp. 1344-1347, 2002.
- [6] B. M. Ebrahimi, J. Faiz, "Configuration impact on eccentricity fault detection in permanent magnet synchronous motors", *IEEE Trans. Magn.*, vol. 48, pp. 903-906, 2012.
- [7] I.J.B.J. Hyon, K. Nam, "Dynamic modeling and control for SPMSMs with internal turn short fault", *IEEE Trans. Power Electron.* vol. 28, pp. 3495- 3508, 2013.
- [8] J. F. Brudny, J. P. Lecoite, "Rotor design for reducing the switching magnetic noise of ac electrical machine variable-speed drives", *IEEE Trans. Ind. Electron.* vol. 58, pp. 5112-5120, 2011.
- [9] N. Leboeuf, T. Boileau, B. Nahid-Mabarakeh, N. Takorabet, F. Meibody-Tabar, G. Clerc, "Inductance calculations in permanent-magnet motors under fault conditions". *IEEE Trans. Magn.* vol. 48, pp. 2605-2616, 2012.
- [10] L. Romeral, J. C. Urresty, J. R. Ruiz, A.G. Espinosa "Modeling of surface-mounted permanent magnet synchronous motors with stator winding interturn faults". *IEEE Trans. Ind. Electron.* vol. 58, pp. 1576-1585, 2011.
- [11] E. Favre, L. Cardoletti, M. Jufer, "Permanent-magnet synchronous motors: a comprehensive approach to cogging torque suppression". *IEEE Trans. Ind. Appl.* vol. 29, pp. 1141–1149, 1993.
- [12] H. Jia, M. Cheng, W. Hua, W. Zhao, W. Li, "Torque ripple suppression in flux-switching pm motor by harmonic current injection based on voltage space-vector modulation". *IEEE Trans. Magn.*, vol. 46, pp. 1527-1530, 2010.
- [13] G. H. Lee1, S. I. Kim, J. P. Hong, J. H. Bahn, "Torque ripple reduction of interior permanent magnet synchronous motor using harmonic injected current". *IEEE Trans. Magn.*, vol. 44, pp. 1582-1585, 2008.
- [14] J. Holtz, L. Springob "Identification and compensation of torque ripple in high-precision permanent magnet motor drives". *IEEE Trans. Ind. Electron.* vol. 43, pp. 309–320, 1996.
- [15] I.J.B.J.Hyon, K.Nam, "Dynamic Modeling and Control for SPMSMs With Internal Turn Short Fault", *IEEE Trans Power electronics*, vol. 28, pp. 3495- 3508, 2013.
- [16] X. Kestelyn, E. Semail, "A Vectorial Approach for generation of optimal current references for multiphase permanent-magnet synchronous machines in real time". *IEEE Trans. Ind. Electron.*, vol. 58, pp. 5057-5065, 2011.
- [17] T.Hamiti, T.Lubin, L.Baghli, A.Rezzoug, "Modeling of a synchronous reluctance machine accounting for space harmonics in view of torque ripple minimization" *Mathematics and Computers in Simulation*, vol. 81, pp.354–366, 2010.
- [18] D.Grenier, L.-A. Dessaint, O.Akhrif, Y.Bonnassieux, and B.Le.Pioufle "Experimental Nonlinear Torque Control of a Permanent-Magnet Synchronous Motor Using Saliency", *IEEE Trans. Ind. Electron*, vol. 44, pp. 680-687, 1997.
- [19] I. Jeong, B.J. Hyon, and K.Nam, "Dynamic Modeling and Control for SPMSMs With Internal Turn Short Fault", *IEEE Trans Power electronics*, vol. 28, pp. 3495- 3508, July 2013.
- [20] R.M. Tallam, T.G. Habetler, and R.G. Harley, "Transient Model for Induction Machines With Stator Winding Turn Faults", *IEEE Trans. Ind. Appl.*, vol.38, pp. 632–637, 2002.
- [21] E. Bahri, R. Pusca, R. Romary, and D. Belkhatay, "Minimization of Torque Ripple Caused by a Stator Winding Dissymmetry in a Surface Permanent Magnet Synchronous Machine (SPMSM)", *XXth International Conference en Electrical Machines, (ICEM 2014)*, BERLIN, Germany, pp. 221-226, 2014.
- [22] E. Bahri, R. Pusca, R. Romary, and D. Belkhatay "Active control of torque ripple in a faulty surface permanent magnet synchronous motor. Case of stator inter-turn short circuit" *Conférence Internationale en Sciences et Technologies Electriques au Maghreb (CISTEM'16)* 26-28, Octobre, ID 319, Marrakech, Maroc.

# Digital Control for the Air Pressure with Multi-Characteristics Selection

Dan MIHAI

University of Craiova / Department for Electromechanics, Environment and Applied Informatics, Craiova, Romania, dmihai@em.ucv.ro

**Abstract** - The paper deals with a preparatory research stage for controlling the air pressure inside a small tank by various characteristics and algorithms. Basic elements both for the hardware design and for the software support are presented. The experimental platform brings together parallel solutions: a microcontroller board using a PIC<sup>TM</sup> 16F877 chip from Microchip and an industrial controller from Honeywell<sup>TM</sup>. The functionality of the platform will be tested in this stage by the on-line commutation of the control characteristics IN (pressure error) – OUT (PWM control for the air pump). A set for the available characteristics of the controller is stored in software. For a fast design with simulation and debugging capabilities, the author used Flowcode<sup>TM</sup> of Matrix Technology Solutions - an Integrated Development Environment with a Very High Level Programming Language. Future research works are intended for some fuzzy control algorithms that could adapt and optimize the control accordingly the dynamic of the process. The main components of the platform are, besides the controllers mentioned above, an industrial pressure sensor, a compressor, the pressurized container and some standard pneumatic devices for a safe operation. Both the hardware and the software design are made so that besides the research aims, the platform could be a flexible and multi – purpose didactic tool for the students.

**Keywords:** *digital control, air pressure, characteristics selection.*

## I. INTRODUCTION

The impact of the digital control solutions in the area of pneumatic systems is more and more obvious during the last decades. If many years ago most of (industrial) applications of microcontrollers concerned the motion control field and the temperature control, now many studies and products integrate microelectronics for different kind of fluidic systems. Ref. [13] makes a synthetic comparison of pneumatic and Direct Digital Control (DDC) in terms of: performance - best DDC, initial cost – comparable, reliability, maintainability, flexibility, easy of use, life cycle cost, cost, management, proprietary – best pneumatic. An analyze of the air compressor production process, as a time-varying, delay and nonlinear complex system, is included in [5]. In order to avoid the drawbacks of classical control systems, affected by pressure instability, a fuzzy pressure controller and an intelligent control method based on the fuzzy PID were proposed.

Many studies and solutions are associated now with the Tire Pressure Monitoring Systems (TPMS) - devices and systems, because the associated equipment became a compulsory one for the new models in automotive. In this

meaning, temperature and pressure sensors values are taken and processed on Programmable System on Chip (PSoC) controller and transmitted via Bluetooth on dashboard or to a smartphone [1]. Using PsoC is possible to minimize the size and power consumption of the system. The main goal in some research works is the power management, considered in [6] to be an important aspect in designing battery operated TPMS as it helps to prolong the lifespan of the battery. The implementation of SLEEP mode to minimize power consumption is discussed and the currents consumed by the microcontroller in SLEEP and ACTIVE modes are measured and recorded. The main tools (hardware and software) belong to the well known producer Microchip (PIC<sup>TM</sup> microcontroller, MPLAB<sup>TM</sup>). An extra study concerns the power minimization for the driver block (based on MOSFET device).

Ref. [7] describes the design of the electric circuit for the control of the piston position for a pneumatic cylinder. The hardware is built around a 32-bit microcontroller Atmel AT91SAM9G20 of ARM9<sup>TM</sup> architecture, in which is implemented a control algorithm. The position control of pneumatic cylinder is designed in the state space and is realized using a predictive controller with online identification of pneumatic system parameters; then, a reduced - order observer uses it for the state vector of the process estimation.

Another application field for the pneumatic actuators and digital control concerns the Heating, Ventilation and Air Conditioning (HVAC) equipment. Ref. [15], aiming to air-condition compressor drive system, proposes a compound control strategy based on sliding-mode observer and high frequency voltage injection method. The study is focused on improving the overall performance for all speed regions. A study focused on how the stepper motor controls the EEV for the air conditioning system is made in [14], the tests and results concerning the very popular device PIC16F877A<sup>TM</sup>. Some works related to the air pressure for HVAC equipment concern both sensor unit and original algorithm / control strategies. In this meaning, [11] developed an approach for whole-house gross movement and room transition detection through sensing at only one point in the home. Disruptions in air-flow, caused by human inter-room movement, result in static pressure changes in the HVAC air handler unit. According to required air pressure, the optimum motor speed is maintained by a variable speed drive which is controlled by a microcontroller. Several control strategies are presented in [2]: On / Off control, Load /Unload control, Modulation control (that meaning the position of the inlet air valve of compressor is modulated from full open to full close, Variable speed control and Blow-off control. An application for the design and development of air

conditioner control card is developed in [12], and the connected circuits to the processors, like drivers, LCD units and sensors, could be standard parts of any other similar project. The main system parameters followed are temperature values for heating and cooling process and speeds for compressor motor and fan.

Beyond research studies, many modern industrial types of equipment, integrating microelectronics or digital control, are now available. Ref. [20] presents such industrial equipment – a high pressure electro-pneumatic regulator providing step-less control of air pressure proportional to an electrical signal with an easy to read digital pressure display and low power consumption. New easy-to-use high-function digital pressure sensor PPX series [23], has dual display to check current value and set value of pressure at the same time, 3-color display, copy function of setting details and 3-mode setting etc. A distinctive application field for the control of pneumatic systems concerns the buildings having a large pneumatic infrastructure [25]. A large number of such buildings are falling behind in energy management as digital systems and networks become more common and critical. New solutions come to improve the situation by converting a building with working but outdated pneumatic control system to a DDC, using wireless technology. Wireless pneumatic DDC provides rapid payback and minimal disruption to gain ongoing energy and maintenance cost savings, while improving comfort and operations. Such high performance equipment has new sensor classes, able to transmit a large amount of data by RF [22].

The paper follows a previous one [8] and the author's intentions are 2 categories: the design and manufacture of a flexible experimental platform for the air pressure control by microcontroller – this is a local goal; and the implementation of various non-conventional control algorithms (like fuzzy control), for future works, when the

platform will prove all necessary capabilities. In this meaning, an inspiration source is [24], a training manual that puts together systemic / theoretical and practical elements associated with an experimental platform. Also, [3] concerns the design of such an experimental platform, where a similar pressure sensor is used. The software design support is totally different. A good source for many examples (including in the pneumatic area) is [4], where is available a project for controlling a pump from a PIC16F877™ processor via an interface made with a D/A converter followed by an integrated power amplifier.

## II. HARDWARE DESIGN

The architecture of the system is presented in Fig.1. The microcontroller unit (MCU) is designed around the processor PIC16F877™ – Microchip Inc. The air pressure sensor is the chip MPX5700 - Integrated Silicon Pressure Sensor On-Chip Signal Conditioned [21].

The industrial controller, as parallel solution, is the equipment UDC 1700 Honeywell [16], able to monitor and control a large variety of temperature, air pressure or fluid flow processes, with options for the output control: Solid State Relay, Relay, Triac, 4-20 mA; 0-20 mA; 0-5 V; 0-10 V.

As driver block, two circuits were used: a predriver based on the chip 74HCT541 and the final power driver for the compressor, build around the MOSFET transistor IRFP150N [19], with galvanic isolation with optocoupler. Other solutions (for a variety of applications) are presented in [9].

The Control board includes, mainly: a.) reference potentiometer for the air pressure in the enclosure; b.) a program RUN switch; c.) selection switch between MCU control and Industrial controller; d.) a double jumper's selector for the characteristics choice, as in Fig. 2. The B

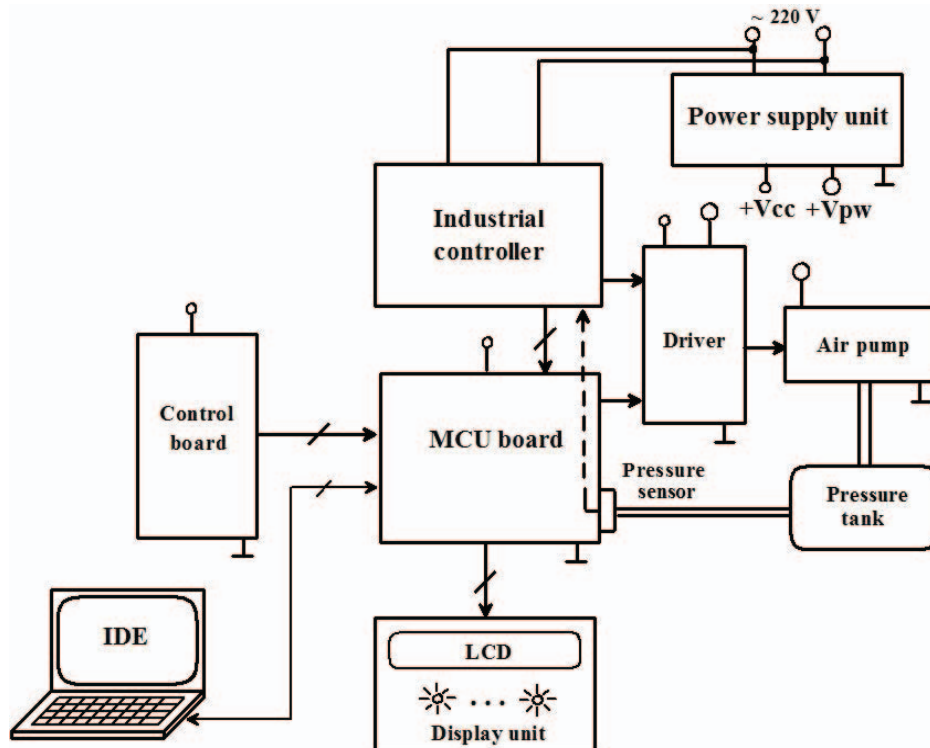


Fig. 1. The simplified structure of the experimental platform.

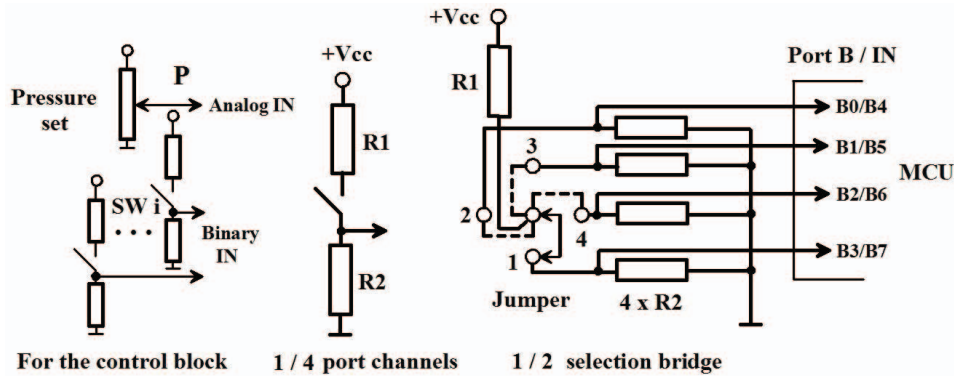


Fig. 2 The circuit for the characteristics selection.

port of the MCU is allocated to the selection function. Each 4 bits set of the port, together with the external circuit, make a 1 to 4 DMUX. B0-B3 bits select the Error thresholds and B4-B7 select the Control thresholds, together defining a characteristic.

The displaying unit has: a.) LEDs circuit for states and real-time tasks; b.) LCD board from Eblocks™ family [17], for displaying alphanumeric data.

The power supply unit has 2 sections: a.) 5 VDC for the controller; b.) 12 V DC for the air pump.

Fig. 3 contains a set of operational characteristics. Each characteristic IN – OUT of the controller is defined by the commutation thresholds: *Thres<sub>ex</sub>* is for the error of the loop and *Thresh<sub>y</sub>* is for the PWM control. For *N<sub>e</sub>* threshold values of the error and *N<sub>c</sub>* threshold values of the PWM control, the resulting number of the available characteristics is *N<sub>e</sub>* x *N<sub>c</sub>* (4 x 4 = 16 in Fig. 3). The characteristic no. 1 has a lower dynamic, with small control values in the region of medium and small error values. The system could behave too slowly to the steady-state regime. The characteristic no. 16 delivers the highest energy but could lead to some overshoot effects. Several experiments must appreciate each control characteristic upon the steady state error, overshoot values, time response and other qualitative and quantitative index.

For the *i*<sup>th</sup> control characteristic, considering both error and control values saturated on 8 bits (0...255), the PWM

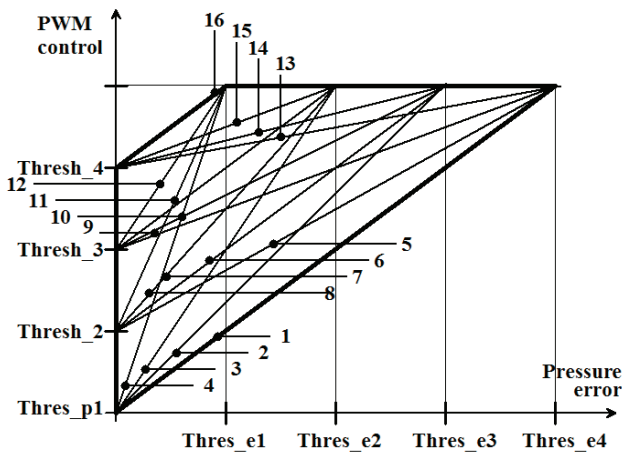


Fig. 3. A set for the control characteristics.

control is computed by program with the relation:

$$PWMcontrol = Thres\_p + \frac{255 - Thres\_p}{Thres\_e} \cdot Error \quad (1)$$

with saturation (255) for errors bigger than 255 .

### III. SOFTWARE DESIGN

The main unit of the program is depicted in Fig. 4, in the Flowcode [18] style. This software has the ability to be accessible for beginners but allowing also very complex Program for digital control by MCU PIC 16F877 or Honeywell industrial controller of the air pressure inside an enclosure. 2016 DM. Variante: 4 x 4 characteristics selectable by hardware.

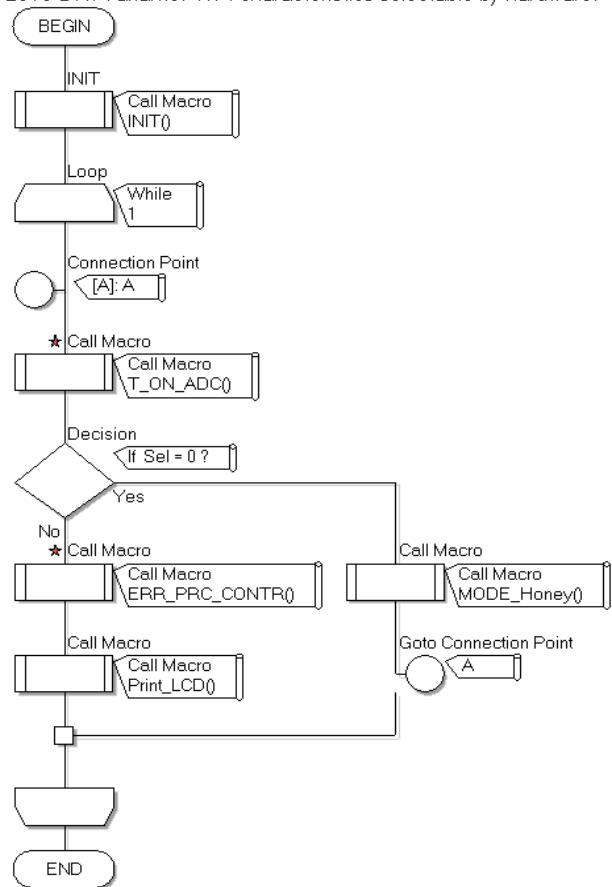


Fig. 4. The image of the Main unit in Flowcode.

programs with many units (macros), interrupts and a rich ready to use library. The author realized many complex applications in motion and temperature control fields, proving that besides CAD facilities (GUI, simulation, debugging), this environment is able to ensure high performance of results [10].

The T\_ON\_ADC Macro asks the state of the RUN switch (sending appropriate messages to LCD), makes the A/D conversion and read the Mode switch (MCU or Honeywell). Two parallel branches make the essential processing for MCU and, respectively, Honeywell modes.

For the characteristic selection, Table 1 has the binary input images B0\_7 and the values involved in the program for a certain set for the threshold values. The procedure for the characteristic identification was conceived in accordance with the multi-decision-switch available in Flowcode, since ver. 4. D val. is the decimal value read from the port B. The quotient Q and the remainder r from modulus division by 8 are:

$$Q = [(Dval. - 1) / 8] \quad r = Dval. - 8 \cdot Q \quad (2)$$

In Fig. 5, Q became v and r remains the same in the program notations. For each 1/16 branches / characteristics, a same generic formula is customized for the thresh-

old values declared in the INIT block. In rel. (1), the program must use an adapted computation formula, accordingly to the arithmetic of the microcontroller CPU

Fig. 6 gives a capture of the program in simulation mode, when the MCU program Mode is selected. The graphical interface allows the viewing of all port bits allocation:

- a.) 3 analog channels for pressure (reference and sensor: A0, A1) and the control output A4, scale [0...5] Vcc, delivered by the industrial controller and processed also by the MCU;
- b.) 10 binary inputs: Control bits (switches) A2 and A3 for RUN program and for the Mode selection (MCU / Honeywell); Selection bits (switches) B0-7 for the jumpers that make the operating characteristic choice);
- c.) PWM output – C2;
- d.) 12 binary outputs: - 6 LCD control bits D0...D5; 6 LEDs bits for the real-time recording of the tasks: C0, 3, 4, 5, 6, 7.

In Fig. 6, for a pressure error of 576 mBar, on the characteristic no. 7, the output PWM control is 46 %, for a 1200 Hz fixed frequency of the pulses sent to the air pump.

TABLE I. DATA FOR SELECTING AN OPERATIONAL CHARACTERISTIC

Q	r	D val.	Bit 7	B 6	B 5	B 4	B 3	B 2	B 1	Bit 0	Thresh error	Thresh pwm	Char. No.
			0	0	0	0	0	0	0	0	-	-	"No sel."
2	1	17	0	0	0	1	0	0	0	1	255	0	1
2	2	18	0	0	0	1	0	0	1	0	192	0	2
2	4	20	0	0	0	1	0	1	0	0	128	0	3
2	8	24	0	0	0	1	1	0	0	0	64	0	4
4	1	33	0	0	1	0	0	0	0	1	255	64	5
4	2	34	0	0	1	0	0	0	1	0	192	64	6
4	4	36	0	0	1	0	0	1	0	0	128	64	7
4	8	40	0	0	1	0	1	0	0	0	64	64	8
8	1	65	0	1	0	0	0	0	0	1	255	128	9
8	2	66	0	1	0	0	0	0	1	0	192	128	10
8	4	68	0	1	0	0	0	1	0	0	128	128	11
8	8	72	0	1	0	0	1	0	0	0	64	128	12
16	1	129	1	0	0	0	0	0	0	1	255	255	13
16	2	130	1	0	0	0	0	0	1	0	192	255	14
16	4	132	1	0	0	0	0	1	0	0	128	255	15
16	8	136	1	0	0	0	1	0	0	0	64	255	16

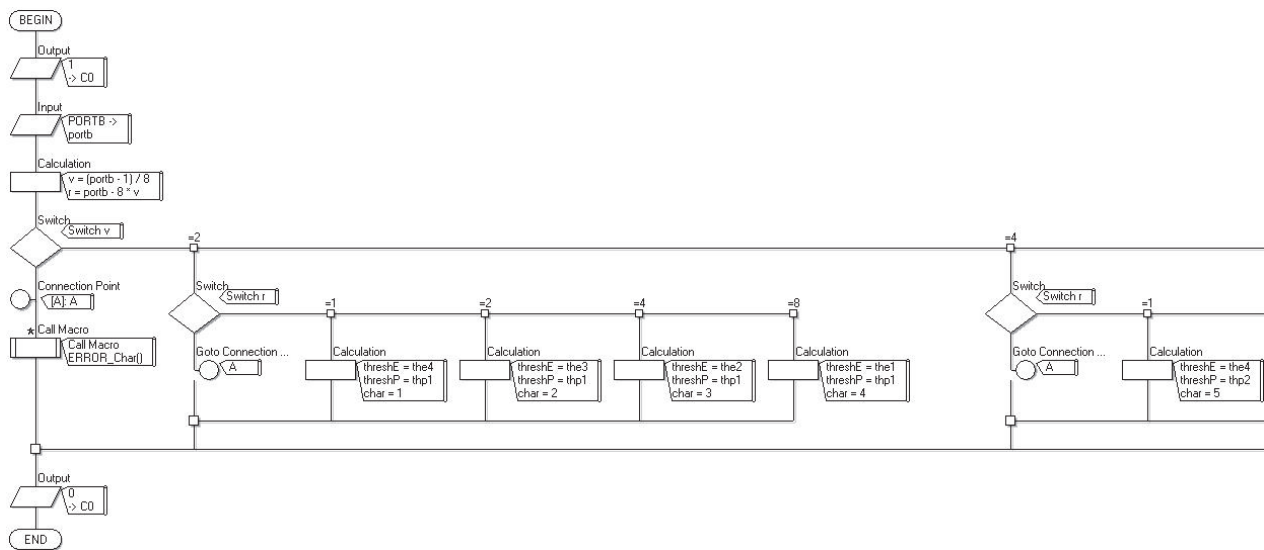


Fig. 5. The Flowcode section for identifying and computing the operating characteristic.

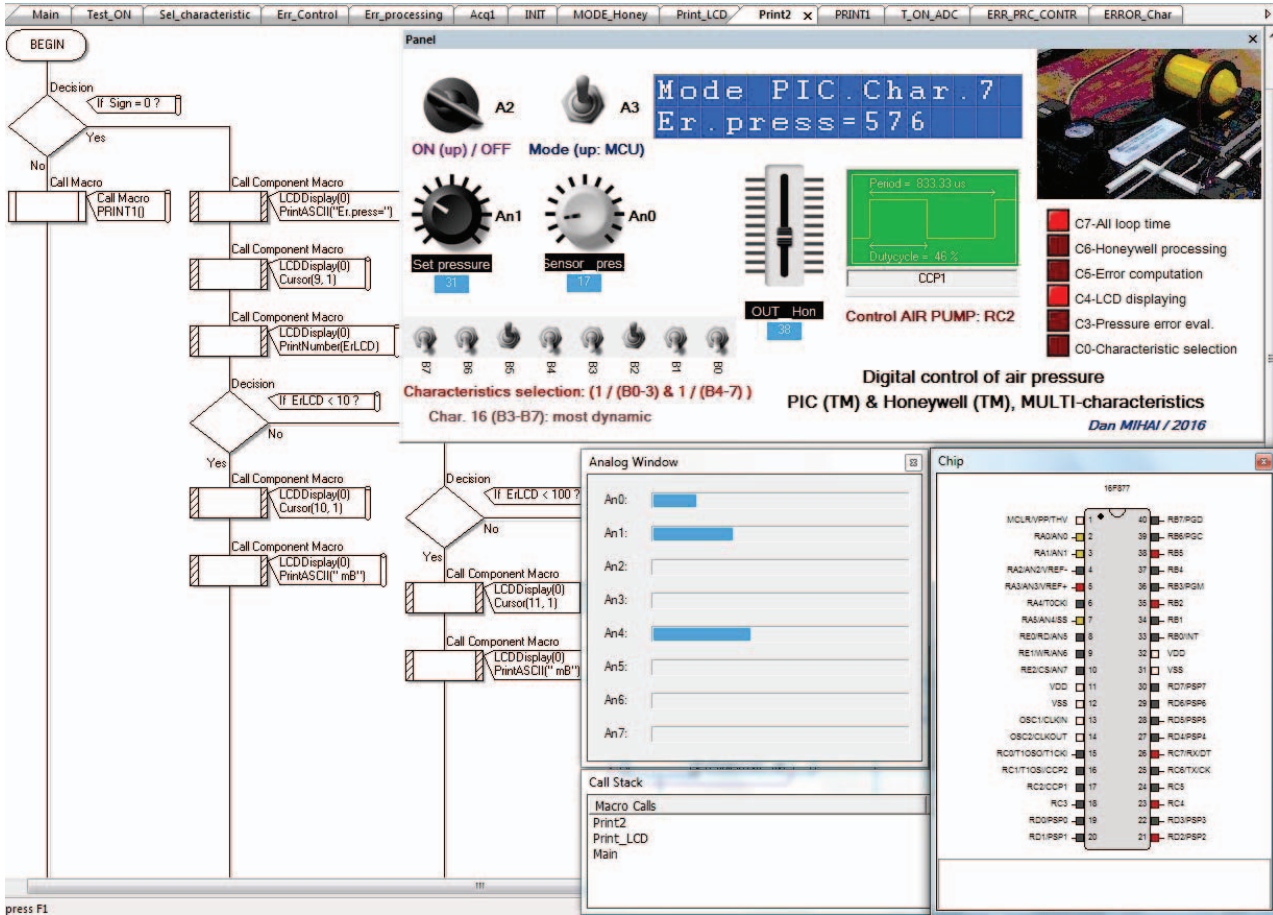


Fig. 6. The program in simulation mode.

#### IV. EXPERIMENTAL RESULTS

An image of the experimental platform is presented in Fig. 7, where the industrial controller is placed on the left side, in front. The air pump (left) and the pressure vessel (right) are visible in the back. The power supply unit and two microcontroller units complete the platform. A second MCU board (having its own pressure sensor) with

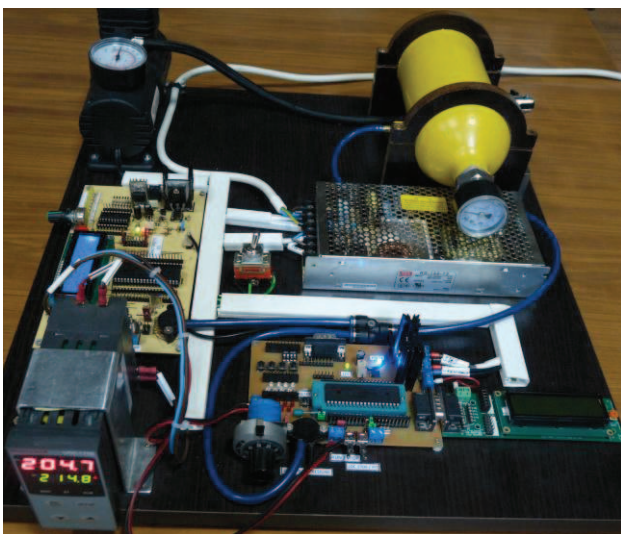


Fig. 7. The experimental platform.

ZIF socket for the processor, was used in some preliminary tests for finding a suitable microcontroller. The local LCD in operation is presented in Fig. 8. The *Mode* (PIC or Honeywell) is indicating which equipment is working. The selected characteristic is displayed and also the value of the air pressure error.

Next images from fig. 9 are captured by an USB logic analyzer and are useful for on-line timing evaluations. The first window has only the essential tasks: *SELECT* - selection of the characteristic: < 15  $\mu$ s; *ERROR\_EV*.: error processing and the control computation: 120  $\mu$ s; *LCD*: displaying task – the longest: 30 ms; *ERR\_COMP*:



Fig. 8. The local display in operation.

routine for scaling and saturating the error for displaying it in technical units (millibar): less than 5  $\mu$ s. These main operational tasks take together 147.4  $\mu$ s. The second window contains the entire loop timing, with a duration of 31.46 ms. It is possible to reduce the time amount for displaying by calling this task only once for several program loops.

The on-line recordings from Fig. 10 are related with different operating points, with different speed for the air pump motor. By these diagrams is possible to follow the right and continuous variation of the PWM factor inside the whole range and to make, also, several quantitative evaluations both for the algorithm and the hardware. The captured signals concern the characteristic no. 11. In rel. (1), for this program branch, Thresh\_p11 = 128 and Thresh\_e11 = 128. The control formula becomes:

$$PWMcontrol\_11 = 128 + 127/128 \cdot Error \quad (3)$$

The values for the pressure error must be arranged into the arithmetic format of the microcontroller. The range for the air pressure is 4 atm., so the LCD format is 4000 units (millibars – the most appropriate unit both for the arithmetic reasons and for the relation with the technical meaning) that corresponds to 255 for 8 bits representation.

Next computations give the theoretical values  $T$  for the sampled values and for those outputted in real-time  $R$ .

Theoretical value for the control at 100 mBar error:

$$PWMcontrol_{11}_{100T} = 128 + \frac{127}{128} \cdot \frac{100}{4000/255} = 134$$

$$PWMcontrol_{11}_{100T} \% = \frac{134}{255} \cdot 100 = 52.54 \%$$

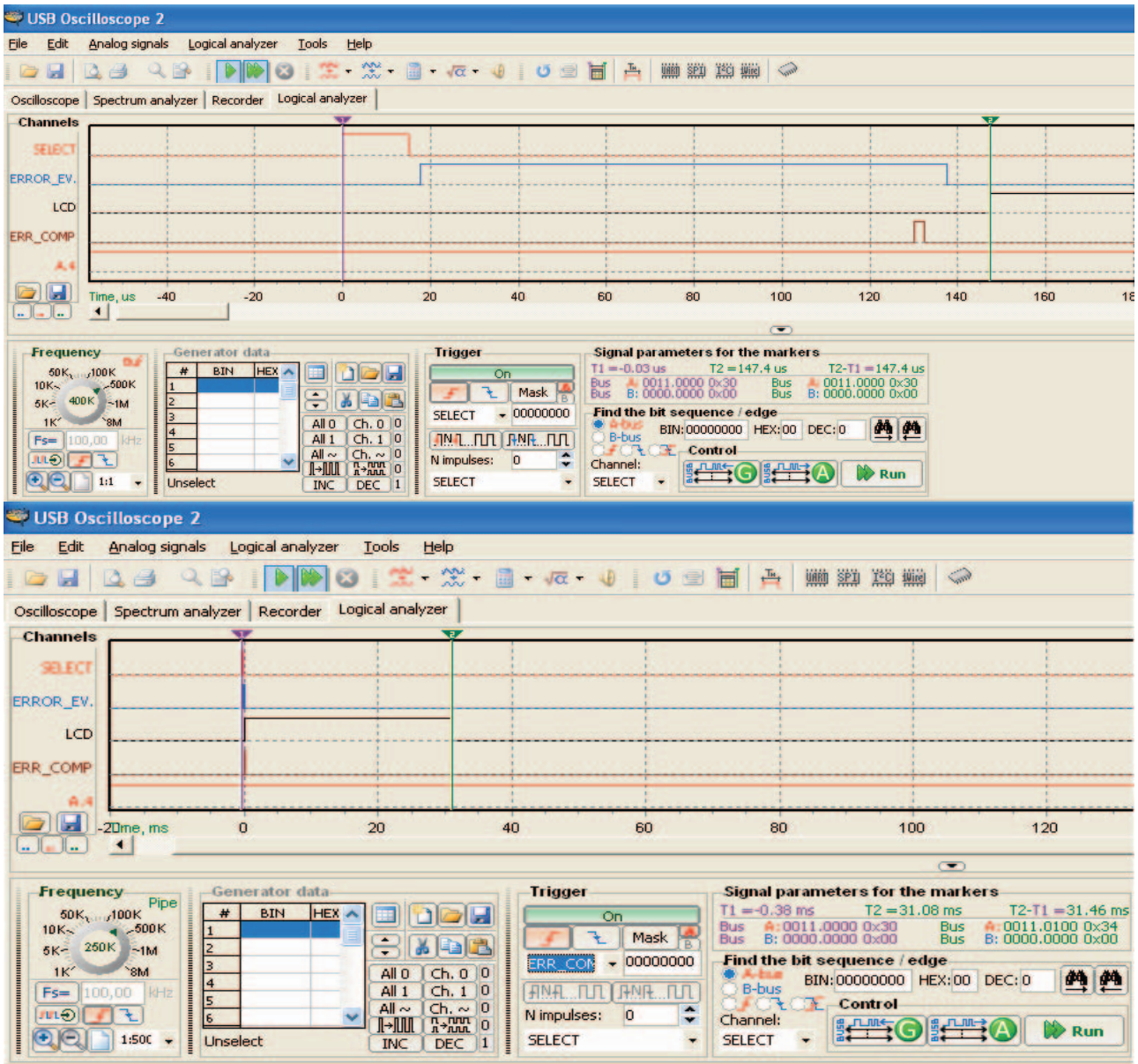


Fig. 9. Recordings for the real-time tasks.

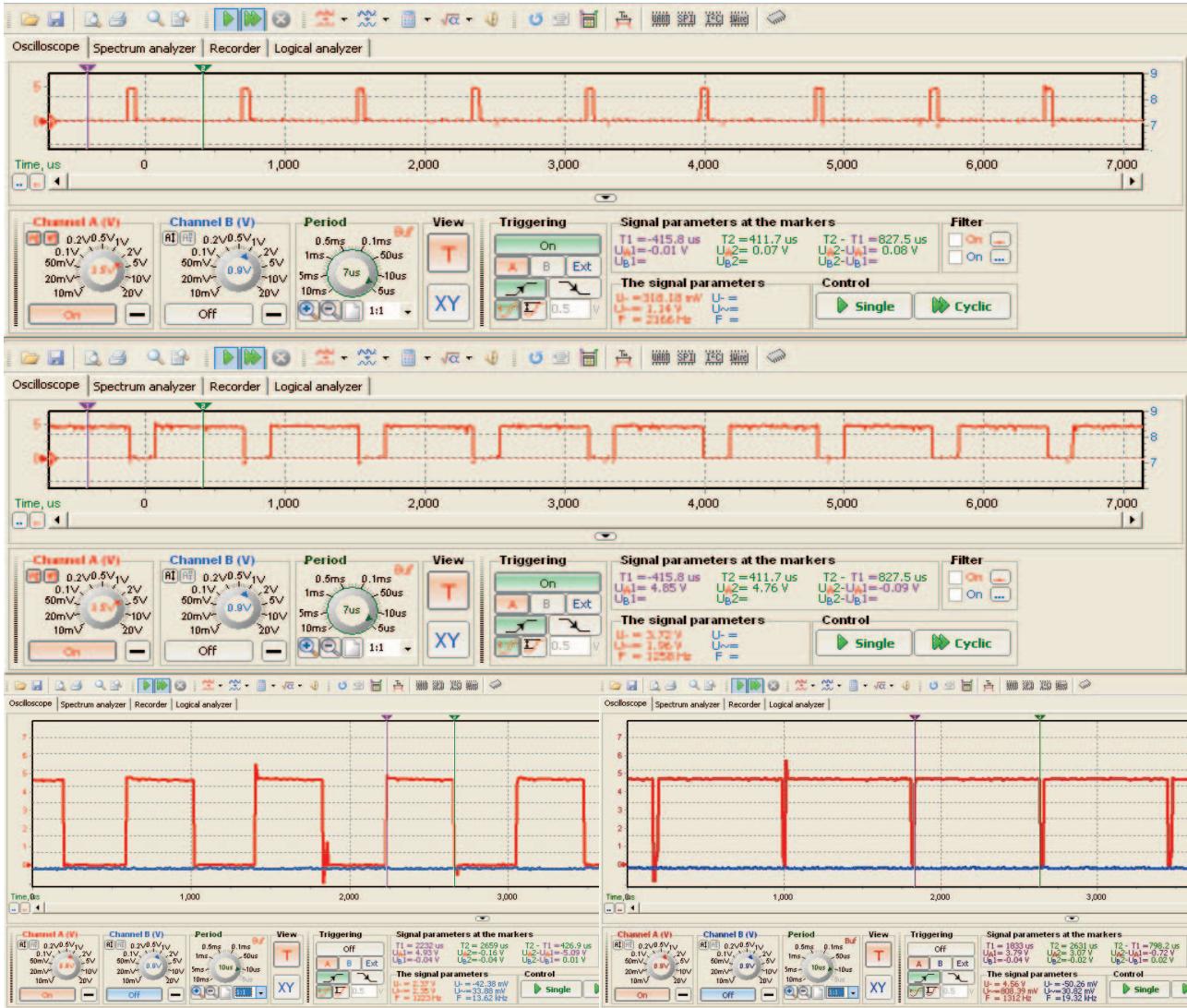


Fig. 10. PWM signals for different operating points.

The real value for the control at 100 mBar error (see T2-T1 in the third diagram):

$$PWM_{control1100R} \% = \frac{426.9}{821.4} \cdot 100 = 51.97 \%$$

The relative difference between  $PWM_{control100R}$  and  $PWM_{control100T}$  is 1.09 %. A similar verification computation error for the operation point with an air pressure error of 2000 mBar, leads to:

$$PWM_{control2000R} = 97.17 \% ; PWM_{control2000T} = 98.83 \%$$

The relative difference for this case is 1.67 %.

### V. CONCLUSIONS

The paper had several goals. The seminal start idea is to offer to the control algorithm the ability to change in real-time the control characteristic so that the dynamic of the pneumatic system could be optimized accordingly to different criterions. The hardware / software design tools

are related, aiming to ensure a fast cycle by using an IDE including a VHLL for programming a modular platform. This approach is not only very efficient but also is able to offer realistic provisional results in simulation and debugging modes.

A standard industrial controller was included into the project so that a parallel operation could be possible. More, the software and the hardware design links these two solutions, the designed microcontroller based system processing some signals delivered by the industrial controller.

Several timing diagrams recorded on-line by an USB logic analyzer made possible a qualitative study (the real-time task distribution, mainly) and quantitative determinations, like the precise measurements of the durations and some evaluations of the errors between the computed (theoretical) values and the real ones obtained by experiment. These errors are very small (maximum 1.7 %) and are related, mainly, with deterministic sources: a quite short format conversion (8 bits) of A/D converter, a sampling rate not very high (tenths of microseconds) of the PCscope, chosen so that a right view of several signals be

relevant (PWM frequency imposed by the air pump is not very high).

The paper did not include a study for the quality and behavior of the pressure loop (all that depending on future intended control algorithms) but to prove the functionality of the experimental platform both on hardware operation and the software tools managing the system.

The resulted experimental platform proved a full functionality and has many educational merits, bringing together many devices, circuits and equipment and involving modern software tools both for design and for acquisition.

*Received on September 20, 2016*

*Editorial Approval on November 5, 2016*

#### REFERENCES

- [1] N. Agalave, U. Patil, "Integration of Tire Pressure Monitoring System using PsoC", International Journal of Science, Engineering and Technology Research (IJSETR), Volume 4, Issue 4, April 2015, pp. 960-964.
- [2] Bahekarl , S. Yadav, "Optimization of Air compressor Motor speed for Reducing Power Consumption", International Journal of Innovative Research in Advanced Engineering (IJIRAE), Volume 1 Issue 6 (July 2014), pp. 430- 434.
- [3] Bindu, "Digital Barometer using PIC Microcontroller and MPX4115A Pressure sensor" – XC8, 2013, in MPLAB X Projects, <http://www.studentcompa nion.co.za/digital-barometer-using-pic-microcontroller-and-mpx4115a-pressure-sensor-xc8/>.
- [4] Ib. Dogan, Microcontroller Based Applied Digital Control, John Wiley & Sons Ltd, England, 2006.
- [5] L. Gongfa, G. Yueheng, J. Kong, G. Po, "Intelligent control of air compressor production process", Applied Mathematics & Information Sciences, 7(3), 2013, pp. 1051-1058, [https://www.researchgate.net/publication/274027567\\_Intelligent\\_Control\\_of\\_Air\\_Compressor\\_Production\\_Process](https://www.researchgate.net/publication/274027567_Intelligent_Control_of_Air_Compressor_Production_Process).
- [6] S. Goparaju, Low Power Tire Pressure Monitoring System, Master degree thesis, University of Akron Ohio, USA, Department of Electrical and Computer Engineering, 2008.
- [7] P. Matousek, " Microprocessor system designated for control pneumatic actuator", Journal of applied science in the thermodynamics and fluid mechanics, Vol.5, No.2/2011, [http://astfm.tul.cz/ladmin/soubory/casopis/File/pdf/3473937matousek\\_microp rocessor\\_system\\_designated\\_forcontrol\\_pneumaticactuator.pdf](http://astfm.tul.cz/ladmin/soubory/casopis/File/pdf/3473937matousek_microp rocessor_system_designated_forcontrol_pneumaticactuator.pdf)
- [8] Mihai, "Designing an experimental platform for the air pressure in a tank by digital control", Paper 3.6, ICATE 2016, Craiova, Romania.
- [9] Mihai, Digital Electronics. Design Elements for Applications, Ed. Sitech, Craiova, 2013, in Romanian.
- [10] Mihai, "Hardware Experiments for Simultaneous Control of Several Motors by a Microcontroller and a VHL Programming Language", Annals of the Univ. of Craiova, Electrical Series, Ed. Universitaria, No. 39, ISSN: 1842-4805, 2015, pp. 61-66.
- [11] S. N. Patel , M. S. Reynolds, G. D. Abowd, "Detecting human movement by differential air pressure sensing in HVAC system", Ductwork: An Exploration in Infrastructure Mediated Sensing, <https://dub.washington.edu/djangosite/media/papers/tmpqiqC-3.pdf>.
- [12] T. T. Soe, K. S. Lwin, Z. M. Naing, A. S. Khaing, "Design and development of microcontroller based air conditioning system, International Journal of Scientific Engineering and Technology Research, Vol. 03, Issue No.10, May-2014, pp. 2000-2004, <http://ijsetr.com/uploads/614523IJSETR1252-341.pdf>
- [13] R. Starr, "Pneumatic controls in a digital age", ENERGY & ENVIRONMENTAL MANAGEMENT, pp. 33-37, <http://www.enterprisevac.com/wp-content/uploads/2015/08/Digital.pdf>
- [14] Thae Su Aye, Zaw Myo Lwin, "Microcontroller based electric expansion valve Controller for air conditioning system", World Academy of Science, Engineering and Technology 42, 2008, pp.387 – 391.
- [15] Z. Wang, L. You , W. Peng, "High performance control on air-condition compressor drive system", Chinese Automation Congress (CAC), Wuhan, China, 2015, pp. 1498 - 1503
- [16] \*\*\*, 1/8 -DIN & 1 /16 -DIN Controller & Indicator Manual, Honeywell, Product Manual, 51-52-25-122, Issue 5 – March 2005, <https://www.honeywellprocess.com/library/support/Public/Documents/51-52-25-122.pdf>
- [17] \*\*\*, EB005, E-blocks LCD board, Matrix Technology Solutions Ltd, <https://www.matrixsl.com/webshop/e-blocks-lcd-board.html>, <http://www.matrixsl.com/resources/files/datasheets/EB005-30-4.pdf>.
- [18] \*\*\*, FLOWCODE 5 E-System design software, <http://www.matrixmultimedia.co.uk/flowcode/>.
- [19] \*\*\*, IRFP150N HEXFET® Power MOSFET, PD-91503D, International Rectifier, <http://www.infineon.com/dgdl/irfp150n.pdf?fileId=5546d462533600a40153562867fa1fd4>.
- [20] \*\*\*, ITVX2000, High Pressure Electro-Pneumatic Regulator, SMC, 2013, <http://www.smcusa.com/top-navigation/cad-models.aspx/127728>
- [21] \*\*\*, MPX5700 Integrated Silicon Pressure Sensor On-Chip Signal Conditioned, Temperature Compensated and Calibrated, Freescale Semiconductor Data Sheet: Technical Data, Rev 10, 10/2012, [http://www.nxp.com/files/sensors/doc/data\\_sheet/MPX5700.pdf](http://www.nxp.com/files/sensors/doc/data_sheet/MPX5700.pdf)
- [22] \*\*\*, MPXY8300: Microcontroller, Pressure Sensor, X-Z Accelerometer and RF Transmitter, <http://www.nxp.com/pages/microcontroller-pressure-sensor-x-z-accelerometer-and-rf-transmitter:MPXY8300>.
- [23] \*\*\*, PPX series, CKD Corporation, CC-825A 2, 2006, [https://www.bibusmenos.pl/fileadmin/editors/countries/bimen/PNEUMA TYKA/Dokumenty /przygotowanie\\_powietrza\\_akcesoria \\_CKD\\_przeka%C5%BAniki\\_ci%C5%9Bnienia\\_PPX.pdf](https://www.bibusmenos.pl/fileadmin/editors/countries/bimen/PNEUMA TYKA/Dokumenty /przygotowanie_powietrza_akcesoria _CKD_przeka%C5%BAniki_ci%C5%9Bnienia_PPX.pdf)
- [24] \*\*\*, Process Control Advanced Process Control Pressure, Flow, and Level, Courseware Sample 86007-F0, 01/2015, Festo Didactic Ltée/Ltd, Quebec, Canada
- [25] \*\*\*, Wireless Pneumatic Direct Digital Control for the Energy Smart Building, 2012-WP-EM-6424020v002, Millenium Net, [http://www.millennialnet.com/MillennialNet/media/Resources\\_Media/WhitePapers/Whitepaper6424Wi-StatIIp.pdf](http://www.millennialnet.com/MillennialNet/media/Resources_Media/WhitePapers/Whitepaper6424Wi-StatIIp.pdf)

# Study of the Reactive Power Side Effects for Tariff and Compensation Purpose at the Transmission Networks' Users

Leonardo Geo Manescu\*, Denisa Rusinaru\*, Marian Ciontu\*, Cosmin Buzatu\*,  
Eugen Butoarca† and Miron Alba†

\* University of Craiova/Faculty of Electrical Engineering, Craiova, Romania, leman78@hotmail.fr

† CEZ Romania/CEZ Distribution SA, Craiova, Romania, Miron.Alba@cez.ro

**Abstract** - The reactive power flows affect voltages, losses and transmission capacities. Thus MVAR flows are a matter of increasing concern for the grid operators and the Romanian Regulatory Authority for Energy has established their importance into a specific Order. The latest corresponding regulation for Romania allows the grid operator to exonerate of payment those injections of reactive which affect in a positive manner positively the voltages in the network. Such exemption is difficult to apply since the influence of MVARs on voltages is locational and time dependent. This paper deals with the assessment of reactive powers related to network users for payment and compensation purposes. The drawbacks are evaluated and compared with the benefits for voltage regulation, according to Romanian regulations. Theoretical skills are combined into one organic methodology, and an in-house software package for reactive power assessment is built. This is based on sensitivities of voltage, loss and transmission capacity to reactive injections into nodes. A case study consisting of a real 110kV network of about 2000 nodes was adopted. The survey was conducted for 6000 hours and outlines voltage to sink's MVARs. The results were used to evaluate the opportunities to compensate and/or to discharge payments the MVARs with positive contribution to voltage regulation. This paper proposes a sensitivity based analysis for a real 110kV network.

**Keywords:** *sensitivity; compensation; reactive; loss; optimal; regulation.*

## I. INTRODUCTION

Reactive power is a topic of constant concern in modern electric network operation. Nowadays everyone agrees on the drawbacks of reactive power: it affects voltage magnitude [1], increases losses [2], reduces the available transmission capacity (ATC) of the network [3] etc. Transmission and distribution companies are interested in reducing reactive power flows [4], mainly by compensation or reciprocal cancelling [5].

The synchronous generator is the most common source of reactive power. It can deliver MVARs at opportunity costs. Another traditional reactive power, spinning too, is the synchronous compensator. It can have no active load and produce more expensive MVARs. The new generation of reactive power sources, employed for compensation purposes as well as for system control, consists of flexible AC transmission devices (FACTS): thyristor controlled reactors (TCR), static VAR compensators (SVC), shunt static synchronous compensator (SSSC) and static compensators (STATCOM), [6], [7].

The features and capabilities of the reactive power sources become crucial in a competitive market environment. The cost characteristics of the solutions able to supply the required reactive powers in secure steady state and dynamic operational conditions also weigh heavily. These elements will be referred in conjunction with the sensitivities of individual elements, depending mainly on their location in the network [8].

The compensation of the reactive power is mainly directed towards voltage control. Optimal voltage control through V/Q ancillary service also aims at loss reduction and capacity relief so as to host additional flows.

The reactive power problem is rather local: one inductive flow seeks to pair with the leading reactive power of the nearest capacitive element. In most cases the consumers are inductive and they shall be compensated either by neighboring under loaded lines or by a specific compensator.

However, transformers and the transmission line exhibit their own reactive powers, which depend on the system load. Nobody pays for these reactive powers, either beneficial or not for the network operation.

In Section II of this paper the authors present the Romanian regulations with regard to reactive power matters and payment settlement. Specific exemption conditions, provided by this regulation, are pointed out in order to be further analyzed in section V.

Section III describes the reactive powers of the network components: transformers and transmission lines. Computing equations and influence factors are outlined.

Section IV outlines the methods available for evaluating the effect of reactive power flows.

Section V presents the proposed methodology and the toolkit developed in order to emphasize the impact of the reactive power on the network voltage, power losses and transmission capacity use.

The results of a case study are delivered and analyzed in section VI and section VII concludes this work.

## II. ROMANIAN REGULATION FOR REACTIVE ENERGY

ANRE, the Romanian Regulatory Authority for Energy, has established the importance of reactive power matter into a specific Order [9]. This order defines all the elements, definitions, formulas and computing methodology for the reactive energy payments.

In accordance with it, the inductive reactive energy (lagging) and capacitive reactive energy (leading) aren't cancelled any more but entitle to separate payments. The tariff for reactive energy at power factors bellow 0.65 is three times higher than for power factors between 0.65 and 0.92. These methodology and tariffs are meant to discourage sinks to exchange intensive reactive powers with the network.

One principle almost obvious in theory has become rather controversial in practice: the possibility to exempt some network users of the payment due for the reactive energy. This exemption is limited to prosumers that:

- participate to the V/Q regulation, under the command of the network operator, for the energy exchanged, injected in/drawn from the network during this service;
- contribute to the improvement of the voltage level by injecting or drawing reactive power.

The last case lacks accuracy in defining the benefits for the voltage regulation service. This opportunity could entitle a prosumer having sometimes fortunate V/Q sensitivity to wait to be exempted for the reactive energy exchanges with the network. In order to characterize the true contribution to this service over a time period, an in-depth analysis, as presented in section VI, is required.

After enforcing this Order in the last 18 months, ANRE has published some global outcomes and decided to continue applying it with minor changes and updates [10]. The results run as follows:

- the inductive energy billed raised by 15% for power factors ranging between 0.65 and 0.92, and by 25% for users operating at power factors bellow 0.65;
- the capacitive energy payments have increased by 12% for power factors ranging between 0.65 and 0.92, and by 200% for users operating at power factors bellow 0.65.

The last case corresponds to situations where the capacitive power is injected in an underloaded network area and has to be discouraged. All these results entitiled the Regulatory Authority for Energy in Romania to maintain these rules and amend some descriptions. Moreover, the network operators were asked to approve of exemptions solely based on an in-depth analysis and measurements. Thus, only beneficial reactive powers have to be rewarded. All the others have to be penalized according to their disruptive effect.

Further in this paper the opportunity of ANRE regulation regarding the reactive power tariff is analyzed by considering a set of operation regimes for a 110 kV distribution network. The presented study cases outline the influence of reactive power on the voltage level by using multiple analysis approaches.

### III. REACTIVE POWER OF NETWORK COMPONENTS

The operation principle of most consumers involves reactive powers in correlation with the active one. These reactive powers are not delivered by some reactive sources, as for the real ones, but exchanged with neighboring branches.

The network components, transformers and lines have their own reactive powers, which depend on the operation

regime. Thus, the reactive power of transformers can be estimated by computing with:

$$Q_T = B_T \cdot V^2 + X_T \cdot I^2 \quad (1)$$

or

$$Q_T = \frac{I_0\%}{100} S_N + \frac{V_{sc}\%}{100} \left( \frac{S}{S_N} \right)^2 \left( \frac{V_N}{V} \right)^2 \quad (2)$$

where:

$B_T$  - the shunt susceptance of transformers – inductive (S);

$X_T$  - the longitudinal reactance of the transformer ( $\Omega$ );

$V$  - the operation voltage of the transformer (kV);

$I$  - the current through the transformer (A);

$I_0\%$  - the no-load current of the transformer (%);

$S_N$  - the rated power of the transformer (MVA);

$V_N$  - the rated voltage of the transformer (kV);

$V_{sc}\%$  - the short-circuit voltage of the transformer (%).

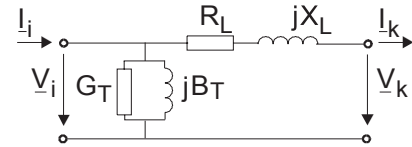


Fig. 1. Model - I of the transformer

This reactive power always lags and exhibits a quadratic flow dependency of the power delivered by the transformer. On the other hand, the transmission lines lead when no-load and become lagging when the line flow increases above the surge impedance loading, SIL:

$$SIL = \frac{V_L^2}{Z_0} \quad (3)$$

where:

$Z_0$  is the surge impedance ( $\Omega$ ):

$$Z_0 = \sqrt{\frac{X_L}{B_L}} = \sqrt{\frac{L}{C}} \quad (4)$$

$L$  the serial inductance of the line (H)

$C$  the shunt capacity of the line (F)

The reactive power loss of the transmission line can be evaluated using the formula:

$$Q_L = \frac{P_i^2 + Q_i^2}{V_i^2} X_L - \frac{V_i^2 + V_k^2}{2} B_L \quad (5)$$

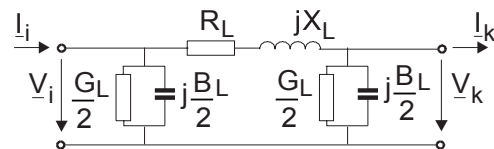


Fig. 2. Model - II of the transmission line

The balance at the network level points out to the reactive power of the whole network. This amount can reach significant values and varies heavily with the operation regime. It can be either positive or negative. Nothing is to be paid for these reactive powers whatever the case.

#### IV. METHODS FOR REACTIVE POWER EVALUATION

Various methods are available for evaluating the effect on voltage control of reactive power injections on voltage control [11, 12, 13].

##### A. Marginal sink variation method

This outlines IQ contributions to voltage upholding for marginal sink variations. The sensitivity of IQ at bus  $i$  to the marginal variation of sink from bus  $j$  is:

$$SQ_{ij} = \frac{dQ_i}{dS_j} = \frac{dQ_i}{dU} \cdot \left( \frac{dS_j}{dU} \right)^{-1} \quad (6)$$

where

$dQ_i$  - the IQ at bus  $i$  which maintains voltage if sink at bus  $j$  varies of  $dS_j$ .

The overall sensitivity of IQ at bus  $i$  is the sum of equations (6) for all sinks:

$$S\Sigma Q_i = \sum_{j=1}^c SQ_{ij} \quad (7)$$

with  $c$  – no. of consumers.

The IQ sensitivity of all the  $g$  reactive “sources” to a marginal variation of the sink from node  $j$  is:

$$S\Sigma Q_j = \sum_{i=1}^g SQ_{ij} \quad (8)$$

Full IQ sensitivity to all sink marginal variations becomes:

$$S\Sigma Q = \sum_{i=1}^g \sum_{j=1}^c SQ_{ij} = \frac{\sum_{i=1}^g dQ_i}{dV} \cdot \left( \frac{\sum_{j=1}^c dS_j}{dV} \right)^{-1} \quad (9)$$

Sensitivities from (6) ... (9) allow to compare technical efficacy of As-V/Q service provider bids. However, these sensitivities deliver no systematic way for ranking bids.

##### B. P/V curves method

In this method the loads are increased not by a marginal value, as in the previous section, but until the system reaches the stability limit. The scenario is chosen to fulfill the purpose of the analysis (e.g. we can increase only the consumption from a region, at various quotas, at constant/variable power factor).

The issues aren't wide-ranging. Moreover, the selection of the scenario can be critical.

By simulating a consumption ( $\Delta S_j |_{j=1, \dots, c}$ ) increase up to the stability limit, balanced by AGC units (all others remaining PV buses at constant specified voltages and powers) we get the IQ variations,  $\Delta Q_j$ . Various specified voltages can be utilized.

The appraisal of different IQ, reveals the efficacy of each reactive power “sources”. The conclusions are useful rather for security analysis than for assessing As-V/Q

tariffs.

##### C. Fictitious compensators method

When the IQs change, voltages alter. Fictitious compensators at each PQ bus can restore system voltages.

We denote by  $Q_j^{(x)}$  the IQ of the As-V/Q service provider from bus  $j$  in regime  $x$  and  $Q_j^{(\min)}$  its IQ minima (lower edge of secondary range for voltage regulation). For synchronous compensators and static „sources” we let  $Q_j^{(\min)} = 0$ .

By simulating a variation  $\Delta Q_j^{(S)}$ :

$$\Delta Q_j^{(S)} = Q_j^{(x)} - Q_j^{(\min)} \quad (10)$$

we determine the IQs of the fictitious compensators which “replace” the missing injection. For a load at bus  $i$ , the resulting fictitious IQ,  $\Delta Q_i^{(C)}$ , defines its “duty” for the  $\Delta Q_j^{(S)}$  service. Because  $\Delta Q_j \neq \sum_i \Delta Q_i^{(C)}$ , the “duties” aren't normalized and must be shared (e.g. pro-rata: load  $i$  pays to provider  $j$  matching to:  $\left( \Delta Q_i^{(C)} / \sum_i \Delta Q_i^{(C)} \right) \cdot \Delta Q_j^{(S)}$ ).

##### D. Back-up generation method

An IQ,  $\Delta Q_j^{(S)}$ , can be “replaced” not only by a fictitious compensator, but also by the IQ of another As-U/Q provider. For the provider from bus  $k$  we note:

- $\Delta Q_k^{(x)}$  IQ in the regime  $x$ ;
- $\Delta Q_k^{(\rightarrow \min_j)}$  IQ in the regime having the same voltages as in  $x$ , and  $Q_j = Q_j^{(\min)}$ .

We can consider that the IQs  $\Delta Q_j^{(S)}$  (at bus  $j$ ) and  $\Delta Q_k^{(\rightarrow \min_j)}$  (at bus  $k$ ) are equivalent. This statement is very useful for assessing tariffs for As-V/Q service in the operating regime  $x$ .

##### E. dV/dQ sensitivity method

The voltage sensitivities to IQ describe a widespread tool in voltage control. The reactive power injection at bus  $k$  meant to correct the voltage at bus  $i$  of about  $\Delta U_i$  is:

$$\Delta Q_k = \frac{\Delta U_i}{S(U_i, Q_k)} \quad (11)$$

where

$$S(U_i, Q_k) = \frac{\mathcal{G}U_i}{\mathcal{G}Q_k} \quad (12)$$

is the reverse, ( $= \mathcal{G}Q_k / \mathcal{G}U_i$ ) of the corresponding element of the Jacobian.

Equation (11) exhibits that the voltage at bus  $i$  can be equally corrected by an IQ of:

$$\Delta Q_j = \Delta Q_k \cdot \frac{S(U_i, Q_j)}{S(U_i, Q_k)} \quad (13)$$

at bus  $j$  or by an injection of  $\Delta Q_k$  at bus  $k$ .

For voltage regulation at bus  $i$ :

- (11) defines the required amount of challenging injections for voltage correction;
- (13) states the tariffs' ratio for two IQs at buses  $j$  and  $k$ , which are equivalent in voltage "correction":  $S(U_i, Q_j) / S(U_i, Q_k)$ .

## V. ASSESSMENT OF REACTIVE POWER OF GRID USERS

The effects of reactive powers injected or drawn by a network user can be quite volatile. Thus, in certain operation regimes, some reactive power injected at specific buses could be helpful for the voltage regulation service. This does not hold true for all operation regimes and isn't true for all network users (it depends on the amount and the location of reactive).

Therefore the impact of each reactive power for all the regimes in question is to be assessed individually. This can be done either *ex-ante* or *ex-post*. In the *ex-ante* approach, the assessment is based on measured data. Hence the corresponding results are undisputable and can be used for payment purposes.

This paper proposes the sensibility-based analysis as the most suitable tool. The voltage sensitivity to nodal reactive power:

$$S_{VQ} = \partial V_i / \partial Q_k \quad (14)$$

and the loss sensitivity to MVAR injected / drawn at node  $k$ :

$$S_{LossQ} = \partial Loss / \partial Q_k \quad (15)$$

outline the impact of  $Q_k$  to voltage regulation and losses.

The contribution to the voltage regulation can be considered useful if the injections  $Q_k$  move the voltage according to the needs for the corresponding operation regime (e.g. if  $Q$  lags, as for most of the loads, than  $S_{VQ}$  should be positive off-peak and negative on-peak). The support to the voltage regulation is stronger if the grid operator lacks available reserves. Further complex analysis can be conducted based on the QV curves, known also as nose curves.

The impact of the reactive power on losses is easy to evaluate based on  $S_{LossQ}$  sensitivity. The injection of reactive power is to be considered useful (loss-friendly) if it diminishes the losses for this operation regime. The magnitude and even the sign of  $S_{LossQ}$  can change during one year.

The reactive power from one node affects the available transmission capacity in the neighborhood. The strongest effect is to be observed over the branches connected to the node. This dependency can be assessed based on direct numerical simulation. Since the nonlinear model of the network is not suitable for superposition, only the full simulation is relevant in this case, [14].

Any exemption regarding the payments for reactive power / energy, as in [9] could be applied, *ex-post*, by reimbursing the prosumers for the reactive energy which help the voltage regulation. The main problem is that these quantities are not measured. Even the latest smart metering system (AMS) does not deliver such kind of data. It should be done by computing these quantities *ex-post*, based on the hourly measurements of reactive power. These measurements are to be set into categories corresponding to their effect on voltage regulation.

The chart flow of the methodology for assessing reactive power impact is presented in Fig. 3. Proprietary software packages, as well as in-house software tools are interfaced in order to reach measurement data, adjust them in a proper format and supply them in order to perform this analysis.

Besides the tariff and payments issues, the main problem is that the reactive power has to be compensated in order to avoid drawbacks. The bills for reactive energy can pay off for the investment in compensators and their operation. The opportunity to invest is based on the analysis cost benefit for each possible scenario. The tariffs for reactive energy from [9] do not generate enough income to pay for compensation at the HV level, where the specific capacity costs (€/MVAR) are more than 10 times higher than at LV.

Moreover, the losses could be decomposed into two components: one depending on the real power flow and the other under the responsiveness of reactive power. This second component can be reduced by proper compensation. Time-dependent performance indexes, "Q/loss", were defined in [15] at the branch level and for entire network.

These indexes could be useful for ranking grid operators as well as for tariff settlement purposes. Thus, the loss component which corresponds to the MVAR flows could be allocated to the grid owner, as an avoidable share of loss. Moreover, this loss share can be carried over the ancillary service dealing with the reactive support to the voltage control - V/Q service.

## VI. CASE STUDY

In order to evaluate the influence of the reactive power flows on the voltages in a studied network the authors propose basically three approaches:

- direct comparison of two simulation cases (the real operation of the test network vs. the suggested compensated configuration);
- using an interpretation of sensitivity based analysis in the buses of the test network;
- analyzing the information given by QV curves.

The analysis was carried out for a real operating 110kV network, consisting of 1994 buses and 2228 branches. The time frame was of 5855 running hours in 2015.

Voltages, real and reactive powers from 481 electric meters were collected during that time.

After undergoing a state estimation process, the data corresponding to each state were processed with an in-house software package, REANS\_CONT, [16][16].

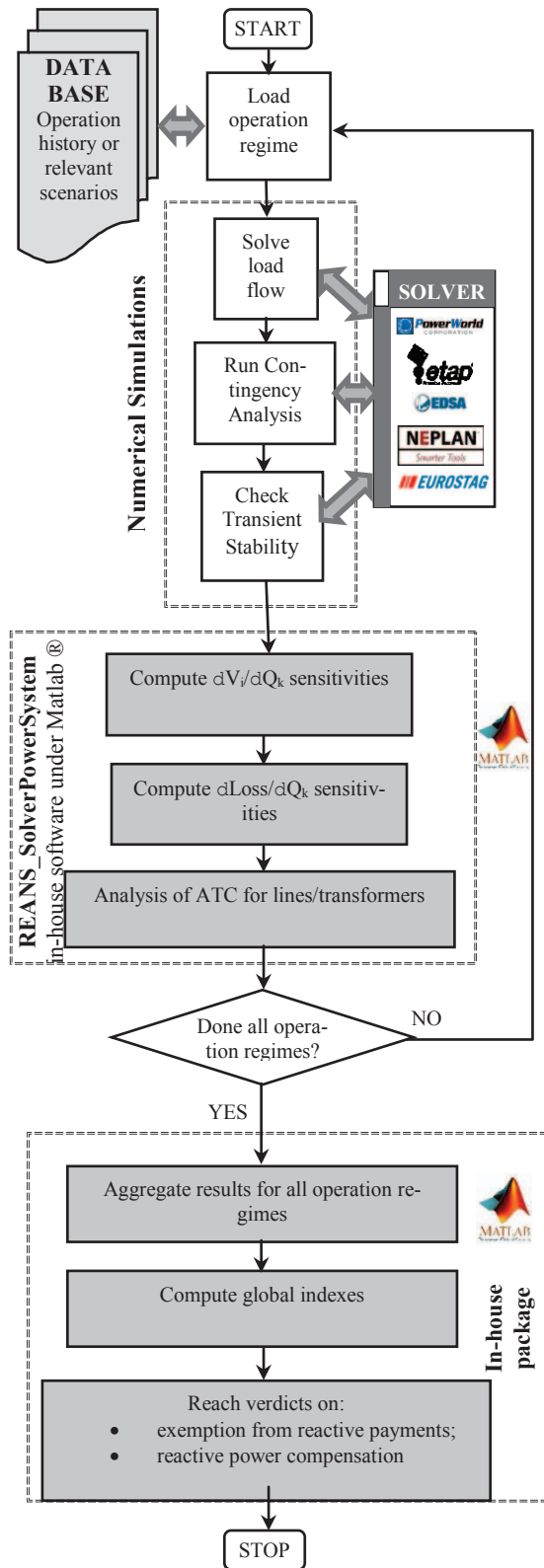


Figure 3: Chart flow of the methodology for assessing reactive power impact.

The generation and load level are presented in Fig. 4 and Fig. 5.

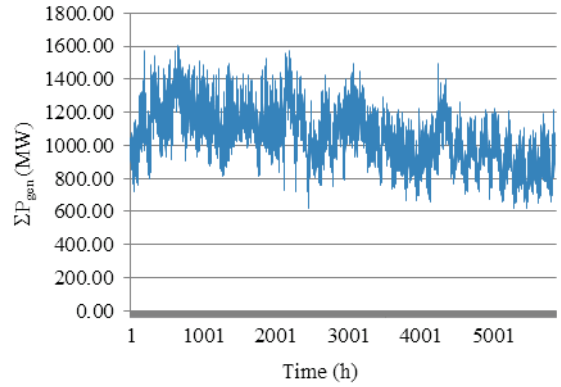


Fig. 4. Generation progression in the time frame.

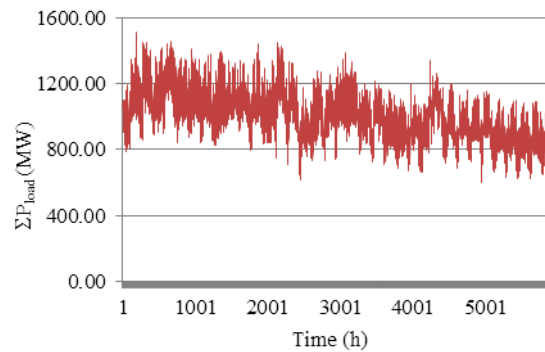


Fig. 5. Consumption progression in the timeframe.

A. Voltage sensitivity to MVARs

Using the REANS\_SolverPowerSystem (in-house software – Matlab ® code) – see Fig. 3, the sensitivity of the voltage to MVAR was calculated.

The results for 1/10 of nodes are illustrated in 3D in Fig. 6 and in 2D in Fig. 7.

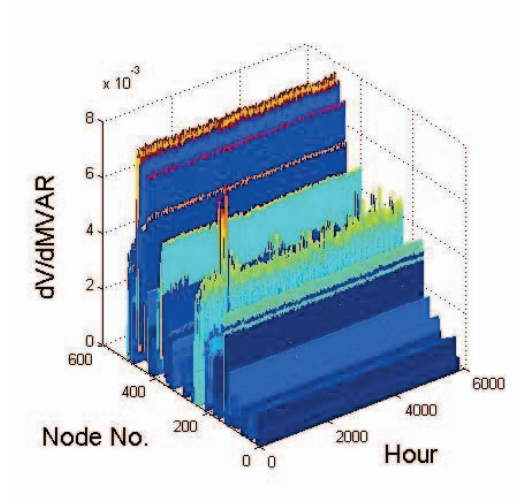
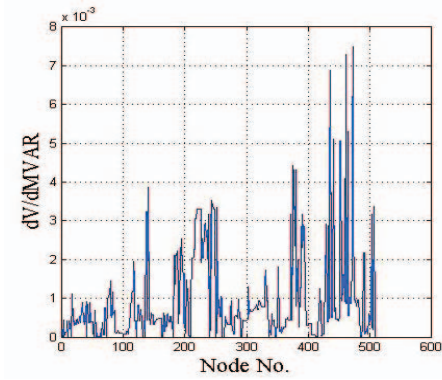
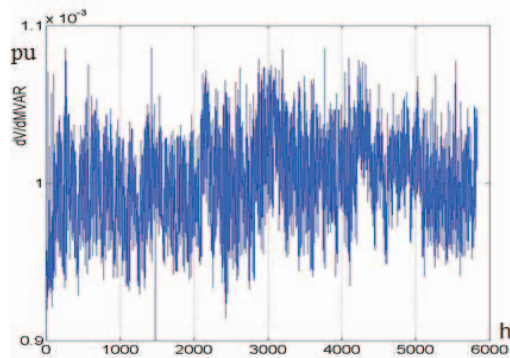


Fig. 6. Voltage sensitivity to MVAR (3D plot)



a)  $dV/dQ$  vs. Node. No at instant t



b)  $dV/dQ$  vs. time for node no. 659

Fig. 7. Voltage sensitivity to MVAR (2D plot).

The QV curves, known also as nose curves could also be useful for describing the impact of one reactive power on the voltage of the node where it is injected.

A sample of such curve for node no. 659 (a high voltage industrial consumer), as delivered by PowerWorld® simulator, [17], is presented in Fig. 8.

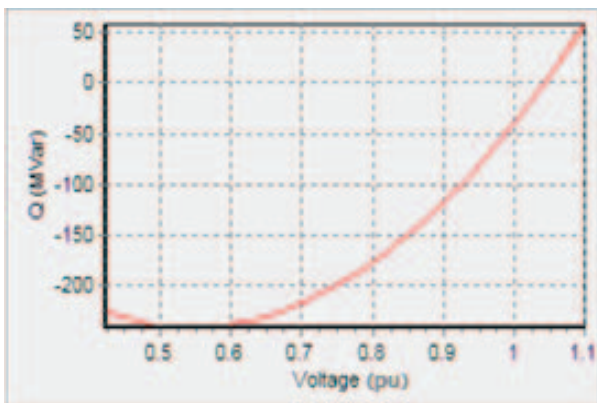


Fig. 8. QV curves for one node.

### B. Loss sensitivity to MVARs

The sensitivity of loss to MVAR was computed using the REANS\_SolverPowerSystem – see Fig. 3.

The results for 1/10 of nodes are shown in 3D in Fig. 9.

The momentary values for the same instant as in Fig. 7a) are 2D, depicted in Fig. 10.

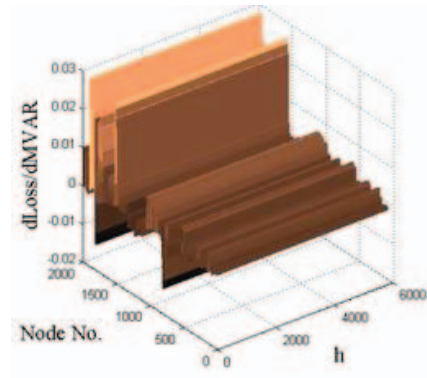


Fig. 9. Loss sensitivity to MVAR (3D plot).

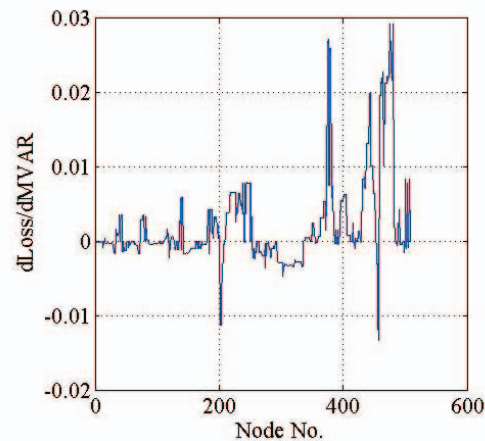


Fig. 10. Loss sensitivity to MVAR (2D plot).

### C. Impact of reactive power on ATC

The impact of the reactive power on the available transmission capacity is outlined by numerical simulation. Thus, the difference between the simulated flows with and without the analyzed MVARs is computed.

Such an approach conducted for node no. 659 (w-w/o) outlines differences in branch loading, which go from -1% (dark blue) up to +2% (red) in Fig. 11.

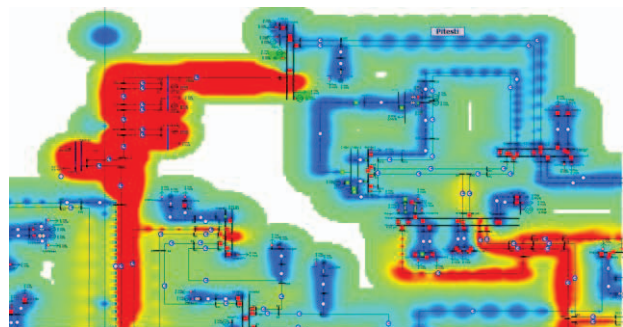


Fig. 11. ATC sensitivity to MVAR.

Information of the same nature could be extracted from the power transfer distribution factors (PTDF), as in [18]. This is faster and more general, but less precise than the method based on the difference in numerical simulation.

### D. Compensation of reactive power

The drawback of reactive power may be avoided by compensation. The compensation presupposes an investment – capital expenditure and operation costs for the running period.

For instance, in the case of the node no. 659 considered for this analysis during the weak load time span, the full compensation of the reactive power (from 19.5 MVAR to 0 MVAR) lowers the voltage by almost 0.02 pu, as it can be seen in Fig. 12.

This MVAR variation also results in a loss reduction of 0.124 MW.

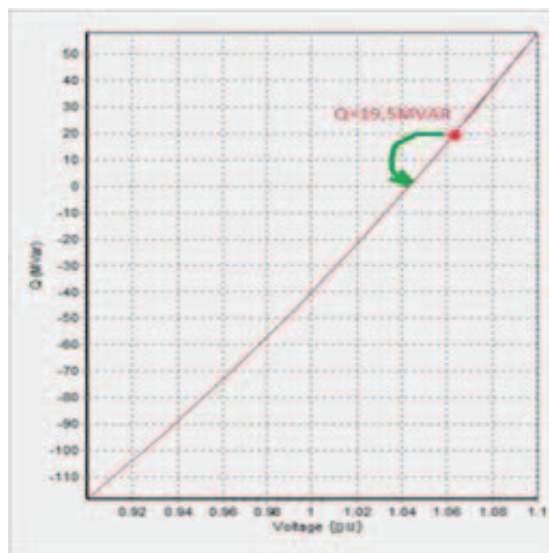


Fig. 12. Full compensation of MVARs in QV curve.

Based on data for 5855 hours, the compensator - STATCOM is to be optimally rated at 15MVAR (unremunerated part – neutral PF is avoided). The capital expenditure (CAPEX) for this compensator is 7.12 M€ and its annual operation expenditure (OPEX) is 17.8 k€. It saves losses of about 71.73 k€/year. For a discount rate of 1.05, the internal rate of return (IRR) is only -31.13 %. This lack of profitability is due to the very high CAPEX for HV compensation with SVC or STATCOM.

Once the technology will advance, the price of static compensators is expected to decrease, leading to a more cost-effective compensation.

## VII. CONCLUSIONS

The paper deals with the reactive power side effect and damping tariff and payments. The drawbacks of the reactive power related to each network user (e.g., voltage drops, additional power losses and useless ATC employment) are to be avoided through compensation.

Based on a case study consisting of a real 110 kV of about 2000 buses, one can conclude that the compensation of prosumers' MVAR for reducing losses is possible but not rewarding, because of the high CAPEX at the HV level (about 5.7 €/MVARh if operating 8760 h/year, fully charged). As the grid operator does not lack providers for the voltage regulation service, new compensators are not advisable, especially at HV. Moreover, the static compensation of MVAR does not free ATC selectively – at the targeted locations.

If the MVARs injected by network users are not necessary to voltage regulation, any exemption from MVARh payments, according to [10], is to be avoided. Beneficial

but volatile support under weak control may generate but not solve problems.

These conclusions are case-based. An in-depth analysis and further tests in various cases would be helpful.

## ACKNOWLEDGMENT

This work was supported by CEZ Distribution (<http://www.cez.ro/ro/cez-distributie.html>). We thank CEZ Distribution not only for funding this work, but also for providing data and generously making available their valuable expertise in dispatching, planning and operation.

Received on July 10, 2016

Editorial Approval on November 5, 2016

## REFERENCES

- [1] Conti and A. M. Greco, "Voltage regulation through optimal reactive power dispatching in active distribution networks," *MELECON 2008 - The 14th IEEE Mediterranean Electrotechnical Conference*, Ajaccio, 2008, pp. 792-798.
- [2] P. Martí, M. Velasco, J. Torres-Martínez, J. Miret and M. Castilla, "Reactive power control for loss minimization in low-voltage distributed generation systems," 2016 12th IEEE International Conference on Control and Automation (ICCA), Kathmandu, 2016, pp. 371-376.
- [3] B. Tamimi, C.A. Cañizares, S. Vaez-Zadeh: "Effect of Reactive Power Limit Modeling on Maximum System Loading and Active and Reactive Power Markets", *IEEE Transactions on Power Systems*, Vol. 25, No. 2, May 2010, pp. 1106 – 1116.
- [4] M. Shicong, G. Jianbo, H. Qing, Z. Jian, D. Mian and Y. Zhao, "Guide for voltage regulation and reactive power compensation at 1000kV AC and above with IEEE P1860 standard," *Power System Technology (POWERCON)*, 2014 International Conference on, Chengdu, 2014, pp. 2092-2097.
- [5] J. Schlabbach and K.-H. Rofalski "Power System Engineering: Planning, Design, and Operation of Power Systems and Equipment", WILEY-VCH Verlag GmbH, 2008
- [6] H. K. Tyll, "FACTS technology for reactive power compensation and system control," *Transmission and Distribution Conference and Exposition: Latin America*, 2004 IEEE/PES, 2004, pp. 976-980.
- [7] P. Preedavichit and S. C. Srivastava, "Optimal reactive power dispatch considering FACTS devices," *Advances in Power System Control, Operation and Management*, 1997. APSCOM-97. Fourth International Conference on (Conf. Publ. No. 450), 1997, pp. 620-625 vol.2.
- [8] S. G. Ghiocel, J. H. Chow, G. Stefopoulos, B. Fardanesh, D. B. Bertagnolli and M. Swider, "A voltage sensitivity study on a power transfer path using synchrophasor data," 2011 IEEE Power and Energy Society General Meeting, San Diego, CA, 2011, pp. 1-7.
- [9] ANRE, "Order – Approval of Methodology on establishing payments for reactive energy and setting the regulated price for reactive energy", ANRE Order No.33/2014 – in Romanian, <http://www.anre.ro/ro/energie-electrica/legislatie/metodologii-tarife/furnizare-energie-electrica>
- [10] ANRE, "Order –Updating and completion of Methodology on establishing payments for reactive energy and setting the regulated price for reactive energy" / Project - in Romanian, <http://www.anre.ro/ro/energie-electrica/legislatie/documente-de-discutie-ee1/metodologii-proceduri-tarife/proiect-de-ordin-privind-modificarea-si-completarea-metodologiei-privind-stabilirea-obligatiilor-de-plata-a-energiei-electrice-reactive-si-a-pretului-reglementat-pentru-energia-electrica-reactiva-aprobata-prin-ordinul-anre-nr-33-2014>
- [11] V. Ajarapu, "Computational Techniques for Voltage Stability Assessment and Control", *Springer Verlag*, 2006.
- [12] H. D. Chiang, A. J. Flueck, K. S. Shah, and N. Balu, "CPFLOW: A practical tool for tracing power system steady-state stationary

- behavior due to load and generation variations”, *IEEE Trans. Power Syst.*, vol. 10, no. 2, pp. 623-634, May 1995.
- [13] X. Lin, A. K. David, and C. W. Yu, “Reactive power optimization with voltage stability consideration in power market systems”, *IEE Gener. Transm. Distrib.*, vol. 150, no. 3, pp. 305-310, May 2003.
- [14] L. G. Manescu: "LQG Decentralized Control for FACTS", International Conference on Applied and Theoretical Electricity ICATE 2002, Nov. 2002, Section 5, pp. 272-278.
- [15] L. G. Manescu and D. Rusinaru, "Loss based performance index for the reactive power control," Optimization of Electrical and Electronic Equipment (OPTIM), 2012 13th International Conference on, Brasov, 2012, pp. 307-312.
- [16] L.G. Manescu, D. Rusinaru, M. Ciontu, et al., “Study about the impact of the reactive power on losses and quality into 110kV distribution network” – in Romanian, Report on Contract 61.1 DJ 31766?27.07.2015 – order from CEZ Distribution.
- [17] Powerworld, “User guide”, <http://www.powerworld.com/knowledge-base/powerworld-simulator-user-guides>
- [18] J. Kumar and A. Kumar, "Multi-transactions ATC determination using PTDF based approach in deregulated markets," 2011 Annual IEEE India Conference, Hyderabad, 2011, pp. 1-6.

# Evaluating RMS of Linearly Variable Magnitude Waveforms by Using FFT and WPT. Theory and Practice.

Ileana-Diana Nicolae<sup>\*</sup>, Petre-Marian Nicolae<sup>†</sup>, Diana Cristina Maria<sup>†</sup> and Scărlătescu Lucian<sup>†</sup>

<sup>\*</sup> University of Craiova, Dept. of Computers and IT, Craiova, Romania, nicolae\_ileana@software.ucv.ro

<sup>†</sup> University of Craiova, Dept. of Electrical, Energetic and Aero-Spatial Engineering, Craiova, Romania  
pnicolae@elth.ucv.ro, maria.diana\_cristina@yahoo.com

**Abstract** - The paper deals with the evaluation of the Root Mean Square (RMS) indices of signals with linearly variable magnitude by using Wavelet Packet Transform (WPT) and Fast Fourier Transform (FFT). Firstly there is presented a synthesis of employed techniques and previous results of the authors with respect to synthetically generated single-harmonic signals. The signals had linearly decreasing/increasing magnitude  $M$ .  $M$  varies according to a constant slope  $G$ . The studied absolute difference between the final and initial values of  $M$  belongs to the set  $\{2, 5, 7.5$  and  $10\}$ % from the initial  $M$ . Results of the RMS evaluation by using both FFT and WPT in a single harmonic approach are recalled, focusing on the maximum absolute values of percent relative errors. New studies are presented now, firstly considering randomly generated synthetic multi-harmonic signals. Three cases are considered, corresponding to harmonic orders belonging to 3 distinct ranges: 3...9, 31...39 and respectively 3...40. The errors associated to the use of FFT and WPT are evaluated for them. Two real multi-harmonic signals are afterward analyzed. Small differences were noticed between the values yielded by FFT and WPT for the total RMS as compared to those computed with Riemann sums. The differences between the RMS yielded by FFT and WPT are also evaluated and discussed.

**Keywords:** *Wavelet packets, Fast Fourier Transforms, power quality, numerical simulation, convergence of numerical methods.*

## I. INTRODUCTION

For real-time applications, in (quasi)stationary regimes with smooth variation of parameters and an insignificant contribution of harmonics of high orders, a standard Fast Fourier Transform (FFT) analysis can provide data with an acceptable accuracy [1]. Interesting wavelet-based algorithms for the harmonic analysis in power systems were proposed in [2]-[4].

Conventional Fourier based analyzing tools have some limitations concerning frequency and time resolutions. Although Wavelet Transforms (Discrete Wavelet Transform - DWT and Wavelet Packet Transform - WPT) overcome these limitations, they suffer from the problem of spectral leakage which is related to the choice of the wavelet family and the mother wavelet used in the analysis. In order to minimize these errors, in [5] is presented to an approach to select the most suitable wavelet family and the most suitable mother wavelet to achieve accurate measurement of steady-state harmonic distortion using DWT. Because WPT is an extended version of DWT, the

useful conclusions for our analysis, provided by [5], [6] are: in the case of low distortion levels the most suitable family is the 'db' (Daubechey) and the accuracy increases with increasing the wavelet order or the number of vanishing moments. Wavelet Packet Transform (WPT) provides a uniform cover of the signal and thus its frequency resolution is superior to that provided by DWT [7].

Our previous studies ([1], [6]) concerned with the accuracy of evaluating Power Quality (PQ) indices considered signals with constant magnitude over a sequence of periods. Special techniques must be used for the evaluation of PQ indices when the signals have linearly growing/decreasing magnitudes [8]. Different values are obtained for the inherent errors (accompanying any numerical method). Their study is compulsory for all applications, because they are specific to every distinct operational context. For signals obtained as sinusoidal waveforms polluted by a single harmonic, an extended study was made in [8]. In this paper, this study is continued, such as to consider sinusoidal signals with linearly variable magnitudes, polluted by more harmonics. The final goal is to estimate the accuracy provided by our original algorithms when analyzing data acquired by our Data Acquisition Systems (DAS) described in [9], which have been using to record and evaluate power quality indices for electrical waveforms acquired from power plants. The mentioned DAS provide 197 samples per period (when providing simultaneously 8 waveforms), respectively of 1576 samples per period for a single waveform.

## II. ALGORITHM RELATED FEATURES

In order to improve the accuracy of analysis, spline interpolations were made, generating  $NP$  equally spaced intervals within each interval defined by 2 adjacent samples.  $NP$  is chosen in different ways, depending on the decomposition method and on the number of samples per period ( $SPP$ ) respectively. When using FFT,  $NP$  was chosen depending on  $SPP$  as follows: for  $SPP=197$ ,  $NP=20$  and when  $SPP=1576$ ,  $NP=3$ .

In order to accomplish the WPT decomposition, two tree configurations were employed, relying on a Wavelet mother (WM) with a filter of length 40. The number of levels was 6 when  $SPP=197$  and respectively 5 when  $SPP=1576$ . The number of calculation points ( $CP$ ) is also variable in the WPT work frame, being computed with:

$$CP = nf \cdot 2^d \quad (1)$$

where  $nf=4$  (it represents the length of the vectors hosted by the tree's terminal nodes) and  $d$  represents the tree's depth (the number of levels).

We also considered a numerical approximation of the total Root Mean Square (denoted by  $RMS_m$ ) which can be computed by using the samples, using a Riemann sum:

$$f_{RMS} = \lim_{T \rightarrow \infty} \sqrt{1/T \int_0^T [f(t)]^2 dt} \quad (2)$$

We used it under the form [10]:

$$V_{RMS\ over\ T} = \sqrt{\frac{\text{area under the curve of } [v(t) \cdot v(t)] \text{ for a period } T}{\text{number of calculation points } s \text{ per period}}} \quad (3)$$

In Eq. (3),  $v(t)$  is a vector obtained: (a) only from the acquired samples from a period, and in this case  $CP = 197$  when the smallest sampling rate is used; (b) as result of the interpolation over a period of the acquired signal ( $CP$  is equal to the number of all points, original plus those yielded by the interpolation).

### III. TECHNIQUES TO EVALUATE POWER QUALITY INDICES AND ERRORS ASSOCIATED TO ALGORITHMS

#### A. Arithmetic averaged values for theoretic RMS values

For our study concerned with sine waves polluted by harmonics, both the magnitudes of the sinusoidal signal ( $M$ ) and respectively of the  $NH$  polluting harmonics ( $H_j$ ,  $j=1...NH$ ) have linear variations all over the sequence whose length is  $Nper=10$  periods.  $M$  was increased / decreased in a linear manner, along all periods. The difference between the initial and final value of  $M$  was defined in a percent relative manner (its absolute value belongs to the set of values  $\{2.5\%, 5\%, 7.5\%, 10\%\}$ ). For a signal with a magnitude  $M$  increasing with 0.1, there is a correlation between the initial and final values of  $M$  as follows:  $M_{final} - M_{initial} = M_{initial} \times 1.1$ . From this point on we will refer this percent increase as "gain" ( $G$ ).

From our point of view, a correct approach when dealing with RMS values corresponding to the whole sequence should make use of the following "theoretical reference values", defined with arithmetic averages [8]:

$$R\tilde{M}S_{FT} = \left( \sum_{i=1}^{Nper \times SPP} M_i / (Nper \times SPP) \right) / \sqrt{2} \quad (4)$$

$$R\tilde{M}S_{j,DT} = \left( \sum_{i=1}^{Nper \times SPP} H_{i,j} / (Nper \times SPP) \right) / \sqrt{2} \quad (5)$$

$$R\tilde{M}S_{DT} = \sqrt{\sum_{j=1}^{NH} R\tilde{M}S_{j,DT}^2} \quad (6)$$

$$R\tilde{M}S_{TT} = \sqrt{(R\tilde{M}S_{FT}^2 + R\tilde{M}S_{DT}^2)} \quad (7)$$

In the above formulas:  $M_i$  represents the magnitude of the pure sine wave ( $S$ ) corresponding to its  $i$ -th synthetically generated sample;  $H_{i,j}$  represents the magnitude of the  $j$ -th harmonic corresponding to its  $i$ -th synthetically generated sample and is raising with  $G$ . In Eqs. (4)...(7),

" $F$ " is used to denote "Fundamental", " $D$ " is used to denote "distorting", " $T$ " stands for "total" and " $Transf$ " can be either FFT or WPT.

#### B. Applying FFT and WPT in a linearly variable magnitude context

When applying both FFT and WPT over the entire signals of  $Nper$  periods length, unacceptable errors were obtained, mainly with respect to the value of the RMS corresponding to distortions ( $RMS_D$ ). This made us apply both transforms in a "per-period" manner. That is, calculations were made for each period individually and finally the following values were computed as arithmetic averaged values over  $Nper$  periods [8] with  $X$  standing for  $F$  or  $D$ :

$$RMS_{XTransf} = \sum_{per=1}^{Nper} RMS_{XTransf}(per) / Nper \quad (8)$$

$$RMS_{TTransf} = \sqrt{(RMS_{FTransf}^2 + RMS_{DTransf}^2)} \quad (9)$$

The compared quantities were: (a) the "node-zero" value yielded by WPT which was compared to the RMS corresponding to the fundamental frequency  $RMS_F$ ; (b) the "non-zero node" value, which was compared to the  $RMS_D$  and (c) the total RMS, denoted by  $RMS_T$ .

The definitions for these indices computed by using WPT are given in [11] and respectively those computed by using FFT are given in [12]. The counterpart definitions in the case when WPT is used consider the following rule:  $RMS_F$  is calculated by using the energy of the leftmost node from the bottom level of the binary tree, whilst  $RMS_D$  is using the energies of the rest of the nodes from the same level [6].

We considered percent relative errors:

$$err = (val_i - val_c) / val_c \cdot 100 \quad (10)$$

where  $val_i$  represents the theoretic values (yielded by Eqs. (4)...(7)) and  $val_c$  represents the computed values (the counterpart of  $val_i$ , computed with the Eqs. (8), (9)).

### IV. PQ EVALUATION FOR SINGLE HARMONIC SIGNALS WITH LINEARLY VARIABLE MAGNITUDE

Simulations were performed with FFT and WPT for the slope defining the variation of  $M$  ( $G$ ) following the rule:  $G = (\text{index of test}) * 2.5\%$ , both for increasing and respectively decreasing  $M$ , in a single harmonic context. Fig. 1 [8], [13] provides graphical representations of the maximum absolute value of the percent relative error (MAVPRE) considering maximum 39 harmonics reaching at most 0.1 from the fundamental's magnitude. The symbol '+' was used for the ascending slope whilst 'o' corresponds to the descending one.

The highest absolute errors are associated to  $RMS_D$ . They appear at small harmonic orders with small magnitudes (Fig. 2). The following symbols were used: „M↑” denotes " $M$  raises"; „M↓” denotes " $M$  falls". Table I depicts the mean values of the MAVPRE (averaged across all values of  $G$ ). This table reveals that the level of all MAVPREs is low, denoting that both methods provide appropriate results for practical applications. The values represented with italicized fonts are used to denote "better accuracy" as compared to the other decomposition technique, for the same value of  $SPP$ .

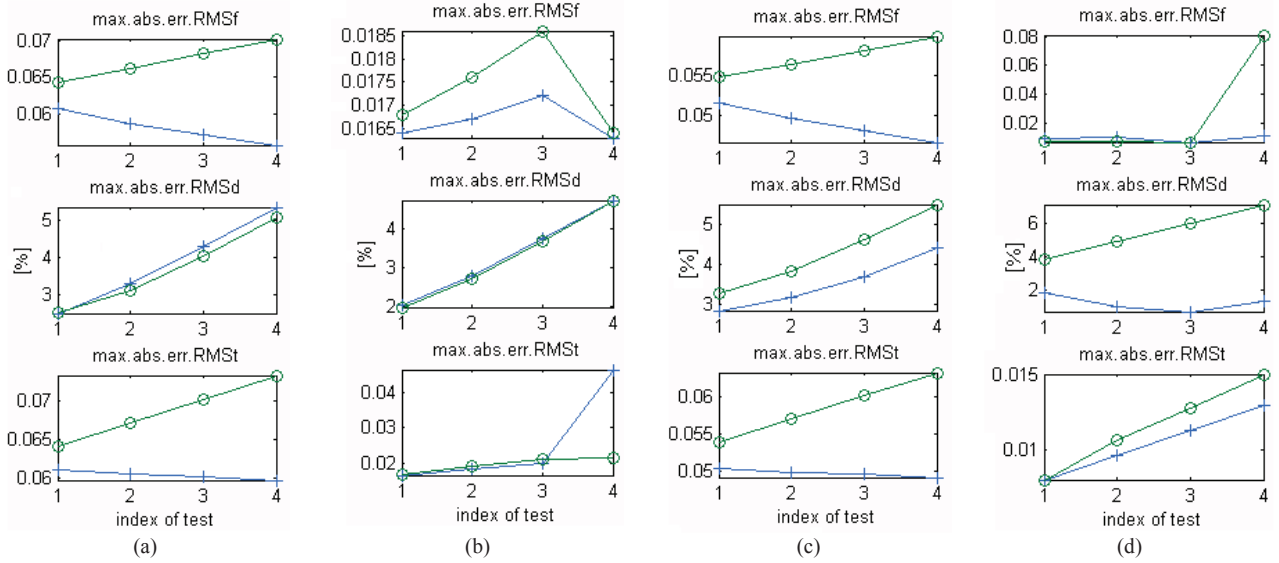


Fig. 1. Maximum absolute values of the percent relative error : (a) , (b) : when using FFT,  $SPP=197$ , respectively  $SPP=1576$ . (c), (d) : when using WPT,  $SPP=197$ , respectively  $SPP=1576$ .

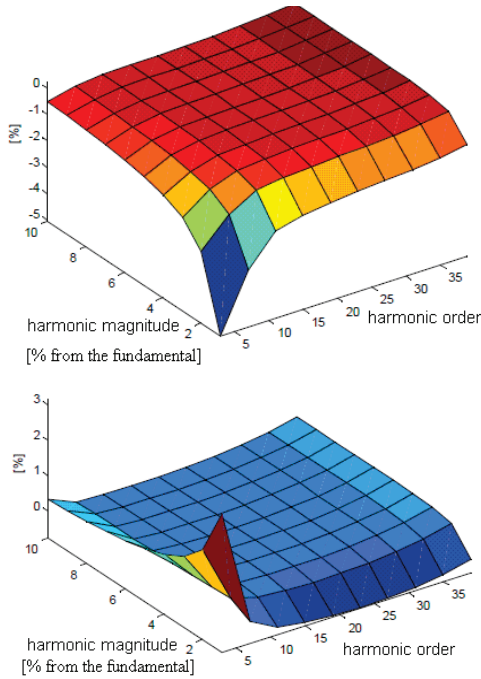


Fig. 2. Minimum (top) and maximum (bottom) of relative percent errors when evaluating  $RMS_D$  with FFT.  $SPP=197$ ,  $G=10\%$ ,  $M$  falls.

TABLE I.  
MEAN VALUES OF THE MAXIMUM ABSOLUTE VALUES OF THE PERCENT RELATIVE ERRORS

PQ index	SPP = 197		SPP = 1576		
	FFT	WPT	FFT	WPT	
$RMS_F$	M $\uparrow$	0.0581	0.0489	0.0167	0.01
	M $\downarrow$	0.0672	0.0573	0.0174	0.02
$RMS_D$	M $\uparrow$	3.8568	3.5436	3.3108	1.288
	M $\downarrow$	3.6738	4.3108	3.2618	5.482
$RMS_T$	M $\uparrow$	0.0604	0.0497	0.0253	0.0104
	M $\downarrow$	0.0687	0.0586	0.0197	0.0116

No systematic trend could be deduced from the quantitative point of view. None of the methods can be declared superior to the other one from the MAVPRE point of view. With 2 exceptions, both yielded by FFT ( $RMS_D$  computed when  $SPP=197$  and  $RMS_T$  computed when  $SPP=1576$ ), MAVPREs are higher for decreasing  $M$  as compared with the cases when  $M$  is raising.

The use of more samples has advantages for both decomposition techniques when computing  $RMS_F$  and  $RMS_T$  (it reduces the associated MAVPREs by a factor of at least 3). Yet, due to the sensibility of WPT analysis relative to phase differences, higher maximum absolute values for the percent relative errors were generated by WPT when more samples were used during the evaluation of  $RMS_D$ , corresponding to certain particular phase differences. For the most critical case ( $G=10\%$ ), actually the mean value of the absolute values for the percent relative errors associated to  $RMS_D$  was around 0, with a “peak” of 2% for the lowest harmonic orders with very small magnitude.

## V. STUDY OF ERRORS IN A MULTI-HARMONIC CONTEXT

Considering the results from Section IV, our attention was afterward focused on 3 test signals spanning over 10 periods, obtained synthetically by superposing over a perfect sinusoid (with the magnitude  $M=10$ ), sets of 4 harmonics with randomly generated magnitudes (correlated to  $M$ ) and respectively with randomly generated phase differences, as depicted by Table II.

The ranges of harmonic orders were chosen such as to cover all areas of interest: the 1-st signal is polluted only by low odd harmonic orders (3, 5, 7 and 9), the 2-nd signal is polluted only by high odd harmonic orders (33, 35, 37 and 39), whilst the 3<sup>rd</sup> signal is polluted with harmonic orders from all the range of interest from the European standard point of view (3, 13, 27 and 39). Similar to our previous studies from Section IV,  $M$  and the harmonics' magnitudes were increased/decreased in a linear manner, along all 10 periods, considering a gain  $G$  calculated with:  $G=(index\ of\ test) * 2.5\%$ , both for increasing and respectively decreasing magnitudes.

TABLE II.  
CHARACTERISTIC FEATURES OF THE SYNTHETIC WAVEFORMS USED FOR TESTS - MULTI-HARMONIC CASES

Synthetic waveform index	Harmonic orders				Harmonic magnitudes [% from the magnitude of the pure sine wave]				Phase differences of harmonics [rad.]			
	1-st	2-nd	3-rd	4-th	1-st.	2-nd.	3-rd	4-th	1-st	2-nd	3-rd	4-th
1	3	5	7	9	13	3.5	2.8	0.7	-2.2	-1.56	2.14	-1.54
2	33	35	37	39	7.7	0.63	0.09	0.8	0.24	3.12	-2.65	-0.36
3	3	13	27	39	4.9	0.49	0.35	0.02	0.19	1.75	2.73	-2.32

Figs. 3 and 4 depict the percent relative errors associated to the use of FFT, respectively WPT. The left column corresponds to positive values of  $G$  and the right column is dedicated to the negative ones. The symbol ‘+’ depicts the results for  $SPP=197$  whilst ‘o’ is used for  $SPP=1576$ .

Table III depicts the mean values of the absolute percent relative errors, averaged across all values of  $G$ . Similar to the single-harmonic case, for the multi-harmonic pollution the greatest errors are associated the evaluation of  $RMS_D$ . Another similarity is related to the “descending over ascending slope” comparison. In all cases, higher errors were recorded for the descending slope, irrespective to the method used for analysis.

Usually WPT provides slightly lower errors (see the italicized fonts). In only 8 out of 72 cases (see the bolded fonts), the FFT yielded slightly smaller errors. All of them are associated to  $RMS_d$ .

The magnitudes of errors in all cases are very low, highly acceptable for industrial applications. Moreover, they did not exceed the maximal values evaluated during the single-harmonic study.

VI. STUDY ON REAL DATA

The next step was to perform analysis over real data, acquired from a test stand. Data correspond to a driving system using a chopper and a DC motor. The 1st set of real data corresponds to unfiltered currents (Fig. 5). The 2nd set of real data (Fig. 6) contains currents with reduced harmonic content, but with a “zig-zag” variation of magnitudes (alternately fallings/risings of signal’s magnitude). The sampling frequency was 19200 Hz.

For a global picture, data were also analyzed considering the reversed order, the final goal being to address both the “ascending” specific and respectively “descending

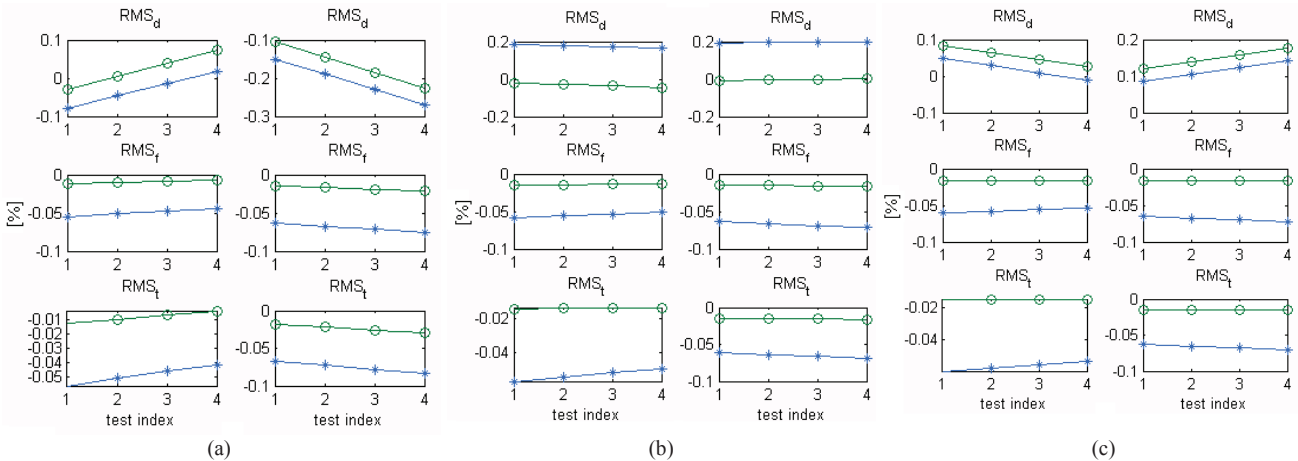


Fig. 3. Percent relative errors yielded by the FFT analysis. (a) – low harmonic orders; (b) high harmonic orders; (c) mixed harmonic orders.

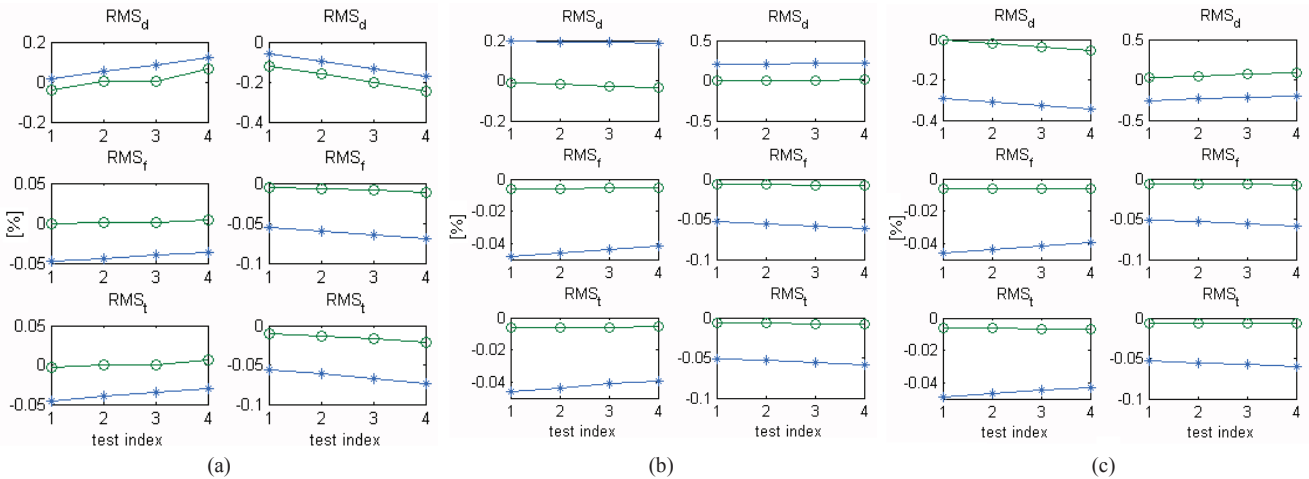


Fig. 4. Percent relative errors yielded by the WPT analysis. (a) – low harmonic orders; (b) high harmonic orders; (c) mixed harmonic orders.

TABLE III.  
MEAN VALUES OF PERCENT RELATIVE ERRORS (ABSOLUTE VALUES)

PQ index mean value of MAVPRE		SPP = 197		SPP = 1576		
		FFT	WPT	FFT	WPT	
Low harmonic orders	$RMS_F$	M↑	0.0495	0.0425	0.0090	0.0013
		M↓	0.0696	0.0627	0.0180	0.0079
	$RMS_D$	M↑	<b>0.0399</b>	0.0684	0.0369	0.0295
		M↓	0.2106	0.1151	<b>0.1663</b>	0.1834
	$RMS_T$	M↑	0.0487	0.0380	0.0077	0.0022
		M↓	0.0754	0.0648	0.0240	0.0151
High harmonic orders	$RMS_F$	M↑	0.0549	0.0448	0.0141	0.0057
		M↓	0.0676	0.0575	0.0157	0.0073
	$RMS_D$	M↑	<b>0.1764</b>	0.1911	0.0330	0.0233
		M↓	<b>0.1964</b>	0.2099	0.0043	0.0055
	$RMS_T$	M↑	0.0526	0.0425	0.0142	0.0059
		M↓	0.0650	0.0549	0.0156	0.0072
Mixed harmo- nic orders	$RMS_F$	M↑	0.0570	0.0429	0.0159	0.0057
		M↓	0.0687	0.0547	0.0165	0.0055
	$RMS_D$	M↑	<b>0.0241</b>	0.3206	0.0553	0.0233
		M↓	<b>0.1149</b>	0.2294	0.1487	0.0073
	$RMS_T$	M↑	0.0562	0.0457	0.0152	0.0059
		M↓	0.0668	0.0565	0.0148	0.0072

specific features.

An interesting aspect is related to the invariance of results yielded by FFT with respect to the sense of variation (identical values were obtained at magnitude's raising and falling respectively). Small differences were instead revealed in particular cases by the WPT analysis.

Tables IV and V gather the results of the joint analysis. The differences between the results yielded by different methods (FFT, WPT and Riemann sum) are evaluated in a percent relative manner. For example the difference "FFT vs WPT" is given by:

$$(value_{FFT} - value_{WPT}) / value_{FFT} \times 100 \quad (11)$$

For the 1-st set of real data, all methods provide almost identical values for all types of RMS. Because the method relying on Riemann sums provides the most accurate value for  $RMS_T$  when considering the theoretical approach, one can deduce that the phenomenon of "spectral leakages" is faced by both FFT and WPT methods. Fortunately the errors associated to it are very small.

For the 2-nd set of real data, WPT is less affected by the spectral leakage phenomena. On the other hand, an over-evaluation of  $RMS_T$  can be noticed when FFT is used, but for both methods the errors are lower than those

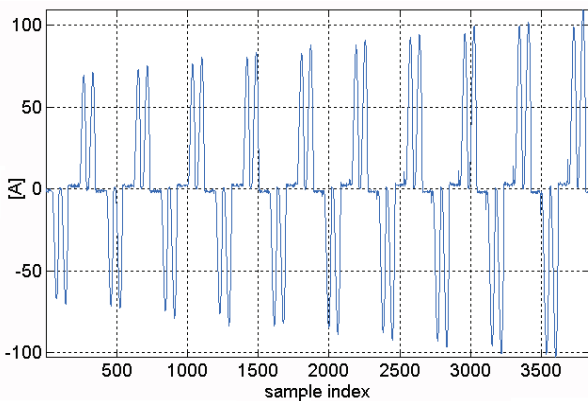


Fig. 5. Phase current from the 1-st set of real data.

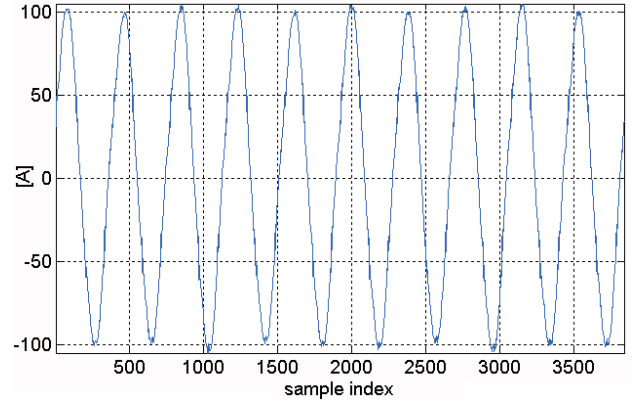


Fig. 6. Phase current from the 2-nd set of real data.

associated to the 1-st set of data.

The opposite signs of errors associated to  $RMS_T$  are in correlation with the significant percent relative differences noticed between the values of  $RMS_D$  yielded by FFT and WPT, mainly for the current flowing through the 1-st phase. The explanation for them might rely on 2 reasons:

- both FFT and WPT can yield positive, respectively negative errors when evaluating  $RMS_D$  which are higher for low harmonic orders with low harmonic magnitudes. They do not occur at the same phase difference and therefore the effects can add, providing differences for counterpart values;
- FFT is more affected by the non-symmetry between the 1-st and 2-nd half-period of the same period and this kind of non-symmetries are frequently noticed in the waveforms from the 2-nd set of data.

Yet, considering the small absolute values of the distorting residues these differences should not be a concern with respect to the accuracy provided by both methods.

## VII. CONCLUSIONS

When dealing with harmonically polluted signals in the context of variable magnitudes, test signals must be generated synthetically such as to simulate as accurate as possible the real signals for which the PQ analysis will be performed by using algorithms with clear specifications relative to the internal data structures and sampling ratios. By varying in a systematic manner the harmonic orders and magnitudes, the phase differences and the value of the slope associated to the magnitude variation it is possible to estimate the level of maximum absolute values of the percent relative errors (MAVPRE) associated to the evaluation of the most important RMSs.

In a single harmonic work frame, the representations of MAVPRE revealed interesting aspects:

- none of the methods can be declared superior to the other one from the MAVPRE point of view;
- the level of all MAVPREs is low;
- usually MAVPREs are higher for decreasing  $M$ ;
- unlike the case when  $M$  raises, when  $M$  falls the behavior of MAVPREs is more predictable;
- the 3D representations revealed that the most significant errors appear when evaluating  $RMS_D$ ;
- a better sampling ratio is always beneficial from the point of view of evaluating with better accuracy  $RMS_F$  and  $RMS_T$ . For certain combinations of phase differences it can instead result into higher MAVPREs associated to  $RMS_D$ , mainly when WPT is used.

TABLE IV.  
VALUES YIELDED BY FFT AND WPT ANALYSIS AND PERCENT RELATIVE DIFFERENCES FOR THE FIRST SET OF REAL DATA

Current PQ index	RMS <sub>D</sub>					RMS <sub>F</sub>					RMS <sub>T</sub>						
	FFT [A]	DWT↑ [A]	FFT vs DWT↑ [%]	DWT↓ [A]	FFT vs DWT↓ [%]	FFT [A]	DWT↑ [A]	FFT vs DWT↑ [%]	DWT↓ [A]	FFT vs DWT↓ [%]	Riemann [A]	FFT [A]	FFT vs R [%]	DWT↑ [A]	DWT↑ vs R [%]	DWT↓ [A]	DWT↓ vs R [%]
I1	26.97	26.95	0.07	26.96	0.04	32.86	32.81	0.15	32.82	0.12	42.89	42.51	0.89	42.46	1.00	42.47	0.98
I2	27.69	27.67	0.07	27.67	0.07	34	33.97	0.09	33.97	0.09	44.26	43.86	0.90	43.81	1.02	43.81	1.02
I3	27.00	26.99	0.04	26.99	0.04	32.96	32.96	0.00	32.96	0.00	43.04	42.61	1.00	42.60	1.02	42.60	1.02

TABLE V.  
VALUES YIELDED BY FFT AND WPT ANALYSIS AND PERCENT RELATIVE DIFFERENCES FOR THE SECOND SET OF REAL DATA

Current PQ index	RMS <sub>D</sub>					RMS <sub>F</sub>					RMS <sub>T</sub>						
	FFT [A]	DWT↑ [A]	FFT vs DWT↑ [%]	DWT↓ [A]	FFT vs DWT↓ [%]	FFT [A]	DWT↑ [A]	FFT vs DWT↑ [%]	DWT↓ [A]	FFT vs DWT↓ [%]	Riemann [A]	FFT [A]	FFT vs R [%]	DWT↑ [A]	DWT↑ vs R [%]	DWT↓ [A]	DWT↓ vs R [%]
I1	4.55	3.86	15.16	3.74	17.80	69.44	69.4	0.06	69.4	0.06	69.52	69.58	-0.09	69.51	0.01	69.51	0.01
I2	4.29	4.17	2.80	3.8	11.42	70.99	70.95	0.06	70.98	0.01	71.09	71.12	-0.04	71.08	0.01	71.08	0.01
I3	4.89	4.39	10.22	4.73	3.27	69.27	69.27	0.00	69.25	0.03	69.42	69.44	-0.03	69.41	0.01	69.41	0.01

The tests on randomly generated multi-harmonic pollutions revealed that:

- the greatest errors are associated to  $RMS_D$ ;
- another similarity to the single harmonic cases is related to the “descending over ascending slope” comparison. In all cases, higher absolute errors were recorded for the descending slope, irrespective to the method ;
- usually WPT provides slightly lower errors. All exceptions are associated to  $RMS_d$ ;
- the magnitudes of errors in all cases are very low, highly acceptable for industrial applications. Moreover, they did not exceed the maximal values evaluated during the single-harmonic study.

For the 1-st set of real data, all methods provide almost identical values for all types of RMS. The phenomenon of “spectral leakages” is faced by both FFT and WPT methods. Fortunately the errors associated to it are very small.

For the 2-nd set of real data, WPT is less affected by the spectral leakage phenomena. On the other hand, an over-evaluation of  $RMS_T$  can be noticed when FFT is used, but for both methods the errors are lower than those associated to the 1-st set of data. The opposite signs of errors associated to  $RMS_T$  are in correlation with the significant percent relative differences noticed between the values of  $RMS_D$  yielded by FFT and respectively WPT, mainly for the current flowing through the 1-st phase.

A final conclusion is relative to the good practice of applying any of the analyzed transform in a per-period manner and performing arithmetic averages.

#### ACKNOWLEDGMENT

This work was supported by a grant of the Romanian National Authority for Scientific Research and Innovation, CNCS/CCCDI –UEFISCDI, project number PN-III-P2-2.1-BG-2016-0240, within PNCIDI III.

Received on July 17, 2016

Editorial Approval on November 15, 2016

#### REFERENCES

- [1] I.D. Nicolae, P.M. Nicolae and M.S. Nicolae, „Tunning the Parameters for the FFT Analysis of Waveforms Acquired from a Power Plant”, *Acta Electrotehnica*, vol. 56 no. 3, pp. 219-224, July 2015, available at [http://ie.utcluj.ro/files/acta/2015/Number3/MPS2015\\_Nicolae-1.pdf](http://ie.utcluj.ro/files/acta/2015/Number3/MPS2015_Nicolae-1.pdf).
- [2] D. Taskovski, L. Koleva, A. Milchevski and V. Dimcev, “Near Perfect Reconstruction Filter Banks for Power Quality Analysis”, *Metrol. Meas. Syst.*, vol. XX, no. 3, pp. 359-370, 2013.
- [3] J. Barros and R. Diego, “Analysis of harmonics in power systems using the wavelet packet transform”. *IEEE Trans. Instrumentation and Measurement*, vol. 57, pp. 63-69, Jan. 2008.
- [4] E.Hamid and Z. Yokoyama Kawasaki „Rms and Power Measurements: A Wavelet Packet Transform Approach”. *Trans. Institute of Elect. Eng. of Japan*, vol. 122-B, no. 5, pp.599-606, May, 2002.
- [5] W. G. Morsi and M. E. El-Hawary, “The most suitable mother wavelet for steady-state power system distorted waveforms”, *Proceedings of CCECE 2008*, pp. 17 –22, Niagara Falls, May 2008.
- [6] I.D. Nicolae, P.M. Nicolae, M.S.Nicolae and I. Smarandescu, “Wavelet Packet Transform, a Reliable and Fast Method to Obtain the Fundamental Components Required for Active Filtering in Power Plants”, in press for *Proceedings of PEMC 2016*, Varna, Bulgaria, Sept. 2016.
- [7] M.R. Mosavi, A. Rezaei a.o., “A fast and accurate anti-jamming system based on wavelet packet transform for GPS receivers”, *GPS solutions*, pp. 1-12, April 2016.
- [8] I.D. Nicolae, P.M. Nicolae, D.C. Maria, L. Scărlătescu, “Dealing with Linearly Variable Magnitudes in Fourier and Wavelet Packet Transform Frameworks”, in press for *Proceedings of ICATE 2016*, Craiova, Romania, Oct. 2016.
- [9] D.M. Purcaru, I. Purcaru and D. Popescu, “Results obtained in monitoring transient electrical events from hydropower plants”, *Proceedings of ICC 2015*, pp. 1-6, Miskolc, Hungary, May 2015.
- [10] K. Cartwright, „Determining the effective or RMS voltage of various waveforms without calculus”, Technology Interface/Fall 2007, pag. 1-20, available at [http://tij.org/issues/issues/fall2007/30\\_Cartwright/Cartwright-Waveforms.pdf](http://tij.org/issues/issues/fall2007/30_Cartwright/Cartwright-Waveforms.pdf), 2007, retrieved 2016.
- [11] W.G. Morsi, M.E. El-Hawary, “Reformulating Power Components Definitions Contained in the IEEE Standard 1459-2000 Using Discrete Wavelet Transform”, *IEEE Trans. on Power Delivery*, vol. 22, no. 3, pp.1910-1916, July 2007.
- [12] A. Tugulea, “Criteria for the Definitions of the Electric Power Quality and its Measurement Systems,” *ETEP*, vol. 6, no.5, pp.357-363, 1996.
- [13] D.C. Maria, “Intelligent Online Monitoring Solutions for Power Groups“, diploma degree project, 2016.

# On the Implementation of FBD-Theory Concepts in the Control of Active DC-Traction Substations

Mihaela Popescu, Alexandru Bitoleanu and Mircea Dobriceanu

University of Craiova, Faculty of Electrical Engineering, Craiova, Romania  
 mpopescu@em.ucv.ro, alex.bitoleanu@em.ucv.ro, mdobriceanu@em.ucv.ro

**Abstract** - This paper is focused on the transformation of a classical DC-traction substation with twelve-pulse uncontrolled rectifier into an active traction substation by adding a dedicated system for active filtering and regeneration called SISFREG. The connection of SISFREG to the AC-side is performed in the primary of the traction transformer via a passive coupling filter and a recovery transformer, whereas an active separating circuit ensures the connection to the DC-traction line. The new functions added to the DC-traction substation lead to the increasing the energy efficiency of the whole system in both traction and braking regimes of the vehicles' traction motors. The control of the current provided by the shunt active filter, which is the main component of SISFREG, is achieved in indirect mode, by means of the current upstream the point of common coupling. In the generation of the set current, the concepts of the Fryze-Buchholz-Depenbrock theory are implemented. Thus, an active current is always imposed at the power supply side and the current control loop guarantees almost sinusoidal current and global unity power factor. A complex Simulink model of the whole system, including facilities for energetic analysis, has been developed and the simulation results show good performances in both steady-state and dynamic regimes.

**Keywords:** *FBD theory, energy efficiency, DC traction, active substation, braking energy recovery, active filtering.*

## I. INTRODUCTION

In the classical DC-traction substations, the existence of the uncontrolled rectifiers to feed the DC-traction line has the effect of current harmonic pollution in the AC power supply and low power factor. Besides the problems in the power quality area, there is a huge waste of energy because of the non-receptivity of the traction power systems for the regenerative energy during the braking regime of the traction motors.

In order to increase the energy efficiency in the DC-traction substations, several solutions are reported in the literature, involving the use of specific static converters, such as static VAR compensators and active power filters [1]-[12].

The flexible and performant shunt active power filter (SAPF) is the most common solution to improve the power quality in traction regime [3]-[6]. As the control algorithm is a key factor, different approaches were formulated, most of them based on synchronously rotating reference frame [3], direct power control [4], or the so-called p-q theory of the powers [5].

On the other hand, in order to send the energy resulted during the braking regime into the power supply, the bidi-

rectional power flow between the DC and AC networks must be ensured. To transform the existing DC-traction substations into reversible substations, controlled converters should be used instead of diode rectifiers [7], [8].

Additional capabilities can be obtained for the DC-traction substation by connecting a regeneration system to the already existing traction transformer, in parallel with the diode rectifier. In [9], a voltage source inverter is coupled in the traction transformer secondary and, on the DC-side, a boost chopper is inserted.

In this paper, the attention is directed to the control system of an active DC-traction substation with 12-pulse diode rectifier which is obtained by adding a SAPF, together with proper connecting circuits, between the catenary line and AC-line [10]-[12]. Both the improvement of the power quality and the reuse of the kinetic braking energy are allowed.

The remaining paper is organized as follows. Section II describes the structure of the system, including the control part. The next section introduces the Fryze-Buchholz-Depenbrock (FBD) theory as a tool for current decomposition and its application in the generation of the reference current. In Section IV, the conceived Simulink model of the whole active DC-traction substation is presented. The performances of the system for active filtering and regeneration in terms of power quality aspects and energy efficiency are then illustrated. The main conclusions and further research are emphasized at the end of the paper.

## II. CONFIGURATION OF THE ACTIVE DC-TRACTION SUBSTATION

As shown in the left side of Fig. 1, the existing DC-traction substation consists of the traction transformer (TT) with wye and delta connections in the two secondary windings and a 12-pulse diode rectifier.

The system for active filtering and regeneration named SISFREG is conceived around a SAPF to allow the regeneration of the braking energy and to lead to an almost unity power factor during traction regime [10]-[12]. It is connected in parallel with the existing traction substation and coupled to the AC power supply by means of a recovery transformer.

It must be mentioned that, by connecting the SAPF directly in the secondary of the traction transformer, the magnitude of the voltage in the point of common coupling (PCC) would be too high compared to the voltage on the DC-side. A correct correlation between the two voltages is required in order to avoid an injected current of poor quality [13].

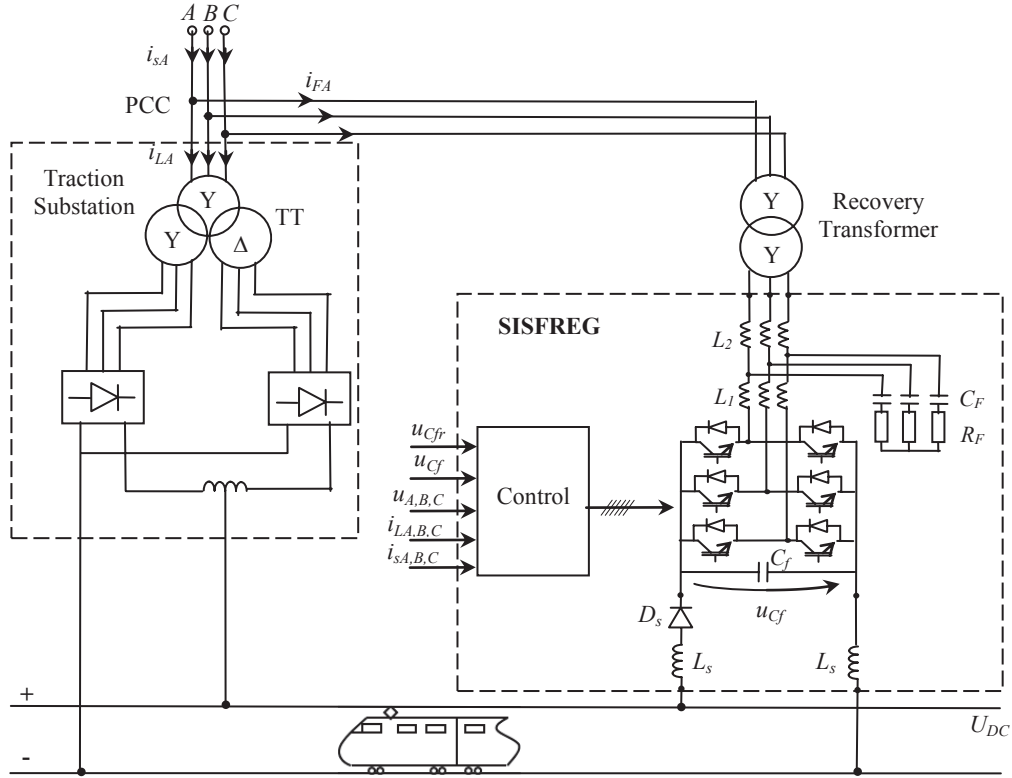


Fig. 1. Structure of the active DC-traction substation with twelve-pulse uncontrolled rectifier.

Indeed, the magnitude of the AC voltage in the traction transformer secondary ( $\sqrt{2}U_s$ ) can be expressed as a function of the no-load average voltage at the output of the 12-pulse rectifier ( $U_{DC0}$ ) as follows [14]:

$$\sqrt{2}U_s = \frac{\pi}{3} \cdot U_{DC0} \approx 1.05 \cdot U_{DC0}. \quad (1)$$

On the other hand, taking into account a voltage drop in the rectifier's output circuit of about 5 %, the no-load average voltage can be expressed by highlighting the rated DC voltage ( $U_{DCN}$ ) as follows:

$$U_{DC0} \approx 1.05U_{DCN}. \quad (2)$$

Consequently,

$$\sqrt{2}U_s \approx 1.1 \cdot U_{DCN}, \quad (3)$$

revealing the need of either decrease the voltage in PCC or increase the voltage on the DC-side.

By adopting an interface filter of third order (LCL type) provided with damping resistance, the behavior of the system against the high order switching harmonics is improved [15], [16].

As shown in Fig. 1, a separating circuit consisting of diode  $D_s$  and inductances  $L_s$  ensures the connection to the DC-traction line. In this manner, the natural transition between the active filtering and regeneration regimes is guaranteed and a correct dynamics of the current is ensured [12].

In the control part, the measured quantities are: the voltage across the compensation capacitor of SAPF ( $u_{cf}$ ), the voltages in PCC ( $u_{A,B,C}$ ), the supply currents upstream

PCC ( $i_{sA,B,C}$ ) and the currents in the traction transformer primary ( $i_{LA,B,C}$ ).

As illustrated in the principle control scheme of Fig. 2, the control of the current injected into PCC by SAPF via the recovery transformer is performed in indirect mode, by means of the current upstream PCC. Thus, the measuring of the SAPF's currents is not required.

First, the prescribed voltage on the DC-side must be ensured by an active component of the current provided at the output of voltage controller ( $i_{sru}$ ) [17]. The measured voltages in PCC are needed too, to generate the shape of these currents.

On the other hand, to improve the waveform of the current drawn from the power supply in traction regime and compensate the reactive power, the associated component of the reference current ( $i_{src}$ ) is generated according the the FBD-theory concepts. Detailed information are given in Fig. 3 and next section.

It must be noticed that, during the operation in regeneration mode, the traction rectifier is blocked due to the increased voltage on the DC-side and, consequently, only reference current  $i_{sru}$  exists.

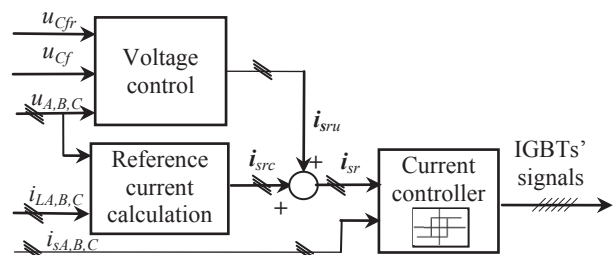


Fig. 2. Simplified structure of the control block.

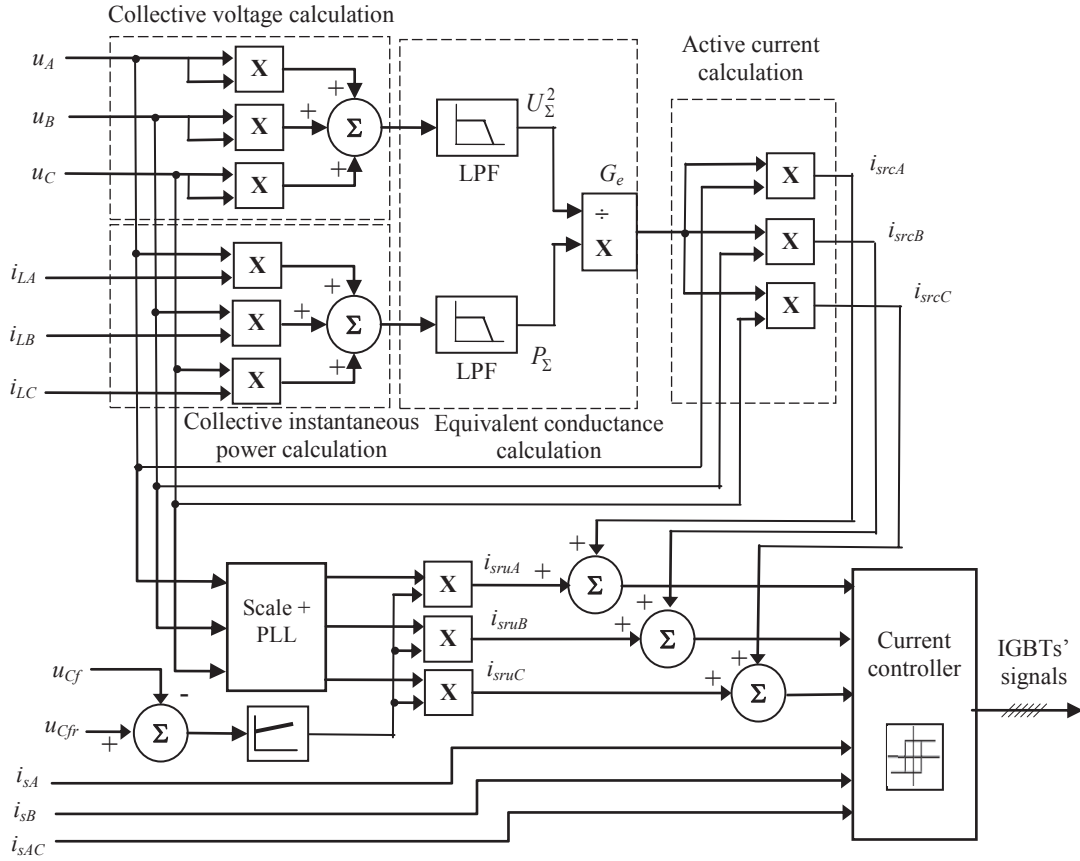


Fig. 3. Detailed structure of the control block based on FBD-theory concepts.

### III. FRYZE-BUCHHOLZ-DEPENBROCK THEORY - A TOOL FOR CURRENT DECOMPOSITION

The mathematical foundation of the so-called Fryze-Buchholz-Depenbrock theory attracted the researchers' attention in the field of the shunt active power filters control. Concretely, the algorithm of the compensating current generation includes the current components defined in the FBD theory [2], [18]-[22].

The FBD time-domain theory was originally proposed in 1931 by S. Fryze for single-phase circuits, and then successively enhanced by F. Buchholz (in 1993) and M. Depenbrock (in 1993) [19], [23].

In accordance with FBD theory, the active components of the currents in the traction transformer primary are calculated as follows:

$$i_{LaA} = G_e \cdot u_A; \quad i_{LaB} = G_e \cdot u_B; \quad i_{LaC} = G_e \cdot u_C, \quad (4)$$

where  $G_e$  is the equivalent conductance,

$$G_e = \frac{P_\Sigma}{U_\Sigma^2}. \quad (5)$$

The quantities used in expression (5) denote:

- the square of the collective rms voltage in the three-phase system,

$$U_\Sigma^2 = \frac{1}{T} \int_{t-T}^t u_\Sigma^2 \cdot dt, \quad (6)$$

where the collective instantaneous voltage ( $u_\Sigma$ ) is:

$$u_\Sigma = \sqrt{u_A^2 + u_B^2 + u_C^2}; \quad (7)$$

- the collective active power ( $P_\Sigma$ ),

$$P_\Sigma = \frac{1}{T} \int_{t-T}^t p_\Sigma \cdot dt, \quad (8)$$

where the collective instantaneous power ( $p_\Sigma$ ) is:

$$p_\Sigma = u_A i_{LA} + u_B i_{LB} + u_C i_{LC}. \quad (9)$$

As shown in Fig. 3,  $U_\Sigma^2$  and  $P_\Sigma$  can be calculated by means of low pass filters (LPFs) as the DC components of the associated instantaneous quantities.

The remaining components of the currents in the primary of the traction transformer are non-active components, i.e.:

$$i_{Lnk} = i_{Lk} - i_{La k}; \quad k = A, B, C. \quad (10)$$

From the compensation point of view, the active components given in (4) are the reference currents and the non-active components given in (10) are related to the compensating currents, that is:

$$i_{srcA} = i_{LaA}; \quad i_{srcB} = i_{LaB}; \quad i_{srcC} = i_{LaC}; \quad (11)$$

$$i_{FrA} = -i_{LnA}; \quad i_{FrB} = -i_{LnB}; \quad i_{FrC} = -i_{LnC}. \quad (12)$$

IV. SIMULINK MODEL OF THE ACTIVE DC-TRACTION SUBSTATION

The entire active DC-traction substation has been modeled under the Matlab-Simulink environment (Fig. 4). The active currents calculation is implemented in the block “FBD”, whereas “Control block” includes the voltage and current control loops and provides the gating signals for the inverter’s IGBTs.

The model of the existing traction substation with 12-pulse parallel rectifier DC-traction contains a Y/y/d traction transformer of rated power of 3.2 MVA and 1.2 kV in each secondary and the two uncontrolled bridge rectifiers connected by reverse magnetically coupled inductances. The rated voltage of the DC traction line is 1500 V.

The Y/y recovery transformer has the rated power of 2.2 MVA and the rated voltages of 820 V/ 33 kV.

Both the compensation capacitor of 100 mF and the separating circuit ( $L_s = 40 \mu\text{H}$ ) are included in the block “DC-link”.

As regards the DC-traction line, during the traction regime, it behaves as an active load with a back electromotive force corresponding to the operation speed, an equivalent resistance and an equivalent inductance. In regeneration mode, the maximal DC-line voltage is maintained and a constant acceleration is imposed, so that the DC-line current is constant.

The LCL interface filter with damping resistance is characterized by  $L_1=21.5 \mu\text{H}$ ;  $L_2=0.21 \text{mH}$ ;  $C_f=29 \mu\text{F}$ ;  $R_f=4.3 \Omega$ .

In the voltage control loop, the proportional constant and integrative time constant of the PI controller are:  $K_p=14.07$ ;  $T_i=7.89 \cdot 10^{-4} \text{s}$ . A hysteresis band (0.5 A) current controller regulates the current upstream PCC.

V. PERFORMANCE OF THE ACTIVE DC-TRACTION SUBSTATION

The developed model for the DC-traction substation (Fig. 4) has been used to verify the proper operation of the

whole system through simulation. Moreover, the performance of SISFREG has been assessed in both operation regimes of the system.

As shown in Fig. 5, the operation in traction regime of the traction substation occurs till  $t=0.4 \text{s}$ . During the first time interval (about 0.14 seconds), the DC-capacitor is charging and reaches the set value of 1783V (i.e. about 10 % higher than  $U_{DC0}$ ), which is maintained during the whole operation period. At  $t=0.4 \text{s}$ , the transition to the regeneration regime is correlated with the increase of the DC-line voltage. A constant acceleration is imposed, so that the DC-line current is constant and the maximal DC-line voltage is handled (maximal 1800 V). The overshoot of DC-line is below 3%. It can be seen that, when the system passes again into the filtering regime ( $t=0.55 \text{s}$ ), the overshoot is higher (below 20%). Fig. 6 shows the nonsinusoidal currents drawn by the traction transformer from the power supply during the traction regime.

The associated harmonic distortion factor (*THD*) is of about 11.91%. This value is determined mainly by the presence of harmonics up to order 37 (Fig. 7). There is a small amount of reactive power, so that the global power factor is of about 0.988.

The collective active power and equivalent conductance calculated in accordance with the FBD theory (Fig. 8) lead to the active and non-active components of the current illustrated in Figs. 9 and 10.

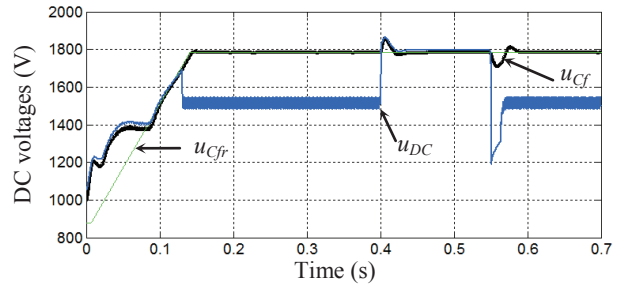


Fig. 5. The DC-line voltage (in blue) along with the compensation capacitor voltage (in black) and its set value (in green).

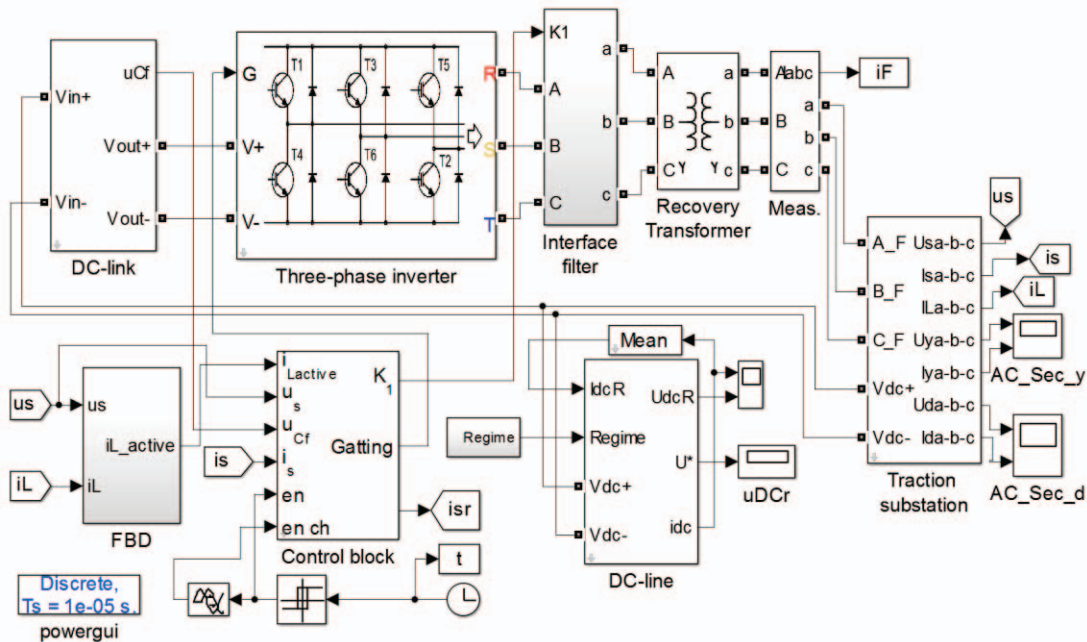


Fig. 4. The Simulink model of the active DC-traction substation with twelve-pulse uncontrolled rectifier..

As expected, the active components of the current in the traction transformer primary are sinusoidal (Fig. 9).

The distorted non-active components of the three currents (Fig. 10) will be the currents needed to be injected in PCC in order to compensate the harmonic distortion and reactive power.

As it can be seen in Figs. 5 and 11, the voltage control circuit succeeds in keeping this prescribed voltage across the compensation capacitor, which is imposed to be by 10 % higher than  $U_{DC0}$ .

When looking at the currents upstream PCC in traction regime (Fig. 12), their waveforms are almost sinusoidal ( $THD = 2.62\%$ ) and the harmonic content hardly can be seen (Fig. 13), which confirms the operation of SISTREG in active filtering mode. The active filtering efficiency, in terms of ratio of  $THD$  values before and after compensation, is of about 4.5.

Moreover, by compensating the reactive power in addition to the current harmonics, the power factor becomes very close to unity ( $PF = 0.999$ ).

The waveforms of the three currents in phase A of PCC (Fig. 14) confirm once again the proper operation of the active DC-traction substation during the traction regime.

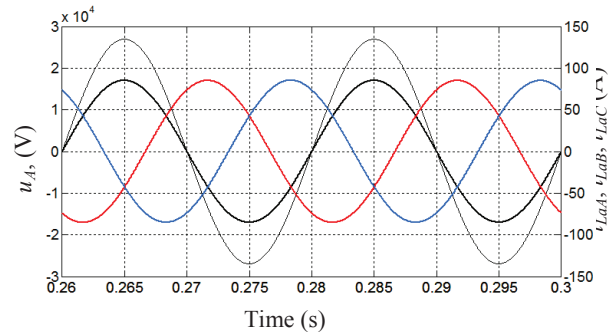


Fig. 9. Active components of the currents and voltage on phase A in the TT's primary.

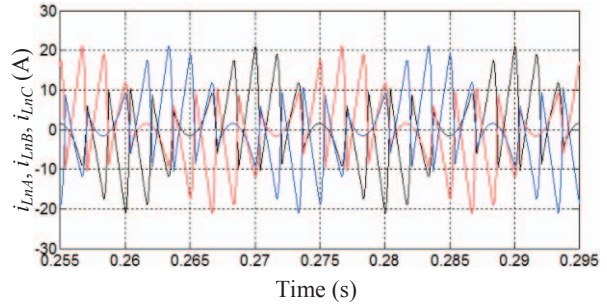


Fig. 10. Non-active components of the currents in the TT's primary.

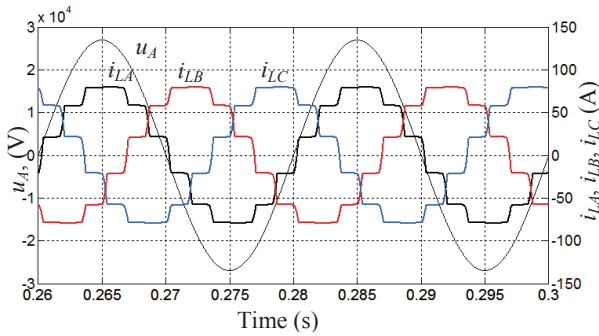


Fig. 6. Currents and voltage on phase A in the TT's primary.

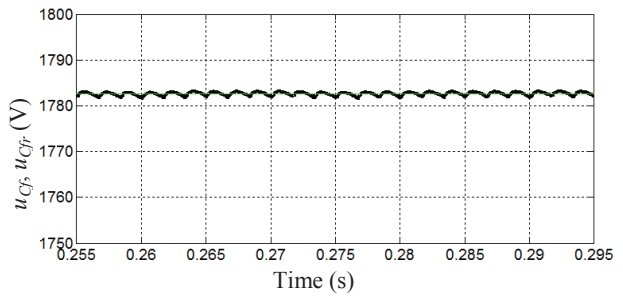


Fig. 11. Voltage across the compensation capacitor and its set value.

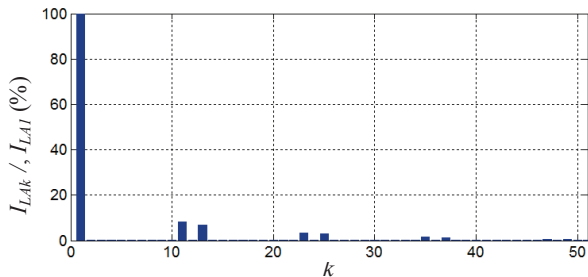


Fig. 7. Harmonic spectrum (p.u.) of the current in the TT's primary.

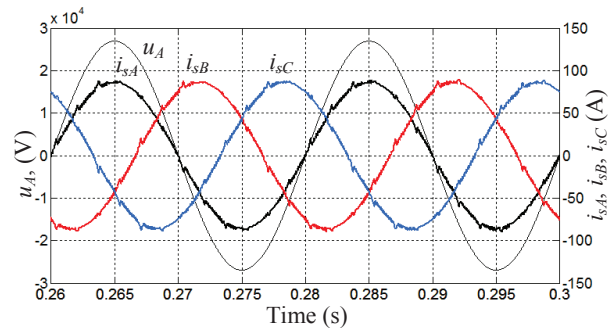


Fig. 12. Currents and voltage on phase A upstream PCC during the operation in traction regime.

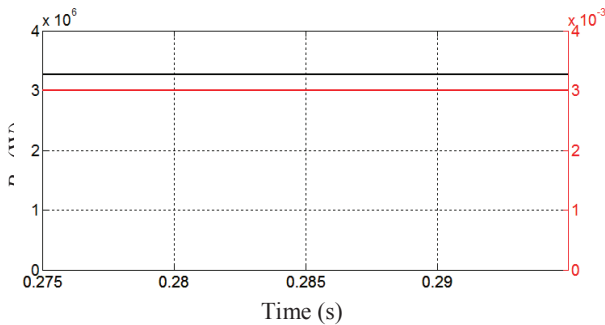


Fig. 8. Collective active power and equivalent conductance.

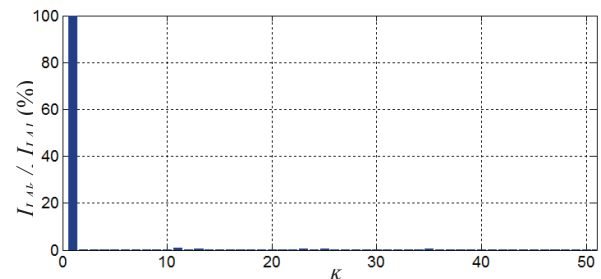


Fig. 13. Harmonic spectrum (p.u.) of the current upstream PCC during the operation in traction regime.

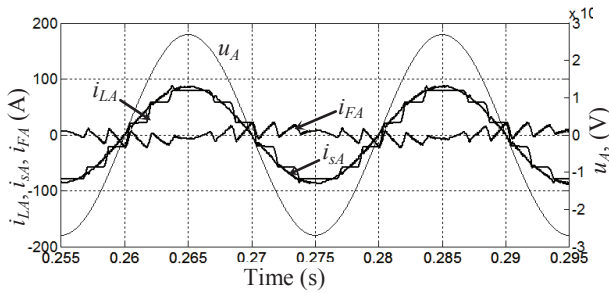


Fig. 14. Currents in phase A of PCC and phase voltage during the operation in traction regime.

When the transition to the braking regime occurs ( $t = 0.4$  s), due to the DC-line voltage increasing (Fig. 5), the separating diode  $D_s$  is forward biased and the traction rectifier is blocked. SISFREG operates in regeneration mode.

The waveform of the current in the traction transformer primary when the system operates in successive regimes of traction and regeneration illustrates the blockage of the traction rectifier in traction regime (Fig. 15).

In order to track the reference current whose components are shown in Fig. 16, SISFREG injects a proper current in PCC (Fig. 17). Fig. 16 illustrates that, during the active filtering regime of SISFREG, the component  $i_{sru}$  of the prescribed active, which comes from the output of the voltage control block and corresponds to the power losses covering, represents about 5.7 % of the prescribed active component  $i_{src}$  provided by the FBD-based reference current calculation block.

As shown in Fig. 18 and Fig. 19, the resulted supply current upstream PCC is almost sinusoidal in both steady-state regimes and it has the same phase as the supply voltage.

As it is clear from Fig. 18, during the regeneration mode, there is a phase-opposition between the currents upstream PCC and the associated voltages.

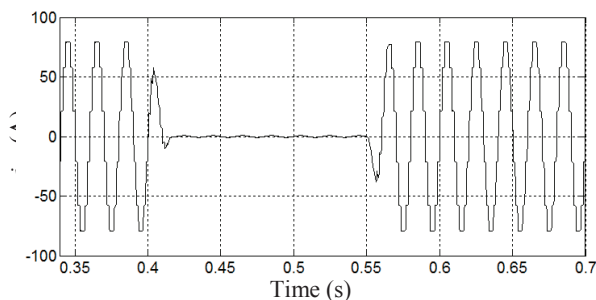


Fig. 15. Current on phase A in the primary of traction transformer when the system operates in successive regimes of traction and regeneration.

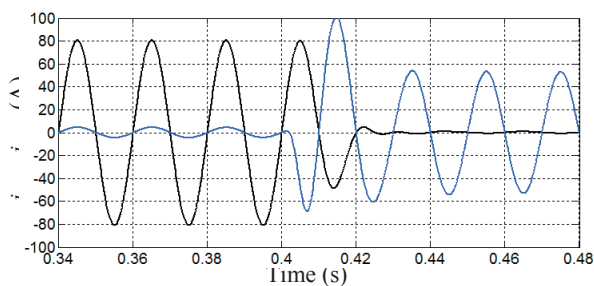


Fig. 16. The two components of the reference current on phase A during two successive regimes:  $i_{srcA}$  (in black);  $i_{sruA}$  (in blue).

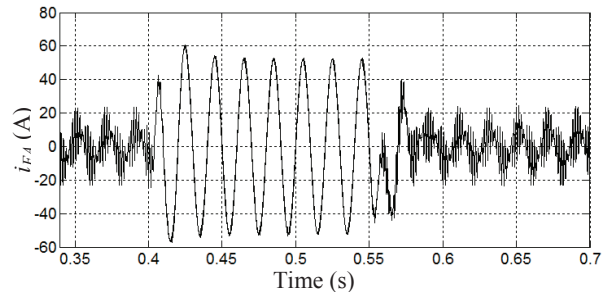


Fig. 17. Current on phase A injected by SISFREG in PCC when the system operates in successive regimes of traction and regeneration.

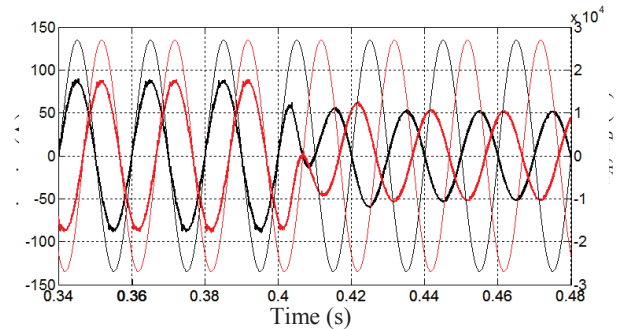


Fig. 18. Currents (thick line) and phase voltages (thin line) on phases A (in black) and B (in red) upstream PCC during two successive traction and regeneration regimes.

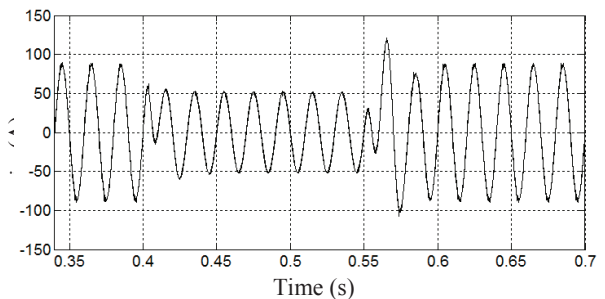


Fig. 19. Current on phase A upstream PCC when the system operates in successive regimes of traction and regeneration.

The active power at the power supply side shown in Fig. 20 highlights the injection of a significant amount of active power during the regenerative braking regime of the traction motors.

Figs. 5, 15, 17 and 19 illustrate a more lasting dynamic regime when SISFREG passes from regeneration mode to active filtering mode, compared to the reverse transition.

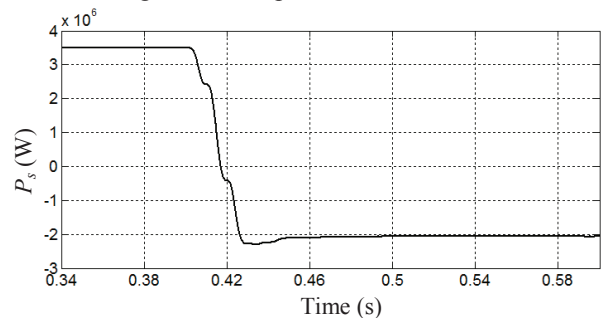


Fig. 20. Active power at the power supply side during the traction and regeneration regimes.

## VI. CONCLUSIONS

The model-based analysis performed in this paper shows that the current decomposition provided by the Fryze-Buchholz-Depenbrock theory can be successfully used in the control of an active DC-traction substation with 12-pulse uncontrolled rectifier, when the indirect control of the current is adopted.

The complete Matlab-Simulink model of the system has been developed and the simulation conducted for the operation in successive regimes of traction and regenerative braking accompanied by power quality analysis show the proper behavior and good energetic performances.

Specifically, there is an almost sinusoidal current at the power supply side, whose harmonic distortion factor is below 3 % in both operation regimes and almost unity power factor is achieved. Thus, the supply current is within the limits stipulated in the IEEE-519 recommendations [24].

Moreover, the natural transition between the two operation regimes is ensured.

In the further research, the proposed control algorithm will be implemented on a dSPACE control board working under Matlab/Simulink environment, within an experimental setup of small scale.

## ACKNOWLEDGMENT

This work was performed through the program Partnerships in priority areas — PN II, conducted with the financial support of MEN – UEFISCDI, project no. PN-II-PT-PCCA-2013-4-0564 (42/01.07.2014).

Received on July 26, 2016

Editorial Approval on November 15, 2016

## REFERENCES

- [1] T. Rekha, A. Bisharathu Beevi, "Power quality control in DC traction systems using static var compensator and harmonic filter," *International Journal of Engineering Research & Technology*, vol. 3, issue 10, pp. 733-740, Oct. 2014.
- [2] Z. Sun, X. Jiang, D. Zhu, and G. Zhang, "A novel active power quality compensator topology for electrified railway," *IEEE Trans. Power Electron.*, vol. 19, no. 4, pp. 1036-1042, Jul. 2004.
- [3] W. Hosny, H.-E. Park, and J.-H. Song, "Investigation of shunt active power filters in railway systems, Substation Installation," *Journal of Energy and Power Engineering*, issue 10, pp. 1974-1979, Oct. 2013.
- [4] A. Bueno, J.M. Aller, J. Restrepo, and T. Habetler, "Harmonic and balance compensation using instantaneous active and reactive power control on electric railway systems," *Twenty-Fifth Annual IEEE Applied Power Electronics Conference and Exposition*, 2010, pp. 1139 – 1144.
- [5] G. Ramos, E. Cantor, M.A. Rios, and L.F. Roa, "Instantaneous p-q theory for harmonic compensation with active power filter in DC traction systems," *International Conference on Power Engineering, Energy and Electrical Drives (POWERENG)*, 11-13 May 2011, pp. 1-5.
- [6] A.M. Rezkalla, "Active filters application for metro a.c substations," *23 rd International Conference on Electricity Distribution*, Lyon, 15-18 June 2015
- [7] Y. Warin, R. Lanselle, and M. Thiounn, "Active substation," *World Congress on Railway Research*, Lille, France, May 2011.
- [8] D. Cornic, "Efficient recovery of braking energy through a reversible dc substation," in *Proc. Electrical Systems for Aircraft, Railway and Ship Propulsion (ESARS)*, pp.1-9, Oct. 2010.
- [9] J.M. Ortega, H. Ibaiondo, and A. Romo, "Kinetic energy recovery on railway systems with feedback to the grid," in *Proc. 9th World Congress on Railway Research*, May 22–26, 2011.
- [10] Mihaela Popescu, A. Bitoleanu, V. Suru, and A. Preda, "System for converting the dc traction substations into active substations," in *Proc. 9th International Symposium on Advanced Topics in Electrical Engineering (ATEE 2015)*, May 2015, pp. 632-637.
- [11] Mihaela Popescu, A. Bitoleanu, and V. Suru, "Indirect current control in active DC railway traction substations," in *Proc. ACEMP-OPTIM-ELECTROMOTION Joint Conference*, Sept. 2015, pp. 192-197.
- [12] Mihaela Popescu, A. Bitoleanu, and A. Preda, "Design and performances of the separating circuit in regeneration and filtering system for active DC-traction substations," in *Proc. SPEEDAM 2016*, Capri, Italy, June 2016, pp. 1180-1185.
- [13] A. Bitoleanu, Mihaela Popescu, *Filtre active de putere*, Universitara Craiova, 2010.
- [14] A. Bitoleanu, S. Ivanov, Mihaela Popescu, *Convertoare statice*. INFOMED Craiova, 1997.
- [15] Mihaela Popescu, A. Bitoleanu, and V. Suru, "On the design of LCL filter with passive damping in three-phase shunt active power filters," in *Proc. SPEEDAM 2016*, Capri, Italy, June 2016, pp. 826-831.
- [16] Mihaela Popescu, A. Bitoleanu, A. Preda, "A New Design Method of an LCL Filter in Active DC-Traction Substations," in *Proc. 17th Int. Conf. on Power Electronics and Motion Control (PEMC) 2016*, Varna, Bulgaria, Sept. 25-30, 2016, pp. 868-873.
- [17] Mihaela Popescu, A. Preda, and V. Suru, "Synchronous Reference Frame Method Applied in the Indirect Current Control for Active DC Traction Substation," *Athens: ATINER'S Conference Paper Series*, No: TRA2015-1552, pp. 1-14, Aug. 2015.
- [18] V. Staudt, "Dynamic parallel compensation of active non-linear loads using the FBD-method," in *Proc. 7th International conference on harmonics and quality of power (ICHQP VII)*, Las Vegas, USA, 1996, pp. 21-26.
- [19] M. Depenbrock and V. Staudt, "The FBD-method as tool for compensating total nonactive currents," in *Proc. 8th IEEE ICHQP'98 Conf.*, Athens, Greece, 1998, pp. 320-324.
- [20] J. Kang, J. Y. Zheng and W. Zeng, "Application of FBD-method to real time current detection in three-phase four-wire system," *Electric Power Automation Equipment*, vol. 26, no. 8, 2006.
- [21] Z. Y. Guo, Y. Q. Zhou and L. M. Guo, "Current detection for four-phase transmission system based on FBD Method", in *Proc. of the Chinese Society for Electrical Engineering*, 2007.
- [22] A. Bitoleanu and Mihaela Popescu, "Shunt active power filter: Overview on the reference current methods calculation and their implementation," *4th International Symposium on Electrical and Electronics Engineering (ISEEE 2013)*, Galati, Romania, 2013, pp.1-12.
- [23] M. Depenbrock, "The FBD-method, a generally applicable tool for analyzing power relations," *IEEE Trans. Power Syst.*, vol. 8, pp. 381-387, May 1993.
- [24] IEEE recommended practice and requirements for harmonic control in electrical power systems, *IEEE Std. 519-1992*.

# New Aspects on the Frequency Splitting and Bifurcation Phenomena in Wireless Power Transfer Systems

Mihai Iordache\*, Andrei Marinescu†, Ioana-Gabriela Sîrbu‡, Lucian Mandache‡, Dragoş Niculae\* and Lavinia Iordache\*

\* Politehnica University of Bucharest, Faculty of Electrical Engineering, Bucharest, Romania, mihai.iordache@upb.ro, dragos.niculae@upb.ro, laviniabobaru@gmail.com

† INCD - ICMET, Craiova, Romania, amarin@icmet.ro

‡ University of Craiova, Faculty of Electrical Engineering, Craiova, Romania, osirbu@elth.ucv.ro, lmandache@elth.ucv.ro

**Abstract** - This paper focuses on the frequency splitting and bifurcation phenomena that appear in the wireless power transfer systems. These two phenomena are analyzed for different possible configurations of the magnetically coupled circuits of the system, through electric circuit methods and mathematical calculus. Considering two printed spiral coils with similar geometrical properties, the study started with a calculus of the splitting frequency. It was made for the series-series connection, but also for series-parallel, parallel-series and parallel-parallel connections. The graphical representations of the load voltage as function of the frequency revealed that this phenomenon is visible only for the series-series and series-parallel connections; even if one or two peaks appear in all cases they are not directly connected to the frequency splitting phenomena, respectively to the spitting factor. The bifurcation phenomenon is analyzed starting from the bifurcation equation defined for the input admittance of the wireless power transfer system. The four types of configurations are analyzed from the graphical representations of the imaginary part of the admittance as function of the frequency. Because an important factor in the frequency splitting and bifurcation phenomena appearance is the ratio between the input resistance and the load resistance, in the last part of the paper the splitting coupling factor as function of the input resistance - load resistance ratio is depicted. The paper brings new contributions in the field through a comparative study on the frequency splitting and bifurcation phenomena for all the four types of configuration of the wireless power transfer systems. Through mathematical calculations, formulas for estimating the frequency (angular frequency) of occurrence of each phenomenon are obtained. The results are validated by comparative simulations related to a system of identical spiral coupled coils. The results of the analysis were commented comparatively and some conclusions could be drawn.

**Keywords:** *inductive power transmission, circuit analysis, equivalent circuits, splitting and bifurcation phenomena.*

## I. INTRODUCTION

Frequency splitting and bifurcation phenomena were often mentioned in the context of the studies, analyzes and applied researches that had as subject the wireless power

transfer (WPT) systems [1–19]. Many researchers have approached tangentially or deeply this topic, trying to explain the theoretical and practical consequences of the occurrence of these phenomena, with their advantages and disadvantages. The researches have focused mostly on the series-series connection, but lately other types of connections were analyzed, too in order to identify the best option.

It is already known now that the frequency splitting phenomenon appears at the magnetically coupled circuits when the coupling factor exceeds a certain critical value called the splitting factor. It is characterized by the fact that in the curves of some output quantities (load voltage, active power load, etc.) represented as functions of the frequency there is not a single point of maximum (peak), but two. In most of the cases they have different values (the first peak is higher than the second one). The regions of the curve bounded by the two peaks are called in literature [2, 3, 12, 18]: the low frequency region, the stagger tuning region and the region of high frequencies. The part of the curve situated between the two peaks (the stagger tuning region) proved to be useful to maintain constantly the voltage transfer factor in the applications characterized by variable load or by inconstant distance between the coils [19]. The high frequency region is preferred for the output voltage controlling [2, 5, 13]. The WPT system behavior under the frequency splitting phenomenon should be well known in order to ensure an optimum power transfer from the source circuit to the receiver circuit. Thus it was observed that the energy transfer is much more efficient if the two circuits operate at the same frequency (resonant circuits) [7 – 9, 11].

If the frequency splitting phenomenon characterizes the output quantities of the WPT system, the frequency bifurcation phenomenon is related to the input quantities of the system (either input impedance or input admittance). Each bifurcation angular frequency is an operating mode of the system. These modes could be stable or unstable. Each operating mode has its own transfer characteristics [18].

This paper has proposed to explore new aspects concerning these two phenomena that may occur in the WPT systems. For the frequency splitting phenomenon the attention was concentrated on finding the splitting frequencies / angular frequencies through a mathematical

calculus. The finding of the extreme points was not made for the load active power - frequency curve as in other previous papers [18], but for another output quantity, i.e. output voltage (load voltage). As for the frequency bifurcation phenomenon, the analysis was centered on the variation with the frequency of the imaginary part of the input admittance, and not of the input impedance as it is treated generally in the literature. The analyses were made for all the possible configurations of the WPT system: series-series, series-parallel, parallel-series, and parallel-parallel. Finally the paper presents some aspects regarding the variation of the splitting coupling factor as function of the ratio between the load resistance and the input resistance. The comparative graphical representations made in each case have revealed the different behavior of the system for different configurations and for various values of the coupling factor. Some important conclusions were drawn in the end of the work.

## II. SYSTEM PARAMETERS

The system used for the analysis consists of two identical printed spiral coils having the inner radius  $r_i = 3.3$  mm, the coil width  $l = 22.8$  mm, the distance between two consecutive turns (the pitch)  $p = 1.2$  mm, the copper section area  $s = 1.2 \times 0.8 = 0.96$  mm<sup>2</sup>, the coil mean radius  $r_m = r_i + l/2 = 14.4$  mm and the number of turns  $N = 10$  (Fig. 2) [18]. A part of its electrical parameters could be determined on the basis of some approximate formulas [20]. However, in order to estimate as accurately as possible all the parameters of interest we preferred to make a numerical calculation using the program ANSOFT EXTRACTOR Q3D [21]. Choosing a distance between coils  $d = 50$  mm and the frequency  $f = 5$  MHz we obtained:  $C_1 = 1.1785$  nF;  $C_2 = 1.18$  nF;  $L_1 = 2.3172$   $\mu$ H;  $L_2 = 2.3098$   $\mu$ H;  $M = 0.8775$   $\mu$ H;  $R_5 = R_{L1} = 0.5971$   $\Omega$  and  $R_6 = R_{L2} = 0.57186$   $\Omega$ . These parameters allowed obtaining the equivalent circuit of the system in the parallel-series (*ps*) configuration (Fig. 1). On its base the other connection types of the equivalent diagram can be obtained relatively easily: series-series (*ss*), series-parallel (*sp*) and parallel-parallel (*pp*). The source has the rms value  $E_i = 15$  V and the internal resistance  $R_7 = R_i = 1.5$   $\Omega$ , and the load has the resistance  $R_8 = R_L = 30$   $\Omega$  (a resistive load).

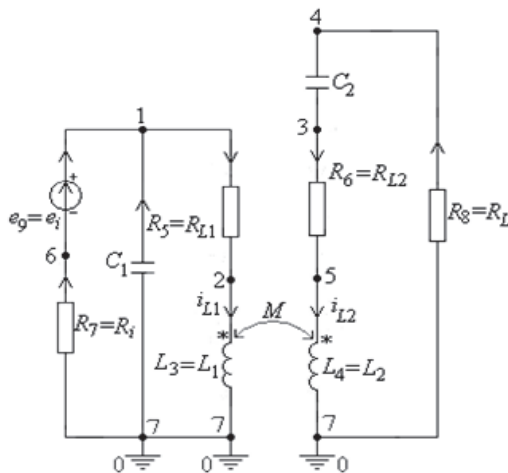


Fig. 1. The equivalent circuit of a WPT system - configuration *ps*.

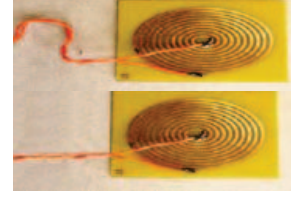


Fig. 2. Printed coils.

## III. THE ANALYSIS OF THE FREQUENCY SPLITTING PHENOMENON

The frequency splitting phenomenon is related to the appearance of two peaks instead of one in the dependence curve of an output quantity (active power load, load voltage, the absolute value of the voltage transfer factor, etc.) on the frequency, when the coupling factor  $k$  exceeds a certain critical value called *frequency splitting coupling factor*,  $k_{split}$ . Therefore  $k_{split}$  is the maximum value of the coupling factor up to which the frequency splitting phenomenon does not appear [18]. Sometimes the two peaks have almost the same value, but there are cases when the first peak has a value higher than the second one. In the coupled modes theory the frequency corresponding to the first peak is called *the odd splitting frequency* and the frequency corresponding to the second maximum value is called *the even splitting frequency* [2, 13, 18].

As output quantity in the study of the frequency splitting phenomenon we considered further the load voltage  $U_L$ . The condition for finding the extreme points of the load voltage - frequency (angular frequency) curve is

$$\frac{\partial U_L}{\partial \omega} = 0 \quad (1)$$

named *the splitting equation* [2, 13].

The points of maximum will correspond to some roots of this equation.

Obviously the equation (1), where the unknown is the angular frequency  $\omega$ , has its coefficients dependent on the circuit parameters (i.e. capacitances, inductances and resistances, as in Fig. 1) and also on the coupling factor  $k$ .

As a remark we could notice that its free term has always a negative value. Also, the final structure of (1) allows the replacement of the term  $\omega^2$  with  $y$ . Because the load voltage - angular frequency curve must have a single peak, the equation (1) must have only one real root.

Equation (1) takes different forms depending on the connection type considered, as it will be seen below.

### A. Series-Series Connection

The equation (1) becomes a 4th degree equation in  $y$  ( $y = \omega^2$ ) in the form [18]

$$ay^4 + by^2 + cy + d = 0, \quad (2)$$

where  $a$ ,  $b$ ,  $c$  and  $d$  depend on the electrical parameters of the circuit, and  $d < 0$ .

Because only one maximum is wanted, the equation (2) must have three equal real roots:  $y_1 = y_2 = y_3 = y_e$  [4, 18].

Thus, using the Vieta's formulas [22], we obtained the system:

$$\begin{cases} 3y_e + y_4 = 0 \Rightarrow y_4 = -3y_e \\ 3y_e(y_e + y_4) = b/a \\ y_e^2(y_e + 3y_4) = -c/a \\ y_e^3 y_4 = d/a \end{cases} \quad (3)$$

from which we obtained

$$y_e = -\frac{3c}{4b} \text{ and } 3\left(\frac{3c}{4b}\right)^4 + \frac{d}{a} = 0. \quad (4)$$

In order to obtain the coupling factor  $k_{split}$  that determines a single peak for the load voltage  $U_L$  curve, from (4) we obtained the solution:

$$\omega_{split\_ss} = \sqrt{\left|-\frac{3c}{4b}\right|}, \quad (5)$$

that depends on the coefficients of the equation (2).

### B. Parallel - Series Connection

In this case the general equation (1) takes the form

$$ay^4 + by^3 + cy + d = 0, \quad (6)$$

with  $d < 0$ .

A condition similar to the previous one is put also in this case (three real roots equal to  $y_e$ ), to obtain a single maximum. Vieta's relations [18, 22] lead now to the conditions:

$$y_e = -\frac{b}{2a}, \quad b^3 + 4a^2c = 0 \text{ and } b^4 + 16a^3d = 0. \quad (7)$$

From (7) we searched for a solution in order to find a minimum value of the coupling factor  $k_{split}$  that ensure a single maximum for the load voltage  $U_L$  curve.

By replacing the coefficients in the last two relations (7) by their expressions (functions of electric parameters and coupling factor  $k = M / \sqrt{L_1 \cdot L_2}$ ) two equations in  $k$  are obtained. The common solution of these two equations that determines a minimum coupling factor has the expression [18]

$$\omega_{split\_ps} = \sqrt{\left|-\frac{b}{2a}\right|}. \quad (8)$$

### C. Series - Parallel Connection

This case offers, from (1), an equation similar to (6), obviously with different expressions for its coefficients  $a$ ,  $b$ ,  $c$  and  $d$ . So the solution (8) is valid also for this connection.

### D. Parallel - Parallel Connection

The equation (1) becomes in this case a 4th degree equation in  $y$  in the form [18]

$$ay^4 + by^3 + cy^2 + d = 0, \quad (9)$$

where  $d < 0$ .

Similarly the condition of having three equal positive real roots together with the Vieta's formulas [18, 22] lead to the relations

$$y_e = -\frac{3b}{8a}, \quad 9b^2 - 32ac = 0 \text{ and } 27b^4 + 8^4 a^3 d = 0 \quad (10)$$

So the common solution of the last two equations (10) that determines a minimum coupling factor has the expression

$$\omega_{split\_pp} = \sqrt{\left|-\frac{3b}{8a}\right|}. \quad (11)$$

As a general remark we could found that formally the equations obtained for each case and thus their solutions are similar to those in [18] where the analysis was done for the output quantity  $P_L$  (load active power). Of course, the equation coefficients have completely different expressions here, but they depend also on the electrical parameters of the circuits and on the coupling factor.

### E. Comparative Results

The four types of connection of the WPT system were analyzed further in a comparative manner. The system to be analyzed has the geometrical and electrical parameters presented in section II. For this system the following parameters were also calculated: the resonance angular

frequency  $\omega_0 = \frac{2}{\sqrt{(C_1 + C_2)(L_1 + L_2)}} = 1.9145 \cdot 10^7$  rad/s;

the resonance frequency  $f_0 = 3.0486$  MHz, and the coupling factor corresponding to the normal operation of the system  $k_n = M / \sqrt{L_1 \cdot L_2} = 0.3793$ .

With these values of the parameters the variation curves of the load voltage  $U_L$  as function of the frequency, for different values of the coupling factor  $k$ , were depicted. Thus Fig. 3 presents the load voltage variations as function of the frequency for the four types of connection:

- *ss* connection and six values of the coupling factor:  $k_1 = 0.1$ ,  $k_c = 1 / \sqrt{Q_1 \cdot Q_2} = 0.181$  (where  $Q_1 = (\omega_0 \cdot L_1) / (R_{L1} + R_i)$  and  $Q_2 = (\omega_0 \cdot L_2) / (R_{L2} + R_L)$  are the quality factors of the two inductively coupled circuits),  $k_n = 0.3793$ ,  $k_{split} = 0.5035$ ,  $k_2 = 0.6$  and  $k_3 = 0.8$  (Fig. 3 (a));

- *sp* connection and seven values of the coupling factor:  $k_c = 1 / \sqrt{Q_1 \cdot Q_2} = 0.024724$  (where  $Q_1 = (\omega_0 \cdot L_1) / (R_{L1} + R_i)$  and  $Q_2 = (\omega_0 \cdot L_2) / R_{L2}$  are the quality factors of the circuits),  $k_1 = 0.15$ ,  $k_n = 0.3793$ ,  $k_2 = 0.45$ ,  $k_{split} = 0.6201$ ,  $k_3 = 0.8$  and  $k_4 = 0.9$  (Fig. 3 (b));

- *ps* connection and seven values of the coupling factor:  $k_c = 1 / \sqrt{Q_1 \cdot Q_2} = 0.09647$  (where  $Q_1 = (\omega_0 \cdot L_1) / R_{L1}$  and  $Q_2 = (\omega_0 \cdot L_2) / (R_{L2} + R_L)$  are the quality factors of the circuits),  $k_1 = 0.15$ ,  $k_2 = 0.25$ ,  $k_n = 0.3793$ ,  $k_3 = 0.6$ ,  $k_4 = 0.75$  and  $k_5 = 0.9$  (Fig.3 (c)), and

- *pp* connection and seven values of the coupling factor:  $k_c = 1 / \sqrt{Q_1 \cdot Q_2} = 0.0132$  (where  $Q_1 = (\omega_0 \cdot L_1) / R_{L1}$  and  $Q_2 = (\omega_0 \cdot L_2) / R_{L2}$  are the quality

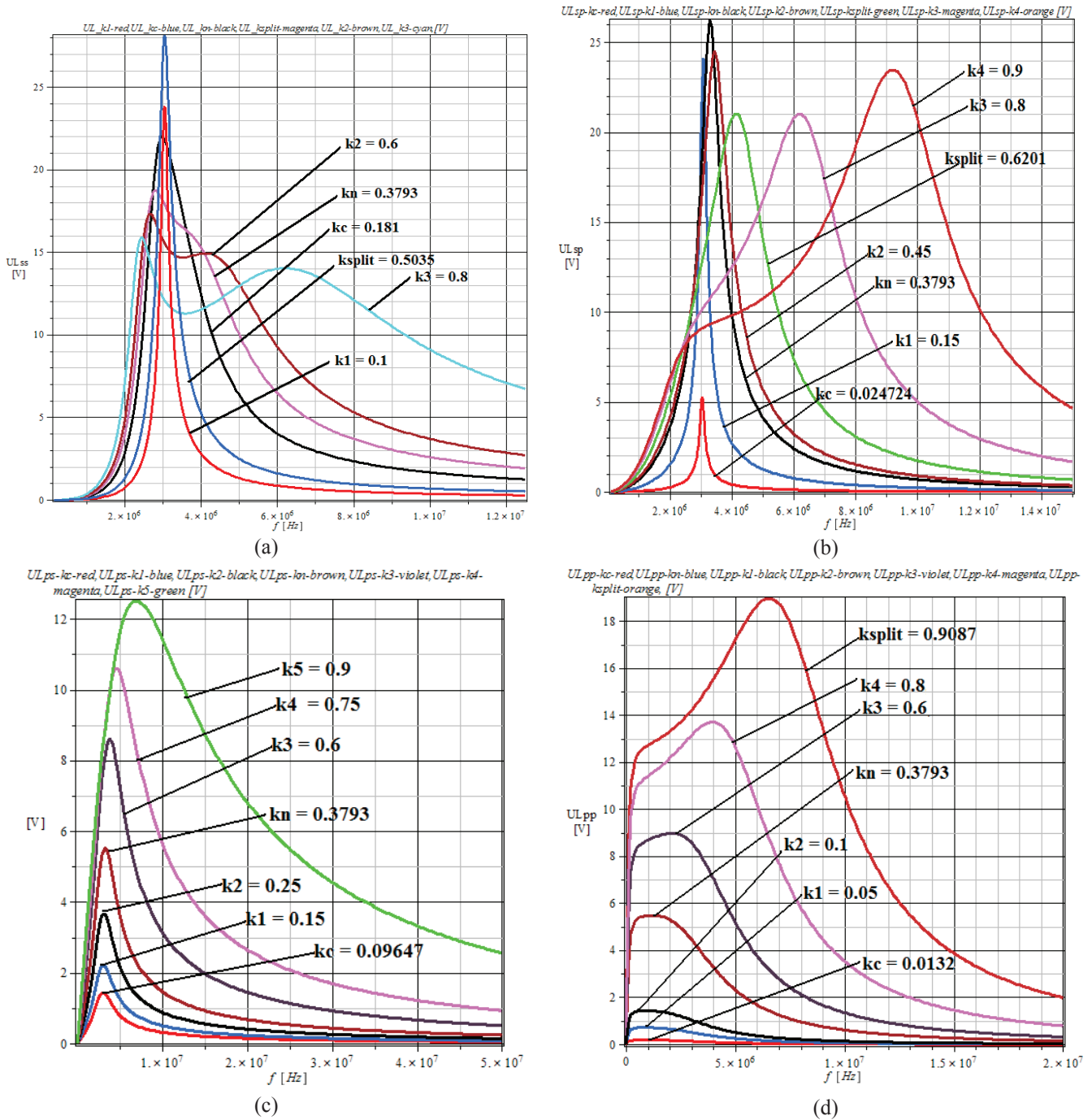


Fig. 3. Load voltage  $U_L$  variations as function of the frequency  $f$ : (a) *ss* connection; (b) *sp* connection; (c) *ps* connection; (d) *pp* connection.

factors of the circuits),  $k_1 = 0.05$ ,  $k_2 = 0.1$ ,  $k_n = 0.3793$ ,  $k_3 = 0.6$ ,  $k_4 = 0.8$  and  $k_{split} = 0.9087$  (Fig.3 (d)).

The curves shapes analysis has shown that the frequency splitting phenomenon is visible for the *ss* and *sp* connections (Figs.3 (a) and (b)). In these cases for the values of  $k > k_{split}$  the load voltage - frequency curves have two peaks. When  $k = k_{split}$ , the three extreme frequencies are equal and only one peak is obtained. For  $k \leq k_{split}$  the load voltage - frequency curves have a single maximum point. In fact  $k < k_{split}$  corresponds to the so-called frequency splitting - free region [18]. For the *ps* and *pp* connections (Figs. 3 (c) and (d)) the frequency splitting phenomenon is not noticeable on the  $U_L - f$  curves. At the

*ps* connection only one peak is obtained for every value of the coupling factor. As for the *pp* connection a change in the shape of the curve is remarked, but it is not directly connected to the value of the  $k_{split}$  (the curve shape is changed even for values of  $k$  lower than  $k_{split}$ ). However the frequency splitting phenomenon exists also at the *ps* and *pp* connections and it could be seen in the curves of the power transfer efficiency  $\eta_{21}$  as function of the frequency [2- 4, 17, 18].

In Figs. 4 (a), (b), (c) and (d) the 3D variations of the load voltage  $U_L$  versus frequency  $f$  and magnetic coupling factor  $k$  - corresponding to the four connections of the magnetically coupled coils system - are presented.

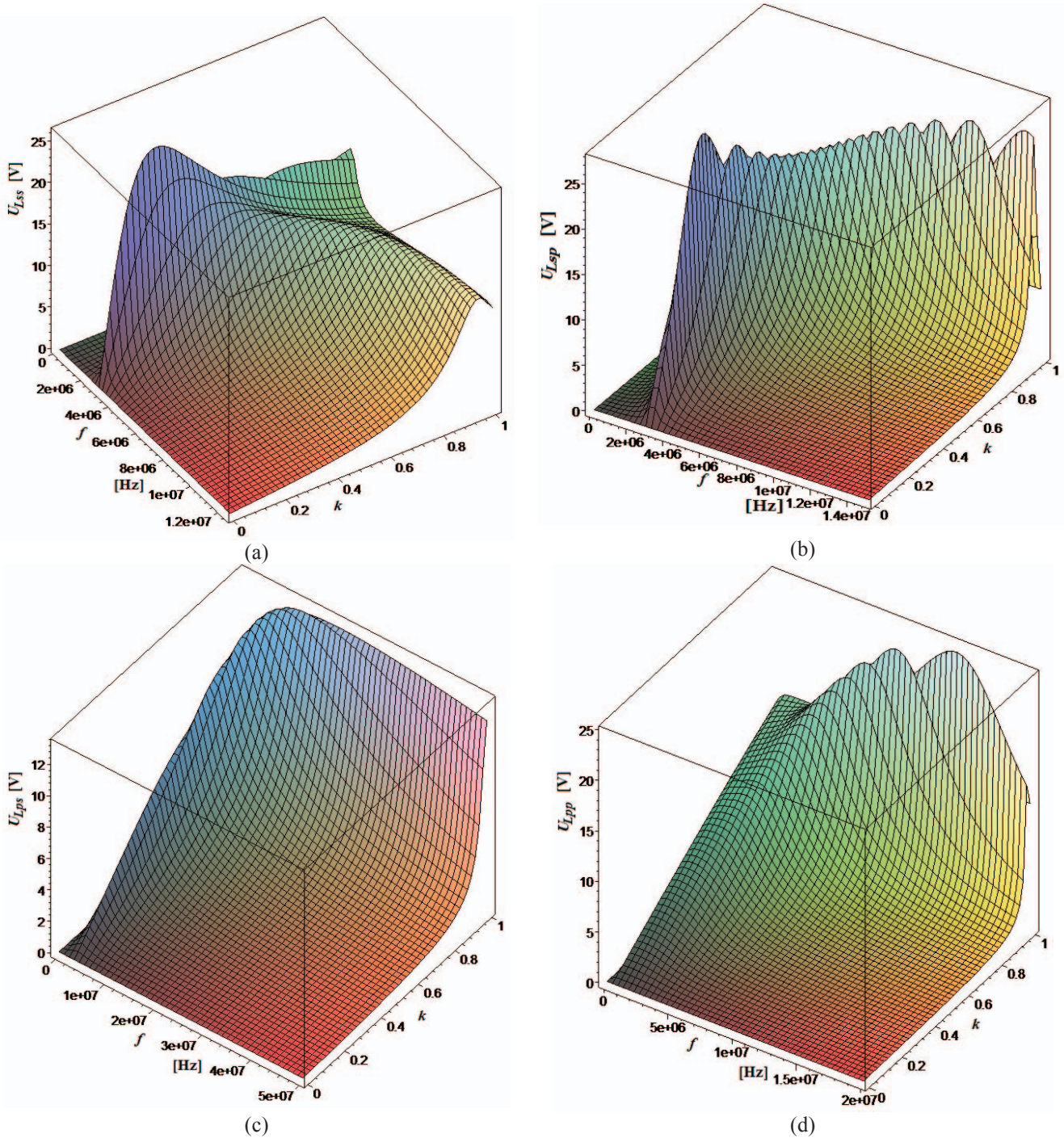


Fig. 4. 3D load voltage  $U_L$  variations as function of the frequency  $f$  and of the magnetic coupling factor  $k$ : (a)  $ss$  connection; (b)  $sp$  connection; (c)  $ps$  connection; (d)  $pp$  connection.

They concentrate the results arising from the analysis of the comparative curves in Fig. 3.

#### IV. THE ANALYSIS OF THE FREQUENCY BIFURCATION PHENOMENON

The bifurcation phenomenon is related to the input characteristics of the wireless power transfer systems. Usually the input impedance is used as reference parameter [3, 17, 18], but also the input admittance could be considered.

Starting from the bifurcation equation defined in the literature [1-18] and using as input parameter the admittance, the bifurcation equation is in this case:

$$\text{Im}(\underline{Y}_{in}) = 0, \quad (12)$$

where  $\underline{Y}_{in}$  is the input complex admittance of the WPT system. By making the substitution  $\omega^2 = x$  in (12), a 3rd degree equation in  $x$  is obtained, of form:

$$a_3 x^3 + a_2 x^2 + a_1 x + a_0 = 0, \quad (13)$$

where  $a_3, a_2, a_1$  and  $a_0$  are the coefficients of the equation. They depend on the values of the parameters of the two resonant circuits.

It can be demonstrated that the bifurcation equation (12) can be brought to a form (13) for each of the four types of possible connections of the two circuits [4, 17, 18].

In order to obtain the value of the coupling factor  $k$  when the bifurcation phenomenon starts we put the condition that all the (three) roots must be equal and real, according to Vieta's formula [2, 4, 16–18, 22]. Thus the following relations must be accomplished:

$$\begin{aligned} 3\left(-\frac{a_2}{3a_3}\right)^2 - \frac{a_1}{a_3} &= 0 \\ \left(-\frac{a_2}{3a_3}\right)^3 + \frac{a_0}{a_3} &= 0 \\ \omega_{bif} = \sqrt{x} &= \sqrt{-\frac{a_2}{3a_3}}. \end{aligned} \quad (14)$$

It can be noticed that these formula are similar to those obtained starting from the bifurcation equation in the complex impedance [18].

The literature offers an analytical approximate solution for the equations (14), obtained for the *ss* connection [2, 4, 16 – 18]:

$$k_{bif} = (1/Q_c) \cdot \sqrt{1 - 1/(4Q_c^2)}, \quad (15)$$

where  $Q_c = \sqrt{Q_1 \cdot Q_2}$ ,  $Q_1 = (\omega_0 L_1)/(R_{L_1} + R_i)$ , and  $Q_2 = (\omega_0 L_2)/(R_{L_2} + R_L)$ .  $k_{bif}$  is named the coupling coefficient of the bifurcation. Also a factor  $k_c = 1/Q_c$  could be defined. Equivalent formulae could be obtained also for the other three types of connection.

The curves of the imaginary part of the input admittance  $\underline{Y}_{in}$  as function of the frequency  $f$  for the system of two magnetically coupled circuits having the parameters presented in section II are represented in Fig. 5, for the four types of connection:

- *ss* connection and six values of the coupling factor,  $k_1 = 0.1$ ,  $k_c = 0.181$ ,  $k_n = 0.3793$ ,  $k_{split} = 0.5035$ ,  $k_{bif} = 0.64045$  and  $k_3 = 0.8$  (Fig. 5 (a));

- *sp* connection and eight values of the coupling factor:  $k_c = 0.024724$ ,  $k_1 = 0.15$ ,  $k_n = 0.3793$ ,  $k_3 = 0.45$ ,  $k_{split} = 0.6201$ ,  $k_{bif1} = 0.62013$ ,  $k_{bif2} = 0.794$  and  $k_4 = 0.9$  (Fig.5 (b));

- *ps* connection and seven values of the coupling factor:  $k_c = 0.09647$ ,  $k_1 = 0.15$ ,  $k_2 = 0.25$ ,  $k_n = 0.3793$ ,  $k_3 = 0.6$ ,  $k_4 = 0.75$  and  $k_{bif} = 0.95125$  (Fig.5 (c)), and

- *pp* connection and seven values of the coupling factor  $k_c = 0.0132$ ,  $k_1 = 0.05$ ,  $k_2 = 0.1$ ,  $k_n = 0.3793$ ,  $k_3 = 0.6$ ,  $k_{bif} = 0.797$  and  $k_{split} = 0.9087$  (Fig.4 (d)).

The variation range of the frequency for  $k > k_{bif}$  is called the bifurcation region, while the variation range when  $k < k_{bif}$  is called the bifurcation - free region. In the bifurcation region the bifurcation equation have two positive real roots: the bigger one is called the big

bifurcation angular frequency and the smaller one is named the small bifurcation angular frequency [18].

By analyzing the curves of the input admittance as function of the frequency from Figs. 5 (a) - (d) a different behavior is remarked for the four types of connection. The *ss* connection presents a strong reduction of the negative peak for the coupling factors bigger than  $k_{bif}$  (in the bifurcation region). At the *sp* connection, if  $k > k_{bif}$ , a displacement of the zero crossing point of the curve is noticed, from the resonance frequency  $f_0 = 3.0486$  MHz towards frequencies even three times bigger (if  $k$  is about 0.9). In the *ps* connection no difference is remarked at the coupling factor variation, so the bifurcation phenomenon is not visible for this type of graphical representation. This phenomenon is again highlighted at the *pp* connection, when for the coupling factors higher than  $k_{bif}$  two extreme points appear.

It should be noted that the studies in the domain of frequency splitting and bifurcation phenomena have shown that a special influence on these phenomena has the ratio between the input resistance  $R_i$  and the load resistance  $R_L$  and also the ratio between the transmitter inductance  $L_1$  and the receiver inductance  $L_2$  [18]. This is why Figs. 6 (a) and (b) present the variation of the splitting coupling factor  $k_{split}$  as function of the ratio  $\alpha = R_L / R_i$ , for two of the four possible connections of the magnetically coupled circuits: *ss* connection and *sp* connection.

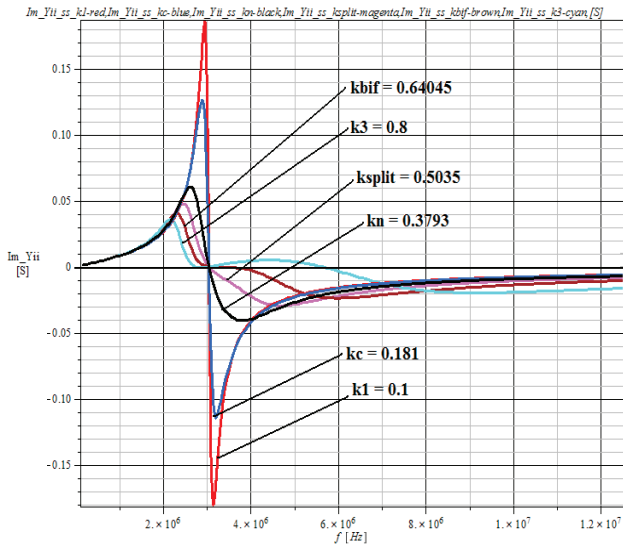
Fig. 6 (a) shows that at the *ss* connection by varying the ratio  $\alpha = R_L / R_i$  between 0 and 40 - all the other parameters of the two resonators remaining constant - the splitting coupling factor  $k_{split}$  increases continuously between 0.04 and 1.0. Fig. 6 (b) highlights that by changing the ratio  $\alpha$  between 0 and 100, at the *sp* connection, the other parameters remaining the same, the splitting coupling factor decreases from 1.0 to 0.06. These variations of the splitting factor confirm once again that at the connections *ss* and *sp* the frequency splitting phenomenon is present. Not the same thing can be said on the other two connections, *ps* and *pp*. The curves of  $\alpha$  (not represented here) presented only very small variations of the  $k_{split}$ , fact that confirms the nonappearance of a clear splitting phenomenon at these connections.

## V. CONCLUSION

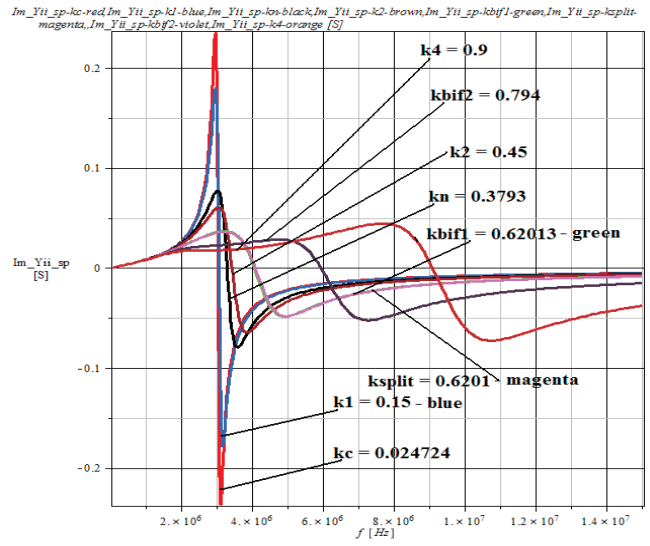
This work brings new aspects on the frequency splitting and bifurcation phenomena, that are present in the wireless power transfer systems. The all four types of connection were analyzed for the system of two magnetically coupled circuits: series-series, series-parallel, parallel-series and parallel-parallel.

The frequency splitting phenomenon focused on the load voltage – frequency characteristic, using thus another output quantity that the usual one (the load active power). The calculus made using the electric circuit theory and algebraic equations is finalized with some useful formulae that permit the calculation of the splitting frequencies for each of the four connection types. These relations, compared with those obtained for the load active power, revealed some important similarities.

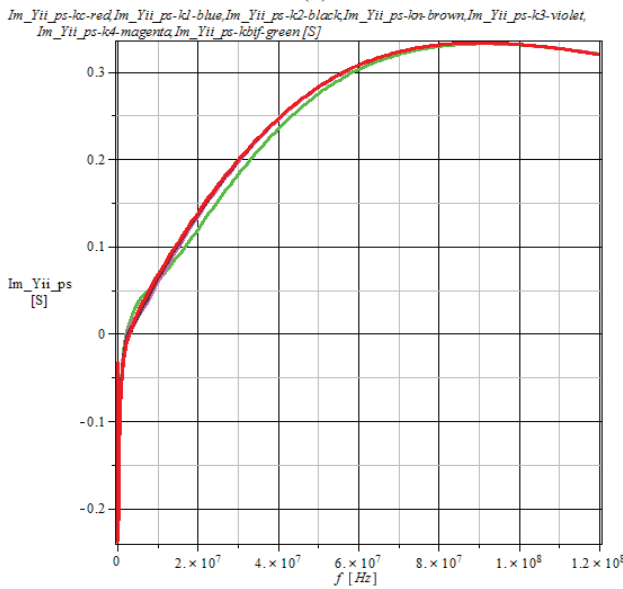
The study of the frequency bifurcation phenomenon was made for the input admittance, and not for the impedance; similarities were found here, too.



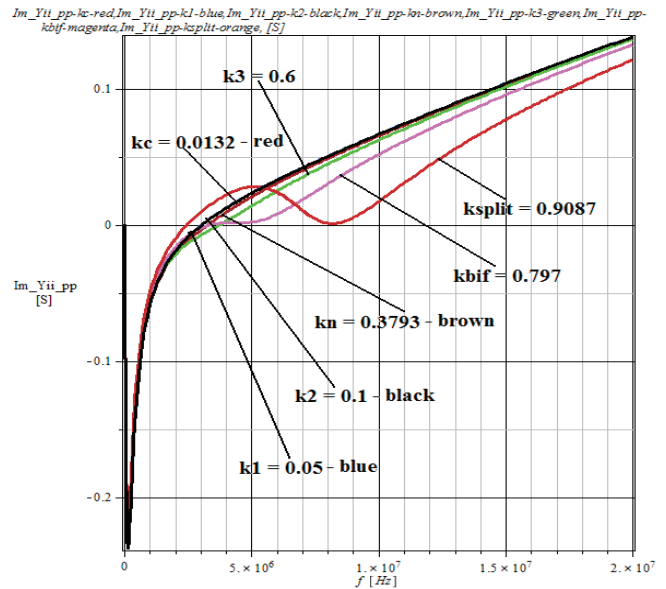
(a)



(b)

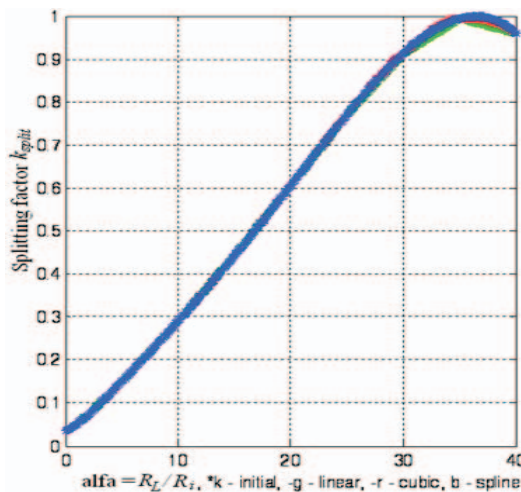


(c)

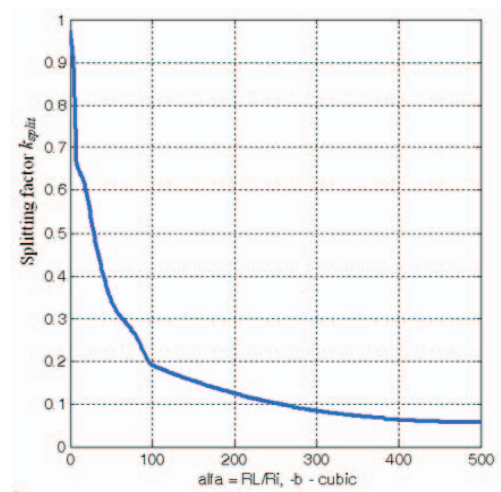


(d)

Fig. 5.  $\underline{Y}_n$  imaginary part variations as function of the frequency  $f$ : (a)  $ss$  connection; (b)  $sp$  connection; (c)  $ps$  connection; (d)  $pp$  connection.



(a)



(b)

Fig. 6. Coupling coefficient  $k$  variations as function of the ratio  $\alpha = R_L / R_i$ : (a)  $ss$  connection; (b)  $sp$  connection.

For each phenomenon the results included also graphical representations, very suggestive, presented comparatively for different values of the coupling factor and for the four alternatives of connection of the circuits. The paper provides also some clues on how it could be estimated, with a rather good accuracy, the limit value of the coupling factor that decides the appearance or the non-appearance of any of the two phenomena. The study on the variation of the splitting coupling factor as function of the load resistance - input resistance ratio ends this work.

The studies presented in this work completes the previous made and published analyzes in the domain of wireless power transfer systems, bringing new and useful information for the researchers and the designers of such systems.

Received on July 29, 2016

Editorial Approval on November 18, 2016

#### REFERENCES

- [1] A. Kurs, A. Karalis, R. Moffatt, J. D. Joannopoulos, P. Fisher, and M. Soljagic, "Wireless power transfer via strongly coupled magnetic resonances", *Science*, vol. 317, no. 5834, pp. 83–86, Jul. 2007.
- [2] W. Q. Niu, J. X. Chu, W. Gu, and A. D. Shen, „Exact analysis of frequency splitting phenomena of contactless power transfer systems”, *IEEE on CAS – I*, Vol. 60, No. 6, pp. 1670 – 1677, June 2013.
- [3] C. S.Wang, G. A. Covic, and O.H. Stielau, “Power transfer capability and bifurcation phenomena of loosely coupled inductive power transfer systems”, *IEEE Trans. Ind. Electron.*, vol. 51, no. 1, pp. 148–157, Feb. 2004.
- [4] M. Iordache, D. Niculae, L. Iordache (Bobaru), and L. Mandache, „Circuit analysis of frequency splitting phenomena in wireless power transfer systems”, *Proc. of the 9th International Symposium Advanced Topics in Electrical Engineering – ATEE’15*, May 7-9, 2015, Bucharest, Romania, pp. 146 - 151.
- [5] M. W. Baker and R. Sarpeshkar, “Feedback analysis and design of RF power links for low-power bionic systems”, *IEEE Trans. Biomed. Circuits Syst.*, vol. 1, no. 1, pp. 28–38, March 2007.
- [6] A. Karalis, J. D. Joannopoulos, and M. Soljačić, “Efficient wireless non-radiative mid-range energy transfer”, *Annals of Physics*, Vol. 323, pp. 34-48, January 2008.
- [7] T. Imura and Y. Hori, “Maximizing air gap and efficiency of magnetic resonant coupling for wireless power transfer using equivalent circuit and Neumann formula”, *IEEE Trans. Ind. Electron.*, vol. 58, no. 10, pp. 4746–4752, Oct. 2011.
- [8] S. Cheon, Y.H.Kim, S.Y. Kang, M. L. Lee, J.M. Lee, and T. Zyung, “Circuit model based analysis of a wireless energy transfer system via coupled magnetic resonances”, *IEEE Trans. Ind. Electron.*, vol. 58, no. 7, pp. 2906–2914, Jul. 2011.
- [9] A. P. Sample, D. A.Meyer, and J. R. Smith, “Analysis, experimental results, and range adaptation of magnetically coupled resonators for wireless power transfer”, *IEEE Trans. Ind. Electron.*, vol. 58, no. 2, pp. 544–554, Feb. 2011.
- [10] J. A. Ricano, H. Rodriguez Torres, H. Vazquez Leal and A. Gallardo del Angel, "Experiment about wireless energy transfer", *1-st International Congress on Instrumentation and Applied Sciences*, Cancun, Mexico, October 26-29, 2010, p.1-10.
- [11] D. Niculae, Lucia Dumitriu, M. Iordache, A. Ilie, L. Mandache, "Magnetic resonant couplings used in wireless power transfer to charge the electric vehicle batteries", *Bulletin AGIR*, No. 4, pp. 155-158, 2011.
- [12] A. J. Moradewicz and M. P. Kazmierkowski, “Contactless energy transfer system with FPGA-controlled resonant converter”, *IEEE Trans. Ind. Electron.*, vol. 57, no. 9, pp. 3181–3190, Sep. 2011.
- [13] J. I. Agbinya (Editor), *Wireless Power Transfer*, 2nd edition, River Publishers Series in Communications, Denmark, 2016.
- [14] F. Zhang, X. Liu, S.A. Hackworth, R.J. Sclabassi, and M. Sun, “In vitro and in vivo studies on wireless powering of medical sensors and implantable devices”, *Proc. of Life Science Systems and Applications Workshop - LiSSA*, April, 9-10, 2009, pp. 84-87.
- [15] Y. Tak, J. Park, and S. Nam, “Mode-based analysis of resonant characteristics for near-field coupled small antennas”, *IEEE Antennas Wireless Propag. Lett.*, vol. 8, pp. 1238–1241, Nov. 2009.
- [16] C. S. Tang, Y. Sun, S. K. Nguang, and A. P. Hu, “Determining multiple steady-state ZCS operating points of a switch-mod contactless power system”, *IEEE Trans Power Electron.*, vol. 24, no. 1-2, pp. 416-425, Jan.-Feb. 2009.
- [17] M. Iordache, L. Mandache, D. Niculae, and L. Iordache (Bobaru), „On exact circuit analysis of frequency splitting and bifurcation phenomena in wireless power transfer systems”, *Proc. of the International Symposium on Signals, Circuits and Systems - ISSCS 2015*, 9 - 10 July, 2013, Iasi, Romania, pp. 24-27.
- [18] M. Iordache, A. Marinescu, I. G. Sirbu, L. Mandache, D. Niculae, and L. Iordache, “Comparative study of the frequency splitting and bifurcation phenomena for equivalent circuits of the wireless power transfer system”, *Proc. of 2016 International Conference on Applied and Theoretical Electricity - ICATE*, October 6-8, 2016, Craiova, Romania, p. 1-7.
- [19] C. M. Zierhofer and E. S. Hochmair, “High-efficiency coupling-insensitive transcutaneous power and data transmission via an inductive link”, *IEEE Trans. Biomed. Eng.*, vol. 37, no. 7, pp. 716–722, Jul. 1990.
- [20] H. A. Wheeler, "Simple inductance formulas for radio coils", *Proceedings of the I.R.E.*, pp. 1398-1400, October 1928.
- [21] Ansoft Q3D Extractor, *User Guide*, [www.ansoft.com](http://www.ansoft.com).
- [22] E. W. Weisstein, *Quartic Equation*. From MathWorld—A Wolfram Web Resource [Online]. Available: <http://mathworld.wolfram.com/QuarticEquation.html>, Nov. 2011.

# Power Control and Energetic Performances of an Induction Heating System Destined for Drying of Current Transformers

Alexandru Bitoleanu, Mihaela Popescu \* and Dinu Roxan Doboşeriu

\* Faculty of Electrical Engineering, University of Craiova, Craiova, Romania, alex.bitoleanu@em.ucv.ro; mpopescu@em.ucv.ro

† S.S.H. Hidroserv, Râmnicu Valcea, Romania, doboşeriu\_constantin@yahoo.com

**Abstract** - This paper is concerned with the design of the power control system for a single-phase voltage source inverter feeding a parallel resonant induction heating load and the analyse of its energetic performances. The control of the inverter output current, meaning the active component of the current through the induction coil when the control frequency is equal or slightly exceeds the resonant frequency, is achieved by a Proportional-Integral-Derivative controller tuned in accordance with the Modulus Optimum criterion in Kessler variant. The control system response, in terms of the rms current at the inverter output when a prescribed step current is applied, shows that the dynamic and static performances are very good. In the second part, the paper presents the energetic performances of a proposed system for drying of current transformer from 110 kV Ciungetu power station. First, based on the actual technical solution and experimental recording of voltage and current, the equivalent parameters of the load circuit have been determined. In the proposed solution, the drying process is based on an induction heating system that contains a half-controlled rectifier and a voltage source inverter that operates with resonant load. The energetic performances have been determined in order to ensure zero-current switching of the inverter.

**Keywords:** *Induction heating, Resonant inverters.*

## I. INTRODUCTION

The voltage source inverters with resonant parallel load are used successfully in medium and high frequency induction heating systems [1]-[5]. The replacement of the current source inverters has been facilitated by both the existence on the market of the high power insulated-gate bipolar transistors (IGBTs) and the advantages of voltage source inverters [3], [5], [6]. These consist primarily in simple limiting the switching overvoltage and simplest achievement of switching at zero current. Last but not least, the use of parallel resonance allows for high load current with a small current through the inverter (only the active component). As the control system handles the operation of the induction coil in parallel with a compensation capacitor at the desired resonant frequency, the current through the induction coil is forced to be sinusoidal. In practice, the parallel resonant circuit is damped when the work piece is inserted into the induction coil by introducing additional losses into the system and increasing the current drawn from the inverter [1], [3], [5], [7].

Currently, at Hidroserv Râmnicu Valcea, the drying of the current transformers used in the high power transformer stations is carried out by a combination between the induction and conduction heating at the industrial frequency of 50 Hz.

Given the technological processes based on heating, a multifunction static system, able to provide both types of energy (DC as well as the AC) and adjust the frequency and the power level, is required, in order to obtain a high degree of flexibility [2], [3], [4]. To substantiate the feasibility of this new technical solution, the associated energetic performance assessment is needed.

For this purpose, the entire system has been modeled in Matlab/Simulink under conditions as close to reality as possible. The determination of energetic performances has been made by using parameters provided by the system design, equivalent load parameters determined based on experimental data and the controller designed in the first part of the paper.

In order to ensure zero-current switching of the inverter, the operating frequency of the square-wave inverter, which is provided by an auto-adaptive loop, is imposed to be slightly higher than the resonant frequency of the equivalent circuit consisting of induction coil-work piece in parallel with the resonant capacitor.

First, the power structure of the system and the role of each components are presented.

The control system structure and block diagram and functions transfer are discussed in Section III. In Section IV, the control of the inverter output current is analyzed and the design of a proportional integral derivative (PID) current controller is performed based on Modulus Optimum criterion in Kessler variant. It is followed by tests on the control system performance. The energetic performances have been determined in section V and some conclusions are finally given in section VI.

## II. STRUCTURE OF THE HEATING SYSTEM

The block diagram of the system for electric induction heating highlights the main components (Fig. 1).

1. Power transformer – that adapts the voltage level to the needs of the process. For the drying process, the existing transformer at Hidroserv Ciungetu will be used.

2. Half-controlled rectifier – that is part of the structure of the static voltage and frequency converter and allows the adjustment of the active power transmitted to the load.

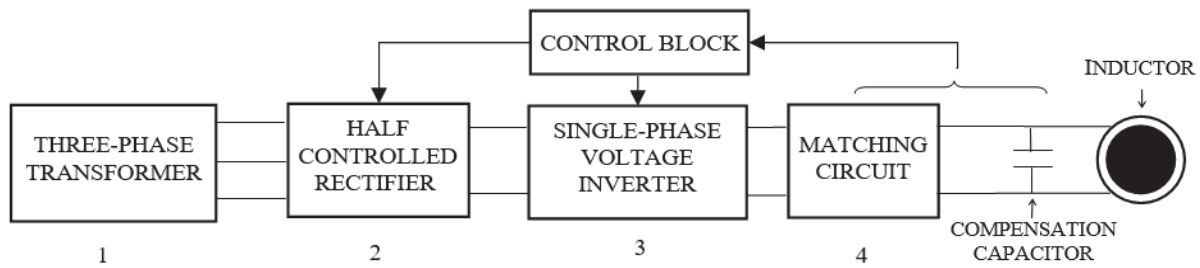


Fig. 1. Block diagram of the electric induction heating system.

3. Inverter – that converts the electrical power from DC to AC and allows the adjustment of the fundamental frequency of the load voltage, in order to obtain superior energetic performance [7] - [13].

4. Matching circuit – that is specific to the converters that supplies inductors for induction heating and aims to improve the energetic performances. Specially, if the control frequencies are close to the resonance frequency, the matching circuit facilitates the high energetic performances [14].

The load of the heating system is the assembly consisting of inductor - heated body - compensation capacitor. It together with the matching circuit represents the load of the inverter.

In many studies of energy analysis, the components of the matching circuit, as well as the compensation capacitor, are considered ideal, lossless. Consequently, the active power at the output terminals of the inverter is equal to the active power dissipation per whole system inductor - heated piece [12], [19].

Basically, the inverter control frequency can be the resonance frequency of the equivalent circuit, the frequency that causes zero current switching, or another frequency that adjusts the power transmitted to the load.

The spectacular developing of the Isolated Gate Bipolar Transistors (IGBTs) determined the reconsideration of the voltage inverters' performances [11]-[21]. It is why, in this work, the use of IGBT-based voltage source inverter is envisaged.

### III. CONTROL SYSTEM STRUCTURE AND BLOCK DIAGRAM

The control of the current through the induction coil can be performed by controlling its active component, which means the control of the inverter output current. As regards the required value of the induction coil current, considering that the heating body is a pipe, there are two possible approaches. a) The work pipe moves through the inductor at a preset speed and the preset current depends on the required temperature gradient.

b) The maximum rated current of the voltage inverter is preset and the work pipe speed is adjusted as a function of the required temperature gradient. This is the option that allows for maximum productivity in terms of the inverter.

When the first approach is adopted, the control system requires two control loops, which are practically independent (Fig. 2).

The following blocks are highlighted in the global block diagram shown in Fig. 2: Ci – current controller;

HCR – half controlled rectifier; DC – DC-link circuit; VSI – single-phase voltage source inverter; MI – matching inductor; HI – heating inductor; RC – resonant capacitor; FAB – frequency adapting block; RMS – rms value calculation; PB - protection block.

The main task of the frequency loop is to achieve the permanent and dynamic observance of the frequency, so that it is equal to or higher than the resonant frequency of the parallel circuit consisting of the equivalent inductor and the resonant capacitor, to facilitate the switching process of inverter's power semiconductors.

As the parameters of the circuit are not constant, the dynamic self adaptation of the frequency is required, by using only quantities provided by system. It results that the frequency loop cannot be controlled by external signals.

On the other hand, in order to obtain the zero-current switching of the inverter's IGBTs, the operating frequency must be slightly higher than the resonant frequency of the load circuit. Consequently, the frequency control loop must be able to achieve this second requirement too.

The block diagram in Fig. 3 illustrates the transfer functions of inverter current control loop [8].

Starting from the equivalent forward transfer function, a Proportional-Integral-Derivative (PID) controller is adopted in order to remove the dominant time constants (the constants of the DC-link circuit). The following specific constants are used:  $K_p$ ,  $K_R$  and  $K_{Ti}$  – the proportional constants of the controller, rectifier and current transducer, respectively;  $T_i$  and  $T_d$  – integral and derivative controllers' time constants;  $T_u$  – the rectifier's integral time constant which corresponds to the average dead-time associated to the firing circuit;  $T_{ed} = R_d \cdot C_d$  and  $T_{emd} = L_d / R_d$  – the electric and electromagnetic time constants of the DC-link circuit;  $T_{ema} = L_a / R_a$  – the electromagnetic time constant of the matching inductor;  $T_{eb} = R_b \cdot C$  and  $T_{emb} = L_b / R_b$  – the electric and electromagnetic time constants of the parallel resonant circuit.

Note that  $L_b$  and  $R_b$  are associated to the equivalent inductance and resistance of the induction coil and heated piece and  $C$  is the capacitance of the resonant capacitor. The transducer was taken into consideration as proportional element.

In the inverter current control loop (Fig. 3), a PID controller is adopted.

Based on the Kirchhoff's laws in the Laplace domain applied to the circuit consisting in the matching induct

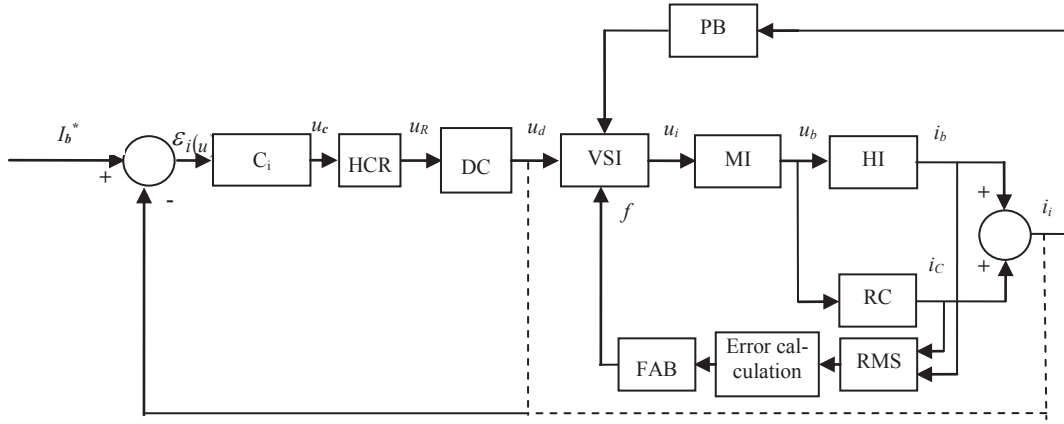


Fig. 2. Block diagram of the closed loop control system

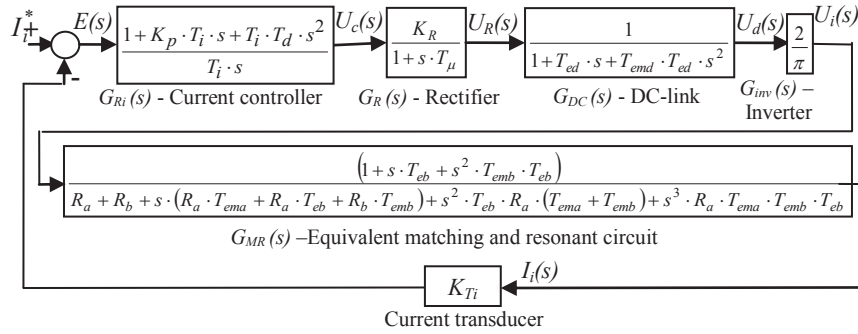


Fig. 3. Operational diagram of the inverter current control loop.

ance and the resonant capacitor in parallel with the equivalent inductor, the transfer function of the matching and resonant circuit can be expressed as follows [8]:

$$G_{MR}(s) = \frac{I_i(s)}{U_i(s)} = \frac{1}{\frac{R_b + sL_b}{1 + sC(R_b + sL_b)} + R_a + sL_a} = \frac{1}{R_a} \cdot \left(1 + T_{eb}s + T_{eb}T_{emb}s^2\right) \left[ \frac{R_b}{R_a} \cdot (1 + T_{emb}s) + (1 + T_{ema}s) \cdot (1 + T_{eb}s + T_{eb}T_{emb}s^2) \right] \quad (1)$$

Assuming that  $T_{eb}T_{emb} \ll T_{eb}$  and  $R_b/R_a \ll 1$ , expression (1) becomes:

$$G_{MR}(s) = \frac{1/R_a}{1 + T_{ema}s} \quad (2)$$

#### IV. CURRENT CONTROLLER TUNING

The current controller design is based on Modulus Optimum criterion in Kessler variant, which is dedicated to the rapid systems [8].

To reach the square modulus of the closed-loop unity feedback transfer function, the open-loop transfer function is expressed first as:

$$G_{di}(s) = G_{Ri}(s) \cdot G_R(s) \cdot G_{DC}(s) \cdot G_{inv}(s) \cdot G_{MR}(s) \cdot K_{Ti} \quad (3)$$

By using the transfer functions shown in Fig. 3 and expression (3), the following expression is obtained:

$$G_{di}(s) = \frac{1 + K_p T_i s + T_i T_d s^2}{s T_i} \cdot \frac{K_R \cdot (2/\pi) \cdot K_{Ti} \cdot (1/R_a)}{(1 + s T_\mu) \cdot (1 + s T_{ema}) \cdot (1 + T_{ed} s + T_{emd} T_{ed} s^2)} \quad (4)$$

To remove the dominant time constants of the DC-link circuit, in accordance with MO criterion, two conditions are imposed in (4):

$$K_p T_i = T_{ed}; \quad T_i T_d = T_{emd} T_{ed} \quad (5)$$

Thus, expression (4) becomes:

$$G_{di}(s) = \frac{K_I}{s T_i \cdot (1 + s T_\mu) \cdot (1 + s T_{ema})}, \quad (6)$$

where,

$$K_I = K_R \cdot (2/\pi) \cdot K_{Ti} \cdot (1/R_a). \quad (7)$$

The integral time constant of the controller is provided by the condition of canceling the denominator term which contains a difference in the modulus square of the closed-loop unity feedback system transfer function [8]:

$$T_i = 2 \cdot K_I \cdot (T_\mu + T_{ema}). \quad (8)$$

When used together with (5), condition (8) gives also the expressions of the proportional and derivative constants of the PID controller:

$$K_p = T_{ed} / [2K_I \cdot (T_\mu + T_{ema})] \quad (9)$$

$$T_d = T_{ed} \cdot T_{ema} / [2K_I \cdot (T_\mu + T_{ema})] \quad (10)$$

From (8) and (10), it is found that the controller's parameters are independent of load parameters, which is an important advantage.

### V. CONTROL SYSTEM PERFORMANCES

To test the performances of the control system, and the energetic performances of the system, the whole induction heating system (power part and control part) has been implemented under Matlab-Simulink environment.

It includes all of the electrical components of the installation and is developed mainly with blocks from Sim Power Systems library.

To avoid using multiple Simulink models or the tandem use of the model and other MATLAB programs such as those of script type, all the needed calculation is included in the model.

Thus, after simulation, all parameters are provided (e.g. rms and average values of the quantities which are of interest, active and apparent powers, power factor, performance indicators).

The main parameters used in the Simulink model are given in Table I.

TABLE I.  
THE NUMERIC VALUES OF THE PARAMETERS IN THE SIMULINK MODEL

Transformer		Rectifier		Inverter	
R <sub>1</sub>	0.0055 Ω	Th	T62-200	IGBT	BSM200GB 120DN2
R <sub>2</sub>	0.0055 Ω	D	1N3274	V <sub>f</sub>	2 V
L <sub>s1</sub>	52.23 μH	V <sub>f</sub>	1.38 V	R <sub>on</sub>	0.01 Ω
L <sub>s2</sub>	52.23 μH	R <sub>on</sub>	0.005 Ω	Fall time	10 <sup>-7</sup> s
M	0.1749 H	Rsnubb	500 Ω	Tail time	2 · 10 <sup>-7</sup> s
		Csnubb	0.25 μF	Rsnubb	150 Ω
				Csnubb	47 μF

It is mentioned that high accuracy results are prefigured by adopting a small simulation step in the discretized model with blocks of type switch (diodes, IGBT, etc).

The control system response, in terms of the rms current at the inverter output when a prescribed step current is applied, is shown in Fig.4 and Fig.5, in perunits.

So, the current is reported on rated value (155A) and the frequency is reported on the resonance value (2kHz). The induction coil and heated transformer parameters are R=0.122Ω and 0.946mH that have been calculated starting from experimentally waves of voltage and current [22].

As it can be seen in Fig.4, the frequency loop searches the value that ensures zero current switching and it finds this value after 0.23 seconds. In this time, in the response of the current are identified three sequences. First, by setting the rms current of the unity value, the overshoot is of about 15% and the transient regime ends in about 0.08 seconds. Follows a second dynamic regime when the frequency closes to the zero current switching value and it

finds this value. Thus, the current has an undershoot (about 20%) followed of an overshoot (about 25%).

In the Fig. 5, the conditions are:

- Initially, the value of the equivalent inductance is increased by 25% (it means that the resonance frequency decreases about 11%) and the current is prescribed at 0.5;
  - After the steady state is obtained, at t=0.4 seconds the current is prescribed at value 1;
  - At t=0.5 seconds the value of the equivalent inductance becomes the rated value.
- Few remarks can be drawn;
- The switching frequency has a lower steady state value; it means that the frequency loop operates properly;
  - Up to t = 0.5 seconds, when equivalent inductance drops to nominal value, overtaking of current are much lower;
  - After this time, the current has a big overshoot (about 65%);
  - The duration of this new dynamic regime is about 0.15 seconds.

Must be underlined that the equivalent inductance value can be changed by temperature, but its change is continuously. In this conditions, the big overshoot of the current shows the sensibility of the frequency loop at changing of the inductance but cannot be really obtained.

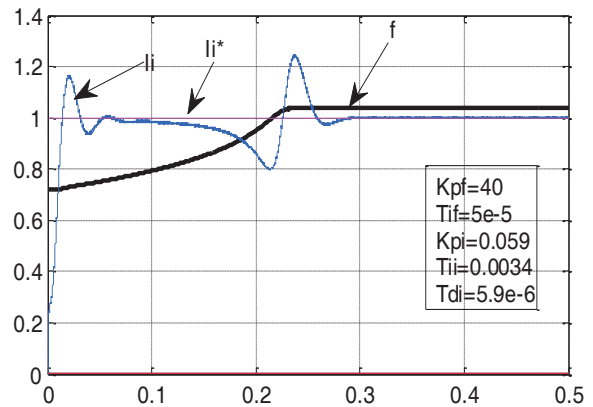


Fig. 4. Response of the inverter current and switching frequency.

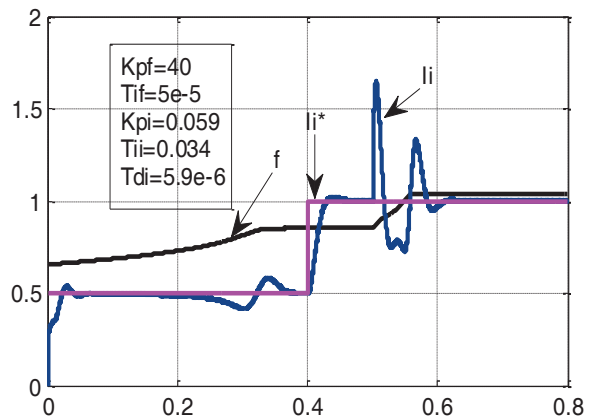


Fig. 5. Response of the inverter current and switching frequency when the prescribed current and inductance value are changed.

## VI. ENERGETIC PERFORMANCES

The operation of the system in the case of prescribing the rated value of the current has been analyzed (active power of the equivalent inductor is about 15 kW). The numerical values obtained by simulation are summarized in Table II. The significance of the involved quantities is as follows:

$f_{sw}$  - the switching frequency of the inverter;  
 $P_s$  and  $S_s$  - the active and apparent powers in the transformer secondary (rectifier input);  
 $PF_s$  - the power factor in the transformer secondary;  
 $P_d$  - the active power at the inverter input;  
 $\eta_R$  - the rectifier efficiency;  
 $P_i$  and  $S_i$  - the active and apparent powers at the inverter output;  
 $PF_i$  - the power factor at the inverter output;  
 $\eta_i$  - the inverter efficiency;  
 $P_{ind}$  - the active power across the equivalent inductor;  
 $S_{ind}$  - the apparent power across the equivalent inductor;  
 $PF_{ind}$  - the power factor across the equivalent inductor;  
 $\eta_{ind}$  - the efficiency of the equivalent inductor;

$\eta_t$  - the total efficiency ( $P_{ind}/P_s$ ).

The analysis of the numerical results (Table II) and the waveforms in Figs. 6 shows the following:

1. The voltage in the transformer secondary is very little affected by the rectifier switches and the waveform of the current is rectangular, and its shape depends of the control angle (Fig. 6a);
2. The voltage in the DC-link circuit is practically constant and the current has pulsations (Fig. 6b);
3. The inverter output voltage is rectangular, and the current is symmetrical and nonsinusoidal (Fig. 6c);
4. The voltage across the inductor, the current through it and the current through capacitor are practically sinusoidal (rms values are equal to the fundamentals rms), (Fig. 6d);
5. The equivalent load has capacitive nature; consequently, the current flow through the compensation capacitor is higher (Fig. 6d);
6. The energetic performances are very good (the efficiencies of the rectifier, of the inverter and of the system have high values).

TABLE II.  
THE ENERGY PERFORMANCES OF THE INDUCTION HEATING SYSTEM

$f_{sw}$ [kHz]	$P_s$ [kW]	$S_s$ [kVA]	$PF_s$ [%]	$P_d$ [kW]	$\eta_R$ [%]	$P_i$ [kW]	$S_i$ [kVA]	$PF_i$ [%]	$\eta_i$ [%]	$P_{ind}$	$S_{ind}$	$PF_{ind}$ [%]	$\eta_{ind}$ [%]	$\eta_t$ [%]
2.116	16.73	1087	1.54	16.51	99.4	15.45	18.16	85.1	93.42	15.02	22.58	66.53	97.21	90.26

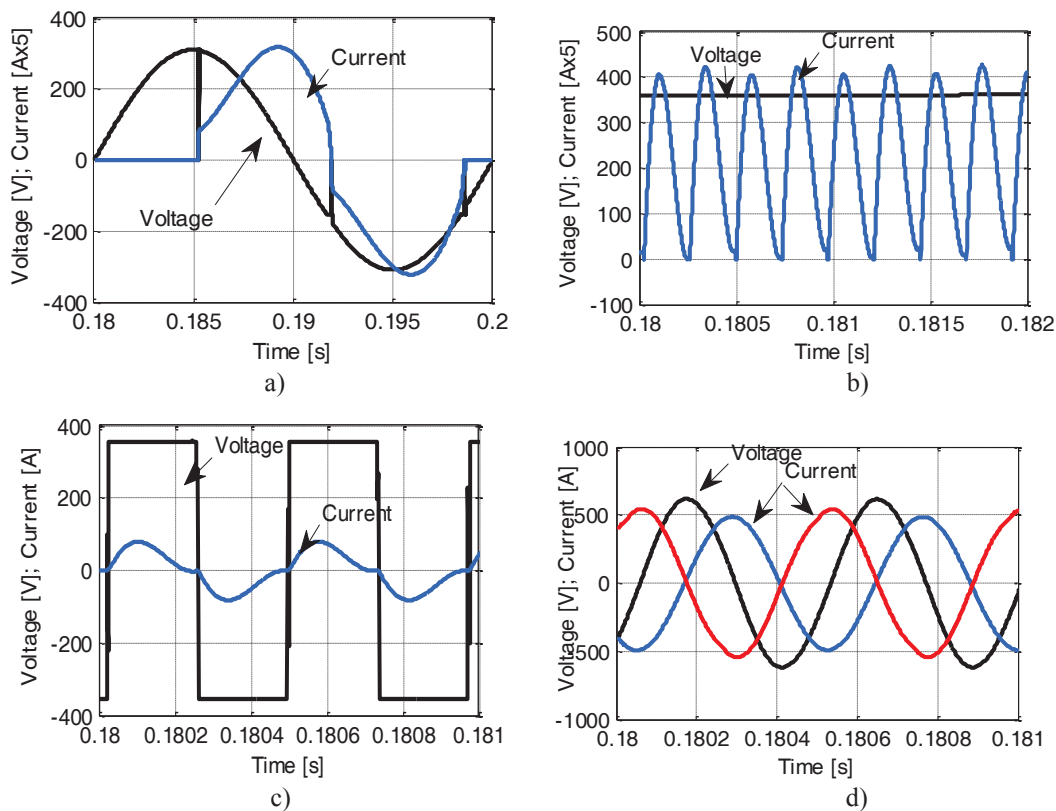


Fig. 6. Waveforms of currents and voltages when the inverter switches at zero current: voltage and current in secondary of the transformer - a); voltage and current to input of the inverter - b); voltage and current to output of the inverter - c); the voltage across the inductor (black), the equivalent inductor current (blue) and the current through the compensation capacitor (red) - d).

## VII. CONCLUSIONS

After designing the inverter current control loop followed by the performance testing through simulation, some concluding remarks can be drawn.

1. The current controller of PID type was successfully tuned based on Modulus Optimum criterion in Kessler variant.
2. The determination of the controller's parameters is unique and leads to the elimination of inertia introduced by the DC-link circuit.
3. The tuned current controller leads to a very good performance of the current loop (the overshoot is missing or is below 25%) and the maximum duration of transient is 0.1 seconds).
4. The overshoot of the current can be reduced if lower value of the current is prescribed (0.5 in per units) until to zero current switching frequency is stabilized.
5. The simulation results illustrate a very good behavior of the control system.
6. It has been shown that the proposed solution for drying applications in maintenance of equipment from hydroelectric plant is viable because it has very good energetic performances.

*Received on July 19, 2016*

*Editorial Approval on November 15, 2016*

## REFERENCES

- [1] Espi Huerta J.M.; Dede Garcia Santamaria E.J.; Garcia Gil R.; Castello Moreno J. Design of the L-LC Resonant Inverter for Induction Heating Based on Its Equivalent SRI. IEEE Trans. on Industrial Electronics[J], Vol. 54, No.6, 2007, PP:3178-3187.
- [2] Espi J.M.; Dede E.J.; Navarro E.; Sanchis E.; Ferreres A. Features and design of the voltage-fed L-LC resonant inverter for induction heating. Proc. Power Electronics Specialists Conference, 1999, PP:1126 - 1131.
- [3] Dieckerhoff S.; Ryan M.J.; De Doncker R.W. Design of an IGBT-based LCL-Resonant Inverter for High-Frequency Induction Heating. The 34th Industry Applications Conference, Vol. 3, Oct. 3-7, 1999, PP:2039-2045.
- [4] Espi J.M.; Navarro A.E.; Maicas J.; Ejea J.; Casans S. Control circuit design of the L-LC resonant inverter for induction heating. Proc. Power Electronics Specialists Conference, 2000, PP:1430-1435.
- [5] Yoo H; Shim E.; Kang J.; Choi G.; Lee C.; Bang B. 100kHz IGBT inverter use of LCL topology for high power induction heating. Proc. 8th IEEE International Conference Power Electronics and ECCE Asia, June 2011, PP:1572-1575.
- [6] Salih A. IGBT for high performance induction heating applications, Proc. 38th Annual Conference on IEEE Industrial Electronics Society, Oct. 2012, PP:3274-3280.
- [7] Rudnev V.; Loveless D.; Cook R.; Black M. Handbook of Induction Heating, Marcel Dekker, NY, 2003.
- [8] Mihaela Popescu and A. Bitoleanu, "Power control system design in induction heating with resonant voltage inverter," in Proc. 6th International Conference on Advanced Computer Theory and Engineering, August 2013, Male.
- [9] F. A. Sprânceană., D. Anghel, Metode și procedee tehnologice. vol. II. Tehnologii Moderne, Printech, Bucuresti, 2006.
- [10] M.K. Kazimierzczuk, D. Czarkowski, Resonant power converters, John Wiley & Sons, 2011.
- [11] A. Bitoleanu, D. Mihai, Mihaela Popescu, C. Constantinescu, convertoare statice și structuri de conducere performante pentru acționări electrice, Sitech, Craiova, 2000.
- [12] V. Esteve, J. Pardo, J. Jordan, E. Dede, E. Sanchis-Kilders, E. Maset, "High power resonant inverter with simultaneous dual-frequency output," Power Electronics Specialists Conference, 2005, pp. 1278-1281.
- [13] S. Dieckerhoff, M.J. Ruan, R.W. De Doncker, "Design of an IGBT-based LCL-resonant inverter for high-frequency induction heating," The 34th Industry Applications Conference, vol. 3, Oct. 3-7, 1999, pp. 2039 – 2045.
- [14] Popescu Mihaela; Bitoleanu A.; Dobriceanu M. Analysis and Optimal Design of Matching Inductance for Induction Heating System with Voltage Inverter, The 8th International Symposium on Advanced Topics in Electrical Engineering, Bucharest, 2013, May 2013,
- [15] F.P. Dawson, P. Jain, "A Comparison of Load Commutated Inverter Systems for Induction Heating and Melting Applications," IEEE Transactions on Power Electronics, vol. 6, no. 3, July 1991, pp.430-441.
- [16] A. Suresh, R.S. Rama, "Parallel resonance based current source inverter for induction heating," European Journal of Scientific Research, vol. 58, no. 2, 2011, pp.148-155.
- [17] Mihaela Popescu, A. Bitoleanu, E. Subțirelu, "Design and performance of the voltage control loop in induction heating systems with L-LC resonant inverters," Annals of the University of Craiova, Electrical Engineering series, No. 37, 2013, pp.39-43.
- [18] S. Chudjuarjeen, A. Sangswang, C. Koopai, "An improved LLC resonant inverter for induction-heating applications with asymmetrical control," IEEE Transactions on Industrial Electronics, vol. 58, issue 7, July, 2011, pp. 2915 - 2925.
- [19] P. Sreenivas, R. Vaddi, J.S. Ranganayakulu, "Full bridge resonant inverter for induction heating applications," International Journal of Engineering Research and Applications (IJERA), vol. 3, issue 1, Jan.-Feb., 2013, pp.066-073.
- [20] V. Suru, Mihaela Popescu, A. Bitoleanu, "Energetic performances of induction heating systems with voltage resonant inverter," Proceedings of International Symposium on Electrical and Electronics Engineering, Galați, România, October 11-13, 2013.
- [21] A. Bitoleanu, Mihaela Popescu, V. Suru, "Maximizing power transfer in induction heating system with voltage source inverter" The 22nd International Conference on Nonlinear Dynamics of Electronic Systems, NDES 2014, Albena, Bulgaria, June 2014.
- [22] D. R. C. Doboseriu, A. Bitoleanu, M. Linca, "Energetic Performances of an Induction Heating System with Half-Controlled Rectifier Destined for Drying of Current Transformers" 2016 International Conference on Applied and Theoretical Electricity (ICATE), Craiova, Romania, 6-8 October, 2016.

# Some Considerations Concerning Radiated Emissions Produced by a Board Display

Petre-Marian Nicolae<sup>\*</sup>, Ileana-Diana Nicolae<sup>†</sup> and Relu-Adrian Aipu<sup>‡</sup>

<sup>\*</sup> Dept. of Electrical Engineering, Energetic and Aeronautics, University of Craiova, Romania, pnicolae@elth.ucv.ro

<sup>†</sup> Dept. of Computer Science and IT, University of Craiova, Romania, nicolae\_ileana@software.ucv.ro

<sup>‡</sup> Continental SA, Timisoara, Romania, aipurelu@gmail.com

**Abstract** - The paper presents some considerations related to the radiated emissions from automotive area of interest. Firstly the equipment used for tests dedicated to radiated emissions is presented. Afterward some considerations on the test equipment, used in a semianechoic chamber are made. Characteristics of the horn antenna used to accomplish tests dedicated to radiated emissions within the range 0.8...1.6 GHz, along with some aspects related to design and simulation are also presented. The analysis of the electric field in the antenna and respectively of the electric field distribution in the remote field area was performed for three different frequencies (1.2GHz, 1.4GHz, 1.6GHz). Tests conditions are also described. Discussions are made with respect to the recorded data. The results of tests concerning the radiated emissions for a board display are presented, both for the horizontal and respectively vertical polarizations. Tests were made firstly for the initial hardware structure and problems related to the vertical polarization were noticed. Measures to improve the display operation are analyzed. Results of tests after the application of improvement measures are presented. Conclusions related to the improvement of the board display operation are deduced.

**Keywords:** radiated emissions, horn antenna, simulation of horn parameters, tests of board display, anti-disturbance measures.

## I. INTRODUCTION

The electric and electronic products designed and conceived to be used in commercial purposes must satisfy specific national and international electromagnetic compatibility (EMC) standards. The tests conceived to certify the compliance with these standards can be grouped in two major categories, as follows:

- tests for radiated and respectively conducted emissions;
- tests for conducted and respectively radiated immunity.

In order to certify the compliance with the norms related to radiated emissions, the Equipment Under Test (EUT) is submitted to the following tests: tests with radiated emissions with antennas, strip line method and current probe.

The tests for radiated emissions (TRE) are defined in order to identify the signals emitted in the surrounding environment by the EUT. These tests are typically developed within the frequency range 30 MHz...1 GHz. Yet some tests for radiated emission which are conceived for the compliance with the American standard FCC extend the upper limit of frequency to 200 GHz [1]. The devices to which these tests are addressed are for example wireless devices for which the carrying frequency is greater than 30 GHz [2].

Sometimes the beneficiaries of some products from the automotive area require additional tests, covering an extended frequency range as compared to the present norms. An improved accuracy of tests is often required for such situations, in order to make sure that the realized products are in compliance with the requirements imposed by norms.

## II. TESTS FOR RADIATED EMISSIONS

The tests for radiated emissions (TRE) are more difficult than those for conducted emissions. TRE are performed in an open space owing to the additional disturbing signals, already present in the environment, which can be superposed over the signals generated by EUT. Fortunately there are methods to identify and separate the external signals coming from external sources such as mobile phones or digital TV.

A different setup for TRE assumes their accomplishing in semi-anechoic chambers. Inside them a "clean" electromagnetic (EM) environment is provided from the interferences point of view. In this case the external signals cannot disturb the accomplished measures. Even if the costs related to the building of a fully functional semi-anechoic chamber often exceed 1 million Euros, because the environment is more and more crowded by the EM spectrum, the tests performed in semi-anechoic chambers represent more and more often the selected alternative.

Assuming that a test configuration is compatible to the applied standard, the TRE can be achieved considering few basic rules to be followed all over the test procedures.

The TRE described in Fig. 1 uses a test antenna placed 1 m behind the EUT and 1 m over the conducting floor [3].

EUT is placed on a table with metallic plan at a height of 90 cm from the floor. An isolating material (with a permittivity lower than 1.4 F/m, similar to that for air) is placed between EUT and floor.

Placing EUT on the test table is made such as to reproduce the real operating conditions [3].

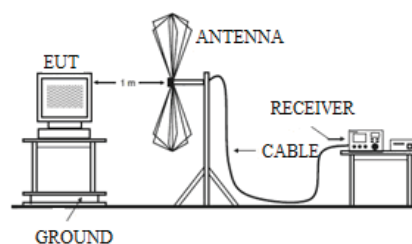


Fig. 1. Setup for TRE

The regulations for the tests concerned with radiated emissions from the automotive area are included in the CISPR 25 standard and, when necessary, are mentioned by the manufacturer's own standards [5], [6]. CISPR 25 mentions that the tested device should be considered as operating in the worst possible conditions, in order to emit the highest disturbances. For these tests, the test received should be set such as to use the appropriate filter (the available options being 9 kHz, 120 kHz or 1 MHz) [5]. Other factors to be considered are the attenuation introduced by the signal cables and respectively the factor of the antenna employed during tests. Fig. 2 depicts a standard configuration of the test equipment for a test concerned with radiated emissions [7].

The symbols used in Fig. 2 are [3]: 1 - EUT (equipment under test); 2 - cable harness; 3 - Load box (provides the operation in normal conditions of the EUT); 4 - Battery; 5 - Line impedance stabilization network (LISN); 6 - Test table with metallic plan; 7. Non-conductive material; 8 - Antenna; 9 - Metallic floor; 10 - Cable for the signal between the antenna and the test receiver; 11 - Input / Output board for the semi-anechoic chamber; 12 - Test receiver; 13 - Materials absorbing electromagnetic radiations; 14 - System for analysis and control.

### III. EQUIPMENT USED FOR RADIATED EMISSIONS TESTS

In order to test the behavior of the EUT considering the emitted radiations, either tests of pre-compliance with the existing standards for the automotive domain, or tests of compliance with the existing more general standards should be performed.

The most important aspect when accomplishing tests from the domain of electromagnetic compatibility (EMC) is represented by the providing of two characteristics of tests: repeatability and respectively reproducibility. Therefore a special attention must be paid to the connecting of test equipment (receivers, antennas, LISN, current probes etc.), as well as to the EUT.

The connections to ground, the cables and connectors of different test equipment must be considered too.

According to CISPR 25, the cables are put together on a cable harness that is placed on the front of the bench for the tests considering the automotive domain. The problem

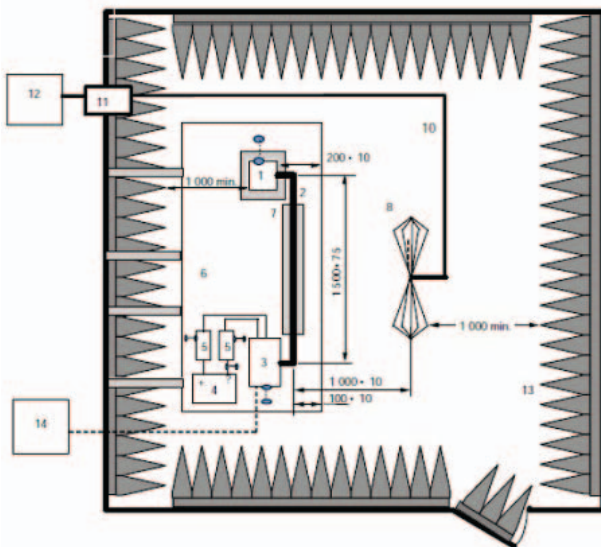


Fig. 2. Standard configuration of the test equipment.

of cable harness is approached because at lower frequencies the main coupling to radiated fields will occur through the cables feeding the device (the same process is used in MIL STD 461 and in ISO 11452) [5]. A LISN is used to bring power to the device [5].

In order to provide correct tests, one should consider all the attenuations introduced in the test procedure by cables and connectors. Therefore the test system (e.g. receiver+antenna+link cables) must be periodically checked. As for the cables, it is required to evaluate the attenuation introduced by them and its compensation during tests.

A series of equipment are required by TRE:

(a) Test receiver (TR). For the cases analyzed in this paper, a receiver Rohde & Schwarz of type ESCI, with range frequency from 9 kHz to 3 GHz was used. It is mainly used for TRE, but it can also be used for various other investigations. The TR performs measurements related to the signal level in a predetermined frequency range.

The new generations of TRs include many blocks used for numerical processing, their operation being fully automated. They allow the operation's control by means of dedicated software packages and interface to a computer [8].

The ordinary operational frequency range of TRs starts from 9 kHz, reaching up to tens of GHz, the new generations of TRs allowing extended frequency ranges [8].

(b) Antennas. At frequencies in the range 30...200 MHz a biconical antenna is used, while for the range 200...1000 MHz, a log periodic dipole array is recommended. From 1 to 2 GHz a pyramidal horn antenna (PHA) is recommended [5].

Because the frequency range for which the effect of EM radiations had to be evaluated was extended to the range 1...2 GHz at the client request, a PHA was used for the tests presented in this paper.

### IV. HORN ANTENNA USED FOR TESTS

The ratio "front / back" (*RFB*) represents a parameter to appreciate the directivity of an antenna for the angles of  $0^{\circ}$  and  $180^{\circ}$  respectively. According to its definition, this ratio is computed considering the voltages occurring across the antenna's terminals when the antenna is irradiated under these angles [8]:

$$RFB = U_0^0 / U_{180}^0 \quad (1)$$

This ratio is often expressed by using logarithms [8]:

$$RFB = 20 \log(U_0^0 / U_{180}^0) \quad (2)$$

A pyramidal horn antenna (PHA) was utilized for the analyzed frequency range. Its gain is given by [9]:

$$G = 10 [1.008 + \log(a/\lambda) \cdot (b/\lambda)] - L_e - L_h \quad [dB] \quad (3)$$

where  $L_e$ ,  $L_h$  represent the coefficient used for correction relative to the maximum deviation of the phase of the field from aperture.

If the aperture of the PHA fits to that corresponding to the maximum gain for the sector - type horn antenna, an optimum PHA is obtained. For it, the gain is [9]:

$$G = 10 [1.008 + \log(a/\lambda) \cdot (b/\lambda)] \quad [dB] \quad (4)$$

For slight modifications of the aperture's opening rela-

tive to the values given by (4), a significant increase of the antenna's frequency range is noticed, the gain being reduced by 2 dB (as compared to the maximum one).

At first simulations were performed in order to get optimal values for one of the PHA's major parameters (gain, radiation characteristics and input impedance). An extensive study on numerical methods usable for simulation of electromagnetic shields behavior was made in [10]. Our simulations were made with the dedicated software tools "ANTENNA MAGUS", and "CST MICROWAVE STUDIO" which allowed for the selection of the PHA's central resonance frequency. For the analyzed cases, the PHA's gain played the role of the optimized parameter.

Once built by using "ANTENNA MAGUS", the physical model of the PHA was loaded into the software tool "CST MICROWAVE STUDIO" (CST) [11]. CST allows the creation of a mesh within the built antenna mode as well as the setting of a port in order to inject the signal into the antenna, in order to study its behavior at various frequencies. CST is using the finite elements method (FEM) for analysis and mesh creations. It also uses an original FEM, with applicability for EM fields [11].

A tetrahedral mesh was built. The mesh for the entire computation domain is depicted by Fig. 3 (a) whilst Fig. 3 (b) depicts a cross section through this domain.

A tetrahedral type of mesh was used because it provides a very good accuracy of results and respectively saves run-time. Considering the spatial symmetry along the central axis (Fig. 3 b), only 34840 tetrahedral were used for computation (half of the number required by the mesh from Fig. 3 a).

In order to evaluate possible reflections of the power inside antenna (caused for example by the poor adaptability between the connection cable and antenna, or between the antenna and the tool used for measurements), the reflection coefficient of the steady wave was analyzed. It is known as "wave standing ratio – VSWR" (Fig. 4) and can be computed with [12]:

$$VSWR = (1 + |\Gamma|) / (1 - |\Gamma|) \quad (5)$$

where  $\Gamma$  stands for the reflection coefficient.

Fig. 4 reveals small reflections, lower than 1.5. Therefore one could conclude that the antenna was well adapted for the impedance of  $50\Omega$ .

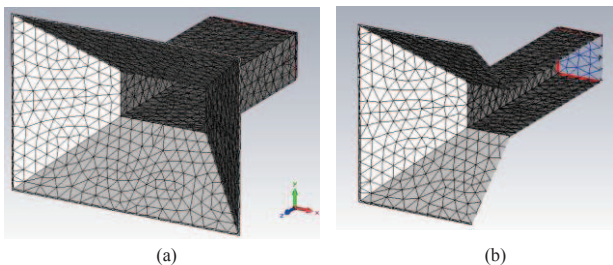


Fig. 3. Mesh (a) of the whole computation domain; (b) in a cross section.

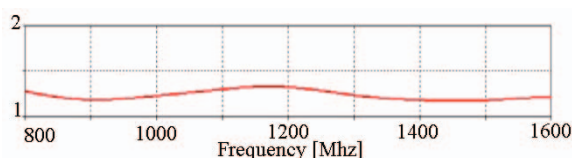


Fig. 4. VSWR as a function of frequency (the range: 0.8...1.6 GHz)

The simulation was made for the frequency range (0.8...1.6) GHz, which matches the range for which the PHA is used during the final tests developed in a semi-anechoic chamber.

The next step consisted in the analysis of results and of PHA behavior at different frequencies. Fig. 5 depicts:

- in the upper part - the electric field in PHA, for the type of analysis "peak". For the analyzed frequencies (1.2 GHz, 1.4 GHz and respectively 1.6 GHz), the maximum 2D values were 213.32 V/n, 284.15 V/n and respectively 207.48 V/n, whilst the phases were  $0^\circ$  for 1.2 GHz and respectively  $158.5^\circ$  for the other 2 frequencies.
- in the bottom part, the electric far field and directivity are represented, the associated numerical results being depicted by Table I.

The polar representations of the radiation characteristics, for different frequencies are depicted by Fig. 6: (a) 1.2 GHz, main lobe magnitude = 12.9 dB, angular width = 34.20 side lobe level = -16.9 dB; (b) 1.4 GHz, main lobe magnitude = 13.5 dB, angular width = 28.90 side lobe level = -18.1 dB; (c) 1.6 GHz, main lobe magnitude = 11.6 dB, angular width = 69.0 side lobe level = -13.4 dB.

A board display (Fig. 7) was used as the EUT submitted to TRE. The EUT's placing on the test table was done such as to reproduce the conditions from the car, the final goal being to provide test conditions as close as possible to the natural ones.

## V. RADIATED EMISSIONS MEASUREMENT

The test setup was accomplished according to the standards for emissions CISPR 2 and its placement is depicted in Fig. 2.

After putting the equipment in the test semi-anechoic chamber and preparing the test software, the appropriate horn antenna was prepared. It was used to make measurements for the frequency range (1...1.6) GHz, the same with that used for simulations, as described in Section V. The horn antenna is of type SCHWARZBECK BBHA 9120 D.

The tests were accomplished for both types of antenna's polarizations: horizontal and respectively vertical.

### A. The Initial Experimental Determination Concerning the Radiated Disturbances

The EUT equipment must be compliant with the limits imposed to the disturbances transmitted through radiation according to CISPR 25 [5].

We used for the tests an electromagnetic disturbances receiver of type ESCI with the frequency range 9 kHz...3 GHz, a LISN and a horn antenna [3].

The receiver's test parameters for all the determinations presented below were: (a) The test range: 1 ÷ 1.6 GHz; (b) Bandwidth: 9 kHz.

TABLE I.  
RESULTS OF ANALYSIS ON ELECTRIC FAR FIELD AND DIRECTIVITY

	Frequency [GHz]		
	1.2	1.4	1.6
Radiation efficiency [dB]	-0.033	-0.054	-0.06
Total efficiency [dB]	-0.114	-0.082	-0.098
Directivity [dBi]	12.9	13.53	11.61

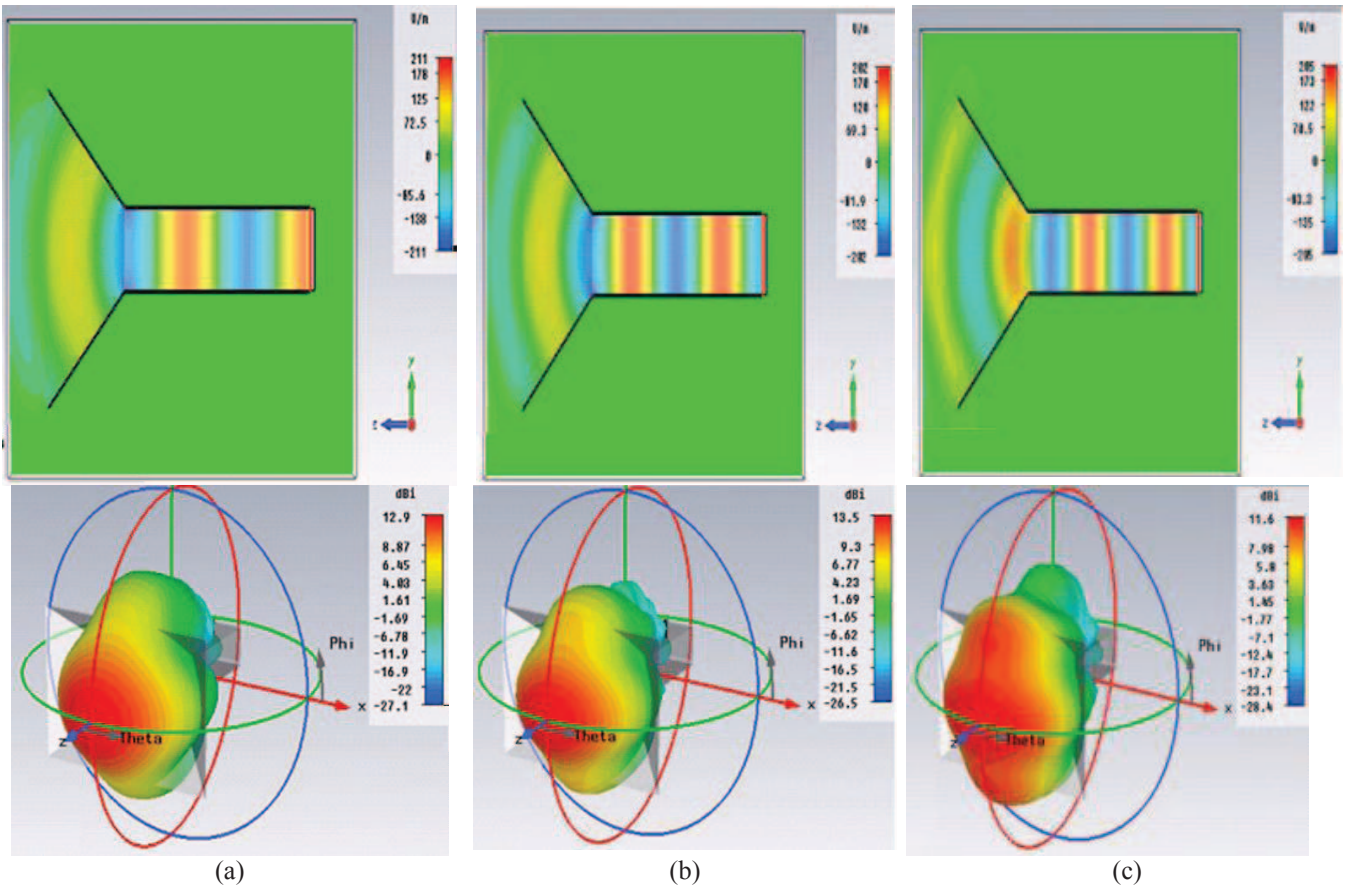


Fig. 5. Electric field in PHA (top) and electric far field and directivity (bottom), at different frequencies: (a) 1.2 GHz; (b) 1.4 GHz; (c) 1.6 GHz.

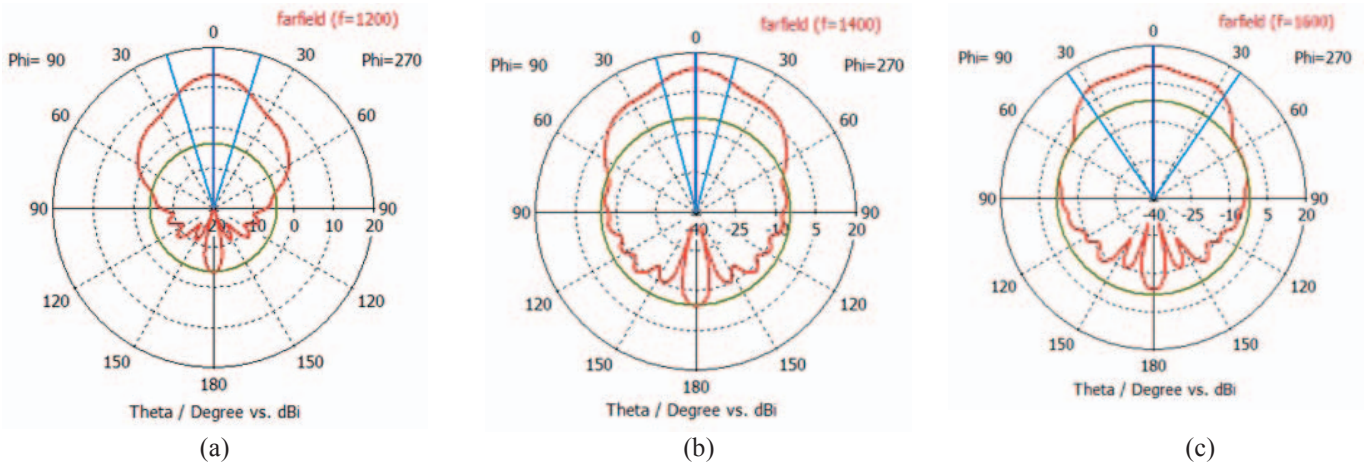


Fig. 6. Polar representation of the radiation characteristics at: (a) 1.2 GHz; (b) 1.4 GHz; (c) 1.6 GHz.



Fig. 7. The board display submitted to TRE

The mean and quasi-peak values of the disturbances transmitted through radiation must not exceed the limits imposed by CISPR 25.

EUT was supplied through an artificial network LISN – in order to provide a constant impedance of  $50 \Omega$  at the EUT supplying and to be able to filter the signals from its supplying cables. Fig. 8 depicts the ensemble used to measure the disturbances transmitted through radiation.

The experimental determinations of the radiated disturbances generated by EUT, before the implementation of anti-disturbances measures are depicted by Fig. 9 (horizontal polarization) and by Fig. 10 (vertical polarization).



Fig. 8. Setup for the determination of disturbances transmitted through radiation for EUT

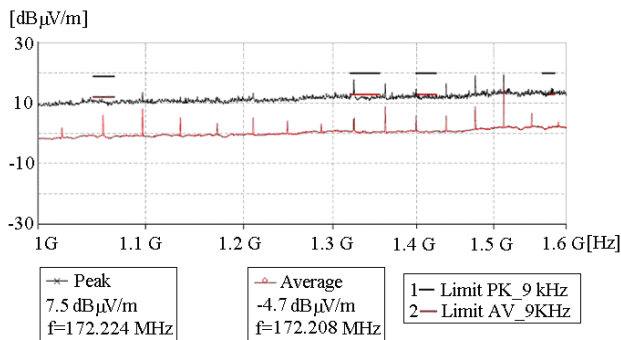


Fig. 9. Disturbances radiated by EUT in horizontal polarization, before the implementation of anti-disturbances measures.

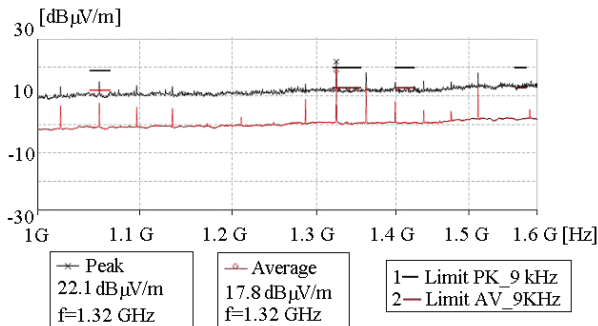


Fig. 10. Disturbances radiated by EUT in vertical polarization, before the implementation of anti-disturbances measures.

The tests revealed that the limits imposed for the peak and average values are under the limits for tests in horizontal polarization (Fig. 9), whilst the limits imposed by CISPR 25 [5], [6] are exceeded for vertical polarization.

#### B. The Anti-disturbances Measures

In order to improve the performances of EUT with respect to its radiated emissions and to provide conformity with the limits imposed by CISPR 25, a shield was added on the supplying side of the display, on its source (Fig. 11 (a)). The EUT's source consists of two dc-dc converters of types boost and buck. Although operating at low frequency, these two converters (of step-up and step-down type) generate all high order harmonics. These latter ones are over the limits imposed by the client.

The shield placed in front of the supplying source behaves like a Faraday cage (Fig. 11(b)). It is made of Aluminum and is 2 mm thick. The connections toward the board were made by clipping and melting.

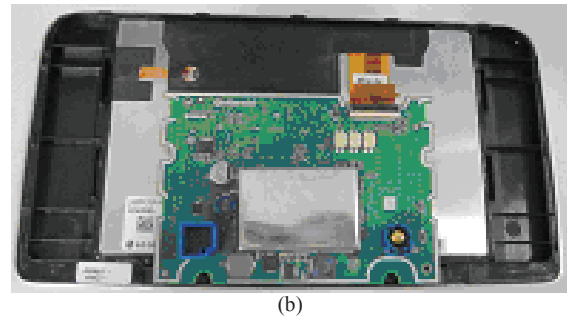


Fig. 11. PCB of the board display: (a) without shield, and (b) with shield, for the supplying source.

The practice of shielding as a solution to reduce the EM radiations is widely used because it is highly efficient and the implementing costs are reasonable. It often represents the “last solution” (it is applied when nothing else can be done to modify the electronic board from the EMC point of view).

#### C. Experimental Determination Concerning the Radiated Disturbances after the Implementation Measures

By adding a shield over the supplying source of the EUT, all the harmonics generated by the converters were removed.

The shield is designed and manufactured such as to let unaffected the normal functionality of the board display. The novelty of this solution consists in extending the frequency range beyond 1 GHz, as the client requested.

The accomplishing of another set of tests revealed that the emissions are now under the imposed limits - Fig. 12.

## VI. CONCLUSIONS

The EMC tests, including the TRE, are very important during the process of designing and realization of a new electronic product [13]. When the limits imposed by the client and current standards are disobeyed, the withdrawal of the EUT from production can be imposed, resulting in waste of money and time.

In order to have the guarantee of some correct measurements of emissions, the results of the simulation concerned with the operation of a horn antenna, used to evaluate the radiated emissions in the semi-anechoic chamber were analyzed.

Several horn antennas were analyzed. The conclusion was that the PHA represents the best option for the case analyzed in this paper.

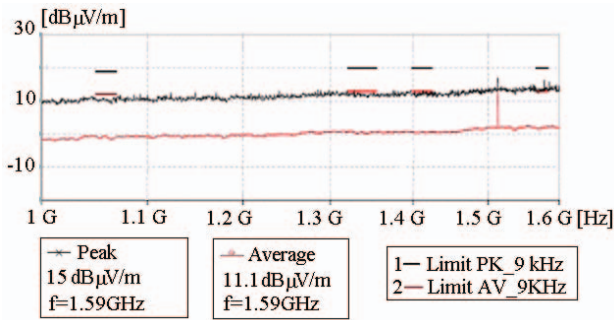


Fig. 12. Disturbances radiated by equipment in vertical polarization, after the implementation of anti-disturbances measures.

For this type of antenna, firstly numerical simulations concerned with the PHA parameters were performed in order to determine the optimum configuration (from the geometrical point of view).

The simulation was performed with the dedicated software CST MICROWAVE STUDIO which used a physical model built with ANTENNA MAGUS.

The simulated horn antenna presents characteristics that are similar to the real horn antenna used for measurements of radiated emissions (gain, directivity and aperture) [14], [15]. Although the simulated antenna proved its efficiency up to frequencies of 20 GHz, the simulations were made only for the frequency range from 1 GHz ... 1.6 GHz, because in this limited range problems were noticed during the tests made in the semi-anechoic chamber.

The FEM analysis revealed that the antenna proposed for the tests accomplishing is compliant with the imposed requirements.

The initial TRE considering the analyzed EUT revealed that the disturbances radiated by exceeded the limits imposed by norms. By adding a shield on the supplying side of EUT, the level of radiated emissions was decreases and consequently the limits imposed by CISPR 25 were no longer exceeded [5], [6].

Therefore the EUT could be certified for the series

production.

Received on July 17, 2016

Editorial Approval on November 15, 2016

#### REFERENCES

- [1] H. Ott, "Electromagnetic Compatibility Engineering," New Jersey, Wiley, 2009.
- [2] C.R. Paul, "Introduction on Electromagnetic Compatibility", 2nd ed., New York, Wiley, 2006.
- [3] \*\*\* IEC EN 61000-4-3, *Electromagnetic compatibility (EMC) - Part 4-3: Testing and measurement techniques - Radiated, radio-frequency, electromagnetic field immunity test*, 2008.
- [4] C. A Balanis, "Antenna Theory: Analysis and Design," John Wiley and Sons, 2005.
- [5] V. Rodriguez, "Automotive Component EMC Testing: CISPR 25, ISO 11452-2 and Equivalent Standards," *2012 IEEE EMC Magazine*, vol. 1, Quarter 1, pp. 83-90, 2012
- [6] S. Mainville, "Automotive EMC Case Study: HMI Graphics Influence on Radiated Emissions", in *Proc. of IEEE Int. Symp. on EMC*, pp. 620-624, Aug. 2010.
- [7] T. Hubing and N. Hubing, "Articles on learnemc.com: EMC Courses & Consulting".
- [8] S.N. Samaddar and E.L. Mokole, "Biconical antenna with unequal cone angles", *IEEE Transactions on Antenna and Propagation*, vol. 46, no. 2, 181-193, 1998.
- [9] S. Kurokawa, M. Hirose, K. Komiyama, "Time-domain three antenna method for evaluation of antenna factors of log-periodic antenna," in *Proceeding of European Microwave Conference 2007*, pp. 94 - 97, Oct. 2007.
- [10] I. Nica, V. David and S. Ursache, "Usage of numerical methods for electromagnetic shields optimization", in *Annals of the University of Craiova, Electr. Engineering Series*, pp. 220-224, 2007.
- [11] CST STUDIO SUITE v2013, *User Manual*, CST AG, available at [www.cst.com](http://www.cst.com), 2013.
- [12] Y. Huang, K. Boyle, "Antennas", John Wiley and Sons, 2008
- [13] D. Johns, S. Mee, "EMC simulation of an automotive display system", *Proceedings of Asia-Pacific Int. Simp. On EMC*, pp. 904-907, 2010.
- [14] C. Burns, P. Leuchtman, and R. Vahldieck, "Analysis of a 1-18 GHz Broadband Double-Ridge Antenna", *IEEE Trans. on Electromagnetic Compatibility*, vol. 45, no. 1, pp. 55-60, Feb. 2003.
- [15] T.K. Sarkar, M. C. Wicks, M. Salazar-Palma, and R. J. Bonneau, "Smart Antennas", Wiley-IEEE Press, Apr. 22, 2003.

# Development of a Barrier Structure Actuated by Three Shape Memory Alloy Springs

Sonia Degeratu\*, Costel Caramida†, Laurentiu Alboteanu\*, Irina Boncea\*, Daniela Coman\*, Monica S. Staicus\* and Gabriela Tont\*\*

\* University of Craiova, Romania, [sdegeratu@em.ucv.ro](mailto:sdegeratu@em.ucv.ro), [lalboteanu@em.ucv.ro](mailto:lalboteanu@em.ucv.ro), [irina.boncea@yahoo.com](mailto:irina.boncea@yahoo.com), [amdcoman@yahoo.com](mailto:amdcoman@yahoo.com), [mstaicus@yahoo.com](mailto:mstaicus@yahoo.com)

† National Institute for Research, Development and Testing in Electrical Engineering, Craiova, Romania, [costica\\_caramida@yahoo.com](mailto:costica_caramida@yahoo.com)

\*\* University of Oradea, Romania, [gtont@uoradea.ro](mailto:gtont@uoradea.ro)

**Abstract** - In this paper, the authors present an experimental analysis in order to highlight the behavior of a barrier structure model, actuated by three shape memory alloy (SMA) helical springs. The authors have developed this new barrier structure to increase the performances of conventional barriers, based on SMAs unique properties and their advantages. SMAs are advantageous for actuation because of their light weight, silent operation and flexibility. SMAs began to be increasingly present in industrial applications as well because they display high reliability and can replace the functions that make the motors or complex gears despite their simple construction. The actuator used in our model works as a linear actuator, contracting itself with great strength and speed, thus exerting the necessary force to lift the barrier arm when the SMA springs are heated by carrying an electric direct current. The designer can control the direction of actuation, the amount of force generated and the stroke of the actuator through various combinations that he can achieve with these three SMA springs. After a description of the accomplished model and of how it works, the authors present an experimental analysis of the behavior displayed by the SMA springs-based barrier structure. The experiments consisted in the determination of the SMA spring functioning time periods at constant value of the SMA spring activating electric current, and while maintaining the barrier arm stroke and weight constant.

**Keywords:** *shape memory alloy (SMA) actuator, SMA spring, barrier structure experimental model, SMA spring functioning time periods.*

## I. INTRODUCTION

In recent years, the use of SMA actuators in a wide variety of applications has had a really dynamic evolution. The increasing interest for the SMA actuators derives from their advantages, as compared to the traditional ones: its high plastic deformation, the force generated, the production of mechanical work, the low voltages for the supply of the SMA element, the high power/weight and stroke/weight ratios [1]–[7]. These advantages are a consequence of the unique and superior properties of SMAs, i.e. pseudo-elasticity, shape memory effects (one-way and two way), hysteresis behavior, vibration damping capacity [4], [6]–[10].

SMAs are smart materials that possess the ability to undergo shape change at low temperatures and retain this deformation until heated, at which point they return to

their original shape [10]. This unique effect of returning to their initial geometry after a large inelastic deformation is known as the Shape Memory Effect (SME) [3], [10], [11]. The SME occurs due to martensitic phase transformation, between a low temperature phase, called martensite (M), and a high temperature parent phase, called austenite (A). A typical shape memory element has four relevant temperatures that define the different stages of actuation, thus providing the designer with a method for control. Simply put, the four temperatures define the start and finish transformations for martensite (Ms, Mf) and austenite (As, Af).

Due to their unique properties, there is increasing technological interest in the use of SMA for various applications: biomedical engineering, automotive industry, high precision engineering, robotics, electro-mechanical engineering, machine craft etc. [8]–[10], [13]–[18].

This paper presents an experimental model of a barrier structure, developed by the authors, that uses an actuator based on three Ni-Ti SMA springs. This barrier structure, dedicated to private parking systems, is an improved version of the experimental model presented in the papers [19]–[21]. The authors intensified the research in this direction given the great interest shown by some Romanian companies that produce such barriers.

The use of SMA spring as actuator in our barrier configuration provides the following advantages: reasonable force/motion characteristics, a compact size, a high work output, silent operation, design simplicity, and near step function operation [8], [10]–[12].

In the first part of this article the authors describe the accomplished experimental model and its operation mode. In the second part, they present an experimental analysis of the SMA springs-based barrier structure behavior.

The study of this experimental model is made with the purpose of anticipating the behavior of a real structure in terms of operating mode, the control and command of the structure through the SMA active elements.

## II. EXPERIMENTAL BARRIER STRUCTURE DESCRIPTION

The experimental model of the accomplished barrier structure driven by three SMA springs is shown in Fig. 1.

The shape memory effect enables any SMA spring to work as a linear actuator by contracting with great strength and at increased speed when heated. In our model, this translational motion is converted into a rotation motion of the barrier arm so that it will be lifted.

In this section, on the one hand, the authors make a description of the barrier structure experimental model, and, on the other hand, they comprehensively explain how the automatic motion of the barrier arm is controlled. The authors also explain how an SMA spring actually works emphasizing the advantages such a device really displays when used as actuator. The active shape-change control of the SMA spring, the miniaturization possibilities, the easy integration into the system structure, the automatic control of the barrier arm motion (using a programmable logic controller) thus underlies an effective increase in the efficiency of such barrier structures.

The so achieved model allows the structure behavior analysis to be made in various drive conditions and control of the SMA springs.

The main positions marked in Fig. 1 are described in detail below.

#### A. The Control Unit

This block (position 2 in Fig. 1) contains the following sources: for the supply of the SMA springs (5V), for LOGO (24V) and for powering the barrier control transmitter (24V).

The control unit block (Fig. 2) has the following outputs:

- 1, 2 - outputs for the stroke transducer;
- 3, 4 - outputs for the supply of the SMA springs;
- 5, 6 - LED for signaling barrier position (red - closed, green - open);
- 7, 8 - terminals for connection to an independent source (of variable voltage) for powering the SMA springs.

#### B. Data Acquisition System Velleman 4 CHANNEL SIGNAL RECORDER

The main features of the Data Acquisition System (position 3 in Fig. 1) are:

- record DC signals or slow moving signals over very long periods;
- the measurements are automatically stored on the hard disk for further processing;
- through the use of USB connection, there is no need for a power supply and installation is easy and straightforward;

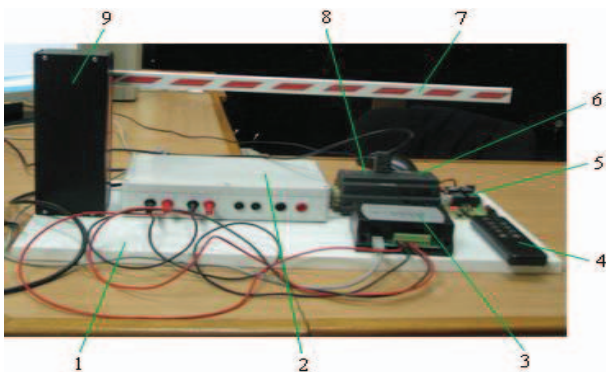


Fig. 1. Latest variant of the experimental arrangement of Ni-Ti SMA-based barrier: 1-seating base; 2-control unit; 3-Signal Recorder (Data Acquisition System); 4-remote control; 5-control receive; 6-Logo!Power; 7-barrier arm; 8-Siemens Logo!24Co (Programmable Logic Controller-PLC); 9-SMA spring-actuated mechanism unit.

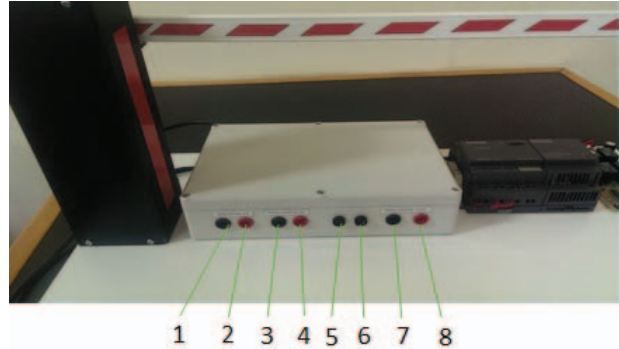


Fig. 2. The control unit of the accomplished model.

- signals are instantly displayed on the PC screen using analog or DVM display.

#### Hardware specification:

- USB connected and powered;
- four DC coupled input channels;
- input resistance: 1mOhm;
- maximum samples per second: 100;
- four input ranges: 3V / 6V / 15V and 30V;
- sensitivity: 10mV;
- accuracy:  $\pm 3\%$  of full scale;
- maximum input: 30V DC;
- power and recording/diagnostic LED.

#### Software specification:

- analogue trace or digital DVM readout;
- 4 simultaneous channels recording;
- minimum/maximum sample hold function for DVM;
- from 1 sec to 1000 sec per division;
- storage and recall of screens or data;
- automatic recording option for extended time recording;
- on screen markers for time and voltage;
- DLL included for own development.

#### System requirements:

- PC, running Win98SE or higher;
- free USB port;
- CD-ROM player [22].

#### C. AD-IR-DRIVER04 Module for the Remote Control

This module (position 5 in Fig. 1) is an electronic module with a microcontroller allowing the command of 4 independent channels using infrared remote controls. The module is provided with 4 relays of 5 A/ 250 V AC (Fig. 3), which can operate various elements of execution.

For the operation, one can utilize TV- COD RC5 remote controls (RCxxx, PILOTxxx type), universal remote controls or other models used frequently by color television sets. The desired buttons for the selections of the commands can be programmed, so one can choose to one's individual liking. By memorizing the operations buttons from the remote control means they remain the same even when the remote is not powered.

A manual K2 remote control is provided to reset the relays' status. The command of the relays can be made in 2 ways:

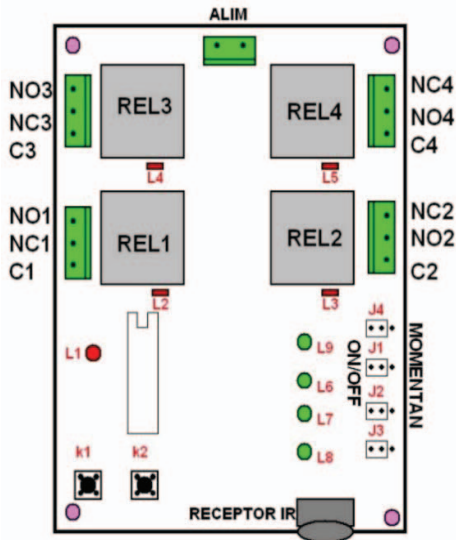


Fig. 3 Block circuit of module AD-IR-DRIVER04 [23].

command type ON/OFF and command type MOMENTAN.

The command module of ON/OFF or MOMENTAN relays is set with the help of PINs found on J1, J2, J3 and J4 modes.

The setting can be made in any configuration, all ON/OFF relays, all MOMENTAN relays or differently.

Remote programming is done as follows. The module should be powered-up so that remote control can be programmed, when LED L1 lights up, and for the start of the operation of learning of the remote controls buttons, press button K1, at which point LED L1 will switch off. Press the remote control button which is utilized for the command of relay REL1. The LED L1 will switch on confirming the takeover of the command. Next, press the desired buttons in order to command the relays REL2, REL3, REL4. LED1 will start blinking at every command. In this way, the desired buttons were memorized.

The main technical characteristics of the module are:

- power supply: 9 ÷ 12 V AC, 50 Hz or 12 V DC;
- the maximum input current: 0.15 A;
- intermediary frequency IR: 38 kHz;
- number of channels: 4;
- command relays: 4 OMRON 5 A per 250 V AC;
- command distance IR: 10 m;
- available remote control RC5: 38 kHz [23].

#### D. Programmable Logic Controller - PLC (Siemens Logo!24Co)

The logic module LOGO! Siemens (position 8 in Fig. 1) is the ideal controller for simple automation tasks in the industry and building services. The consistently modular design of LOGO! makes it extremely flexible. A wide range of modules allows individual expansion of LOGO! to 24 digital inputs, 16 digital outputs, 8 analog inputs and 2 analog outputs.

PLC LOGO! 24Co, used in the barrier model, is compact, easy to use and provides a low cost solution for control tasks of low complexity.

Together with the LOGO! Soft Comfort software, the configuration of the logical module is simply intuitive: program generation, project simulation and documentation are accomplished using drag and drop functions, allowing maximum ease of operation

The main technical data of the PLC LOGO! 24Co are:

- inputs: 8;
- input/supply voltage: 24 V DC;
- permissible range: 20.4 V – 28.8 V DC;
- „0” signal: 5 V DC;
- „1” signal: minim 12 V DC;
- input current: 2 mA (I3 - I6), 0.1 mA (I1, I2, I7, I8);
- outputs: 4;
- direct current: 0.3 A;
- short-circuit protection: electronic, approx. 1 A;
- switching frequency: 10 Hz;
- cycle time: <0.1 ms/function;
- display: no;
- emitted interference: in accordance with EN 55011;
- maximum program memory: 200 blocks;
- external memory module: LOGO! memory card [24].

Description of the command LOGO! Soft of the accomplished model is as follows.

The LOGO!Soft program for the barrier command is presented in Fig. 4. The digital input I3 controls the barrier (up/down) depending on the signal from the receiver output which in turn is driven by the remote control.

The signal from the stroke transducer is connected to the AI1 analog input. Through B004 Analog Threshold Trigger block, the output Q1 is set or reset depending on the threshold triggers On / Off corresponding to the position of the barrier, the SMA springs being powered up or not.

Barrier position is determined by the stroke transducer ( $T_c$ ) positioned on the axis of the arm. The transducer supply voltage,  $U_{Tc}$ , is 5 V. The transducer stroke is  $360^\circ$ .

Lifting barrier arm angle was set at  $86^\circ$ , resulting in:

$$U_{Tc} * On = (U_{Tc} * 86) / 360 = 1.2 V \quad (1)$$

The amplification parameter of the Analog Threshold Trigger block is 100. Resultantly, the output  $Q_1$  is 1 if the actual value of the input functions  $A_x$  is greater than Threshold On.

$$Threshold\ On = U_{Tc} * 100 = 120 \quad (2)$$

$$Threshold\ Off = 118 \quad (3)$$

The B002 and B003 Analog Threshold Trigger blocks command, at the outputs Q2 and Q3, the LEDs functioning which indicates the barrier position, respectively the red LED for the lowered position of the barrier and the green LED for the raised position of the barrier. These LEDs function as elements which signal when it is possible or not to go through the space of the barrier.

#### E. LOGO!Power Module

The mini power supply devices designed into the LOGO!POWER module (position 6 in Fig. 1) offer great performance in the smallest space and the excellent efficiency over the complete load range.

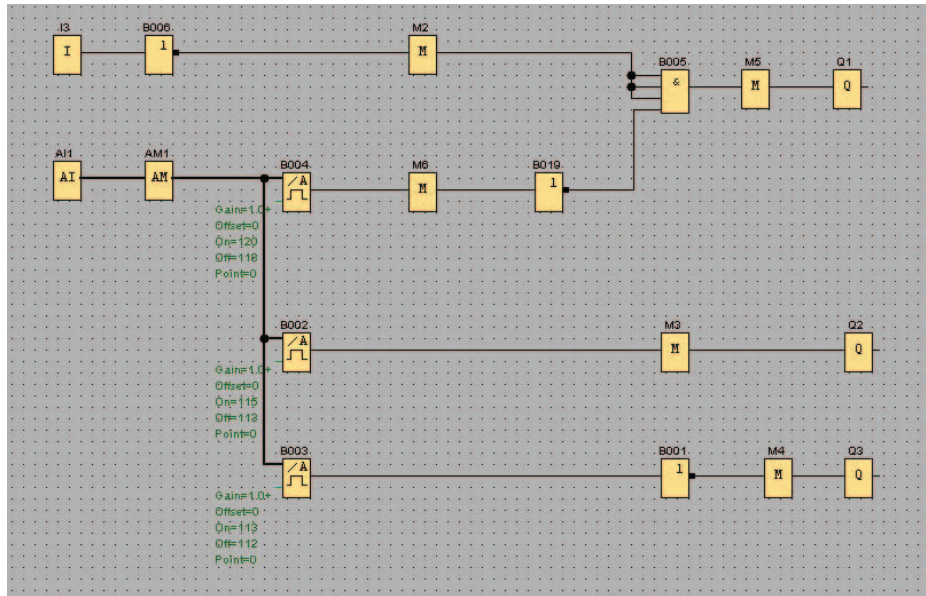


Fig. 4. LOGO!Soft barrier command.

The technical characteristics of the module are:

- power supply, type: 24 V / 1.3 A;
- input: 1 – phase AC or DC;
- rated voltage value  $V_{in}$  rated: 100 – 240 V;
- voltage range AC: 85 – 264 V;
- input voltage for DC: 110 – 300 V;
- overvoltage resistance: 2.3 x  $V_{in}$  rated, 1.3 ms;
- rated line frequency: 50 – 60 Hz;
- rated line range: 47 – 63 Hz;
- input current at rated input voltage 120 V rated value: 0.7 A;
- input current at rated input voltage 230 V rated value: 0.35 A;
- switch-on current limiting (+ 25 °C), max.: 25 A;
- rated voltage  $V_{out}$  DC: 24 V;
- setting range: 22.2 – 26.4 V (set via potentiometer on the device front);
- status display: green LED for output voltage OK;
- startup delay, max.: 0.5 s;
- output current: 1.3 A;
- active power supplied typical: 30 W;
- efficiency at  $V_{out}$  rated,  $I_{out}$  rated: 85%;
- power loss at  $V_{out}$  rated,  $I_{out}$  rated: 6 W;
- active power loss during no-load operation max.: 2 W;
- current limitation: 1.7 A [25].

#### F. Driving Mechanism Block

The barrier driving mechanism block (position 9 in Fig.1) is presented in Fig. 5. The actuator of this block is based on three SMA Electric Pistons (3) rigidly fixed at their piston-free ends on the fixed support (4). The other ends of the SMA Electric Pistons are fixed on a mobile support (5), from which the traction wires (6) depart towards the driving barrier arm system (8) on which a rotating stroke transducer,  $T_c$  (7) is mounted. This transducer is powered up by a voltage of 5 V and can accomplish a

maximum stroke of 360°. The accomplished mechanism allows a rotation of the barrier arm by 86 degrees at a complete stroke of 16 mm of the SMA Electric Pistons (when they are commanded electrically).

The main elements of this experimental arrangement are the three SMA Electric Pistons. The SMA Electric Piston is a linear actuator mechanism that shortens in length with great strength and speed when it is activated by carrying an electric direct current. An SMA spring placed inside makes all these possible.

The SMA Electric Piston was purchased from the Mondotronics, Inc. [26].

The SMA spring displays two entirely different forms or "phases" at the distinct temperatures  $M_f$  and  $A_f$ . At the "low" temperature ( $M_f$ ), the SMA spring is extended, and can be stretched easily or deformed by a small force. But

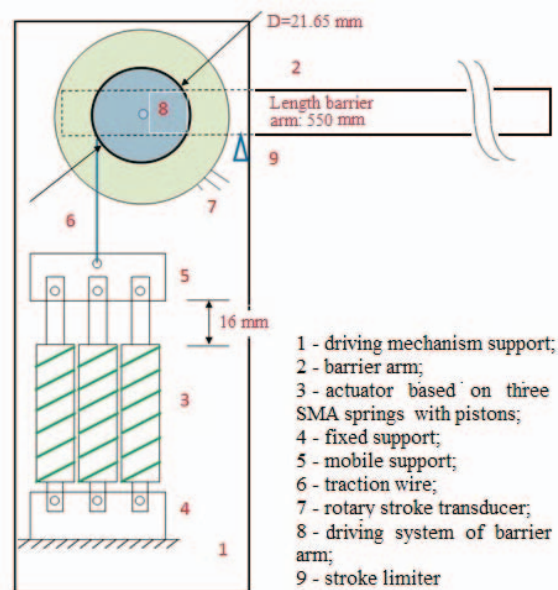


Fig. 5. Driving mechanism block of the experimental barrier structure.

when raised to the "high" temperature  $A_f$ , by applying an electric direct current, the SMA spring changes to a much harder form. In this phase, it shortens in length, and exerts the necessary force to lift the barrier arm.

The SMA Electric Piston used in our model can lift to 4.5 N against gravity, yet the SMA Electric Piston itself weighs only 0.1 N. The SMA Electric Piston was presented in detail in [17], [19], and [21]. Therefore, because of the way the mechanical coupling of the three SMA Electric Piston occurs the total force developed by the driving mechanism will be 13.5 N.

### III. ELECTRICAL CIRCUIT OF REALISED MODEL

The electrical circuit, with its component blocks, is shown in Fig. 6.

The power supply block comprises:

- source of 5V, for powering the three SMA springs and the race transducer;
- source of 24V, for supplying PLC (LOGO! POWER);
- source of 12V, for supplying lifting/lowering command receptor of the barrier arm (TRACO POWER).

The command part is composed of an infrared transmitter-receiver, which applies a voltage of 24V to the I3 digital input of PLC through a normally closed contact of the command receptor. The race transducer, whose axis is secured to the movable part of barrier, transmits a proportional signal to the A11 analog input of PLC.

PLC uses the Q1 output and the R1 relay for powering the SMA springs. The Q3 output is used for signaling lowered position of the barrier through the red LED. The Q2 output is used for signaling raised position of the barrier by the green LED.

The switch K is used for powering the SMA springs from:

- a) a 5 V internal power source, which ensures a constant direct current (2.89 A);
- b) a 0-5 V external power source, which ensures a variable direct current.

### IV. EXPERIMENTS AND RESULTS

Because the SMA spring activates by electric heating, the contraction time varies greatly with the applied current; the higher the current, the faster the heating, and the faster the contraction. In the case of our model, the electric current for powering the SMA springs can come from two sources: internal power source or external variable source.

This paper presents the test results obtained with the experimental arrangement presented in Fig.1, using the internal power source.

The experiments consisted in the determination of the SMA spring functioning time periods:  $t_{sc}$ ,  $t_a$ ,  $t_{rel}$ , and  $t_r$ . These parameters have the following meaning:

- $t_{sc}$  = time to start contracting, or the necessary time from the start of current application to reach the temperature  $A_s$ ;
- $t_a$  = time to actuate, or the contraction time, or the necessary time for the arm to reach the angular displacement of  $86^\circ$ ;

$t_{rel}$  = time to relax, or the necessary time for the SMA spring to cool from a temperature greater or at least equal to  $A_f$  to the temperature  $M_s$ . In all cases the cooling process ended at  $23.1^\circ\text{C}$ ;

-  $t_r$  = time to reset, or the necessary time for the arm to return to its initial position. In this status, the SMA temperature is under  $M_f$ .

This test was carried out to analyze the operating mode and to have control over the active shape change of the SMA actuator.

The result for a complete up-down cycle of the barrier arm is shown in Fig. 7.

The supply voltage of the three SMA springs was  $U=2.79$  V, DC, as seen in Fig. 8. This value is indicated by the voltage markers.

By using the two markers from the transducer race signal we were able to determine the values for all SMA spring functioning time periods:  $t_{sc}$ ,  $t_a$ ,  $t_{rel}$ , and  $t_r$ . As an example, in Fig. 9 the two transducer markers indicate the value for the time to actuate,  $t_a=1$ s.

The values obtained for  $t_{sc}$ ,  $t_a$ ,  $t_{rel}$ ,  $t_r$  and for the supply voltage of the SMA springs are presented in Table 1

It follows that one can choose a corresponding value for the supply voltage of the three SMA springs so as to obtain a desired pair of actuate-reset time periods.

### V. CONCLUSIONS

It is known that the barrier structures' performances are directly related to the actuators' driving systems' performance. Systems using shape memory alloys are used extensively in applications requiring high reliability, weight reduction of the dimensions, the absence of vibration, high precision when operating in repeated cycles.

The proposed barrier structure is relatively lightweight and has a simple configuration due to the fact that an SMA spring actuator offers efficiency in terms of energy, weight and space.

The analysis of the experimental results has demonstrated that our proposed model behaves quite well.

The results presented in this paper describe the behavior of analyzed barrier structure in case of a constant value for the supply voltage of the SMA springs and, therefore, for a constant value of their activating current.

For a given barrier structure, choosing the activating current values for the SMA actuator will be done so as to obtain the functioning times of the barrier required by the customer. Therefore, in future work, we will analyze the behavior of this structure at different values of SMA spring activating electric current in order to correctly choose the type of application.

These new barrier structures could prove potentially useful in: parking lots, toll gates, goods yards, railway and bridge barriers, apartment block access etc.

### ACKNOWLEDGMENT

This work was supported by the grant number 7C/2014, awarded in the internal grants competition of the University of Craiova.

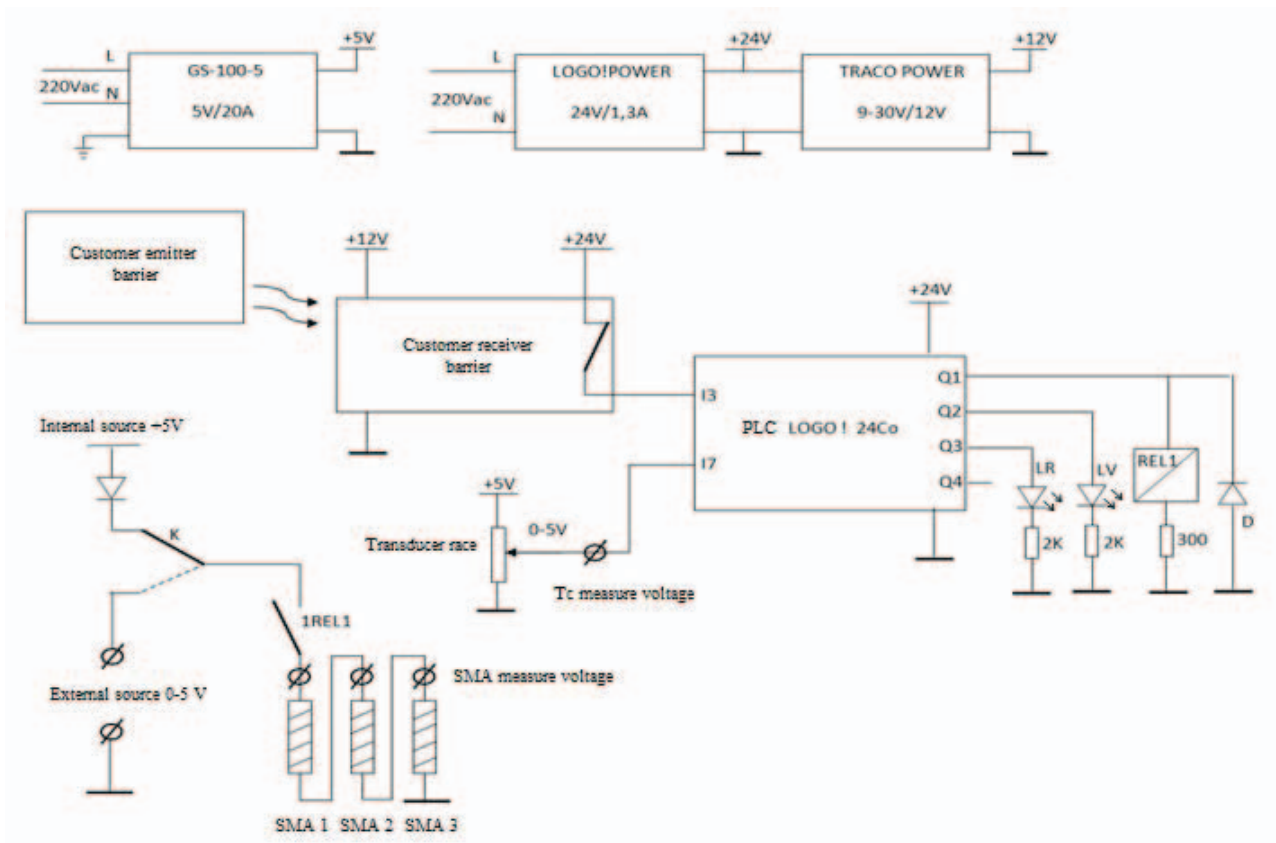


Fig. 6. Electrical circuit of accomplished model

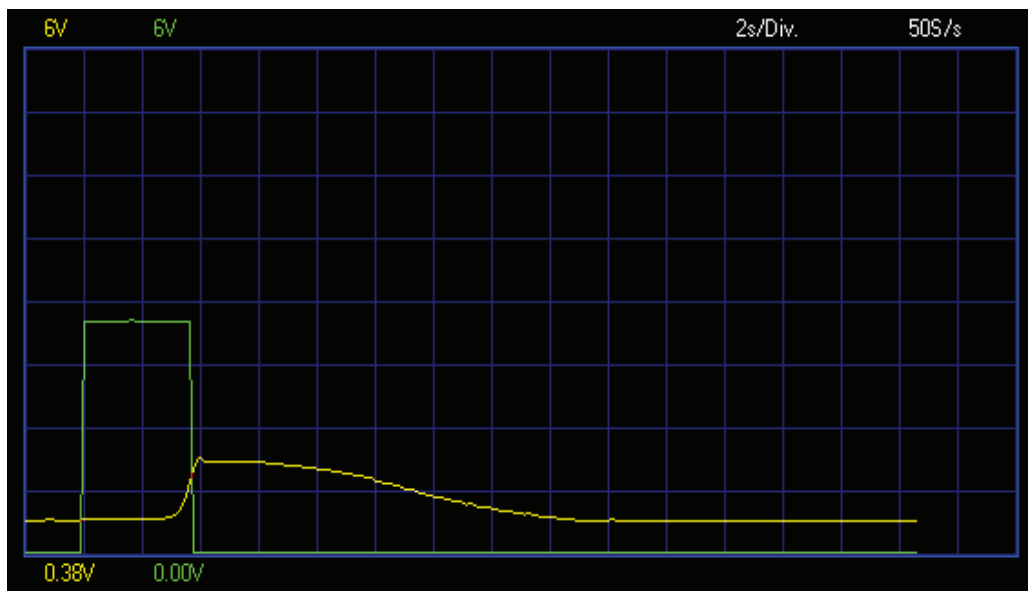


Fig. 7. A complete up-down cycle of the barrier arm:  
 — signal from Tc transducer (SMA spring working time periods);  
 — signal from power source of SMA springs.

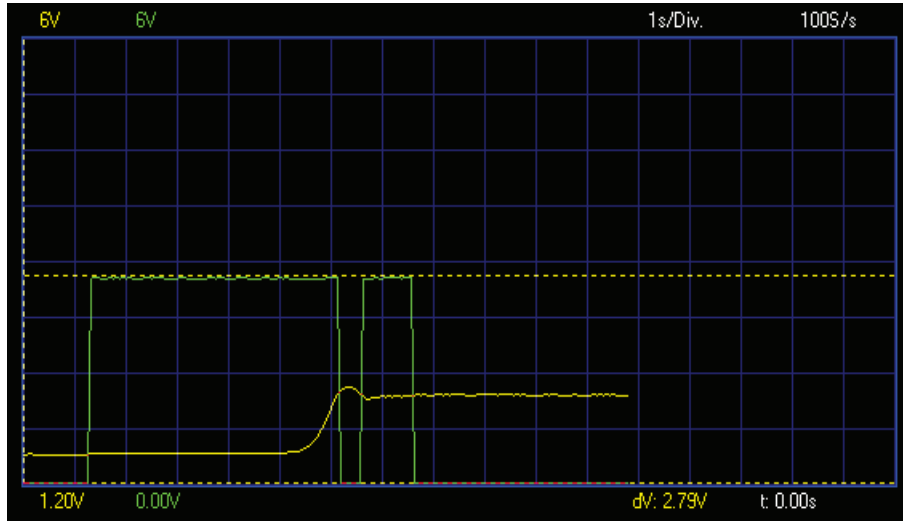


Fig. 8. The supply voltage of the three SMA springs (2.79 V) indicated by the voltage markers:

— signal from Tc transducer (SMA spring working time periods);  
 — signal from power source of SMA springs.

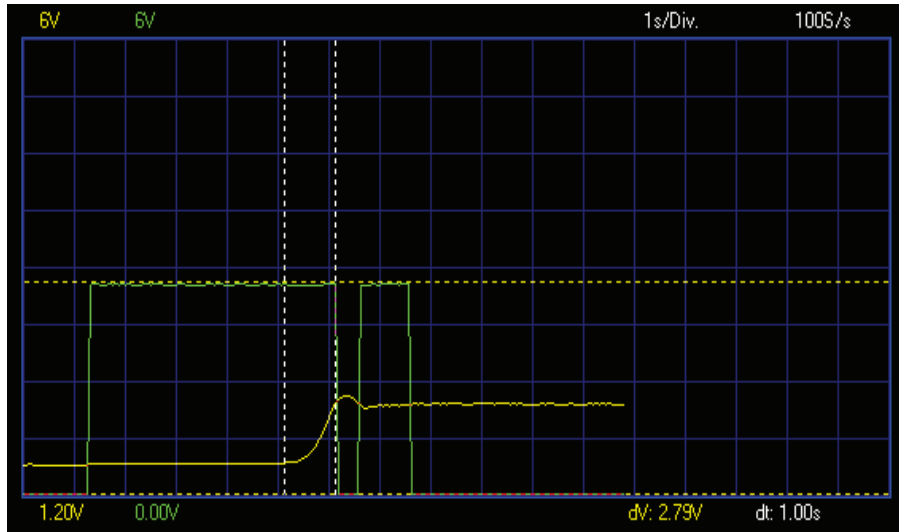


Fig. 9. The value for the time to actuate ( $t_a=1s$ ) indicated by the transducer markers:

— signal from Tc transducer (SMA spring working time periods);  
 — signal from power source of SMA springs.

TABLE I.  
 FUNCTIONING TIMES FOR THE ANALYZED BARRIER CORRESPONDING TO  
 A COMPLETE UP-DOWN CYCLE

U [V]	$t_{sc}$ [s]	$t_a$ [s]	$t_{rel}$ [s]	$t_r$ [s]
2.79	3.91	1	3.81	13.56

Received on Jun 16, 2016

Editorial Approval on November 15, 2016

REFERENCES

[1] E. Torres-Jara, K. Gilpin, J. Karges, R.J. Wood, and D. Rus, "Compliant Modular Shape Memory Alloy Actuators," *IEEE Robotics & Automation Magazine*, pp. 78–87, December 2010.

[2] K. Seung, K. Byungkyu, "Design parametric study based fabrication and evaluation of in-pipe moving mechanism using shapememory alloy actuators," *J. Mech Sci.*, vol. 22, pp. 96–102, 2008.

[3] W. Huang, *Shape memory alloys and their application to actuators for deployable structures*, Ph.D. Thesis, University of Cambridge, 1998.

[4] C. Mavroidis, "Development of actuators using shape memory alloys and electrorheological fluids," *J. Res Nondestr. Eval.*, vol. 14, pp. 1–32, 2002.

[5] G. Knowles, R. Bird, V. Birman, "Shape memory alloy springs used as reduced power/weight actuators," *Proceedings of ASME 2004 international mechanical engineering congress and exposition*, Anaheim, California, USA, pp. 17–25, November, 2004.

[6] Yang K, Gu CL. "A compact and flexible actuator based on shape memory alloy springs," *J Mech. Eng. Sci.*, vol. 222, pp.1329–1337, 2008.

- [7] H. Morawiec, "Structure formation and its effect on properties of shape memory alloys", Physics of Advanced Materials, Winter-school, Thessaloniki, Greece, pp. 14-18, January, 2008.
- [8] S. Degeratu, N. Bizdoac, *Shape memory alloys: fundamentals, design and applications*, Universitaria Press, Craiova, Romania, 2003.
- [9] H. Wu Ming and L. McD. Schetky, "Industrial applications for shape memory alloys", Proceedings of the International Conference on Shape Memory and Superelastic Technologies, Pacific Grove, California, pp. 171-182, 2000.
- [10] T. C. Waram, *Actuator Design Using Shape Memory Alloys*, Ontario Press, Canada, 1993.
- [11] T. W. Duerig, et al, *Engineering Aspects of Shape Memory Alloys*, ButterworthHeinemann, London, 1990.
- [12] K. Otsuka and C. M. Wayman, *Shape Memory Materials*, chap. 2, Cambridge Univ. Press, 1999.
- [13] G. Songa, N. Ma and H.-N. Li, "Applications of shape memory alloys in civil structures," Engineering Structures, vol. 28, pp. 1266-1274, 2006.
- [14] D. Mandru, I. Lungu, S. Noveanu, and O. Tatar, "Applications of shape memory alloy actuators in biomedical engineering," Annals of the Oradea University, vol. VII, pp. 922-927, 2008.
- [15] T. Anson, "Shape memory alloys – Medical applications," Materials World, Vol. 7, No. 12, pp 745-747, December 1999.
- [16] L.G. Machado and M.A. Savi, "Medical applications of shape memory alloys", Brazilian Journal of Medical and Biological Research, vol.36, pp. 683-691, 2003.
- [17] S. Degeratu, L. Alboteanu, S. Rizescu, D. Coman, N. G. Bizdoaca, C. Caramida, "Active Solar Panel Tracking System Actuated by Shape Memory Alloy Springs," Proceedings of the International Conference on Applied and Theoretical Electricity-ICATE, October 23-25, 2014, Craiova, Romania, publisher IEEE, pp.: 5.
- [18] N. Bizdoaca, S. Degeratu, "Robotic Finger Actuated with Shape-Memory Alloy Tendon," WSEAS Proceedings of Soft Computing, Optimization, Simulation & Manufacturing Systems, Malta, pp. 897-906, 2003.
- [19] S. Degeratu, P. Rotaru, S. Rizescu, N. G. Bizdoacă, "Thermal study of a shape memory alloy (SMA) spring actuator designed to insure the motion of a barrier structure," Journal of Thermal Analysis and Calorimetry, February 2013, vol. 111, Issue 2, pp. 1255-1262.
- [20] S. Degeratu, S. Rizescu, N.G. Bizdoaca, C. Caramida, V. Degeratu, "Analyzing and Modeling Performance of a New SMA Actuator-based Barrier Structure," Proceedings of 7th International Conference on Electrical and Electronics Engineering, ELECO 2011, Bursa, Turkey, 1-4 December, 2011, vol. 2, pp. 110-114.
- [21] S. Degeratu, N.G. Bizdoaca, S. Rizescu, P. Rotaru, V. Degeratu, and G. Tont, "Barrier structures using shape memory alloy springs," Proceedings of WSEAS International Conference DEEE, 2010, Tenerife, December 29-October 2, pp. 367372.
- [22] <http://www.velleman.eu/products/view/?country=be&lang=en&id=350526>.
- [23] [www.adelaida.ro](http://www.adelaida.ro)
- [24] [http://www.industry.siemens.nl/automation/nl/nl/industriële-automatisering/industrial-automation/simatic-controller/logica-module-logo/logo-modulair-uitbreidingsmodules/Documents/e20001-a1120-p271-x-7600\\_20-21.pdf](http://www.industry.siemens.nl/automation/nl/nl/industriële-automatisering/industrial-automation/simatic-controller/logica-module-logo/logo-modulair-uitbreidingsmodules/Documents/e20001-a1120-p271-x-7600_20-21.pdf).
- [25] <http://w3.siemens.com/mcmsg/power-supply-sitop/en/logo-power/Pages/default.aspx>.
- [26] Jameco electronics catalog. 2012;625. p. 61.  
<ftp://ftp.jameco.com/Archive/PreviousCatalogs/624catalog.pdf>

# Energetic Analysis of the Drying Process of Current Transformers from 110 kV Ciungetu Power Station

Dinu Roxan Doboşeriu<sup>\*</sup>, Alexandru Bitoleanu<sup>†</sup> and Mihaela Popescu<sup>†</sup>

<sup>\*</sup> S.S.H. Hidroserv Ciungetu, Râmnicu Vâlcea, Romania, [doboseriu\\_constantin@yahoo.com](mailto:doboseriu_constantin@yahoo.com)

<sup>†</sup> University of Craiova, Faculty of Electrical Engineering, Craiova, Romania, [alex.bitoleanu@em.ucv.ro](mailto:alex.bitoleanu@em.ucv.ro)

**Abstract** - Currently, at company Hidroserv Râmnicu Vâlcea, the drying of current transformers used in power transformer stations is done by a combination between induction and conduction heating at the frequency of 50 Hz. Obviously, this solution is outdated in terms of technology and the performed energetic analysis proves it. In order to achieve the design of a multifunction static system intended to replace the existing one, so as to respond as best as possible to the specific needs, it is necessary to analyze the drying process from energetic point of view. The knowledge of the equivalent parameters of the loads is needed too. To substantiate the feasibility of this new technical solutions, the goal of the paper is the analysis of the actual technology from energetic point of view. Considering that the current transformer of the 110 kV power station Ciungetu is the typical load, experimental determinations relating to the its drying process have been performed. Two heating coils are used, of 33 turns and 38 turns, respectively. In order to determine the associated parameters for both coils, the current and voltage across the equivalent inductor have been recorded by using an oscilloscope Tektronix TDS3000. It is obvious, and the performed energetic analysis demonstrates this, the solution currently used is outdated in terms of technology.

**Keywords:** *current transformer, electric drying, experimental recording, harmonics, numeric filtration.*

## I. INTRODUCTION

In the operation of current transformers from transformer stations of hydropowers, their resistance of insulation can become lower than the limits imposed by norms. Consequently, it is necessary to dry them. The wetting of the insulation can be due to the loss of tightness between component parts and to the atmospheric moisture penetration because the insulating oil is hygroscopic.

The Norm PE116/94 for tests and measurements on electrical equipment requires that, for current transformers working at voltages in the domain 110 kV – 400 kV, the insulation resistance value to be greater than 5000 MΩ. Otherwise, their connection to the line voltage is not allowed.

The drying of the current transformers can be done through various methods: by outdoor heating, by heating with current from an independent source, by heating with short-circuit current, through ventilation, through active iron losses into the transformer. In cases where through a certain method it fails to obtain the necessary drying tem-

perature or when heating of different parts is not uniform, two methods are combined [1], [2].

Currently, at Hidroserv Râmnicu Vâlcea, a combination of the induction heating at the industrial frequency and the conduction heating is the adopted solution to dry the current transformers used in the power transformer stations. Given the technological processes that use heating, in order to have a high degree of flexibility, it is considered that a static multifunction system is required. It could provide both DC and AC energy and, in the same time, allow the adjustment of the frequency and power level [3] - [13].

After introduction, this paper contains three background sections and ends with some conclusions.

In the following section, the structure currently used for drying by induction and conduction heating is presented and some details on the apparatus used for recording the current and voltage are given.

The next section is dedicated to the processing of the recorded data, needed for the graphical representation and harmonic analysis. Because the waveforms contain high frequency noise, their filtration is done with first order filters having the cutting frequency of 10 kHz.

Then, the electric powers in system and the total power factor are calculated by using both unfiltered and filtered waveforms. Finally, some conclusions are drawn.

## II. EXPERIMENTAL SETUP

The current transformer that must be dried is covered with an insulating film of textolit, over which a coil that has shape of a truncated cone is achieved (Fig. 1). The size of the obtained coil depends on number of its turns.

The conductor used is made of flexible copper class 5 according to EN 60228, profile stranded (wire diameter of 0.51 mm), with an outer diameter of 15.8 mm. In this way, the parameters' variation depending on the frequency can be neglected.

The power supply is ensured by using the autotransformer of a source for welding capable to adjust the output voltage in large limits.

Two structures of the induction heating coil have been achieved, as follows:

1. Coil with 33 turns, when the rms values of the voltage and current are 59 V and 150 A;
2. Coil with 38 turns, when the rms values of the voltage and current are 56 V and 130 A.

In order to determine the associated parameters for both coils, the current and voltage across the equivalent induc-



Fig. 1. Detail about the drying of current transformers in actual technology.

tor have been recorded by using an oscilloscope Tektronix TDS3000. The current has been recorded by a shunt  $0.5\text{m}\Omega/100\text{mV}$  precision class 0.2% [14]. The acquisition frequency was 100 kHz.

For the subsequent use in the calculation of the parameters, the waveforms of the two quantities have been filtered by means of first order filters having a period of  $10^{-4}$  seconds. Thus, a significant attenuation of the high order harmonics has been achieved (Fig. 2).

It is estimated that the value of  $10^4$  rad/sec for the cutting pulsation represents an acceptable compromise between the mitigation of the high order harmonics and how the phases of the first 31 harmonics are affected. Thus, for a lower value of the cutting pulsation, the mitigation of the high order harmonics could be more pronounced, but the phases' changing of the first 31 harmonics would become unacceptable. Conversely, a higher value of the cutting pulsation would not mitigate sufficiently the magnitude of the high order harmonics.

### III. WAVEFORMS AND HARMONIC ANALYSIS

As it can be seen in Fig. 3a), the waveform of the acquired current in the case of the coil with 33 turns contains harmonics of high frequency. Their presence is due to the induced voltages by the electromagnetic disturbances existing in the external environment.

The harmonics spectra of the raw and filtered waveforms of the current show that the harmonics up to order 31 have very little influence and the most apparent of these are of orders from 2 to 6 and 11 (Fig. 4).

Two indicators have been taken into consideration to quantify the degree of harmonic distortion, i.e. [15], [16]:

- The total harmonic distortion factor (THD),

$$THD = \sqrt{\left(\frac{I}{I_1}\right)^2 - 1}, \quad (1)$$

where  $I$  and  $I_1$  are the global rms value of the current and the fundamental rms value, respectively;

- The partial harmonic distortion factor (PHD),

$$PHD = \frac{\sqrt{\sum_{k=2}^N I_k^2}}{I_1}, \quad (2)$$

where  $N$  is the order of the last harmonic taken into consideration.

It was obtained that the total harmonic distortion factor for the unfiltered wave is 6.33% and the partial harmonic distortion factor corresponding to the first 31 harmonics is 2.63%.

As regards the filtered waveform of the current, the total distortion factor is 3.8% and the partial harmonic distortion factor associated to the first 31 harmonics is 2.54%. It can be seen that the last one is slightly lower than the corresponding value related to the unfiltered wave (2.63%). It follows that the filtering process does not affect the low order harmonics, impacting on energetic quantities.

As illustrated in Fig. 5, the high frequency noises contained in the acquired waveform of the voltage are lower. The harmonic spectrum shows that the highest weight corresponds to the harmonics 2, 3, 5 and 11 (Fig. 6a).

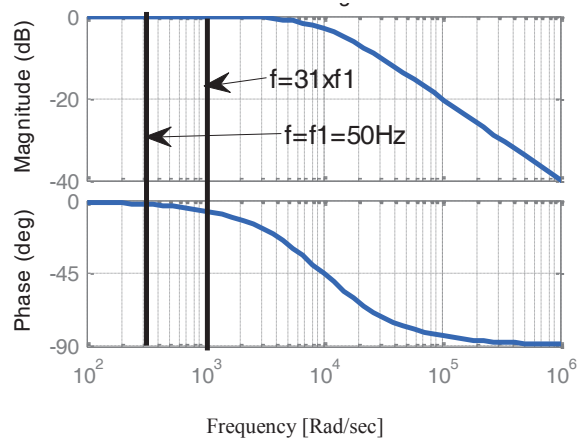


Fig. 2. Bode diagrams of the first order filter.

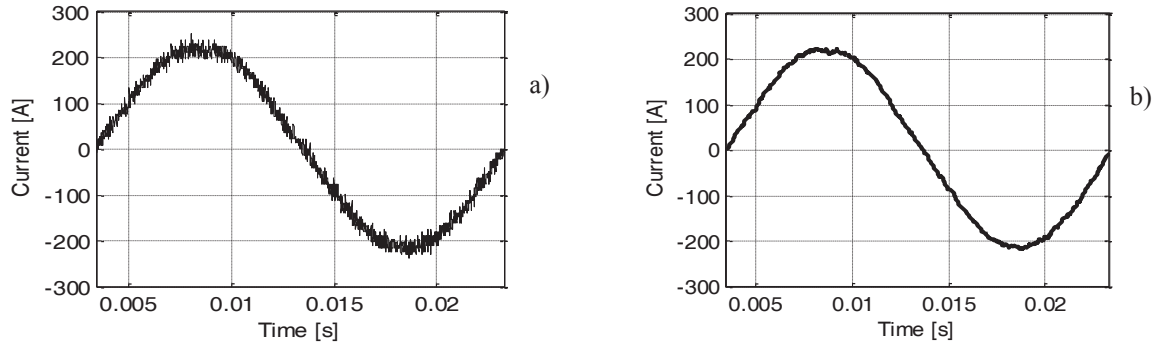


Fig. 3. The waveform of current for the coil with 33 turns: a) recorded; b) filtered.

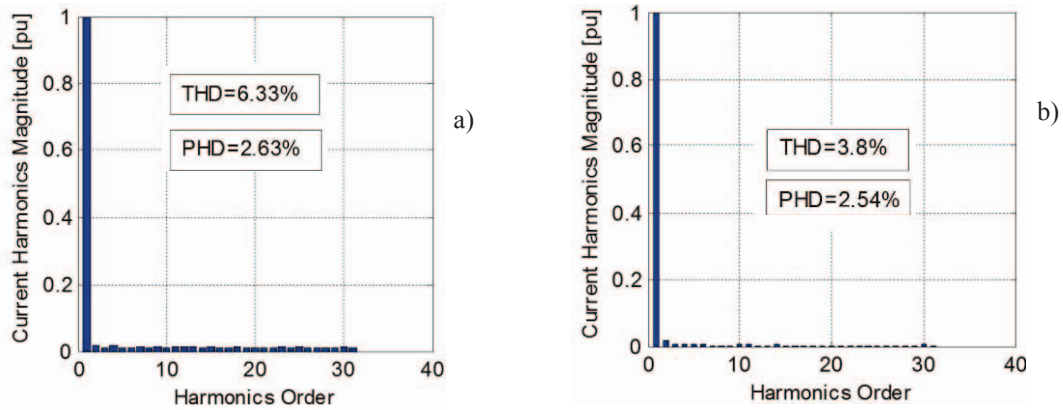


Fig. 4. Harmonic spectra of the current (p.u.) for the coil with 33 turns: a) for the acquired wave; b) for the filtered wave.

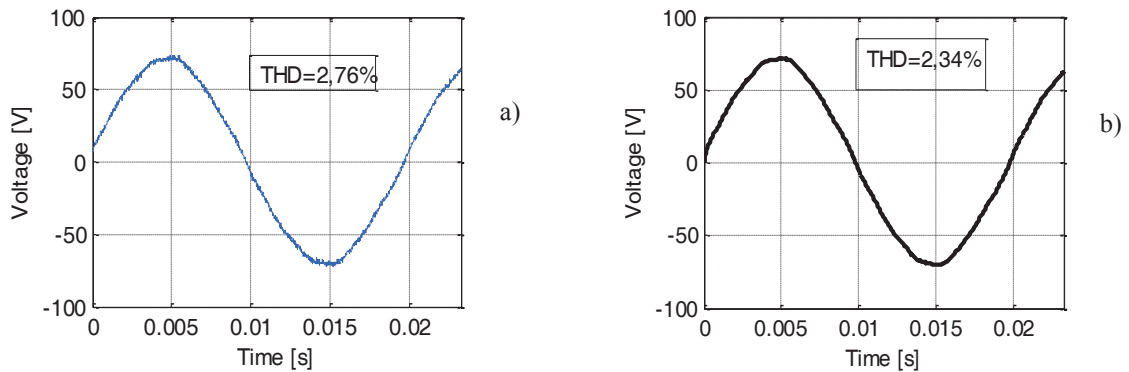


Fig. 5. The waveform of voltage for the coil with 33 turns: a) recorded; b) filtered.

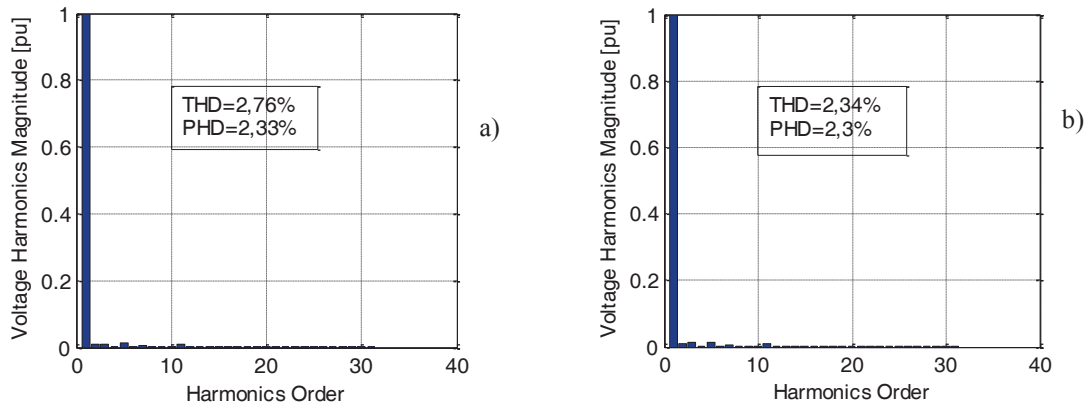


Fig. 6. Harmonic spectra of the voltage (p.u.) for the coil with 33 turns: a) acquired wave; b) filtered wave.

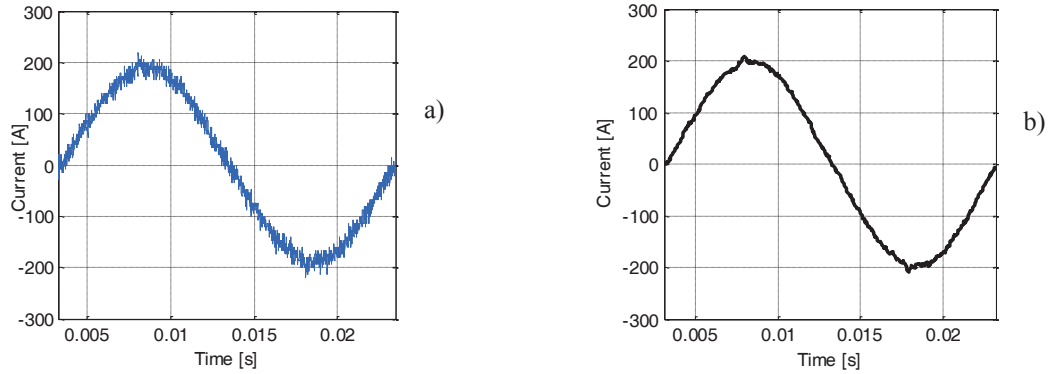


Fig. 7. The waveform of current for the coil with 38 turns: a) recorded; b) filtered.

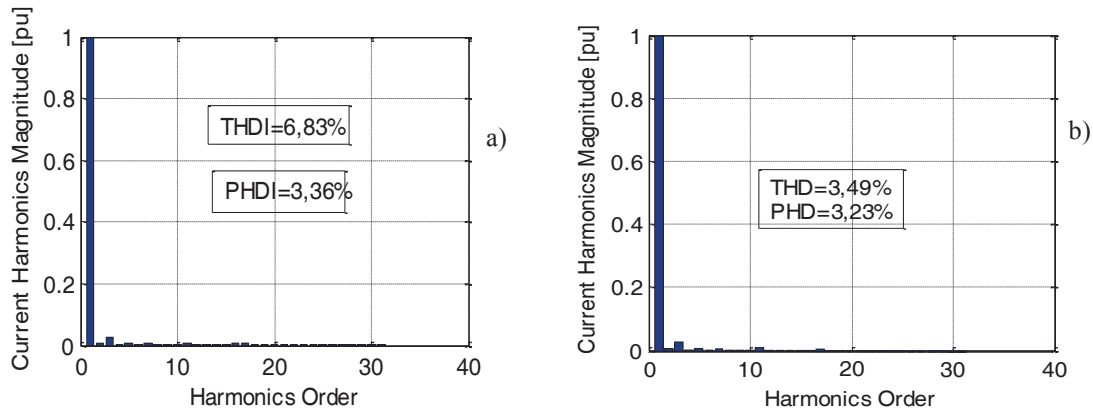


Fig. 8. Harmonic spectra of the current (p.u.) for the coil with 38 turns: a) acquired wave; b) filtered wave.

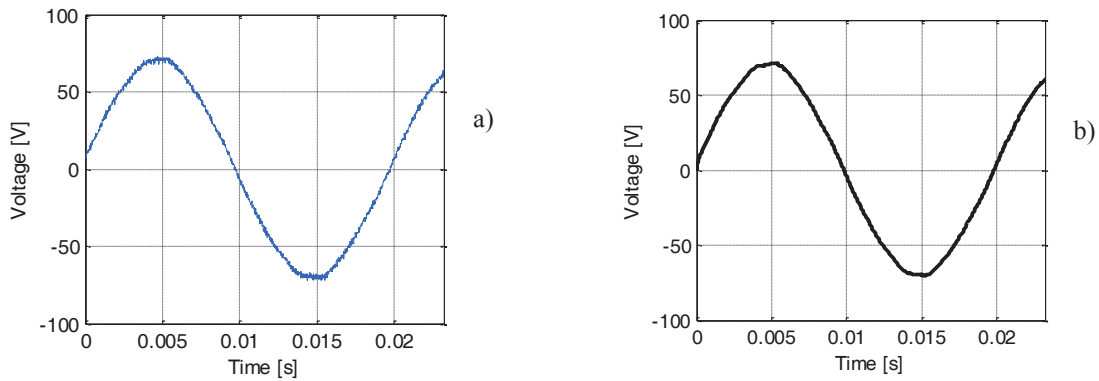


Fig. 9. The waveform of voltage for the coil with 38 turns: a) recorded; b) filtered.

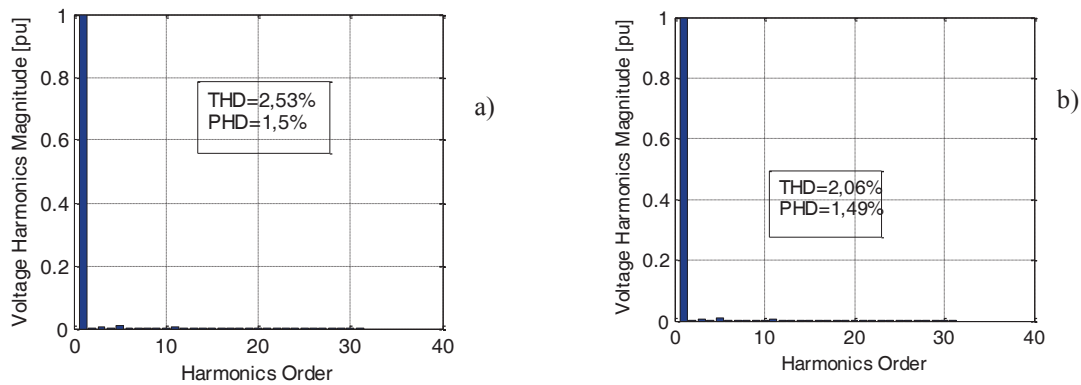


Fig. 10. Harmonic spectra of the voltage (p.u.) for the coil with 38 turns: a) acquired wave; b) filtered wave.

The total harmonic distortion factor of the unfiltered and filtered waves of voltage is 2.76 % and 2.34 % respectively. The partial distortion factors by considering only the first 31 harmonics have the values 2.33 % for the raw wave and 2.3 % for the filtered wave.

As it can be seen from Fig. 4b) and Fig. 6b), the weight of harmonic of order 31 is 0.12 % for voltage and 0.15 % for current. This aspect and the very close values of the partial harmonic distortion factors show that the consideration of the first 31 harmonics is enough.

In the case of the 38 turns coil, the phenomena are similar in terms of quality aspects (Fig. 7-Fig. 10). There are, however, few quantitative differences, as follows:

- The total harmonic distortion of the current is 6.83 % for the acquired wave and 3.49 % after filtration;
- The partial harmonic distortion of the current is 3.36 % for acquired wave and 3.23 % for after filtration;
- The total harmonic distortion of the voltage is lower, respectively it is 2.53 % for the unfiltered wave and 2.06% for the filtered wave;
- The partial harmonic distortion of the voltage is lower, that is 1.5% for unfiltered wave and 1.49% for filtered wave;
- The weight of the harmonic voltage of order 31 is about 0.066 %;
- The weight of the harmonic current of order 31 is about 0.35 %.

It must be mentioned that the measurements for the two coils were performed on different days. Accordingly, the supply conditions were not identical. Even the frequency of the supply voltage was different, namely 50.5 Hz in the case of coil with 33 turns and 50 Hz in the case of coil with 38 turns.

#### IV. ENERGETIC ANALYSIS

In order to perform the energetic analysis, the active power ( $P$ ), the apparent power ( $S$ ) and the global power factor ( $PF$ ) have been calculated. The following expressions have been implemented by modeling under MATLAB/Simulink software:

- for the active power,

$$P = \int_{t-T}^t u \cdot i \cdot d\tau; \quad (3)$$

- for the apparent power,

$$S = U \cdot I; \quad (4)$$

- for the global power factor, which is a synthetic indicator on powers,

$$PF = \frac{P}{S}. \quad (5)$$

The rms values values of the voltage and current ( $U$  and  $I$ ), which intervene in (4), have been implemented through their definitions [16]:

$$U = \sqrt{\int_{t-T}^t u^2 d\tau}; \quad (6)$$

$$I = \sqrt{\int_{t-T}^t i^2 d\tau}. \quad (7)$$

The power that could be compensated ( $P_C$ ) has been calculated too,

$$P_C = \sqrt{S^2 - P^2}, \quad (8)$$

and its weight in the active power ( $W_{CP}$ ) and apparent power ( $W_{CS}$ ) are expressed as:

$$W_{CP} = \frac{P_C}{P}; \quad (9)$$

$$W_{CS} = \frac{P_C}{S}. \quad (10)$$

It must be noted that the power that could be compensated to reach the unity power factor contains both the reactive power and the distortion power [16].

In the same time, the undimensional indicators WCP and WCS are a measure of additional expenses because of unused power.

The numerical results given in Table I show that the energetic performances are weak.

Thus, low values are obtained the the global power factor (about 38 % for the coil with 33 turns and about 45 % in the case of the coil with 38 turns).

If it is obvious that the drying process by heating the current transformer is more effective if the coil covers better the transformer's height and the number of turns of the coil is higher. This second aspect is confirmed by the results shown in Table 1.

TABLE I.  
THE NUMERICAL RESULTS OF ENERGY PARAMETERS

Coil	33 turns		38 turns	
	Filtered wave	Unfiltered wave	Filtered wave	Unfiltered wave
Frequency	50.5 Hz		50 Hz	
$U$ [V]	49.41	49.43	49.41	49.44
$I$ [A]	153.5	153.8	138.3	138.6
$P$ [W]	2885	2887	3091	3093
$S$ [VA]	7583	7601	6832	6851
$PF$	0.3816	0.3798	0.4595	0.4515
$P_C$ [VA]	7013	7031	6093	6113
$W_{CP}$ [%]	243.08	243.55	197.11	197.64
$W_{CS}$ [%]	92.48	92.51	89.18	89.23

The need to search for new sources and technologies based on the heating process, dedicated to the drying of the current transformers and other components of the hydropower plants, is better illustrated by the high values of indicators  $W_{CP}$  and  $W_{CS}$ .

Thus, the power that could be compensated represents about 90 % of the apparent power and 200 % of the active power.

## V. CONCLUSIONS

1. The detailed energetic analysis of the drying process by heating of a current transformer from a power station in a hydropower plant shows that the existing technology and equipment are “energy-intensive”.

2. The data obtained through this analysis can be used to calculate the equivalent parameters of the system, which are required in identification and the design of new equipment with better energy performance.

3. The power that could be compensated, with favorable consequences on the supply system, is about  $2 \div 2.5$  times higher than the active power.

4. A simple solution to compensate this useless power is to use a compensation capacitor connected in parallel with the inductor.

5. It is estimated that a complete way to improve the energetic performances requires supplying from a static system based on a resonant voltage inverter.

6. A multifunction static system able to provide both AC and DC voltage, continuously adjustable in large limits, may be obtained by supplying the voltage source inverter from either a fully controlled rectifier or a half controlled rectifier.

Received on July 17, 2016

Editorial Approval on November 15, 2016

## REFERENCES

- [1] R. G. Ghemke, *Defectele masinilor electrice*, Editura Tehnică, București, 1960.
- [2] Felicia Anghel Sprânceană., D. Anghel, *Metode și procedee tehnologice. vol. II. Tehnologii moderne*, Printech, București, 2006.
- [3] M. K. Kazimierczuk, D. Czarkowski, *Resonant power converters*, John Wiley & Sons, 2011.
- [4] A. Bitoleanu, D. Mihai, Mihaela Popescu, C. Constantinescu, *Convertoare statice și structuri de comandă performante*, Sitech, Craiova, 2000.
- [5] V. Suru, Mihaela Popescu, A. Bitoleanu, “Energetic performances of induction heating systems with voltage resonant inverter”, *Proceedings of International Symposium on Electrical and Electronics Engineering*, October 11-13, Galați, România, 2013.
- [6] A. Bitoleanu, Mihaela Popescu, V. Suru, “Maximizing power transfer in induction heating system with voltage source inverter,” *The 22nd International Conference on Nonlinear Dynamics of Electronic Systems*, Albena, Bulgaria, 2014.
- [7] V. Esteve, J. Pardo, J. Jordan, E. Dede, E. Sanchis-Kilders, E. Maset, “High power resonant inverter with simultaneous dual-frequency output,” *36th Power Electronics Specialists Conference*, 2005, pp. 1278-1281.
- [8] S. Dieckerhoff, M. J. Ruan, R. W. De Doncker, “Design of an IGBT-based LCL-resonant inverter for high-frequency induction heating,” *The 34th Industry Applications Conference*, vol. 3, Oct. 3-7, 1999, pp. 2039 – 2045.
- [9] F. P. Dawson, P. Jain, “A comparison of load commutated inverter systems for induction heating and melting applications,” *IEEE Transactions on Power Electronics*, vol. 6, no. 3. July 1991, pp. 430-441.
- [10] A. Suresh, R. S. Rama, “Parallel resonance based current source inverter for induction heating,” *European Journal of Scientific Research*, vol. 58, no. 2, 2011, pp. 148-155.
- [11] Mihaela Popescu, A. Bitoleanu, E. Subțirelu, “design and performance of the voltage control loop in induction heating systems with L-LC resonant inverters,” *Annals of the University of Craiova, Electrical Engineering Series*, no. 37, 2013, pp. 39-43.
- [12] S. Chudjuarjeen, A. Sangswang, C. Koopai, “An Improved LLC resonant inverter for induction-heating applications with asymmetrical control,” *IEEE Transactions on Industrial Electronics*, vol. 58, issue 7, July 2011, pp. 2915 - 2925.
- [13] P. Sreenivas, R. Vaddi, J.S. Ranganayakulu, “Full bridge resonant inverter for induction heating applications”, *International Journal of Engineering Research and Applications (IJERA)*, vol. 3, issue 1, Jan.-Feb. 2013, pp. 066-073.
- [14] K. Agoston, *Instrumentatie si masurari electrice*, Matrixrom, Bucuresti, 2009.
- [15] Mihaela Popescu, *Electronique de puissance: composants semi-conducteurs et convertisseurs*, Universitaria, Craiova, 2006.
- [16] A. Bitoleanu, Mihaela Popescu, *Filtre active de putere*, Universitaria Craiova, 2010.

# Improving the Power Quality and Controllability of PV Power Plants for Microgrids Integration

Luminita Barote, Corneliu Marinescu, Ioan Serban and Daniel Munteanu

Transilvania University of Brasov/Department of Electrical Engineering and Applied Physics  
Brasov, Romania  
luminita.barote@unitbv.ro

**Abstract** - This paper deals with the implementation of the control strategy for a three-phase voltage source inverter (VSI) system with the purpose of improving the power quality and controllability of photovoltaic (PV) system for microgrids (MGs) integration by means of energy storage system. The proposed model comprises of a PV power plant with an energy storage system coupled to the grid by means of a VSI. The PV system and the battery storage are integrated with the help of DC-DC and DC-AC converters in such a way that bidirectional flow of active and reactive powers can be achieved. The required power for the connected loads can be effectively delivered and supplied by the proposed PV system and energy storage systems, subject to an appropriate control method. The ultimate goal of any power system is to maintain a balance between demand and supply of active power at any set point in time. Controllers integrating energy sources respond to the received signals and attempt to fulfil the grid demand. The system response is almost instantaneous and thus can be very helpful in grid frequency and voltage support. The grid voltage harmonic generation influences the PI current controller and generates current harmonics; the used harmonic compensator is effective for both positive and negative sequence fifth and seventh harmonics. The proposed control system is validated by means of simulation results.

**Keywords:** microgrid, PV source, energy storage, harmonic compensator, power quality.

## I. INTRODUCTION

The introduction of renewable energy sources (RES) is associated with the development of distributed power generating systems. The classical energy unidirectional distribution grid is replaced with a smart grid containing a multitude of microgrids (MGs), using RES and loads where the energy flow is bidirectional in respect with the main Grid. The control of the issues related to the stability of supply and energy quality in such grids are falling in the responsibility of the automated MGs, because the exponential increase of the control complexity makes not anymore possible the human dispatcher to perform it. From this point of view the RES have to participate to the quality control issues [1], [2]. This responsibility will be shared by sources and customers (loads) in the grid. In this way the dynamic stability of the MG has to be sustained by the RES power plant, too. One of the RES, the PV source,

has, due to the electronic converters implied in its structure, the greatest answer speed capability to face with the stability problems, part of which are created in large extent by its own inherent variability of energy production. The premise used until now, to maximize the energy production using the maximum power point tracking (MPPT), will be replaced by the request to participate to the MG's operational stability [3-4]. This will mean to keep some part of the rated power as a reserve to be exploited in case of need. Also that request will require an associated energy storage facility besides the PV power plant. The difference between the PV power generation and local load consumption being directed to or supplied by the battery energy storage system connected via the power electronic interface. In our study we are starting to create a PV system on which study and, later, experiment some issues related to the dynamic stability and power quality of an MG supplied by a PV power plant. We will present aspects related not only on the grid connected MG, but to the possibility to operate it in an islanded way, too.

The system considered in the present study consists of a PV plant of 5.2 kW rated power, a battery banks (48V/100 Ah), a 5 kW three-phase VSI used to interface the DC-link to the grid through an LC filter. The simplified block diagram of the proposed system is shown in Fig 1.

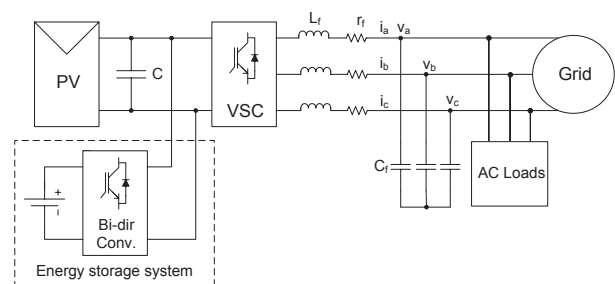


Fig. 1. Block diagram of analyzed system.

There are a lot of researches developed around the PV based MGs. Many of them are building around the same system adopted by us, [5]-[8], or without the storage facility, [9]. The dynamic control of the power supply to the grid and the stability of the MG related to the stability of grid in case of transients are at the beginning in many aspects as it can arise from the review papers such us [10]-[12].

The main objective of the present work is to implement a structure for improving the power quality and controllability of PV power plants for MG integration by means of

This work was supported by a grant of the Romanian National Authority for Scientific Research and Innovation, CNCS - UEFISCDI, project number PN-II-RU-TE-2014-4-0359.

energy storage system. The paper is organized as follows: in Section II the system configuration with the control methods, Section III describes the simulation results while the main conclusions are provided in Section IV.

## II. SYSTEM CONFIGURATION AND CONTROL

The analyzed PV power plant consists on 1 string of 22 series panels ( $\approx 5200$  W) directly to the VSI DC-link, the rated DC voltage produced by the string being around  $650V_{DC}$ . The PV panel's model is detailed in [13] and the datasheet parameters are given in [14]. The energy storage system consists of a storage element, in this case a bank of batteries and a bidirectional converter.

The lead acid batteries are the dominant energy storage technology, with their advantages of low price, high-unit voltage, stable performance and a wide operating temperature range [15], [16].

The battery bank consists of four 12 V batteries connected in series. The battery is able to supplement the power provided to the load by the PV, when the irradiation is too low. Batteries are the storage devices which cannot be overcharged or depleted completely. Their charging /discharging have to be controlled in order to maintain it for longer life. This care can be taken while generating the capability. For battery state of charge (SOC) estimation, the control method updated the SOC variable from one time step to the next, based on the power that goes through the cell stack. The control algorithm uses two variable parameters ( $I_{Batt}$ ,  $V_{Batt}$ ) and one constant block (c). With a discrete time-integrator block by accumulation the SOC is thus computed each cycle based on the previous SOC, depending on the input values. The change in SOC is implemented as follows:

$$SOC_{t+1} = SOC_t + \Delta SOC \quad (1)$$

$$\Delta SOC = \frac{\Delta E}{E_{capacity}} = \frac{P_{LAB} \cdot Time_{Step}}{E_{capacity}} = \frac{I_{Batt} \cdot V_{Batt} \cdot Time_{Step}}{P_{rating} \cdot Time_{rating}} \quad (2)$$

The basic principle of an SOC indication system is shown in Fig. 2.

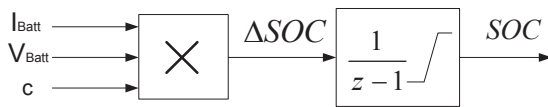


Fig. 2. Simplified battery SOC control method.

$$c = \frac{Time_{Step}}{P_{rating} \cdot Time_{rating}} = \frac{100 \cdot 10^{-6}}{5000 \cdot 4 \cdot 3600} \quad (3)$$

Where the values in (3) are corresponding to the practical studied system, the battery thus modeled is integrated in parallel with the DC link via the bidirectional DC-DC converter.

The bidirectional charge controller provides suitable charging conditions and regulates the current flow to avoid overcharge for battery protection. Connecting the battery through a DC-DC converter provides flexibility in choosing the DC-link voltage level, and the battery volt-

age and configuration. It also enables the battery to provide the necessary power to maintain a constant load voltage.

The simplified layout of the bidirectional charge controller is presented in Fig. 3. This control algorithm uses a constant DC reference voltage ( $V_{DC\_ref}$ ) to charge/discharge a battery.

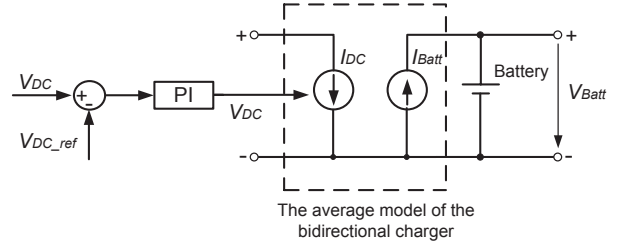


Fig. 3. The control mode of the bidirectional charge controller.

The DC voltage ( $V_{DC}$ ) is compared with a reference voltage ( $V_{DC\_ref}$ ) and an error signal is obtained. With a PI (proportional-integrator) controller, the DC value of the charge/discharge current ( $I_{DC}$ ) is obtained. When  $I_{DC} > 0$  the battery is charging, and when  $I_{DC} < 0$  the battery is discharging. It measures the power output of the PV system and the state of charge (SOC) of the battery and decides how much energy can be delivered/absorbed at a given moment.

A 5000  $\mu F$  capacitor is considered on the DC-link of the PV battery system. The 5 kW three-phase VSI is responsible for converting the DC power from the PV-battery system into AC mains power and feeds it into the grid.

The whole system was sized to ensure the adequate output for the load and to the grid. The PWM of the inverter and the LC filter ( $L_f = 2$  mH,  $C_f = 10$   $\mu F$ ) was adequately sized to reduce the THD under the standard value. To have the desired reference AC currents at the output, the magnitude and phase information is essential.

A simple PI loop generates the magnitude of the current by comparing the DC link voltage to the reference value, and a phase locked loop provides the voltage phase angle information. Thus PI controller takes care of the voltage at the DC bus. The controller generates a positive reference current for a positive error and a negative reference current for a negative error.

The control structure of the grid side converter based on PI current controllers in  $dq$  frame is presented in Fig. 4. The  $i_q$  current component determines reactive power while  $i_d$  decide the active power flow.

The input of the current controller is the error between the measured and reference grid current. The current controller output is the reference grid voltage, which divided by the DC source voltage gives the duty cycle for the inverter. The power quality problem of the power supplied by the PV-battery source is related to the harmonics content of the AC wave generated by the inverter.

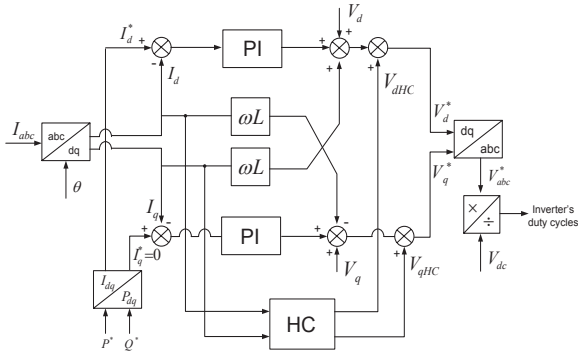


Fig. 4. The dq current control based on PI controller with HC.

In order to reduce the harmonics content, expressed by the THD, a supplementary Harmonics Compensator (HC) is applied in synchronous reference frames, where the currents being regulated are DC quantities, which eliminates the steady-state error, in order to obtain an improved power quality in the analyzed configuration.

Among numerous current control schemes reported in the literature [17]-[19], in the studied HC control structure (Fig. 5) two controllers are implemented in two frames rotating at  $-5\omega$  and  $+7\omega$ , one frame for each harmonics. As the most important harmonics in the current spectrum are the 5<sup>th</sup> and 7<sup>th</sup>, in this paper HC is designed to compensate these two selected harmonics.

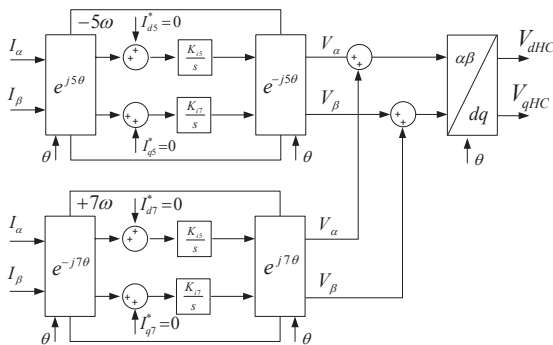


Fig. 5. The HC diagram for PI controller.

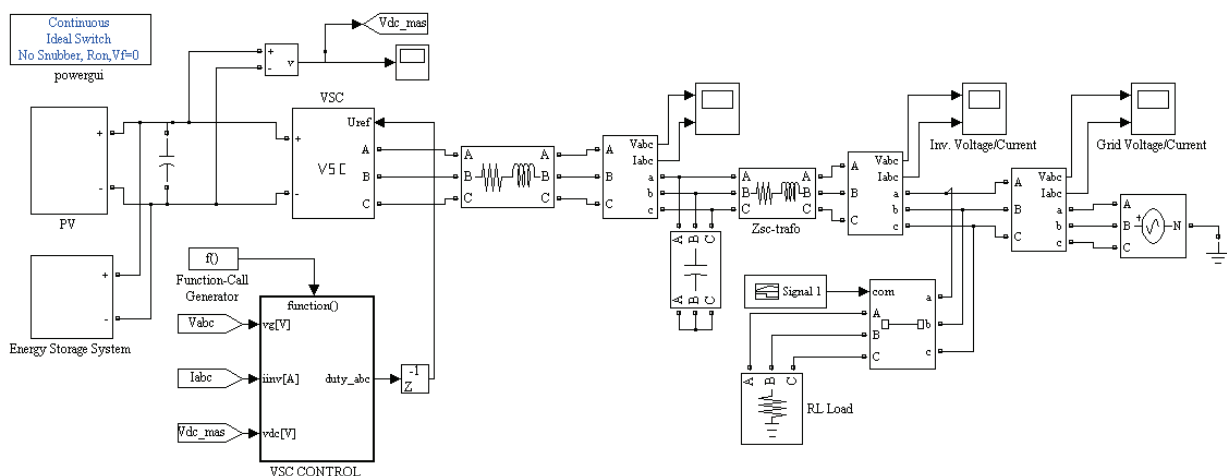


Fig. 6. Simulink diagram of the studied system.

In order to synchronize the grid connected VSI and control of injected current to ensure unity power factor at point of common coupling (PCC), a PLL block is used. Also, PLL system can be used to detect the frequency and phase of the harmonics in order to select the proper speed of the synchronous frame. The implemented PLL structure in our analyzed control structure is based on [21], where the positive-sequence voltage vector is translated from the  $\alpha\beta$  stationary reference frame to the  $dq$  rotating reference frame by means of Park's transformation.

### III. SIMULATION RESULTS

The proposed PV-battery MG system has been modeled and simulated using the Matlab/Simulink environment. Fig. 6 presents the Simulink diagram of the PV-battery connected to the MG by means of a three-phase inverter.

In order to investigate the system's operation, the system is tested under different scenarios to show that operation is quick enough in response to the commanded signals. The system is tested in the synchronous  $dq$ -PI, for two different cases as follows:

- constant reference inverter power ( $P_{inv}=3 \text{ kW}$ ) and constant AC loads ( $P_{load} = 5 \text{ kW}$ ), with harmonic generation, without and with HC for variable irradiation PV levels.
- step change in the inverter power reference for 3 kW to 5 kW at  $t=3 \text{ s}$  and variable AC loads (see Fig. 16 – green line), with harmonic generation, without and with HC for a constant PV irradiation level.

The following figures show the simulation results followed by a discussion about improving the power quality and controllability of PV power plants for microgrids integration by means of energy storage system.

#### A. Case 1: PV-battery system variation at constant local load

In the first case, a variation in the PV irradiation was applied, (see Fig. 7) in order to simulate a real PV operating condition. The simulations were performed at 3 kW constant inverter reference power value and 5 kW total load power demand. The reactive power reference is set to zero.

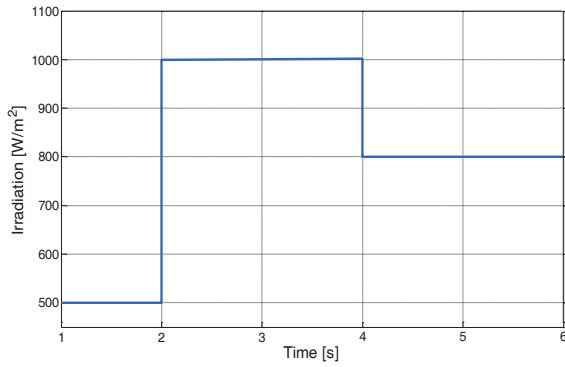


Fig. 7. Variable irradiation of PV array input.

By using a PI regulator, the DC inverter voltage link, presented in Fig. 8, is maintained around 650 V<sub>DC</sub> according to the PV irradiation levels. For testing the effectiveness of HC, a 5<sup>th</sup> and 7<sup>th</sup> harmonic order injection by the three phase voltage grid is applied into the system for whole duration of the simulation.

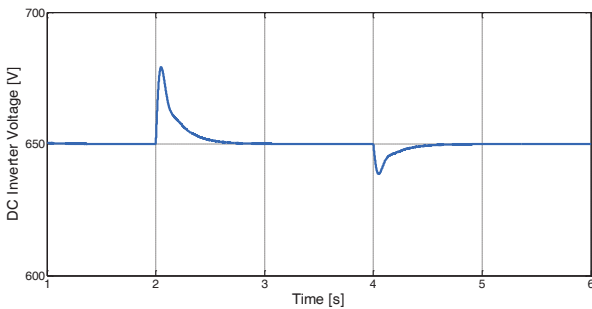


Fig. 8. DC inverter voltage link variation.

In Fig. 9, during this process, the negative current implies that the battery is in discharging mode. When the battery is charging, the battery voltage increases by about 2 V (at t=2 s for 1000 W/m<sup>2</sup>) and decreases by about 1 V (starting with t=4 s for 800 W/m<sup>2</sup>).

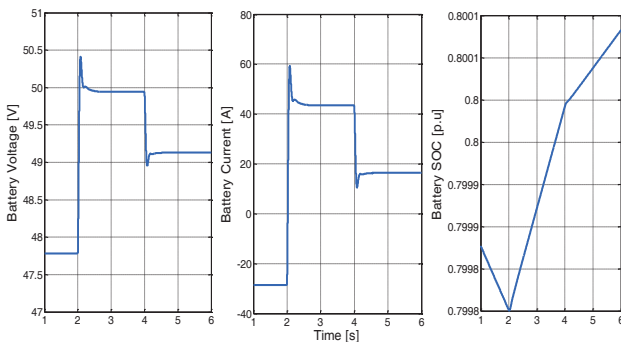


Fig. 9. Battery voltage, current and SOC variation.

The initial battery SOC is considered 80 %. In the transient regime, the battery SOC passes from discharging to charging mode in order to ensure the stability of the supply for the loads.

As it can be seen in Fig. 10, at 500 W/m<sup>2</sup>, the power produced by the PV system cannot supply the entire load

energy demand (5 kW), therefore the battery will supply the difference.

The excess power (at 1000 W/m<sup>2</sup>) is stored in the battery bank. Consequently, Fig. 10 shows that the power balance of the PV-battery system is maintained.

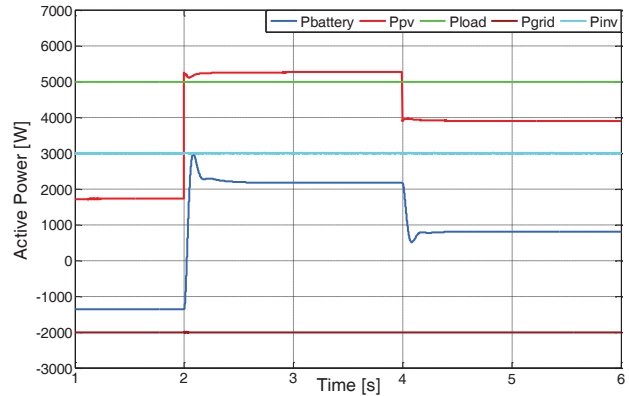


Fig. 10 Active power balance in the PV-battery system.

The grid currents variation waveforms without/with HC are presented in Fig. 11.

According to [20] the injected current and voltage in the grid should not have a THD larger than 5 % (for current) and 8 % (for voltage). The FFT analysis was made for 3 kW inverter active power reference value to obtain the graphical representation of the harmonic spectrum for phase A (*I<sub>a</sub>*) with harmonic injection in both cases: without and with HC starting at t= 5.08 s for 1 cycle.

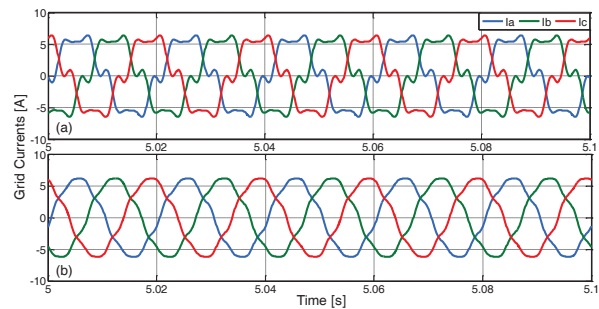


Fig. 11. Grid currents variation: (a) without HC; (b) with HC.

The grid currents THD containing the 5<sup>th</sup> and 7<sup>th</sup> harmonics are processed in Matlab/Simulink with a Powergui block.

As can be seen in Fig. 12, when is applied a harmonic injection is enabled (i.e. the grid has harmonic components), without HC, the level of THD current is 23.26 % for 3 kW inverter power reference. After the HC activation, the THD level decreases at 6.00 %.

By compensating the 5<sup>th</sup> and 7<sup>th</sup> harmonics, the THD current is drastically reduced, while the PI-HC controller implemented in *dq* frame having good performances at partial powers representing 60 % of the rated value (5 kW).

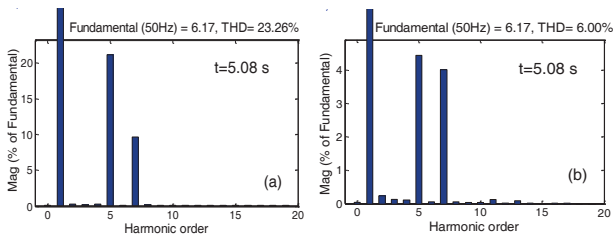


Fig. 12. Grid current ( $I_a$ ) harmonic spectrum: (a) without HC; (b) with HC.

The measured grid voltages variation with harmonic injection is shown in Fig. 13. In Fig 14, the resulted voltage THD (5.91 %) calculated for 1 cycle starting at  $t=5.08$  s is in accordance with the standards.

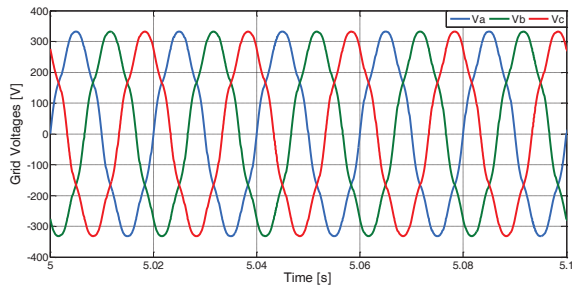


Fig. 13. Grid voltages variation with harmonic injection.

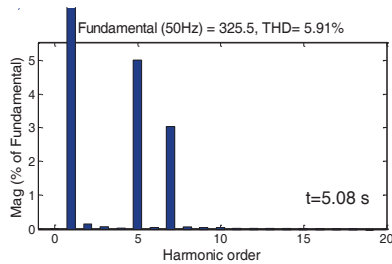


Fig. 14. Grid voltage ( $V_a$ ) harmonic spectrum with harmonic generation content

**B. Case 2: PV-battery system variation at variable local load**

In order to test again the transient performance of the proposed PV-battery control method, a variation of the full power load demand is considered (at  $t=2$  s, a 5 kW load is connected and disconnected at  $t=4$  s) for a constant PV irradiation level ( $1000 \text{ W/m}^2$ ). Also, a step change in the inverter power reference from 3 kW to 5 kW at  $t=3$  s is applied. The battery voltage, current and SOC variation results are presented in Fig. 15. For this case, the battery is in charging mode for the whole duration of the simulation. Until the load is connected, all the power produced by PV plant is stored in the battery. Also, at  $t=2$ s when a 5 kW local load is connected, the PV ensure stable supply for the loads (the approximately 0.2 kW excess power is stored in the battery), and the battery charging mode is maintained during the transient event. When the inverter power is changed, the battery voltage decreases by about 1.5 V (at  $t=3$  s), and the positive current implies that the battery remains in charging process.

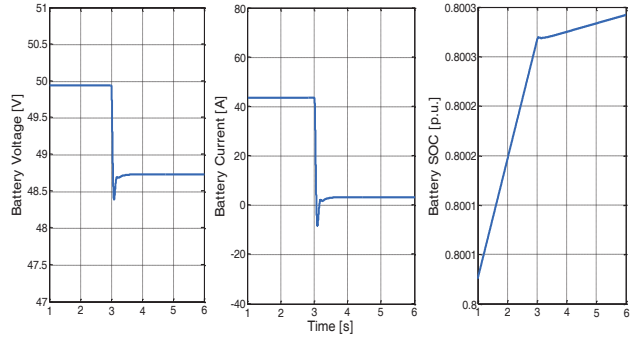


Fig. 15. Battery voltage, current and SOC variation.

The case of VSI output power increasing from 3000W up to around 5000W is shown in Fig. 16, which highlights the power balance of the PV-battery connected to the grid system.

A good transient behavior of the PI controller can be noticed in this situation. The current is controlled according to its new reference and the output power of the VSI smoothly reaches its new operating point. These results confirm that the proposed control algorithm is stable, achieving zero steady-state error at fundamental frequency and having a good transient response. A zoom in the grid currents starting at  $t=5$ s in both situations without/with HC can be seen in Fig. 17.

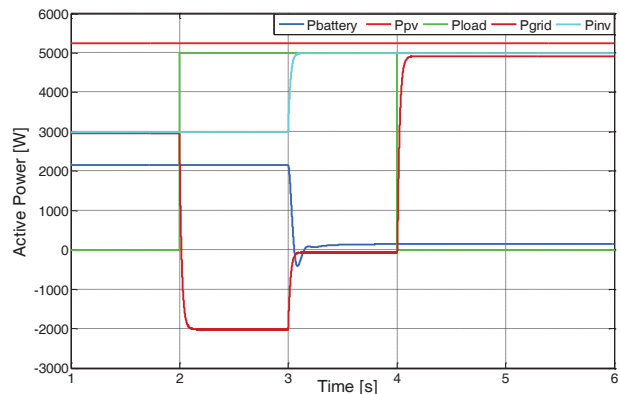


Fig. 16. Active power balance in the PV – battery system.

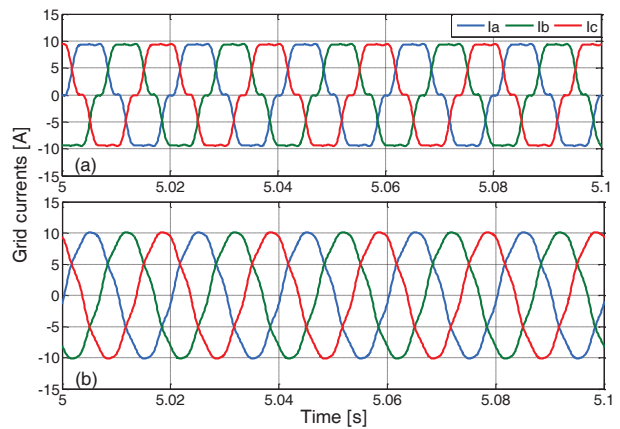


Fig. 17. Grid currents variation: (a) without HC; (b) with HC.

As can be seen in Fig. 18, when a harmonic injection is applied, without HC, the level of THD current is 14.21 % for 5 kW, while after HC implementation, the THD level decreases at 3.78 % and the system is within the standards at rated power.

The grid voltages are balanced and unaffected by the step change in the inverter power reference for 3 kW to 5 kW and the grid voltage THD is similar by the previously case (see Fig. 13 and Fig. 14).

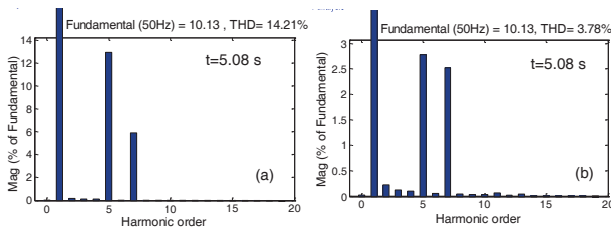


Fig. 18. Grid current ( $I_a$ ) harmonic spectrum: (a) without HC; (b) with HC.

#### IV. CONCLUSIONS

The behaviour of an interfacing system for improving power quality and controllability of PV power plants for MG integration has been presented in this paper.

This includes an associated energy storage system facility in the PV DC link besides the PV power plants with the role to enhancing the control for MG integration. A  $dq$ -PI control strategy has been applied in order to design a current controller for grid-connected VSI, with the main focus on harmonics distortion and tracking performance. The control strategies are performing well under normal and transient PV irradiation conditions.

The analyzed two cases were provided in terms of the harmonic generation dependent on the PI controller structure without and with HC for constant and variable loads.

With harmonic injection and without HC, the system does not comply with the IEEE 1547.2 standard in terms of harmonic content. By compensating the 5<sup>th</sup> and 7<sup>th</sup> harmonics, the system is within the standards, at rated power and at partial powers representing 60 % from the rated value. Stair change in the PV power shows good battery response in the case of increase/decrease in load.

The simulations results show that the enhance control method ensures good effectiveness in meeting the stringent grid harmonic standard it is suitable for MG integration.

Received on July 18, 2016

Editorial Approval on November 11, 2016

#### REFERENCES

- [1] A. Choudar, D. Boukhetala, S. Barkat, J.M Brucker, "A local energy management of a hybrid PV-storage based distributed generation for microgrids", *Energy Conversion and Management*, vol. 90, 2015, pp. 21–33.
- [2] J. M. Guerrero, P. C. Loh, T.-L. Lee, and M. Chandorkar, "Advanced control architectures for intelligent microgrids—Part II: Power quality, energy storage, and ac/dc microgrids", *IEEE Transaction on Industrial Electronics*, vol. 60, no. 4, Apr. 2013, pp. 1263, 1270.
- [3] S-T Kim, S. Bae, Y. C. Kang and J-W Park, "Energy management based on the photovoltaic HPCS with an energy storage device", *IEEE Transactions on Industrial Electronics*, vol. 62, no. 7, July 2015, pp. 4608-4617.
- [4] Y. Guan, J. C. Vasquez, J. M. Guerrero, Y. Wang, and W. Feng, "Frequency stability of hierarchically controlled hybrid photovoltaic-battery-hydropower microgrids", *IEEE Transactions on Industry Applications*, vol. 51, no. 6, Nov. 2015, pp. 4729-4742.
- [5] J. Quesadaa, R. Sebastiánb, M. Castrob, J.A. Sainz, "Control of inverters in a low voltage microgrid with distributed battery energy storage. Part I: Primary control", *Electric Power Systems Research*, vol. 114, 2014, pp. 126–135.
- [6] T. L. Vandoorn, J. D.M. De Kooning, B. Meersman, B. Zwaenepoel, "Control of storage elements in an islanded microgrid with voltage-based control of DG units and loads", *Electrical Power and Energy Systems*, vol. 64, 2015, pp. 996–1006.
- [7] H. Mahmood, D. Michaelson, and J. Jiang, "A power management strategy for PV/battery hybrid systems in islanded microgrids", *IEEE Journal of Emerging and Selected Topics in Power Electronics*, vol. 2, no. 4, Dec. 2014, pp. 870-882.
- [8] S. Gaurava, C. Birlaa, A. Lambaa, S. Umashankara, S. Ganesanb, "Energy management of PV-battery based microgrid system", *Procedia Technology*, vol. 21, 2015, pp. 103 – 111.
- [9] M. Mahzarnia, A. Sheikholeslami, "Improvement the dynamic voltage profile by a voltage stabilizer in microgrids with a type of inverter based resource", *Intelligent Systems and Applications Journal*, 2013, pp. 39-46.
- [10] F.M Uriarte, C. Smith, S. VanBroekhoven, R.E. Hebner, "Microgrid ramp rates and the inertial stability margin", *IEEE Transaction on Power Systems*, vol. 30, no.6, Nov. 2015, pp. 3209-3216.
- [11] J.G de Matos, F. S.F.e Silva, L.A.de S Ribeiro, "Power control in ac isolated microgrids with renewable energy sources and energy storage systems", *IEEE Transaction on Industrial Electronics*, vol.62, no.6, June 2015, pp.3490-3498.
- [12] S. Parhizi, H. Lotfi, A. Khodaei, S. Bahramirad, "State of the art in research on microgrids: a review", *IEEE Access*, vol. 3, 2015, pp.890-925.
- [13] L. Barote, C. Marinescu, "Renewable Hybrid System with Battery Storage for Safe Loads Supply", *IEEE PowerTech*, 19 - 23 June 2011, Trondheim, Norway, pp. 1-5.
- [14] Poly-crystalline solar panel 200-250 W, <http://www.risenenergy.com>.
- [15] C.A. Hill, M.C. Such, D. Chen, J. Gonzalez and W.M. Grady, "Battery energy storage for enabling integration of distributed solar power generation", *IEEE Transactions on Smart Grid*, vol. 3, no. 2, June 2012, pp.850 - 857.
- [16] M. T. Lawder, V. Viswanathan, V. R. Subramanian, "Balancing autonomy and utilization of solar power and battery storage for demand based microgrids", *Journal of Power Sources*, vol. 279, 2015, pp. 645-655.
- [17] R. Teodorescu, M. Liserre and P. Rodríguez, "Grid converters for photovoltaic and wind power systems", *John Wiley & Sons, Ltd, Publication*, 2011.
- [18] J. Rocabert, A. Luna, F. Blaabjerg, P. Rodriguez, "Control of power converters in ac microgrids", *IEEE Transaction on Power Electronics*, vol.27, no.11, Nov. 2012, pp. 4734-4748.
- [19] I. Serban, C. Marinescu, "Control strategy of three-phase battery energy storage systems for frequency support in microgrids and with uninterrupted supply of local loads", *IEEE Transaction on Power Electronics*, vol. 29, no. 9, Sept. 2014, pp 5010-5021.
- [20] \*\*\* IEEE 1547.2-2008, "IEEE standard for interconnecting distributed resources with electric power systems", 2009.
- [21] N. Jaalam, N.A. Rahim, A.H.A. Bakar, C. Tan, A.M.A. Haidar, "A comprehensive review of synchronization methods for grid-connected converters of renewable energy source", *Renewable and Sustainable Energy Reviews*, vol. 59, 2016, pp. 1471–1481.

# Simulation and Implementation of Sensorless Control Using Estimators in Electric Drives with High Dynamic

Marcel Nicola\*, Dumitru Sacerdotianu\* and Adrian Hurezeanu†

\* ICMET Craiova/ Research and Development Department, Craiova, Romania,  
marcel\_nicola@yahoo.com, dumitru\_sacerdotianu@yahoo.com

† CESI Automation Craiova/ Research and Development Department, Craiova, Romania,  
adrian.hurezeanu@cesiautomation.ro

**Abstract** - In this article we'll tackle the control of electric drive with high dynamic, with rapid changes in torque and speed, where the control strategy is FOC (Field Oriented Control). In the surface mining industry, from which the electric drive application for this article is selected, the general trend is toward using asynchronous motors with short-circuit rotor, due to the advantages of this motor both in terms of design and operation. In order to achieve the variable speed, must be used the static frequency converters. Simulations were carried out using a converter with FOC control strategy and a 45kW motor. The simulations also followed the direction from simple to complex in order to emphasize both qualitative and quantitative elements with respect to the overall dynamic behavior. Simulations were carried out both in the case where the overall structure contains an encoder for speed information, and where the sensorless approach is used the implementation of an estimator is strictly necessary. Such cases were dealt with where speed is measured directly with an encoder, compared with the case of sensorless control, where speed is estimated using a Model References Adaptive Control Estimator. Simulations were carried out in MATLAB/Simulink environment, highlighting the control structures and comparative results achieved for a drive application commonly used in surface mining industry. Following these directions a functional application was implemented and tested.

**Keywords:** *sensorless control; electric drives; controller; estimator.*

## I. INTRODUCTION

The development of electric drive systems was characterized in recent years by a special dynamic, linked both with technological advancements in the manufacture of semiconductor switching elements and new topologies of electric drive. Electric drives represent complex equipment designed to ensure optimal power supply and command of actuators during the operating processes [1-6].

To study the behavior of the system of frequency converter plus motor prior to the actual construction of the converter, a series of numerical simulations have been carried out using MATLAB/Simulink environment [7-9].

Trial and error type iterations are necessary to avoid the rough design errors, but also to identify a series of complex effects and phenomena, even if in the simulated environment, which should converge towards a positive purposefulness of the whole project.

We are showing the control of electric drive with high dynamic, with rapid changes in torque and speed, where the control strategy is FOC. Such cases were dealt with where speed is measured directly with an encoder, compared with the case of sensorless control, where speed is estimated using an Estimator. Simulations were carried out in MATLAB/Simulink environment, highlighting the control structures, the tuning parameters and comparative results achieved for a drive application commonly used in surface mining industry.

The technical data of the electric drive system which includes static frequency converter designed with superior technical features providing speed regulation between zero and the rating value for asynchronous motors with short-circuit rotor, are as follows: supply voltage: 3 x 400 Vac/50 Hz; rated output power: 45 kW; peak output: 1.5 x PN/2 minutes; operating temperature: -25°C to 45°C; stator resistance: 0.041  $\Omega$ ; rotor resistance: 0.050  $\Omega$ ; stator/rotor inductance: 0.8 mH; mutual inductance: 20.7 mH.

Sensorless control has a lot of advantages in terms of hardware technology, as well as performance, but the price is an additional encumbrance on the control system. Therefore, the main function of the control subsystem is prediction of speed. Fortunately, achievements in control theory, such as Kalman or Luenberger estimators, have largely contributed to solving this problem. This emphasizes the importance of continuous migration of new approaches and achievements in control theory to the field of electric drives [10].

In this article we will focus on a different type of estimator than the ones mentioned above, namely a MRAC-Model References Adaptive Control type estimator [11]. Although it doesn't have the advantage of the Kalman type estimator (which provides a good prediction even for additional uncertainty added to the measured values), this estimator has the advantage of simplicity in terms of its structure, because obviously beside the simulations which ensure a good design, it also performs the implementation of algorithms for measurement, control and prediction in a DSP, where the number of variables and performed operations must be optimized.

The structure of the paper is as follows. In second section will briefly present the basics of Field Oriented Control for the induction motor. The simulations performed with the same parameterization sets of the controllers and the references for speed and torque are presented in Section 2 and 3 for a good comparison between the cases of



The output of speed controllers supply the torque ( $T^*$ ) and flux ( $\Phi^*$ ) references for inner loop control. Following [1] and Fig. 5 for usual electrical parameters given above we can write the equations and transfer functions for calculate the  $I_d$ ,  $I_q$  and the intermediate value of flux used at each iteration by de FOC strategy control.

$$I_q^* = \frac{2}{3} \cdot \frac{1}{p} \cdot \frac{L_r}{L_m} \cdot \frac{T_e}{\Phi^*} = 0.346 \cdot \frac{T_e}{\Phi^*}, \quad (3)$$

$$I_d^* = \frac{\Phi^*}{L_m} = \frac{\Phi^*}{20.7}, \quad (4)$$

$$\frac{\Phi^*(s)}{I_d(s)} = \frac{L_m}{1+T_r} = \frac{20.7}{1+0.43s}, \quad (5)$$

where the symbol \* mean that the value is calculated and will be used to the next iteration. In this way we can write the equations for each block from Fig. 5.

The simulation results for the parameterization sets of the controllers and the references for speed and torque from below are given in Fig. 6-10.

Set no.1: Speed controller:  $K_p=30$ ,  $K_i=20$ ; Flux controller:  $K_p=100$ ,  $K_i=3$ , hysteresis band of current controller=10A; the speed reference is given by the sequence: [0 0.5 2]s  $\rightarrow$  [0 150 700]rpm; the torque reference is given by the sequence: [0 0.5 3]s  $\rightarrow$  [10 100 200]Nm.

Set no.2: Speed controller:  $K_p=300$ ,  $K_i=2000$ ; Flux controller:  $K_p=100$ ,  $K_i=30$ , hysteresis band of current controller=10A; the speed reference is given by the sequence: [0 0.5 2]s  $\rightarrow$  [0 150 700]rpm; the torque reference is given by the sequence: [0 0.5 3]s  $\rightarrow$  [10 100 200]Nm.

Set no.3: Speed controller:  $K_p=300$ ,  $K_i=2000$ ; Flux controller:  $K_p=100$ ,  $K_i=30$ , hysteresis band of current controller=10A; the speed reference is given by the sequence: [0 0.5 2]s  $\rightarrow$  [0 150 700]rpm; the torque reference is given by the sequence: [0 0.5 3]s  $\rightarrow$  [10 100 200]Nm; rotor resistance is doubled:  $2 \times 0.05 \Omega$ .

Set no.4: Speed controller:  $K_p=300$ ,  $K_i=2000$ ; Flux controller:  $K_p=100$ ,  $K_i=30$ , hysteresis band of current controller=10A; the speed reference is given by the sequence: [0 7]s  $\rightarrow$  [800 300]rpm; the torque reference is given by the sequence: [0 3 7]s  $\rightarrow$  [10 300 10]Nm.

Set no.5: Speed controller:  $K_p=300$ ,  $K_i=2000$ ; Flux controller:  $K_p=100$ ,  $K_i=30$ , hysteresis band of current controller=10A; the speed reference is given by the sequence: [0 0.5 2 4 7 8 9]s  $\rightarrow$  [0 150 300 500 350 450 700]rpm; the torque reference is given by the sequence: [0 3 6 9 10]s  $\rightarrow$  [10 100 200 300 100]Nm.

IN FOC control strategy (see Fig. 1 and Fig. 5) the flux and current controllers are in inner loop and the speed controller is in outer loop control. Besides the good dynamic performance are achieved (stationary error, settling time, rising time, overshooting and oscillating index), due to proper tuning of the regulators PI using Ziegler-Nichols method and varying the hysteresis band of current controller between 5A and 20A. Using a quality index given by de sum of squared errors between desired speed and measured speed, after a lot of simulations the best tuning is achieved in Fig. 7. The actual parameters of the motor can vary in time from the rated parameters (particularly due to temperature), in such a way that through simula-

tion, it is found that controllers have a good tuning even for a fluctuation of 100% in rotor resistance (see Fig. 8).

In Fig. 9 at second 7, when the torque reference decreases from 300Nm to 10Nm regenerative braking occurs and the voltage in the intermediate circuit increases. In Simulink, in order to analyze this phenomenon we have set the limits of the braking chopper between 750V (Activation Voltage) and 650V (Shutdown Voltage). For actual implementation, instead of the braking chopper, a regenerative inverter will be used.

The simulations for an increasing dynamic of the references torque and speed are presented in Fig. 10.

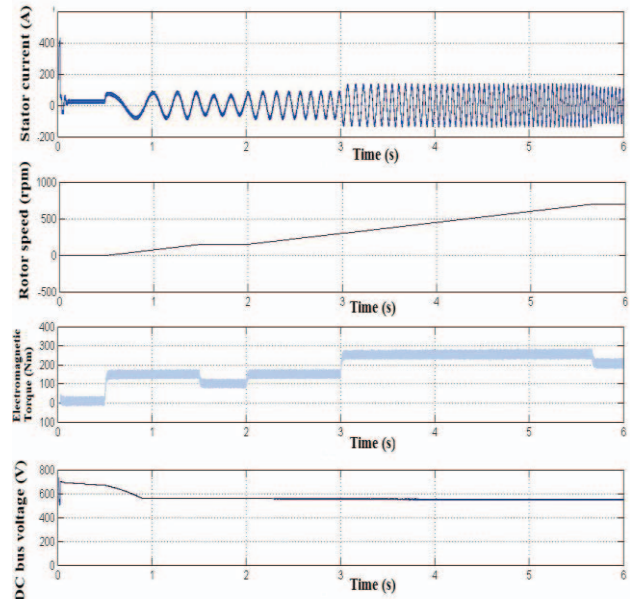


Fig. 6. The simulation of model for the set no.1 of parameters of the controllers and references.

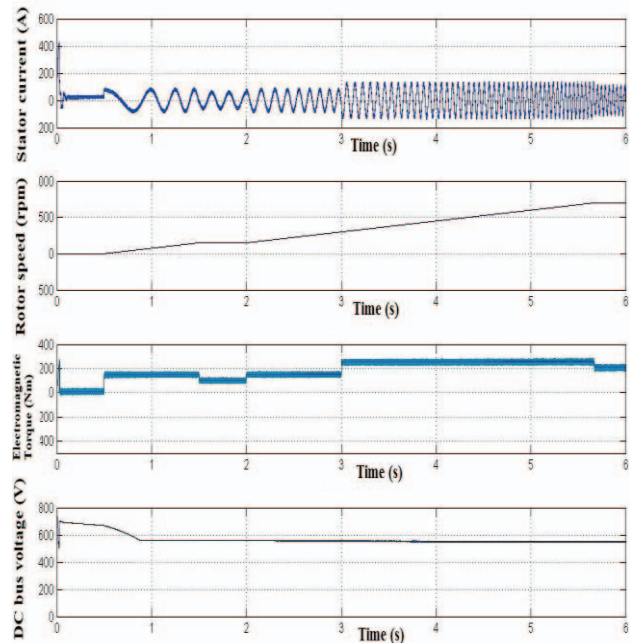


Fig. 7. The simulation of model for the set no.2 of parameters of the controllers and references.

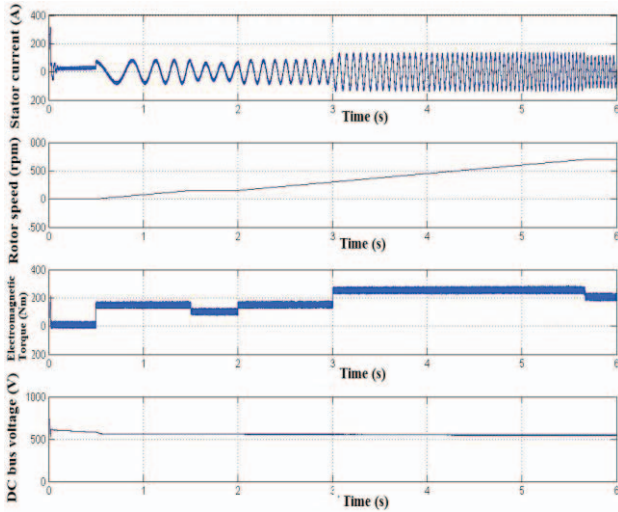


Fig. 8. The simulation of model for the set no.3 of parameters of the controllers and references.

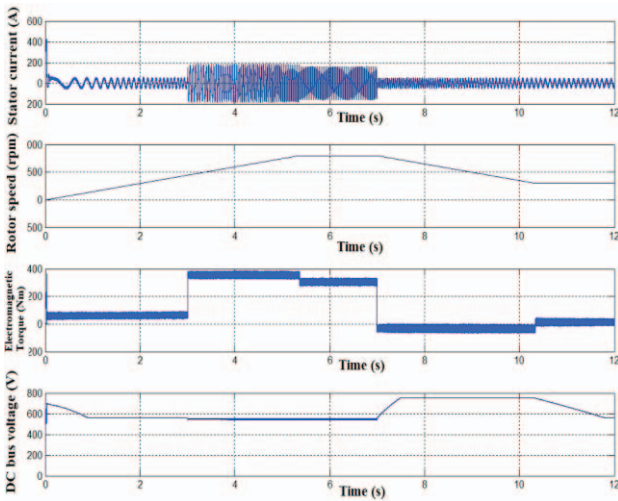


Fig. 9. The simulation of model for the set no.4 of parameters of the controllers and references.

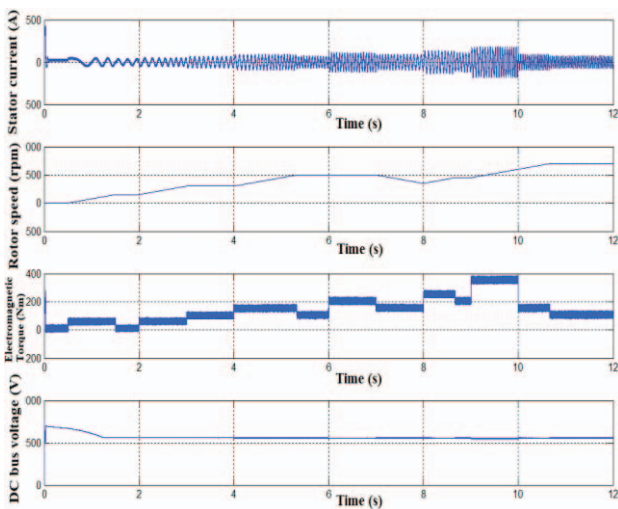


Fig. 10. The simulation of model for the set no.5 of parameters of the controllers and references.

### III. CONTROL SENSORLESS OF ELECTRIC MOTORS DRIVES

The model Simulink for the sensorless version is shown in Fig. 11, [1]. As opposed to the model in Figure 1, an additional estimator block will be noticed (see Fig. 12), [11]. The type of estimator for angular speed is MRAS.

The model Simulink for the sensorless version is shown in Fig. 11, [1]. As opposed to the model in Fig. 1, an additional estimator block will be noticed (see Fig. 12), [11]. The type of estimator for angular speed is MRAS.

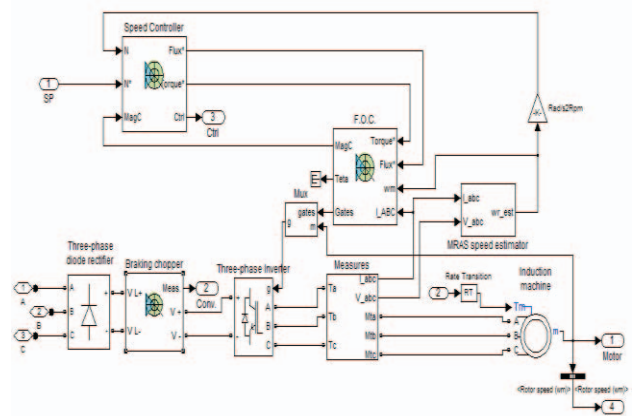


Fig. 11. Simulink block diagram for sensorless model.

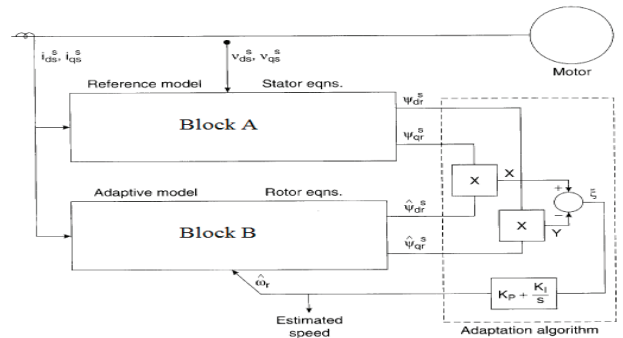


Fig. 12. Speed estimator block diagram.

The equations of Blocks A and B are [11]:

$$\begin{bmatrix} \dot{\psi}_{dr}^s \\ \dot{\psi}_{qr}^s \end{bmatrix} = \frac{L_r}{L_m} \left\{ \begin{bmatrix} u_{ds}^s \\ u_{qs}^s \end{bmatrix} - \begin{bmatrix} R_s + \sigma L_s S & 0 \\ 0 & R_s + \sigma L_s S \end{bmatrix} \begin{bmatrix} i_{ds}^s \\ i_{qs}^s \end{bmatrix} \right\}, \quad (6)$$

$$\begin{bmatrix} \dot{\psi}_{dr}^s \\ \dot{\psi}_{qr}^s \end{bmatrix} = \begin{bmatrix} -\frac{1}{T_r} & -\omega_r \\ \omega_r & -\frac{1}{T_r} \end{bmatrix} \begin{bmatrix} \psi_{dr}^s \\ \psi_{qr}^s \end{bmatrix} + \frac{L_m}{T_r} \begin{bmatrix} i_{ds}^s \\ i_{qs}^s \end{bmatrix}, \quad (7)$$

For the speed Estimator implemented in Simulink, let note  $\sigma = 1 - \frac{L_m^2}{L_r L_s}$  and starting with equations [11,12] we obtain:

$$\frac{d}{dt} (\Psi_{dr}^s) = \frac{L_r}{L_m} v_{ds}^s - \frac{L_r}{L_m} (R_s + \sigma L_s S) i_{ds}^s, \quad (8)$$

$$\frac{d}{dt}(\Psi_{qr}^s) = \frac{L_r}{L_m} v_{qs}^s - \frac{L_r}{L_m} (R_s + \sigma L_s s) i_{qs}^s, \quad (9)$$

and using that  $\theta = \tan^{-1} \frac{\Psi_{qr}^s}{\Psi_{qd}^s}$ , after calculus we obtain:

$$\omega_r = \frac{1}{\hat{\Psi}_r^s} \left[ (\Psi_{dr}^s \dot{\Psi}_{qr}^s - \Psi_{qr}^s \dot{\Psi}_{dr}^s) - \frac{L_m}{T_r} (\Psi_{dr}^s i_{qs}^s - \Psi_{qr}^s i_{ds}^s) \right]. \quad (10)$$

The encoder is thus eliminated, and the angular speed is estimated from current and voltage measurements. Using Popov hyperstability criterion, in order to achieve the overall asymptotic stability, an estimator will be achieved as follows [11]:

$$\hat{\omega}_r = \xi \left( K_p + \frac{K_i}{s} \right), \quad (11)$$

$$\xi = \hat{\Psi}_{dr}^s \Psi_{qr}^s - \Psi_{dr}^s \hat{\Psi}_{qr}^s. \quad (12)$$

In the following simulations without encoder version, the behavior of the converter unit plus motor will be analyzed, in terms of the following quantities: stator current, rotor speed, torque and voltage in the intermediate circuit.

The varying parameters were: for the speed regulator  $K_p$  and  $K_i$ , for the flux controller  $K_p$  and  $K_i$ , speed ramps and the hysteresis band for the current regulator. In addition with the encoder case, the estimator which is implemented around a PI controller will also have tuning parameters  $K_p$  and  $K_i$ .

The simulation results for the parameterization sets of the controllers and the references for speed and torque from below are given in Fig. 13-17.

Set no.1: Speed controller:  $K_p=300$ ,  $K_i=2000$ ; Flux controller:  $K_p=100$ ,  $K_i=30$ , hysteresis band of current controller=10A; speed estimator controller:  $K_p=500$ ,  $K_i=5000$ ; the speed reference is given by the sequence: [0 0.5 2]s  $\rightarrow$  [0 150 700]rpm; the torque reference is given by the sequence: [0 0.5 3]s  $\rightarrow$  [10 100 200]Nm.

Set no.2: Speed controller:  $K_p=30$ ,  $K_i=20$ ; Flux controller:  $K_p=100$ ,  $K_i=3$ , hysteresis band of current controller=10A; speed estimator controller:  $K_p=500$ ,  $K_i=5000$ ; the speed reference is given by the sequence: [0 0.5 2]s  $\rightarrow$  [0 150 700]rpm; the torque reference is given by the sequence: [0 0.5 3]s  $\rightarrow$  [10 100 200]Nm.

Set no.3: Speed controller:  $K_p=30$ ,  $K_i=20$ ; Flux controller:  $K_p=100$ ,  $K_i=3$ , hysteresis band of current controller=10A; speed estimator controller:  $K_p=500$ ,  $K_i=5000$ ; the speed reference is given by the sequence: [0 0.5 2]s  $\rightarrow$  [0 150 700]rpm; the torque reference is given by the sequence: [0 0.5 3]s  $\rightarrow$  [10 100 200]Nm; rotor resistance is doubled:  $2 \times 0.05 \Omega$ .

Set no.4: Speed controller:  $K_p=30$ ,  $K_i=20$ ; Flux controller:  $K_p=100$ ,  $K_i=3$ , hysteresis band of current controller=10A; speed estimator controller:  $K_p=500$ ,  $K_i=5000$ ; the speed reference is given by the sequence: [0 7]s  $\rightarrow$  [800 300]rpm; the torque reference is given by the sequence: [0 3 7]s  $\rightarrow$  [10 300 10]Nm.

Set no.5: Speed controller:  $K_p=30$ ,  $K_i=20$ ; Flux controller:  $K_p=100$ ,  $K_i=3$ , hysteresis band of current controller=10A; speed estimator controller:  $K_p=500$ ,  $K_i=5000$ ;

the speed reference is given by the sequence: [0 0.5 2 4 7 8 9]s  $\rightarrow$  [0 150 300 500 350 450 700]rpm; the torque reference is given by the sequence: [0 3 6 9 10]s  $\rightarrow$  [10 100 200 300 100]Nm.

Because the speed estimator must operate faster than the outer control loops, maintaining the tuning parameters for the speed regulator like in the case with the encoder will result in an insufficient response like the one in Fig. 13. Therefore, by considerably lowering the tuning values for the speed regulator (so that they will be much smaller than the values of the controller from the estimator), the optimum tuning is achieved in Fig. 14 and it is found that controllers have a good tuning even for a fluctuation of 100% in rotor resistance (see Fig. 15). In Fig. 16 occur the regenerative braking and the simulations for an increasing dynamic of the references torque and speed are presented in Fig. 17.

Besides the good dynamic performance are achieved due to proper tuning of the controllers, even in sensorless case. Both in simulations and in implementation in DSP, a special attention is given to the phenomenon of saturation of component blocks. For the control loops, limiting and anti wind-up components will be implemented in the PI controllers.

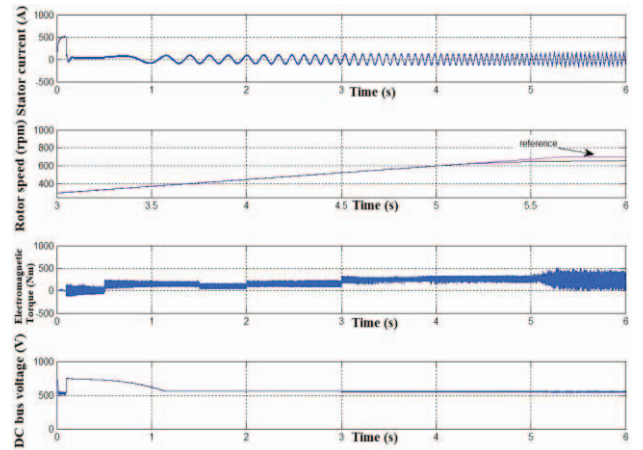


Fig. 13. The simulation of sensorless model for the set no.1 of parameters of the controllers and references.

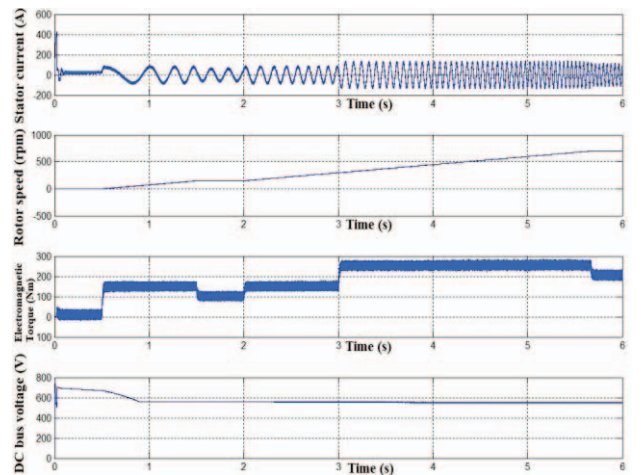


Fig. 14. The simulation of sensorless model for the set no.2 of parameters of the controllers and references.

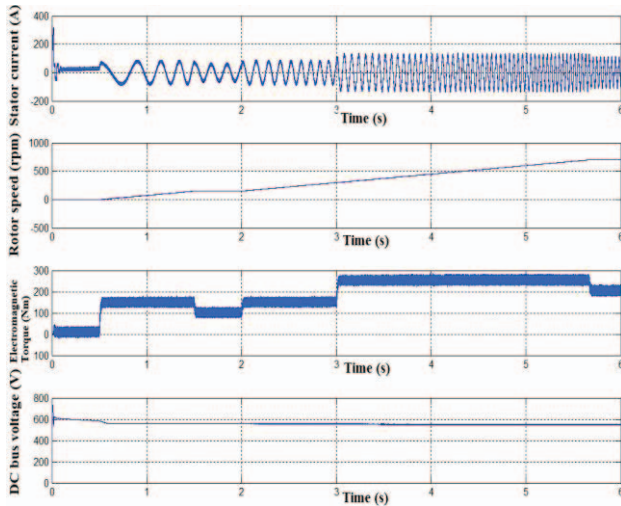


Fig. 15. The simulation of sensorless model for the set no.3 of parameters of the controllers and references.

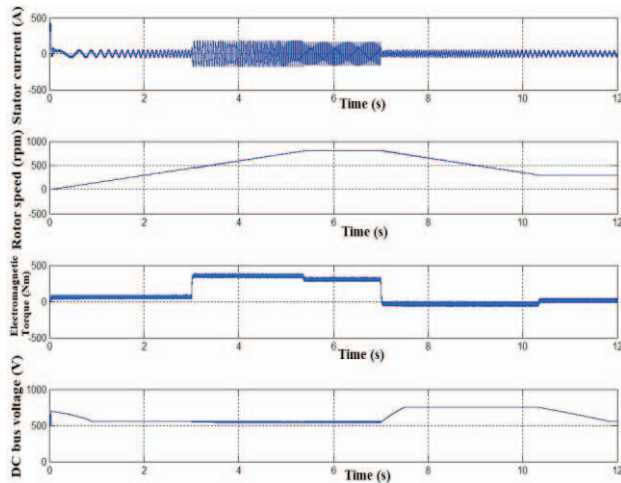


Fig. 16. The simulation of sensorless model for the set no.4 of parameters of the controllers and references.

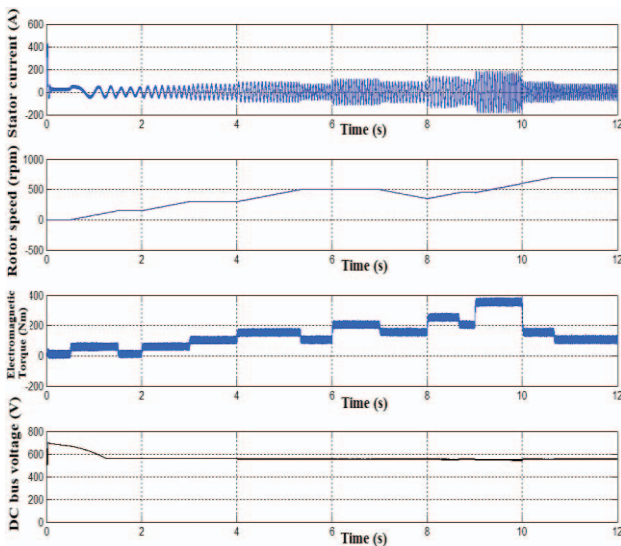


Fig. 17. The simulation of sensorless model for the set no.5 of parameters of the controllers and references.

#### IV. HARDWARE AND SOFTWARE IMPLEMENTATION

For hardware implementation of Command and Control Unit we used the DSP dsPIC33EP810MU810 Microchip. This DSP have Harvard Architecture, 70 MIPS, Acc 40bits, PWM hardware blocks, USB, SPI and ECAN interfaces.

For the three-phase diode rectifier block we used DD160N 160A / 2200V modules from Infineon and for three-phase inverter block we used LNC2W562M modules from Infineon. The current transducers are HAT 500-S from LEM with IPN = 500A, IPM=  $\pm 1500$ A and  $U_a = \pm 15$ V. The voltage transducers are LV 25-P-1000 from LEM with UPN = 10...500V and IPN = 10mA.

The block diagram of hardware implementation is presented in Fig. 18 and contain the blocks: 1- c.c. circuit, 2- three-phase main inverter, 3- synchronization block, 4- PWM block, 5- induction motor, 6- output filter, 7- PWM block for recovery inverter, 8- three-phase recovery inverter, 9- estimation block, 10- voltage controller, 11- flux controller, 12- speed controller, 13- current controller, 14- data bus. The blocks 9 to 13 are implemented software in main DSP.

An image of cabinet of hardware structure for driving application is presented in Fig. 19.

The software implementation is realized in MPLAB from Microchip. MPLAB is a integrated and development environment IDE, who contain editor, project manager, debugger, profiler and C/C++ optimizer.

The software application supply the following features:

- o Sensorless vectorially control of induction motors
- o Automatically identification of electrical motor parameters
- o Stability and fast response at fast changes of load
- o Implementation of PWM Space Vector modulation
- o Implementation of PI controllers and estimators
- o Implementation of communication with PC host.

The main software blocks are:

- o Init- make the configuration of registers and the limits of CAN converters
- o Clarke- implement the Clarke transformation
- o iClarke- implement the inverse Clarke transformation
- o Control- make the configuration of DSP
- o eCAN- make the configuration and activate the communication on CAN interface with other DSP
- o Ethet- make the configuration on Ethernet
- o Park- implement the Park transformation
- o iPark- implement the inverse Park transformation
- o Measure- implement the read and conversion of digital and analog ports
- o PI- make the configuration and implement the software PI controllers
- o Estim- implement the software estimators
- o SVgen- implement the software PWM Space Vector modulation
- o Timer- make the configuration of timers
- o Main- implement the main loop.

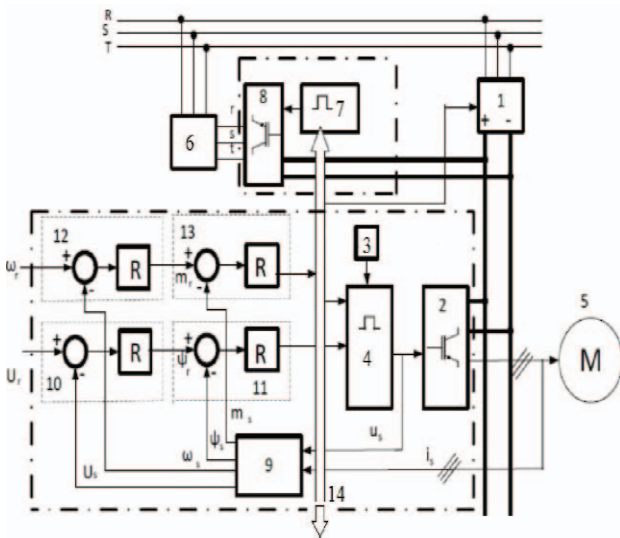


Fig. 18. Hardware block diagram.



Fig. 19. Picture of electric drives equipment.

Following [13] all the software blocks that make the control of hardware structure are implemented on DSP, resulting a functional application.

The code for software blocks are implemented in MPLAB IDE, like a C language but optimized for DSP, where in a special format data Q15, the execution speed is increased even through the replacement of divide operations (large time consumer) by the shifting bit operations (low time consumer).

When are make the implementation of the equation of speed Estimator in DSP, can appear some little errors due

the data format representation instruction and the algorithm for increasing of accuracy of estimated speed value is presented in [13].

It's worth to say that the software implementation in DSP is not a trivial task and represent the last stage and the validation of the chain: theory, design, simulation and implementation.

Similar results with those of Section III are obtained even in the case of the functional application. In Fig. 20 are presented the signals recorded on the PC host for 1 minute. The signals presented are: speed reference and speed output, output torque, DC bus voltage, output current and voltage filtered.

The reference and output speed (the brown and red line) are overlaid, indicating a very good control and stationary and dynamic performance. The prescribed and actual output frequency (running and slope frequency) are overlapping under acceleration and braking ramps. The controllers follows the prescribed values properly in both cases: increase and decrease the frequency.

Output voltage is directly proportional to engine speed, based on the operation principle of inverter the  $U/f = \text{constant}$ . Observe correct output voltage variation depending on engine speed. The current through motor is influenced by the functioning regime of drive motor (acceleration or braking) and by the variation of the shaft load (at constant speed). The variation of current is correct and correlated with the engine operating conditions.

DC voltage value from intermediate circuit is the rectified and filtered voltage value of three-phase line voltage and is influenced by the functioning regime of drive motor (motor/generator) and the current through the motor.

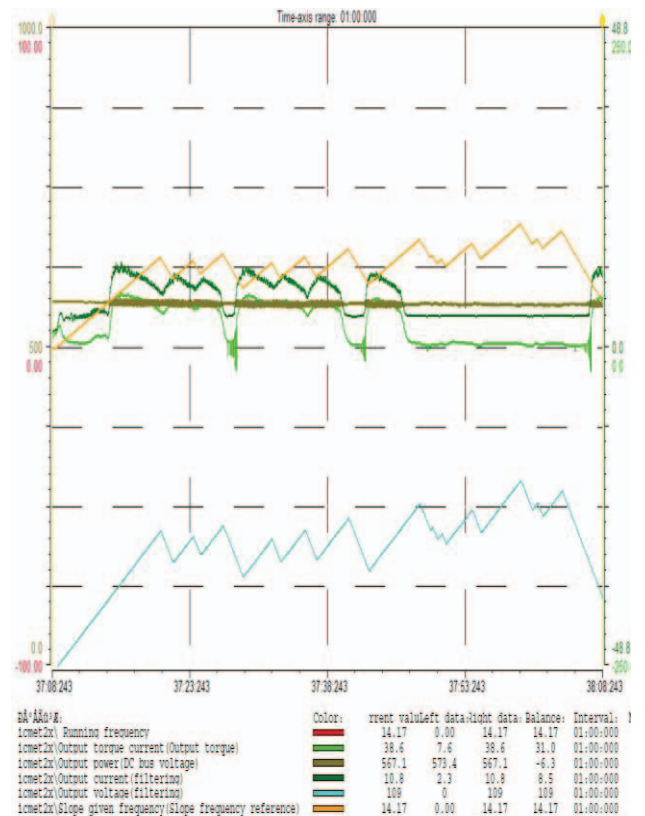


Fig. 20. Signals recorded on the PC host from driving application

It is obvious that the tuning of the controllers from the DSP will be slightly different from the one achieved through simulation, since simulations cannot identify every single mode and dynamic from practice, but the qualitative aspect will surely be maintained, and the good results achieved through simulations and the implementation of algorithms in the DSP which follow the direction of the ones in Simulink is a guarantee that the actual model will also function with good results. The practical experiment proved us this fact.

#### V. CONCLUSIONS

In this article was presented the control of electric drive with high dynamic, with rapid changes in torque and speed, where the control strategy is FOC.

Such cases were dealt with where speed is measured directly with an encoder, compared with the case of sensorless control, where speed is estimated using an Estimator and the references for speed and torque are same.

Simulations were carried out in MATLAB/Simulink environment, highlighting the control structures and comparative results achieved for a drive application commonly used in surface mining industry. Following these directions a functional application was implemented.

Due to proper tuning of the controllers the good dynamic performance are achieved, even in sensorless case for a structure of estimator like a MRAC.

The results of the research consist in the implementation of the FOC sensorless control for an industrial drive which will be offered on the market.

In future approaches, based on the results presented in this article, the problem of multi-engine drive will inherently occur, where cases of combined constant or variable speed and torque drive will be analyzed.

#### ACKNOWLEDGMENT

This work was carried out through the Partnerships in priority areas - PN II, developed with the support of MEN - UEFISCDI, project no. PN-II-PT-PCCA-2013-4-0157.

*Received on July 13, 2016*

*Editorial Approval on November 18, 2016*

#### REFERENCES

- [1] SimPowerSystem [Online]. Available: <http://www.mathworks.com/products/simpower/model-examples.html>.
- [2] A.R. Beig, G. Narayanan, and V. T. Ranganathan, "Space vector based synchronized PWM algorithm for three level voltage source inverters: principles and application to V/f drives," Proc. of IEEE Ind. Electron. Conf. (IECON'2002), pp. 1249-1254, 2002.
- [3] S.B. Veeranna, U.R. Yaragatti, and A.R. Beig, "Synchronized SVPWM algorithm for overmodulation region for three-level VSI," Proc. of IEEE Ind. Electron. Conf. (IECON'2010), pp. 1004-1010, 2010.
- [4] V. Oleschuk and G. Grandi, "Algorithms, schemes and techniques of space-vector modulation for dual-inverter systems with symmetrical multilevel phase voltage," International Review on Modelling and Simulations (IREMOS), vol. 5, no. 5, pp. 1877-1866, 2012.
- [5] V. Oleschuk, "PWM methods providing phase voltage symmetries in dual-inverter fed systems," Przegląd Elektrotechniczny (Electrical Review), vol. 89, no. 6, pp. 61-65, 2013.
- [6] N. Mohan et al., "Restructuring of first courses in power electronics and electric drives that integrates digital control," IEEE Trans. Power Electronics, Vol. 18, No. 1, pp. 429-437, Jan. 2003R.
- [7] X. M. Chen et al., "An Economical Rapid Control Prototyping System Design with Matlab/Simulink and TMS320F2812 DSP," IMECS 2010, Hong-Kong, Vol. II, March 17-19, 2010.
- [8] O.A. Mohammed, N.Y. Abed, and S.C. Ganu, "Real-time simulations of electrical machine drives with hardware-in-the-loop," in Proc. IEEE Power Engineering Society General Meeting, pp. 1-6, 2007.
- [9] A. L. Gelen and S. Ayasun, "Realization of power electronic converter based DC motor speed control methods using MATLAB/Simulink," Int. Journal on Engineering Education, Vol. 25, No. 1, pp. 33-41, 2009.
- [10] J. Rodriguez and P. Cortes, *Predictive control of power converters and electrical drives*. John Wiley & Sons, Ltd., Publication, 2012.
- [11] B.K. Bose, *Modern Power Electronics and AC Drives*. New Jersey: Prentice Hall, 2002.
- [12] G. Sieklucki, "Analysis of the transfer-function models of electric drives with controlled voltage source," Przegląd Elektrot., no. 7a, pp. 250-255, 2012.
- [13] Microchip dsPIC33EP256MU810 datasheet [Online]. Available: <http://www.microchip.com/wwwproducts/en/dsPIC33EP256MU810>.

# Monitoring and Analysis of the Electrical Parameters for an Industrial Consumer using LabVIEW Environment

Claudiu-Ionel Nicola, Viorica Voicu, Sebastian Popescu, Maria Cristina Nițu,  
Daniela Iovan, Marian Duță, Alin Benea, Silviu Andreescu

ICMET Craiova / Research, Development Division for Electric Equipment and Energy Efficiency, Craiova, Romania,  
nicolaclaudiu@icmet.ro

**Abstract** - This<sup>1</sup> paper presents a case study for monitoring the quality of electric energy in an industrial consumer. The measurements were carried in the power supply point where the quality of the electric energy is influenced by the activity of the manufacturer, the transmission and distribution provider, the supplier as well as the electric power consumer activity. Transients occur at this limiting point, with negative effects on the consumer, as well as on the electric power supply network. There are two types of electric energy quality indicators, depending on the point of occurrence. Primary quality indicators are given by the production, transport and distribution of electric energy. Secondary indicators are given by the disruptive operation of industrial consumers. The data processing was achieved using LabVIEW software in terms of the two types of quality indicators. Based on the data obtained from the measurements and using the interface created in LabVIEW, it was possible to carry out the analysis of the average hourly consumption, the power factor, the wave forms of the current and voltage, the analysis of the current and voltage harmonics. The software application enables creation of customized reports with varying ease of use and flexibility. Using the software application developed in LabVIEW, full quality analysis of electric energy can be done at the user's premises.

**Keywords:** *quality analysis, electric energy, consumer, LabVIEW environment.*

## I. INTRODUCTION

The quality of the electric energy is influenced by the activity of the manufacturer, the transmission and distribution provider, the supplier as well as the electric power consumer activity. The operation of industrial users can be accompanied by the input of significant disturbances in the electric power supply network in the form of voltage fluctuations, voltage dips and swells, unbalance which can translate into a reduction in the quality of electricity supplied to the consumers connected in the network [1].

An incident in any of these grids can lead to an interruption in the supply and / or dips that - depending on the structure of the grid - can produce effects on consumers and producers connected in a same power supply points and even further. An incident in the facilities of a manufacturer or a consumer may lead to a transient that would affect all consumers connected at the same power supply points [2], [3].

Quality indicators of electric energy, depending on the place of occurrence of disturbances are indicators of primary and secondary quality indicators.

The quality of electric energy – is assessed using quality indicators for specific electrical quantities, voltage, frequency and respectively for the electricity supply utility in terms of the duration of power failure. The quality indicators are determined at the limiting points between the electric wiring of the supplier and of the consumer which constitute the load:

- primary quality indicators (power supply frequency variations, voltage variations, dips, power failure, temporary surges, transients) are given by the production, transport and distribution of electric energy;

- secondary indicators (harmonics, interharmonics, voltage fluctuations, unbalances) are given by the disruptive operation of industrial consumers [4-7].

The values accepted for most quality indicators are standardized by energy standards and prescriptions. According to the standard of performance for the electricity supply utility with regulated tariffs, approved by ANRE's decision no. 34/1999, the supplier has the obligation to meet the following parameters of electric energy quality [8], [9]:

- frequency: during 95% of the week, the frequency must be within the range  $50 \text{ Hz} \pm 1\%$  and during 100% of the week, within the range  $50 \text{ Hz} + 4\%$  up to  $50 \text{ Hz} + 6\%$  ;

- voltage: during 95% of the week, the voltage mustn't have higher deviations than  $\pm 10\%$  of the contracted voltage. In case you are dissatisfied with the quality of the electricity, you have the right to challenge this to the provider, who has the obligation to check the quality parameters, to analyze together with the supplier solutions for providing the stipulated quality level, reporting the results of the analysis carried out and the actions that were taken.

In case of voltage deviations higher than  $\pm 10\%$  of the contracted voltage, during 95% of the week, and if the contracted frequency exceeds the  $50 \text{ Hz} \pm 1\%$  range, during 95% of the week, and the range of  $50 \text{ Hz} + 4\%$  up to  $50 \text{ Hz} + 6\%$ , during 100% of the week, you are entitled to a reduction in tariffs. The amount of tariff reductions for households is of 1% for each deviation percentage outside the stipulated quality limits.

Based on these considerations and according to Law 121/2014 on energy efficiency, industrial consumers are obliged to carry out an energy balance once every four years.

<sup>1</sup> The paper was developed with funds from the Ministry of Education and Scientific Research as part of the NUCLEU Program: PN 09 01 02 27.

In order to improve quality evaluation of energy to industrial consumers, we proposed a specialized software developed in LabVIEW that allows reading of measured data obtained from a network analyzer (in this case CHAUVIN ARNOUX - CA 8352), processing data to create a clear picture about the quality of electric energy in an industrial consumer.

The LabVIEW is a programming environment based on G language (graphic language) core intended mainly to develop applications for data control and acquisition, their analysis and results presentation. LabVIEW contains a comprehensive set of tools for acquiring, analyzing, displaying, and storing data, as well as tools to help you troubleshoot the code you write [10-14].

This paper presents a case study for monitoring the quality of electric energy in an industrial consumer using an interface developed in LabVIEW.

## II. MEASUREMENT METHOD

The energy measurements carried out on the audited outline presented in Fig. 1 were based on the use of the following three-phase power analyzer - CA 8352 power analyzer [15].

The audited outline is presented in Fig. 1

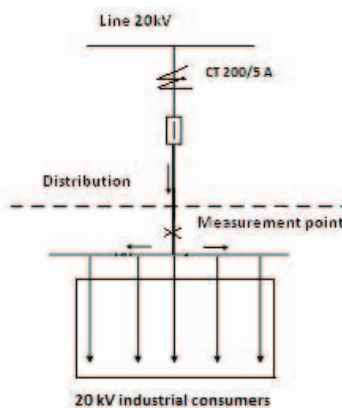


Fig. 1. Single-wire electrical circuit diagram.

The measurements were carried in the power supply point of an independent contour.

The C.A 8352 is an electrical network analysis instrument (harmonics, power, EN 50160, flicker, etc.), easy to use, this instrument can be programmed and read at the touch of the screen, in the particularly user-friendly Windows environment, includes FFT analysis functions and an oscilloscope mode for displaying curves. The instrument's configuration is defined by the user according to the option chosen: "RMS hp" (half-period) power analysis/ monitoring of minimum, maximum and average values calculated over a half-period (i.e. 10 ms) during the integration period defined; flicker measurement/ EN 50160 standard analysis; recording of transients; data logger: analogue data recording; location and recording of control and remote control signals; "Symmetry" option displaying the direct, indirect and homopolar values in U and I and indicating the unbalance of the system in terms of voltage and current/measurement and monitoring of load and short-circuit impedances on each phase of the electrical grid; remote communication via ETHERNET of the various graphic screens and the data recorded [16].

## III. DESCRIPTION OF THE SOFTWARE

The ability to analyze, interpret and manipulate data is a fundamental need in many scientific and engineering applications. LabVIEW provides built-in analysis capabilities in an integrated environment, enabling to obtain results faster. LabVIEW is the tool of choice due to its unparalleled connectivity to instruments, powerful data acquisition capabilities, natural dataflow-based graphical programming interface, scalability, and overall function completeness. One need that persists regardless of the area of expertise is the fact that users must manipulate data and measurements, and make decisions based on it.

The network analyzer CA 8352 has a software package allowing the user to download the data stored in the internal storage to a PC and using an interface developed LaVIEW, full quality analysis of electric energy can be done at the user's premises. The LabVIEW is often viewed as primarily a measurement tool, but it also provides powerful analysis libraries, routines, and algorithms that range from basic math to advanced signal processing which can be easily integrated into any LabVIEW program. The stages of the analysis achieved using the software application for the measured data of quality indicators consist of loading text files, processing, achieving graphs with their evolution in time and generating excel type reports.

According to the analysis stages the main structure used to develop the software application is flat sequence structure. Data flow for the flat sequence structure differs from data flow for other structures. Frames in a flat sequence structure execute from left to right and when all data values wired to a frame are available. The data leaves each frame as the frame finishes executing. This means the input of one frame can depend on the output of another frame.

### A. Description of the software for primary quality indicators

The software application presented in Fig. 2 we used for the performs reading of text files from the results of measurements carried out using the network analyzer for primary quality indicators. The primary quality indicators that we process are voltage, current, active power, reactive power, apparent power, power factor, active energy and reactive energy.

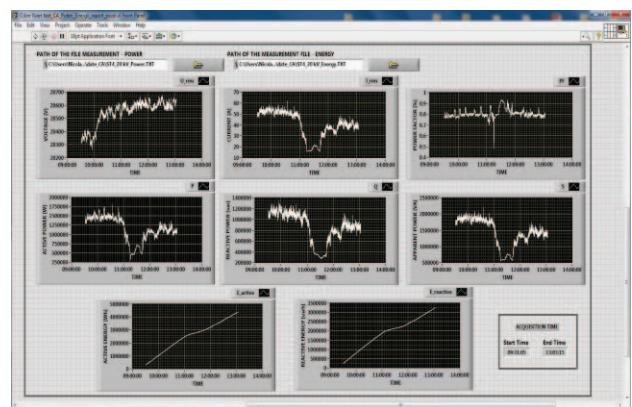


Fig. 2. The software interface for power quality.

Figure 3 shows a part of the application software block diagram with the function that performs reading from text

files to be processed mathematically. The minimum, average and maximum values of the primary quality indicators are determined and the graphs for the evolution in time are achieved for each quality parameter with the whole set of recordings, as noticed in the software interface.

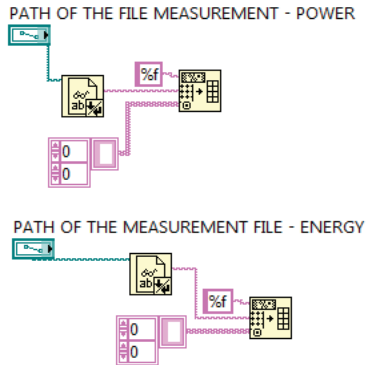


Fig. 3. Single-wire electrical circuit diagram.

Every report generation program is based on the same model. New Report.vi must be called to specify the report type (standard, HTML, Word, or Excel), and we can then populate the report with data using the VIs from the report generation function palette. Once we have completed the report, we can print, save, or e-mail it. We must close all the references at the end of the program with the Dispose Report VI.

Fig. 4 and Fig. 5 shows a part of the block diagram of the application software with the table result from processing data and the report generation of the measured data. The first table contains measured data with date and time properly.

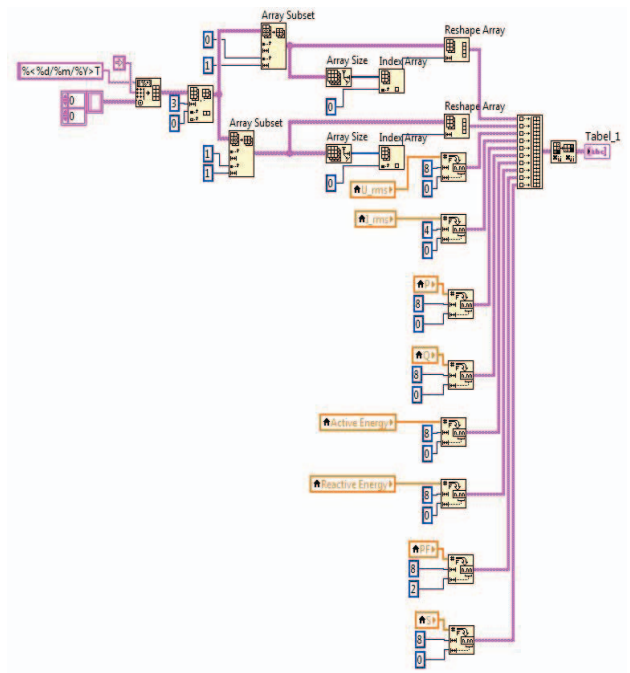


Fig. 4. Build table with measurement data.

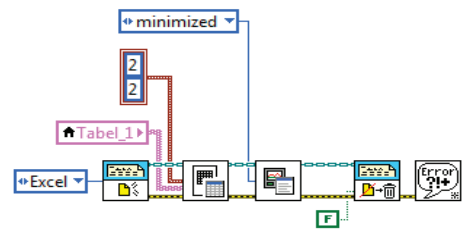


Fig. 5. Generate excel report for measured data with date and time properly.

Fig. 6 and Fig. 7 shows a part of the block diagram of the application software with the second table contains the minimum, average and maximum of the measured data and the report generation.

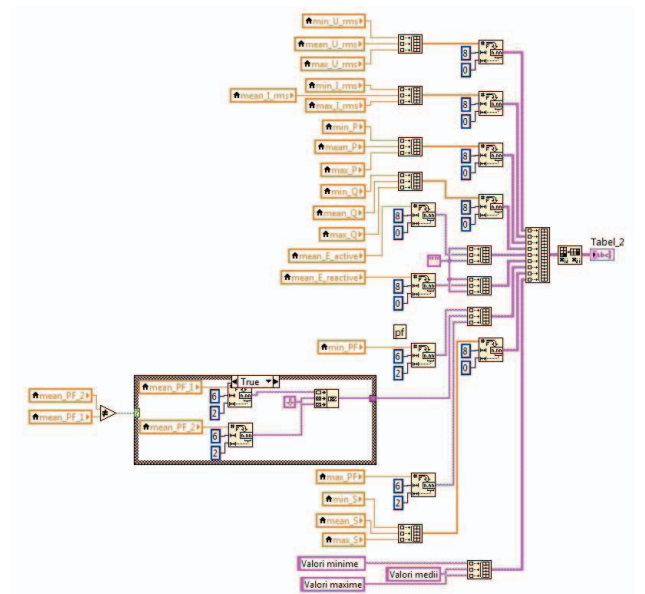


Fig. 6. Build table with processed data.

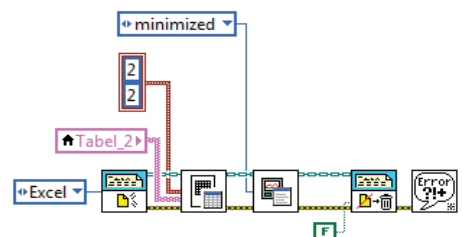


Fig. 7. Generate excel report with the processed data.

*B. Description of the software for secondary quality indicators*

The software application presented in Fig. 8 we used for performs reading of text files from the results of measurements carried out using the network analyzer for secondary quality indicators. The secondary quality indicators that we process are individual current harmonics, individual voltage harmonics, the total harmonic distortion for current and the total harmonic distortion for voltage.

LabVIEW MathScript RT Module adds math-oriented, textual programming to LabVIEW. The MathScript Node

offers an intuitive means of combining graphical and textual code within LabVIEW, both are currently used in a number of science, engineering and technology programs and industries for simulation and analysis [17], [18].

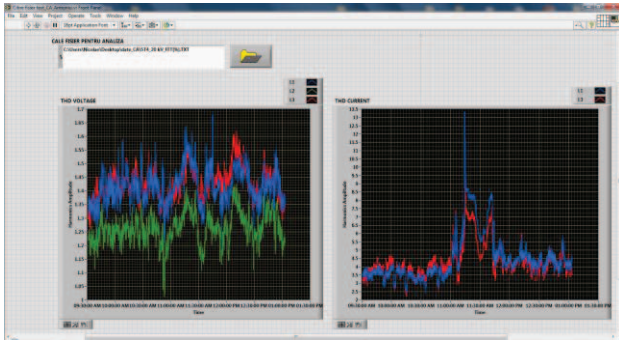


Fig. 8. The software interface for harmonic analysis.

Fig. 9 shows the MathScript node for plotting bar graph with harmonics and Fig. 10 show MathScript node for calculate means of columns and rows.

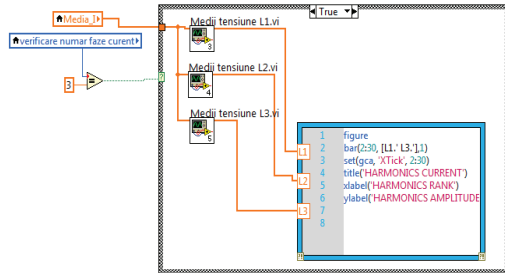


Fig. 9. Plot the bar graph with harmonics.

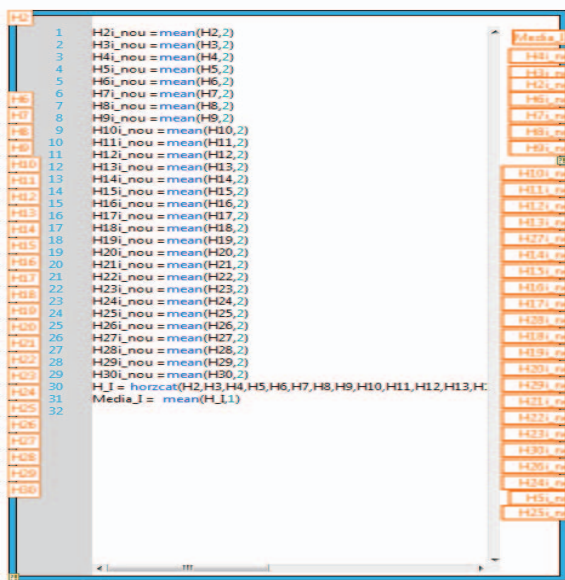


Fig. 10. MathScript Node for calculate means of columns and rows.

Fig. 11 and 12 shows a part of the block diagram of the application software with the excel report generation with individual current harmonics and individual voltage harmonics.

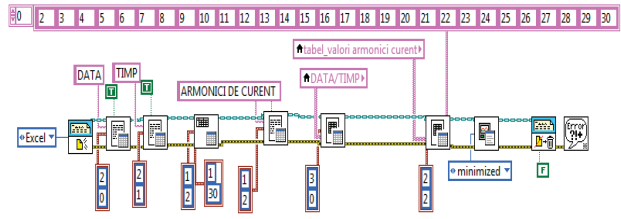


Fig. 11. Generate excel report with individual current harmonics

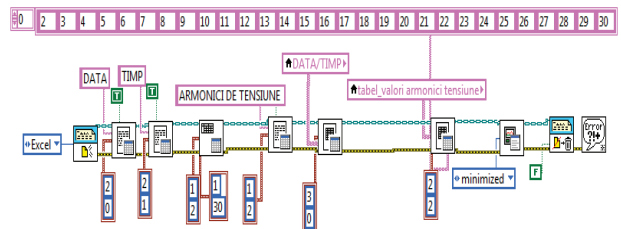


Fig. 12. Generate excel report with individual voltage harmonics.

#### IV. RESULTS OBTAINED WITH LABVIEW

The measurements were carried out at the level of 20 kV voltage on the outgoing circuit on the consumer switchboard, with a 5 seconds sampling rate of measurements.

The measurements were carried out at the level of 20 kV voltage on the outgoing circuit on the consumer switchboard, with a 5 seconds sampling rate of measurements.

Processing the measured data in LabVIEW revealed the following charts for the evolution in time of the data resulting from measurements are:

TABLE I. SUMMARY OF MEASURED AVERAGE HOURLY LEVELS OF CONSUMPTION:

Measurement point	Power supply of consumer
Voltage (V)	20543
Current (A)	40
Active Power (W)	1142405
Reactive Power L (var)	846673
Active Energy (Wh)	1142334
Reactive Energy (varh)	846593
Apparent Power (VA)	1425421
Power Factor	0.81

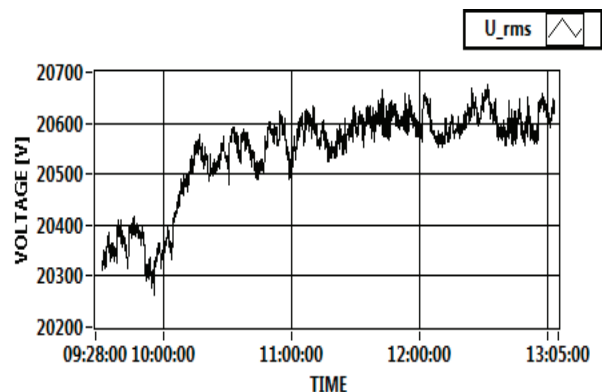


Fig. 13. Time evolution of voltage.

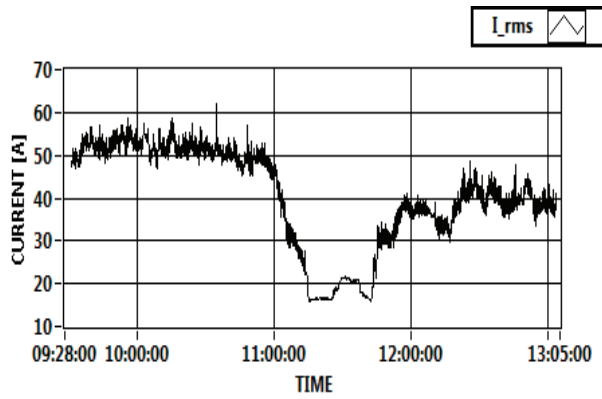


Fig. 14 Time evolution of current.

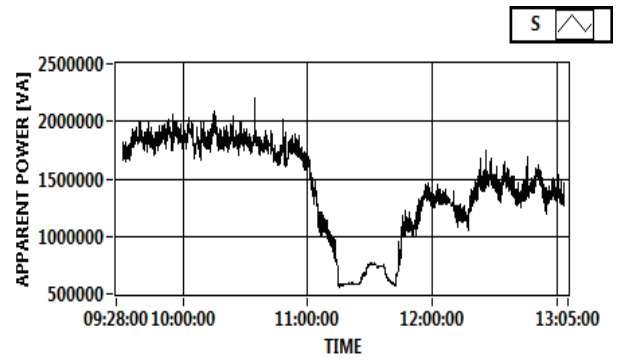


Fig.18. Time evolution of aparent power.

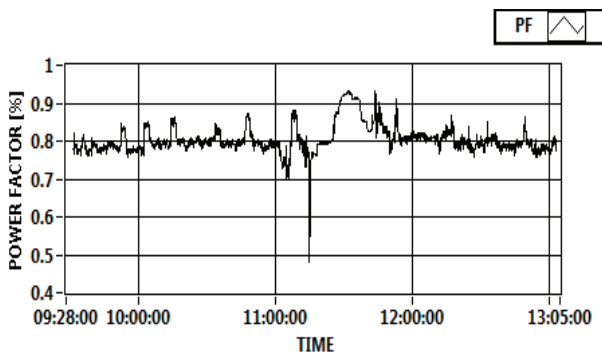


Fig. 15. Time evolution of power factor.

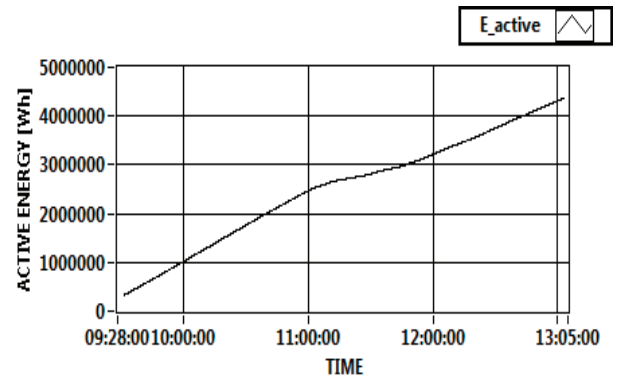


Fig. 19. Time evolution of active energy.

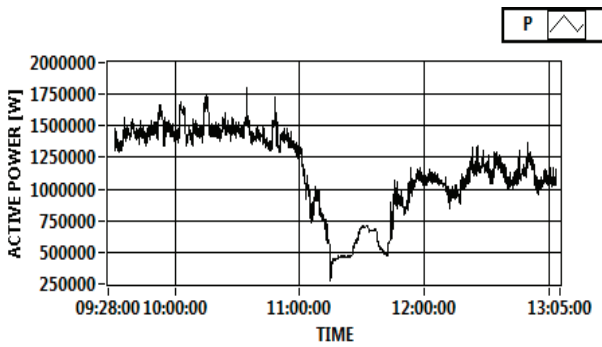


Fig. 16. Time evolution of active power.

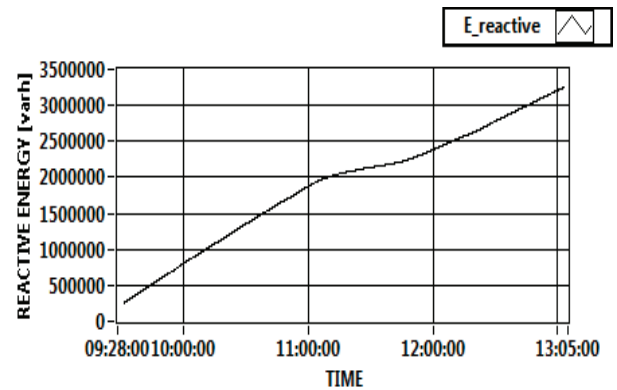


Fig. 20. Time evolution of reactive energy.

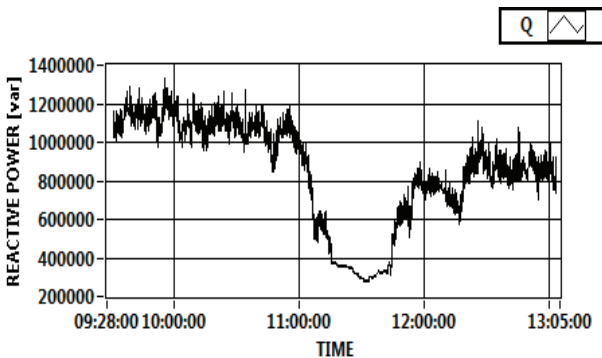


Fig. 17. Time evolution of reactive power.

TABLE II. THE HARMONIC DISTORTION CONDITION IS PRESENTED IN THE TABLE BELOW:

Circuit	General Power Distributor 20 kV
Total harmonic current distortion factor -THD <sub>i</sub> (%)	4,30
Total harmonic voltage distortion factor -THD <sub>u</sub> (%)	1,37
Individual current harmonics (%)	5- 2,32% 7- 2,04%
Individual voltage harmonics (%)	5- 1,33% 7- 0,50%

Processing the measured data in LabVIEW revealed the following charts for the evolution in time of the data resulting from measurements are:

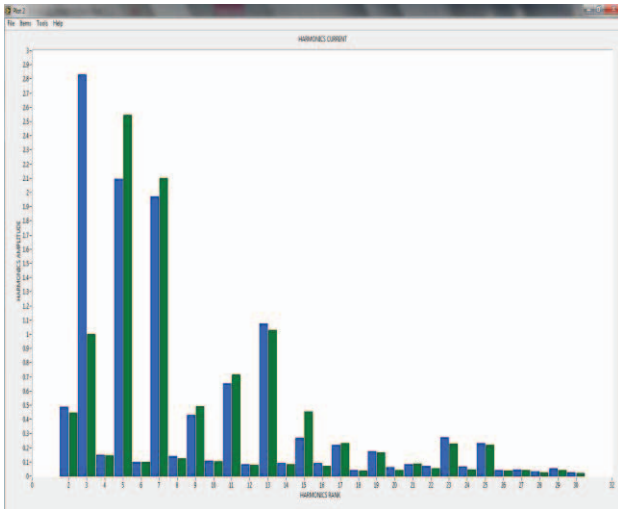


Fig. 21. Individual current harmonics.

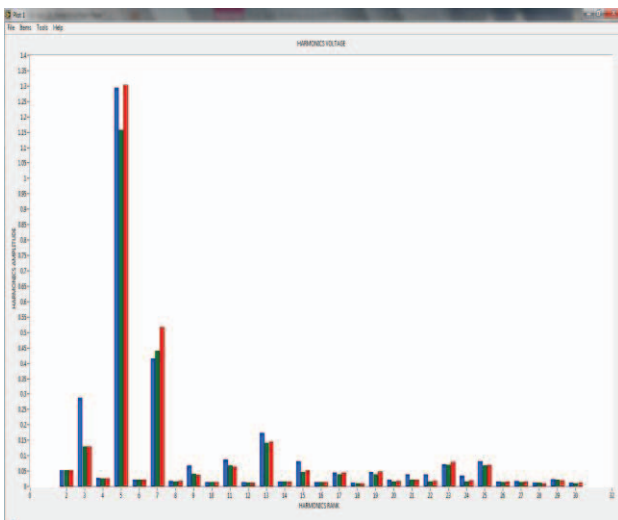


Fig. 22. Individual voltage harmonics.

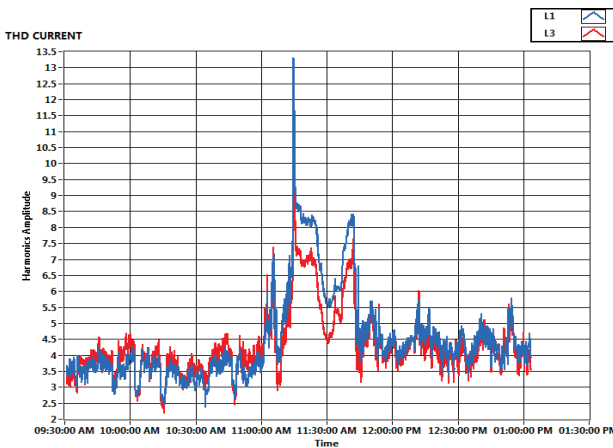


Fig. 23. Total harmonic current distortion factor -THD<sub>I</sub>.

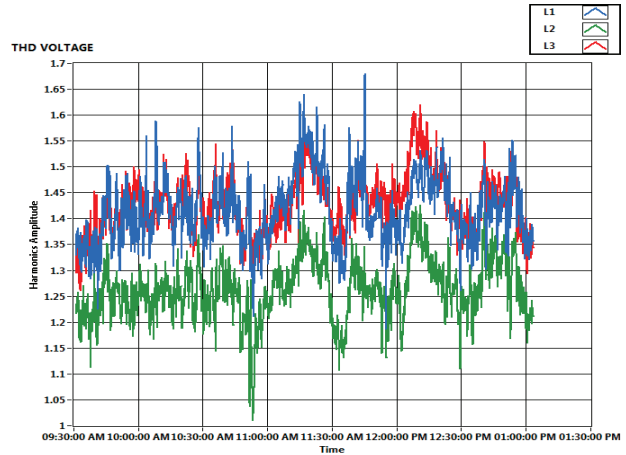


Fig. 24. Total harmonic voltage distortion factor -THD<sub>U</sub>.

From the data analysis we can conclude the following:

- in power factor metering point average is 0.81 (see table 1), situated below the neutral value (0.92);
- the total harmonic current distortion factor (THD<sub>I</sub>) in the 20 kV power supply point has a high average value of 4,30% (see table 2 and Fig. 21) and does not exceed the 15% required by the IEEE 519/2014-[16] for ratio  $I_{SC}/I_{load}=100\div1000$ ;
- the total harmonic voltage distortion factor (THD<sub>U</sub>), in the 20 kV power supply point has a high average value of 1,37% (see table 2 and Fig. 22) and does not exceed the 8% required by the IEEE 519/2014-[16].
- in the Fig. 21 may observe that harmonic 5 (2,32%) and harmonic 7 (2,04%) had the highest values of the current harmonics;
- in the Fig. 22 may observe that harmonic 5 (1,33%) and harmonic 7 (0,50%) had the highest values of voltage harmonics.

### V. CONCLUSIONS

The ability to analyze, interpret and manipulate data is a fundamental need in many scientific and engineering applications. LabVIEW provides built-in analysis capabilities in an integrated environment, enabling to obtain results faster.

The software developed in LabVIEW allows reading of measured data analyzer, processing data to create a clear picture about the quality of electric energy in an industrial consumer, full power quality analysis can be done at the user's premises [19], [20].

The data processing was achieved using LabVIEW software in terms of the two types of quality indicators. Based on the data obtained from the measurements and using the inter-face created in LabVIEW, it was possible to carry out the analysis of the average hourly consumption, the power factor, the wave forms of the current and voltage, the analysis of the current and voltage harmonics.

The software application enables creation of customized reports with varying ease of use and flexibility. Using the software application developed in LabVIEW, full quality analysis of electric energy can be done at the user's premises.

Developing the interface in LabVIEW facilitates the analysis of power quality at industrial consumer level. This can also be applied to other types of consumers.

*Received on July 19, 2016*

*Editorial Approval on November 14, 2016*

#### REFERENCES

- [1] F. Vatra, P. Postolache, and A. Poida, "Power quality - Manual for Professionals", vol.1, editura SIER, Bucuresti, March 2013.
- [2] I. Drovtar, J. Niitsoo, A. Rosin, J. Kilter and I. Palu, "Electricity consumption analysis and power quality monitoring in commercial buildings", Electric Power Quality and Supply Reliability Conference (PQ), Tartu, pp.1-6, June 2012.
- [3] C. Stanescu, F. Vatra, and A. Poida, "Power quality in romanian electricity market", Electrical Power Quality and Utilisation (EPQU)- 9th International Conference on, Barcelona, pp.1-4, October 2007.
- [4] J. Desmet, and A. Baggini, "Harmonics - Neutral Sizing in Harmonic heavily polluted installations", Copper Development Association, June 2003.
- [5] D. Chapman, "Harmonics - Causes and effects", Copper Development Association, March 2001
- [6] J. Desmet, and A. Baggini, "Harmonics - Neutral Sizing in Harmonic heavily polluted installations", Copper Development Association, June 2003.
- [7] K. L. Koo, "Power Quality Monitoring in U.K. National Grid electricity transmission system", Universities Power Engineering Conference (UPEC)- 45th International, Cardiff, Wales ,pp.1-6, September 2010.
- [8] *Voltage Characteristics of Public Distribution Systems*, Standard EN 50160, 2010
- [9] *Law 121/2014 on energy efficiency*
- [10] LabVIEW™ Basics I Course Manual, March 1998 Edition.
- [11] J. A. Baesso Grimoni, and O. S. Nakao, " Using LabVIEW in a Mini Power System Model Allowing Remote Access and New Implementations", in Proc. of International Conference on Engineering Education – ICEE, Coimbra, Portugal, , pp.1-5, September 2007.
- [12] S. Dang, R. Kakimzhanov, M. Zhang, and A. Gholamzadeh, "Smart grid-oriented graphical user interface design and data processing algorithm proposal based on LabVIEW", Environment and Electrical Engineering (EEEIC)-14th International Conference on, Krakow, pp. 323 - 327, May 2014.
- [13] A. Baloi, F. Molnar-Matei, A. Pana, F. Baloi, and F. Dilerte, "LabVIEW implementation for three-phase voltage dip classification", Electric Power Engineering (EPE)- 16th International Scientific Conference on, Kouty nad Desnou, pp.116-121. May 2015.
- [14] D.L. Brooks, R.C. Dugan, and A. Sundaram, "Using simulations to enhance PQ monitoring [of industrial power systems]", Power Engineering Society Summer Meeting, Edmonton, Alta., vol.1, pp. 476 - 480, July 1999.
- [15] *User Guide CA 8352 power analyzer*, Chauvin Arnoux, France.
- [16] *IEEE Recommended Practice and Requirements for Harmonic Control in Electric Power Systems*, IEEE STANDARD 519, 2014.
- [17] H. P. Halvorsen. (2014, Mar. 07). Introduction to LabVIEW. [Online]. Available: <http://home.hit.no/~hansha/documents/labview/training/Introduction%20to%20LabVIEW/Introduction%20to%20LabVIEW.pdf>
- [18] LabVIEW MathScript RT Module [Online]. Available: <http://www.ni.com/LabVIEW/mathscript/>
- [19] R.K. Tripathi, and C.P. Singh, "Power quality control of unregulated non-linear loads", Power, Control and Embedded Systems (ICPCES)-International Conference on, Allahabad, pp. 1-6, December 2010.
- [20] S. Nuccio, "A digital instrument for measurement of voltage flicker", Instrumentation and Measurement Technology Conference, 1997. IMTC/97. Proceedings. Sensing, Processing, Networking, Ottawa, Ont., pp. 281 - 284, May 1997.

# Modeling and Simulation of the Coal Flow Control System for the Longwall Scraper Conveyor

Olimpiu Stoicuța\*, Teodor Pană†

\*University of Petrosani / Department of Control Engineering, Computers, Electrical Engineering and Power Engineering

†Technical University of Cluj – Napoca / Department of Electrical Machines and Drives

\*[OlimpiuStoicuta@upet.ro](mailto:OlimpiuStoicuta@upet.ro), †[Teodor.Pana@edr.utcluj.ro](mailto:Teodor.Pana@edr.utcluj.ro)

**Abstract** - In this paper, the modeling and simulation of a coal flow control system for the longwall scraper conveyor is presented. The coal flow on the scraper conveyor, it is controlled by the following variables: the coal flow, advance speed and cutting speed of the longwall shearer. The electrical drive system of the longwall scraper conveyor together with the electrical drive system of the advancement and the cutting mechanism of the longwall shearer are done by means of induction motors. The control of speeds and electromagnetic torque of induction motors is realized by using sensorless vector control systems. Within these control systems, the estimation of position and of components of the rotor flux space-phasor, as well as the rotor speed of the induction motor, is done by an extended Gopinath observer. The advantages of a coal flow control system are control of productivity and also that electric motors of the flow of transport can be optimally chosen, leading ultimately to a much lower consumption of electricity for coal extraction. Modeling and simulation of control systems is done taking into account the mathematical equations that make the connection between constructive and functional parameters of the longwall shearers with the features of the strata of mining coal, specifically the coal deposits from the Jiu Valley, Romania.

**Keywords:** coal flow control system; induction motor; sensorless vector control; longwall mining; longwall shearer; scraper conveyor.

## I. INTRODUCTION

A longwall mining system consists of the longwall shearers, scraper conveyor, powered roof supports and auxiliary equipment (see Fig.1) [1].

The current technology of extracting the coal in the longwall mining is based on three main technological processes that are made with the elements of a longwall system.

The three technological processes are [1]:

- extracting and loading coal onto a conveyor (of the longwall shearers);
- the coal transport (scraper conveyor);
- the roof support longwall mining (powered roof supports).

The longwall shearers are mining machines that are designed to dislodge, break and load the broken material on the means of transport.

The automation of the longwall shearers for the cutting of the coal layers from the longwall face is done in order to achieve the following objectives: achieving maximum

productivity; getting minimum energy consumption; protection of electric motors and removing the human operator.

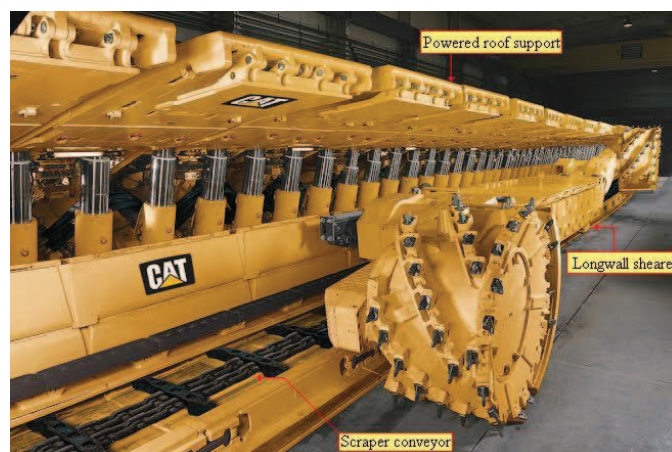


Fig. 1. The elements composing the longwall mining system [2].

Until now, the vast majority of firms producing the longwall shearers have partially solved the objectives mentioned above.

The constant control of the flow of coal on the scraper conveyor currently accounts for one of the most important issues in the field of automation of longwall systems.

The main objective of the article is presentation and analysis of a new control system for the flow of coal on the scraper conveyor of the longwall system. Automatic control of the flow of coal on the scraper conveyor is made by means of a control system where in the main loop there is a flow of coal, while the secondary loop is for advancement and cutting speed of the longwall shearers. The advancement and the cutting speed are considered components of the input vector of the longwall shearers, regarded by the control theory as an element execution. The control systems of induction motors speeds in the conveyor system, advancement system and the cutting system are built based on a sensorless vector control systems with direct rotor flux orientation.

Position estimation and dq components of rotor flux space-phasor, as well as the rotor speed of the induction motor are built on an extended Gopinath observer (EGO).

The constant control of the flow of coal on the scraper conveyor offers the optimal choice for the induction motors and of the gear reducers from the conveyor system of coal.



$$v_t^* = \frac{k_b \cdot \tan(\psi)}{2 \cdot d - b} \cdot v_a^* \quad (7)$$

$$\omega_r^* = \frac{i_T}{R_a} \cdot v_r^* \quad (8)$$

The block diagram of the control system for the cutting speed, respectively of the advance speed, are shown in Fig.4.

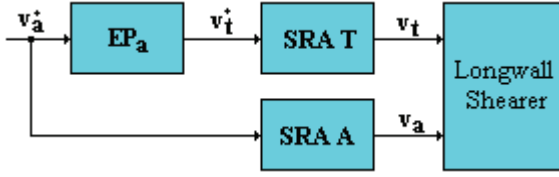


Fig.4. The block diagram of the optimal of the speed control system.

The control system shown in Fig.4, allows for the control of the maximum splinter thickness cut by controlling the advancement speed as well as the cutting speed [3]. In Fig. 4, by the “SRA T” and “SRA A” is noted cutting speed control system, respectively, advance speed control system.

### III. THE CUTTING SPEED CONTROL SYSTEM

This system is intended for dislocation of coal from the massive and for the coal loading onto the conveyor.

The drive of the cutting organs is usually done with the help of squirrel cage induction motors ( $M_1$  and  $M_2$ ), located inside cutting arms.

The electromagnetic torques developed by electric motors are submitted to the cutting organs (1 and 2), through some planetary transmissions and the coupling elements located inside the arms. The cutting control system of longwall shearers is presented in Fig 5.

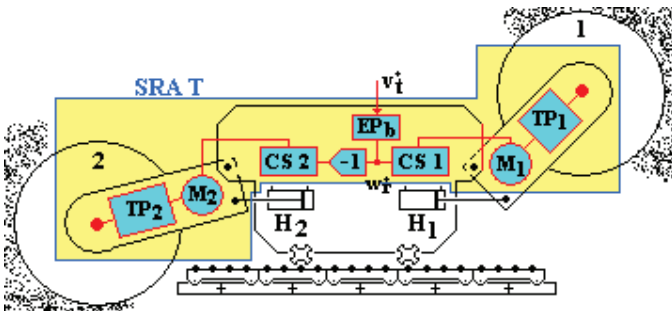


Fig.5. The block diagram of the cutting speed control system (SRA T).

The cutting organs are in form of a helicoidal rotor, and the cutting knives are arranged in a helicoidal shape.

The planetary transmissions  $TP_1$  and  $TP_2$  are considered identical, having an equal transmission report (see Fig.6).

In this paper,  $TP_1$  and  $TP_2$  the planetary transmissions are considered identical to the planetary transmissions of the longwall shearer KSW-460NE (see Fig.6). The control of speeds and electromagnetic torque of induction motors ( $M_1$  and  $M_2$ ) is realized using a sensorless vector control systems ( $CS_1$  and  $CS_2$ ). On the other hand, to be able to control the same speed for both cutting organs, the prescribing element of the two tuning systems ( $CS_1$  and  $CS_2$ ), has to be the same.

The prescribing element ( $EP_b$ ) is defined by the following relation:

where  $R_a = D/2$ ,  $D$  is the diameter of the cutting organs measured from the tip of the splintering knife and  $i_T$  is the gear ratio for  $TP_1$  and  $TP_2$ .

The gear ratio of the  $TP_1$  and  $TP_2$ , presented in the Fig. 6, is calculated by the following formula:

$$i_T = \left(1 + \frac{z_3}{z_1}\right) \cdot \frac{z_5}{z_4} \cdot \frac{z_{10}}{z_6} \cdot \left(1 + \frac{z_{13}}{z_{11}}\right) \quad (9)$$

where:  $z_i$  is the number of teeth in the gears.

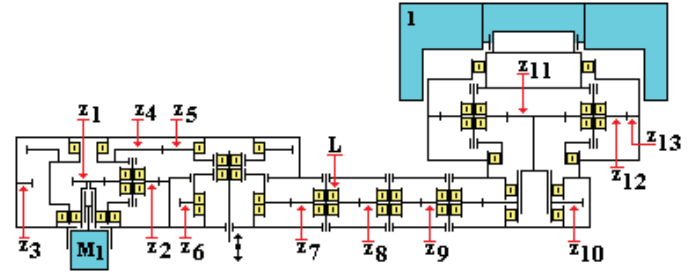


Fig.6. The block diagram of the planetary transmission  $TP_1$  [4].

The equations that define the planetary transmissions ( $TP_1$  and  $TP_2$ ), are:

$$\omega_k^{out} = \frac{\omega_k^{in}}{i_T} \quad (10)$$

$$M_T^{out} = \eta_T \cdot i_T \cdot M_e \quad (11)$$

where:  $k = \{1, 2\}$ ;  $M_e$  is electromagnetic torque of the induction motor ( $M_1$  or  $M_2$ );  $M_T^{out}$  is torque at the shaft of the cutting organs (1 and 2);  $\eta_T$  is the total efficiency of the planetary transmission ( $TP_1$  or  $TP_2$ ).

### IV. THE ADVANCE SPEED CONTROL SYSTEM

This system is intended for the displacement of the longwall shearers during work and mining of various maneuvers as well as for the maintenance of a permanent contact between the cutting body and massive. The displacement of the longwall shearers during operation can be done through some type of advancement systems, either mechanical, hydraulic or electric. If the case in which the coal layers have a small or medium tilt, the actuating system of the advance system component is mounted on the longwall shearers.

In recent years, the vast majority of the longwall shearers for the coal strata that have had a small or average inclination, having an advancement system that is electrically powered, generally a drive through two induction motors ( $M_L$  and  $M_R$ ). The torque developed by the electric motor is transmitted to the advance mechanism mechanical with planetary equipment ( $TP_L$  and  $TP_R$ ), see Fig.7. Between the advancement mechanisms, the most commonly used in European Union countries are: Rollrack mechanisms, Eicotrack and Dynatrack.

In this article, the drive system chosen for analysis is an electric one, developed around the two induction motors, and the advancement mechanism is of Eicotrack type.

The Eicotrack advance mechanism has been developed by the Eickhoff company and consists of two pinions - driving ( $R_L$  and  $R_R$ ) that enter in gearing with a rack gear (3) fixed on the edge of the conveyor (rack and pinion mechanism). The pinions - driving are driven through planetary transmission and the two electric motors, see Fig.7. The raising and the lowering arms, on which are mounted cutting organs is usually done by means of hydraulic actuators ( $H_1$  and  $H_2$ ).

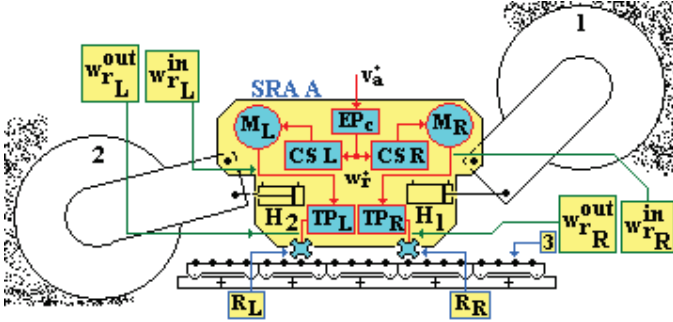


Fig.7. The block diagram of the advance speed control system (SRA A).

In the case of the advancement mechanisms, the rack pin has a circular profile and the tooth of the wheel has evolventic profiles, the line of gearing is determined by line (d), what is defined by the point of contact (P) and the axis pin (A), see Fig.8.

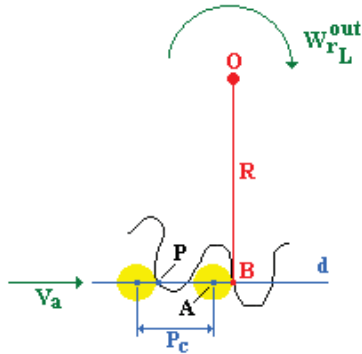


Fig.8. The interaction mode of the pinion with rack [3].

The rack with bolts that has the step ( $P_c$ ) it is mounted into space exploited what improves the loading conditions of the coal on the conveyor while it eliminates the dangers of blocking. In the case of the advancement mechanism, the items located in the gear have the above mentioned profiles and advancement speed is given by the next relation

$$v_a = R \cdot \omega_{rL}^{out} \quad (12)$$

where  $\omega_{rL}^{out}$  is the angular speed of the leader element, and  $R$  is the distance between points  $O$  and  $B$  what is constant during the whole phase of gearing.

The control of speeds and electromagnetic torque of induction motors ( $M_L$  and  $M_R$ ) is realized using the sensorless vector control systems ( $CS_L$  and  $CS_R$ ).

The prescribing element ( $EP_c$ ) of the two control systems is the same and is defined by the following relation:

$$\omega_r^* = \frac{i_A}{R} \cdot v_a^* \quad (13)$$

where  $R$  is the distance between the points  $O$  and  $B$ , and  $i_A$  is the gear ratio for  $TP_L$  and  $TP_R$ .

In this paper,  $TP_L$  and  $TP_R$ , the planetary transmissions, are considered identical to the planetary transmissions of the longwall shearer KSW-460NE (see Fig.9).

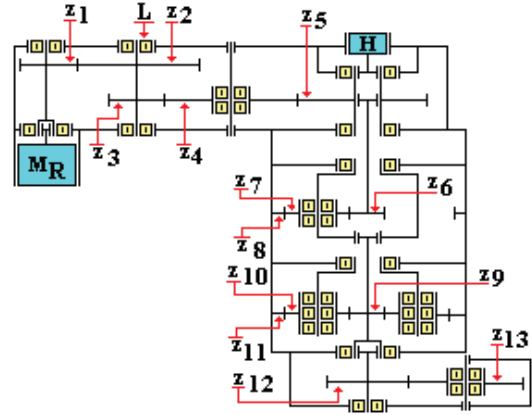


Fig.9. The block diagram of the planetary transmission  $TP_R$  [4].

The gear ratio of the  $TP_L$  and  $TP_R$ , presented in the Fig. 9, is calculated by the following formula

$$i_A = \frac{z_2 \cdot z_4 \cdot z_5}{z_1 \cdot z_3 \cdot z_4} \left( 1 + \frac{z_8}{z_6} \right) \cdot \left( 1 + \frac{z_{11}}{z_9} \right) \cdot \frac{z_{13}}{z_{12}} \quad (14)$$

where:  $z_i$  is the number teeth of the gears.

The equations that define the planetary transmissions ( $TP_L$  and  $TP_R$ ), are:

$$\omega_k^{out} = \frac{\omega_r^{in}}{i_A} \quad (15)$$

$$M_a^{out} = \eta_a \cdot i_A \cdot M_e \quad (16)$$

where:  $k = \{L, R\}$ ;  $M_e$  is electromagnetic torque of the induction motor ( $M_L$  or  $M_R$ );  $M_a^{out}$  is torque at the shaft of the pinion ( $R_L$  or  $R_R$ );  $\eta_a$  is the total efficiency of the planetary transmission ( $TP_L$  or  $TP_R$ ).

## V. THE SENSORLESS VECTOR CONTROL SYSTEM

The automatic control of the advancement speed and of the cutting speed is done through the speeds control systems of the induction motors from the component of the advancement and cutting system of the longwall shearers. In the article, the speed control of the induction motors is built on sensorless vector control systems, with direct orientation after the rotor fluxes (see  $CS_1$ ,  $CS_2$ ,  $CS_L$  and  $CS_R$  in the previous figures).

Within these control systems, the estimation of the position and dq components of the rotor flux space-phasor, as well as the rotor speed of the induction motor, are done by an

extended Gopinath observer (EGO) [5]. The control systems of induction motor speeds in the mining machines are of the same type. The block diagram of a speed control system for induction motors is presented in Fig. 10.

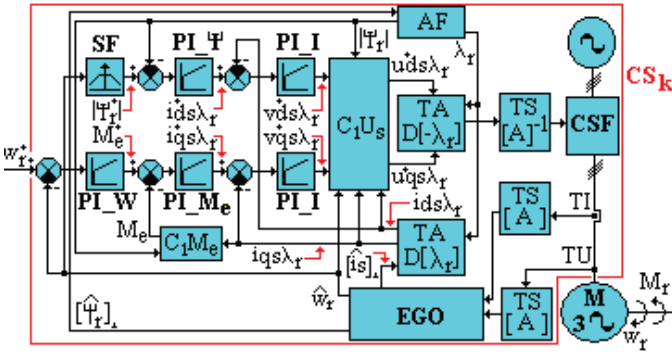


Fig.10. The sensorless vector control system of the speed induction motor.

In the following, we will present the mathematical equations that define the main blocks of the control system [3], [5], presented in Fig. 10.

- *The analyzer block of the rotor flux phasor (AF).* The equations defining the phasor module and position of the rotor flux are:

$$\psi_r = |\underline{\psi}_r| = \sqrt{\psi_{dr}^2 + \psi_{qr}^2} \quad (17)$$

$$\sin \lambda_r = \frac{\psi_{qr}}{\psi_r}; \quad \cos \lambda_r = \frac{\psi_{dr}}{\psi_r} \quad (18)$$

- *Extended Gopinath Observer (EGO).* The equations that define this type of observer are presented on the following relations [5]

$$\frac{d}{dt} x = A_a \cdot x + A_b \cdot x + B \cdot u + \underline{G} \cdot C \cdot \frac{d}{dt} e_x \quad (19)$$

$$\hat{\omega}_r(t) = k_R \cdot \varepsilon(t) + \frac{k_R}{T_R} \cdot \int_0^t \varepsilon(\tau) \cdot d\tau \quad (20)$$

where  $x = [i_s \quad \underline{\psi}_r]^T$ ;  $\hat{x} = [\hat{i}_s \quad \hat{\underline{\psi}}_r]^T$ ;  $e_x = x - \hat{x}$ ;

$$A_a = \begin{bmatrix} a_{11}^* & a_{12}^* \\ 0 & a_{22}^* \end{bmatrix}; A_b = \begin{bmatrix} a_{21}^* & 0 \\ a_{31}^* & 0 \end{bmatrix}; B = \begin{bmatrix} b_{11}^* \\ 0 \end{bmatrix}; \underline{G} = \begin{bmatrix} 0 \\ \underline{g} \end{bmatrix}; C = [1 \quad 0];$$

$$a_{11}^* = a_a^* + a_b^*; a_{21}^* = a_{31}^*; a_{31}^* = \frac{L_m^*}{T_r^*}; a_{12}^* = a_{13}^* - j \cdot a_{14}^* \cdot z_p \cdot \omega_r;$$

$$a_{22}^* = a_{33}^* + j \cdot z_p \cdot \omega_r; a_{33}^* = \frac{-1}{T_r^*}; b_{11}^* = \frac{1}{L_s^* \cdot \sigma^*};$$

$$a_{13}^* = \frac{L_m^*}{L_s^* \cdot L_r^* \cdot T_r^* \cdot \sigma^*}; a_{14}^* = \frac{L_m^*}{L_s^* \cdot L_r^* \cdot \sigma^*}; T_s^* = \frac{L_s^*}{R_s^*}; T_r^* = \frac{L_r^*}{R_r^*};$$

$$\sigma^* = 1 - \frac{(L_m^*)^2}{L_s^* \cdot L_r^*}; a_a^* = -\frac{1}{T_s^* \cdot \sigma^*}; a_b^* = -\frac{1 - \sigma^*}{T_r^* \cdot \sigma^*};$$

$$\begin{aligned} \varepsilon &= e_1 \cdot \psi_{qr} - e_2 \cdot \psi_{dr}; e_1 = i_{ds} - \hat{i}_{ds}; e_2 = i_{qs} - \hat{i}_{qs}; \\ u &= \underline{u}_s; \hat{i}_s = i_{ds} + j \cdot i_{qs}; \underline{\psi}_r = \psi_{dr} + j \cdot \psi_{qr}; \underline{u}_s = u_{ds} + j \cdot u_{qs}; \\ \hat{i}_s &= \hat{i}_{ds} + j \cdot \hat{i}_{qs}; \hat{\underline{\psi}}_r = \hat{\psi}_{dr} + j \cdot \hat{\psi}_{qr}; \underline{g} = g_a + j \cdot g_b. \end{aligned}$$

The coefficients which define the Gopinath matrix G, are [5]:

$$g_a = -k \cdot \frac{a_{31}^* \cdot a_{33}^*}{(a_{33}^*)^2 + (z_p \cdot \omega_r)^2} \quad (21)$$

$$g_b = k \cdot \frac{a_{31}^* \cdot z_p \cdot \omega_r}{(a_{33}^*)^2 + (z_p \cdot \omega_r)^2} \quad (22)$$

where  $k$  is a coefficient of proportionality ( $k > 0$ ).

In the above relations, we marked with „\*”, the electrical parameters, determined experimentally, of the induction motor.

The dynamic controlling of the speed observer is done via constants  $k_R$  and  $T_R$ . The other blocks of Fig.10, are presented in detail in [5], [6].

## VI. THE COAL FLOW CONTROL SYSTEM

The constant control of the flow of coal on the scraper conveyor currently accounts for one of the most important issues in the field of automation of longwall systems.

The most significant consumption of electricity in coal exploitation in mining of coal is due to electric motors in the transmission of coal flow in an underground silo, and then, with the help of the extraction machine, at the surface.

The electric motors from the conveyor flux component are oversized, which entail a very high consumption of electric energy.

The advantage of a system to control the flow of coal on the scraper conveyor is that electric motors from the flow of transport can be optimal chosen, leading ultimately to a much lower consumption of electricity for coal extraction.

In order to design the control system of the flow of coal on the scraper conveyor, in the following we will define the masic flow rate cut by the longwall shearer. It is given by the following relation:

$$Q_c = \rho_a \cdot v_a \cdot A_a \cdot \delta(v_i) \quad (23)$$

where  $Q_c$  is the masic flow of coal that is achieved by the longwall shearer,  $A_a = B \cdot H$  the domain of the area exploited,  $B$  is the width cuted of the longwall shearer,  $H$  is the height cuted of the longwall shearer,  $\rho_a$  is the average density of coal, and  $v_a$  is the advance speed of the longwall shearer,  $\delta$  is Kronecker function.

The flow of loading coal on the scraper conveyor using two cutting devices is given by the following relation [7]:

$$Q_i = k_c \cdot \rho_a \cdot v_i \cdot A_b \quad (24)$$

where  $Q_i$  is the mass of coal loaded on the scraper conveyor,  $A_b = \pi \cdot (R_a^2 - R_b^2)$  is the area of the snail section;  $R_a$  is the radius of the cutting;  $R_b$  is the radius of the hub cutting organs;  $v_t$  is the cutting speed;  $\rho_a$  is the average density of coal;  $k_c$  is a dimensionless coefficient.

Under these conditions, in the dynamical regime can write the following differential equation:

$$Q_c(t) - Q_i(t) = \frac{dM(t)}{dt} \quad (25)$$

where  $M$  is the mass of accumulated coal on the hearth between the conveyor and the coal massive.

In the context of the relationship (25) is observed that, in order to reduce the mass of coal left on the hearth, the mass flow rates must satisfy the following equality  $Q_c \cong Q_i$ .

Under these conditions, the equality  $Q_c \cong Q_i$ , can be put under the following form

$$v_t \cong \frac{A_a}{k_c \cdot A_b} \cdot v_a \quad (26)$$

The relation (26) has an essential role in the proposed control system. From relation (26) and (7), obtain:

$$\frac{k_b \cdot \tan(\psi)}{2 \cdot d - b} \cong \frac{A_a}{k_c \cdot A_b} \quad (27)$$

If the relationship (27) is respected, remaining coal mass variation is very small.

In these conditions, the load per unit length of the scraper conveyor is given by the following relations:

$$q = \frac{Q_c}{v_t} = \rho_a \cdot A_a \cdot \frac{v_a}{v_t} \cdot \delta(v_t) \quad (28)$$

In the context of the relation (28), coal load per unit length of the scraper conveyor can be controlled on the basis of the ratio of the advancement speed and the cutting speed, respecting the condition (7) and (27).

In order to control the mass flow of coal on the scraper conveyor, in the following we will keep in mind that the mass flow rate of the conveyor is given by the following relation

$$Q_r = q \cdot v_r \quad (29)$$

where  $q$  is the loads of charcoal per unit length of the conveyor and  $v_r$  is the speed of the conveyor.

In the relation (29) is observed that when the speed  $v_r$ , is maintained constant, mass flow control of coal on the scraper conveyor can be done by modifying the cargo of coal per unit length of the conveyor. In other words, the mass flow rate control of the conveyor is provided by means of the ratio between the advance speed and the cutting speed.

The mass flow measurement of coal that is at some point of time on the conveyor is provided by means of a scale with continuous measurement (FT).

On the other hand, is observed that when the conveyor speed is chosen based on the following relation:

$$v_r^* = \frac{v_a^*}{2} \quad (30)$$

the mass flow of coal from the conveyor is:

$$Q_r = \rho_a \cdot A_a \cdot \frac{v_a}{2} \cdot \delta(v_t) \quad (31)$$

The relation (31) reveals that the mass flow of coal from the conveyor can be controlled directly through the advancement speed, if the expression (30) is satisfied.

The speed control system of the conveyor is presented in Fig.11 [3].

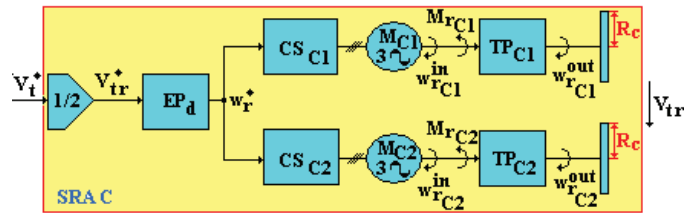


Fig.11. The block diagram of the speed control system of the conveyor.

The system consists of two conveyors ( $T_1$  and  $T_2$ ), electrically operated through two induction motors ( $M_{C1}$  and  $M_{C2}$ ).

The speed of the two induction motors is controlled via two sensorless vector control systems ( $CS_{C1}$  and  $CS_{C2}$ ).

The control systems for the speed of the induction motors in the scraper conveyors component have the same form as in Fig.10.

The electromagnetic torques and the speeds of the two induction motors are submitted to the drive mechanisms of the conveyors, using the planetary transmissions ( $TP_{C1}$  and  $TP_{C2}$ ).

On the other hand, the prescribing element ( $EP_d$ ) of the speed of the two control systems is defined by the following relation

$$\omega_r^* = \frac{i_r}{R_c} \cdot v_r^* \quad (32)$$

where  $i_r$  is the gear transmission ratio for  $TP_{C1}$  and  $TP_{C2}$ , and  $R_c$  is the reel radius by drive.

The equation that define the planetary transmissions ( $TP_{C1}$  and  $TP_{C2}$ ), is identical with (32).

The block diagram of the control system of the mass flow of coal, of the scraper conveyor, based on equation (31), is shown in Fig. 12.

The automatic controller of the mass flow ( $PI_F$ ), is one of the integral proportional type.

The weighing scale is placed on the scraper conveyor, located outside the hewing coal.

Due to the above considerations, the mathematical model is affected by a dead time.

The dead time can be calculated as in the following relation:

$$T_m = \frac{L_c(t)}{v_{tr}} \quad (33)$$

where  $L_c(t) = L_a(t) + L_b$  is distance (the position) of the longwall shearer compared with the measurement element to the flow mass (the weighing scale conveyor).

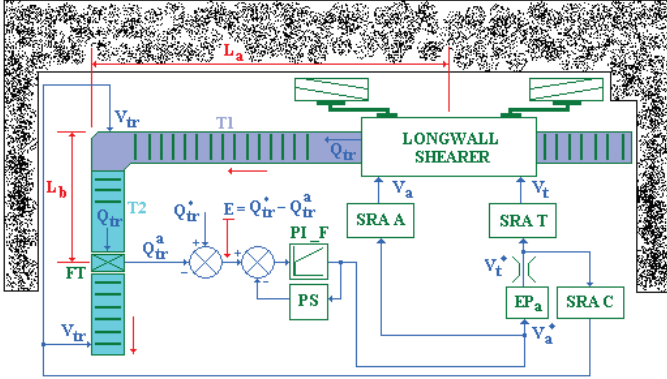


Fig. 12. The coal flow control system of on the scraper conveyor [3].

The coal flow  $Q_{tr}^a$  (see Fig.12), is affected by a dead time. The mathematical equation that define this flow of coal, is:

$$Q_{tr}^a(s) = Q_{tr}^s(s) \cdot e^{-T_m s} \quad (34)$$

where  $T_m = L_c/v_{tr}$ ;  $L_c = L_a + L_b$ ;  $L_b$  is a constant distance and the  $L_a$  is a variable distance.

In the relation (34), variable  $s \in C$  it results from applying Laplace transform. To compensate for dead time effects, we use the control strategy that uses a Smith predictor (SP) [8].

## VII. ANALYSIS BY SIMULATION OF THE CONTROL SYSTEM

The simulation of the control system proposed is based on the equations presented in the article and the block diagram in Fig. 12. The simulation is performed in Matlab-Simulink [9], [10]. In the simulation of the control systems at the advancement and cutting speeds of the longwall shearer, are taken into account the dynamic effects introduced by static frequency converter (CSF). Switching frequency of the IGBT transistors in the inverter is 2 kHz. The equations that define the resistance torques are presented in detail in [3].

The electrical and mechanical parameters of the induction motor from the control system component of the flow of the coal are presented below:

- the electrical and mechanical parameters of the induction motors from the advancement system:

$$\begin{aligned} P_n &= 45[\text{kW}]; U_n = 440[\text{V}]; I_n = 74[\text{A}]; z_p = 2; \\ n_n &= 1459[\text{rot/min}]; M_n = 295[\text{N}\cdot\text{m}]; L_s = L_r = 0.0253[\text{H}]; \\ L_m &= 0.024823[\text{H}]; R_s = 0.229133[\Omega]; R_r = 0.096662[\Omega]; \\ J &= 0.17[\text{kg}\cdot\text{m}^2]; F = 0.028[\text{N}\cdot\text{m}\cdot\text{s/rad}]; \eta_n = 90[\%]; \\ f_n &= 50[\text{Hz}]; \cos(\varphi) = 0.98 \end{aligned}$$

- the electrical and mechanical parameters of the induction motors from the cutting system:

$$\begin{aligned} P_n &= 200[\text{kW}]; U_n = 1000[\text{V}]; I_n = 155[\text{A}]; z_p = 2; \\ n_n &= 1470[\text{rot/min}]; M_n = 1300[\text{N}\cdot\text{m}]; L_s = L_r = 0.0224[\text{H}]; \\ L_m &= 0.021507[\text{H}]; R_s = 0.137388[\Omega]; R_r = 0.083842[\Omega]; \\ J &= 2.2[\text{kg}\cdot\text{m}^2]; F = 0.06[\text{N}\cdot\text{m}\cdot\text{s/rad}]; \eta_n = 93.5[\%]; \\ f_n &= 50[\text{Hz}]; \cos(\varphi) = 0.8 \end{aligned}$$

- the electrical and mechanical parameters of the induction motors from the scraper conveyors:

$$\begin{aligned} P_n &= 200[\text{kW}]; U_n = 1000[\text{V}]; I_n = 142[\text{A}]; z_p = 2; \\ n_n &= 1480[\text{rot/min}]; M_n = 1290[\text{N}\cdot\text{m}]; L_s = L_r = 0.0273[\text{H}]; \\ L_m &= 0.026736[\text{H}]; R_s = 0.14769[\Omega]; R_r = 0.058708[\Omega]; \\ J &= 5.8[\text{kg}\cdot\text{m}^2]; F = 0.065[\text{N}\cdot\text{m}\cdot\text{s/rad}]; \eta_n = 94.5[\%]; \\ f_n &= 50[\text{Hz}]; \cos(\varphi) = 0.86 \end{aligned}$$

The mechanical parameters of the gears and the main technical data of the longwall shearer and scraper conveyor are given below:

- The gear ratios of the gear units:  $i_A = 196.185$ ;  $i_T = 36.725$ ;  $i_r = 33$ .
- The radius of the wheels drive:  $R_a = 0.6[\text{m}]$ ;  $R = 0.179[\text{m}]$ ;  $R_c = 0.23[\text{m}]$ ;  $R_b = 0.225[\text{m}]$ .
- The other parameters used in the simulation are:  $c = 2$ ;  $d = 0.05[\text{m}]$ ;  $b = 0.015[\text{m}]$ ;  $H = 2[\text{m}]$ ;  $B = 0.6[\text{m}]$ ;  $\tan(\psi) = 1.28$ ;  $L_b = 5[\text{m}]$ .

For the tuning of PI controllers from the control system component in Fig.2, we used the following values of the constants  $T_{d1}^*$  and  $T_{d2}^*$ :

- For SRA T and SRA C:  $T_{d1}^* = 3 \cdot 10^{-3}$ ;  $T_{d2}^* = 6 \cdot 10^{-3}$
- For SRA A:  $T_{d1}^* = 3 \cdot 10^{-3}$ ;  $T_{d2}^* = 9 \cdot 10^{-3}$

Parameters that define the extended Gopinath observer are:

$$k = 0.2; k_R = \frac{1}{T_{d1}^* \cdot k_u}; T_R = \frac{T_r^*}{2}$$

$$\text{where: } k_u = a_{14} \cdot z_p \cdot \psi_r^*; \psi_r^* = \frac{U_{\max}}{2 \cdot \pi \cdot f_n}; U_{\max} = U_n \cdot \frac{\sqrt{2}}{\sqrt{3}}$$

This dead time in the process of the model makes it difficult the control the flow of coal by the scraper conveyor.

In this sense, the parameters which defining the PI (Proportional Integral) flow control are:

$$k_q = \frac{T_{d1}^*}{30}; T_q = \frac{10}{3} \cdot T_{d1}^*$$

To compensate for dead time effects, we use the control strategy that uses a Smith predictor [8]. So, the transfer function of the Smith predictor used is:

$$G_H(s) = G_0(s) \cdot (1 - e^{-T_m \cdot s}) \quad (35)$$

where  $G_0(s) = \frac{a_1 \cdot s + a_0}{s^2 + b_1 \cdot s + b_0}$ , and the coefficients that define the transfer function are:  $b_1 = 52$ ;  $b_0 = 65^2$ ;  $a_1 = -479.4521$ ;  $a_0 = 2.026 \cdot 10^6$ .

In these conditions, the simulation program and the simulation results are presented in the following.

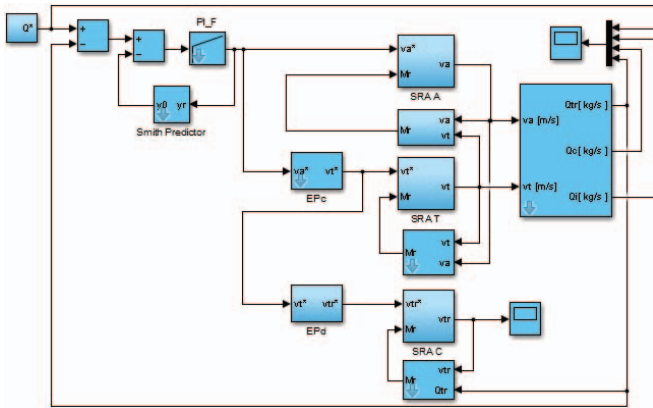


Fig.13. The simulation program of the coal flow control system.

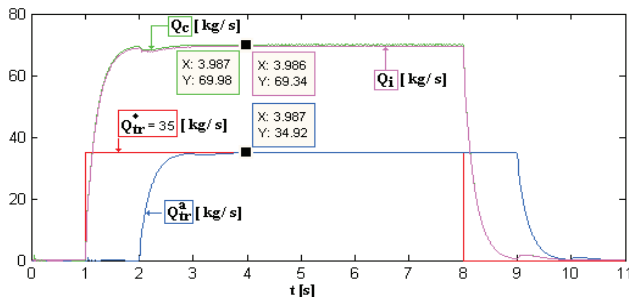


Fig.14. The step response of the coal flow control system – case 1.

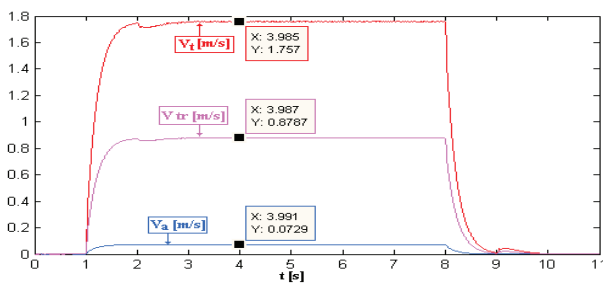


Fig.15. The time variation of the speeds ( $v_a$ ,  $v_t$  and  $v_{tr}$ ) – case 1.

From the graphs of Figures 14 and 15, it is observed that when coal flow imposed is 35 [kg/s], advance speed is stabilized at 4.374 [m/min].

The cutting speed is stabilized at 1.75 [m/s] and conveyor speed is 0.87 [m/s].

From the graphs of Figures 16 and 17, it is observed that when coal flow imposed is 20 [kg/s], advancement speed stabilizes at 2.499 [m/min]. In this case, the cutting speed is stabilized to 1 [m/s] and conveyor speed is by 0.5 [m/s].

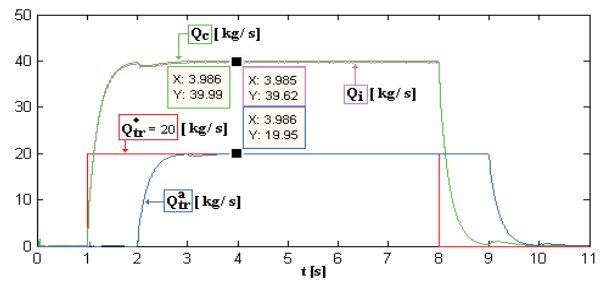


Fig.16. The step response of the coal flow control system – case 2.

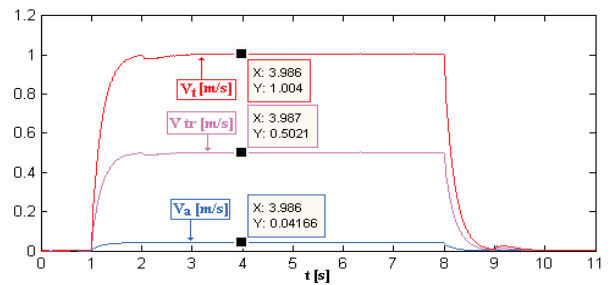


Fig.17. The time variation of the speeds ( $v_a$ ,  $v_t$  and  $v_{tr}$ ) – case 2.

### VIII. CONCLUSIONS

In this article, the modeling and simulation of a new coal flow control system for the longwall scraper conveyor is presented.

After analyzing by simulation in the Matlab-Simulink of the coal flow control system, we find that the control system works properly, having good dynamic performances. Given the above, we believe that the control system of the coal flow, presented in this article, can be successfully used in practice.

Received on July 20, 2016

Editorial Approval on November 15, 2016

### REFERENCES

- [1] I. Kovacs, N. Ilias, M.S. Nan, "The Working Regime of the Cutter Loaders", Universitas Publishing House, Petrosani, 2000.
- [2] \*\*\*, [www.cat.com](http://www.cat.com)
- [3] O. Stoicuta, T. Pana, C. Mandrescu, "The Control System Analysis of the Coal Flow on the Scrapers Conveyor in a Longwall Mining System", Int. Conf. IEEE ICATE, Oct. 2016.
- [4] \*\*\*, The technical documentation of the longwall shearer - KSW460NE, [www.kopex.com.pl](http://www.kopex.com.pl)
- [5] Pana T., Stoicuta O., "Small Speed Asymptotic Stability Study of an Induction Motor Sensorless Speed Control System with Extended Gopinath Observer", Journal of Advances in Electrical and Computer Engineering, vol.11, no.2, pp.15-22, 2011.
- [6] T.Pana, O. Stoicuta, "Controllers Tuning for the Speed Vector Control of Induction Motor Drive Systems", Int. Conf. IEEE AQTR, vol.1, pp.1-6, May 2010.
- [7] S.S.Peng, H.S. Chiang, Longwall Mining, John Wiley&Sons, 1984.
- [8] O.J. Smith, "A Controller to Overcome Dead Time", ISA J., vol.6, no.2, pp. 28-33, Feb. 1959.
- [9] C.H. Ong, "Dynamic Simulations of Electric Machinery: using Matlab/Simulink", Prentice Hall, 1998.
- [10] T. Pană, "Matlab Application Toolbox – Electrical Drives – Induction Motor", Mediamira Publishers, Cluj-Napoca, Romania, 1997.

# Design and Simulation of Wireless Power Transfer Systems

Mihai Iordache, George Andronescu, Victor Bucată, Maria-Lavinia Iordache (Bobaru),  
Marilena Stăculescu, Dragoș Niculae

University Politehnica of Bucharest / Department of Electrical Engineering, Bucharest, Romania,  
mihai.iordache@upb.ro, george.andronescu@upb.ro, victor.bucata@upb.ro, laviniabobaru@gmail.com, marilena.stanculescu@upb.ro, dragos.niculae@upb.ro

**Abstract** – This paper presents a set of diagrams for wireless power transfer systems (WPTS) with a lot of applications in key domains such as: medical, electrical engineering, military etc. Our research is based on circuits working as WPTS. All the circuits are using sets of two magnetically coupled coils whose parameters were extracted by simulations using the specialized software ANSOFT Q3D EXTRACTOR. The simulations of the circuits were performed using TINA, SPICE and SIMULINK in MATLAB. We used existing parts from Texas Instruments libraries. WPTS are more appropriate for small distances transmission, distances up to twice the coils dimensions, because the magnetic field strength produced by the transmitter becomes very weak when the distance increases. In contrast to other WPTS methods, the efficiency of the system can reach up to 95% for short distance. The circuits were also physically built and tested and the results were very close to the numerical ones. We also compared the results with data in existing literature and we obtained a bound of the error of less than 5%. We also studied the efficiency of the power transfer and presented some practical applications for these systems such as low power battery chargers. The results done by simulations were almost identical with the experimental ones and those in existing literature, the error being less than 5%.

**Keywords:** *Wireless Power Transfer Systems, coupled resonators, circuit simulations, power transfer efficiency, wireless battery charger.*

## I. INTRODUCTION

The major sections of the system that implements Ampere and Faraday's laws are transmission and receiver of the two magnetically coupled coils, named "inductive connection" of the WPTS (Wireless Power Transfer System) (Fig. 1).

The coupled coils can have different shapes and sizes. The inductive components can be considered as an AC transformer with inductive high transmission. This transformer is called "weakly coupled transformer". In such a transformer, a small quantity of the magnetic flux produced by the first coil enters the second one. As a consequence, the energy to be transmitted in the weakly coupled system is in general reduced. This problem limits the use of WPTS based on inductive coupling.

WPTS are more appropriate for small distances transmission, distances up to twice the coils dimensions, because the magnetic field strength produced by the transmitter becomes very weak when the distance increases. In

contrast to other WPTS methods, the efficiency of the system can reach up to 95% for short distance.

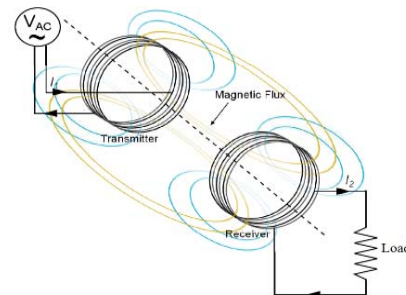


Fig. 1. WPTS functioning principle.

The set of diagrams for WPTS presented in this paper are suitable for applications such as: medical implants, mobile phones batteries charging, wireless sensors networks, electrical networks monitoring etc. To model the power source, we used on one hand Tina and Spice [1-3, 16] libraries and on the other hand Simulink in Matlab [4]. The two coil parameters were computed using the specialized software ANSOFT EXTRACTOR Q3D, [5].

The standard diagram of a WPTS is presented in Fig. 2.

The oscillator and the power amplifier (PA) are playing important roles for the WPTS. The oscillator should produce a high frequency sinusoidal signal with the frequency equal to the resonance frequency of the two magnetically coupled resonators, TX and RX, [6-9, 11-15, 18, 19]. The power source circuit of the transmitter contains a tuning device for adjusting the frequency at the input of the transmitter TX at the resonance frequency of the two resonators which varies as the distance between the two coils to modify. Other important blocks are the voltage rectifier and regulator which must provide constant current and voltage on the load.

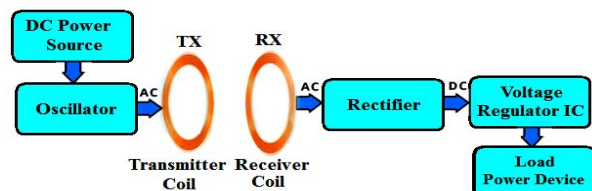


Fig. 2. Standard diagram of a WPTS.

In this paper we designed the schematics used for building WPTS and we made the numerical analysis of these schematics in Tina, SPICE [15] and SIMULINK (MATLAB).

The results we obtained with the aforementioned software were compared with the experimental ones and with those in existing literature. By the end we inferred that the results done by simulations were almost identical with the experimental ones, the error being less than 5%.

II. WPTS DESIGN AND ANALYSIS USING TINA AND SPICE

In Fig.3 we present the first WPTS that was designed and built in our research laboratory from UPB.

We took into considerations two sets of coils built in University Politehnica of Bucharest (UPB) electrical engineering laboratory.

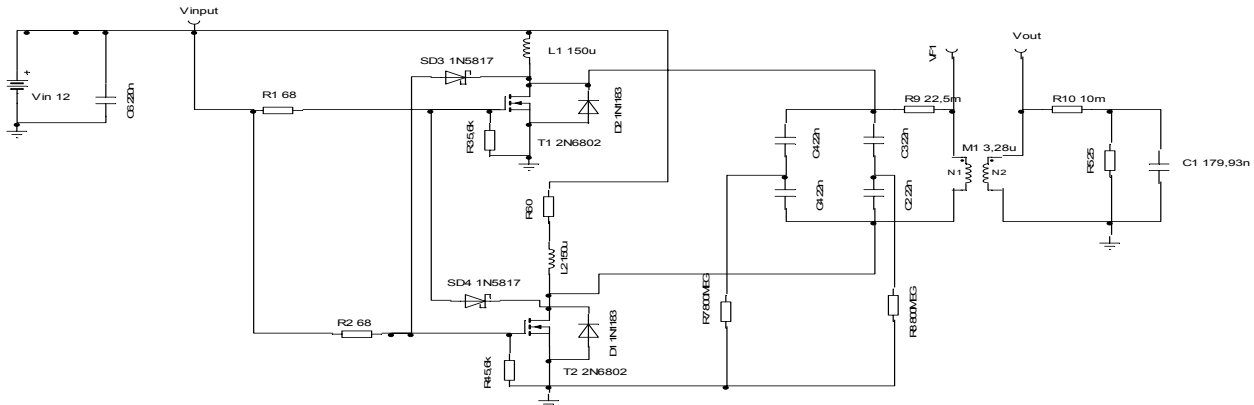


Fig. 3. WPTS corresponding to the parameters from Case 2.

The parameters of the two coils sets were identified using the software ANSOFT EXTRACTOR Q3D, [5].

The schematics of the WPTS from Fig. 3 was simulated by Tina, [1 – 3], and SPICE [16], which uses as input file, the .cir file exported from Tina.

Fig. 4 presents a photo of the WPTS built in our laboratories for Case 1 (Two identical helicoidally coils).

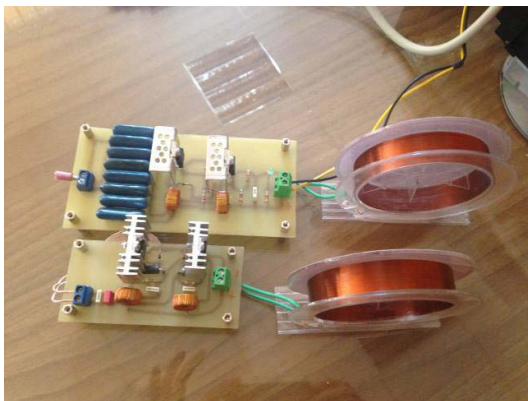


Fig. 4. Case 1. WPTS with Helicoidally coils.

Fig. 5 presents a photo of the WPTS built in our laboratories for Case 2 (different shaped coils).

A. Case 1.

Input data: Two identical coils; Shape: helicoidally; Parameters:

$$L_1 = L_2 = 1.4 \mu\text{H}, C_1 = 22 \text{ nF}, C_2 = 22 \text{ nF}, R_{L1} = R_{11} = 0.0225 \Omega, R_{L2} = R_{10} = 0.01 \Omega \text{ and } k = M/\text{sqrt}(L_1 * L_2) = 0.3.$$

B. Case 2.

Input data: Two different coils; Shape: spiral (printed coils); Parameters:

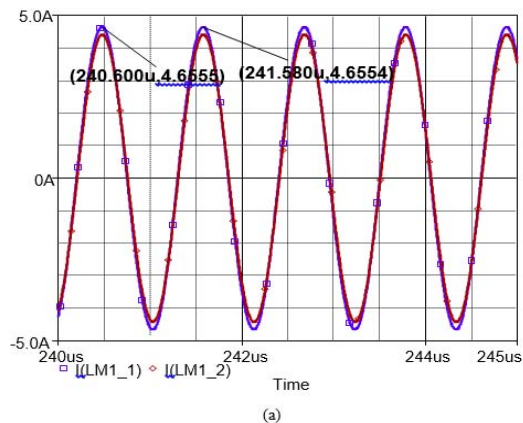
$$L_1 = 3.275 \mu\text{H}, L_2 = 0.585 \mu\text{H}, C_1 = 22 \text{ nF}, C_2 = 179 \text{ nF}, R_{L1} = R_{11} = 0.0225 \Omega, R_{L2} = R_{10} = 0.01 \Omega \text{ and } k = M/\text{sqrt}(L_1 * L_2) = 0.5.$$

Fig. 8 presents a WPTS with the following specifications: a constant output voltage  $U_{out} = 11.347 \text{ V}$ ; a constant output current  $I_{out} = 453.899 \text{ mA}$ ; on the branch of coil  $L_2$  we connected a voltage rectifier with diodes.

The output of the bridge is connected to a RC filter for regulating the ripples in the time dependency of the output voltage  $u_{R5}$  and the output current  $i_{R5}$ .



Fig. 5. Case 2. WPTS with printed coils.



From Fig. 6, b we notice that the main frequency of 905 kHz is very close to the resonance frequency of 907.33 kHz, and the error is of -0.257%.

The dependencies on frequencies for the two cases are given in Fig. 6, b (Case 1), respectively Fig. 7, (Case 2).

The time dependencies of the currents  $i_{L1}$  and  $i_{L2}$  for Case 1, respectively Case 2, are given in Fig. 6, respectively Fig. 7, a.

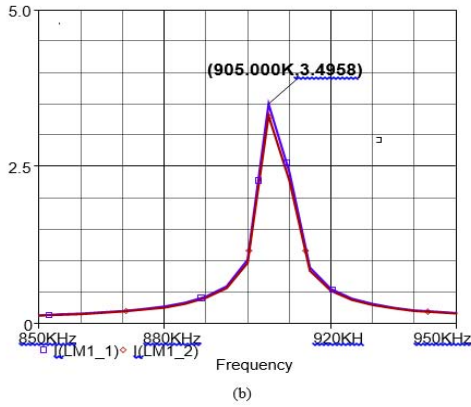


Fig. 6. Dependencies of currents  $i_{L1}$  and  $i_{L2}$ , for the first set of coils: a) vs time; b) vs frequency.

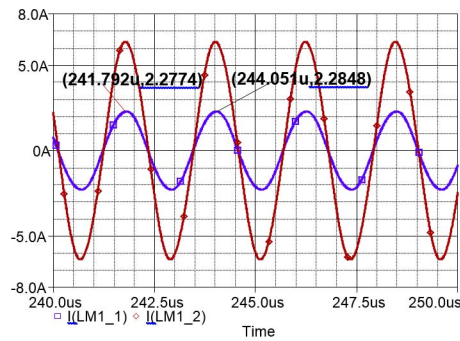


Fig.7.a Dependencies of currents  $i_{L1}$  and  $i_{L2}$ , for the second set of coils vs. time;

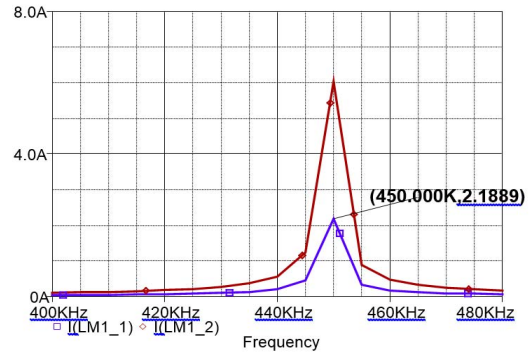


Fig.7.b Dependencies of currents  $i_{L1}$  and  $i_{L2}$ , for the second set of coils vs frequency.

The two sets of magnetic coupled coils from Fig. 8 have the parameters:

1.  $L_1 = 2.265 \mu\text{H}$ ,  $L_2 = 0.54655 \mu\text{H}$ ,  
 $k = M / \sqrt{L_1 \cdot L_2}$ ;
2.  $L_1 = 37 \mu\text{H}$ ,  $L_2 = 23.15 \mu\text{H}$ ,  
 $k = M / \sqrt{L_1 \cdot L_2} = 0.22619$ .

The dependencies on time of the output voltage  $u_{R5}$ , the output current  $i_{R5}$  and the output power on the load  $P_{R5}$  are depicted in Fig. 9. From Figs. 9, a, and b as a conclusion, we notice the considered dependencies are almost the same for both versions of the two resonators.

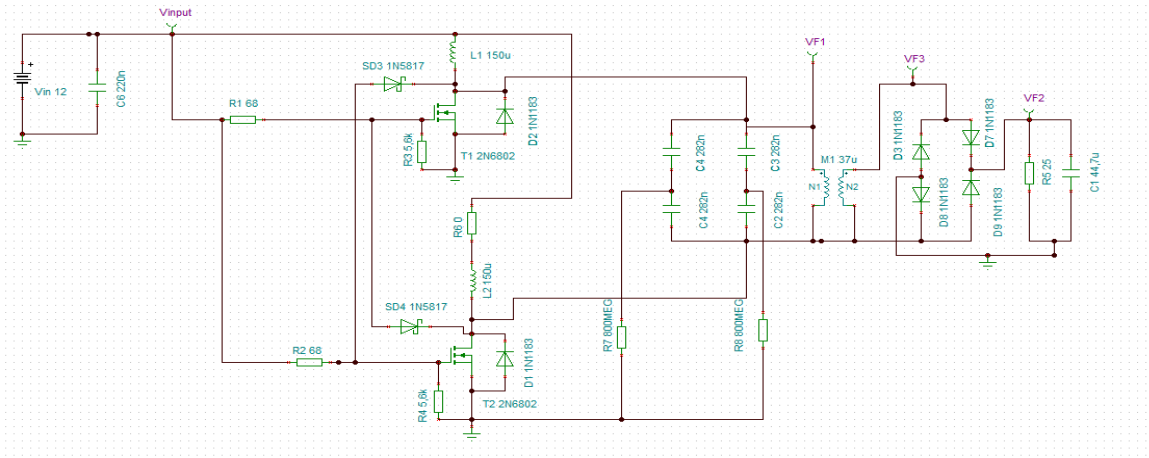


Fig.8. Wireless Power Transfer System (WPTS) which produces constant output voltage and current (dc).

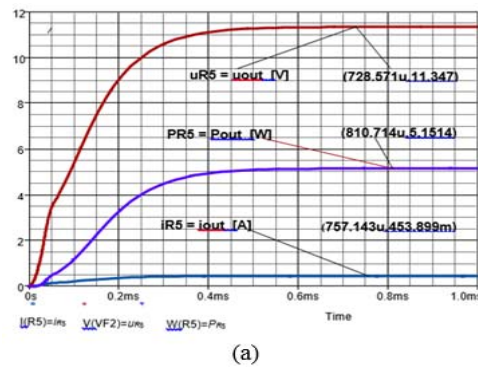


Fig. 9.a Time dependencies of the output voltage  $u_{R5}$ , the output current  $i_{R5}$  and the output power on the load  $P_{R5}$ : the parameters of the two coils as variant 1;

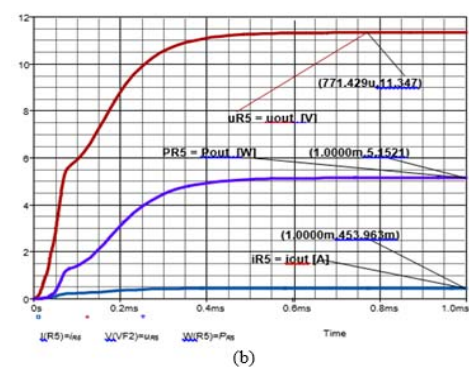


Fig. 9.b Time dependencies of the output voltage  $u_{R5}$ , the output current  $i_{R5}$  and the output power on the load  $P_{R5}$ : the parameters of the two coils as variant 2

In Fig. 10 we present a WPTS used for charging low power batteries which need a constant voltage 0.565 V dc and a constant current 30 mA on all charging time.

We build in our lab the coils for the two variants and the parameters were identified using ANSOFT EXTRACTOR Q3D, [5]. For the system in Fig. 10 we considered two variants for the two magnetic coupled coils:

1.  $L_1 = 0.674 \mu\text{H}$ ,  $L_2 = 1.235 \mu\text{H}$ ,  
 $k = M / \sqrt{L_1 \cdot L_2} = 0.3$ ,
2.  $L_1 = 2.265 \mu\text{H}$ ,  $L_2 = 0.54655 \mu\text{H}$ ,  
 $k = M / \sqrt{L_1 \cdot L_2} = 0.5$

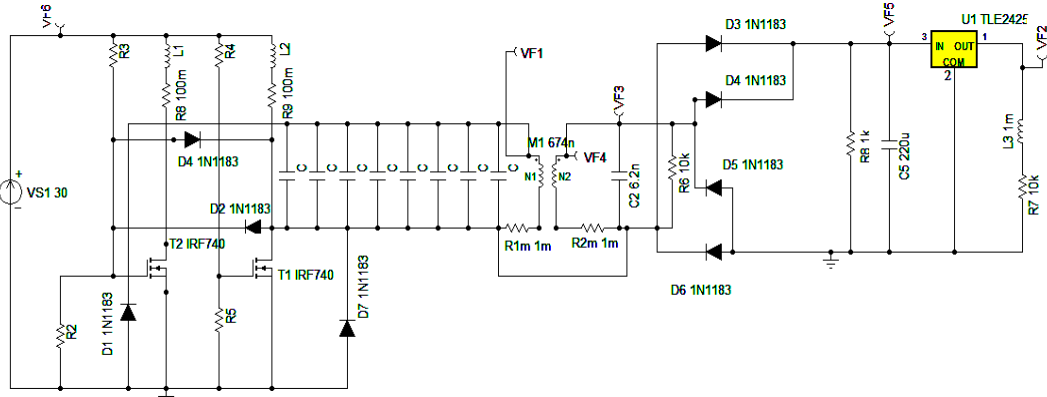


Fig. 10. Wireless electromagnetic energy transfer used for low power battery charging.

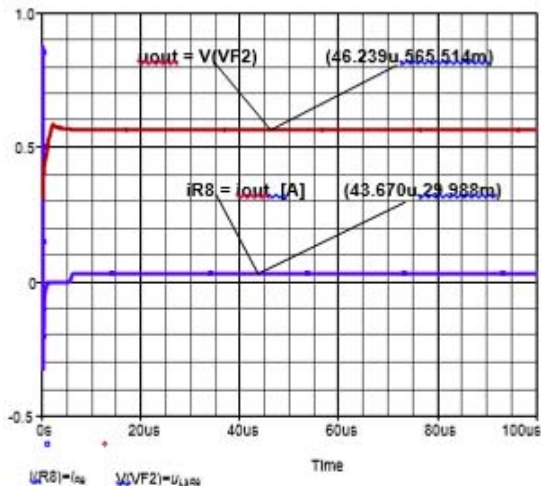


Fig.11. Time dependency of the current  $i_{RS} = i_{out}$  and of the voltage  $u_{RS} = u_{out}$ , for the variant  $L_1 = 0.674 \mu\text{H}$ ,  $L_2 = 1.235 \mu\text{H}$ ,

$$k = M / \sqrt{L_1 \cdot L_2} = 0.3$$

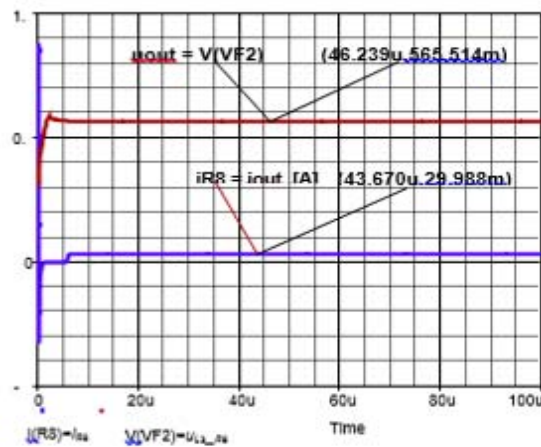


Fig.12. Time dependency of the current  $i_{RS} = i_{out}$  and of the voltage  $u_{RS} = u_{out}$ , for the variant  $L_1 = 2.265 \mu\text{H}$ ,  $L_2 = 0.54655 \mu\text{H}$ ,

$$k = M / \sqrt{L_1 \cdot L_2} = 0.5.$$

We build in our lab the coils for the two variants and the parameters were identified using ANSOFT EXTRACTOR Q3D, [5].

To output a constant current and voltage, a voltage regulator was attached to the load (Fig. 9). Fig. 11 presents the WPTS for Case 1, while Fig. 12 presents the WPTS for Case 2.

As a conclusion, we notice from Figs. 11 and 12 that the two output variables are almost identical for both cases for the parameters of the two magnetically coupled resonators.

### III. WPTS DESIGN AND ANALYSIS SIMULINK

WPTS requires a wide range of electronic parts, so, at a first glance, it's very useful and natural to use MALAB SIMULINK toolbox [4]. The SIMULINK toolbox from MATLAB, [4], facilitates the design and dynamic analysis for wireless power transfer systems.

The first designed and analyzed WPTS is shown in Fig. 13. The system WPTS\_1\_2 (WPTS\_2) contains the following files: *red\_bifazat.c*, *WPT\_2\_dat.m*, *WPT\_2.mdl*, *redr\_bifazat.mexw64*, and *redr\_bifazat.mexw64.pdl*.

The input file *WPT\_2\_dat.m* is:

clear all	C1=54.4e-09;	L2m=1.235e-06;
close all	C2=6.2e-9;	R2m=0.001;
%Datele initiale	C3=47e-06;	M=0.2737e-06;
U_DC=12;	L1=8.6e-06;	hist=0.001;
R1=1e+03;	L2=8.6e-06;	Up=2;
R2=0.2;	L3=1e-4;	Us=5;
R3=1e+06;	L4=1.0e-06;	T=1e-06;
R4=0.01;	L1m=0.674e-06;	%mex -v -g redr_bifazat.c;
R5=5;	R1m=0.001;	END
R6=1e+04;		

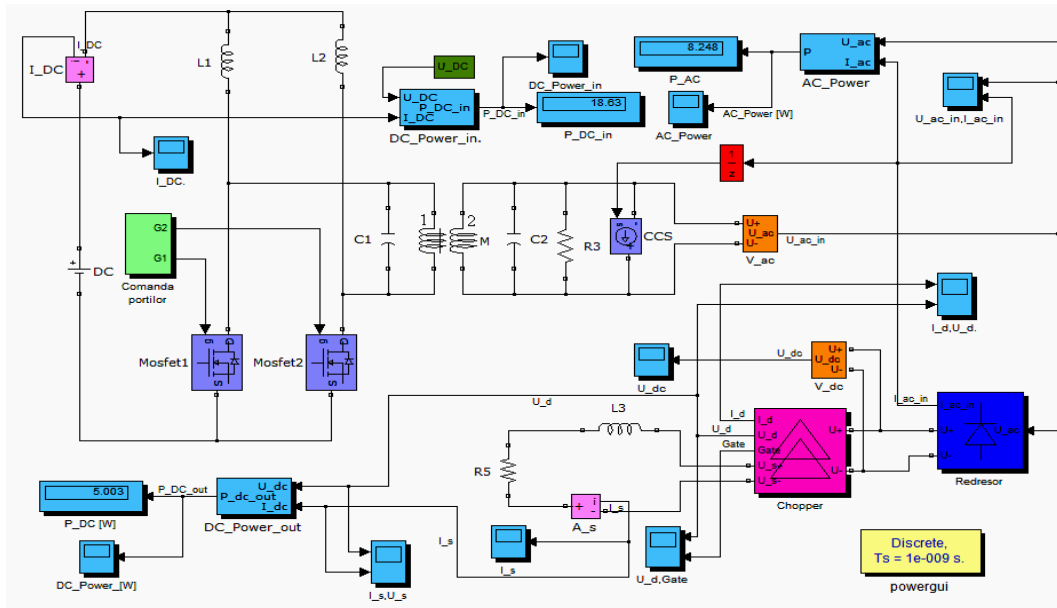


Fig.13. Equivalent diagram of a wireless electromagnetic power transfer used for charging cell phones.

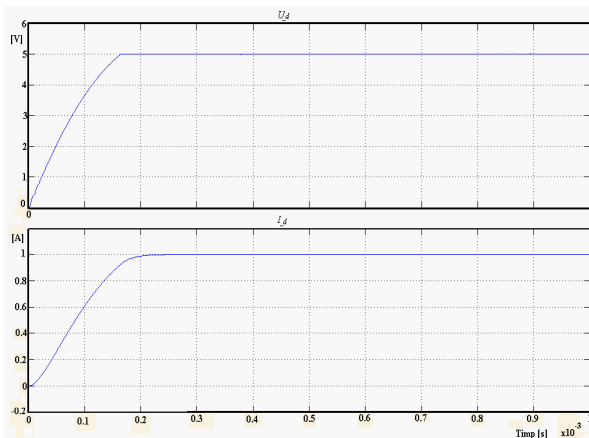
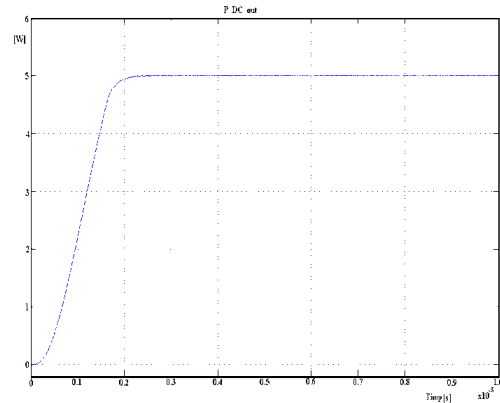
From Fig. 13, we deduce that the schematics of the WPTS allows for the power transfer efficiency computation:

$$\eta_{21\_2} = 100.0 \cdot \frac{P_{dc\_in}}{P_{ac\_out}} = 100.0 \cdot \frac{5.003}{8.248} = 60.66 \%$$

$$\eta_{21\_1} = 100.0 \cdot \frac{P_{dc\_in}}{P_{dc\_out}} = 100.0 \cdot \frac{5.003}{18.63} = 26.85 \%$$

Fig. 14 depicts the time dependencies of the output current  $I_d$  and voltage  $U_d$ . The time dependency of the output power  $P_{DC\_out}$  is given in Fig. 15.

The schematics of the next wireless power transfer system SWTP\_3, designed and analyzed with the SIMULINK toolbox in MATLAB, is presented in Fig. 16. For the WPTS in Fig. 16, the two resonators have the following parameters, [6]:  $C_1 = 46.171$  nF,  $C_2 = 46.091$  nF,  $L_1 = 66.56$   $\mu$ H,  $L_2 = 66.49$   $\mu$ H,  $M = 13.438048$   $\mu$ H,  $R_{L1} = 1.12$   $\Omega$ ,  $R_{L2} = 0.78$   $\Omega$  and  $R_L = 7.93$   $\Omega$ .


 Fig. 14. Time dependencies of voltage  $U_d$  and current  $I_d$ .

 Fig. 15. Time dependency of power  $P_{dc\_out}$ .

We preferred to use the values of the parameters of the two coils for the system SWTP\_3 identical as in [6] in order to check the results we obtained with those measured in [6]. In Fig. 16 the magnetic couple for the two coils  $L_1$  and  $L_2$  was eliminated.

In figure 17 we give the time dependencies of the voltage  $u_2$  and current  $i_2$  in the receptor coil. The resonance frequency is:

$$f_0 = \frac{1}{2\pi\sqrt{L_1 C_1}} \cong \frac{1}{2\pi\sqrt{L_2 C_2}} = 90.9 \text{ kHz.}$$

is very close to the frequency of the curves given in figures 17 and 18,  $f_{0\_grafic} = 90.85$  kHz. From Fig. 17, the diagram of the wireless power transfer system allows for calculating the efficiency of power transfer:

$$\eta_{21\_1} = 100.0 \cdot \frac{P_{ac\_out}}{P_{ac\_inp}} = 100.0 \cdot \frac{7.788}{9.788} = 79.567 \%$$

The waves for the WPTS in Figs. 17 are identical with those in [6].

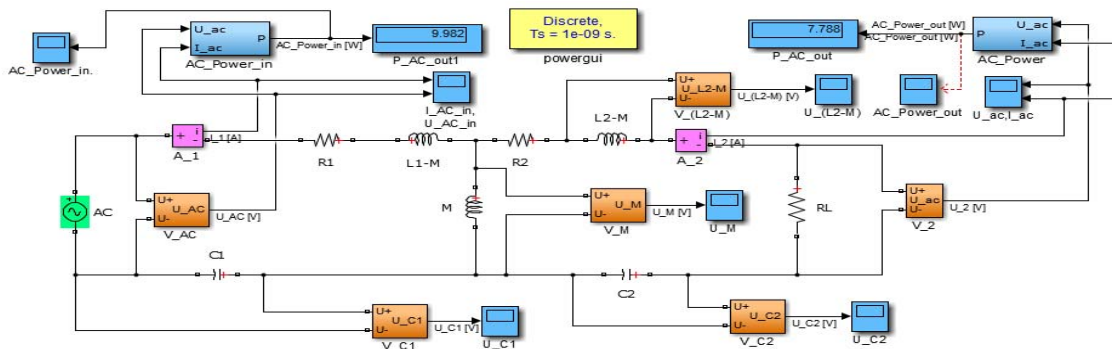


Fig. 16. Equivalent diagram of the wireless power transfer system used for checking experimental results.

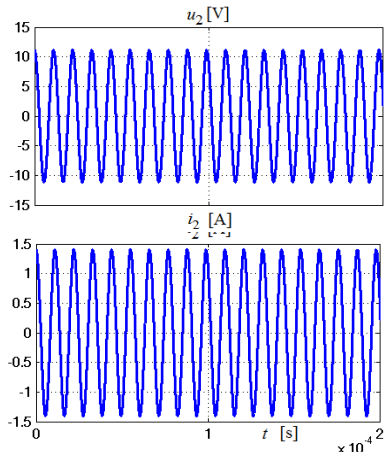


Fig. 17. Time dependencies of the voltage  $u_2$  and current  $i_2$  in the receptor coil.

#### IV. CONCLUSIONS

In this paper we presented a set of diagrams for WPTS with applications in many important domains. Our research used circuits working as WPTS. The originality consists of designing WPTS for which the parameters and the configuration of the two magnetically coupled resonators from the system are known. The user can impose some values for the current and the voltage corresponding to the load. These circuits use sets of two magnetically coupled coils built in our lab from UPB. The parameters of the two coils were determined using specialized software. For designing the power source circuit, the output circuit and the schematics for WPTS, electronic parts from Tina, SPICE and Simulink have been used. Analyzing the results obtained by simulations, we can conclude that TINA, SPICE and MATLAB are suited for the design and analysis of a wide range of WPTS. WPTS are more appropriate for small distances transmission, distances up to twice the coils dimensions. In contrast to other WPTS methods, the efficiency of the system can reach up to 95% for short distance. The results done by simulations were compared with those with the experimental ones and those in existing literature, the error being less than 5%.

#### REFERENCES

- [1] TINA Users Manual”, DesignSoftware, web site: <http://www.designsoftware.com>.
- [2] “National Semiconductors Analog Databook”, web site: <http://www.ni.com>.
- [3] D. Ibrahim, “Circuit Design, Simulation, And Implementation Using TINA”, Near East University, Department Biomedical Engineering, Iefkosa, TRNC, 2012.
- [4] E. W. Weisstein, Nov. 2011, Quartic Equation. From MathWorld—A Wolfram Web Resource [Online]. Available: <http://mathworld.wolfram.com/QuarticEquation.html>.
- [5] Ansoft Q3D Extractor, User Guide, [www.ansoft.com](http://www.ansoft.com).
- [6] W. Q. Niu, J. X. Chu, W. Gu, and A. D. Shen, “Exact Analysis of Frequency Splitting Phenomena of Contactless Power Transfer Systems”, IEEE on CAS – 1: Vol. 60, NO. 6, June 2013, pp. 1670 – 1677.
- [7] Y. Tak, J. Park, and S. Nam, “Mode-based analysis of resonant characteristics for near-field coupled small antennas”, IEEE Antennas Wireless Propag. Lett., vol. 8, Nov. 2009, pp. 1238–1241.
- [8] T. Imura and Y. Hori, “Maximizing air gap and efficiency of magnetic resonant coupling for wireless power transfer using equivalent circuit and Neumann formula”, IEEE Trans. Ind. Electron., vol. 58, no. 10, Oct. 2011, pp. 4746–4752.
- [9] S. Cheon, Y.H.Kim, S.Y. Kang, M. L. Lee, J.M. Lee, and T. Zyung, “Circuit model based analysis of a wireless energy transfer system via coupled magnetic resonances”, IEEE Trans. Ind. Electron., vol. 58, no. 7, Jul. 2011, pp. 2906–2914.
- [10] A. P. Sample, D. A. Meyer, and J. R. Smith, “Analysis, experimental results, and range adaptation of magnetically coupled resonators for wireless power transfer”, IEEE Trans. Ind. Electron., vol. 58, no. 2, Feb. 2011, pp. 544–554.
- [11] M. W. Baker and R. Sarpeshkar, “Feedback analysis and design of RF power links for low-power bionic systems”, IEEE Trans. Biomed. Circuits Syst., vol. 1, no. 1, March 2007, pp. 28–38.
- [12] A. J. Moradewicz and M. P. Kazmierkowski, “Contactless energy transfer system with FPGA-controlled resonant converter”, IEEE Trans. Ind. Electron., vol. 57, no. 9, Sep. 2011, pp. 3181–3190.
- [13] J. Sallan, J. L. Villa, A. Llombart, and J. F. Sanz, “Optimal design of ICPT systems applied to electric vehicle battery charge”, IEEE Trans. Ind. Electron., vol. 56, no. 6, Jun. 2009, pp. 2140–2149.
- [14] J. I. Agbinya (Editor), Wireless Power Transfer, 1st edition, ISBN: 978-87-92329-23-3, River Publishers Series in Communications, Denmark, 2012.
- [15] J. I. Agbinya (Editor), Wireless Power Transfer, 2nd edition, ISBN: 978-87-92329-23-3, River Publishers Series in Communications, Denmark, 2016.
- [16] M. Iordache, Lucia Dumitriu, Aided Simulation of Analog Circuits- Algorithms and Computing Techniques (in RO), Vol I and Vol. II, Publishers POLITEHNICA Press, Bucharest 2014.
- [17] J. A. Ricano, H. Rodriguez, H. Vasquez, “Experiment About Wireless Energy Transfer”, 1-st International congress on instrumentation and applied sciences, Cancun, Mexico, october 2010.
- [18] D. Niculae, M. Iordache, Lucia Dumitriu, “Magnetic coupling analysis in wireless transfer energy”, The 7th International Symposium on Advanced Topics in Electrical Engineering (ATEE), 2011, Bucharest, 12-14 May 2011.
- [19] Mihai Iordache, Dragos Niculae, Lavinia Iordache (Bobaru), Lucian Mandache, “Circuit Analysis of Frequency Splitting Phenomena in Wireless Power Transfer Systems”, Proceeding of the 9th International Symposium Advanced Topics in Electrical Engineering – ATEE’15, May 7-9, 2015 Bucharest, Romania, Editura Politehnica Press, pp. 146 - 151, Print ISBN: 978-1-4673-5979-5.

# Small Scale Model of Automatic Barrier Powered by Photovoltaic Panel

Laurențiu Alboteanu\*, Gheorghe Manolea\*, Alexandru Novac†

\* University of Craiova/Department of Electromechanical, Environmental and Industrial Informatics, Craiova, Romania, [alboteanu@em.ucv.ro](mailto:alboteanu@em.ucv.ro), [ghmanolea@gmail.com](mailto:ghmanolea@gmail.com)

† S.C. Promat S.A., Craiova, Romania, [alexandru\\_novac@yahoo.com](mailto:alexandru_novac@yahoo.com)

**Abstract** - Access control systems offer numerous benefits and are able to constitute extremely good solutions for securing an area of high or very high importance. An access control system allows restriction, monitoring and directing human trafficking as cars to a location or from a location. In generally at access control systems call the managers of circulated spaces or areas where must enter only authorized persons. To access the vehicles in different areas are frequently used automatic barriers. This paper presents such an access system, achieved a small scale named "automatic barrier model", that uses photovoltaic panels (PV) as main energy source. Automatic operation of barrier is provided by a development system achieved around a microcontroller. In the first part of paper is presents the structure and minimum requirements of development system. Also are highlighted aspects of dimensioning and design for both parts hardware and software respectively. To achieve electrical diagrams and PCBs was used a dedicated software. Finally was tested the achieved automatic barrier model. The tests consist of verifying the correct operation of the automated system. Were made test regarding to automation and to power supply from PV panel. Experimental results show a smooth functioning of experimental automatic barrier powered by PV panel and can be successfully expanded at real scale.

**Keywords:** *vehicles access system; automatic barrier; microcontroller; photovoltaic panels; automation.*

## I. INTRODUCTION

To restrict access to a parking or an area, usually there are used electromechanical barriers of different sizes, and in the case of restricting access for a single parking space there is widely used lock parking, which is either manually or electromechanical controllable from the remote control [15].

In some cases the electrical grid is situated at considerable distances, or power supply works of the automatic access point are expensive.

The paper presents an alternative solution for small-scale automated access of vehicles. Automatic access system can be supplied with electricity, either from photovoltaic panels or from another source of energy. Automatic operation is provided by a development system achieved around a microcontroller.

We chose this variant of control because the microcontroller is suitable for operation in an industrial environment, it can operate in a wide range of temperature and humidity, it is easily adapted to interfacing with any process and it has no particular problems on the training of service personnel due to offered programming facilities.

Microcontrollers were imposed in an increasingly wide range of applications, programming because of their high simplicity, affordability and reliability [8], [9], [11].

## II. STRUCTURE OF AUTOMATIC BARRIER MODEL

### A. Requirements

Experimental model called "automatic barrier" proposed for design must meet the following requirements [1]:

- development will be carried out around a microcontroller;
- it must be possible the purchase of five digital signals (barrier up, barrier down, present car, signal access control, fault reset);
- programming will be in a higher level language;
- the user interface will be managed by a seven-segment display;
- microcontroller programming is done via a connector provided on PCB;
- fast status signaling of model is done through two LEDs;
- it must be possible to control a DC motor;
- to allow power supply from alternative power sources.

### B. Bloc Diagram of the Automatic Barrier Model

In the design of development systems can take into account the cost, complexity PCB (printed circuit board), speed of execution of the instructions, the existence of media performance written code etc.

It is possible to ensuring the requirements above by a structure built around a microcontroller ATmega8 product type ATMEL [13].

Ensuring the requirements above is possible using two modules: power supply module and control module (Fig. 1).

The energy from the photovoltaic (PV) panel or from another power source is taken from a constant current source. Then it follows a voltage source. In this way it is controlled the charge current and battery voltage in the circuit.

A switching source with high efficiency (92%) allows obtaining supply voltage of control module developed around a microcontroller.

Detailed status of the installation is presented through a seven-segment display and a global signalling is possible via two LEDs.

The DC motor that acts barrier is controlled via an amplifying circuit.

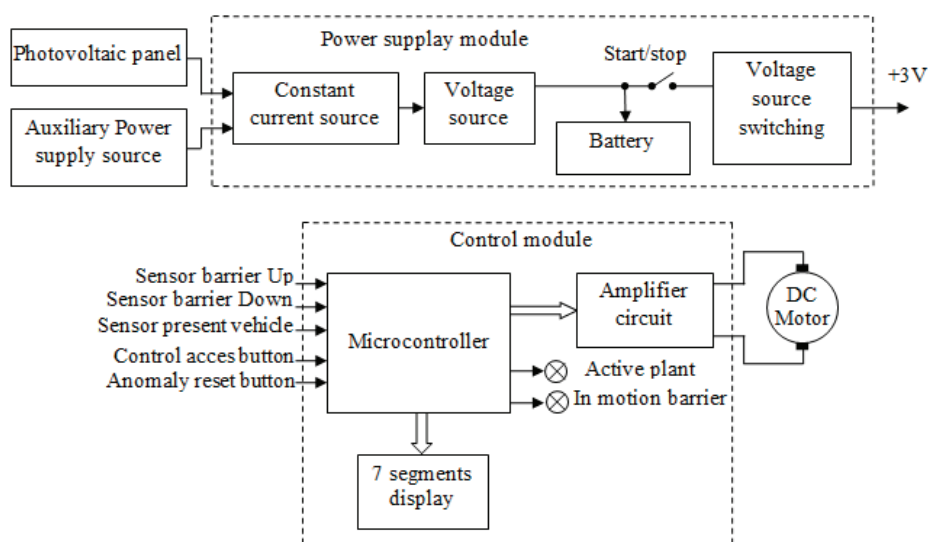


Fig. 1. Block diagram of "automatic barrier" model.

### III. DESIGN OF AUTOMATIC SYSTEM

#### A. Design of Hardware Part

The design of electronic schemes was performed using the program Orcad 9.1, Capture module [14].

In the power supply module (Fig. 2), the diodes D4 and D5 mix the two power supplies: a PV panel and an auxiliary power source. Value of  $R2 = 10$  Ohms allows battery charging at a current of  $1,25 / 10 = 0,125 = 125$  mA. Neglecting the voltage drop across D2 then the voltage across the battery is determined by the resistors R1 and R3. To obtain the values in the figure (to J2 connector):

$$U_{batt} = 1,25 \cdot \left(1 + \frac{R3}{R1}\right) = 1,25 \cdot \left(1 + \frac{660}{120}\right) = 8,125V \quad (1)$$

The J2 connector is coupled to the battery. It consists of two cells in series type SAMSUNG ICR18650-22E. The nominal voltage of such cells is 3.7 V (2,75V minimum, maximum 4,2V). The corresponding maximum voltage the two cells is  $4.2 * 2 = 8,4V$ . It chose to limit the voltage  $U_{ac} = 8,125V$ .

The LTC1474 circuit is powered from the battery circuit and is capable of providing an output voltage of 3 V at a yield of about 92% (Fig. 3). The battery capacity (mAh 2200 for a cell) and a good yield of the switching source cause increased autonomy of the installation.

For R4 and R5 resistors,

$$R4 = 2 \cdot 390k\Omega = 780k\Omega \quad (2)$$

$$R5 = 820k\Omega + 330k\Omega = 1150k\Omega \quad (3)$$

obtain the output voltage (to J4 connector):

$$U_{out} = 1,23 \cdot \left(1 + \frac{R5}{R4}\right) = 1,23 \cdot \left(1 + \frac{1150}{780}\right) = 3,043V \quad (4)$$

The voltage blocking of the switching source to protect the battery ( $U_{in}$ ) is given by resistances R7 and R9.

$$R7 = 1500k\Omega + 470k\Omega = 1970k\Omega \quad (5)$$

$$R9 = 390k\Omega + 120k\Omega = 510k\Omega \quad (6)$$

with the formula:

$$U_{trip} = U_{In} = 1,23 \cdot \left(1 + \frac{R7}{R9}\right) = 5,98V \quad (7)$$

$$> 2 \cdot 2,75 = 5,5V$$

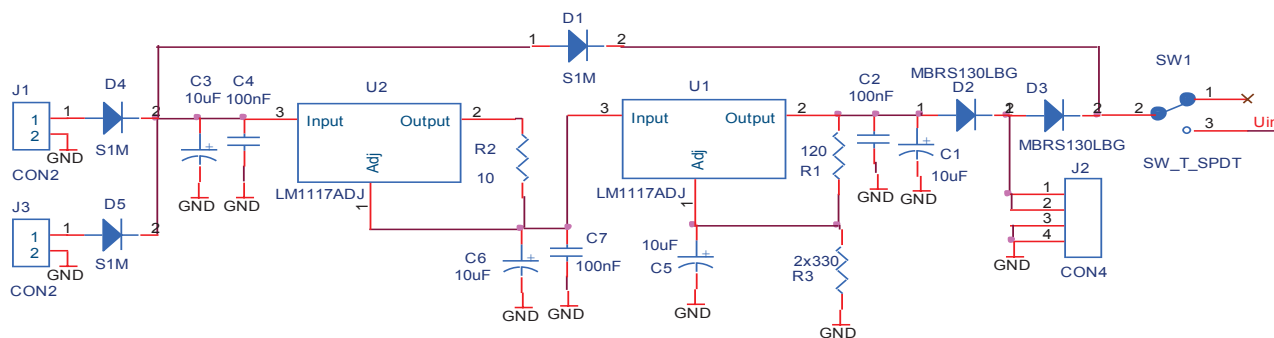


Fig. 2. Wiring diagram of the power supply module – voltage source and current source.

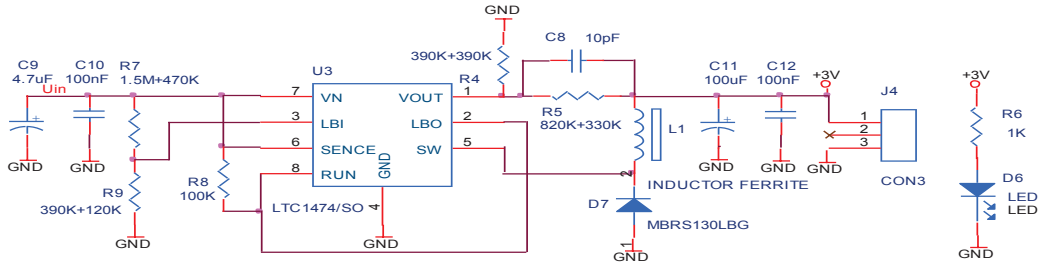


Fig. 3. Wiring diagram of the power supply module - switching source.

The control module (Fig. 4, 5) contains, in addition to the circuit U2 - ATmega8, a connector of programming (J2), a cell display with seven segments (U1), a connector allocated to DC motor (J1), two LED signaling D9 and D10 and an amplifying circuit composed of transistors Q1, Q2, Q3 and Q4.

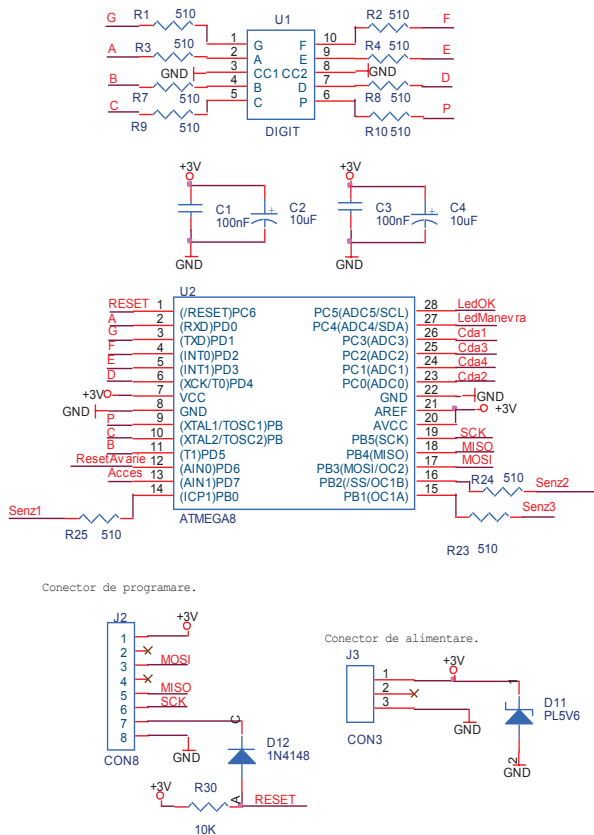


Fig. 4. Wiring diagram of the control module- part with microcontroller.

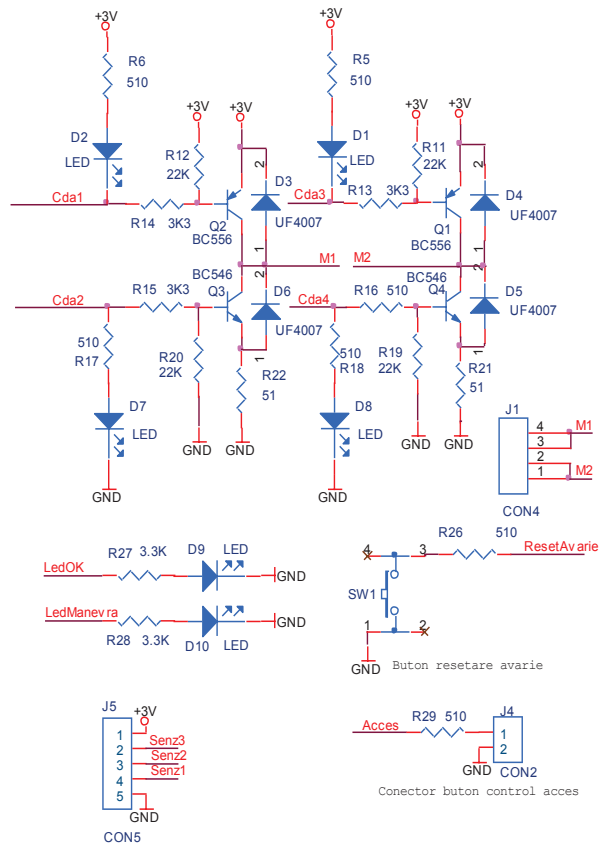


Fig. 5. Wiring diagram of the control module – part with amplifying circuit

The conduction state of the four transistors is indicated by LEDs D1, D2, D7 and D8. J5 connector provides the interface between the control module and sensors in the system. For "barrier up" and "barrier down" is using two reed sensors [6] commanded by a magnet jointly with barrier.

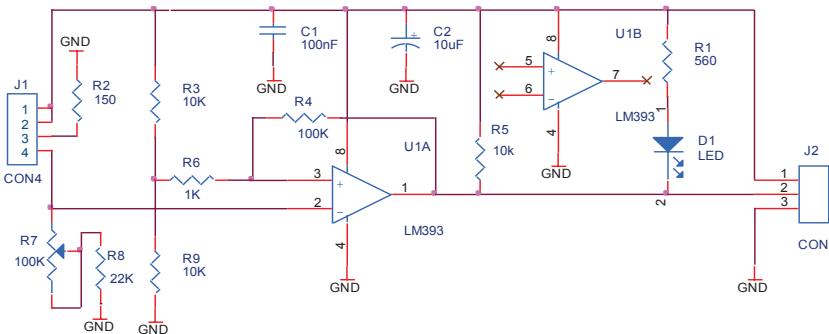


Fig. 6. Wiring diagram of the present car sensor.

Sensor "present car" (Figure 6) contain a type LM393 comparator. At J1 pins 2-3 there is connected an infrared (IR) LED emission and at pins 1 and 4 there is connected an IR receiver. Resistor R7 adjusts threshold of detection the light beam.

### B. Design of Software Part

The general structure of software for microcontroller is shown in Figure 7.

The program starts with microcontroller initialization and variables used [2],[3]. Implementation of various timings is possible by using a sequence of decrement of all counters used. Then follows purchase of five digital signals, execution of algorithm, then transmitting the synthesized commands.

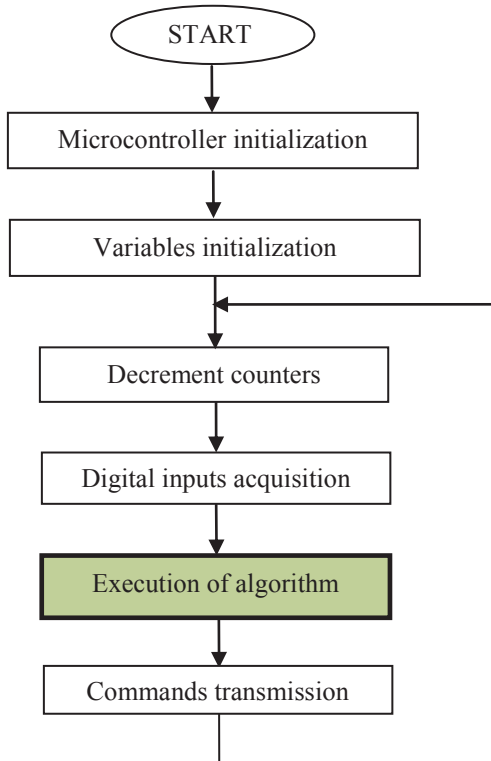


Fig. 7. Flow diagram of microcontroller program.

Program operation is based on a tact generated with a timer 0. The interrupt is generated at every 10 ms, which determines setting of variable "Tact" (fig. 8).

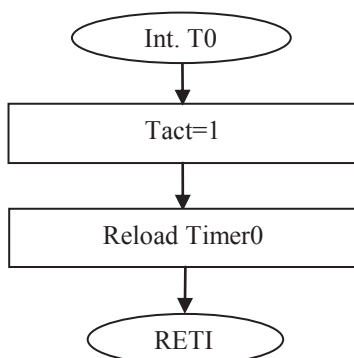


Fig. 8. Flow diagram of timer 0.

Chart of Figure 9 captures the decremental routine for three work counters: "Counter", "CounterLedOK" and "CounterLedManevra".

This method allows working with hundreds of independent counters.

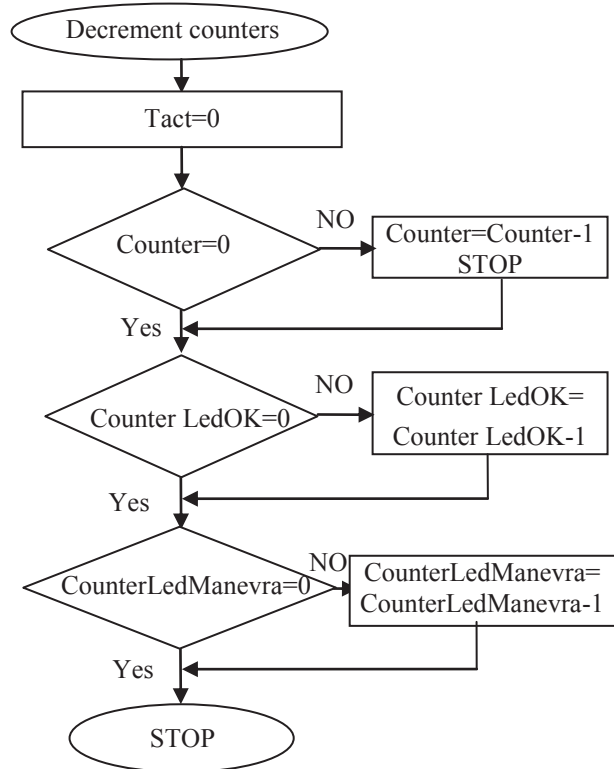


Fig. 9. Flow diagram of routine for counters decrement.

The proper algorithm includes six distinct states encoded by variable "CounterState" (Fig. 10).

The 6 states have the following meaning:

- State 0- Barrier rest, waiting command;
- State 1- Barrier in course of erection;
- State 2-Barrier up, braked a countercurrent;
- State 3-Barrier up, the rest;
- State 4-Barrier being lowering;
- State 5- Barrier down, braked a countercurrent.

The program remains in the state "0" until activation of the "Access" signal. Immediately it is given the command to lift the barrier. This sequence ends with activation of the "Barrier Up" signal.

In order to avoid moving the barrier of inertia for about 0,4 sec. there is activated a countercurrent braking mode. After this sequence the system enters a delay of 6 seconds.

The descent begins only if the infrared beam is not interrupted. Its disruption in the sequence lowering or braking downhill has the effect of automatically switching to state 1 (lifting barrier). After termination of the braking mode (CounterState = 5) it returns to "0" state.

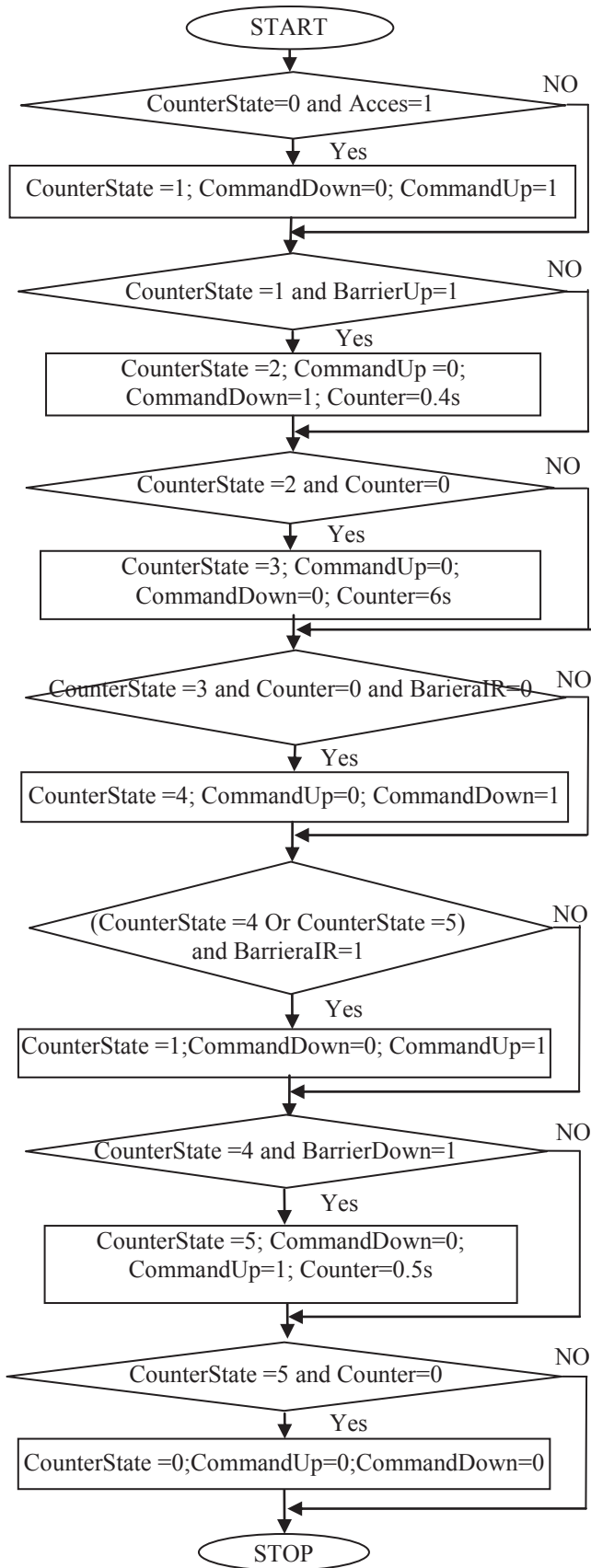


Fig. 10. Flow diagram of proper algorithm – normal operation mode.

Also in the proper algorithm it is part of an operation sequence for detection of possible anomaly (Fig. 11). Thus, while the "CommandUp = 1" or "CommandDown = 1" more than 9 sec., it means that there appeared at least an anomaly in the motor operation.

The system passes into a state (CounterState = 6), which, for the reset involves pressing the button "ResetAnomaly".

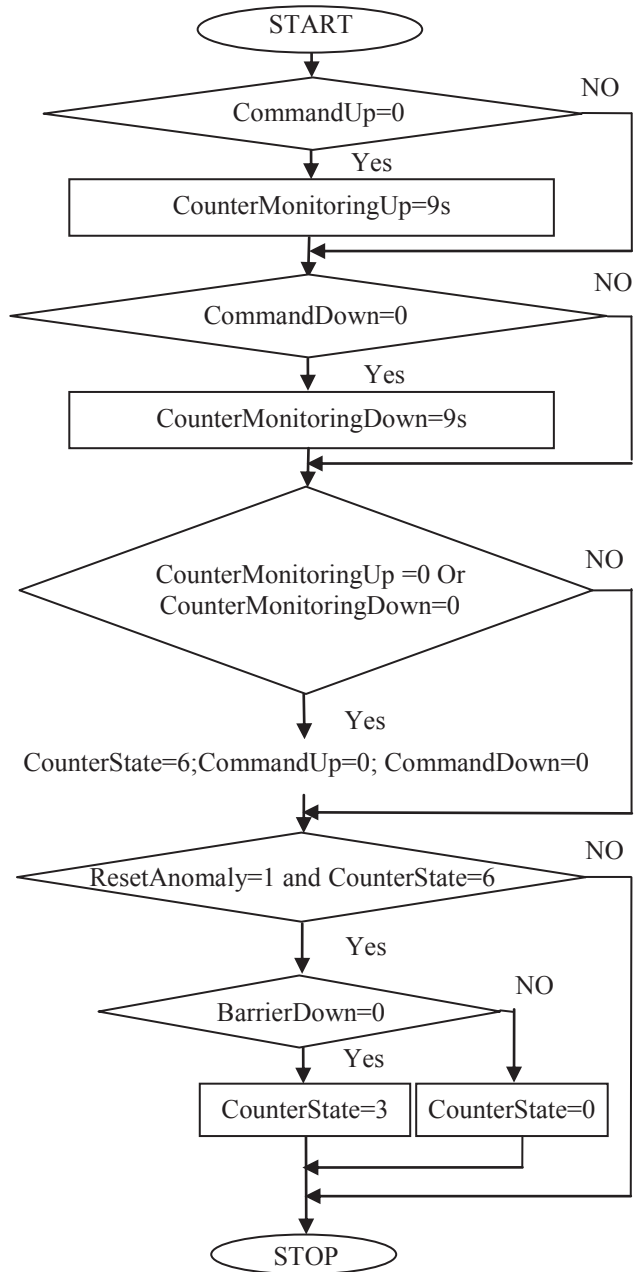


Fig. 11. Flow diagram of proper algorithm– anomaly processing.

The microcontroller program, which provides automatic control of the barrier, was written in high level language C, because it is easier to understand and maintain [4], [5] [7].

The code for the microcontroller used was written using the software package StudioAVR4 [12].

IV. ACHIEVEMENT AND TESTING OF AUTOMATIC MODEL

A. Achievement of Automatic Model

After designing of electronic schemes there were performed printed wiring boards using the program Orcad 9.1, Layout module [14] and electronic components were assembled. It began the assembly with passive circuit elements and they ended with the active components.

Components of the "automatic barrier" model are explained in Figure 12.

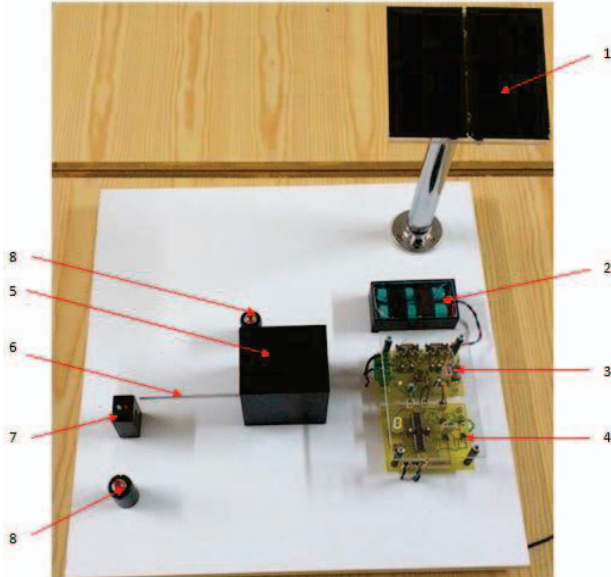


Fig. 12. Experimental model of "automatic barrier": 1-PV panel; 2-battery; 3-power supply module; 4-module with microcontroller; 5-module of barrier drive; 6-barrier; 7- infrared detector module and LED signalling; 8- access buttons.

B. Experiments Regarding to Automation Part

Experimentation actually consists of correct working verification according to the protocol and conditions imposed by design.

In figures 13 ... 18 there are captured the 6 operating states in a work cycle lifting-lowering of barrier. These states were predefined in the design stage of automatic vehicle access system for the purpose of verification and easier debugging of system.

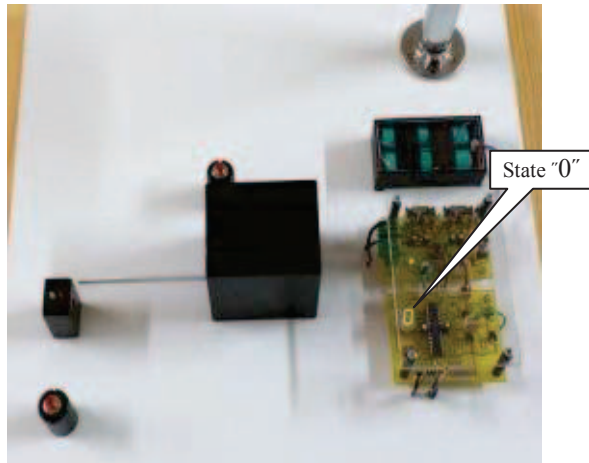


Fig. 13. Testing of model: State 0- Barrier at rest, waiting command.

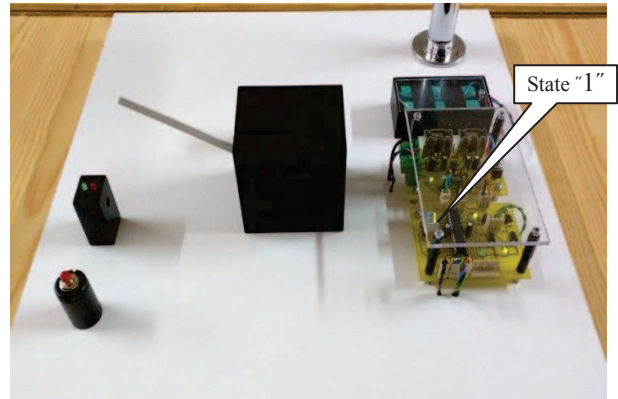


Fig. 14. Testing of model: State 1- Barrier in course of rise.

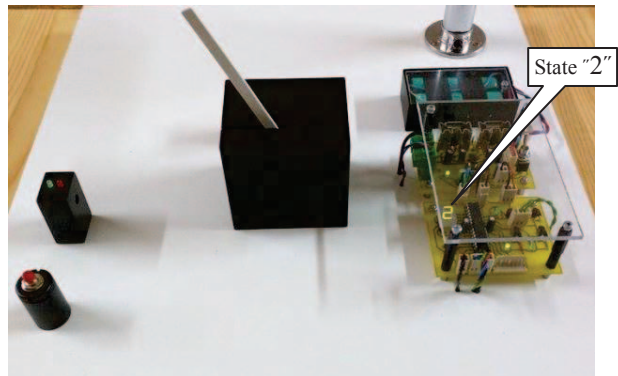


Fig. 15. Testing of model: State 2- Barrier up, braked a countercurrent..

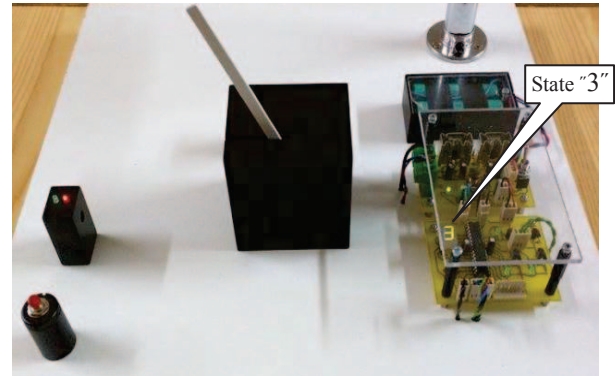


Fig. 16. Testing of model: State 3- Barrier up, the rest.

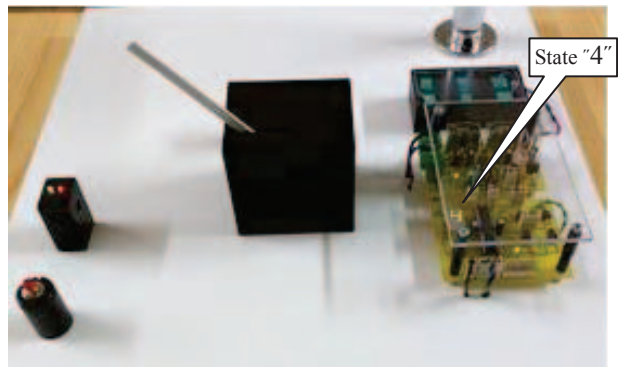


Fig. 17. Testing of model: State 4- Barrier being lowering.

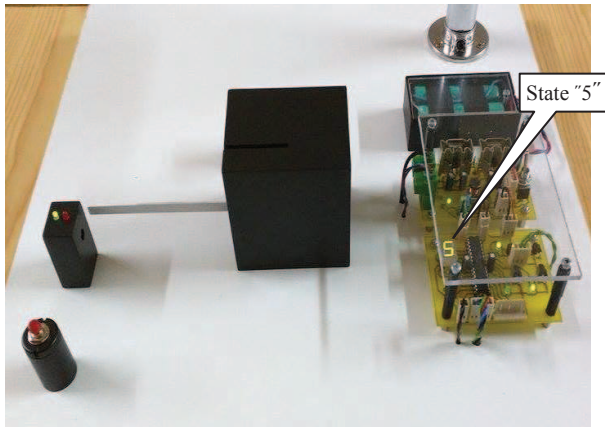


Fig. 18. Testing of model: State 5- Barrier down, braked a countercurrent

For automatic operation of the barrier was opted for the use of distinct states of operation for programming and debugging easier.

C. Experiments Regarding to Power Supply from Photovoltaic Panel

The purpose of the experimental determinations is to visualize the measured values of the PV panel voltage and auxiliary power supply source both at without load operation, and the operation of a work cycle up-down of barrier.

The structure of the experimental equipment for the measurement of voltage is depicted in Figure 19.

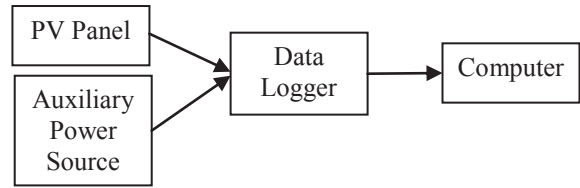


Fig. 19. Structure of experimental equipment.

In the first stage was recorded [10] the voltage supplied from two sources (PV panel and auxiliary power supply) at no load functioning. The experimental result is shown in Figure 20.

In the first moment both sources are connected. The voltage is 12V for two sources. The voltage is sufficient for charging a battery, having a nominal voltage 9V.

After 20 sec. PV panel was covered. Observe that the voltage supplied to it drops to zero. The voltage of PV panel returns to 12V after it is discovered (t = 1min, 10sec.).

In the next stage was recorded evolution of PV panel voltage (Fig. 21) during two cycle of operation of the barrier.

In Figure 21 are marked some states of the first cycle of operation, as follows:

- 1 - State 1- Barrier in course of rise
- 2 - State 2- Barrier up, braked a countercurrent
- 3 - State 4- Barrier being lowering
- 4 - State 5- Barrier down, braked a countercurrent

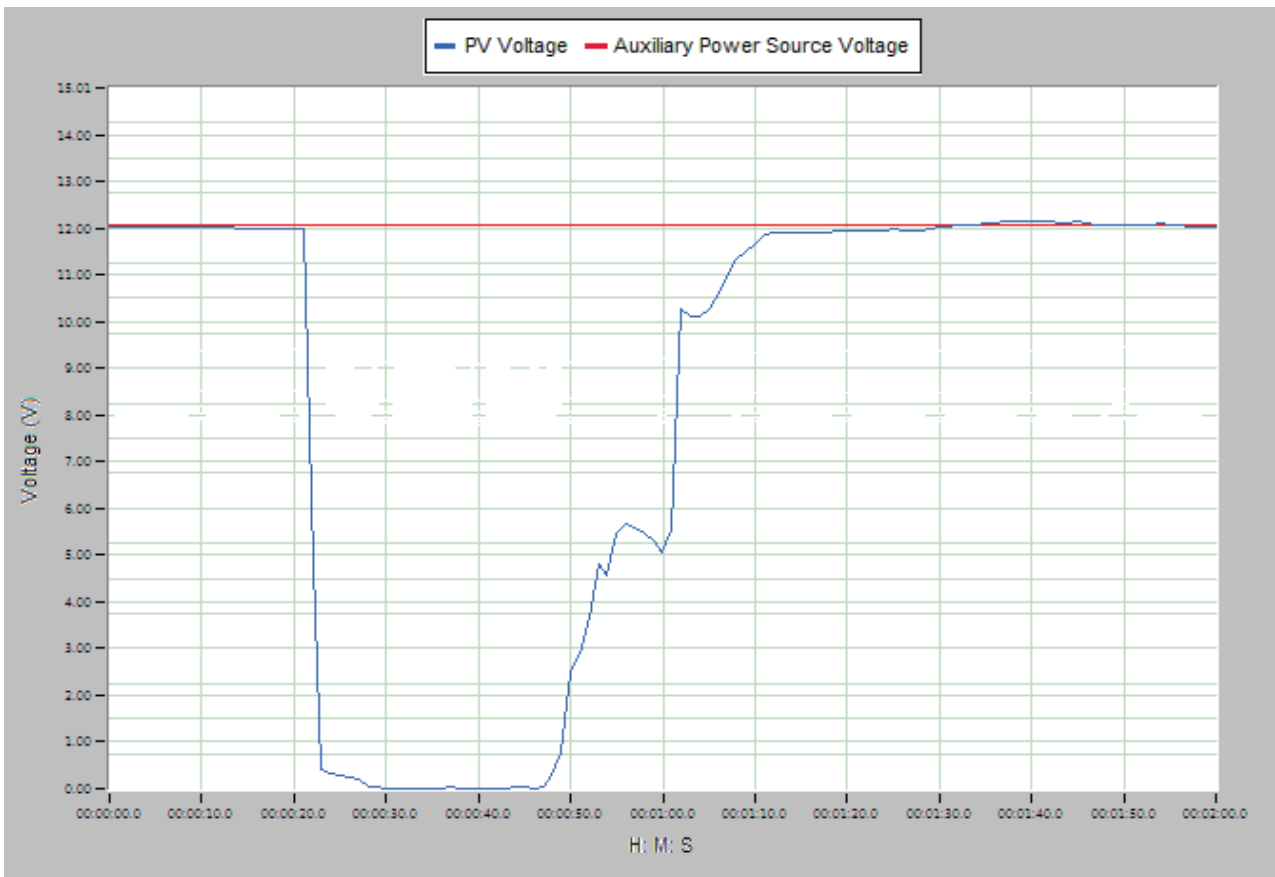


Fig. 20. Voltage of power supply sources without load.

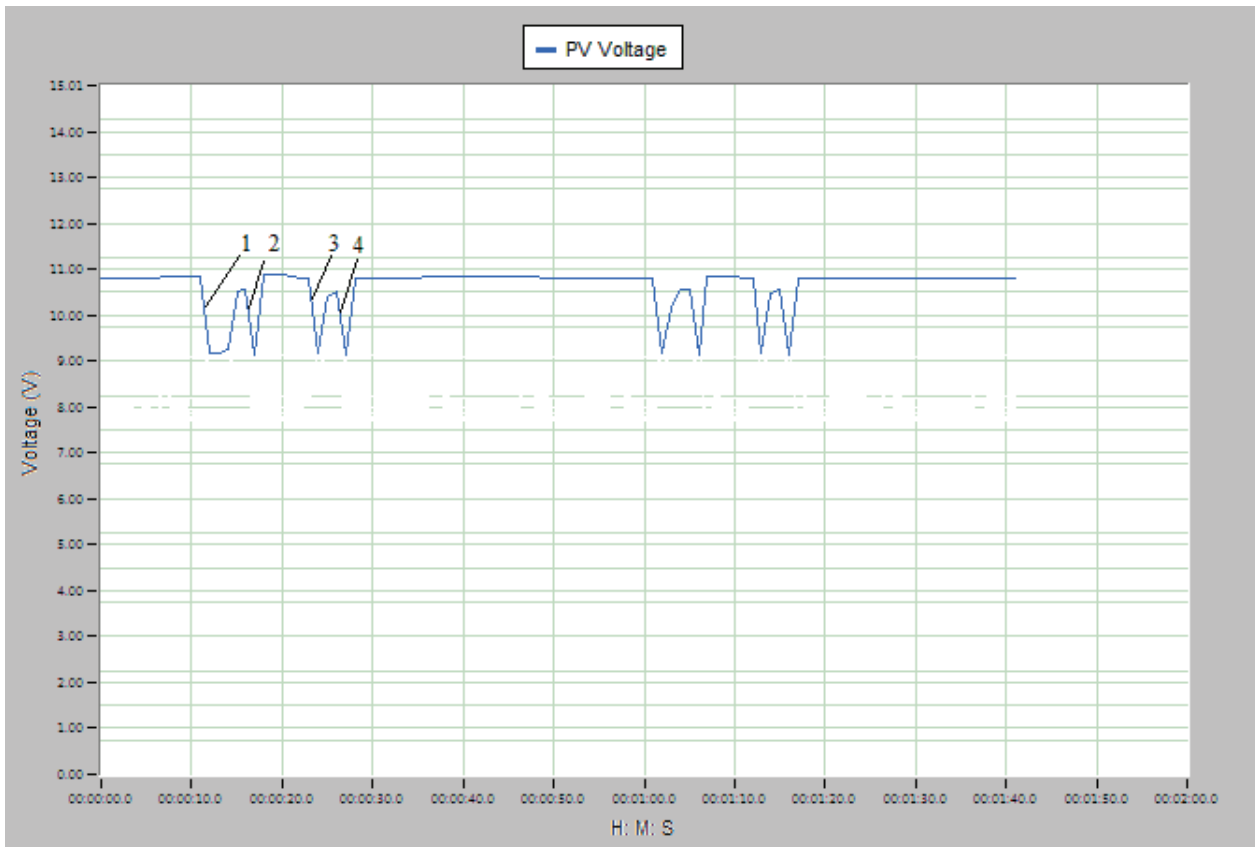


Fig. 21. Evolution of PV panel voltage at two work cycle up-down of barrier.

## V. CONCLUSION

The paper presented an automatic access system powered by photovoltaic panels, achieved small scale as an experimental model.

The solution of using two power sources for supply vehicle access system from PV panels or other sources represents an innovative solution for efficient energy use.

Experimental results show a smooth functioning of experimental automatic access system powered by PV panel and can be successfully expanded at real scale.

Received on July 17, 2016

Editorial Approval on November 15, 2016

## REFERENCES

- [1] L. Alboteanu, Gh. Manolea, and Al. Novac, "Automtion o a pumping station for alow power applictions", "Hidraulica"-Magazine of Hydraulics, Pneumatics, Tribology, Ecology, Sensorics, Mechatronics no. 1/2014, ISSN 1453 – 7303, pp.58-64.
- [2] L. Alboteanu, F. Ocoleanu, Al. Novac, Gh. Manolea, "Remote monitoring system of the temperature of detachable contacts from electric cells" Annals of the University of Craiova, Electrical Engineering series, No. 34, 2010; ISSN 1842-4805.
- [3] L. Alboteanu, F. Ravigan, Al. Novac, "Design of a Sun Tracking Automaton for Photovoltaic Panels with Low Concentration of Solar Radiation," Procc. of International Conference on Applied and Theoretical Electricity (ICATE), 2014, pp. 1-5, Craiova, Romania.
- [4] Ch. Cullens, "Use of Visual C++", Teora Publisher, 1996.
- [5] M. Marzband, A. Sumper, M. Chindris, and B. Tomoioga, "Energy management system of hybrid microgrid with energy storage", Buletinul AGIR, nr. 3/2012, pp. 635-642.
- [6] W. Nawrocki, "Measurement Systems and Sensors", London, ARTECH HOUSE, 2005.
- [7] A.M. Simionescu, "Modular system for acquisition, monitoring and processing electrical parameters of a distribution network," Buletinul AGIR, ISSN: 1224-7928, vol. 3, 2012, pp. 69-74.
- [8] C. Șulea, Gh. Manolea, "The hardware structure of the monitoring system for the Romanian anti-hail rockets launch units"; Annals of the University of Craiova, Electrical Series, Ed. Universitaria, ISSN: 1842-4805, Craiova, Romania, No. 36, 2012, pp. 339-244.
- [9] C. Șulea-Iorgulescu, E. Petre, "Specialized device – Slave – for monitoring the antihail systems", Published in: System Theory, Control and Computing (ICSTCC), 2015, IEEE, DOI: 10.1109/ICSTCC.2015.7321371
- [10] Toma L., "Acquisition systems and digital signal processing, . "Vest" Publsher , Timișoara, 1996.
- [11] C. Zoller, R. Dobra, "Microcontroller Implementation In The Electrical Networks For The Hazardous Areas", microCAD 2008, International Scientific Conference, University of Miskolc, Hungary, 2008.
- [12] \*\*\* <http://www.atmel.com/Microsite/atmel-studio/>
- [13] \*\*\* Atmega8 User datasheet.
- [14] \*\*\* [www.orcad.com](http://www.orcad.com) , Orcad software.
- [15] \*\*\* <http://cwbsolutions.net/parking-and-access-control>

# Dynamic Regime Electromagnetic Torque in Brushless Direct Current Motors

Ion Vlad, Sorin Enache, Monica Adela Enache

University of Craiova, Faculty of Electrical Engineering, Craiova, Romania  
ivlad@em.ucv.ro, senache@em.ucv.ro, menache@em.ucv.ro

**Abstract** - This study aimed at establishing the mathematical model for determining the dynamic regime torque and at emphasizing constructive aspects which influence its magnitude and variation. Brushless direct current motors are very present and there have been carried out researches regarding their design and optimum construction. The technology evolution in several areas has caused an increase in production of permanent-magnet BLDC motors, which has good technical-economic performances for a large range of controlled-speed applications. The study carried out, by the simulations we presented, shows that these motors have high torque oscillations in a complete rotation. There are identified the slots which create high torques, respectively low torques, in a complete rotation, thus justifying the oscillations. In this paper there is emphasized that the optimum variant of maximum torque involves a supply by six pulses per period in direct direction, also indicating the value of the control angle. The most unfavourable variant occurs at brushless direct current motor supplied by three pulses per period and reverse succession of phases, where the average value of the torque decreases by 56.7% over the optimum machine. A complete elimination of oscillations in this type of motor is not possible, but an optimal design can reduce them considerably.

**Keywords:** brushless direct current motor, design, simulation, optimization.

## I. INTRODUCTION

Classical direct current motors are replaced by brushless direct current motors in several applications due to low energy consumption, their high reliability and low maintenance. The main advantage of this motor is high specific power obtained by means of rare-earth permanent magnets, so a much decreased weight [1-5].

The possibility to replace the assembly comutator-brushes of direct current motor by a contactless commutation device emphasized the advantages of this machine [6-10].

For electrical devices and installations supplied by local energy sources, it is advisable to use permanent-magnet direct current fractional-horsepower motors which have a low weight per unit of power, high efficiency, linear mechanical characteristic, very high rotating speeds; they are noiseless motors, with safe operation, without monitoring and maintenance etc.

The motors used for two-wheeler vehicles (electrical scooter, electrical bicycle, electrical motor-scooter) are permanent-magnet direct current motors manufactured with "brushless" technology.

Brushless direct current motors are used in peripheric equipments of computers, in potentiometers with motor and in devices following advance of copying machines [3], [6], [11-14]. There is experienced using brushless direct current motors rated at high power, in electrical cars and auto-trucks.

At present [13], [15], [16-19], there are fabricated magnetic materials with special features, being possible to carry out brushless permanent-magnet direct current motors rated at low and middle powers.

In order to simplify the scheme of the commutation device and to reduce its cost, an armature winding having a minimum number of coils is used in these motors.

## II. CONSTRUCTION AND OPERATION

The motor construction uses permanent magnets made of rare earths [7], [16-19]. Good perspectives have the materials of type Nd-Fe-B, which have good magnetic features, are less breakable and have a low cost (much less than the magnets of type Sm-Co), but have a low operation temperature (80-100)°C. The temperature has an important effect upon the magnet characteristics, so upon the motor characteristics.

High currents and high temperatures cause demagnetization. In case of drives using brushless direct current motors, demagnetization is not a problem because the current is permanently followed and it is limited by controller and measuring motor temperature is a simple problem.

Brushless direct current motors are now frequently used for two-wheeler vehicles. They are carried out as a close construction IP 44, are assembled in the very wheel hub, have a solid construction, facing shocks, vibrations, bad weather. The producer pays a special attention to aspect and operation because the motor is integrated in the hub of the back wheel and the battery accumulator and the display have low dimensions.

Modern computation tools have enabled the capitalization of complex mathematical models for investigating and computing the electromagnetic torque of such motors.

An important aspect is the *functional criterion*, meaning to carry out the motor with certain technical characteristics imposed by customer, these being defined by means of the parameters: resistances, inductances, inertia moment, steady state and transient time constants etc. These parameters depend upon geometry, construction and electromagnetic stresses of the machine. In these circumstances, the theme we approached in this paper is a subject of interest for engineering.

### III. MATHEMATICAL MODEL FOR ESTABLISHING DYNAMIC REGIME ELECTROMAGNETIC TORQUE

The mathematical model carried out for establishing instantaneous values of electromagnetic torque [3], [4], [6], [8-9] is based on relations known in literature. The study we have carried out and presented below has considered:

$$\beta = p \cdot \alpha + \gamma \quad (1)$$

$\alpha$  - geometrical angle corresponding to the rotor displacement Fig.1,  $\beta$  -control angle of the a-phase current,  $\gamma$  -delay angle for the control of the current  $I_a$ .

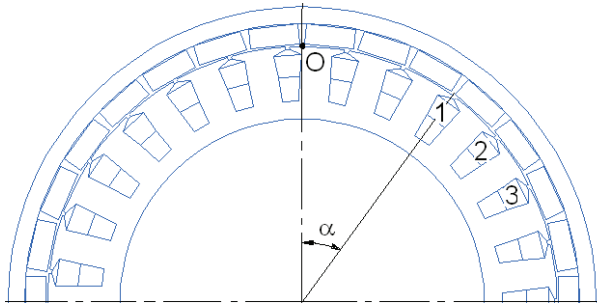


Fig.1. Cross-section through the motor.

There has been established the space origin in the point O, ( $\alpha = 0$  -neutral axis, Fig. 1) and the lines of the magnetic field have been modelled as follows: the opposite armature has been taken as being smooth (the slot opening is very small) and it has been considered that the field lines are radial over the whole magnet width, while they are modelled by arcs and segments outside that area.

The design data of the motor provide the magnetic voltage of the air-gap and its size in the magnet zone. In crossing points (ferromagnetic core-air) where the tangential component of magnetic induction preserves, there has been imposed the condition of continuity and derivability of the curve modelling the field line.

The air space between the magnets  $b_{0mg}$ , makes the air-gap size variable at the armature periphery, thus modelling the distribution curve of the air-gap magnetic induction (Fig.2), with a polynom-function of the third degree where continuity and derivative conditions have been imposed.

This way, we have modelled numerically the air-gap magnetic induction relatively to the rotor position:

$$B = f(\alpha) \quad (2)$$

and, by using this relation, there has been simulated the curve of air-gap magnetic induction, Fig. 2.

The armature winding is in star connection, distributed in slots (on tooth). The armature winding is radial, star connection, distributed in two layers into slots, with the pitch  $y=1$  (on tooth).

According to literature, for having a high rotating torque, during the operation we will have two coils connected in series and the third one at rest. Consequently, there are rectangular alternating currents, the duration of a pulse is of 120 electrical degrees.

There has been established the time origin  $t=0$  when  $\alpha = 0$  and there has obtained the numerical modelling of

currents relatively to the rotor position and the currents control:

$$I_a, I_b, I_c = f(\alpha, \gamma) \quad (3)$$

The control device models, on a polar pitch, the three currents of the windings relatively to  $\beta$  -electrical angle. The phase currents b and c are displaced in phase by 120 electrical degrees.

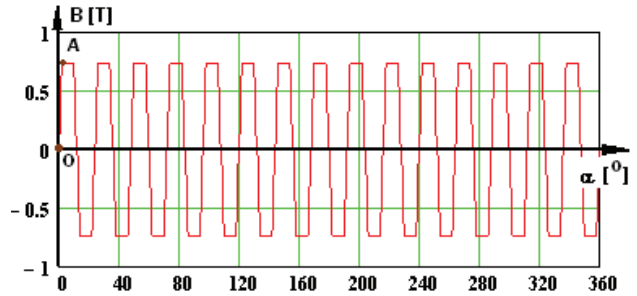


Fig.2. Distribution curve of air-gap magnetic induction on the whole machine.

It is considered that the point O -the space origin, is on the axis of the first slot, taken as a reference. Consequently, the position of the slot  $N_{cx}$  is established by the geometrical angle as below:

$$\zeta_{N_{cx}} = \alpha + \frac{360}{N_c} N_{cx} \quad (4)$$

There has been computed the ampere-turns corresponding to the conductors placed in the upper layer crossed by the current  $I_x$ , respectively to the conductors placed in the under layer where we have the current  $I_y$  for each slot:

$$\theta_{N_{cx}} = 0.5 \cdot n_c I_x + 0.5 \cdot n_c I_y \quad (5)$$

where we have:  $n_c$  -number of conductors/slot,  $N_{cx}$  - number of slot,  $I_x, I_y$  are the currents  $I_a, I_b$  or  $I_c$  relatively to the slots distribution on zones and phases, carried out according to literature.

There are considered the conductors and the afferent ampere-turns concentrated in the slot axis and at the air-gap level:

$$\theta_{N_{cx}} = f(\alpha, \gamma, N_{cx}) \quad (6)$$

In this stage there are known the air-gap magnetic induction  $B(\alpha)$ , the ampere-turns of each slot  $\theta_{N_{cx}}(\alpha, \gamma, N_{cx})$ , the iron length  $l_{Fe}$ , so it is possible to compute the torques determined by each slot with the relation:

$$T_{N_{cx}} = 0.5 \cdot D \cdot B(\alpha) \cdot \theta(\alpha, \gamma, N_{cx}) \cdot l_{Fe} \quad (7)$$

This way, we have modelled numerically the electromagnetic torque of a slot:

$$T_{N_{cx}} = f(\alpha, \gamma, N_{cx}) \quad (8)$$

For the total torque we have:

$$T = \sum_{i=1}^{N_c} T_{N_{cx}} \quad (9)$$

On the basis of the mathematical model presented, it is possible to carry out a computation program, where  $N_p$  – number of points per a complete rotation and  $N_{pi}$  – number of points by which the control is delayed, per a pole pair. This way, elementary angles result:

$$\alpha_e = k_p \frac{360}{N_p} \quad k_p = 1, 2, 3, \dots, N_p \quad (10)$$

$$\gamma_e = k_{pi} \frac{360}{N_{pi}} \quad k_{pi} = 1, 2, 3, \dots, N_{pi} \quad (11)$$

For values assigned to  $N_p$  and  $N_{pi}$  there are computed and memorized the instantaneous values and the average value in a complete rotation of torque given by a slot, respectively the total average torque.

IV. RESULTS, SIMULATIONS AND CONCLUSIONS

Using the mathematical model presented before and advanced numerical computation methods [20-24], there have been carried out simulations and, with the results obtained, there have been pointed out conclusions regarding electromagnetic torque of the motor.

All the results we have obtained and the simulations presented here are emphasized by a concrete example of permanent-magnet brushless direct current motor. The motor is rated as follows:  $P_N=100$  W;  $U_N= 20$  V;  $I_N=6.0$  A,  $n_N= 450$  r/min, and is built with 27 slots,  $2p=30$  magnetic poles of type Nd-Fe-B.

A.1. Supply by six pulses per a pair of poles and direct succession of phases

The control device, which supply the motor, sets the phase current for three phases (Table I), during an operation period.

TABLE I. The matrix of the three phase currents

$\alpha$ [°] el.	0÷60	60÷120	120÷180	180÷240	240÷300	300÷360
$I_a$ [A]	$I_N$	$I_N$	0	$-I_N$	$-I_N$	0
$I_b$ [A]	$-I_N$	0	$I_N$	$I_N$	0	$-I_N$
$I_c$ [A]	0	$-I_N$	$-I_N$	0	$I_N$	$I_N$

For criterion “maximum electromagnetic torque” the optimum variant of winding has been found, where the distribution of slots per zones and phases is that presented in Table II. Because we have three overlapped stars, there have been presented the ampere-turns produced by currents which cross the conductors from the nine slots.

TABLE II. Slot ampere-turns

Slot no.	1	2	3	4	5	6	7	8	9
Ampere-turn in the upper layer	$\theta_A$	$-\theta_A$	$-\theta_B$	$\theta_B$	$-\theta_B$	$-\theta_C$	$\theta_C$	$-\theta_C$	$-\theta_A$
Ampere-turn in the lower layer	$\theta_A$	$-\theta_A$	$\theta_A$	$\theta_B$	$-\theta_B$	$\theta_B$	$\theta_C$	$-\theta_C$	$\theta_C$

In Fig.3 there is presented the curve of the electromagnetic torque average value, for a complete rotation, for different control angles of currents.

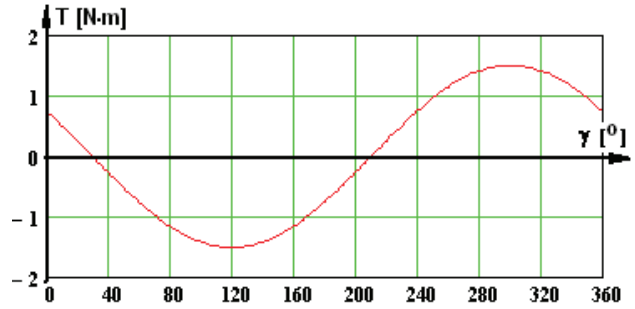


Fig.3. Torque average value at a complete rotation for different control angles of currents.

In order to obtain a maximum torque for a complete rotation, the control electrical angle is  $\gamma=294^\circ$  or the geometrical angle  $\xi=294/15=19.6^\circ$  shows where the first position transducer is placed on the rotor (fixed armature) relatively to the origin –point O, in the rotation direction. The next positions where the transducers are placed are at  $120^\circ$  electrical degrees in the rotation direction.

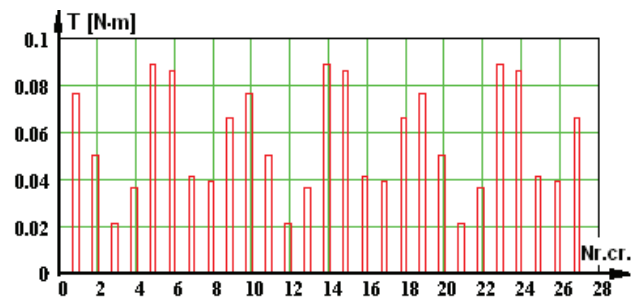


Fig.4. Torque values relatively to the number of slot.

For the angle  $\gamma$  -fixed and ( $\alpha= 0 \div 360^\circ$ ), by means of the program there have been computed the average value of the torques given by the currents which cross the conductors from the armature slots. The total torque of the motor has resulted as  $T_N=1.52$  N.m, for a speed of  $n_N=450$  r/min, so, the useful mechanical power results as  $P_2=72.2$  W.

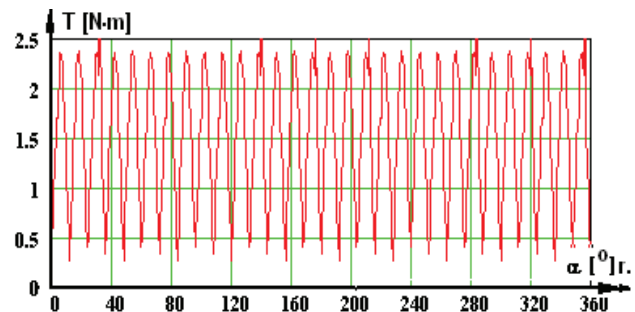


Fig.5. Variation curve of the motor torque at a complete rotation.

By analyzing Fig.4, we notice the slots and their contribution at producing the motor torque: 5, 6, 14, 15, 23, 24 –very important slots, 1, 10, 14 –important slots, 4, 8, 13, 22 –slots with mild torques, 3, 12, 21 –slots with low torques.

In Fig.5 we can see how the total torque of brushless direct current motor modifies for a complete rotation (a lot of peaks and variations within large limits).

There are presented below the torque variation curves, for a complete rotation, at different slots, Fig. 6.

From the analysis of these figures we notice that, at slots 3, 12, 21 the average value of the torque is very low and the torque has large positive and negative oscillations and slots 5, 6, 14, 15, 23, 24 provide high torques.

Periodical oscillations of torque are a major cause of vibrations, which in some cases can produce the mechanical resonance of the system.

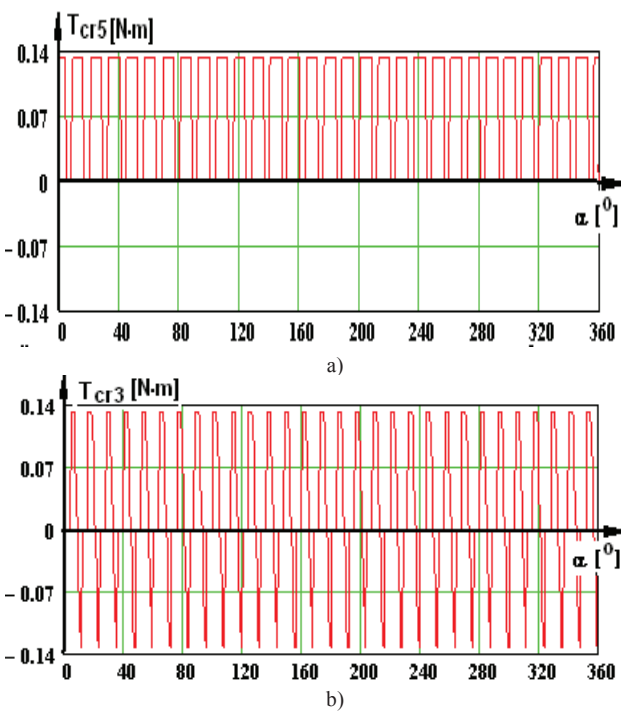


Fig.6. Variation curves of torques for a complete rotation: a) provided by the currents which cross the conductors from the slot 5; b) for the slot 3.

*A.2. Supply by six pulses per a pair of poles and reverse succession of phases*

In the matrix of the three phase currents from table no. 1, the phases b and c are reversed during a period.

The curve of the average value of the electromagnetic torque for a complete rotation, for different control angles of currents is presented in Fig.7.

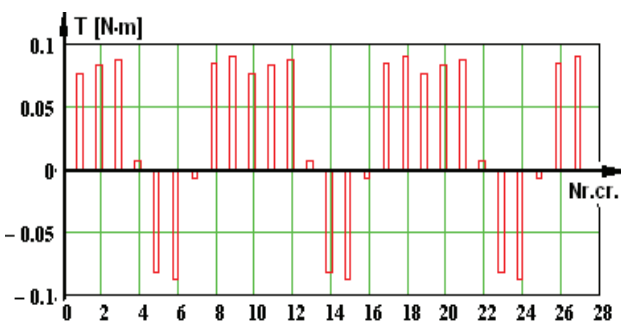


Fig.7. Values of torques relatively to the slot number.

For the electrical angle  $\gamma=10$  and  $(\alpha= 0 \div 360^\circ)$ , by means of the program, there have been computed the average values of the torques provided by the currents which cross the conductors from the armature slots.

The total torque of the motor has resulted as  $T_N=0.755$  N·m, at a speed of  $n_N=450$  r/min, so the useful power is  $P_2=35.3$  W.

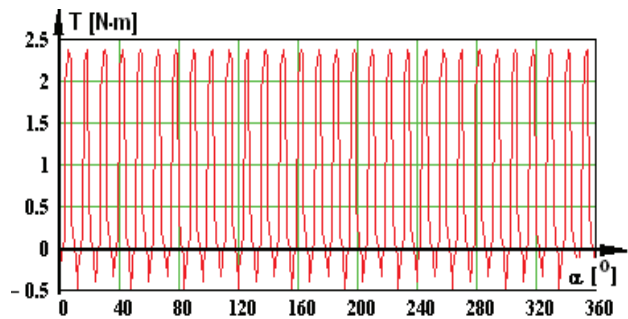


Fig.8. Variation curve of the motor torque for a complete rotation.

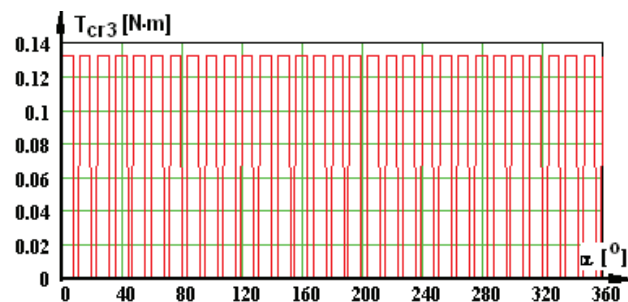


Fig.9. Variation curve of torque for the slot 3 for a complete rotation.

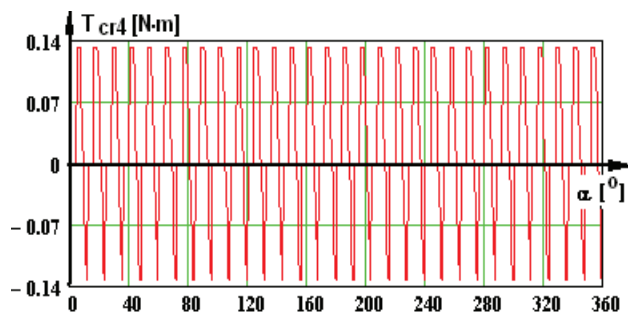


Fig.10. Variation curve of torque in a complete rotation for the slot no. 4.

The most important slots are multiple of three, with an average torque of  $T_{cr3}=0.084$  N·m, and the representative torque is presented in Fig.9. The slot no. 4 causes a torque having very high oscillations (positive and negative), Fig.10, the average value being  $T_{cr4}=0.012$  N·m.

*B.1. Supply by three pulses per a pair of poles and normal succession of phases*

The values of the three phase currents during a period are given by a three-pulse control device. The program of numerical computation enables this analysis which, on the basis of the simulations we carried out and the results we obtained, shows how many drawbacks this supply variant has. The matrix of the three phase currents (table no. 3), during a period is given by a three pulses control device.

TABLE III.  
The matrix of the three phase currents

$\alpha$ [°] el.	0÷60	60÷120	120÷180	180÷240	240÷300	300÷360
$I_a$ [A]	$I_N$	$I_N$	0	0	$-I_N$	$-I_N$
$I_b$ [A]	$-I_N$	$-I_N$	$I_N$	$I_N$	0	0
$I_c$ [A]	0	0	$-I_N$	$-I_N$	$I_N$	$I_N$

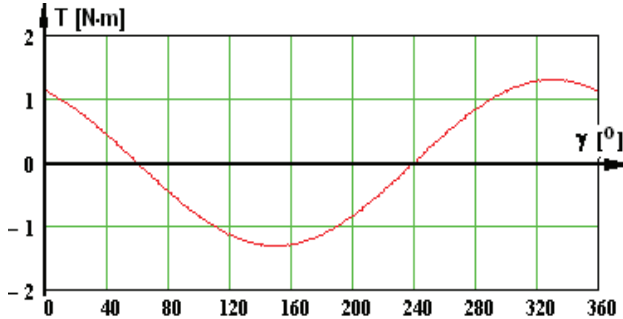


Fig.11. Average value of torque at a complete rotation for different control angles of currents.

For different control angles of currents there is obtained the curve of the electromagnetic torque for a complete rotation, Fig.11. There results two maximum torques, a positive one for  $\gamma=330$  electrical degrees and a negative one for  $\gamma=150$  electrical degrees.

Corresponding to the control angle  $\gamma=330^\circ$  and  $\alpha=0 \div 360^\circ$ , there have been established the torques provided by the currents which cross the conductors from the armature slots.

The total torque of the motor has resulted as  $T_N=1.314$  N.m, for a speed of  $n_N=450$  r/min, so we have a useful power of  $P_2=61.9$  W.

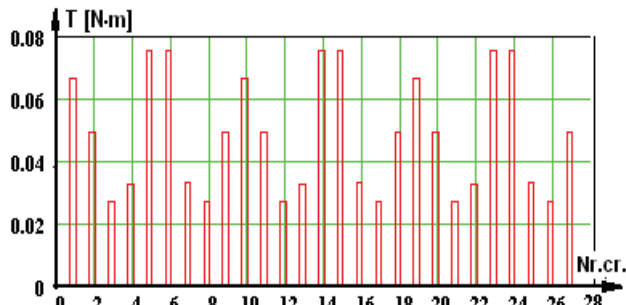


Fig.12. Torque values relatively to the slot number.

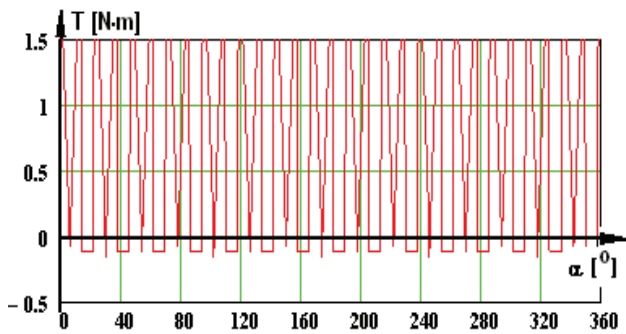


Fig.13. Variation curve of the motor torque for a complete rotation.

In Fig. 12 there can be seen the curve of the total torque, for a complete rotation (a lot of peaks and variations within large limits).

B.2. Supply by three pulses on a pair of poles and reverse succession of phases

There are preserved three pulses on a period but there are interchanged the phases b and c. There is simulated the curve of the electromagnetic torque for different control angles of currents.

There result two maximum torques, a positive one for  $\gamma=30$  electrical degrees and a negative one for  $\gamma=210^\circ$  electrical degrees. For the control angle  $\gamma=30^\circ$  and  $\alpha=0 \div 360^\circ$ , there have been computed the torques provided by the currents which cross the conductors from the armature slots, Fig.14.

There resulted a total average torque of  $T_N=0.657$  N.m, for a speed of  $n_N=450$  r/min, so we have a useful power of  $P_2=30.96$  W.

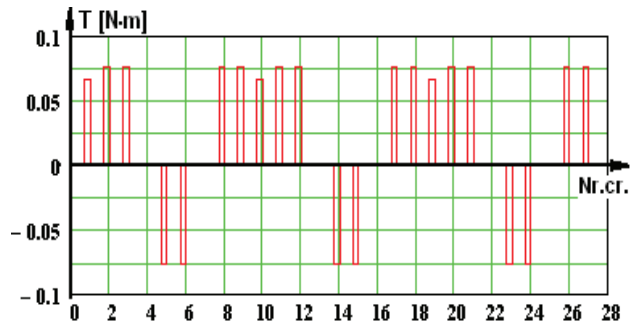


Fig.14. Torque values relatively to the slot number.

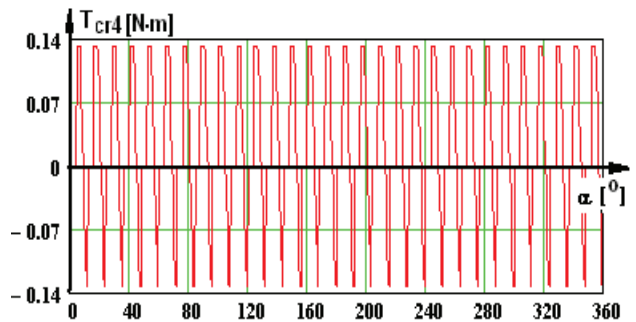


Fig.15. Variation curve of total torque in a complete rotation.

In this case, Fig.15, the torque has very high oscillations (positive and negative) and the average value is lower  $T_N=0.657$  N.m.

The most important results of the study we have carried out are filled in table no. 4, where:  $T_{med}$  –average value of the torque for a complete rotation,  $T_{cr,max}$ ,  $T_{cr,min}$  –minimum/maximum value of the slot torque,  $N_{crt}$  with  $T>0/<0$  –number of slots which provide positive/negative torque.

Table IV.  
Couples notches created by the rotor

	Supply by six pulses per period		Supply by three pulses per period	
	Succession a, b, c	Succession a, c, b	Succession a, b, c	Succession a, c, b
$T_{med}$ [Nm]	1.52	0.755	1.314	0.657
$T_{cr,max}$ [Nm]	0.084	0.092	0.076	0.075
$T_{cr,min}$ [Nm]	0.021	0.007	0.026	0.063
$N_{crt}$ -cu $T>0$	27	21	27	15
$N_{crt}$ -cu $T<0$	0	6	0	6

## V. CONCLUSIONS

A constant wave of torque is important, especially in servo-drives, where a high precision, a control of speed and rotor position are required. For instance, in tool-machines, finishing the processed piece is negatively affected by torque oscillations of driving motor. Periodical torque oscillations or *ripple* are, in a lot of situations, the cause of vibrations which are annoying when mechanical resonance occurs in equipment structure.

The study we have carried out and the results presented in table no.4 recommend the supply by six pulses and direct succession of phases, because there results the highest torque for a complete rotation, all the slots are active and provide positive torques, so the oscillations are lower.

We can notice that in all these cases we have some very active slots ( $T_{cr}=0.084$  N·m) and some almost inactive slots ( $T_{cr}=0.021$  N·m). The most unfavourable variant is the supply by three pulses and reverse succession of phases, when the torque gets high oscillations and decreases to 56.7% over the torque corresponding to the optimum variant.

An almost constant torque cannot be obtained for brushless direct current motor, but we can draw near this requirement. The inertia moment of the rotor and the high speed decrease the speed oscillations caused by torque oscillations. A performing control system, with a reaction loop by speed, can reduce considerably the torque oscillations for low speed, too, if the amplification and the bandwidth are high enough.

## ACKNOWLEDGMENT

This paper was realized under the frame of the grant POC-A1-A1.2.3-G-2015 ID 40 401.

Received on July 17, 2016

Editorial Approval on November 24, 2016

## REFERENCES

- [1] C. Bianchini, F. Immovilli, E. Lorenzani, A. Bellini, M. Davoli, "Review of Design Solutions for Internal Permanent Magnet Machines Cogging Torque Reduction", 2011, *IEEE Transactions on Magnetics*, vol. 48, no.10, Oct. 2012, pp 2685-2693.
- [2] A. Campeanu, I. Vlad, S. Enache, "Numerical Analysis of the Dynamic Behavior of a High Power Salient Pole Synchronous Machine by using a Corrected Model", *AECE Journal*, Vol.12, Issue 1, Year 2012, pp.97-102.
- [3] L. Dosiek, P. Pillay, "Cogging Torque Reduction in Permanent Magnet Machines", *IEEE Trans. On Industry Applications*, vol. 43, no. 6, 2007, pp 1565-1571.
- [4] W. Fei, P.C.K. Luk, "A New Technique of cogging Torque Suppression in Direct-Drive Permanent-Magnet Brushless Machines", *IEEE Trans. on Industry Applications*, vol 46, no. 4, July/Aug. 2010, pp. 1332-1340.
- [5] M.S. Islam, S. Mir, T. Sebastian, "Issues in reducing the cogging torque of mass-produced permanent magnet brushless DC motor", *IEEE Trans. on Industry Applications*, vol. 40, no. 3, 2004, pp.813 – 820.
- [6] J. Kaňuch, Z. Ferková, "Design and simulation of disk stepper motor with permanent magnets", *Archives of Electrical Engineering*, vol. 62, no. 2 (2013), pp. 281-288.
- [7] T. Koch, A. Binder, "Permanent magnet machines with fractional slot winding for electric traction", *International Conference on Electrical Machines, ICEM 2002, Brugge, Belgium, 2002*.
- [8] M. Miyamasu, K. Akatsu, "Efficiency Comparison between Brushless DC Motor and Brushless AC Motor Considering Driving Method and Machine Design", *IEEE Industrial-Electronics-Society (IECON 2011), 2011*, pp.1830-1835.
- [9] I. Vlad, S. Enache, M.A. Enache, "Optimization of Low-Power Brushless Direct Current Motors", *The 9 th International Symposium on ADVANCED TOPICS IN ELECTRICAL ENGINEERING*, 7-9 mai 2015, București, pp.176-181.
- [10] I. Vlad, S. Enache, L. Mandache, M.A. Monica, "Transversal Shape Optimization of a Brushless DC Motor for Electric Vehicles", *Annals of the University of Craiova, Electrical Engineering series*, nr. 39, Anul 2015, pp.144-149.
- [11] T. Sebastian, S. Mir, M. Islam, "Electric Motors for Automotive Applications", *EPE Journal*, vol. 14, no.1, 2004, p.31-37.
- [12] T. Tudorache, L. Melcescu, M. Popescu, "Methods for Cogging Torque Reduction of Directly Driven PM Wind Generators", *12th International Conference on Optimization of Electrical and Electronic Equipment, OPTIM, 2010*.
- [13] S.H. Zareh, M. Khosroshahi, M. Abbasi, K.G. Osgouie, "The select of a permanent magnet brushed DC motor with optimal controller for providing propellant of a Home Mobile Robot", *IEEE (ICMA)*, 2010, pp.1137 – 1141.
- [14] Y.L. Zhang, W. Hua, M. Cheng, G. Zhang, X. F. Fu, "Static Characteristic of a Novel Stator Surface-Mounted Permanent Magnet Machine for Brushless DC Drives", *38th Annual Conference on IEEE-Industrial-Electronics-Society (IECON 2012)*, 2012, pp.4139-4144.
- [15] N. Vasile, V. Dogaru, C. Sălișteanu, *Electrical machines. Construction, technology and special applications*, ICPE Publishing House, Bucuresti, 2000 (in Romanian).
- [16] \*\*\* Catalog ICPE Bucharest, Sintered magnets Al-Ni-Co and Nd-Fe-B –magnetic characteristics.
- [17] [http://neomagnet.ro/produse-in-stoc/D165\\_H15\\_mm\\_magnet\\_inel\\_sm2co17](http://neomagnet.ro/produse-in-stoc/D165_H15_mm_magnet_inel_sm2co17).
- [18] [http://www.icpe-me.ro/motoare\\_magneti\\_permanenti.ht](http://www.icpe-me.ro/motoare_magneti_permanenti.ht)
- [19] <http://www.et.upt.ro/admin/tmpfile/fileM1369636748file51a2ff8c8b180.pdf>
- [20] O. Cira, *Lessons of MathCad*, The Blue Publishing House, Cluj-Napoca, 2000 (in Romanian).
- [21] I. Daniel, I. Munteanu, *Numerical methods in electrical engineering*. Bucharest, MATRIX ROM Publishing House, 2004 (in Romanian).
- [22] V. Fireșteanu, M. Popa, T. Tudorache, *Numerical modeling in the study and design of electrical devices*, Editura Matrix Rom, Bucuresti, 2004 (in Romanian).
- [23] St. Nagy, *Numerical modelling of electromagnetic and thermic field*, Applications, Oradea 2004 (in Romanian).
- [24] P. Năslău, R. Negrea, s.a., *Computer aided mathematics*, Timișoara, Politehnica Publishing House, 2005 (in Romanian).

# Enhancing the dynamic frequency of microgrids by means of PV power plants with integrated energy storage

Daniel Munteanu, Ioan Serban, Corneliu Marinescu, Luminita Barote

Department of Electrical Engineering and Applied Physics, Transilvania University of Brasov, Brasov, Romania

Email: munteanu.d@unitbv.ro

**Abstract** - Achieving<sup>1</sup> a high-level of stability represents one major concern in autonomous microgrids (MGs) with high penetration levels of renewable energy sources. The aim of this paper is to study how photovoltaic (PV) power plants can provide dynamic frequency support in MGs, in order to obtain an improved stability for the entire power system. On the PV side an energy storage subsystem is added, with the main purpose of better control and higher power reserve of the PV power plant. By this way the necessary input power is provided by the PV system along with the battery block. The required output power is supplied by a three-phase voltage source converter (VSC). The VSC control is implemented in a rotating  $dq$  reference frame, including a harmonic compensation loop for the output current. To improve the dynamic frequency stability of the MG, specific functions are implemented within the PV inverter control. To highlight the performance of the proposed system, a comparative analysis is provided, which cover four cases of interest depending on the status of the storage system and dynamic support (i.e. with/without storage and with/without dynamic support). Simulation results are included to validate the power control system, showing that the dynamic frequency control can be improved by the proposed solution.

**Keywords:** *Frequency control; microgrid; power system dynamic stability; PV power generation, energy storage.*

## I. INTRODUCTION

The rapid development growth of distributed generation systems is mainly associated with the sector of Renewable Energy Sources (RES). Aiming to maximize the use of local energy resources as close as possible to the consumers and to reduce the losses on the conventional networks have led to the necessity of developing small self-sustaining power systems, namely microgrids (MGs) [1]. Moreover, the MG is considered the building block in the future smart grid [2]. The automated MGs will take the control of the power systems related to the stability of supply and energy quality, mainly because the exponential increase of the control complexity makes no longer possible the human dispatcher to perform it. Within this framework, the RES-base generators should also have to participate to ensuring the MG power quality and stability. Therefore, the main tasks have to be shared among all the resources in the MG, sources, energy storage systems and consumers [3].

A major issue of the grids with high RES penetration levels consists in ensuring the power control and predictability. In this regard, the RES generators must become controllable in a similar way to conventional ones. In autonomous MGs, maintaining the stability both in normal operating conditions and during severe dynamic regimes represents a more difficult task mainly because of its reduced inertia and power reserve [19]. Therefore, besides enhancing the MG stability and power availability by means of energy storage systems and active loads, improving the RES generators control mainly during dynamic regimes represents a new real concern.

The current research is focused on the photovoltaic (PV) source, because of its high potential in terms of answer speed capability to face with the stability problems, part of which are created in large extent by its own inherent variability of energy production. The premise used to date, consisting in maximising the energy production using a maximum power point tracking (MPPT) algorithm, will be replaced by the higher priority request to participate to the MG operational stability. The main studied solutions to achieve a more flexible power control of PV power plants consist in integrating energy storage systems within the power plant structure [4]-[7], curtailing the PV output power to a certain degree [8]-[11], or combination of both solutions. Although such solutions increase the costs – either in terms of additional resources (e.g. energy storage system), or because of not using the entire available solar energy when operating outside the maximum power point – they are justified when ensuring the security and stability in MGs with limited resources becomes a priority.

Integrating an energy storage system within a PV power plant to enhance its power control can be accomplished in several ways. The solution of interest for the current study involves connecting a battery bank to the DC-link of the PV inverter by means of a bidirectional DC-DC converter [13], [15]. To be mentioned that this paper is an extension of a previous study [20], being mainly focused on the operation strategy and control of the PV-battery system in order to increase the active power control of the PV power plant and thus, to be able to participate in the MG dynamic frequency control mechanism [12]-[14],[16].

After introduction, the paper is organized as follows: Section II presents the three-phase inverter (VSC) and system configuration, in Section III the control principle and control methods of the VSC are detailed, Section IV describes the simulation cases and results while the main conclusions are provided in Section V.

<sup>1</sup> This work was supported by a grant of the Romanian National Authority for Scientific Research and Innovation, CNCS – UEFISCDI, project number PN-II-RU-TE-2014-4-0359.

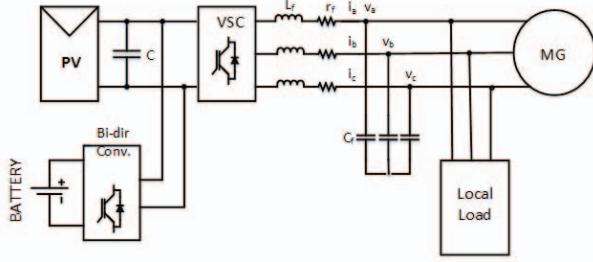


Fig. 1. Block diagram of the analysed system

## II. PV SYSTEM CONFIGURATION

Fig. 1 shows the block diagram of the studied PV system, consisting of a three-phase VSC connected to a MG. The inverter is supplied from a PV system and a battery block is connected on the DC-link to support either a local load connected when operating islanded, or to provide dynamic support when connected to the MG.

The analysed PV power plant consists in a single string with 22 series connected panels each having 245 W. The PV string is connected directly to the VSC DC-link, the rated DC voltage produced by the string being around 650V.

A 48V battery is connected to the VSC DC-link by means of a DC-DC bidirectional converter. It should be mentioned that the discussion about the converter structure and its impact on the overall system efficiency are issues outside the focus of the current paper and, therefore, a generic DC-DC half-bridge converter is considered. Another important aspect that is reserved for future studies implies the optimization of the converter power and battery capacity. If the PV system is intended to support the MG only during severe dynamic regimes, a short-term energy storage system is to be considered.

## III. SYSTEM CONTROL

### A. VSC Power control

The control of the VSC output power is accomplished in rotating  $dq$  reference frame, with the block diagram developed as in Fig. 2a and Fig. 2b. The inner current loop is based on proportional-integrator (PI) controllers on each axis, with voltage feed-forward and cross-coupling elimination terms [17]. The synchronization of the inverter is done by a conventional three-phase phase-locked loop (PLL). Based on the active and reactive power references ( $P_{PV}^*$ ,  $Q_{PV}^*$ ), the  $dq$ -axis reference currents are calculated as follows [17]:

$$I_d^* = \frac{2 P_{PV}^* V_d + Q_{PV}^* V_q}{3 (V_d^2 + V_q^2)} \quad (1)$$

$$I_q^* = \frac{2 P_{PV}^* V_q - Q_{PV}^* V_d}{3 (V_d^2 + V_q^2)} \quad (2)$$

For limiting the output current distortion to the standard level (i.e.  $THD_1 < 5\%$ ), the VSC control also includes a harmonic compensation (HC) loop, presented in Fig. 2c. The HC is implemented in rotating reference frames, one for each harmonic that is required to be compensated. In this case, targeting for the 5<sup>th</sup> and 7<sup>th</sup> harmonics, two

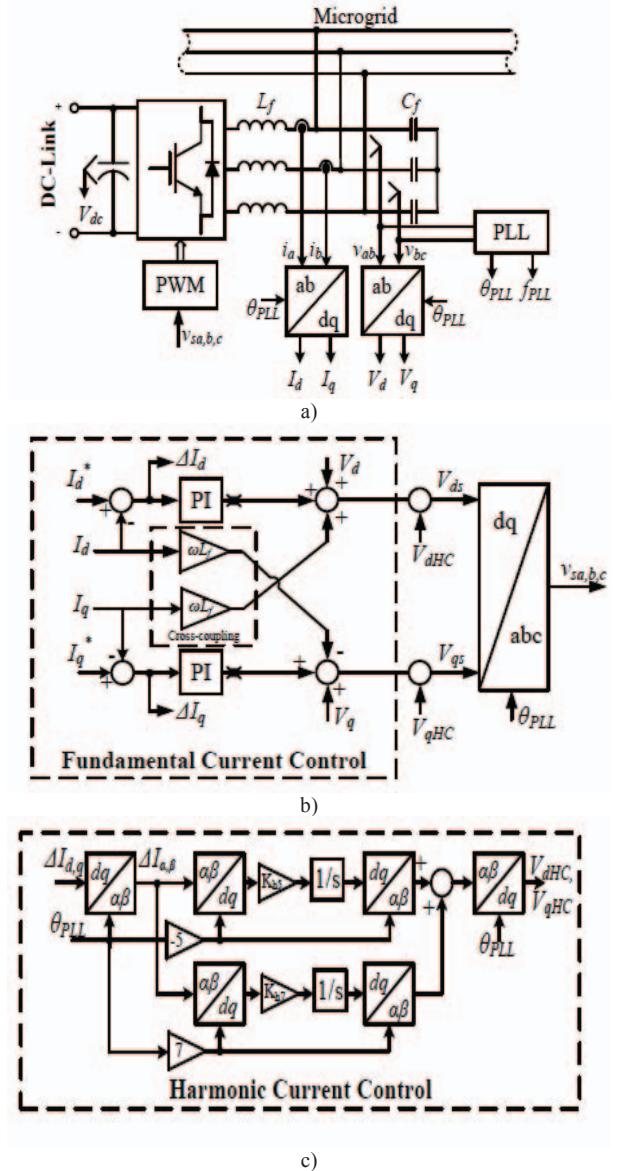


Fig. 2. VSC command: a) general structure; b) fundamental current control diagram; c) harmonic current control diagram

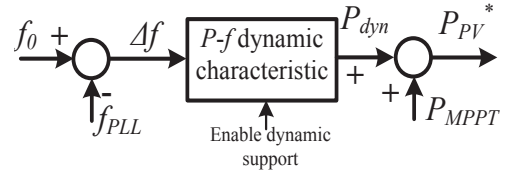


Fig. 3. Block diagram of PV Frequency controller

rotating frames at  $-5\omega$  (negative sequence) and  $7\omega$  (positive sequence) are employed. The converted current signals are provided to two integral controllers with the corresponding gains of  $K_{h5}$  and  $K_{h7}$ . The obtained compensation voltages are then added to the main  $dq$  VSC reference voltages.

When the energy storage system is connected to the VSC DC-link the battery acts as an energy buffer to balance the power between the PV production and the VSC output requirements. By this way the VSC output power is decoupled from the PV available power and, therefore, achieving a better control of the PV power

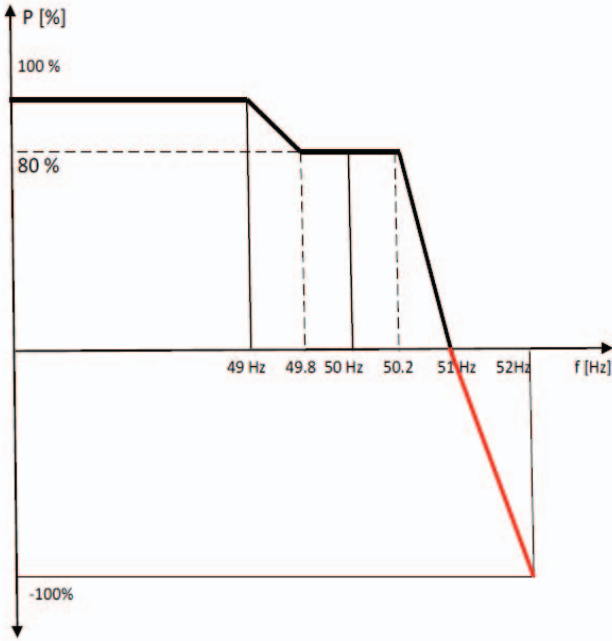


Fig. 4. Dynamic Frequency characteristic of the PV power plant

plant. In this paper, this characteristic is used to provide a certain level of support for the MG frequency.

When the support is enabled, the battery energy storage system is controlled to maintain the DC-link voltage constant by absorbing or injecting power by means of the bidirectional DC-DC converter. For a better assessment of the system performance, the conventional operation case of the PV power plant (i.e. without integrated storage) is also included in Section IV. In this case, the DC-link voltage is no longer regulated by the battery system, but by the internal VSC control.

### B. Frequency Control

For the purpose of PV power plant participation in the MG frequency control process, a frequency controller is developed with the block diagram shown in Fig. 3. The frequency deviation  $\Delta f$  from the reference value  $f_0$  – which may be fixed or controlled by the MG central controller – is used to determine the active power reference according

to a predefined P-f characteristic. The signal  $P_{MPPT}$  comes from the MPPT block, which is not detailed in the current paper.

In order to analyse the proposed PV plant response to the frequency changes, for the simulations presented in section V an aggregate dynamic MG model is developed, based on the transfer function from (3) to represent the primary frequency control process, in per units (p.u.) [18].

$$G_{MGf}(s) = \frac{\Delta f_{MG}}{\Delta P} \quad (3)$$

$$= \frac{1 + sT_R}{2Hf_0T_Rs^2 + (DT_R + 2Hf_0)s + D + \lambda_{MG}}$$

where:  $\Delta f_{MG}$  is the MG frequency deviation;  $\Delta P$  is the active power disturbance;  $T_R$  represents the composite time constant of the primary frequency control of the MG;  $\lambda_{MG}$  is the composite power-frequency characteristic of the MG;  $H$  is the inertial time constant of the MG;  $D$  is the load damping coefficient;  $f_0$  is the initial steady-state frequency.

The active power-frequency characteristic is inspired from the existing PV grid code standards (Romanian grid code was targeted), being adapted for the required operation in MGs. As Fig. 4 illustrates, this characteristic is based on a 20 % reserve of the inverter when the frequency falls within normal operation range. Featuring an enhanced active power control due to the integrated storage, the characteristic can be expanded to the bottom quadrant also (i.e.  $P < 0$  – absorbing active power from MG). Therefore, the system can react to both signs of the frequency deviation. To be mentioned that, the current paper does not cover the cases when the battery reaches its state of charge (SOC) limits and when the system cannot longer operate as described. This aspect is reserved for future studies.

In order to highlight the proposed system behaviour in comparison with the conventional PV operation mode, two methods of generating the active power reference are used. In the first case a fixed reference value is used (i.e.

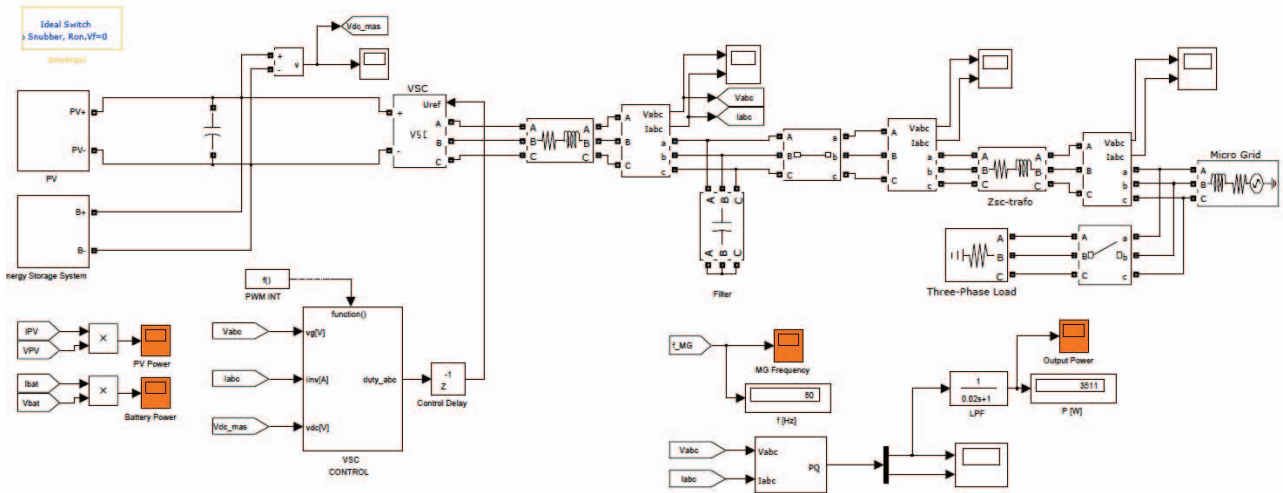


Fig. 5. Simulink block diagram Simulink of the studied system

provided by  $P_{MPPPT}$ ), while in the second case the dynamic frequency support is enabled.

Voltage regulation can also be provided through exchange of reactive power control [21], but in this case the reactive power reference is set to zero ( $Q_{PV}^*=0$ ) in order the VSC to operate at unity power factor.

#### IV. SIMULATION RESULTS

The PV system presented in Fig. 1 is modelled in Matlab/Simulink, and the main simulations of interest are discussed hereinafter. Fig. 5 presents the Simulink diagram of the PV inverter connected to the MG and main system parameters are presented in Table I. The VSC used here is a 5 kW three-phase inverter, sized to support the PV system above and to supply a 5 kW load connected to the MG. As for the simulation of the MG, is used a dynamic MG model in Simulink. The dynamic characteristic of the frequency presented in Fig. 4 is implemented in Simulink by means of a look-up table function. The MG model is developed according to expression (3), the frequency changing according to the active power balance in the MG. By this way, it is possible to analyse and optimize the PV power plant response during dynamic events in the MG.

In order to highlight the support capabilities of the studied system, the presented analysis includes the following operating cases: with and without dynamic support from the PV power plant, applied for different irradiation values and one more case, in which are applied the above conditions, but without battery support. There are three operating cases. In the first case there is a fixed value for the irradiation ( $G=1000\text{W/m}^2$ ) and two assumptions with and without dynamic support, while in the second case the irradiation drops to a lower value ( $G=500\text{W/m}^2$ ) in order to simulate a real PV operating condition also with the same assumptions. In the third case there are the same aforementioned conditions but without using the battery support.

The measurements include the MG frequency and the main active powers in the system (i.e. PV string, battery and VSC). For all cases, the MG is considered initially at steady-states with  $f_0=50$  Hz.

As Fig. 6 shows, at  $t=2\text{s}$  when the load is connected, the frequency decreases rapidly to 48.72 Hz without dynamic support and to 48.86 Hz with dynamic support. After the primary frequency control is finished in about three seconds after the disturbance occurred, the frequency is restored in both cases to the rated value of 50Hz. Regarding the system active power flow, as shown in Fig. 7, without support the VSC output power has a small reaction to the MG frequency deviation. All the powers remain constant and the battery block is charged. The output power is constantly around 5000 W, after the load is switched on. With dynamic support, the PV power remains unchanged at around nominal value with a fluctuation after 2 second when the load is switched on. The VSC output power changes according to the characteristic from Fig. 4, increasing from 4000 W up to around 5000 W when the load is switched on, and again at 4000 W after that. During this time, the battery provides the balance of around 1250W between the PV and VSC power. This difference is smaller when the system operates without dynamic support and higher with

dynamic support, the reason being the imposed operating characteristic of the frequency dynamic control for the VSC with power reserve, as described in section III.

TABLE I.  
THE MAIN SYSTEM PARAMETERS

Parameters	Values
VSC rated output power	5 kW
DC link voltage	650 V
Battery voltage	48 V
VSC output filter inductance and capacitance	3.1 mH; 10 $\mu\text{F}$
MG rated frequency ( $f_0$ )	50 Hz
MG time constant of the primary frequency control ( $T_R$ )	0.1 s
MG inertia constant (H)	1 s
MG damping factor (D)	2 %
MG power frequency characteristic ( $\lambda_{MG}$ )	20 kW/Hz

In the second studied case, the PV irradiation changes from  $G=1000\text{W/m}^2$ , to  $500\text{W/m}^2$  at  $t=4\text{s}$ . For a better comparison these tests are accomplished for two operating conditions, i.e. without dynamic support and with dynamic support. As shown in Fig. 8, the frequency starts from the 50 Hz and after 2 seconds when the load is connected, it drops to 48.72 Hz without dynamic support, while with dynamic support being limited to 48.86 Hz. It should be mentioned that the frequency response is similar to the case presented in Fig. 6, since the integrated battery energy storage system ensures the power balance on the DC-link side of the VSC and, therefore, the VSC maintains its power response capability regardless of the PV production. As shown in Fig. 9, without dynamic support the PV power is constant around nominal value. After 4 seconds when the irradiation changes, the PV string power drops proportionally to 2000 W. However, due to the integrated energy storage system, the VSC output power is not affected, because during this time, when the irradiation drops the battery provides the balance between the PV and VSC power with a small fluctuation in both cases. The VSC output power being higher than the PV production, the battery provides the difference and starts discharging. Similar to the previous case, the balance is lower when the support is enabled in contrast to the operation without support. As a consequence, the MG frequency is undisturbed by the PV string power reduction at  $t=4\text{s}$ , as illustrated in Fig. 8.

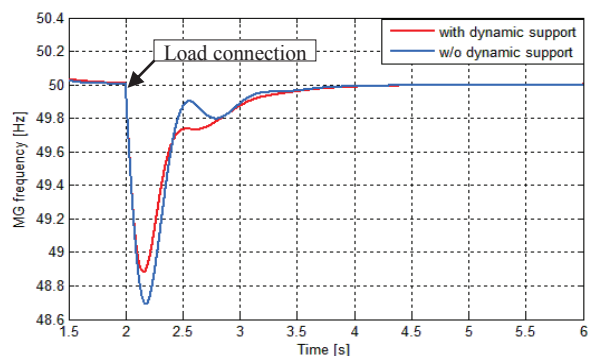


Fig.6. MG frequency for  $G=1000\text{W/m}^2$  without and with dynamic support.

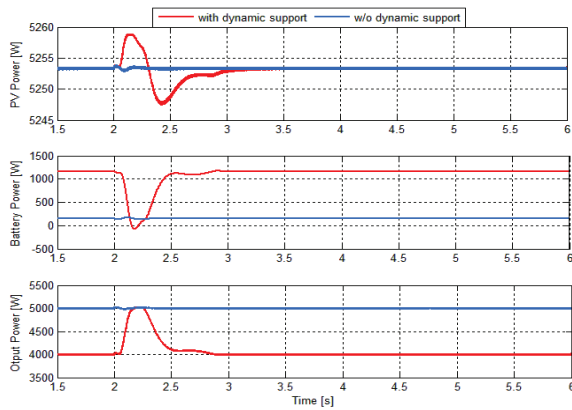


Fig.7. PV power, Battery power, Output power for  $G=1000 \text{ W/m}^2$  without and with dynamic support.

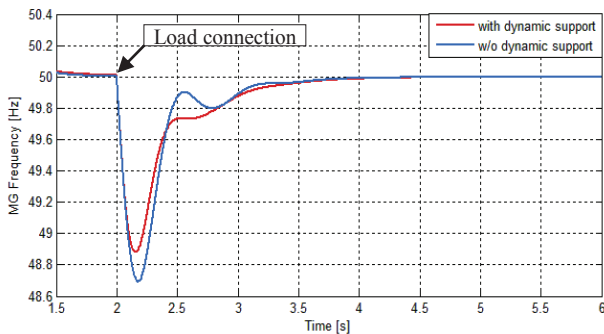


Fig.8. MG frequency for  $G=1000 \text{ W/m}^2$  and  $G=500 \text{ W/m}^2$  without and with dynamic support and with integrated battery.

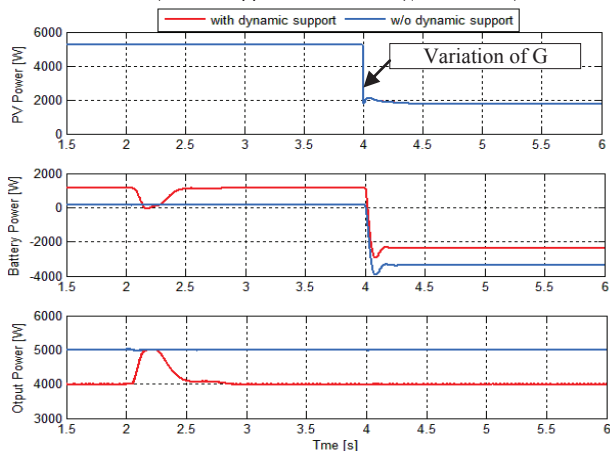


Fig.9. PV power, Battery power, Output power for  $G=1000 \text{ W/m}^2$  and  $G=500 \text{ W/m}^2$  without and with integrated battery.

In the third studied case, the PV irradiation changes from  $G=1000 \text{ W/m}^2$ , to  $500 \text{ W/m}^2$  at  $t=4\text{s}$  as in the previous case, but now the battery is removed from the DC-link. In order to compare this case with the other two above, these tests are accomplished in the same operation conditions, without dynamic support and with dynamic support. As shown in Fig. 10, frequency starts from the 50 Hz, and after 2 seconds when the load is connected, the frequency starts declining to 48.72 Hz without dynamic support and to 48.86 Hz with dynamic support. At around  $t=4\text{s}$  the frequency is restored to the rated value in both cases, i.e. with and without dynamic support. However, after  $t=4\text{s}$ , when the irradiation changes to  $500 \text{ W/m}^2$  the MG frequency is dropping to 49.4 Hz without dynamic support, while being limited to around 49.7 Hz when the

support is enabled. After 5.8 seconds the frequency is brought back to 50 Hz in both cases.

As shown in Fig. 11, without dynamic support the PV power is at a constant value around the nominal value of 5000 W, while in the other case the PV power changes from 4000 W to 5000 W after 2 seconds when the load is switched on and again at 4000 W. The output power is 5000 W without dynamic support, whereas with dynamic support being maintained at 4000 W, according to the characteristic from Fig. 4, with a minor fluctuation when the load is switched on.

After 4 seconds, when the irradiation changes, the PV string power drops proportionally to the irradiation to approximately 1700 W and remains constant in both cases, i.e. with/without dynamic support. However, due to the lack of integrated energy storage system, the VSC output power now follows the PV string production and, therefore, it can no longer sustain the MG frequency, until the MG frequency is stabilized again after 5.8 s at 50 Hz. As a consequence, the irradiation change perturbs the MG and the frequency drops according to the PV active power decrease (i.e. 4000 W), but this perturbation is limited due to the dynamic characteristic of the frequency when the system is working with dynamic support.

Further improvements are under study, one of these consisting in adapting the PV power plant response capability according to the battery state-of-charge. Enhancing the frequency controller to respond to the rate-of-change-of-frequency is another improvement taken into consideration.

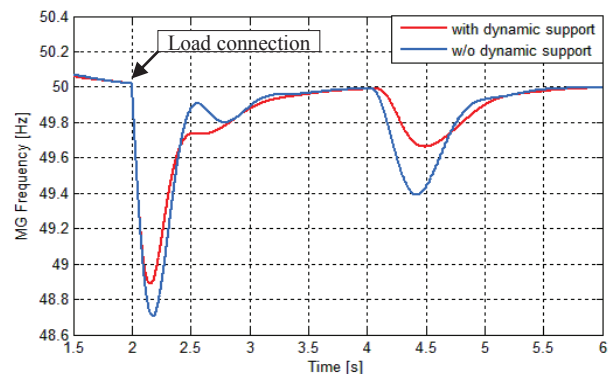


Fig.10. MG frequency for  $G=1000 \text{ W/m}^2$  and  $G=500 \text{ W/m}^2$  with and without dynamic support and without integrated battery.

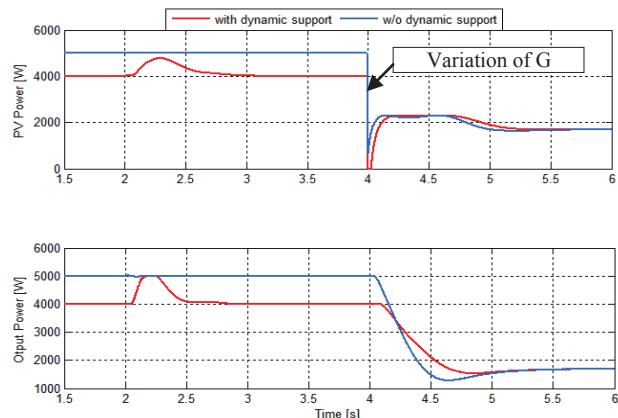


Fig.11. PV Power, Output power for  $G=1000 \text{ W/m}^2$  and  $G=500 \text{ W/m}^2$  without and with dynamic support and without integrated battery.

## V. CONCLUSIONS

The paper has presented a solution for dynamic support of frequency in microgrids (MGs) by means of photovoltaic (PV) power plants. In order to improve the PV system control and power reserve, an energy storage system is integrated into the structure of the PV power plant. The PV response to frequency deviations is adapted from the existing Romanian grid code, a modified  $f$ - $P$  characteristic being developed according to the system characteristics. The simulation results have clearly shown that, as long as the battery storage system operates in normal conditions (i.e. without storage limitations), the considered PV system is able to improve the MG frequency response and for sure the dynamic frequency support according to existing power reserve, ensures an increased stability of the entire MG output power. Regarding the PV power it was demonstrated that, according to irradiation values, the battery compensates for the difference between the PV string production and the imposed PV plant output power according to the frequency controller characteristic. The case without integrated energy storage system was also analyzed, the results showing that the PV power plant can provide a certain level of support according to its power reserve operation, which depends on the irradiation level.

*Received on July 17, 2016*

*Editorial Approval on November 15, 2016*

## REFERENCES

- [1] N.W.A. Lidula, A.D. Rajapakse, Microgrids research: A review of experimental microgrids and test systems, *Renewable and Sustainable Energy Reviews*, Volume 15, Issue 1, January 2011, Pages 186-202.
- [2] N.Hatziargyriou, "Microgrids: Building Blocks of the Smart Grid", IEEE PES ISGT Europe, Berlin, Germany, 14-17Oct., 2012.
- [3] S. Parhizi, H. Lotfi, A. Khodaei and S. Bahramirad, "State of the Art in Research on Microgrids: A Review", IEEE Access, vol. 3, pp. 890-925, 2015.
- [4] M. Rezkallah, S. Sharma, A. Chandra and B. Singh, "Hybrid standalone power generation system using hydro-PV-battery for residential green buildings", 41st Annual Conference of the IEEE Industrial Electronics Society (IECON), Yokohama, pp. 003708-003713, 2015.
- [5] K. F. Krommydas and A. T. Alexandridis, "Modular Control Design and Stability Analysis of Isolated PV-Source/Battery-Storage Distributed Generation Systems", IEEE Journal on Emerging and Selected Topics in Circuits and Systems, vol. 5, no. 3, pp. 372-382, Sept. 2015.
- [6] H. Mahmood, D. Michaelson and J. Jiang, "A Power Management Strategy for PV/Battery Hybrid Systems in Islanded Microgrids", IEEE Journal of Emerging and Selected Topics in Power Electronics, vol. 2, no. 4, pp. 870-882, Dec. 2014.
- [7] S. Adhikari and F. Li, "Coordinated V-f and P-Q Control of Solar Photovoltaic Generators With MPPT and Battery Storage in Microgrids", IEEE Transactions on Smart Grid, vol. 5, no. 3, pp. 1270-1281, May 2014.
- [8] H. Mahmood, D. Michaelson and J. Jiang, "Strategies for Independent Deployment and Autonomous Control of PV and Battery Units in Islanded Microgrids", IEEE Journal of Emerging and Selected Topics in Power Electronics, vol. 3, no. 3, pp. 742-755, Sept. 2015.
- [9] Y. Guan, J. C. Vasquez, J. M. Guerrero, Y. Wang and W. Feng, "Frequency Stability of Hierarchically Controlled Hybrid Photovoltaic-Battery-Hydropower Microgrids", IEEE Transactions on Industry Applications, vol. 51, no. 6, pp. 4729-4742, Nov.-Dec. 2015.
- [10] Y. Yang, F. Blaabjerg and H. Wang, "Constant power generation of photovoltaic systems considering the distributed grid capacity", IEEE Applied Power Electronics Conference and Exposition (APEC), Fort Worth, TX, pp. 379-385, 2014.
- [11] A. Sangwongwanich, Y. Yang and F. Blaabjerg, "High-Performance Constant Power Generation in Grid-Connected PV Systems", IEEE Transactions on Power Electronics, vol. 31, no. 3, pp. 1822-1825, March 2016.
- [12] J. Quesadaa, R. Sebastián, M. Castro, J.A. Sainz, "Control of inverters in a low voltage micro-grid with distributed battery energy storage. Part I: Primary control", Electric Power Systems Research, vol. 114, pp. 126-135, Sept. 2014.
- [13] S. Gaurava, C. Birlaa, A. Lambaa, S. Umashankara, S. Ganesanb, "Energy Management of PV - Battery based Micro-grid System", Procedia Technology, vol. 21, pp. 103 - 111, 2015.
- [14] F.M. Uriarte, C. Smith, S. VanBroekhoven, R.E. Hebner, "Micro-grid Ramp Rates and the Inertial Stability Margin", IEEE Transactions on Power Systems, vol.30, no.6, pp.3209-3216, Nov. 2015.
- [15] J. G. de Matos, F. S. F. e Silva and L. A. d. S. Ribeiro, "Power Control in AC Isolated Microgrids With Renewable Energy Sources and Energy Storage Systems", IEEE Transactions on Industrial Electronics, vol. 62, no. 6, pp. 3490-3498, June 2015.
- [16] J. M. Guerrero, M. Chandorkar, T. L. Lee and P. C. Loh, "Advanced Control Architectures for Intelligent Microgrids—Part I: Decentralized and Hierarchical Control", IEEE Transactions on Industrial Electronics, vol. 60, no. 4, pp. 1254-1262, April 2013.
- [17] R. Teodorescu, M. Liserre, P. Rodriguez, "Grid Converters for Photovoltaic and Wind Power Systems", IEEE-Wiley, 2011.
- [18] I. Serban, R. Teodorescu, C. Marinescu, "Energy storage systems impact on the short-term frequency stability of distributed autonomous microgrids, an analysis using aggregate models," IET Renewable Power Generation, vol. 7, no. 5, pp. 531-539, Sept. 2013.
- [19] Tang X, Deng W, Qi Z. "Investigation of the Dynamic Stability of Microgrid", IEEE Transactions on Power Systems, vol. 29, no.2, pp: 698-706, 2014.
- [20] D. Munteanu, C. Marinescu, I. Serban, L. Barote, "Control of PV Inverter with Energy Storage Capacity to Improve Microgrid Dynamic Response" ICATE- Craiova, Oct. 2016.
- [21] B. I. Craciun, D. Sera, E. A. Man, T. Kerekes, V. A. Muresan, R. Teodorescu, "Improved voltage regulation strategies by PV inverters in LV rural networks," 3rd IEEE International Symposium on Power Electronics for Distributed Generation Systems (PEDG), Aalborg, 2012, pp. 775-781.

# The Analysis of Magnetic Field Measurements in a Public Access Area

Georgiana Roșu<sup>\*</sup>, Octavian Baltag<sup>†</sup>

<sup>\*</sup> Military Technical Academy, Bucharest, Romania, georgianamarin01@gmail.com

<sup>†</sup> University "Gr. T. Popa" of Medicine and Pharmacy, Iasi, Romania, octavian.baltag@bioinginerie.ro

**Abstract** - This paper describes a case study referring to the magnetic field measurements performed in a public access area. Compared to the standard limits regarding the human exposure to electromagnetic fields, the measurement results were significantly higher. Based on these results and the scarce data regarding the magnetic field sources in the area, there are discussed several cases of power lines configurations and their corresponding magnetic field levels.

**Keywords:** *electromagnetic exposure, electromagnetic pollution, magnetic field measurement, standards*

## I. INTRODUCTION

The case study described in this paper is based on a set of magnetic field measurements performed in a market place area [1]. The paper aims to identify the magnetic fields sources that could generate such high levels registered in the measurement stage. Because the analyzed area is a public access area, determining the electromagnetic field exposure of the general public is highly important [2-9]. Based on an analytical model and the scarce data regarding the magnetic field sources in the area, there are discussed several cases of power lines configurations and their corresponding magnetic field levels.

## II. DESCRIPTION OF THE ANALYZED CASE

The case presented herein refers to an area located North of Constanta, Romania, illustrated in Fig. 2, where a transformer substation 400/110/20 kV operates as part of the national power grid. Also, in the close vicinity of the

substation, there is located a market place. People working and visiting this public access area are exposed to the electric and magnetic fields generated by the power lines converging to and from the substation, as the map in Fig. 2 shows clearly.

In the center of the market place there is situated one of the very high voltage (400 kV) power line towers, carrying electric power from the national grid to the transformer substation. Also, crossing above the southern side of the market area, there are three high voltage power line towers, each supporting a three-phase system of 110 kV. In Fig. 1 there is illustrated the 400 kV power line tower which is located in the north-eastern corner of the market place, and the inscription of the tower, stating that there should be maintained a protection area of 75 meters width from the power line axis.



Fig. 1. The 400 kV power line tower in the center of the market place



Fig. 2. The market place adjacent to the substation and converging power lines (Google Maps)

In order to determine the magnetic field levels affecting all exposed persons around, a set of measurements of magnetic flux density was performed on the contour of the market place. The measurement device was a gauss-meter with transversal Hall probe, which was calibrated before the measurements. The space coordinates corresponding to the magnetic field data were recorded with a GPS device. The measurements were performed at 1 meter above ground; there was measured the vertical component of the magnetic field. Magnetic flux density ranging from a few  $\mu\text{T}$  to several hundred  $\mu\text{T}$ , was measured on the boundary of the selected area. Fig. 3 outlines the measurement area border and Fig. 4 illustrates the values of the magnetic induction measured therein. The highest measured values range from 300  $\mu\text{T}$  to 460  $\mu\text{T}$ .

At the analyzed location, the human factor is present almost 24 hours a day, particularly in the warm months of the year, performing a commercial activity. It is in fact a public access area, with continuous exposure, the human factor not being aware, instructed, nor protected. By com-

paring the measured values with the standard imposed levels [7, 8, 10,11], several observations can be made:

- high values of magnetic field are determined by the close proximity of high voltage overhead power lines;
- in most points located on the Southern side of the area, near the 110 kV power line, the magnetic flux density exceeds the safety level of 100  $\mu\text{T}$ , indicating a dangerous area for the humans therein;
- the safety level for the magnetic flux density is also exceeded in the N-E corner of the area, next to the 400 kV power line tower, beneath the overhead power line conductors.

Since the measured values were significantly higher than the usual magnetic field within the area of high voltage substations or beneath high voltage power lines [11, 12], there is imposed the analysis of the available data. There are analyzed several models of magnetic fields sources, such as overhead and underground three-phase power lines.

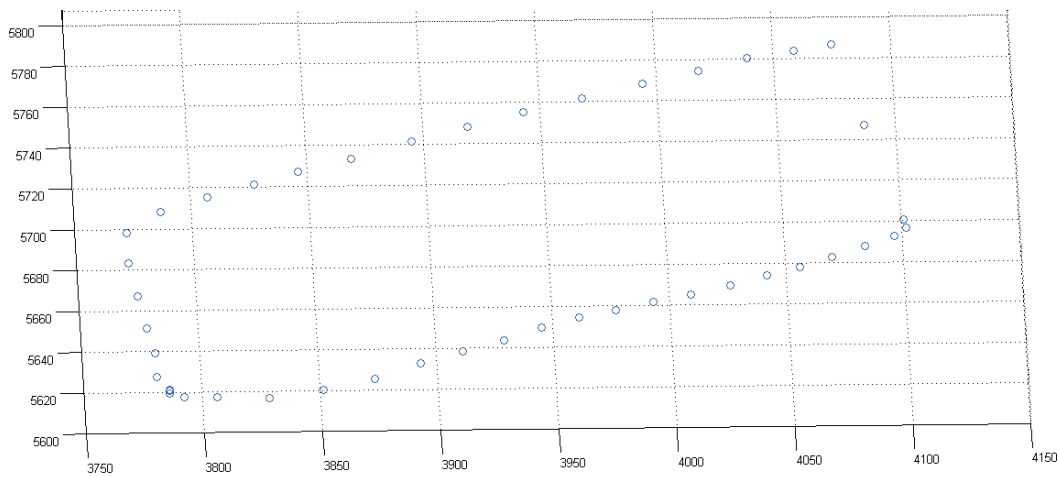


Fig. 3. The measurement points location expressed relative to a reference point

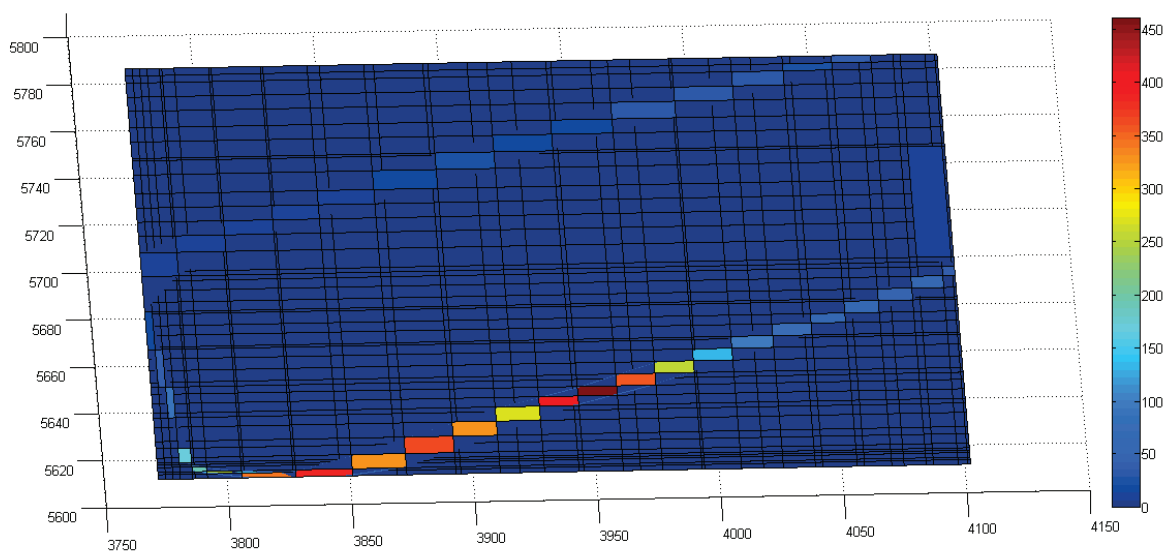


Fig. 4. The magnetic flux density registered in the measurement points

### III. THE MAGNETIC FIELD COMPUTATION MODEL

The computational model of the magnetic field generated by a power line is based on the Biot-Savart-Laplace equation; the magnetic field density generated in point M by the current  $i_k$  passing through the k-th electric circuit ( $k = 1, 2$  or  $3$ ) is determined by the electric current  $i_k$ , the magnetic permeability of free space, the distance vector  $r$  between the position of the observation point M and that of the cable, and the regular distance element on the electric wire  $dl$ .

$$\vec{B}_k \Big|_M = \frac{\mu_0 i_k}{4\pi} \int_{\Gamma_k} \frac{d\vec{l} \times \vec{r}}{r^3} \quad (1)$$

The integral is computed along the wire of the k-th circuit (phase)  $\Gamma_k$ ; in literature, different shapes of the aerial cable are considered (straight cable or with a proper droop due to its connection between two points at the same elevation or at different elevations, by considering different three-phase line configurations, etc.) [10, 11].

By considering a cross-section through a three-phase power line, there is obtained a simplified 2D computational configuration. Still, the three currents passing through the cables  $i_k$  ( $k = 1, 2, 3$ ) form a symmetrical system. The magnetic field computation is performed in the  $(x, y)$  plane, illustrated in Fig. 5. For the three-phase line system, the total magnetic field is obtained through fields' superposition, considering the symmetrical phase shift between the currents.

The magnetic field density generated by the three-phase line, computed in the observation point  $M(x_M, y_M)$  has the orthogonal components  $B_x$  and  $B_y$ :

$$B_x = \frac{\mu_0}{2\pi} \sum_{k=1}^3 i_k \left[ \frac{-(y_M - y_k)}{(y_M - y_k)^2 + (x_M - x_k)^2} \right] \quad (2)$$

$$B_y = \frac{\mu_0}{2\pi} \sum_{k=1}^3 i_k \left[ \frac{(x_M - x_k)}{(y_M - y_k)^2 + (x_M - x_k)^2} \right] \quad (3)$$

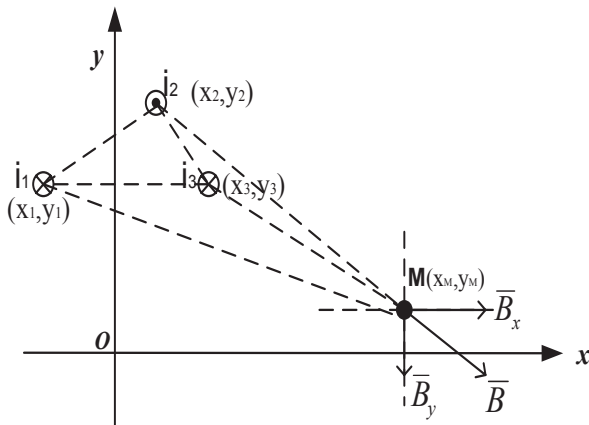


Fig. 5. The components of the magnetic field generated by the three-phase power line

### IV. THREE-PHASE OVERHEAD POWER LINE

For the adopted computational model, there is further considered an overhead three phase power line. For a standard a power line tower of 110 kV supporting a three phase power line at approximately 20 meters above the ground, the cable positions expressed in the selected Cartesian system are as follows:  $(x_1, y_1) = (-4; 20)$ ,  $(x_2, y_2) = (2; 24)$ , and  $(x_3, y_3) = (4; 20)$  meters.

The observation point M is 1 meter above the ground ( $y_M = 1$  m), and its horizontal coordinate ( $x_M$ ) ranges from -10 to 10 meters. The load current is considered to be 400 A (which represents the effective value admissible for a 110 kV power line). The orthogonal components of the magnetic field density are illustrated in Fig. 6 and Fig. 7; as one could observe, the magnetic field components resulting from (2) and (3) render values lower than  $1 \mu\text{T}$ . Such low values are determined by the large distance between the observation point M and the aerial cables - approximately 20 meters.

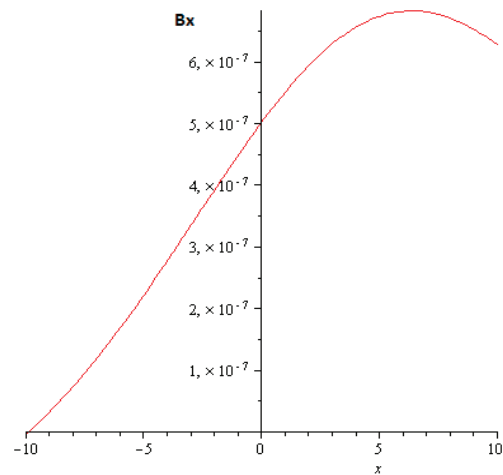


Fig. 6. The horizontal component of the magnetic field  $B_x$  generated by the overhead three-phase power line on the  $x$  axis, perpendicular to the power line

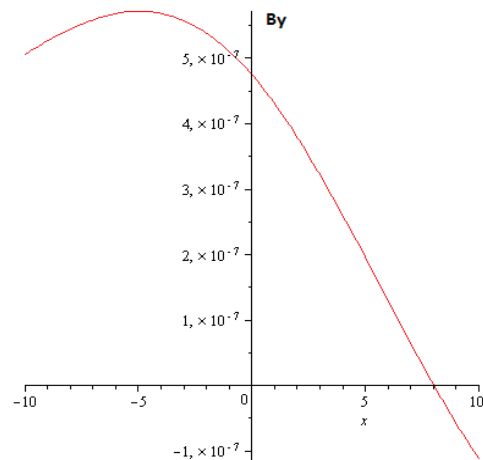


Fig. 7. The vertical component of the magnetic field  $B_y$  generated by the overhead three-phase power line on the  $x$  axis, perpendicular to the power line

### V. THREE-PHASE UNDERGROUND POWER LINE

The computational model needs further improvement and adequacy to the true circuits' configuration; superposition of magnetic field components from many different circuits and possibly the true effective value of the line current could influence the results.

Power distribution specialists state that the magnetic field generated by an underground cable can reach up to 5 times the value of the magnetic field produced by an overhead line, mainly because of the distance between the line and the ground. [13].

For the scope of determining the magnetic field of an underground power line, the computation model was adapted for a 20 kV underground three-phase power line. Two configurations were considered: an axial (horizontal) distribution of the cables and a triangular distribution, respectively. The configurations are illustrated below in Fig. 8.

The reason of choosing the 20 kV voltages lies in the fact that the transformer substation in the analyzed region is distributing the following voltages 400/110/20 kV. Therefore, it was taken into consideration the fact that an underground cable of medium voltage (20 kV) could also be present in the area.

For the 20 kV underground cable, there was considered a copper cable of section  $S = 240 \text{ mm}^2$  [14]. The maximum load current differs with the cable distribution: it is 445 A for the horizontal distribution and 456 A for the triangular distribution, respectively.

The burial depth is 0.8 meters, and the observation point is located 1 meter above the ground. So, in the case of an underground power line, the distance between the power line and the measurement point is approximately ten times lower. For both cable configurations, there were taken into account two different distances between cables: 7 cm and 25 cm, respectively.

As one can notice in Fig. 9 – Fig. 16, there is registered a field increase with the distance between cables, in both configurations. Still, the obtained values are below  $10 \mu\text{T}$  and lower than the measured values.

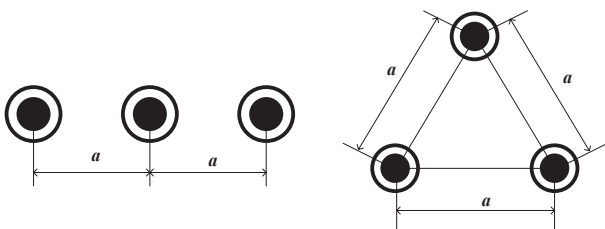


Fig. 8. The selected configurations of the underground three-phase power line - horizontal distribution and triangular distribution, respectively

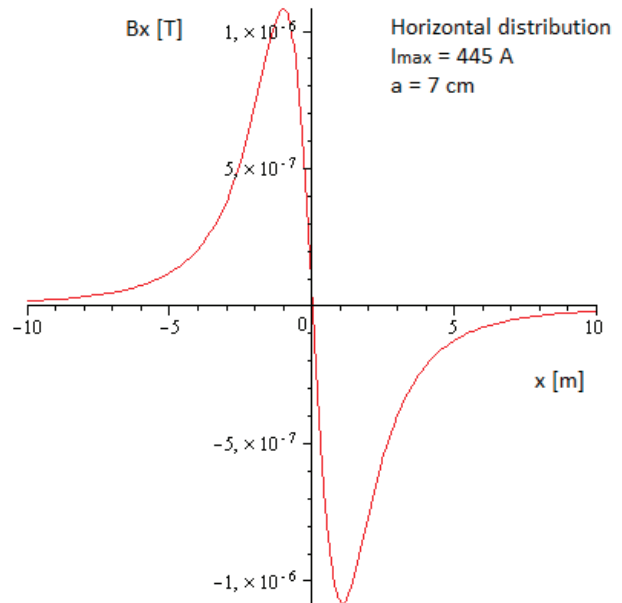


Fig. 9. The horizontal component of the magnetic field  $B_x$  generated by the underground three-phase power line, with cables placed in horizontal line configuration, at 7 cm distance

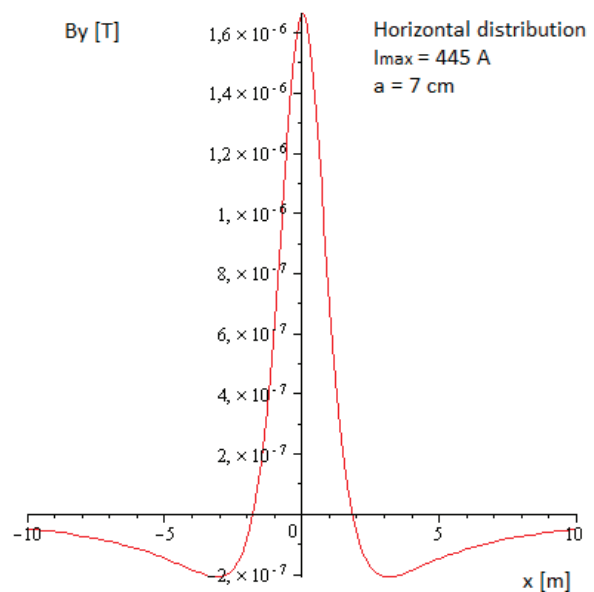


Fig. 10. The vertical component of the magnetic field  $B_y$  generated by the underground three-phase power line, with cables placed in horizontal line configuration, at 7 cm distance

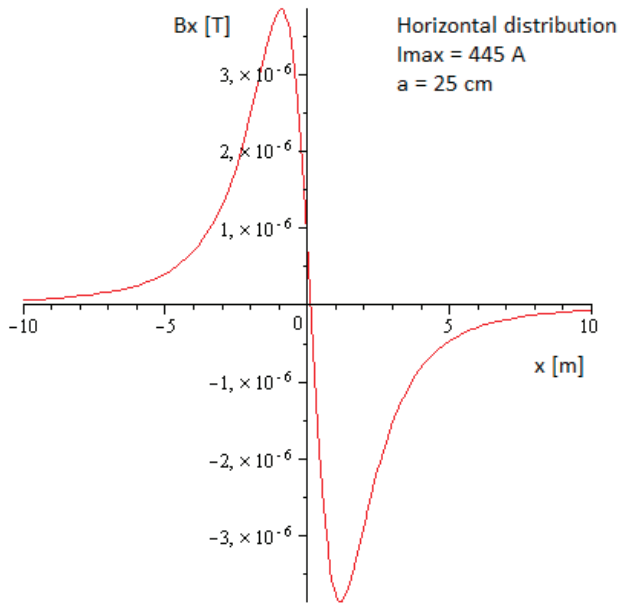


Fig. 11. The horizontal component of the magnetic field  $B_x$  generated by the underground three-phase power line, with cables placed in horizontal line configuration, at 25 cm distance

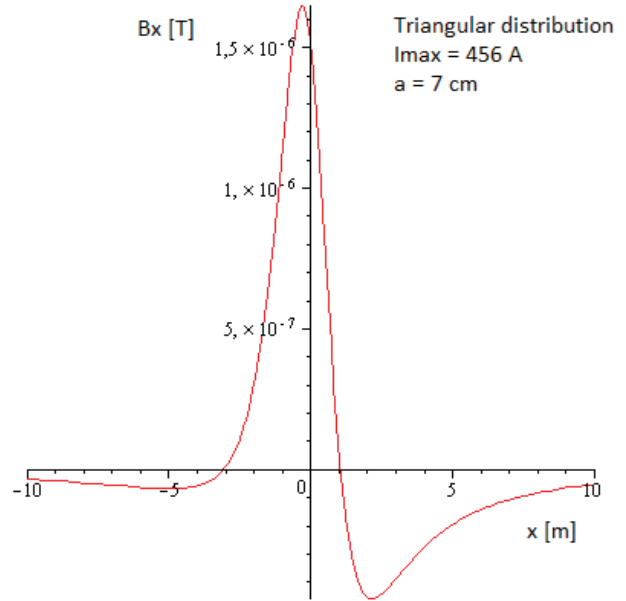


Fig. 13. The horizontal component of the magnetic field  $B_x$  generated by the underground three-phase power line, with cables placed in triangle configuration, at 7 cm distance

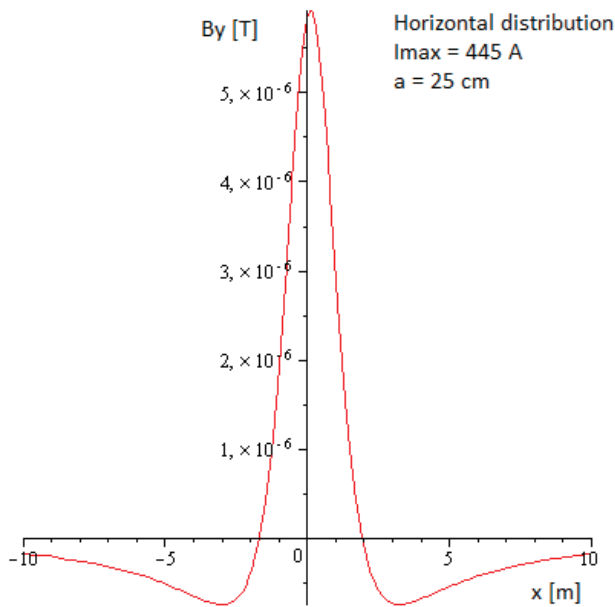


Fig. 12. The vertical component of the magnetic field  $B_y$  generated by the underground three-phase power line, with cables placed in horizontal line configuration, at 25 cm distance

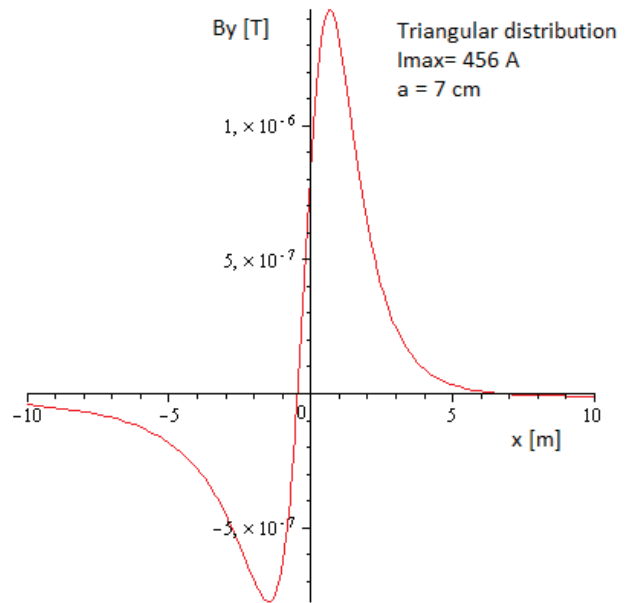


Fig. 14. The vertical component of the magnetic field  $B_y$  generated by the underground three-phase power line, with cables placed in triangle configuration, at 7 cm distance

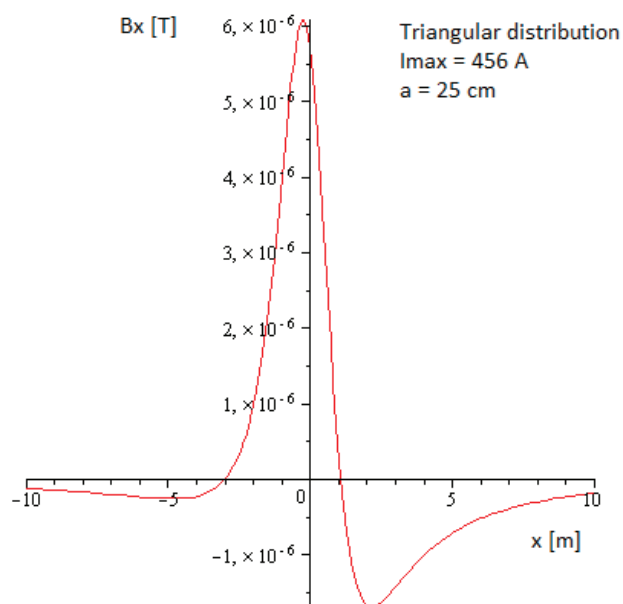


Fig. 15. The horizontal component of the magnetic field  $B_x$  generated by the underground three-phase power line, with cables placed in triangle configuration, at 25 cm distance

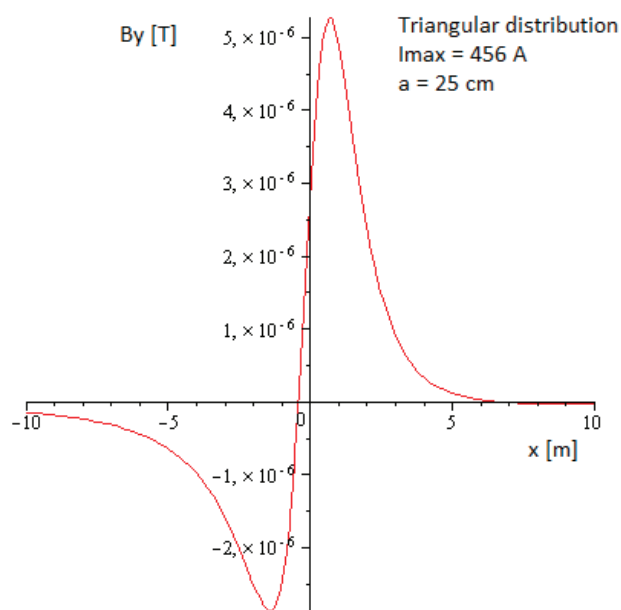


Fig. 16. The vertical component of the magnetic field  $B_y$  generated by the underground three-phase power line, with cables placed in triangle configuration, at 25 cm distance

## VI. CONCLUSIONS

Starting from a set of measurements performed in a market place area, indicating very high levels of magnetic field, there were analyzed several types of power lines considered to be magnetic field sources. The analyzed area presents a particular type of exposure, being simultaneously populated with workers and ordinary people. The people working there are not aware of electromagnetic field emissions, body exposure, the need for protective measures and limitations, etc.

The analyzed sources render magnetic field values in the range of 1 -10  $\mu\text{T}$ . The maximum measured values reach levels with the order of hundreds of  $\mu\text{T}$ . This cannot be explained through the presence of multiple power lines, both overhead and underground, crossing the market area.

Even though it is a market place – therefore a public access area, it is a private property, meaning that the owner is the authority responsible for the assessment of the workplace and for all the needed protective measures. Due to the negative attitude of the market administration, it was not possible to repeat the measurements or to perform supplementary ones. Still, the paper aims to increase awareness to the fact that people perform professional activities in areas unsuitable in terms of electromagnetic field exposure, and to determine measurements resuming.

Received on October 3, 2016

Editorial Approval on November 15, 2016

## REFERENCES

- [1] G. Rosu, F. Enache, O. Baltag, M. Morega, "Environmental Magnetic Field Assessment. A Case Study", Proceedings of the 2016 International Conference on Applied and Theoretical Electricity, Craiova, 2016.
- [2] ICNIRP, „Guidelines for Limiting Exposure to Time-Varying Electric and Magnetic Fields (up to 300 GHz)”, Health Physics 74(4):494-522, 1998.
- [3] ICNIRP, "Guidelines for Limiting Exposure to Time-Varying Electric and Magnetic Fields (1 Hz - 100 kHz)", Health Phys., vol. 99(6)/2010, pp. 818-836, 2010.
- [4] World Health Organisation, „ Static fields. Environmental health criteria Monograph No.232”, Health risk assessment, pp. 210-217, ISBN 92 4 157232 9.
- [5] IEEE, (2002), Safety Levels with Respect to Human Exposure to Electromagnetic Fields, 0-3 kHz, IEEE Standard C95.6-2002, ISBN: 0-7381-3389-2.
- [6] Council of the European Union, "Council Recommendation of 12 July 1999 on the Limitation of Exposure of the General Public to Electromagnetic Fields (0 Hz to 300 GHz)", Official Journal of the European Communities L1999/519/EC, 59-70, 1999.
- [7] Directive 2013/35/EC of the European Parliament and of the UE Council, of 26 June 2013, on the minimum health and safety requirements regarding the exposure of workers to the risks arising from physical agents (electromagnetic fields).
- [8] The Order of the Health Ministry no. 1193 of Sept. 29, 2006, regarding the approval of the national norms for limiting general exposure to electromagnetic fields from 0 to 300 GHz (published in Romanian by MO 895/03.11.2006).
- [9] EN 50413:2009 "Basic standard on measurement and calculation procedures for human exposure to electric, magnetic and electromagnetic fields (0 Hz - 300 GHz)", IEC Standard, 2009.
- [10] M. Atudori, M. Rotariu, "Electromagnetic radiation field near power lines and its environmental impact", U.P.B.Sci.Bull., Series C, vol. 74, no. 1, pp. 231 – 238, 2012.
- [11] E. Lunca, M. Istrate, A. Salceanu, „Comparative analysis of the extremely low-frequency magnetic field exposure from overhead power lines”, Environmental Engineering and Management Journal, Vol.12, No. 6, pp. 1145-1151, 2013.
- [12] G. Filippopoulos, D. Tsanakas, "Analytical calculation of the magnetic field produced by electric power lines", IEEE Transactions on Power Delivery, vol. 20, no. 2, pp. 1474 – 1482, 2005.
- [13] "A Guide to the Debate On Electric and Magnetic Fields and Health" (Available on-line: <http://www.emfs.info/>)
- [14] Order 38/2008 of ANRE, "Normative on Designing and Executing Electric Cables Networks - NTE 007/08/00", S.C. Electrica S.A.

# Comparisons Among p-Channel, n-Channel and Mixed n/p -Channel OTFTs

Cristian Ravariu\*, Georgeta Alecu†

\*Politehnica University of Bucharest, The Faculty of Electronics, Telecommunications and Information Technology, Bucharest, Romania, cristian.ravariu@upb.ro

†National Institute for Research and Development in Electrical Engineering ICPE-CA, Bucharest, Romania, georgeta.alecu@icpe-ca.ro

**Abstract** - Some theoretical approaches of an alternative organic semiconductor device are presented in this work. The Organic transistors are based either on n-type or p-type or mixed p/n overlapped layers. The carrier modulation insides different films is carried out by two gates electrodes, as is usual in the thin film transistor field. This paper introduces some novel aspects for these kinds of organic transistors, selecting a suitable biasing regime. The simulations emphasize a stronger influence on the static characteristics when the superior gate is acted. One of the novelties of this paper concerns the electrical conduction occurrence by two simultaneous channels, in comparison with one volume channel conduction, for different gate voltage regimes. A similar work regime is also encountered in the SOI devices with ultra-thin films that develop a volume channel. The volume channel regime is advantageously when the technology of fabrication of the organic semiconductors on different insulators provides an extremely charged interface, which can degrade the surface currents. Comparisons and applications for both situations - with one volume channel or two accumulation channels - are finally discussed. The vertical n/p junction arose between the upper n-channel and the bottom p-channel, offers novel physical properties and prevented any interaction among channels. The device simulations revealed multiple behaviors, depending on the Top and Bottom Gate voltages, if a positive drain-source voltage is applied.

**Keywords:** organics transistors, thin films, simulations, alternative materials in electronics.

## I. INTRODUCTION

The organic technology provides facile methods of the thin film transistors manufacturing, at room temperature processes as inkjet printing, sol-gel process, roll-to-roll printing, which provides low cost technologies, against the classical lithography from the silicon technology, [1-3].

Even with the last years rapid progress in the organic materials manufacturing [4], an Organic Thin Film Transistor (OTFT) with better characteristics than a Metal Oxide Semiconductor Field Effect Transistor (MOSFET), rests a major issue, [5].

For example, the Organic METal Semiconductor Field Effect Transistor (OMESFET) developed by another researcher group [6], operates at lower voltages than usual OTFT, with better ON/OFF current ratio, but only use the conduction thru a channel with p-type conduction, [6].

The well-known technologies of the Pentacene OTFT transistors frequently demand conduction thru a p-type organic layer, except for a few low band-gap organic polymers. Recently, other authors claim that n-type conduction can be used in conjunction with convenient organic gate dielectrics [7], even in special low band-gap organic semiconductors, where the electrons mobility increases to  $0.05\text{cm}^2/\text{Vs}$ , [8].

Till nowadays, the more performant Organic-TFTs are fabricated by the p-type organic polymers, offering conduction regime with accumulation channel. An additional reason for the n-type organic-TFT avoiding is the electrons entrapping at the semiconductor-oxide interface by hydroxyl groups, present as silanols in the usual  $\text{SiO}_2$  insulator, [8]. OTFTs with pentacene onto a dielectric polymer layer enriched the drain current excursion from 8nA to 80nA at the same gate voltage biasing, [9].

Therefore, in this paper, a mixed solution - with a p-organic layer on an n-organic layer - is considered to enrich the current way. The source to drain conduction is possible by accumulation channels [10] or by volume channels, [5]. In this paper we take into account the possibility to ensure a superior conduction by the superposition of both these two mechanisms. The polyimide material is considered as buried organic insulator and the oxide material is considered as the upper insulator, for the proposed Organic-TFT. The compatibility between the circuit integration technology and the surface oxide is wellknown, while the matching with polyimide material was proved elsewhere, [11]. The expected results envisage a larger current capability by a suitable work regime and alternative functions for these transistors.

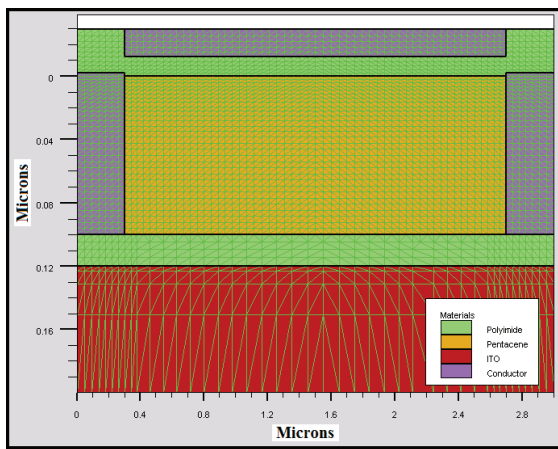
## II. THE DEVICES STRUCTURE AND PHYSICAL PARAMETERS

This organic thin film transistor also belongs to the Semiconductor on insulator SOI transistor class [12], due to similar configuration with sub-100nm organic films placed onto an insulator support from polyimide. Therefore, the back and front gates from SOI architectures [13] are labeled here as bottom and top gates, to be in agreement with the TFT terminology, [6, 7].

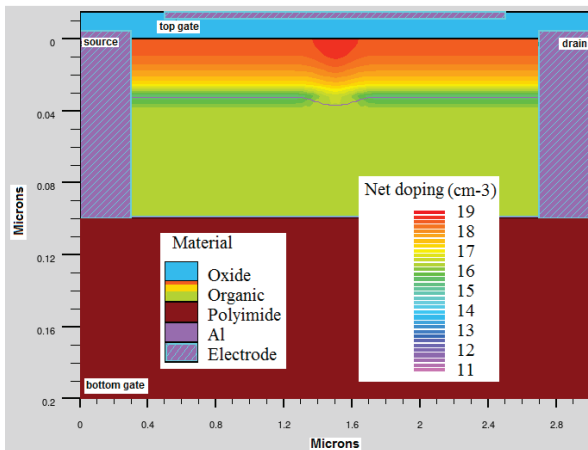
The investigation software tools from this paper involve the Atlas 2D from Silvaco, adapted for our OTFT device. In fig. 1.a is presented the proposed structure besides to the mesh for a sole p-channel transistor or similar

for n-channel and in fig. 1.b is presented the adopted structure with mixed n/p channels with modified geometry. In this last case, the structure gathers an accumulation current localized at the upper interface with oxide and with the inferior interface with polyimide. In this way, multiple conduction routes occur: by upper n-channel and bottom p-channel. However, the metallic shortcut on the vertical direction, achieved by the deep source and drain contacts, ensure a zero current within the pn junction on the Oy axis.

From the material point of view, the organic semiconductor can be depicted either as the default pentacene from the Atlas library [14], or as optimized organic semiconductors from literature [15] simply labeled as Organic.



(a)



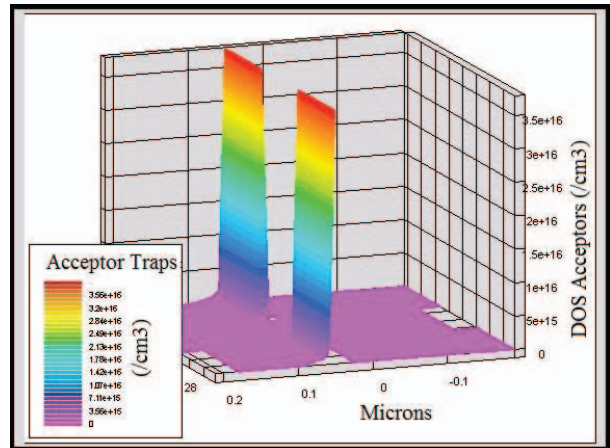
(b)

Fig 1. Materials and doping profile within the O-TFT with (a) sole p-channel; (b) mixed p/n-channels.

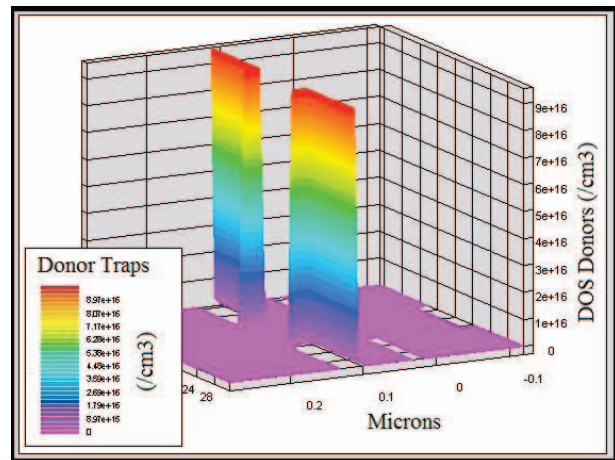
In the literature, the carrier motilities inside the organic semiconductors are typically of  $0.1...1\text{cm}^2/\text{Vs}$ , or more, [16]. We considered an average value of  $0.8\text{cm}^2/\text{Vs}$  in these simulations. In order to make possible both electrons and holes charge transport, the Lowest Unoccupied Molecular Orbital (LUMO), besides to the Highest Occu-

ried Molecular Orbitals (HOMO) - energy levels must be localized as close as possible and the gate dielectrics must suppress the electron capture at the organic-dielectric interface.

In order to be closer to a real behavior, in this paper, the the Density Of States (DOS) are distinctly defined at the organic semiconductor / polyimide interface by for ionized acceptor states -  $g_A=3.75 \times 10^{16}\text{cm}^{-2}$ , fig 2.a, and ionized donor states  $g_D=9.5 \times 10^{16}\text{cm}^{-2}$ , fig. 2.b, [17].



(a)



(b)

Fig. 2. The ionized states density taken into account in simulations: (a) for acceptors; (b) for donors.

For the presented OTFT structure, the aluminum contacts provide a Schottky barrier, while the gold contacts offers better ohmic contacts and they are finally included in simulations. Also the simulations show a strong dependence of the contact resistance on the doping concentrations in the n or p type layers. On the other hand, the contact resistances are variable for different gates biasing, due to the carriers concentration ranging, [15].

The physical parameters of the standard pentacene, noted as Pentacene [14], enhanced new organic semiconductors noted as Organic [15, 19] and polyimide as insu-

lator [20] are included in the Atlas models by the "material" instruction and centralized in table 1. Those parameters that are missing from table 1, for pentacene, organic or insulators, get the default values from the Atlas library, [14]. The sizes and doping concentrations of each layer are selected from a real organic technology [11-21], and they are indicated as main references in table 1. The n-type layer is defined by a Gaussian doping concentration, with a maximum value of  $10^{19} \text{ cm}^{-3}$ , while the p-type substrate has  $10^{17} \text{ cm}^{-3}$ .

TABLE I.  
INITIAL DEVICE CHARACTERISTICS

Material	Thickness ( $\mu\text{m}$ )	$E_G$ (eV)	Mobility ( $\text{cm}^2/\text{Vs}$ )
n-Pentacene	40 <sup>[15]</sup>	2.11 <sup>[21]</sup>	$1 \times 10^{-5}$ , <sup>[21]</sup>
p-Pentacene	60 <sup>[9]</sup>	2.11 <sup>[21]</sup>	$4 \times 10^{-4}$ , <sup>[21]</sup>
n-Organic	40 <sup>[15]</sup>	1.20 <sup>[19]</sup>	0.80 <sup>[15]</sup>
p-Organic	60 <sup>[9]</sup>	1.21 <sup>[19]</sup>	0.80 <sup>[15]</sup>

### III. FIRST ATLAS SIMULATIONS

The Atlas input file is prepared to simulate electrical conduction thru organic materials, activating some key parameters in the "model" instruction: pfmob singlet langevin, to activate the Poole-Frenkel mobility model and the Langevin recombination for the existent carriers, [14].

In Atlas 2D output files, the drain currents are expressed in Amperes per  $1 \mu\text{m}$ , as default depth. Therefore, in our simulations, the current densities are more relevant than the currents itself.

The potential distribution over the mixed OTFT structure is presented in fig. 3, accordingly with an expecting work regime, for low positive drain voltage and negative top-gate voltage and also negative bottom-gate voltage. In another work regime, the drain voltage is increased, when the mixed device is biased at  $V_S=0\text{V}$ ,  $V_D=40\text{V}$ ,  $V_{TG}=-10\text{V}$  and  $V_{BG}=30\text{V}$ , the maximum electric field occurs on a  $0.2 \mu\text{m}$  length of oxide, between the edges of top gate and drain electrodes.

Subsequently, the maximum electric field reaches  $2.5 \times 10^6 \text{ V/cm}$ , still lower than  $1.1 \times 10^7 \text{ V/cm}$ , but under increasing alert for the critical electric field in the right corner of the oxide, near the drain contact. Hence, a limit drain voltage can be  $+40\text{V} \dots +50\text{V}$  to avoid the breakdown. A thicker polyimide provides a lower residual current thru polyimide versus oxide, at the same voltages. For the device safety, the gate currents are monitored. After simulations, the top and bottom gate current densities possess few orders of magnitude lower than the drain current, so far away from the breakdown conditions and far away from the loss of the gate control.

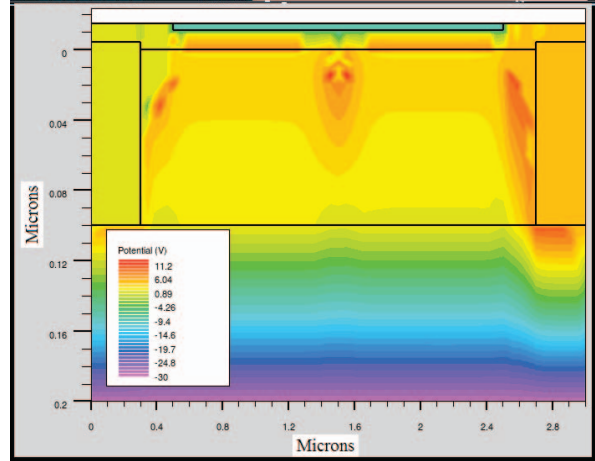
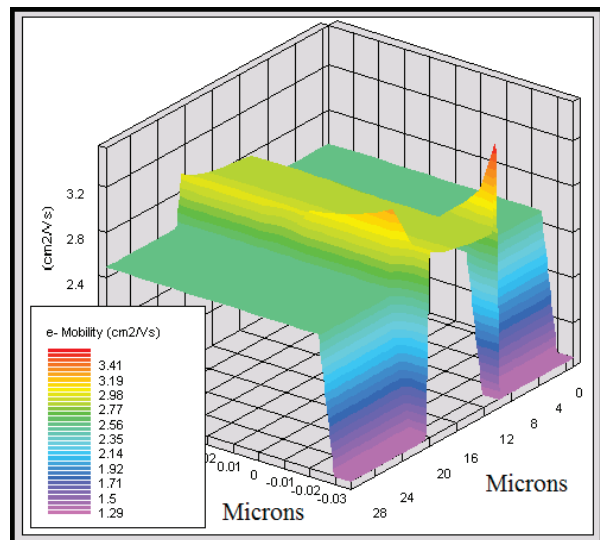


Fig 3. The potential distribution at  $V_S=0\text{V}$ ,  $V_D=+4\text{V}$ ,  $V_{TG}=-10\text{V}$  and  $V_{BG}=-30\text{V}$  in mixed OTFT.

Because the mixed OTFT structure comprises a vertical n/p junction, two types of electrical carriers ensure the longitudinal conduction, as in any pn junction.

A top gate biased at negative voltage can foster the holes accumulation. An additional negative bottom gate voltage enhances the holes accumulation, while positive bottom gate voltage depletes the p-type film, fig. 3. Holes accumulation occurs near the polyimide interface for  $V_{BG}=-30\text{V}$ , up to  $2 \times 10^{18} \text{ cm}^{-3}$ , higher than the native doping concentration of  $10^{17} \text{ cm}^{-3}$ , while holes accumulation occurs near the oxide interface for  $V_{TG}=-10\text{V}$ , up to  $9 \times 10^{19} \text{ cm}^{-3}$ . In this case, an electrons volume channel coexists with the upper holes surface channel, near the source vicinity. The work regime with positive top gate voltage provides two conduction channels, near oxide and polyimide interfaces, depending on the bottom gate biasing.

Figure 4 presents a comparison between the electrons and holes mobility, under usual biasing conditions.



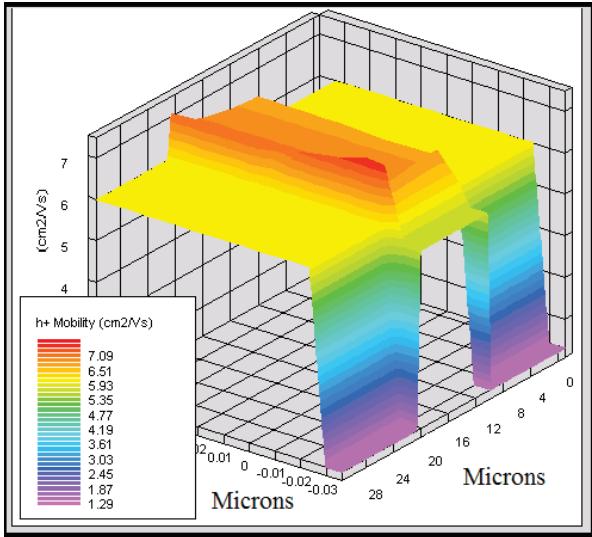


Fig 4. The electrons and holes concentration for different top and bottom gate voltages.

The specific models included in Atlas to capture the organic semiconductors becomes obviously, due to the results with higher holes mobilities and lower electron mobilities (opposite to the inorganic semiconductors), as is specifically encountered in literature, [22].

#### IV. STATISTIC REGIME ANALYSIS

The output characteristics simulations,  $I_D$ - $V_{DS}$ , consists in drain-source voltage ranging from 0V to positive values at maximum +40V, keeping a negative bottom gate voltage and associating different top-gate voltages, fig. 5. In the simulations from fig. 5, the organic semiconductor noted by organic, is envisaged. The current decreases when the negative top or bottom voltages increase in modulus, due to the n-channel diminishing.

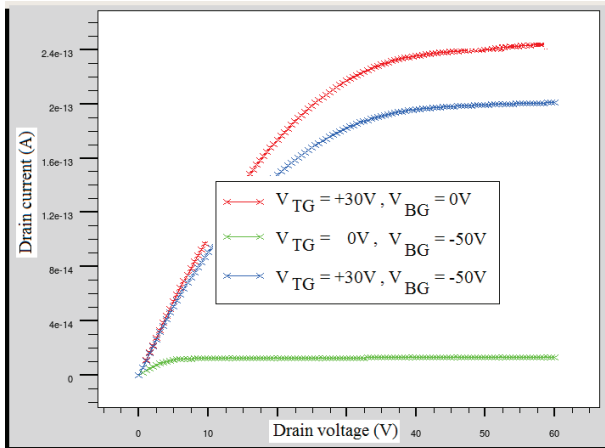


Fig 5. The output characteristics at different top and bottom gate voltages.

Selecting the optimum "organic" semiconductor, the drain current reaches in the saturation region for a saturation voltage,  $V_{DSat}$  of minimum +5V and maximum +42V in fig. 5. The maximum drain current reaches a value of  $2.38 \times 10^{-13}$  A that is 2.3 times higher than in a previous

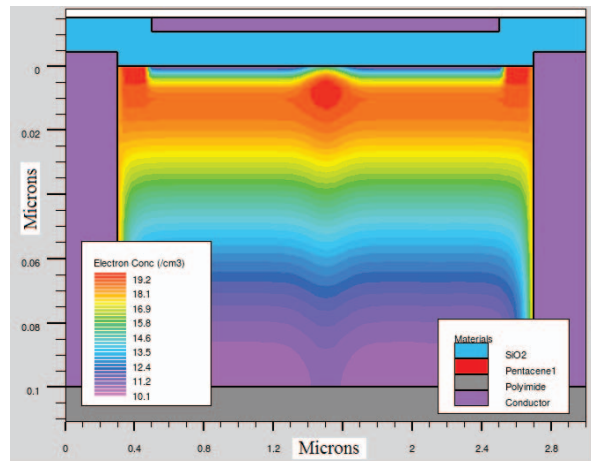
analysis [11], when  $I_D$  was 100fA. Now, the maximum saturated drain current of 238fA occurs for  $V_{TG}=+30$ V,  $V_{BG}=0$ V, instead old conditions for  $V_{TG}=+10$ V,  $V_{BG}=+50$ V.

In this study results that a higher positive top gate voltage produces higher drain currents. A lower dependence of the drain current on the bottom gate voltage is simulated.

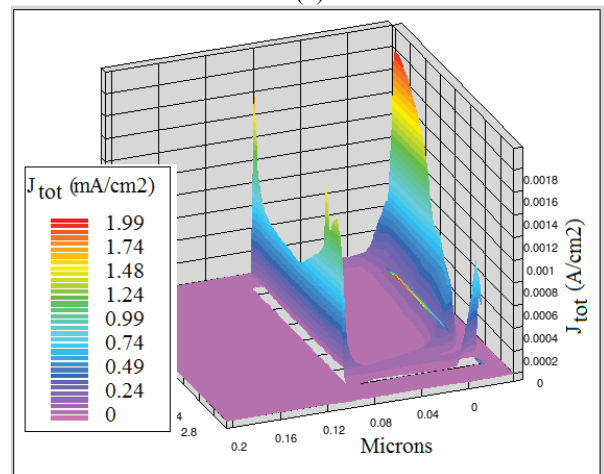
#### V. DISCUSSIONS

The applications of the proposed OTFT are in agreement with the applied voltages in each work regime. Because the n and p layers possess different doping concentrations, the conduction through the longitudinal n-channel is stronger than the conduction through the longitudinal p-channel.

The conduction superiority has to be established by the static characteristics analysis, forcing the device to use a p-type channel or a n-type channel. This evolution is emphasized once for a maximum electron concentration reached deeply in the n-type film of  $10^{19}$ cm<sup>-3</sup>, but rather closer to the oxide layer, fig. 6.a.



(a)



(b)

Fig 6. The electron concentration through the proposed OTFT with overlapped channels as contours traces proving a thin volume channel onset; two accumulation channels onset at  $V_S=0$ V,  $V_D=40$ V,  $V_{TG}=10$ V.

When positive voltages are applied on both gate terminals, two accumulation channels occur near the interfaces with oxide and with polyimide, fig. 6.b. This work regime with two simultaneous channels acted by two gates represents the main explanation to support a 2.3 higher drain current during the saturation regime.

If the positive voltage is applied on the top-gate, ( $V_{TG}>0$ ), the electron concentration increases in a thin volume channel, at 10nm close under the upper oxide interface (where  $n > 10^{19} \text{cm}^{-3}$ ), offering the specific volume channel conduction way [4], with a maximum of efficiency now, 2.3 times higher drain current. Weather the work regime is changed ( $V_{TG}<0$  or  $V_{BG}>0$ ), the holes channel is onset within the p-type layer and systematically the hole current density rests much lower than the electron current density, due to the initial asymmetry in the doping concentrations. To capture an as favorable as possible work regime for the holes transport, it is necessary to invert the biasing (e.g. for  $V_{TG}>0$ ,  $V_{BG}<0$ ), to increase the hole concentration  $p > 10^{19} \text{cm}^{-3}$  near the polyimide interface, so that two distinct accumulation channels occurs and both get the same order of magnitude for the current density,  $j_{p, n} = 1.2 \dots 1.8 \text{ mA/cm}^2$ , fig. 6.b. The localization of these two channels is near the oxide interface and near the polyimide interface. In this case, the vertical n/p junction is reverse biased, with two depleted regions, n-type and p-type that touch each other by the median coordinate of the organic mixed layers. This reverse bias prevents any leakage between the upper n-channel and the bottom p-channel, ensuring a firm behavior of the device.

Some comparisons of the main voltages and saturated drain current for the proposed device biased at  $V_{TG}>0$ , with similar organic thin film transistors, are presented in table 2.

TABLE II.  
THE OTFTS DEVICE PARAMETERS

Parameters	$ V_G $ (V)	$ I_{d, \max} $ ( $\mu\text{A}$ )	$V_{Dsat}$ (V)
Actual OTFT	1 ... 30	0.238	2...42
Other OTFT	17... 33 <sup>[22]</sup>	0.102 <sup>[11]</sup>	24...54 <sup>[21-29]</sup>

The studied organic OTFTs are suitable for the industrial low power display, due to a low drain current consumption, versus other variants, [22]. Also the organic devices are suitable for any biomimetic applications, which require carriers mobility under  $0.1 \text{ cm}^2/\text{Vs}$ , [24] and transducer with organic materials as biocompatible interfaces, [25-29].

The volume channel regime is advantageously when the technology of fabrication of the organic semiconductors on different insulators provides an extremely charged interface, which can degrade the surface currents.

## VI. CONCLUSIONS

This paper studied some new configurations of Organic Thin Film Transistors, which usually used a sole p-channel, or a sole n-channel. When a mixed structure with n-type layer on a p-type layer was used in the organic semiconductor region, some novel kinds of conduction channels occurred. The vertical n/p junction arose between the upper n-channel and the bottom p-channel, offers novel physical properties and prevented any interaction among channels.

The device simulations revealed multiple behaviors, depending on the Top and Bottom Gate voltages, if a positive drain-source voltage is applied.

## ACKNOWLEDGMENT

This work was partially supported by POSDRU/89/1.5/S/62557 Project.

*Received on October 6, 2016.*

*Editorial Approval on November 20, 2016.*

## REFERENCES

- [1] Alejandro de la Fuente Vornbrock, Donovan Sung, Hongki Kang, Rungrot Kitsomboonloha, Vivek Subramanian, Fully gravure and ink-jet printed high speed pBTTT organic thin film transistors, Organic Electronics, Volume 11, Issue 12, pp. 2037-2044, 2010.
- [2] K. Bock, Polymer electronics systems—Polytronics, Proceedings of IEEE, vol. 93, no. 8, pp. 1400–1406, 2005.
- [3] Tariel Ebralidze, Nadia Ebralidze, Giorgi Mumladze, Molecular Aggregations and Anisotropy Photoinduction in Organic Compounds, Optics. Vol. 3, No. 4, 2014, pp. 33-36.
- [4] C. Ravariu, D. Dragomirescu, F. Babarada, D. Prelipceanu, B. Patrighi, C. Gorciu, D. Manuc, A. Salageanu, Organic Field Effect Transistor OFET Optimization Considering Volume Channel Conduction Mechanism, 38-th IEEE International Annual Conference of Semiconductors, 12-14 Oct, 2015, Sinaia, Romania, pp. 113-117.
- [5] Anita Risteska, Kah-Yoong Chan, Thomas D. Anthopoulos, Aad Gordijn, Helmut Stiebig, Masakazu Nakamura, Dietmar Knipp, Designing organic and inorganic ambipolar thin-film transistors and inverters: Theory and experiment, Organic Electronics, Volume 13, Issue 12, pp. 2816–2824, 2012
- [6] Arash Takshi, Alexandros Dimopoulos, and John D. Madden, Simulation of a Low-Voltage Organic Transistor Compatible With Printing Methods, IEEE Transactions on electron devices, vol. 55, no. 1, pp. 276-282, 2008.
- [7] Satria Zulkarnaen Bisri, Taishi Takenobu, Yohei Yomogida, Hidekazu Shimotani, Takeshi Yamao, Shu Hotta, and Yoshihiro Iwasa, High Mobility and Luminescent Efficiency in Organic Single-Crystal Light-Emitting Transistors, Adv. Funct. Mater., vol. 19, pp. 1728–1735, 2009.
- [8] L.-L. Chua, J. Zaumseil, J.-F. Chang, E.-C. W. Ou, P. K.-H. Ho, H. Sirringhaus, and R. H. Friend, General observation of n-type field effect behavior in organic semiconductors, Nature, vol. 434, no. 7030, pp. 194–199, 2005.
- [9] J. Jakobovic, J. Kovac, M. Weis, D. Hasko, R. Smanek, P. Valent, R. Resel, Preparation and properties of thin parylene layers as the gate dielectrics for organic field effect transistors, Microelectronics Journal, vol. 40, pp. 595– 597, 2009.
- [10] C. Ravariu, Deeper Insights of the Conduction Mechanisms in a Vacuum SOI Nanotransistor, IEEE Transactions on Electron Devices, vol. 63, no. 8, 2016, pp. 3278 - 3283.
- [11] C. Ravariu, D. Dragomirescu, Different Work Regimes of an Organic Thin Film Transistor OTFT and Possible Applications in Bioelectronics, American Journal of Bioscience and Bioengineering, vol. 3, issue 3-1, June 2015, pp. 7-13.

- [12] C. Ravariu, F. Babarada, Modeling and simulation of special shaped SOI materials for the nanodevices implementation, *Hindawi Journal of Nanomaterials*, ID 792759, pp. 1-11, July 2011.
- [13] C. Ravariu, F. Ravariu, A test two-terminals biodevice with lipophylic and hidrophylic hormone solutions, *Journal of Optoelectronics and Advanced Materials JOAM*, vol. 9, nr. 8, pp. 2589-2592, Aug. 2007.
- [14] \*\*\*, Atlas Manual 2012, available at: [www.silvaco.com](http://www.silvaco.com).
- [15] Franziska D. Fleischli, Katrin Sidler, Michel Schaer, Veronica Savu, Jürgen Brugger, Libero Zuppiroli, The effects of channel length and film microstructure on the performance of pentacene transistors, *Organic Electronics*, vol. 12, pp. 336-340, 2011.
- [16] P. Singh, A. Sellinger, A. Dodabalapur, Electron transport in copper phthalocyanines *J. Appl. Phys.*, 107, 044509, 2010.
- [17] G. Bersuker, P. Zeitzoff, G. Brown, and H. R. Huff, Dielectrics for future transistors, *Materials Today*, vol. 7, no. 1, pp. 26-33, 2004.
- [18] Burgi, L.; Richards, T. J.; Friend, R. H.; Sirringhaus, H., Close look at charge carrier injection in polymer field-effect transistors, *J. Appl. Phys.*, vol. 94, issue 9, 6129: 1-9, 2003.
- [19] Prashant Sonar, Samarendra P. Singh, Yuning Li, Mui Siang Soh, and Ananth Dodabalapur, A Low-Bandgap Diketopyrrolopyrrole-Benzothiadiazole-Based Copolymer for High-Mobility Ambipolar Organic Thin-Film Transistors, *Adv. Mater.*, vol. 22, pp. 5409-5413, 2010.
- [20] Stefan Chisca, Ion Sava, Valentina-Elena Musteata, Maria Bruma, Dielectric and conduction properties of polyimide films, *IEEE International Semiconductor Conference CAS 2011*, Volume: 2, pp. 253 - 256, 2011.
- [21] Jana Zaumseil and Henning Sirringhaus, Electron and Ambipolar Transport in Organic Field-Effect Transistors, *Chem. Rev.*, 107, pp. 1296-1323, 2007.
- [22] Hagen Klauk, Organic thin-film transistors, *Chem. Soc. Rev.*, vol. 39, pp. 2643-2666, 2010.
- [23] P. F. Babarada, C. Ravariu, J. Arhip, Electrophysiological Data Processing Using a Dynamic Range Compressor Coupled to a Ten Bits A/D Conversion Port, in *Proceedings IEEE-CCP*, Lisa O'Conner Editor, Conference Publishing Services CPS, IEEE Computer Society, pp. 257-262, 2011.
- [24] G. S. Costa, A. M. Salgado, P. R. G. Barrocas, Advances on Using a Bioluminescent Microbial Biosensor to Detect Bioavailable Hg (II) In Real Samples, *American Journal of Bioscience and Bioengineering*. Vol. 1, No. 3, 2013, pp. 44-48.
- [25] Tae-Jun Ha, Prashant Sonar, Samarendra P. Singh, and Ananth Dodabalapur, Characteristics of High-Performance Ambipolar Organic Field-Effect Transistors Based on a Diketopyrrolopyrrole-Benzothiadiazole Copolymer, *IEEE Transactions on electron devices*, vol. 59, no. 5, pp. 1494-1500, 2012.
- [26] Bremner, Y. Liu, M. Samie, G. Dragffy, A. G. Pipe, G. Tempesti, J. Timmis and A. M. Tyrrell, SABRE: a bio-inspired fault-tolerant electronic architecture, *Bioinspir. Biomim.* IOP, 8 016003, 2013.
- [27] Poornima Mittal, B.Kumar, Y.S.Negi, B.K.Kaushik, R.K.Singh, Channel length variation effect on performance parameters of organic field effect transistors, *Microelectronics Journal*, Volume 43, Issue 12, pp. 985-994, 2012.
- [28] Yoshinori Ishikawa, Yasuo Wada, and Toru Toyabe, Origin of characteristics differences between top and bottom contact organic thin film transistors, *Journal of applied physics*, 107, 053709, 2010.
- [29] Na Liu, Yulei Hu, Jianhua Zhang, Jin Cao, Yinchun Liu, Jun Wang, A label-free, organic transistor-based biosensor by introducing electric bias during DNA immobilization, *Organic Electronics*, vol. 13, pp. 2781-2785, 2012.

# On the Immunity of Data Acquisition Systems Used in Power Systems

Livia-Andreea Dina<sup>1</sup>, Ileana-Diana Nicolae<sup>2</sup>, Petre-Marian Nicolae<sup>1</sup>,  
Dorina-Mioara Purcaru<sup>3</sup>

<sup>1</sup>University of Craiova, Dept. of Electr., Energetic and Aero-Spatial Eng., Craiova, Romania, dina.liviaandreea@yahoo.com, pnicolae@elth.ucv.ro

<sup>2</sup>University of Craiova, Dept. of Computers and IT, Craiova, Romania, nicolae\_ileana@software.ucv.ro

<sup>3</sup>University of Craiova, Dept. of Automation, Electronics and Mechatronics, Craiova, Romania, dpurcaru@yahoo.com

**Abstract** - The paper deals with some tests regarding the immunity for radiated emissions and compliance with international standards for electromagnetic compatibility (EMC) measurements for an industrial data acquisition system (DAS) used in power systems. The behavior of the DAS, when functioning near electromagnetic disturbance sources, is studied. The goal is to test its robustness in similar conditions as those encountered in its normal environment. It is known that multiple factors may affect the accuracy of data acquired by DAS. The Equipment Under Test (EUT), which in this case is represented by DAS is tested for immunity in a specialized enclosure (GTEM Cell). The immunity based on the analysis of the influences of an electric field with constant magnitude and variable frequency in the range of 80 MHz...1 GHz is studied. After analyzing the initial tests results, partial and, afterwards, full shielding of the EUT's case is performed in order to remove the EM influence. The tests' results drive to the conclusion that it is necessary to design and build an enclosure from conductive material for the DAS. After the implementation of the measures, the EUT passed the tests concerning the immunity. The GTEM Cell construction, GTEM model, generation and distribution of electric and magnetic field inside the GTEM Cell, equipment under test (EUT), radiated emission measurement scheme, EMC standards for GTEM Cell, are exposed.

**Keywords:** Data Acquisition System, immunity tests, electromagnetic shield, electromagnetic interferences.

## I. INTRODUCTION

Immunity to radiation is the condition when the existence of radio-frequency waves into the atmosphere is likely to affect the normal operation of a device. In order to exemplify this phenomenon, we can mention the case of voltage fluctuations, harmonics etc.

Passing the immunity tests for a data acquisition system (DAS) means that the equipment has the capacity of functioning undisturbed in the environment where it is installed.

DAS purpose is to acquire the input analogical signals, to measure, analyze, process and display the measurement. The acquired data accuracy in our test isn't always high.

Because of some disturbance sources, significant errors

can occur during measuring related operations.

By testing the immunity to EM radiations of DAS, one intends to analyze and remove the negative effects that appear in the measurement process.

Testing the equipment's immunity to radiations can be done with a specialized enclosure, such as the Gigahertz Transverse Electromagnetic Mode (GTEM) Cell [1].

GTEM cell is an improved version of TEM cell, with extended frequency range to GHz and increased working volume.

Unlike the anechoic chamber, the GTEM cell makes possible for easy testing using less power, when the size of the EUT allows this [2].

## II. DATA ACQUISITION SYSTEM

Data acquisition systems are complex structures for processes monitoring in which usually a lot of physical quantities are occurring (Fig. 1).

The purpose of data processing differs with equipment destination. It can be the control of physical process, for protection, or it can be used informatively about the process evolution by data visualization.

DAS acquires analogical or digital signals, using transducers, in order to record, to display or process the information based on the transducer's nature.

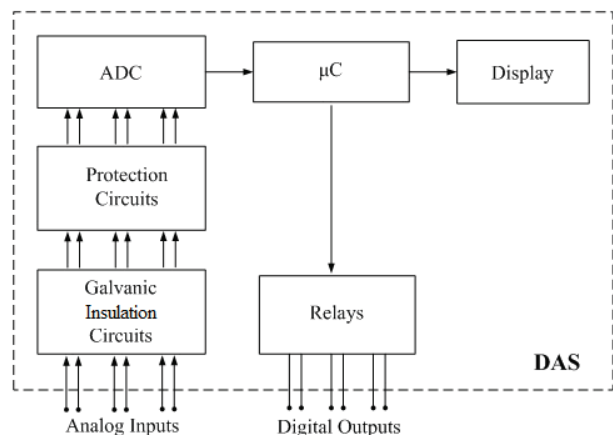


Fig. 1. The basic schematic of a data acquisition system.

<sup>1</sup> This work was supported by a grant of the Romanian National Authority for Scientific Research and Innovation, CNCS/CCCDI –UEFISCDI, project number PN-III-P2-2.1-BG-2016-0240, within PNCDI III.



Fig. 2. The tested data acquisition system.

The specifications of the tested DAS (Fig. 2) are:

- Equipment used for measurements in the time domain, with eight analogical input channels of  $\pm 10$  V and eight digital outputs;
- The Voltage inputs are completely differential, in order to connect it easily both to star (Y) and respectively delta ( $\Delta$ ) schemes;
- The analogical voltage input circuits provide the galvanic isolation of inputs signal to the analog to digital converters (ADC);
- The input circuits preserve the characteristic accuracy for more than 1.5 times the rated input quantities;
- The measuring equipment allows both synchronous acquisition of eight input signal, and over-sampling features.

In case of DAS, the electromagnetic disturbances can be generated by different equipment functioning nearby.

### III. DAS Measurement Errors

The errors which appear in DAS measurement can have many causes, as detailed below. Among these, the EM pollution represents the most important sources which can radically influence the DAS operation, often altering the real input values. Removing this effect is the main goal of our research. In this case, the other causes can be neglected.

#### A. The analog to digital conversion of the signal, conversion errors

A first error is caused by the analog to digital (A/D) converter (ADC) which converts every value of the analogical signal to digital divisions.

In Fig. 3 one can observe that the real sinusoidal input signal recomposition is not precise. Because the resolution increases towards 16-bit, the number of steps increases to  $2^{16} = 65536$ , and one obtain a near perfect signal representation. Our data acquisition system uses 12-bit A/D converters for  $-10$  V  $\div$   $+10$  V input voltage.

The 12-bit resolution A/D converter has the following minimum variation of voltage [3]:

$$U_d = \frac{U_{\max} - U_{\min}}{2^{12}} \quad (1)$$

$$U_d = \frac{10 - (-10)}{4096} = 4.88 \text{ mV}$$

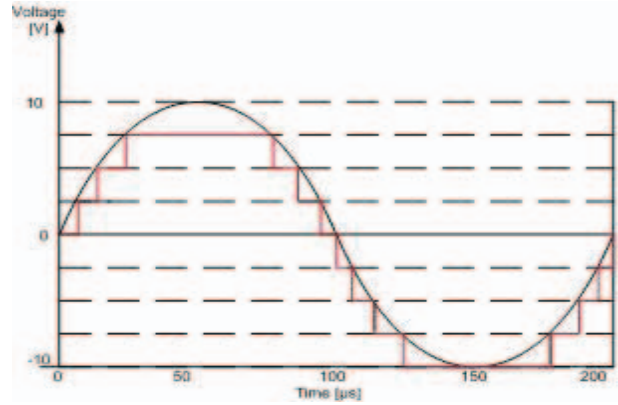


Fig. 3. Truncation errors at the 3-bit conversion of signal.

This minimum voltage variation represents one step. For signals between  $-10$  and  $+10$  V, the minimum detectable variations is  $4.88$  mV.

The continuous (DC) voltage is constant for a certain time interval:

$$U_{DC} = \frac{1}{(t_2 - t_1)} \cdot \int_{t_1}^{t_2} U(t) dt. \quad (2)$$

For a digitized signal the voltage becomes [14]:

$$U_{DC} = \frac{1}{N} \cdot \sum_{i=1}^N U_i \quad (3)$$

The root mean square (RMS) is computed with [14]:

$$U_{RMS} = \sqrt{\frac{1}{(t_2 - t_1)} \cdot \int_{t_1}^{t_2} U^2(t) dt}. \quad (4)$$

The quantization error ( $\epsilon$ ) can be determined with [14]:

$$\frac{0.5 \cdot U_{\min}}{U_{\max}} = \frac{1}{2^{N+1}} \leq \epsilon \quad (5)$$

where:  $N$  – number of bits of the ADC.

When one can estimate the limits of the signal values, it is recommended to choose a domain where the error is as small as possible.

#### B. Errors introduced by protection and isolation circuits

Another source of errors is represented by the ripple voltage (noise) introduced by the galvanic isolation and over-voltage protections circuits, or the supply. Typically, the ripple voltage value is  $20 - 100$  mV peak to peak.

Figs. 4 and 5 represent the waveform of a signal before and after filtering [3].

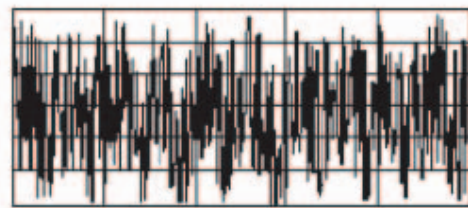


Fig. 4. The waveform of the original signal.

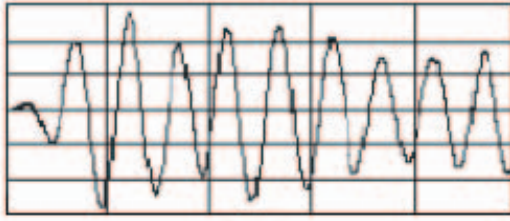


Fig.5. The waveform of the processed signal.

The noise removal can be realized by signal filtering. A data analysis is necessary (the acquired signal must be processed such as to get a reconstructed signal approximating as much as possible the original signal).

The signal filtering is performed using low-pass filters, which do not affect the low frequency components, but they mitigate the high frequency components. The frequency where the signal is attenuated (cutoff frequency) must be sufficiently high such as to preserve the useful components of the signal. Usually, it is chosen to be half the operating frequency of the circuits.

EM pollution represents an important source of perturbation. The removal of its effect is the primary purpose of our research. In the analyzed case, it has the greatest negative effect on the DAS operation.

### C. Errors caused by EMC

The EM radiation affects directly the DAS behavior, having effects like: malfunctioning of the microcontroller, erroneous measurements and wrong digital outputs. They main sources of EM perturbations from the operating environment of the tested DAS are equipment built with controlled power semiconductors, which are functioning nearby DAS.

The detection of these problems is the starting point of this paper. One intended to test the DAS to immunity, using a GTEM 750 cell and eventually to take corrective measures if problems are detected.

## IV. IMMUNITY TESTING OF DAS

Testing the DAS in the GTEM cell is realized in compliance with the generic standard IEC 61000-4-20, which refers to immunity testing in transverse electromagnetic (TEM) waveguides.

The GTEM Cell is a transmission line that simulates the electromagnetic energy transmission in the TEM mode (Transversal Electro-Magnetic) through which the electromagnetic wave propagates into the surrounding space. The GTEM cell, as a new measurement facility in electromagnetic compatibility (EMC), needs to be evaluated, especially considering its electric field distribution. It is important to determine the field strength and distribution in a GTEM cell for EMC and calibration measurements.

The field strength inside a GTEM Cell is a function depending on the input power as well as on the location along the longitudinal axis or septum height. Immunity measurements require field uniformity (75 dB according to IEC 61000-4-3 Standard) over certain test areas [4], [5].

Immunity tests assume that the equipment under test (EUT) must withstand a certain level of interference (level specified by the standard) such as to receive a positive opinion and pass the tests [6].

One used the software WIN 6000, compatible with GTEM 750 Cell and the related equipment.

The measurements have been done with a frequency step of 1%, the EUT being positioned in three different ways on the coordinate system's axes [1].

In this case, for testing, the EUT is placed in the cell and the amount of power is increased until the required value of the field is reached. For each measurement the EUT is monitored for the respective frequency (30 MHz – 1 GHz). The configuration of the test is depicted by Fig. 7 [7].

Test arrangement was performed in accordance with the standard IEC 61000-4-3, and the following equipment was included: amplifier; generator; bi-directional coupler; meter (power meter) depicted by Fig. 6.

The electric field values within the cell and the measured forwarded and reversed powers during tests are depicted in Fig. 8. The “+” marker suggests the frequencies for which errors appeared.

The stationary step time for each analyzed frequency was 5 seconds. The testing was done for a value of 30 V/m for the reference input field, with an error tolerance of 1 %.

The DAS testing was performed with and without the signal's modulation in amplitude (AM). During tests, the DAS was operating with no inputs (the voltages and currents values were null). The measurements display (voltages and currents) on the DAS' screen is realized in a sequential mode.

No errors were recorded during tests with not AM.

During tests with AM one noticed that the DAS had an abnormal behavior, as explained in Table I.

As a consequence of the above, one proposed the shielding of the DAS.

Shielding is essential firstly for the limitation of the radiate emission of a system (EN55022 standard, for radiated emission between 30 MHz and 1 GHz), and on the other hand, for system protection against perturbations emitted by local equipment or more commonly against electromagnetic radiation in the environment.

Several standards define the method for testing the immunity to radiated perturbations, depending on the source of field and respectively on the frequency: incidental electromagnetic field – IEC 61000-4-3, 61000-4-10 and so on.

Shielding is generally acquired through a metal or metal plated casing, which surrounds the equipment (Fig. 11).

TABLE I.  
ERRORS OCCURRED DURING TESTS.

Frequency [MHz]	Voltages [V]
0÷110	0
116	10
120	12
124	26
130	29
132	31
136	36
137÷438	0
451	restarted
471	Stopped working and restarted
495÷1000	0

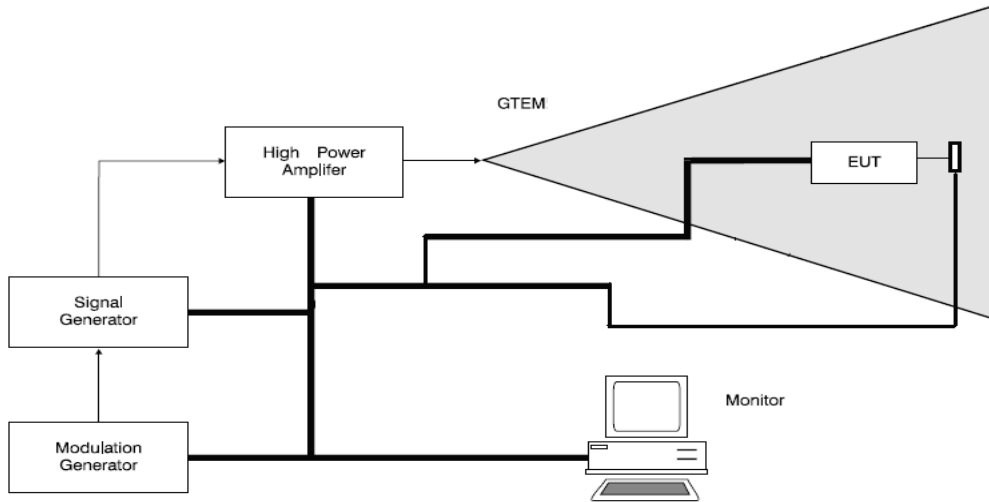


Fig. 6. Equipment disposal for the immunity test.

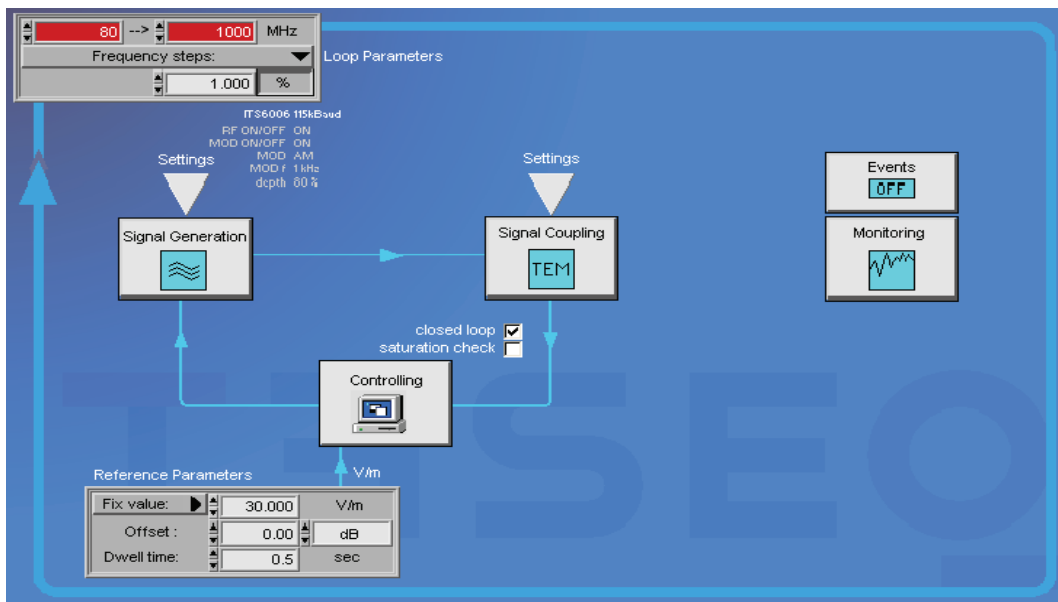


Fig. 7. Test equipment configuration.

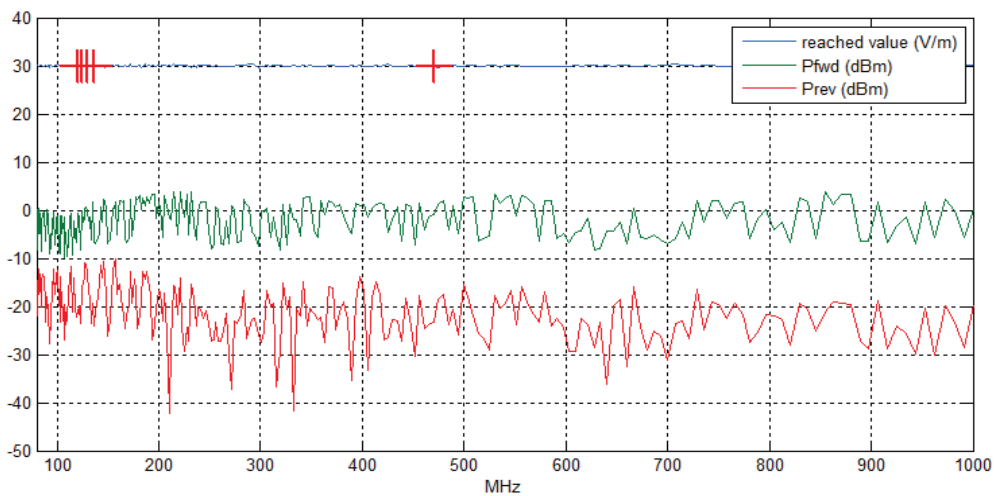


Fig. 8. Reached value of E-field, the forwarded and reversed power.

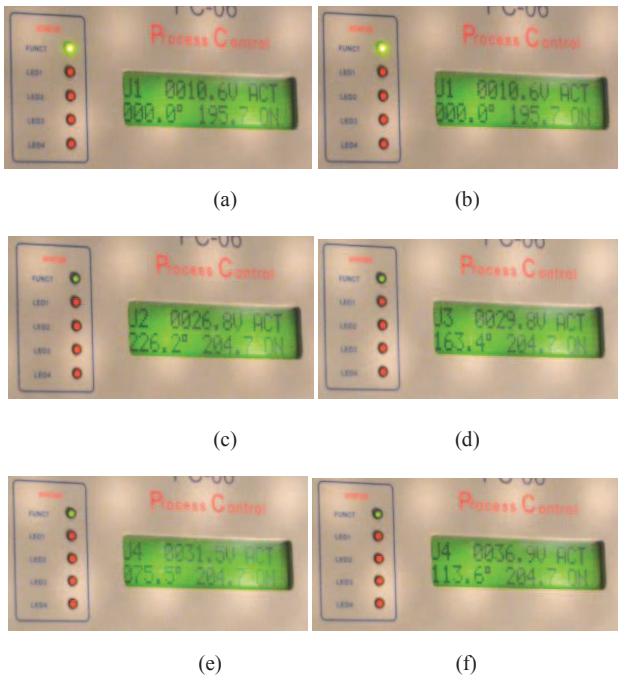


Fig. 9. Voltages measured by DAS during testing within 110 MHz ÷ 140 MHz range.



Fig. 10. DAS behavior at resetting for 451 MHz.

The shielding must protect the sensitive part of a device against exterior electromagnetic fields.

Because the tangential component of the electric field and the normal component of the magnetic field are null at the surface separating the shield from the environment, the conducting surfaces are absorbing electric field whilst rejecting the magnetic field. In the same time, the reflection (shielding) is improved along with the electric conductivity  $\sigma$  and therefore it is stronger for the Copper shields and weaker for the Iron ones.

Following the partial shielding, one noticed that for the 110 MHz ÷ 140 MHz range, parasite voltages were recorded, having values between 26 – 41 V (Fig. 12).

For the 430 MHz ÷ 480 MHz range one noticed a normal behavior of the DAS, the voltage remaining constant at 0 V (Fig. 13).

Further, a decision on DAS fully shielding DAS was made. The shielding was done with copper foil (which has high shielding properties), the shield being connected to ground (Fig. 14).

After the DAS's fully shielding, the voltages measured were at 0 V for the analyzed frequency range of 30 MHz ÷ 1 GHz.

In the first stage one partially shielded the DAS. The shielding was made with copper foil with a width of 0.08mm applied on the outer case of the DAS in the direction of the electric field's propagation.

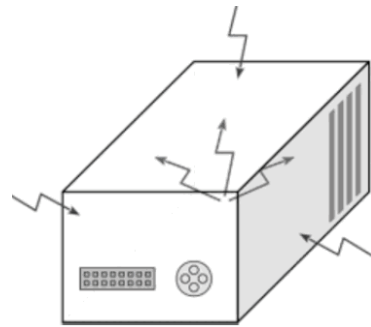


Fig. 11. Metallic case used to shield the equipment.

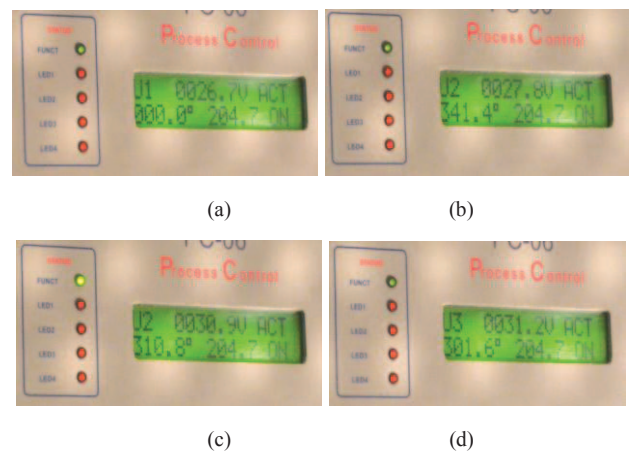


Fig. 12. Voltages measured by the partially shielded DAS during tests in the 110 MHz ÷ 140 MHz range.

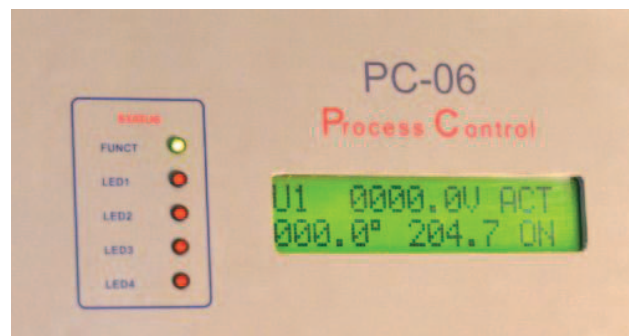


Fig. 13. Voltage measured by the partially shielded DAS during tests in the 430 MHz ÷ 480 MHz range.

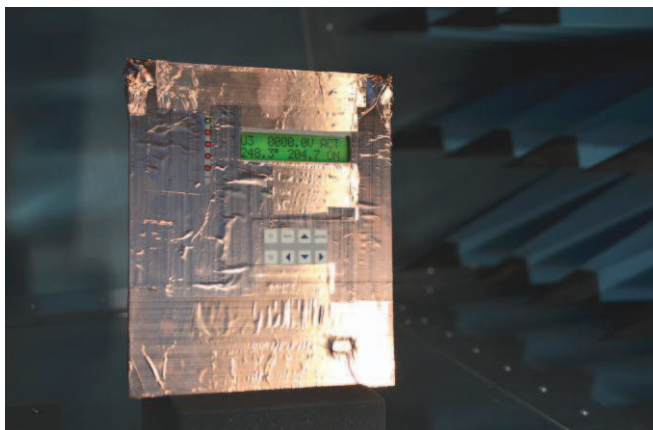


Fig. 14. DAS fully shielded with copper foil.

## V. CONCLUSIONS

The tests concerned with the DAS revealed that the original case, made of Iron, did not provide immunity to electromagnetic radiation. Therefore a Copper foil was used to cover the DAS.

The advantage of the partially shielded DAS is that one managed to remove the unwanted effects that appeared within the 430 MHz ÷ 480 MHz frequency range, namely the DAS' resetting, blocking and shutting down.

The initial solution of a partially shielded DAS had limited effects, because one could not manage to remove all the negative aspects of EMC.

Further, one decided to fully shield the DAS with a shield connected to the DAS' ground.

In the end, the obtained results were satisfactory, the input sizes being null for the entire test period.

An important role, from the DAS' construction point of view, will be the DAS' case substituting by a metallic case made from a material with high EMC shielding properties (such as copper foil).

This solution should considerably reduce the negative effects of electromagnetic interference.

Received on July 17, 2016

Editorial Approval on November 15, 2016

## REFERENCES

- [1] P. M. Nicolae; I. D. Nicolae; D. G. Stănescu, "Using GTEM cells for immunity tests on electronic boards with microcontroller", *Proceedings of EMC 2012*, pp: 44 – 49, Pittsburg, USA, 2012.
- [2] IEC 61000-4-20 Edition 2.0, Electromagnetic compatibility (EMC) – Part 4-20: Testing and measurement techniques – Emission and immunity testing in transverse electromagnetic (TEM) waveguides, *Basic EMC Publication*, Geneva, Switzerland, Aug. 2010.
- [3] D.M. Purcaru, I. Purcaru, D. Popescu, "Results obtained in monitoring transient electrical events from hydropower plants", *Proceedings of ICC 2015*, pp. 414-419, Miskolcz, Hungary, May, 2015.
- [4] IEC EN 61000-4-3:2010, *Electromagnetic compatibility (EMC) – Part 4-3: Testing and measurement techniques - Radiated, radio-frequency, electromagnetic field immunity test*, 2010.
- [5] A. Ubin and M. Z. M. Jenu, "Characterization of electric fields in a GTEM Cell", *Proceedings of RF and Microwave Conference*, pp. 209-214, Subang, Selangor, Malaysia, Oct. 2004.
- [6] P. M. Nicolae, D. G. Stănescu and M.Ș. Nicolae, „Aspecte privind teste de emisii și imunitate la perturbațiile electromagnetice în celula G-TEM”, *Proceedings of SNET'12*, Bucharest, 2012 (in Romanian).
- [7] H. Schaffner, "GTEM test cells, test cells for EMC radiated & immunity testing DC to 20 GHz," Zurich, Switzerland, Feb. 2005, available at <http://docslide.us/documents/gtem-test-cells-e.html>.
- [8] B. Adascalitei, D. L. Dretu and M. P. Salceanu, "Electromagnetic Compatibility Testing and Measurement" – *Theoretic manual*, Iasi, 2003.
- [9] H. Chen, Z. Qian, Z. Zeng, and C. Wolf, "Modeling of Parasitic Inductive Coupling in a Pi-Shaped Common Mode EMI Filter", *IEEE Trans. on Electromagnetic Compatibility*, vol. 50, no.1, pp. 71-79, Feb., 2008.
- [10] S. Ishigami, K. Harirna and Y. Yamanaka, "Estimation of E-field distribution in a loaded GTEM cell", *Proceedings of EMC 2001*, vol. 1, pp. 129-134, Quebec, Canada, Aug. 2001.
- [11] IEC 61000-6-3 Edition 2.1, Electromagnetic compatibility (EMC) – Part 6-2: Generic Standard – *Emission standard for residential, commercial and light-industrial environments*
- [12] A. Ubin and M. Z. M. Zenu, Characterization of Electric Fields in a GTEM Cell [EMC measurement applications], *Proceedings of RF and Microwave Conference*, pp. 209-214, Subang, Selangor, Malaysia, Oct. 2004.
- [13] P. M. Nicolae, D. M. Purcaru, I. D. Nicolae, G. Mihai and M. Duță, "On EM Disturbances over Digital Equipment Used for Monitoring and Events Recording in a Power System", *Proceedings of EMC 2011*, pp. 465-470, Long Beach, USA, Aug. 2011.
- [14] CISPR16-1-1 Ed. 3.1, Specification for radio disturbance and immunity measuring apparatus and methods Part 1-1: Radio disturbance and immunity measuring apparatus - Measuring apparatus. International Electrotechnical Commission, 2010.
- [15] S. Braun, A. Frech, and P. Russer, "CISPR Specification and Measurement Uncertainty of the Time-domain EMI Measurement System," *Proceedings of EMC 2008*, pp. 1-4, Detroit, USA, Aug. 2008.
- [16] S. O. Land, M. Ramdani, R. Perdriau, Y. Braux and M. Drissi, Using a Modified Taylor Cell to Validate Simulation and Measurement of Field-to-Shorted-Trace Coupling, *IEEE Trans. on Electr. Compatibility*, vol. :56, issue: 4, pp. 864 – 870, Aug. 2014,.
- [17] IEC EN 61000-4-3, Electromagnetic compatibility (EMC) – Part 4-3: Testing and measurement techniques - Radiated, radio-frequency, electromagnetic field immunity test, *Basic EMC Publication*, Geneva, Switzerland, Aug. 2010.

# Aspects of Behavior Regarding Certain Electronic Equipment Subject to Electrostatic Discharge

Mircea-Emilian Ardeleanu<sup>1</sup>, Paul Nicolescu<sup>2</sup>

1. University of Craiova, Electrical Engineering Faculty, e-mail : mircea\_emilian@yahoo

2. National Institute for Research Development and Testing in Electrical Engineering of Craiova (ICMET), cem@icmet.ro

**Abstract** - Electrical discharge due to human operators may cause disturbances with very fast variation reaching the sensitive equipment by conduction and radiation and can affect and even destroy them. Therefore, between a human, possible to load electrostatic voltages of 10-15kV ordinal, and an electronic device (computer, laptop, memory stick, etc.), system connected to the grounding, an electrostatic discharge can occur as a result of electric charging (electrification) the person wearing clothes made of synthetic fibers, due to friction with the air. This paper proposes a study of the transient arrangement produced by human electrostatic discharge and the disruptive or destructive effects that may occur. Experimental tests have been performed to determine the degree of immunity to electrostatic discharge (ESD) into the air and through direct contact, in accordance with the regulations in force, in the specialized laboratory of ICMET Craiova, subjecting a memory stick and a wireless Internet connection stick to electrostatic discharge. The results obtained revealed the individualized behavior for each device tested.

**Keywords:** *electromagnetic compatibility, electrostatic discharge, immunity to a disturbance, contact discharge, air discharge.*

## I. INTRODUCTION

Industrial development, especially in the light industry, widely producing synthetic fibers and clothes made of synthetic fibers and semiconductor manufacturing industry has led to the importance of electrostatic discharge studies and analyses.

Electrical discharge, due to human operators, may cause disturbances with very fast variation reaching the sensitive equipment by conduction and radiation that can affect and even destroy them.

Therefore, between a human, possible to load electrostatic voltages of 10-15kV ordinal, and an electronic device (computer, laptop, memory stick, etc.), system connected to the grounding, an electrostatic discharge can occur as a result of electric charging (electrification) the person wearing clothes made of synthetic fibers, due to friction with the air.

This paper proposes a study of the transient arrangement produced by human electrostatic discharge and the disruptive or destructive effects that may occur.

Experimental tests have been performed to determine the degree of immunity to electrostatic discharge (ESD) into the air and through direct contact, in accordance with

the regulations in force, in the specialized laboratory of ICMET Craiova, subjecting a memory stick type ADATA of 8GB and a wireless Internet connection stick to electrostatic discharge. The results obtained revealed the individualized behavior for each device tested.

## II. THEORETICAL NOTIONS RELATED TO ELECTROSTATIC DISCHARGES

Electrostatic discharges shall be recorded between broadband disturbance sources.

Electrostatic discharges arising from the accumulation of electrical charge with a certain polarity in the separation of the two areas that previously have been in contact and one of the two environments is isolating [1].

Electrostatic discharge are classified between non-functional sources of electromagnetic interference along with other sources such as: automotive ignition installations, welding equipment, electronic converters, etc. [2]

The development of electronics, microelectronics and generally of IT equipment and the production of synthetic fibers and clothes made of synthetic fibers has led to increasing emphasis on studying and analyzing the effects of disturbing or destructive effects of electrostatic discharges produced by humans.

Electrostatic discharges from humans are important in terms of electromagnetic compatibility.

Depending on the clothes worn by a human operator, humidity environment, etc. a person can be charged with a voltage up to 30 kV, which can produce large amounts of undesirable electrostatic discharge (disturbing or destructive) on electronic equipment. In general, a person walking on a carpet can be charged with a voltage up to 15 kV.

In the case of electrostatic discharge from the point of view of electromagnetic compatibility and determining the level of immunity, the essential problem is the fact that these discharges are very fast and under the form of impulses measured in nanoseconds.

Disturbing phenomena produced by electrostatic discharges are produced by discharge currents under the form of impulses and by time-varying magnetic fields [2]

## III. GENERAL ASPECTS OF ESD TESTS

The tests on immunity to electrostatic discharge can be performed in specialized laboratories and on-site (on-site operation).

The tests are done in accordance with the specified standard IEC 61000-4-2 [3].

For ESD testing a high voltage source is required, an energy accumulator and discharge electrode. In general, the discharge electrode is mounted in a device called test gun that can move towards the object tested (EUT) starting from a certain distance until spark discharges occur, known as air discharge. In case the test gun comes into contact with metal parts of the EUT, discharge occurs through direct contact.

In Table I [3] we have presented immunity levels and the tensions the equipment must be tested at.

TABLE I.  
TEST LEVELS

Contact discharge		Air discharge	
Level	Test voltage kV	Level	Test voltage kV
1	2	1	2
2	4	2	4
3	6	3	8
4	8	4	15
x	special	x	special

The contact discharge is the preferred test method and the second method by air discharge shall be used where contact discharge method cannot be applied.

It is important to achieve with the equipment used, through the laboratory simulation of electrostatic discharge, the ideal wave shape of the discharge current through direct contact.

This waveform is shown in figure 1 [2,3].

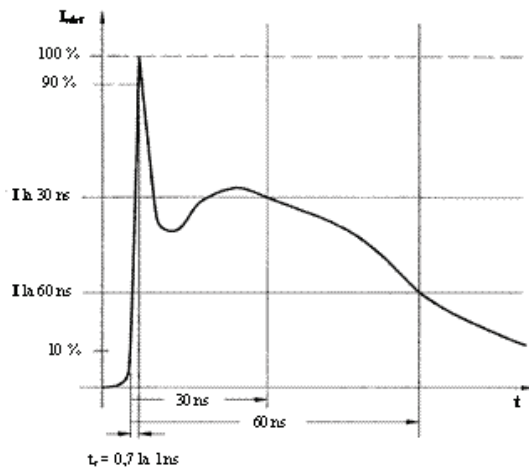


Fig.1 Ideal wave shape of the discharge current

Also, it is important to analyze the results on EST immunity, represented by knowing the environmental conditions in which the tests were performed, namely [3]:

- ambient temperature 15-30 °C;
- relative humidity 30-60%
- atmospheric pressure 860 – 1.060 mbar.

The test result shall be classified in terms of loss of function or degradation of performance of the equipment under test (EUT), as follows [3]:

- a) normal performance within limits specified by the manufacturer;
- b) temporary loss of function or degradation of performance which ceases after the disturbance ceases, and from which the equipment under test recovers its normal performance, without operator intervention;
- c) temporary loss of function or degradation of performance, the correction of which requires operator intervention;
- d) loss of function or degradation of performance which is not recoverable, owing to damage to hardware or software, or loss of data.

#### IV. EXPERIMENTAL DETERMINATIONS ON ESTABLISHING THE DEGREE OF IMMUNITY TO ESD

This article has proposed to present the ESD test results for a memory stick (fig. 2 a) and an Internet connection stick (fig. 2 b) in order to establish the degree of immunity



a)



b)

Fig.2 Article proposed to the ESD test

We selected these devices because they can be directly connected to a computing equipment (computer, laptop) and may be subject to human nature ESD (electrostatically charged human operator)

*A. Equipment used*

The tests were conducted in the specialized laboratory of ICMET Craiova.

The high voltage generator is an electrostatic discharge simulator for immunity tests by air and contact discharges (25 kV), ESD30C (EM Test) (fig. 3.a) equipped with test gun (fig. 3.b).

The ESD30C/ (EM test) is a mains supply powered ESD simulator that generates ESD up to 25 kV in both air discharge and contact discharge mode [8].



a)



b)

Fig.3 Equipment used

The test gun is equipped with two interchangeable tips for air discharge and for direct contact discharge (fig. 4). The two tips are made in accordance with the requirements specified in international standards.



a)



b)

Fig.4 The accessory for test gun

a) top for testing by contact discharge; b) top for testing by air discharge

The tests were conducted at an ambient temperature of 25.5 ° C and a humidity of 54.5%, sizes falling in the range of values provided in [3].

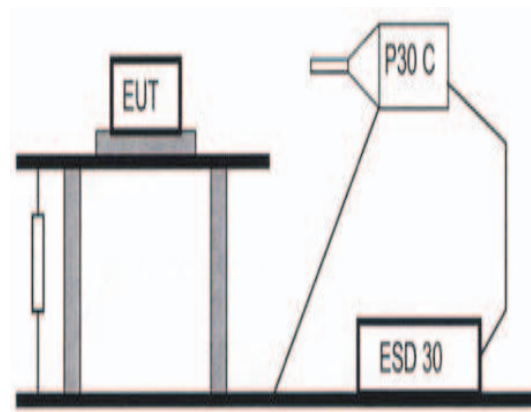


Fig.5 Experimental assembly which is performed in laboratory for the ESD tests [6]

Before carrying out the tests, we carried out a verification of waveform signal produced by the equipment used on a calibration ESD resistance (EM Test) of 2 Ω for a test voltage of 2kV( fig.6).

The result obtained is shown in fig. 7 and is within the limits imposed by [3] and presented in Table II, being similar to the waveforms obtained in similar experimental conditions and found in specialized literature [4].

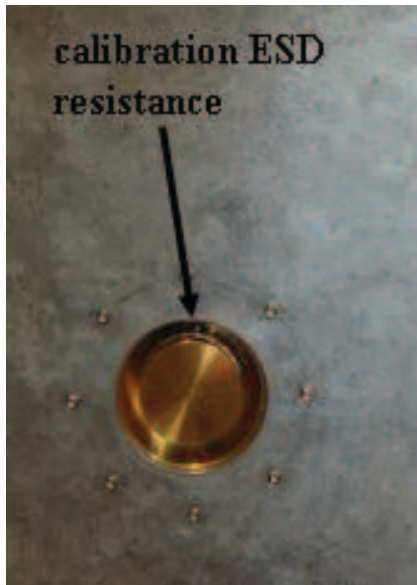


Fig.6 Calibration ESD resistance (EM Test) of 2 Ω

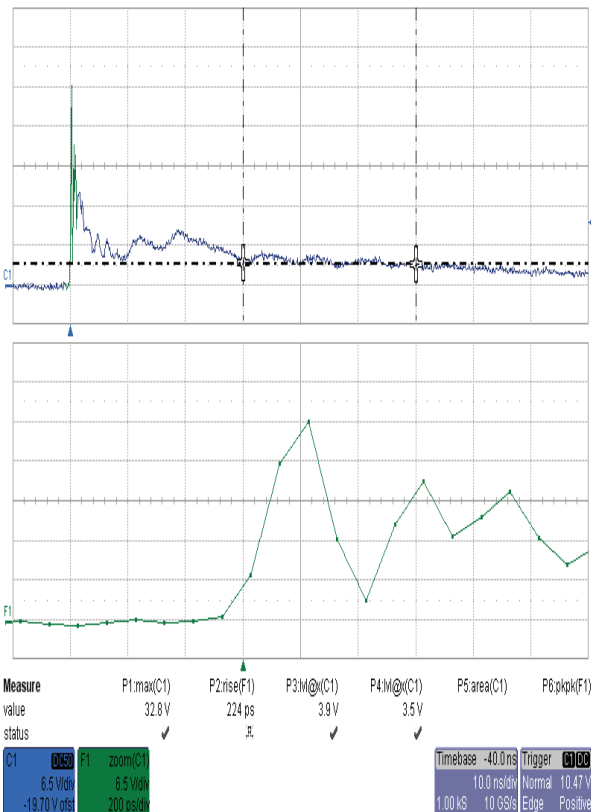


Fig. 7. Waveforms obtained experimental.

TABLE II. CONTACT DISCHARGE CURRENT WAVEFORM PARAMETERS

Level	Indicated voltage [kV]	First peak current of discharge ± 15% [A]	Rise time $t_r$ (± 25%) [ns]	Current (± 30 %) at 30 ns [A]	Current (± 30 %) at 60 ns [A]
1	2	7.5	0.8	4	2
2	4	15	0.8	8	4
3	6	22.5	0.8	12	6
4	8	30	0.8	16	8

The reference point for measuring the time for current at 30 ns and 60 ns is the instant when the current first reaches 10% of the 1<sup>st</sup> peak of discharge current



Fig.8 Issues during tests

*B. Results of the experimental tests*

The test points were selected so that the requirements IEC 61000-4-2 and thus can be considered:

- points on metallic sections of a cabinet which are electrically isolated from ground;
- any point in the control or keyboard area and any other point of man-machine communication, such as switches, knobs, buttons, indicators, LEDs, slots and other operator-accessible areas.

The ESD shall be applied only to those points and surfaces of the EUT which are accessible to persons during normal use [3]:

- those points and surfaces which are only accessible under maintenance;

- those points and surfaces which are only accessible under service by the (end-) user (for example : battery contacts while changing batteries, a cassette in a telephone answering machine etc.);
- in the case of the contacts of coaxial and multi-pin connectors which are provided with a metallic connector shell, the test point (contact discharges) shall only be applied to the metallic shell of the connectors;
- those points and surface of equipment which are no longer accessible after fixed installation or after following the instructions for use;
- contacts within a non- conductive connector and which are accessible shall be tested by the air- discharge test only. In this case is used the rounded tip finger on the ESD generator.

The test results obtained by the two electronic devices are shown in Table III for the Internet connection stick and in Table IV for the memory stick.

“Good” means behavior so that the EUT behaved normal performance within limits specified by the manufacturer.

### C. Analysis of the results obtained

By analyzing the results presented in Table III and Table IV, we can conclude that the wireless Internet connection stick tested behaved well for each ESD level, for both air and direct contact discharge. After testing with 15 kV voltage air discharge, we observed the occurrence of discharges in the form of light luminescent effluvia.

Regarding the memory stick type ADATA 8GB, we observed that for an ESD voltage of 2kV, 4 kV and 8 kV it behaved well, as there were no operational problems. At the ESD air discharge tests, at a voltage of 15 kV, we observed perturbations in operation, namely after charging with positive polarity, a blockage occurred in operation and after charging with negative polarity, a reset occurred in operation.

It is important to remember is that electrostatic discharges did not lead to destroying the equipment tested.

## V. CONCLUSIONS

The development of light industry for the large scale manufacture of synthetic fibers and clothes made of synthetic fibers correlated with the technological advances in IT (computers, laptop, mobile phones and other electronic devices, etc.) has led to an increased importance of studying electrostatic discharges and immunity tests of electronic equipment on ESD.

Therefore, between a human, possible to load electrostatic voltages of 10-15kV ordinal, and an electronic device (computer, laptop, memory stick, etc.), system connected to the grounding, an electrostatic discharge can occur as a result of electric charging (electrification) the person wearing clothes made of synthetic fibers, due to friction with the air.

ESD can cause distortions in the operation of various electronic equipment or even their destruction.

ESD tests can be performed in specialized laboratories certified for this purpose, or on site.

In this paper, we subjected to ESD a memory stick and a wireless internet connection stick.

The tests were conducted with special equipment (power source, test gun) found at ICMET Craiova and in normal environmental conditions.

By analyzing the test results determining the degree of ESD immunity of the equipment tested, we observed that the wireless Internet connection stick behaved well, as there were no problems in operation and in the case of the memory stick, we reported loss in performance at a voltage of 15kV, namely blockage of operation after testing with positive polarity and a resetting of its operation after testing with negative polarity.

Following these tests, as a conclusion, it is worth noting that the electrostatic discharges did not lead to the destruction of the equipment tested, as they behaved well in this regard.

The results of these experimental tests have highlighted the importance and necessity of establishing ESD immunity of electronic equipment which may be subjected, incidentally, to human-type ESD.

TABLE III.  
TEST RESULTS FOR INTERNET CONNECTION STICK

Contact discharge			Air discharge		
Level	Test voltage kV	Performance	Level	Test voltage kV	Performance
1	2	good	1	2	good
2	4	good	2	4	good
3	6	good	3	8	good
4	8	good	4	15	good – small glow discharge

TABLE IV.  
TEST RESULTS FOR MEMORY STICK

Contact discharge			Air discharge		
Level	Test voltage kV	Performance	Level	Test voltage kV	Performance
1	2	good	1	2	good
2	4	good	2	4	good
3	6	good	3	8	good
4	8	good	4	15	a) positive electrode- temporary loss of function (the correction of which requires operator intervention) b) negative electrode – temporary loss of function (reset the system)

Received on July 17, 2016

Editorial Approval on November 15, 2016

#### REFERENCES

- [1] Schwab,A.J., *Compatibilitate electromagnetica*, Editura Tehnica Bucuresti, 1996.
- [2] Schwab,A.J.,Kürner,W.,*Compatibilitate electromagnetica*, Editura AGIR, Bucuresti, 2013.
- [3] IEC 61000-4-2 International standard, Electromagnetic compatibility (EMC) – part. 4-2: testing and measurement techniques – Electrostatic discharge immunity test.
- [4] Beniugă,O.,Beniugă,R.,Kovac,K., Electromagnetic Compatibility Problems Involved by ESD Magnetic Field Radiation, 5<sup>th</sup> International Conference on Modern Power Systems MPS 2013, 28-31 May, Cluj-Napoca, 2013,pp.55-58.
- [5] IEC 60050 (161) International Electrotechnical Vocabulary (IEV)-Chapter 161; Electromagnetic compatibility
- [6] [www.emchire.co.uk/products](http://www.emchire.co.uk/products)
- [7] IEC 60068-1 Environmental testing- Part 1: General and guidance
- [8] \* \* \* - Electrostatic Discharge Simulator – ESD 30C/ P30C – Documentatie tehnica, [www.pci-card.com/ESD30c.pdf](http://www.pci-card.com/ESD30c.pdf).
- [9] [www.iota.ee.tuiasi.ro/~lides/rezultate.htm](http://www.iota.ee.tuiasi.ro/~lides/rezultate.htm)
- [10] Salceanu,Al.,David,V.,cretu,M., *Upon the influence of ESD gun on the immunity repetability tests*, Buletinul Universitatii politehnice Iasi, Tomul LII(LVI), Fasc.5, 2006,pp.1081-1084.
- [11] IEC 61000-6-1 – Electromagnetic compatibility (EMC) – Part. 6 - 1: Generic standards- Immunity for residential, commercial and light-industrial environments.

# Load Flow Analysis of Unbalanced Distribution Networks using Symmetrical Components Based Software

Denisa Rusinaru\*, Leonardo Geo Manescu\*, Marian Ciontu\*, and Miron Alba†

\* University of Craiova/Faculty of Electrical Engineering, Craiova, Romania, drusinaru@elth.ucv.ro

† CEZ Romania/CEZ Distribution, Craiova, Romania, Miron.Alba@cez.ro

**Abstract** - This paper presents the algorithm and the main features of a Matlab (R2014a)-based software conceived by the authors for analysis of the asymmetrical operation of the three-phase distribution networks. The software's algorithm is based on an iterative procedure of Newton-Raphson type. This algorithm is independently applied on three equivalent sequence networks and includes an equivalent model for the unbalanced loads supplied from the analysed distribution grid. In order to outline the capabilities of this software tool named PFASYM and illustrate the key concepts a comprehensive case study was considered. This one summarizes the results of a three-phase load flow analysis performed for a real representative 110/20 kV distribution network supplying industrial unbalanced loads. The PFASYM's results are validated by comparison with those generated by a proprietary software package. The analysis methodology used in this illustrative case study and the results generated for different grid configurations could assist the grid operator in conducting the power flow studies of operational areas of interest. This work is part of an overall energy systems modelling and analysis project developed by the authors, in collaboration with the local power distribution operator. This one has as objective to facilitate the understanding of the power flow concepts for the present distribution networks operating in asymmetry conditions and to assist the grid operator in applying optimal mitigation measures.

**Keywords:** *symmetrical components; three-phase load flow; unbalanced load; asymmetry factor.*

## I. INTRODUCTION

The purpose of the three-phase analysis is to give the proper information required by the control and planning activities of the present power networks, whose operation is strongly affected by electromagnetic perturbations amplified by the extending renewable generation units. Therefore, the power networks' operators are nowadays constrained to highly consider not only safety, continuity or economic issues in their activity and in relation with customers, but also the power quality.

The large number of single phase loads connected in the distribution network, as well as the very numerous variable speed drives in industry, cause the unbalance in the line voltages at terminals in the absence of a proper line voltage regulation. Since the asymmetry of the line voltages causes poor performance of the three-phase loads and an unbalanced real and reactive power demand, the evaluation of the asymmetrical operation of the power

grids, location of the asymmetry sources and evaluation and mitigation of their effects became an essential concern for the power grids' operators.

Based on these facts, a proper adjusted analysis should be performed in order to take into consideration the differences between phase values for the networks operating in asymmetrical conditions and/or supplying unbalanced loads.

So that, this task might be ensured by applying different analysis algorithms, described usually with phase components or associated to other different types of components. Tars, El-Abiad, Birt and Graffy have investigated the three-phase load flow since 1970' [1], being followed by Arrilaga and Harker [2]. There were also registered probabilistic approaches [3]. But no matter the state values representation, their non-linear dependency asks for iterative type algorithm – e.g. Gauss-Seidel, Newton-Raphson and others, whose application should take into account the different behavior and values between the phases of the unbalanced networks [4, 5, 6, 7].

The principle was applied and further developed by the authors for a three-phase load flow model, which became the core of a Matlab (R2014a)-based power system analysis and simulation tool, an in-house developed software named PFASYM [8].

## II. PARTICULARITIES OF THE LOAD FLOW ALGORITHM FOR THREE-PHASE ANALYSIS OF POWER GRIDS

The principle of the power flow algorithms for analysis of unbalanced networks - PFASYM is mainly similar to those applied for one-phase approach. There are some differences required by the new level of information [5, 8].

- a. The conventional PV or PQ-buses with symmetrical loads are counted further on up or down. The last indexes are assigned to the buses with unbalanced loads.
- b. Power mismatches of the network buses  $\Delta P$ ,  $\Delta Q$  are defined similarly to the symmetrical conventional case, since the nodal admittance matrix includes components describing all three phase and couplings between them, in phase terms or symmetrical components.
- c. The output results contain three-phase information.
- d. The voltage-controlled (generator) bus model has certain particularities describe as following.

The generator bus model includes three bus types, as in Fig.1 [1, 8]:

- i. INT bus – PV type: it is an internal bus where the machine’s total power ( $P_A+P_B+P_C$ ) is injected and represents the induced internal voltage;
- ii. BG bus – PQ type: it represents the terminal of the generator;
- iii. P bus (optional) – PQ type: the high voltage bus at which the power transmission system is connected; it is approached as a usual PQ bus.

For those generators located in the slack buses the A-phase voltage of the BG-bus is constant and assumed as reference for phase of other buses’ voltages.

If the algorithm is written in terms of symmetrical components, there are some additional particularities aiming to simplify the computing process, given as in Table I.

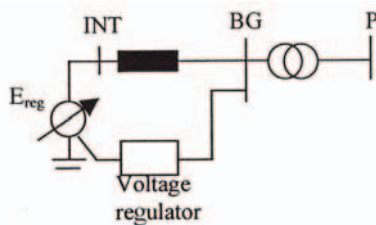


Fig. 1. Generator model for three-phase load flow analysis.

TABLE I. CHARACTERISTICS OF THE GENERATOR BUS MODEL

Algorithm type	Buses of generator model	Characteristic equations	State values
Three-phase representation	INT	- Voltage at regulator terminals $E_{reg}$ - Active power of generators, $P_g$	A-phase voltage - $\underline{E}_{INT}^A$
	BG	- Phase bus powers ( $P_a, P_b, P_c, Q_a, Q_b, Q_c$ )	$\underline{U}_{BG}^A, \underline{U}_{BG}^B, \underline{U}_{BG}^C$
	P	- Phase bus powers ( $P_a, P_b, P_c, Q_a, Q_b, Q_c$ )	$\underline{U}_P^A, \underline{U}_P^B, \underline{U}_P^C$
Symmetrical components (+, -, 0)	INT	- Bus voltage phasor $\underline{E}_{INT}$ - Bus active powers $P_g$	- Argument of positive sequence voltage - $\delta_{INT}^+$ - Positive sequence reactive power - $Q^+$
	BG	- Bus complex power $\underline{S}$ in sequence circuits	$\underline{U}_{BG}^+, \underline{U}_{BG}^-, \underline{U}_{BG}^0$

The equations describing the unbalanced operation of the power networks are:

- The power balance equations for phase circuits or equivalent sequence components circuits;
- The slack bus voltage;
- The complex power balance for all the network’s buses.

The output data of the analysis are:

- The phase or symmetrical components of the voltages in the network’s buses;
- The phase or phase or symmetrical components of the currents in the network’s buses;
- The phase or phase or symmetrical components of the

powers in the slack buses.

### III. THE LOAD FLOW SOLUTION INDEPENDENTLY APPLIED ON THE EQUIVALENT SEQUENCE CIRCUITS OF THE ASYMMETRICAL POWER GRIDS

The significant advantages of the symmetrical components justify the frequent utilization of the load flow problem decomposition into three subsequent problems. These ones correspond to the positive, negative and zero sequence equivalent circuits, with a reduced mutual coupling between them [6].

The symmetrical components solution for the three-phase load flow has proven good performances meaning a low computing time, low computer storage requirements, stable convergence no matter the asymmetry level, as well as the validation for the mono-phase representation of the correspondent symmetrical network.

The differences between the one-phase load flow problem and the three-phase case refer to:

- the size of the bus admittance matrix;
- the number and type of variable;
- the value field of input data for the positive sequence equivalent circuit;
- the dependence of the bus voltages in each sequence circuit on all the symmetrical components of the bus voltages resulted in the previous iteration.

In addition a model of the unbalanced loads was proposed and further integrated in the three-phase load flow, allowing running independently the solution on the three sequence circuits of the studied network [9].

#### A. The Bus Types

The three-phase load-flow problem describes the static unbalanced operating conditions of a power system with respect to power and/or voltage constraints in the network buses. Generally, the buses are classified as in the conventional symmetrical cases, as slack/swing buses, PV buses, and PQ buses.

It should be specified that a INT-type bus will be introduced for each generator, to the back of its equivalent internal impedance, as in Fig. 1. Since the internal phase voltages are symmetrical, these buses will not be contained obviously in the negative and zero sequence equivalent circuits of the network.

The unbalanced loads will be introduced as PQ buses with non-zero power consumptions only in the positive equivalent circuit. The negative and zero sequence circuits will be connected precisely in these buses through the equivalent phase-to-phase impedance  $\underline{Y}_m$ , which describes the unbalance of the load accordingly to the model given in the following section.

Details of the bus classification are given in Table II.

TABLE II. BUS DETAILS FOR THE THREE-PHASE LOAD FLOW PROBLEM

Bus type	Number of buses		
	Positive sequence	Negative sequence	Zero sequence
PQ or Load Bus	$N_l+N_u+N_g+N_{sl}$	$N_l+N_u+N_g+N_{sl}$	$\begin{matrix} Max \\ N_l+N_u+N_g+ \\ N_{sl} \end{matrix}$
Generator Bus (PV ≈ INT)	$N_g$		

Bus type	Number of buses		
	Positive sequence	Negative sequence	Zero sequence
PQ or Load Bus	$N_l + N_u + N_g + N_{sl}$		
Slack Bus (INT)	$N_{sl} (\text{min } 1)$		
TOTAL	$N_+$	$N_-$	$N_0$

TABLE II. (CONTINUATION)

with notations:

$N_+ = N_l + N_u + 2N_g + 2N_{sl}$  – the total bus number of the positive sequence circuit of the studied network;

$N_- = N_l + N_u + N_g + N_{sl}$  – the total bus number of the negative sequence circuit;

$N_0 \leq N_l + N_u + N_g + N_{sl}$  – the total bus number of the zero sequence equivalent circuit and depends on the configuration type of the power transformers;

$N_{sl}$  – the number of the slack buses;

$N_g$  – the number of the generator INT buses;

$N_l$  – the number of the buses with symmetrical loads;

$N_u$  – the number of the buses with unbalanced loads.

### B. The Equivalent Phase-to-phase Admittance Model of the Unbalanced Loads

The model used for the unbalanced loads in the load flow problem is given in Fig. 2. Basically this one includes two equivalent loads: a three-phase perfectly balanced load model (three phase admittances equal to  $\underline{Y}_e$ ) and a phase-to-phase model (an admittance connected between two phases of the network,  $\underline{Y}_m$ ), which takes over the level of the load unbalance [9, 10].

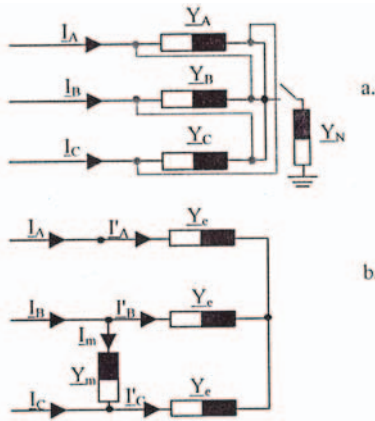


Fig. 2. The unbalanced load model: a. three-phase representation of the load; b. equivalent phase-to-phase admittance load model.

There is a correspondence between the two load representations, with matrixal terms defined by the connection type:

$$[\underline{I}_n] = [\underline{Y}_{n,unb}][\underline{U}_n] = [\underline{Y}_{n,eqv}][\underline{U}_n] \quad (1)$$

with:

$[\underline{I}_n]$ ,  $[\underline{U}_n]$  – the column vector of the currents, respectively voltages at the model terminal buses;

$[\underline{Y}_{n,unb}]$  – the bus admittance matrix of the unbalanced load;

$[\underline{Y}_{n,eqv}]$  – the bus admittance matrix of the equivalent phase-to-phase admittance unbalanced load model.

For the symmetrical component representation, the correspondent circuit (see Fig. 3) and equations are given as following:

$$[\underline{I}_{sim}] = [\underline{Y}_{sim}][\underline{U}_{sim}] \quad (2)$$

with:

$[\underline{I}_{sim}]$ ,  $[\underline{U}_{sim}]$  – the column vector of the symmetrical components of the currents, respectively voltages of the equivalent load model;

$[\underline{Y}_{sim}]$  – the sequence admittance matrix of the equivalent unbalanced load model.

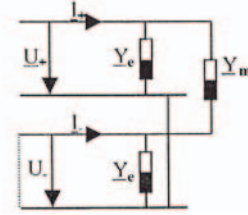


Fig. 3. Sequence circuits connection for the equivalent phase-to-phase admittance load model.

### C. The Bus Admittance Matrix

A bus admittance matrix can be computed for each sequence network as following:

i. The sequence admittances of the network components are determined.

ii. The bus admittance submatrices of each network's sequence circuit are determined according to the physical links between the network components.

iii. The resulting parameters will be organized according to the nature and position of the symmetrical components into the global symmetrical components admittance matrix.

$$[\underline{Y}_{sim}] = \begin{bmatrix} \underline{Y}^{00} & \underline{Y}^{0+} & \underline{Y}^{0-} \\ \underline{Y}^{+0} & \underline{Y}^{++} & \underline{Y}^{+-} \\ \underline{Y}^{-0} & \underline{Y}^{-+} & \underline{Y}^{--} \end{bmatrix} \quad (3)$$

where  $\underline{Y}^{ij}$  are the symmetrical components admittance submatrices, with  $i, j = 0, +, -$  denoting the index of the symmetrical component.

The resulting bus admittance matrix has some features that should be taken into account:

- the off diagonal submatrices (describing the mutual connection between the sequence circuits) are generally empty;

- its parameters are non-zero only for the buses with unbalanced loads (e.g.  $[\underline{Y}^{+-}]$ ,  $[\underline{Y}^{-+}]$  of the model described in the previous section), as well as those at the ends of asymmetrical transmission lines.

### D. The Load Flow Algorithm Equations

A rough outline of solution of the power-flow problem supposes firstly to make an initial guess of all unknown bus voltage magnitudes and angles [8].

The initial bus voltages for the sequence circuits of the analyzed network  $\underline{U}^{s(0)} = [\underline{U}_1^{s(0)} \quad \underline{U}_2^{s(0)} \quad \dots \quad \underline{U}_N^{s(0)}]$  are commonly chosen as:

$$\underline{U}_k^{s(0)} = \begin{cases} U_{sp} \angle 0^\circ & k = 1, \dots, N_g \\ 1 \angle 0^\circ & k = N_g + 1, \dots, N_c, N_c + 1, N_+ \end{cases} \quad (4)$$

$$\underline{U}_k^{-(0)}, \underline{U}_k^{0(0)} = 0 \angle 0^\circ \quad (4')$$

where  $s$  denotes the index of the symmetrical components  $0, +, -$ ;

$\underline{U}_{sp}$  – the specified initial value of the bus voltage.

The former experience has proven that such a choice is still undesirable, since the solution does not reach the convergence for some operational conditions. Instead of this, the results of load flow in the balanced network can be used as input data in the positive sequence circuit.

Further the powers' balances for the network phases and sequences are solved using the most recent iteration values of voltage angles and magnitudes, as in further equations:

$$\underline{S}_k = \underline{S}_{k,g} - \underline{S}_{k,cons} = \underline{S}_k^A + \underline{S}_k^B + \underline{S}_k^C = P_k + jQ_k \quad (5)$$

$$P_k = P_k^A + P_k^B + P_k^C; Q_k = Q_k^A + Q_k^B + Q_k^C \quad (5')$$

$$\underline{S}_k = 3(\underline{U}_k^0 \underline{I}_k^{0*} + \underline{U}_k^+ \underline{I}_k^{+*} + \underline{U}_k^- \underline{I}_k^{-*}) \quad (6)$$

where  $\underline{S}_{k,g}$ ,  $\underline{S}_{k,cons}$  are the complex generated/consumed power in  $k$ -th bus and the symmetrical components of voltage given by (7) for the successive iterations:

$$[\mathbf{Y}^{00}][\mathbf{U}^0] = [\mathbf{I}^0] - [\mathbf{Y}^{0+}][\mathbf{U}^+] + [\mathbf{Y}^{0-}][\mathbf{U}^-] \quad (7)$$

$$[\mathbf{Y}^{++}][\mathbf{U}^+] = [\mathbf{I}^+] - [\mathbf{Y}^{+0}][\mathbf{U}^0] + [\mathbf{Y}^{+-}][\mathbf{U}^-] \quad (8)$$

$$[\mathbf{Y}^{--}][\mathbf{U}^-] = [\mathbf{I}^-] - [\mathbf{Y}^{-0}][\mathbf{U}^0] + [\mathbf{Y}^{-+}][\mathbf{U}^+] \quad (9)$$

Taking into consideration their physical significance and weights by comparison with the other symmetrical components, the positive sequence values given by (8) will be considered as reference for developing the load flow solution.

The solution of the previous equation system associated to the load flow problem is reached by applying an iterative procedure to (8), (9) and (7), with respect to this order. For the positive sequence circuit, the iterated bus powers are given by (10):

$$\underline{S}_k^+ = \underline{U}_k^+ \left( \sum_{n=1}^{N_+} \underline{Y}_{kn}^{++} \underline{U}_n^+ \right)^* + \underline{U}_k^+ \left( \sum_{n=1}^{N_0} \underline{Y}_{kn}^{+0} \underline{U}_n^0 + \sum_{n=1}^{N_-} \underline{Y}_{kn}^{+-} \underline{U}_n^- \right)^* = \quad (10)$$

$$= \frac{1}{3} (\underline{S}_{k,g} - \underline{S}_{k,cons}) - \underline{U}_k^0 \underline{I}_k^{0*} - \underline{U}_k^- \underline{I}_k^{-*}$$

#### E. The Load Flow Algorithm Steps

The load flow study involves the following steps:

1. The state values of the positive sequence circuit are iteratively calculated according to a Newton-Raphson algorithm [2, 8], described by (11):

$$\begin{bmatrix} \mathbf{J}_1(i) & \mathbf{J}_2(i) \\ \mathbf{J}_3(i) & \mathbf{J}_4(i) \end{bmatrix} \begin{bmatrix} \Delta \delta(i) \\ \Delta \mathbf{U}(i) \end{bmatrix} = \begin{bmatrix} \Delta \mathbf{P}(i) \\ \Delta \mathbf{Q}(i) \end{bmatrix} \quad (11)$$

with:

$\mathbf{J}_1, \mathbf{J}_2, \mathbf{J}_3, \mathbf{J}_4$  – the Jacobian term at the  $i$ -th iteration;

$\Delta \mathbf{U}, \Delta \delta$  – the magnitude, respectively phase of the bus voltages at the  $i$ -th iteration;

$\Delta \mathbf{P}, \Delta \mathbf{Q}$  – the bus power mismatches at the  $i$ -th iteration.

2. The power mismatches having the initial values set according to (10) are given in Table III, while the Jacobian components are summarized in Table IV.

TABLE III.  
BUS POWER MISMATCHES

Mismatch type	Equation	Number of equations
$\Delta P_k$	$\frac{1}{3} (P_{k,g} - P_{k,cons}) - U_k^+ \sum_{n=1}^{N_+} [U_n^+ (G_{kn}^{++} \cos \delta_{kn}^+ + B_{kn}^{++} \sin \delta_{kn}^+)] - U_k^+ [\sum J_{Re,k} \cos \delta_k^+ - (\sum J_{Im,k}) \sin \delta_k^+] \quad (12)$	$N_+ - N_{sl}$
$\Delta Q_k$	$-(Q_{k,g}) - U_k^+ \sum_{n=1}^{N_+} [U_n^+ (G_{kn}^{++} \sin \delta_{kn}^+ - B_{kn}^{++} \cos \delta_{kn}^+)] - U_k^+ [\sum J_{Re,k} \sin \delta_k^+ + (\sum J_{Im,k}) \cos \delta_k^+] \quad (13)$	$N_+ - N_{g-}$ $N_{sl}$

with:

$$J_{Re,k} \stackrel{def}{=} J_{Re,k}^{+0} + J_{Re,k}^{+-}, \quad \sum J_{Im,k} \stackrel{def}{=} J_{Im,k}^{+0} + J_{Im,k}^{+-} \quad (14)$$

$$J_{Re,k}^{+0} \stackrel{def}{=} \operatorname{Re} \left( \sum_{n=1}^{N_0} \underline{Y}_{kn}^{+0} \underline{U}_n^0 \right)^* = f_1(\mathbf{U}^0, \delta^0) \quad (15)$$

$$J_{Im,k}^{+0} \stackrel{def}{=} \operatorname{Im} \left( \sum_{n=1}^{N_0} \underline{Y}_{kn}^{+0} \underline{U}_n^0 \right)^* = f_2(\mathbf{U}^0, \delta^0) \quad (15')$$

$$J_{Re,k}^{+-} \stackrel{def}{=} \operatorname{Re} \left( \sum_{n=1}^{N_-} \underline{Y}_{kn}^{+-} \underline{U}_n^- \right)^* = f_3(\mathbf{U}^-, \delta^-) \quad (16)$$

$$J_{Im,k}^{+-} \stackrel{def}{=} \operatorname{Im} \left( \sum_{n=1}^{N_-} \underline{Y}_{kn}^{+-} \underline{U}_n^- \right)^* = f_4(\mathbf{U}^-, \delta^-) \quad (16')$$

$$G_{k,n}^{++} = \operatorname{Re}(\underline{Y}_{k,n}^{++}) \quad B_{k,n}^{++} = \operatorname{Im}(\underline{Y}_{k,n}^{++}) \quad \delta_{k,n}^{++} = \delta_k^+ - \delta_n^+ \quad (17)$$

TABLE IV.  
THE JACOBIAN OF THE POSITIVE SEQUENCE CIRCUIT

Bus ID	Jacobian Component
$n \neq k$	$\mathbf{J}1_{kn} = \frac{\partial P_k}{\partial \delta_n^+}; \mathbf{J}2_{kn} = U_n^+ \frac{\partial P_k}{\partial U_n^+}; \mathbf{J}3_{kn} = \frac{\partial Q_k}{\partial \delta_n^+}; \mathbf{J}4_{kn} = U_n^+ \frac{\partial Q_k}{\partial U_n^+} \quad (18)$
$n = k$	$\mathbf{J}1_{kk} = \frac{\partial P_k}{\partial \delta_k^+}; \mathbf{J}2_{kk} = U_k^+ \frac{\partial P_k}{\partial U_k^+}; \mathbf{J}3_{kk} = \frac{\partial Q_k}{\partial \delta_k^+}; \mathbf{J}4_{kk} = U_k^+ \frac{\partial Q_k}{\partial U_k^+} \quad (19)$

3. The Jacobian system (11) is iteratively solved and the voltage values in the buses of the positive sequence circuit are updated, resulting the components  $\mathbf{U}^{+(i+1)}$  and  $\delta^{+(i+1)}$  of the voltages' vector at the  $i+1$ -th iteration.

4. The negative and zero sequence bus currents are consequently updated, as in (20):

$$\begin{bmatrix} \underline{I}_k^0 \\ \underline{I}_k^- \end{bmatrix}^{(i+1)} = \frac{1}{3} \begin{bmatrix} 1 & 1 & 1 \\ 1 & a^2 & a \end{bmatrix} \begin{bmatrix} \underline{I}_k^A \\ \underline{I}_k^B \\ \underline{I}_k^C \end{bmatrix}^{(i+1)} \quad (20)$$

with:

$$\begin{bmatrix} \underline{I}_k^A \\ \underline{I}_k^B \\ \underline{I}_k^C \end{bmatrix}^{(i+1)} = \begin{bmatrix} \underline{S}_{k,cons}^A / \underline{U}_k^{A(i+1)*} \\ \underline{S}_{k,cons}^B / \underline{U}_k^{B(i+1)*} \\ \underline{S}_{k,cons}^C / \underline{U}_k^{C(i+1)*} \end{bmatrix} - \text{the column vector of}$$

the bus phase currents for the  $i+1$ -th iteration;

$$\begin{bmatrix} \underline{U}_k^A \\ \underline{U}_k^B \\ \underline{U}_k^C \end{bmatrix}^{(i+1)} = \begin{bmatrix} 1 & 1 & 1 \\ 1 & a^2 & a \\ 1 & a & a^2 \end{bmatrix} \begin{bmatrix} \underline{U}_k^{0(i)} \\ \underline{U}_k^{+(i+1)*} \\ \underline{U}_k^{-(i)} \end{bmatrix} - \text{the column vector}$$

of the bus phase voltages for the  $i+1$ -th iteration.

5. The reactive powers of the voltage-controlled buses in the positive sequence circuit ( $Q_k^{+(i+1)}$ ) are iteratively calculated, as well as the associated injected powers:  $Q_{k,g}^{(i+1)} = Q_k^{+(i+1)} + Q_{k,cons}$ . If the resulting values exceed their limits  $Q_{MAX}$  or  $Q_{MIN}$  for any iteration, then the PV-type bus is changed as a PQ-type one, with the value of  $Q_{k,g}$  set to its limit.

6. The negative and zero sequence bus voltages are updated at the  $i+1$ -th iteration:

$$\begin{bmatrix} \underline{U}^0 \\ \underline{U}^+ \\ \underline{U}^- \end{bmatrix}^{(i+1)} = \begin{bmatrix} \underline{Y}^{00} \\ \underline{Y}^{0+} \\ \underline{Y}^{0-} \end{bmatrix}^{-1} \left[ \begin{bmatrix} \underline{I}^0 \\ \underline{I}^+ \\ \underline{I}^- \end{bmatrix}^{(i+1)} - \left( \begin{bmatrix} \underline{Y}^{0+} \\ \underline{Y}^{0-} \end{bmatrix} \begin{bmatrix} \underline{U}^+ \\ \underline{U}^- \end{bmatrix}^{(i+1)} + \begin{bmatrix} \underline{Y}^{00} \\ \underline{Y}^{0+} \end{bmatrix} \begin{bmatrix} \underline{U}^0 \\ \underline{U}^+ \end{bmatrix}^{(i)} \right) \right] \quad (21)$$

$$\begin{bmatrix} \underline{U}^0 \\ \underline{U}^+ \\ \underline{U}^- \end{bmatrix}^{(i+1)} = \begin{bmatrix} \underline{Y}^{00} \\ \underline{Y}^{0+} \\ \underline{Y}^{0-} \end{bmatrix}^{-1} \left[ \begin{bmatrix} \underline{I}^0 \\ \underline{I}^+ \\ \underline{I}^- \end{bmatrix}^{(i+1)} - \left( \begin{bmatrix} \underline{Y}^{0+} \\ \underline{Y}^{0-} \end{bmatrix} \begin{bmatrix} \underline{U}^+ \\ \underline{U}^- \end{bmatrix}^{(i+1)} + \begin{bmatrix} \underline{Y}^{00} \\ \underline{Y}^{0+} \end{bmatrix} \begin{bmatrix} \underline{U}^0 \\ \underline{U}^+ \end{bmatrix}^{(i+1)} \right) \right] \quad (22)$$

7. The problem converges to a valid solution in the positive sequence circuit at once the mismatch condition is fulfilled ( $\Delta P^+, \Delta Q^+ \leq \varepsilon$ ) or the rate of convergence is exceeded.

8. Once the load flow solution was obtained, the active and reactive powers of the slack buses are determined, as well as the phase bus currents and the current and power flows along the network's branches.

The solution of the three-phase load flow problem can be written as in Table V.

TABLE V.  
THREE-PHASE LOAD FLOW SOLUTION DISPLAY

Bus ID	Voltage		Current		Power			
	$\underline{U}^{+,0}$	$\underline{U}^{A,B,C}$	$\underline{I}^{+,0}$	$\underline{I}^{A,B,C}$	$P^{+,0}$	$Q^{+,0}$	$S^{+,0}$	$S^{A,B,C}$

The three-phase load flow method is based on a double iterative algorithm: one is related to the powers of the positive sequence circuit buses; the second one is related to the state values and currents in the buses of the negative and zero sequence circuits.

#### IV. SUBROUTINES OF THE THREE-PHASE LOAD FLOW PROGRAM

The three-phase load flow algorithm makes the core of the MATLAB-based software analysis tool PFASYM.

Though PFASYM does not have any GUI, it has some other certain advantages such as an information query system designed to access load flow parameters and other electrical system information, integrated unbalanced loads' models and a robust and efficient algorithm to solve

three-phase load flow. The simulation results can be obtained as static reports (text output), as well as plots (graphical output).

The reason behind developing this computational tool with MATLAB programming environment is the easiness of matrix-oriented programming, attractive graphical capabilities and the integration with MATLAB Simulink.

PFASYM contains 12 subroutines [8]. These are designed to compute the network parameters for the sequence circuits of the network, as well as the bus and branch state values describing the asymmetrical operation: voltages, currents and powers on phases and sequence circuits, as well as the voltage asymmetry factors.

The PFASYM subroutines are described in Table VI.

TABLE VI.  
COMPONENTS OF PFASYM LOAD FLOW PROGRAM

Subroutine	Description
PARIN.mat	Reads and validates the input network branch parameters
TRANSFORM.m	Computes the sequence parameters and the primitive matrix for the network's power transformers
LINE.m	Computes the sequence parameters and the primitive matrix for the network's symmetrical ( <b>Linsim</b> ) and asymmetrical lines ( <b>Linnes</b> )
SHUNTS.m	Computes the sequence admittance matrix for the network's reactive shunt components
CONDEZ.m	Computes the admittance matrix of the coupled sequence networks in buses with unbalanced loads
YNODSECV.mat	Computes and stores the bus sequence submatrices <b>YPP, YNN, YZZ, YPN, YNP, YPZ, YZP, YNZ, YZN</b> with sparsity technique
INVYNZ.m	Computes the inverse bus admittance matrices for the negative and zero sequence circuits <b>ZNN, ZZZ</b>
MSTIN.mat	Reads and validates input bus data
CSPOZ.m	Computes the Jacobian for the positive sequence circuit, as well as the correspondent iteration values
MSTNZ.m	Computes the present iteration negative and zero components of bus voltages and currents
FINAL.m	Validates the solution convergence and computes the phase bus and branch values, as well as asymmetry factors
EDIT.mat	Writes the output data

#### V. SIMULATION RESULTS

In order to outline the capabilities of PFASYM software an asymmetrical electric utility system is considered in order to validate a power flow case study suitable for simulating and evaluating alternative scenarios for the system's phases loading [11].

The selection of a local 110 kV distribution network given in Fig. 4 has taken into consideration two criteria: (1) the technical complexity of the network configuration, which allowed all major concepts pertaining to power flow studies to be addressed; (2) the proximity of the network position to our research center, which facilitated site visits and access to data.

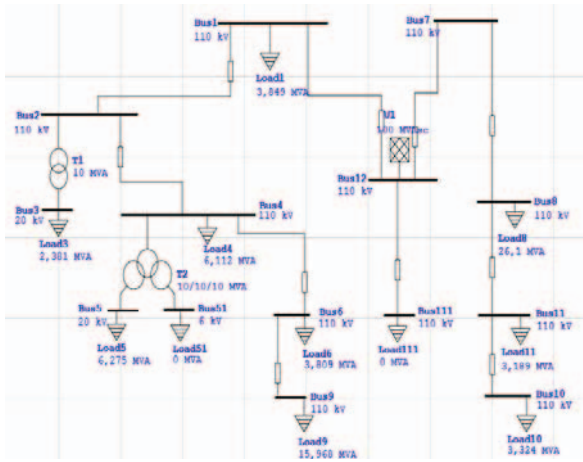


Fig. 4. The test network configuration.

The network includes 12 buses and 9 lines, with branch data given in Table VII.

TABLE VII.  
BRANCH DATA OF THE TEST NETWORK

Branch		R (Ω)	X (Ω)	Y (mS)
From	To			
#1	#2	0.7336	1.5298	0.0711
#1	#12	0.8263	1.7231	0.0820
#2	#4	0.9885	2.0612	0.0960
#4	#6	0.9885	2.0612	0.0960
#6	#9	0.1421	0.2963	0.0129
#7	#8	0.1421	0.2963	0.0129
#7	#12	3.1044	6.4736	0.3014
#8	#11	0.8263	1.7231	0.0800
#11	#10	4.2241	8.0860	0.4103

TABLE VIII.  
BUS DATA OF THE TEST NETWORK

Bus ID	P (MW)	Q (MVA <sub>r</sub> )
#1	3.464	1.679
#2	0.000	0.000
#3	2.176	0.966
#4	5.887	1.642
#5	6.001	1.833
#6	3.615	1.201
#7	0.000	0.000
#8	22.498	12.231
#9	14.400	6.900
#10	3.226	0.803
#11	3.087	0.799

Three buses are connecting points for railway traction substations (#1, #10, #11) for which an asymmetry higher than 2.5% was registered. The bus input data are

measurements of the local distribution operator, given in Table VIII. For this purpose, the following six study cases are considered:

*Case I.* The network described by the previous information in accordance with the real field data is studied. This case configuration includes 3 buses (#1, #10, #11) with unbalanced loads and is considered as reference (named here initial configuration) for the following ones. By running PFASYM for this case, the simulation results are given in Table IX.

*Case II.* The load in bus #10 is replaced by a balanced one in the initial configuration, with results given in Table X.

*Case III.* The load in bus #1 is replaced by a balanced one in the initial configuration, with results given in Table XI.

*Case IV.* The load in bus #1 is added to one in #2 in the initial configuration, with results given in Table XII.

*Case V.* The load value in bus #1 is added to one in #6 in the initial configuration, with results given in Table XIII.

*Case VI.* The asymmetry of the load in bus #1 is doubled in the initial configuration, with results given in Table XIV.

TABLE IX.  
BUS RESULTS FOR THE INITIAL CONFIGURATION (CASE I)

Bus ID	PA	QA	PB	QB	PC	OC
	(MW)	(MVA <sub>r</sub> )	(MW)	(MVA <sub>r</sub> )	(MW)	(MVA <sub>r</sub> )
#1	1.223	1.823	2.215	0.157	0.000	0.000
#2	0.000	0.000	0.000	0.000	0.000	0.000
#3	0.724	0.326	0.704	0.304	0.710	0.320
#4	2.543	0.509	1.906	0.550	1.945	0.550
#5	1.968	0.580	1.867	0.578	2.010	0.628
#6	1.128	0.405	1.178	0.400	1.223	0.365
#7	0.000	0.000	0.000	0.000	0.000	0.000
#8	7.635	4.736	7.347	4.612	7.730	4.007
#9	4.662	2.234	4.679	2.242	4.681	2.243
#10	1.950	0.447	0.000	0.000	1.166	1.258
#11	2.068	1.895	0.556	0.582	0.626	0.523
Pgen (MW) 250.783			Qgen (MVA <sub>r</sub> ) 211.541			

TABLE X.  
BUS RESULTS FOR CASE II

Bus ID	PA	QA	PB	QB	PC	OC
	(MW)	(MVA <sub>r</sub> )	(MW)	(MVA <sub>r</sub> )	(MW)	(MVA <sub>r</sub> )
#1	1.223	1.823	2.2150	0.1570	0.000	0.0000
#2	0.000	0.0000	0.0000	0.0000	0.000	0.0000
#3	0.724	0.3260	0.7040	0.3040	0.710	0.3200
#4	2.543	0.5090	1.9060	0.5500	1.945	0.5500
#5	1.968	0.5800	1.8670	0.5780	2.010	0.6280
#6	1.128	0.4050	1.1780	0.4000	1.223	0.3650

Bus ID	PA	QA	PB	QB	PC	OC
	(MW)	(MAVr)	(MW)	(MAVr)	(MW)	(MAVr)
#7	0.000	0.0000	0.0000	0.0000	0.000	0.0000
#8	7.635	4.7360	7.3470	4.6120	7.730	4.0070
#9	4.662	2.2340	4.6790	2.2420	4.681	2.2430
#10	1.950	0.4470	1.9770	0.4540	1.981	0.4550
#11	2.068	1.8950	0.5560	0.5810	0.626	0.5250
Pgen (MW) 253.552			Qgen (MVar) 209.355			

TABLE X. (Continuation)

In the Case II, the system phase loading determines a slight change repartition of the powers in the vicinity bus #11. It also minimally discharges the injection sources of reactive power.

TABLE XI.  
BUS RESULTS FOR CASE III

Bus ID	PA	QA	PB	QB	PC	OC
	(MW)	(MAVr)	(MW)	(MAVr)	(MW)	(MAVr)
#1	1.223	1.823	1.224	1.823	1.224	1.822
#2	0.000	0.000	0.000	0.000	0.000	0.000
#3	0.724	0.326	0.704	0.304	0.710	0.320
#4	2.423	0.518	2.006	0.545	2.045	0.545
#5	1.968	0.580	1.864	0.578	2.006	0.627
#6	1.128	0.405	1.178	0.400	1.220	0.465
#7	0.000	0.000	0.000	0.000	0.000	0.000
#8	7.635	4.736	7.347	4.612	7.730	4.007
#9	4.662	2.234	4.673	2.239	4.672	2.238
#10	1.950	0.447	0.000	0.000	1.166	1.258
#11	2.068	1.895	0.556	0.582	0.626	0.523
Pgen (MW) 250.985			Qgen (MVar) 215.347			

TABLE XII.  
BUS RESULTS FOR CASE IV

Bus ID	PA	QA	PB	QB	PC	OC
	(MW)	(MAVr)	(MW)	(MAVr)	(MW)	(MAVr)
#1	1.222	1.819	2.214	0.157	0.000	0.000
#2	1.213	1.805	2.200	0.156	0.000	0.000
#3	0.722	0.325	0.703	0.303	0.710	0.320
#4	1.912	0.507	1.903	0.549	1.907	0.551
#5	1.965	0.578	1.864	0.577	2.010	0.628
#6	1.127	0.405	1.170	0.399	1.223	0.365
#7	0.000	0.000	0.000	0.000	0.000	0.000
#8	7.635	4.736	7.256	4.555	7.683	3.983
#9	4.655	2.230	4.672	2.239	4.682	2.243
#10	1.950	0.447	0.000	0.000	1.955	1.254
#11	2.057	1.934	0.556	0.592	0.626	0.534
Pgen (MW) 259.932			Qgen (MVar) 215.9640			

In the Case III, a balanced repartition of the phase loads has a minimal influence over the vicinity load buses #4, #6 and leads to a higher network injection, which seems to be influenced by the low overall load on the B-phase.

TABLE XIII.  
BUS RESULTS FOR CASE V

Bus ID	PA	QA	PB	QB	PC	OC
	(MW)	(MAVr)	(MW)	(MAVr)	(MW)	(MAVr)
#1	1.220	1.823	2.215	0.157	0.000	0.000
#2	0.000	0.000	0.000	0.000	0.000	0.000
#3	0.722	0.325	0.703	0.303	0.710	0.320
#4	1.906	0.506	1.902	0.549	1.907	0.551
#5	1.959	0.570	1.862	0.577	2.010	0.628
#6	2.831	2.170	3.335	0.245	1.223	0.365
#7	0.000	0.000	0.000	0.000	0.000	0.000
#8	7.635	4.730	7.256	4.555	7.683	3.983
#9	4.628	2.210	4.663	2.235	4.682	2.243
#10	1.950	0.440	0.000	0.001	1.166	1.258
#11	2.068	1.895	0.568	0.595	0.626	0.523
Pgen (MW) 260.381			Qgen (MVar) 216.005			

For the Cases IV, V, the aggravation of the overall asymmetry following the increase of the loads unbalance leads to a higher network injection up to 3% compared to the initial case.

TABLE XIV.  
BUS RESULTS FOR CASE VI

Bus ID	PA	QA	PB	QB	PC	OC
	(MW)	(MAVr)	(MW)	(MAVr)	(MW)	(MAVr)
#1	2.444	3.638	4.427	0.314	0.000	0.000
#2	0.000	0.000	0.000	0.000	0.000	0.000
#3	0.723	0.325	0.704	0.304	0.710	0.320
#4	1.910	0.508	1.905	0.550	1.945	0.550
#5	1.969	0.579	1.865	0.578	2.010	0.628
#6	1.129	0.405	1.177	0.400	1.223	0.365
#7	0.000	0.000	0.000	0.000	0.000	0.000
#8	7.635	4.736	7.347	4.612	7.730	4.007
#9	4.663	2.235	4.679	2.240	4.681	2.243
#10	1.950	0.447	0.000	0.000	1.166	1.258
#11	2.068	1.895	0.556	0.582	0.626	0.534
Pgen (MW) 254.206			Qgen (MVar) 213.241			

In the Case VI, the active power injection in the network has a lower increase by comparison with the two previous cases ( $\approx 1.3\%$  compared to the initial case).

Based on the results given in Table IX...XIV, the voltage asymmetry factors are given in Fig. 5, Fig. 6 and Fig. 7.

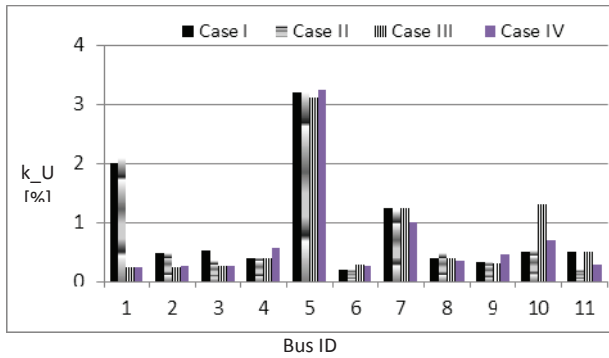


Fig. 5. Voltage asymmetry factors for Cases I...IV.

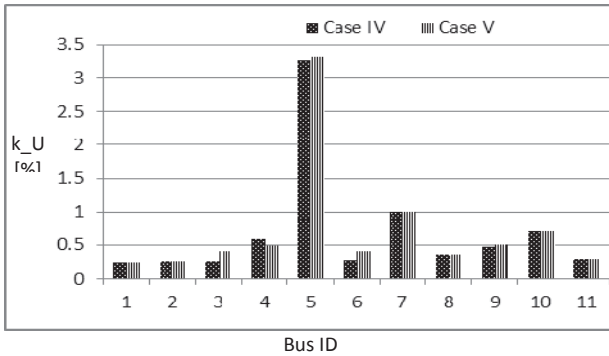


Fig. 6. Voltage asymmetry factors for Cases IV vs. Case V.

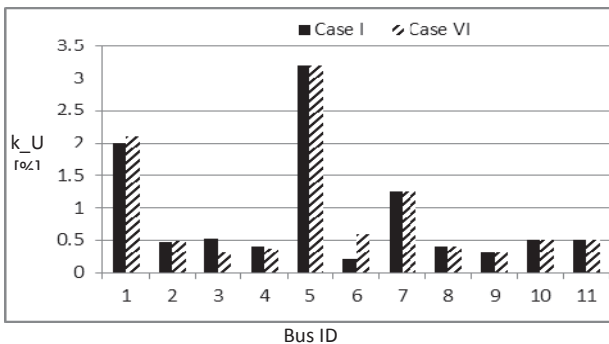


Fig. 7. Voltage asymmetry factors for Case I vs. Case VI.

The validation of the PFASYM results was made by running the load flow program of ETAP 14.1.0 [12].

For the studied network, the PFASYM load flow solution exhibited a maximum deviation of 3.184% (in bus # 1) from the results generated by ETAP program.

## VI. CONCLUSIONS

This paper presents a novel load flow method adjusted to the particularities of the real power distribution network operating in unbalanced conditions. The method's algorithm was developed using a Newton-Raphson solution in the equivalent positive sequence circuit. The negative and zero sequence components are independently determined as a function of the positive sequence components. For the unbalanced loads supplied by the network a particular model is used. This one includes an equivalent phase-to-phase load connected between of the negative and positive sequence circuits. This approach leads to a lower convergence rate. Here are also summarized the

results of a load flow analysis performed with PFASYM program, the in-house Matlab-based software for three-phase power system analysis. The program solves a singular power quality aspect, but it has the great advantage of a low cost/ no cost for the owner of a Matlab license, by comparison with the commercial software packages. The analysis of data generated by PFASYM outlined that the load symmetrization in a bus with unbalanced load leads to decreasing of the voltage asymmetry in the buses of its vicinity, while the voltage asymmetry tends to increase in those buses nearby those with unbalanced load. The longer is the distance between the highly unbalanced loads and the system injection bus, the higher is the voltage asymmetry. In some buses of the studied network the voltage asymmetries exceeds the standards limits [13, 14]. The voltage asymmetry is high in the buses with unbalanced loads, but mostly in the bus placed centrally in the network configuration related to the three railway traction substations. The PFASYM results were validated by comparison with those of an ETAP load flow on the same network configuration. Though the convergence of solution was reached more rapidly (up to 5 iterations) in the case of the proprietary tool, the PFASYM's results are similar, with an average error within 3.2% related to the ETAP ones.

Received on July 19, 2016

Editorial Approval on November 15, 2016

## REFERENCES

- [1] K.A Birt, J.J. Graffy, J.D. McDonald, A.H.El-Abiad, "Three phase load flow program", IEEE Trans. On Power Apparatus and Systems, vol.PAS-95, no.1, Jan/Febr. 1976, p. 59-65.
- [2] J. Arrillaga, C.P. Arnold, and B.J. Harker, Computer Modelling of Electrical Power Systems, Chicester Wiley, 2<sup>nd</sup> edition, 2001.
- [3] R.N. Allan, A.M. Leite da Silva, and R.C. Burchett, "Evaluation methods and accuracy in probabilistic load flow solutions", IEEE Trans. On Power Apparatus and Systems, vol. PAS-100, no.5,1981, p.2539-2546.
- [4] A Garces, "A linear three phase load flow for power distribution networks", IEEE Trans. on Power Systems, vol.31, issue 1, Jan. 2016, p. 827-828.
- [5] T.H.Chen, and Y.L. Chang X.P. Zhang, "A novel and fast three-phase load flow for unbalanced radial distribution systems", IEEE Trans. on Power Systems, vol.17, issue 4, Nov. 2002, p. 1238-1244.
- [6] J. Arrillaga, and C.P. Arnold, Three-phase load flow, in Computer Analysis of Power Systems, John Wiley & Sons, Ltd., West Sussex, England. doi: 10.1002/9781118878309.ch3, 1990.
- [7] E. Demirok, S.B. Soren, D. Sera, and R. Teodorescu, "Three-Phase Unbalanced Load Flow Tool for Distribution Networks", Proceedings of the 2nd International Workshop on Integration of Solar Power Systems. Energynautics GmbH, 2012.
- [8] D. Rusinaru, The permanent unbalanced operation of the power networks (in Romanian), Craiova, Universitaria Publ., 2005.
- [9] D. Rusinaru, L.G. Manescu, and R.C. Dinu, "Compensator configurations for load currents' symmetrization", International Conference on Applied Sciences ICAS2015, Book Series: IOP Conference Series-Materials Science and Engineering, Vol: 106, 2016, 012030.
- [10] D. Rusinaru D, L G Manescu, and M. Merfu, "The Load Unbalance Influence on the Power Factor Value in Three-Phase Distribution Networks", Recent Advances in Electrical Engineering Series 22 314-319, 2013.
- [11] D. Rusinaru, L.G. Manescu, M. Merfu, and P. Postolache, "Power quality general levels in distribution networks", 16th International Conference on Harmonics and Quality of Power (ICHQP), 2014 IEEE, Romania, 2014, p: 58 – 62.
- [12] ETAP 14.1. User Guide. ETAP Operation Technology, Inc., 2015.

[13] Romanian Performance Standard for Electricity Distribution Service, ANRE, 2015.

[14] EN 50160, Voltage characteristics of electricity supplied by public distribution systems, 1999.

# Technical Aspects Regarding Electromagnetic Compatibility Compliance of the Electric and Electronic Integrated Systems

Stoica Dan<sup>1</sup>, Cosereanu Liviu<sup>2</sup>, Enache Mihai<sup>3</sup>, Ploșniță Albert<sup>4</sup>, Mazăre Petru<sup>5</sup>

<sup>1</sup>Military Equipments and Technologies Research Agency, Bucharest, Romania [dstoica@acttm.ro](mailto:dstoica@acttm.ro)

<sup>2</sup>Military Equipments and Technologies Research Agency, Bucharest, Romania [liviuc@acttm.ro](mailto:liviuc@acttm.ro)

<sup>3</sup>Military Equipments and Technologies Research Agency, Bucharest, Romania [menache@acttm.ro](mailto:menache@acttm.ro)

<sup>4</sup>Military Equipments and Technologies Research Agency, Bucharest, Romania [aplosnita@acttm.ro](mailto:aplosnita@acttm.ro)

<sup>5</sup>Military Equipments and Technologies Research Agency, Bucharest, Romania [pmazare@acttm.ro](mailto:pmazare@acttm.ro)

**Abstract** - The modern world's needs of electric and electronic devices and systems lead to a continuously electromagnetic interferences growing in ways that were hard to predict few decades ago, a serious reason to consider the electromagnetic compatibility (EMC) regulations a top priority for the developers and the end-users as well. An important segment of these products is represented by integrated systems, and not only the large scale ones, as a natural consequence of the increased equipments interoperability and versatility. The integrated systems developers are facing many issues regarding EMC products compliance, although the individual components of their systems are fully or partially compliant with the EMC standards and regulations. Practical solution to identify and solve these problems consists in preliminary pre-compliance tests deployed in specialized EMC laboratories. Unlike the classic EMC tests, the specialized pre-compliance probes enable the developers to improve their products, according to the provided feedback, and to minimize their efforts to reach that goal. Our specialized EMC laboratory has been involved in many testing and evaluation projects for different types of electric and electronic systems compliance characterization. The authors participated in experimentation activities as well as software simulation sfor EMI protection solutions design and realization. The accumulated experience allow us to investigate the associated phenomena related to EMC problems and to find solutions for these inconveniences

**Keywords:** EMC, compliance, Electromagnetic compatibility, EMI, shielding

## I. INTRODUCTION

The electric and electronic systems developers meet many challenges regarding their final products EMC compliance. Most of the EMI/EMC issues are a natural consequence of their functionality, caused by electric currents and voltage drops specific to all modern electric system [1]. Even, most of these problems are solved during the initial development phase, starting with the lowest design levels, there are many cases when a system integrator has very low control of these effects, and tries to get more information for a specialized EMC laboratory [10] in order to identify and to implement adequate measures. Our paper presents a general guidance for this process,

taking into account the accumulated experience in this field by participating in national research programs.

## II. THEORETICAL BACKGROUND

The main idea behind all EMI/EMC protection solutions is based on electromagnetic field attenuation and currents filtering [5], [9] solutions implementation in order to provide a proper environment for equipments correct functionality.

These solutions can be evaluated by specific tehcnical parameters which are directly dependent on materials type and geometry, constructive solutions and medium properties.

The shielding effectiveness, noted  $SE$ , is one of the most important parameter [1], [6], [7], [8] for the characterization of an electromagnetic screen and is defined as the report between the field's intensity (electric or magnetic) measured without screen  $E_s$  and with screen  $E_0$ .

$$SE = 20 \cdot \log_{10} \left( \frac{E_s}{E_0} \right) \quad [dB] \quad (1)$$

$$\text{or} \quad SE = 10 \cdot \log_{10} \left( \frac{P_i}{P_t} \right) \quad (2)$$

A screen action on the electric or magnetic field through the following mechanisms:

- absorption (characterized by the factor of attenuation through absorption  $A$ ),
- reflection (characterized through the factor of attenuation through reflection  $R$ ),
- multiple scintillations (with significant effects in the thin screen's case) (characterized through the factor of attenuation through scintillations  $R_r$ ).

Expressing the attenuations  $A$ ,  $R$  and  $R_r$  in dB, it's obtained, through their summarization, the (total) efficacy  $SE$  of the screen.

$$SE = A + R + R_r \quad (3)$$

where:

$R$  - through the factor of attenuation through reflection at the frontier surfaces,

$A$  - the factor of attenuation through absorption within the screen (the transformation of the electromagnetic energy in heat through the losses due to currents circulation through the screen),

$Rr$  - the factor of attenuation that considers the multiple scintillations in the inside of the screen.

The efficacy of the screening depending on:

- the perturbation source's frequency
- the material of the screen (generally: copper, iron, aluminium, silver)
- the field's type that must be attenuated (electric, magnetic, TEM)
- the screen's geometry (parallelepipedal, cylindrical, spherical, etc.) and thickness
- the incidence angle of the field, etc.

Each of the previously enlisted mechanisms actions in specific modes, that can be appreciated objectively through characteristic values.

The absorption is characterized through the attenuation constant,  $\alpha_a$ , specific for every material.

A material with a attenuation constant  $\alpha_a$ , of high value, has higher values for permeability and conductivity and implicitly has the attenuation factor  $A$ , high. It must be remarked that the attenuation of the material increases once with the increase of the work frequency.

### III. MULTIPLE-STEP APPROACH

In some situations the end-users are able to conduct their own research activities in order to solve their EMC compliance problems, taking advantage of the existing specialized infrastructure and personnel or the financial support to conduct these activities "outside". This approach offers the advantage of getting more knowledge in this field, having more economic and efficient solutions for similar cases with the risk of an initial major investment which may not be economically feasible for their long term projects. In this sense, we conducted a case study for informatics equipment trying to reduce its electromagnetic radiated emissions using simple solutions.

We choose a standard desktop computer as EUT (Equipment Under Test) including a central unit, mouse, keyboard and LCD display. We tested it according with MIL-STD 461F EMC standard, RE-102 probe [2]. The configuration setup is presented in figure 1. In figure 2 there are presented the radiated emissions of the EUT in the 30 MHz – 1 GHz frequency band.

We tried to decrease the EUT emissions by usage of special ferrite across the external cables. The expected results were not very surprising, but it still proved that we can reduce some EM noise; even the solution is more used as an EMF protection than a reduction technique.



Fig.1 RE-102 probe configuration setup

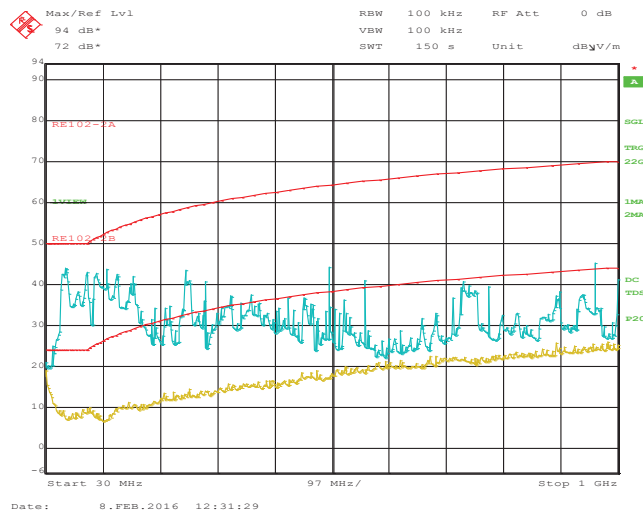


Fig.2 Initial EUT RE-102 test results



Fig.3 Ferrite installed on USB cable

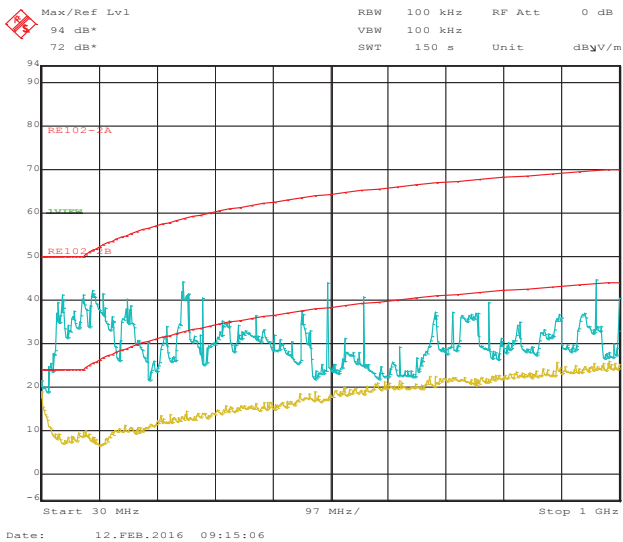


Fig.4 EUT RE after ferrites installing

In figures 5 and 6 there are presented the results obtained in third phase of our study. We shielded the interconnection cables using special metallic shielding tube. There are good results, but we still faced some EMF spikes over the limit.



Fig.5 VGA shielded cable

The final step consisted in usage of a special electromagnetic shielding system for EUT, which was developed in a previous research project. The EUT has been installed in this special system and tested according RE-102. The special electromagnetic shielding system for EUT (SPE) is presented in figure 7.

The SPE design was created in accordance with informatics systems specific requirements for electromagnetic emissions reduction [4], [6] and product functionality assurance. In order to establish these requirements we conducted several EMI measurements for a representative set of informatics systems (classical architecture including central unit, display unit and standard peripherals). In figure 7 there is presented the central unit SPE component including attenuation system (shielded enclosure, shielded cables, EMI gaskets) and filtering equipments (power line filters, honeycomb vents).



Fig.7 Special EM Protection System

In figure 8 there is presented the comparison between initial EUT and the special protection system EM emissions.

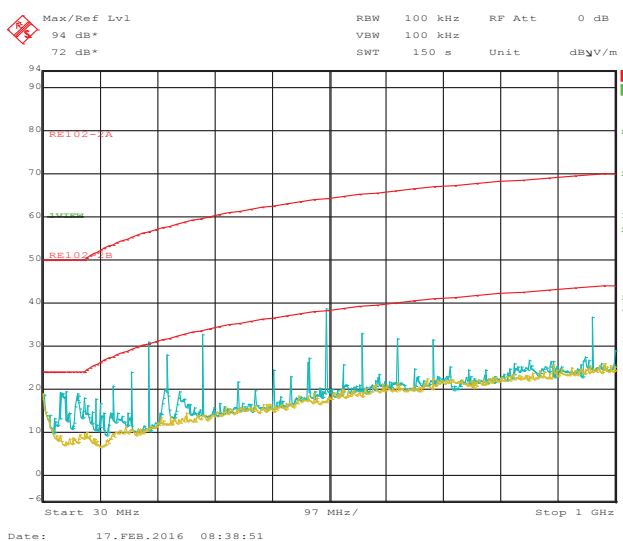


Fig.6 EUT with shielded cables RE test results

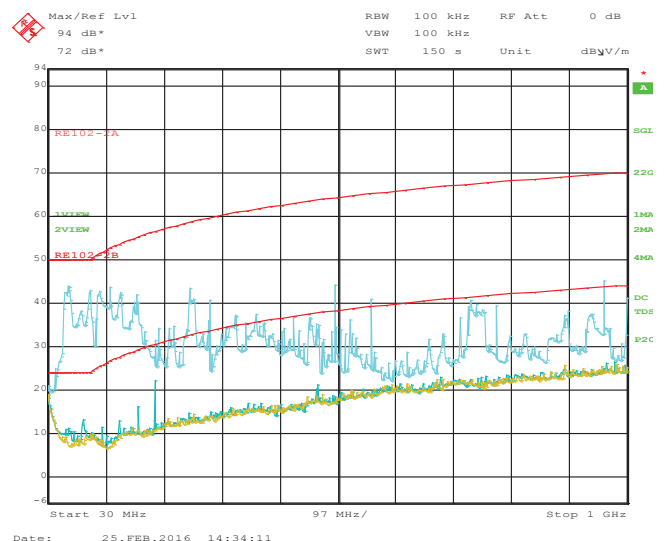


Fig.8 Initial EUT emissions vs SPE results

#### IV. PRE-COMPLIANCE EMC TESTS

A modern specialized EMC testing and evaluation infrastructure must include measurement equipment and platforms that allow more data to be collected and to be analyzed in order to offer an “answer” for system developer. The advantage of this approach is the fact that the end-user can “find” in a more efficient and more economic way a solution to the EMC/EMI problems without investing time and personnel for it.

The main purpose of the EMC pre-compliance testing is to find and to investigate the EMI sources that cause product incompliance. In order to achieve that, the first step consists in a general EUT standard evaluation followed by a data analysis and interpretation. The intermediary tests will focus on physical regions testing by using special antenna arrays or near field probes set. If there is a technical specification available, the provided feedback will be more consistent, testing engineers being able to indicate the accurate source of the problem and possible ways to counterattack the undesired effects [3].

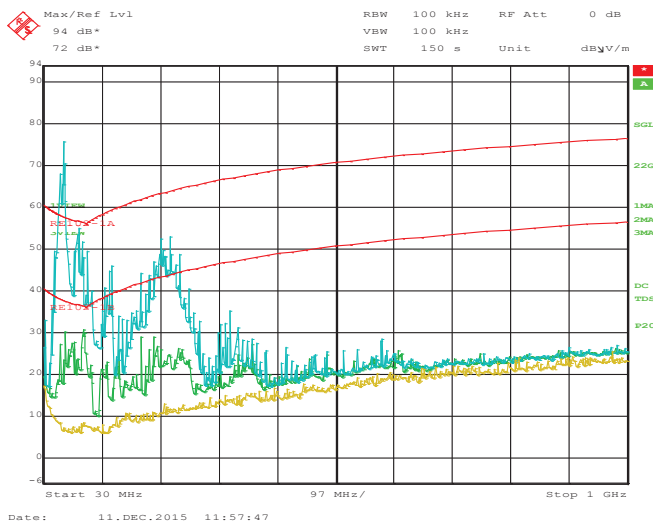


Fig. 9 Preliminary EUT evaluation (2 operational modes)

In the figure 9 there are presented the standard EUT first evaluation results, carried out in our specialized laboratory for an integrated command and control system, which consisted of a standard console (keyboard and joystick), display device, multisensory data interface device and an engine control device. There were two operational modes tested (idle, maximum functionality) and at a first glance the product was far of being compliant with the EMC regulations specific to its working destination.

Using a near field probes set we conducted several measurements in the “hot” frequency band areas and we collected enough data for EMI source identification. We also made some suggestions for product EMI improvement, like cables shielding, connectors replacement, display protection, EMI gaskets usage and others. After all, the provided feedback was useful and helpful for the developer because of the results obtained after several EMI shielding/filtering implementations, as it is shown in figure 10.

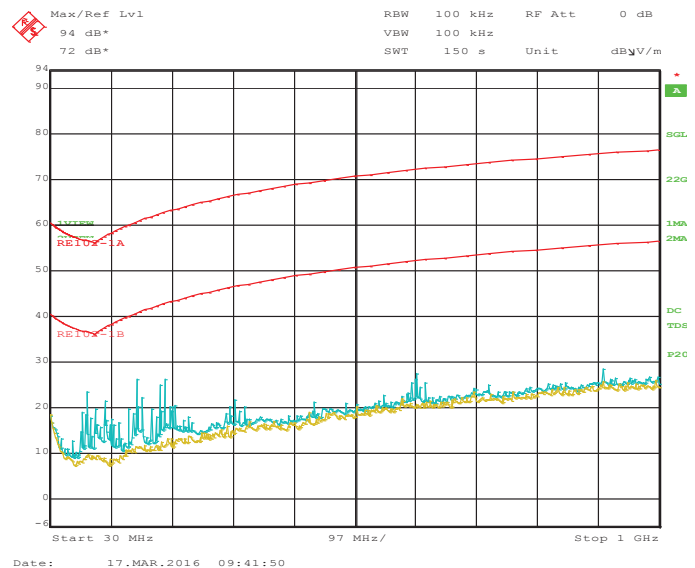


Fig. 10 Final EUT evaluation

#### V. CONCLUSIONS

The information technologies market is in a continuous evolution and change and there are many economical agents involved in many complex projects design and development. The EMC compliance problems must be threaten seriously, considering the risks involved regarding products safety and reliability, as well as human health and security. Our presented cases show some possible approaches that can be taking into account by a system integrator/developer in a EMI/EMC improvement process.

Both presented solutions conducted the end-user to its goal but a preliminary analysis should be carried out before access one of them, considering the advantages and disadvantages related to economical, technical and quality aspects.

Received on July 17,2016

Editorial Approval on November 15, 2016

#### REFERENCES

- [1] Gh. Hortopan, Principii si tehnici de compatibilitate electromagnetica, Ed Tehnica, Bucuresti, 1998
- [2] MIL-STD 461F, Requirements for the Control of Electromagnetic Interference Characteristics of Subsystems and Equipment, 2013
- [3] Precompliance EMC Measurements, Henry Ott, John Wiley & Sons, 2009
- [4] J. P. Berenger, "Perfectly matched layer for the absorption of electromagnetic waves," J. Comput. Phys., vol. 114, pp. 185-200, October 1994.
- [5] C. A. Balanis, Advanced Engineering Electromagnetics; John Wiley & Sons; New York, 1989.
- [6] E. S. Siah, K. Sertel, J. L. Volakis, V. V. Liepa and R. Wiese, "Coupling studies and shielding techniques of electromagnetic penetration trough apertures on complex cavities and vehicular platforms," IEEE Trans. ElectromagnCompat., vol. 45, pp. 245-256, May. 2003.
- [7] H. A. Mendez, "Shielding theory of enclosures with apertures," IEEE Trans. Electromagn. Compat., vol. EMC-20, pp. 296-305, May 1978
- [8] D. Căzânaru „Protecția echipamentelor de tehnologia informației și sistemelor de comunicații din punct de vedere al compatibilității electromagnetice”, Teză de doctorat, București, 30.11.2010.

- [9] Robert Armstrong : “Measurement of shielding in electrically large metallic enclosures”, University of York, February 2013
- [10] Clayton R. Paul : “ Introduction to electromagnetic compatibility”, Second edition, John Wiley and Sons, Inc. Publication, February 2006, ISBN : 978-0-471-75500-5

# Electromagnetic Shielding System for Information and Communication Equipments

Stoica Dan<sup>1</sup>, Cosereanu Liviu<sup>2</sup>, Enache Mihai<sup>3</sup>, Boteanu Adina<sup>4</sup>, Ploşniță Albert<sup>5</sup>

<sup>1</sup>Military Equipments and Technologies Research Agency, Bucharest, Romania [dstoica@actm.ro](mailto:dstoica@actm.ro)

<sup>2</sup>Military Equipments and Technologies Research Agency, Bucharest, Romania [liviuc@actm.ro](mailto:liviuc@actm.ro)

<sup>3</sup>Military Equipments and Technologies Research Agency, Bucharest, Romania [menache@actm.ro](mailto:menache@actm.ro)

<sup>4</sup>Military Equipments and Technologies Research Agency, Bucharest, Romania [aboteanu@actm.ro](mailto:aboteanu@actm.ro)

<sup>5</sup>Military Equipments and Technologies Research Agency, Bucharest, Romania [aplosnita@actm.ro](mailto:aplosnita@actm.ro)

**Abstract** - Today, most of the human activities are computer-controlled with respect to equipments and platforms functionality, quality of the process and people and goods safety. Unlike the specialized platforms, where this feature is already implemented and developed according to the system architecture, in many other applications this function can be achieved by including a simple desktop or laptop and the specific software application in the platform original configuration. These applications can be also very sensitive, in terms of safety, quality and costs, so the whole controlling process must be accurate, stable and robust. One of the main problems that can occur and affect these systems workability is represented by electromagnetic interference (EMI) presence and the complementary issues, especially when the scenario takes place in a hard electromagnetic environment (industrial, military, IT&COM high-density areas etc.). There are some technical approaches to solve this inconvenience, but most are focused to adapt the current equipment configuration, which was intended to work in a specific environment and to provide specific features, to the new place working requirements. Our solution is to develop a self-independent EMI protection system that can be easily adapted to a large range of the IT&COM equipments in order to minimize costs, product performances distortion and overall time implementation.

**Keywords:** EMC, shielding, Electromagnetic compatibility, EMI

## I. INTRODUCTION TO ELECTROMAGNETIC SHIELDING

Electromagnetic shielding and filtering represent the most common solutions used for equipments EMI/EMF protection, consisting of special materials and devices integrated into the original system configuration, through different implementation methods.

Electromagnetic shielding main application is to reduce the levels of electromagnetic fields radiated by the intrinsic equipment EMF sources or to protect [3] the equipment against external interferences in order to immunize it and provide a controlled EMF environment.

The electromagnetic emissions of equipments represent a natural consequence of their operation, a phenomenon that can be reduced or amplified depending on many factors, often difficult to be estimated by electrical and electronic equipment manufacturers.

The classical solution considered by most manufacturers of electromagnetic protected equipments / systems consists in the construction of new enclosures for

equipments, use of shielded [1], [4], [6], [7], [8] cables, and external / internal power supply filtering circuits. Regardless of the implementation, in the absence of a specialized laboratory able to measure the quality of the solution used, it is difficult to quantify SE using only analytical calculation methods, since there are phenomena which can be difficult to predict, such as:

- diffusion waves through the wall screen,
- couplings by accessing screen conductors,
- the penetration aperture.

Despite these drawbacks, analytical calculation may still be considered for a base estimation of the shielding performance specific to a particular solution.

In the case of high electric conductivity materials (which is the most common situation), the diffusion phenomenon hasn't a significant weight when in the conductors are present couplings and / or penetration through the apertures. The exception is the region of low frequency and the magnetic field radiation.

Couplings by conductors who access the screen have a significant share in the total field radiated but are significantly less dependent on the design of shielding, but are influenced more by the embodiment of filtrations and joints bonding (welding) of the access points in the outer shielding cables.

## II. SHIELDING EFFECTIVENESS CALCULUS

Regardless design and realization, the electromagnetic shielding solutions are measured by shielding effectiveness - SE (Shielding Effectiveness) parameter. Additionally it can be also considered other criteria for assessing the technical solution, namely ergonomics, reliability, modularity, implementation costs etc...

Furthermore, knowing the screening material, we can estimate the value of SE. In theory, if it's considered a simplified case of a plane wave passing [2] through an infinitely long screen, then it is possible to define the following components of shielding effectiveness: absorption, reflection and multiple scintillations attenuation.

In figure 1 there is represented the simplified model of electromagnetic shielding. As we mentioned above there are figured the main components of shielding with respect to the radiation source and material design and properties.

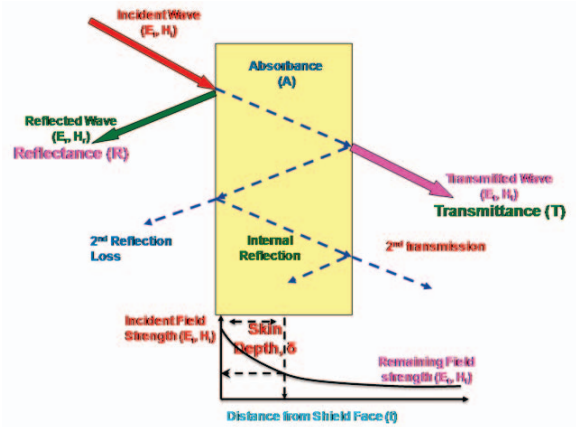


Fig.1 Microwave absorption [8] and EMI shielding behavior

If there is considered the case of plane wave radiated by a dipole or a winding looped at distance  $r$ , corresponding to far field condition ( $r \gg \lambda/2\pi$ ), the sizes of shielding components (in dB) are respectively:

$$A \langle \text{dB} \rangle = 3,34 \cdot \sqrt{\mu \cdot \sigma \cdot f \cdot d} \quad (1)$$

$$R \langle \text{dB} \rangle = 168 - 20 \cdot \log_{10} \left( \sqrt{\frac{\mu \cdot f}{\sigma}} \right) \quad (2)$$

$$R_r = 20 \cdot \log_{10} \left\{ 1 - 10^{-\left(\frac{A}{10}\right)} \cdot [\cos(0,23 \cdot A) - j \cdot \sin(0,23 \cdot A)] \right\} \quad (3)$$

and  $R_r = 0$  if  $A > 15 \text{ dB}$ ;

where:

- A - attenuation by absorption,
- R - attenuation by reflection,
- $R_r$  - mitigation by internal reflections in the material,
- f - wave frequency,
- $\mu$  - magnetic permeability of the material,
- $\sigma$  - electrical conductivity of the material.

To characterize a screen size using electromagnetic shielding effectiveness called, SE, defined as the ratio of the field strength (electric or magnetic) measured in the absence of the screen ( $E_s$ ) and with the screen ( $E_0$ ) we can use:

$$SE = 20 \cdot \log_{10} \left( \frac{E_s}{E_0} \right) \langle \text{dB} \rangle \quad (4)$$

or by expression of powers:

$$SE = 10 \cdot \log_{10} \left( \frac{P_i}{P_t} \right) \quad (5)$$

If the attenuation A, R and  $R_r$  are expressed in dB, by summing the quantities of the components of the shielding, then we obtain:

$$SE = A + R + R_r \quad (6)$$

The main factors influencing the SE are:

- frequency field;
- material type and thickness;

- screen geometry (rectangular, cylindrical, spherical, etc.);

### III. NUMERICAL METHODS USED FOR ELECTROMAGNETIC SHIELDING CALCULUS

Full description of macroscopic magnetism phenomena is performed using Maxwell's equations (considered as postulated), equations describing the behavior of space-time field. Maxwell's equations can be presented and used in two forms: differential (local) or integral (global).

In the case of stationary environments, the most important difference between the two forms of Maxwell's equations lies in the treatment of discontinuities of the materials and / or sources.

The most common methods for calculating numerical electromagnetic problems are: method of moments (MoM), the method of transmission line modeling (TLM), finite element method (FEM) and finite difference method (FDM - with different variations and sub- options). Not all of these methods are the same in terms of the accuracy of the results of the processing time and computing resources required to be used by each of them.

### IV. SOFTWARE MODELING AND SIMULATION

In our case study we conducted researches in order to optimize the electromagnetic protection system design, in order to be used for EMF reduction generated by a standard PC. Protection system modeling and simulation were performed within ANSYS HFSS software, in the 10 MHz - 9 GHz frequency band.

The conducted analyzes allowed us to establish the constructive details of the shielded enclosure, taking into account the electromagnetic protection requirements established for the whole system.

In order to find more accurate, reliable and fast solutions to our problem we decided to start our work by simulating a simplified model of the electromagnetic protection system, considering it a rectangular single material enclosure. We had the opportunity to conduct many parametrical analysis in order to take a final decision regarding system design.

In this respect, simulations were performed for:

- a. Study regarding the influence of apertures shapes on the overall system electromagnetic shielding performance;

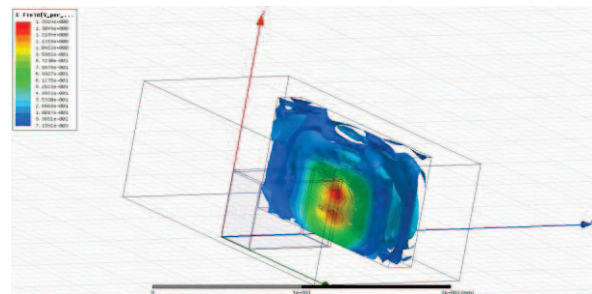


Fig. 2 Electric field distribution in rear of the shielded enclosure with rectangular gaskets at 1 GHz

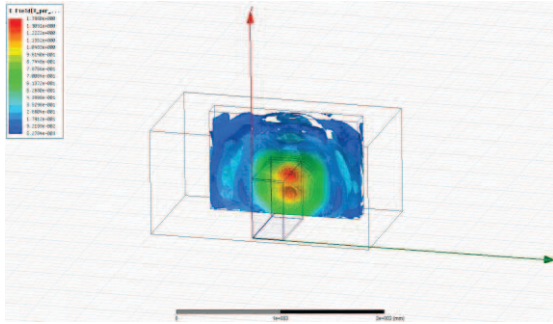


Fig. 3 Electric field distribution in rear of the shielded enclosure with circular gaskets at 1 GHz

The above simulations revealed the influence of an aperture on overall shielding performance, and underlined the idea that we must specific connectors for data input/output interfaces.

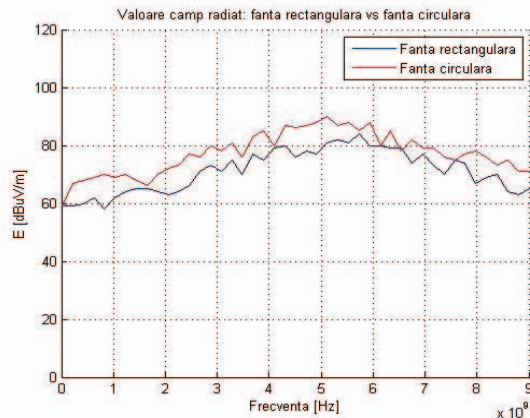


Fig.4 Electric field radiated at 1 GHz rectangular gaskets vs circular gaskets

b. The optimization of the I/O connector panel position, on the rear panel;

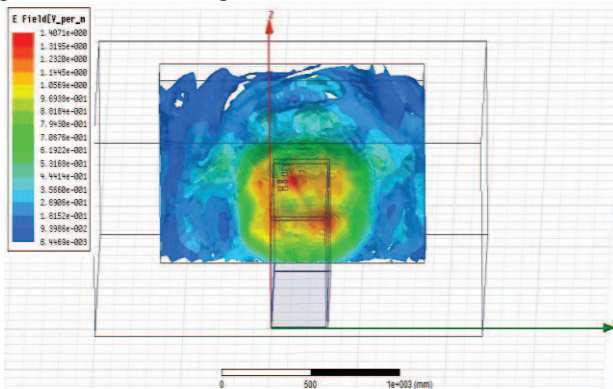


Fig.5 Electric field distribution in rear of the shielded enclosure with top lateral position of connectors panel at 1 GHz

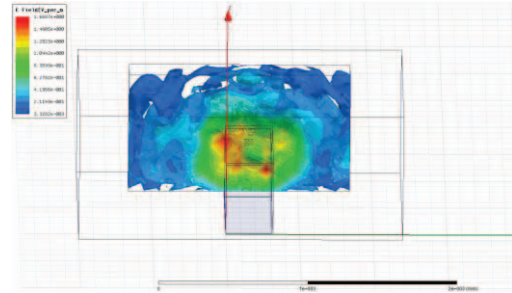


Fig.6 Electric field distribution in rear of the shielded enclosure with central position of connectors panel at 1 GHz

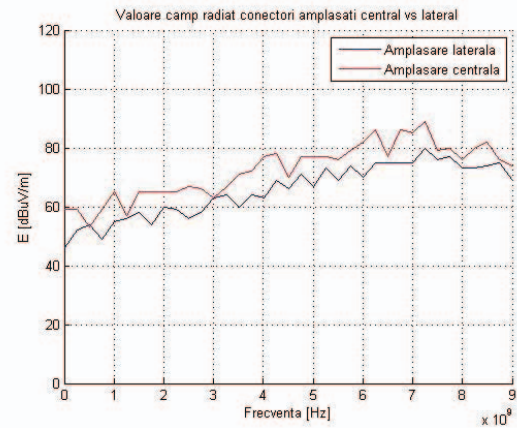


Fig.7 Electric field radiated at 1 GHz central position panel vs lateral position panel

The obtained results helped us to “fit” the connector panel in the “right” position, considering the above stated objectives.

c. The optimization of the filter vent Panel position, on the rear/side panels;

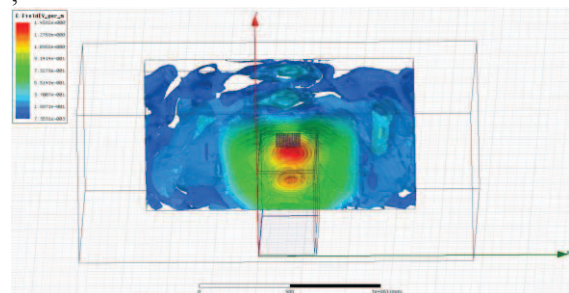


Fig.8 Electric field distribution in rear of the shielded enclosure with top lateral position of filter vent at 1 GHz

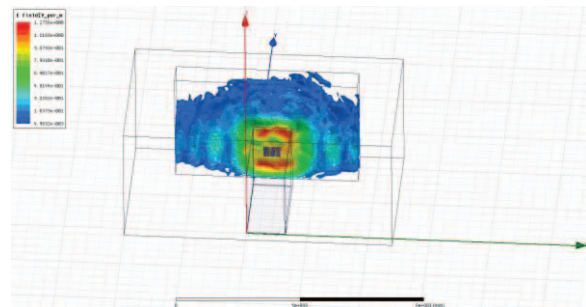


Fig.9 Electric field distribution in rear of the shielded enclosure with top central position of filter vent at 1 GHz

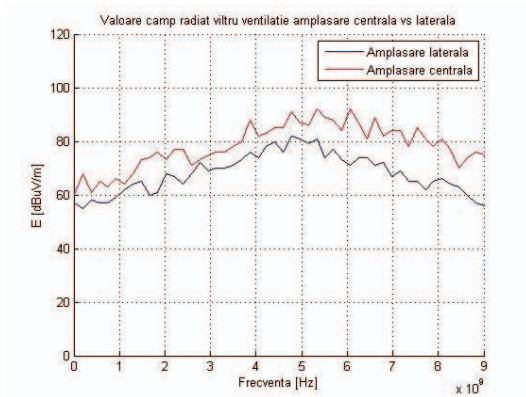


Fig.10 Electric field radiated at 1 GHz top central position vs top lateral position panel

As well as the previous study the obtained results allowed us to find the best solution for air filter position.

## V. CONCLUSIONS

There are many aspects to be taken into account during the system design and realization phases, especially those related to constructive details and materials type.

Simulations have led to specific conclusions about how to achieve a shielded enclosure. There were also other factors that contributed to our final decision regarding system design and realization, like technologies and materials availability, implementation costs, ergonomics and reliability. Other good practices were taken into account, like EMI gaskets or shielded cables usage.

The main scientific objective of our project was to develop a modular and versatile electromagnetic protection system that could “fit” different types of informatics systems.

The conducted research activities allowed us to find an optimal solution for system design, taking advantage of powerful simulation software and testing infrastructure availability. There is known that a shielded enclosure could be improved if better and larger materials are used, but in particular case there is possible to improve the overall system performance by elements repositioning or replacement.

Received on July 17, 2016

Editorial Approval on November 15, 2016

## REFERENCES

- [1] C. R. Paul, "Shielding Effectiveness," in Introduction to Electromagnetic Compatibility, John Wiley & Sons, 2006
- [2] ASTM Standard 4935-10, Standard Test Method for Measuring the Electromagnetic Shielding Effectiveness of Planar Materials
- [3] MIL-STD 461F, Requirements for the Control of Electromagnetic Interference Characteristics of Subsystems and Equipment, 2013
- [4] D. R. J. White, M. Mardigian: "Electromagnetic Shielding: A Handbook Series on EMI and Compatibility", vol. 3. Gainsville, VA: Interference Control Technology, 1988
- [5] IEEE Std. 1302-1998: "IEEE Guide for the Electromagnetic Characterization of Conductive Gaskets in the Frequency Range of DC to 18 GHz", IEEE, Inc., 345 E 47th Street, New York, NY 10017, 1998
- [6] D. J. Angelakos: "Radio frequency shielding properties of metal honeycomb materials and of wire-mesh", IEEE Int. Symp. Electromagnetic Compatibility, pp. 265-280, 1960
- [7] W. A. Bereuter, D. C. Chang: "Shielding effectiveness of metallic honeycombs", IEEE Trans. Electromagn. Compat., vol. 24, no. 1, pp. 58
- [8] Informații prezentate pe diferite site-uri de profil: [www.hollandshielding.com](http://www.hollandshielding.com), [www.aronia.com](http://www.aronia.com), [www.lessemf.com](http://www.lessemf.com), [www.lairdtech.com](http://www.lairdtech.com), [www.shieldingsystems.eu](http://www.shieldingsystems.eu)